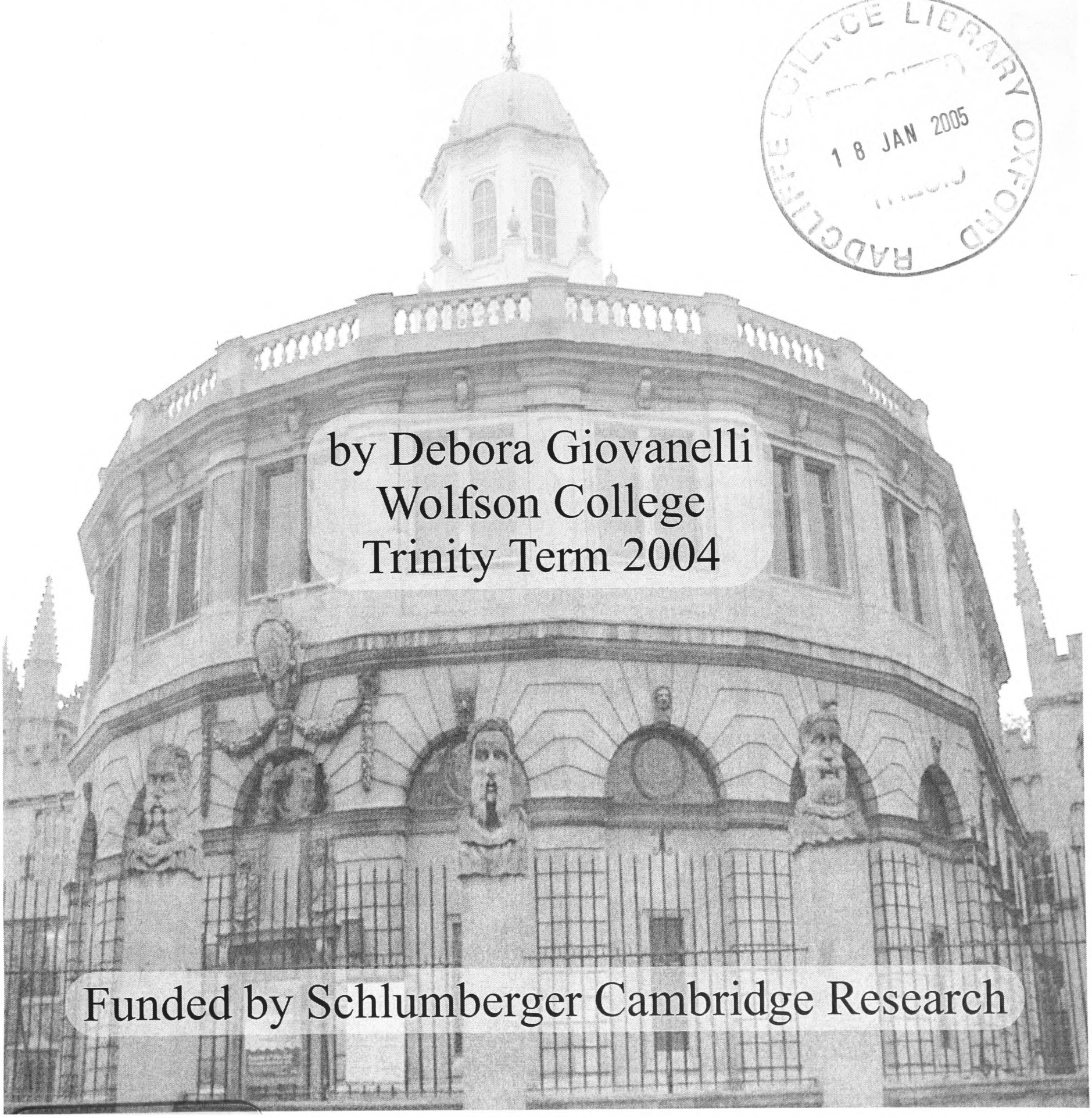
Electrochemical Detection of Gases

A thesis submitted for the
degree of Doctor of Philosophy

University of Oxford

RADCLIFFE SCIENCE LIBRARY OXFORD
18 JAN 2005



by Debora Giovanelli
Wolfson College
Trinity Term 2004

Funded by Schlumberger Cambridge Research

Electrochemical Detection of Gases — Debora Giovanelli

D. Phil Thesis — Trinity Term 2004

Abstract

This thesis discusses diverse electrochemical strategies for the determination of the concentration of the gases hydrogen sulfide, ammonia and halothane.

The chemical tagging of sulfide by a variety of structurally diverse substituted benzoquinone species was studied over a wide range of pH ($2<pH<10$). Each derivative was found to respond to increasing concentration of sulfide (typically over a range 10-200 μM). The electrochemically initiated reaction of N,N-diethyl-p-phenylenediamine (DEPD) with sulfide in N,N-dimethylformamide (DMF) was next examined with quantitative detection of sulfide (linear range= 28-3290 μM, LoD= 22 μM) achieved by analysis of the increase in the second oxidation wave. This is consistent with the sulfide attacking the doubly oxidised species in a 1,4-Michael addition. The direct oxidation of sulfide at a nickel hydroxide film on a nickel electrode in alkaline solution has provided the basis for the design of a simple and inexpensive sensor for monitoring H_2S in the range 20-200 μM. More sensitive (LoD= 1 μM) amperometric detection of sulfide was obtained at modified nickel electrodes in acidic media in which sulfide was stripped from the nickel oxide layer. This approach was exploited further by using nickel modified screen printed carbon (Ni-SPC) electrodes as economical and disposable sensors for sulfide.

Next, two different strategies for determining gaseous ammonia in the ionic liquid 1-ethyl-3-methylimidazolium bis(trifluromethylsulfonyl)imide, [EMIM][$N(Tf)_2$], and in DMF are described. The first approach exploits the effect of ammonia as a proton acceptor species on the anodic oxidation of hydroquinone, resulting in a linear detection range from 10 to 95 ppm ammonia (LoD= 4.2 ppm). The second approach is based on the direct oxidation of ammonia in either DMF or [EMIM][$N(Tf)_2$].

The possibility of photochemically induced electrocatalytic processes within microdroplets containing p-chloranil (2,3,5,6-tetrachloro-1,4-benzoquinone, TCBQ) was examined as a means of detecting the anaesthetic gas halothane.

Finally, two of the more promising routes for sulfide detection were studied at elevated temperatures (up to 70 °C) with a view to developing H_2S sensors capable of meeting the demands of oilfield applications.

Acknowledgements

First I would like to thank my supervisor Richard Compton for giving me the opportunity to carry out a D.Phil in his group and for his help, advice and supervision.

I would next like to thank Schlumberger Cambridge Research for providing fundings to support this research, and I am particular grateful to Li Jang and Tim Jones for their invaluable assistance and suggestions.

Of my colleagues in the group to whom I owe a special debt Dr. Nathan Lawrence has my especial gratitude for his substantial contribution to the work on sulfide detection and for his tremendous help and encouragement over my first two years.

I am also indebted to some other members of the RGC group with whom I have been working for the duration of my PhD. Thanks to Marisa, for the help with experiments with ionic liquids (Chapter 9 and 10), to Greg and Ian for carrying out the experimental work detailed in Chapter 14 and 15 respectively, to Oleksiy for the mathematical modelling for the simulation study in Chapter 5, to Neil for the high-speed channel electrode experiments in Chapter 5, to Trevor for the computational work reported in Chapter 11, to Craig for making the nickel microdisc electrodes and finally, to Dr. Shelley Wilkins for undertaking the surface imaging presented in Chapter 8.

I would like to express my gratitude to all the other members of the RGC group, notably to Marisa for being such a lovely person, Mike for knowing just about everything you ever needed to known about computers, Neil for always being willing to help, Russ for recording all those tapes and for tips on ionic liquids, Trev for introducing me to the finest British comedy and for the Cooperative Fantasy Compton League wooden spoon.

From previous years, I would like to thank Dr. César Prado for his help and contagious enthusiasm and Dr. Victor Climent for being characteristically calm and supportive. Many thanks also to Ben, Camilla, Matt, Mike, James and Simon for the jokes at tea-time and the evenings spent in the pub.

I conclude with a big thank you to my friends outside the lab who don't care about the thesis, who won't read the thesis, and who had to put up with me while I was writing it. Thanks also to the many friends I met over these last three years which I have spent in England for giving me so many happy memories which I shall cherish always; I will not mention you all by name but I will remember all of you fondly.

Finally, I would like to thank my family and my friends back home in Italy for being always there for me and I would like to dedicate this thesis to my father: Papá, spero che tu sia orgoglioso di me. Ti voglio bene.

Contents

Contents.....I

Acknowledgments.....X

Part 1: "Introduction and Experimental" 1

Aims and Scope.....1

Chapter 1: "Electrochemical Background" 2

1.1 Dynamic Electrochemistry.....2

1.2 The Electrical Double Layer.....2

1.3 Electron Transfer Kinetics.....5

1.4 Mass Transport.....10

1.4.1. Diffusion.....11

1.4.2 Convection.....12

1.4.3 Migration.....13

1.5 Potential Sweep Methods.....14

1.5.1 Linear Sweep Voltammetry (LSV).....15

1.5.2 Cyclic Voltammetry (CV).....17

1.5.3 Square Wave Voltammetry (SWV).....20

1.6 The Testa-Reinmuth Notation for Electrochemical Processes.....22

1.6.1 CE Reaction.....22

1.6.2 EC Reaction.....23

1.6.3 EC' Reaction.....24

1.6.4 ECE and $EC_{2x}E$ Reaction.....24

1.7 Microelectrodes.....25

1.8 Rotating Disk Electrode.....27

1.9 Standard Addition Plot and Detection Limits.....29

1.10 Chapter 1 References.....31

Chapter 2: "Experimental".....**33**

2.1 Chemicals.....33

2.2 Electrochemical Equipment.....33

2.3 Rotating Disk Electrodes.....34

2.4 Atomic Force Microscopy (AFM).....34

2.5 Scanning Electron Microscopy (SEM).....34
2.6 UV / Visible Spectrometry.....35
2.7 Chapter 2 References.....35

Part 2: "Electrochemical Detection of Hydrogen Sulfide".....36

Aim and Scope.....36

Chapter 3: "A Review of the Analytical Detection Strategies for Sulfide".....37

3.1 Introduction.....37
3.2 Analytical Detection Strategies for Sulfide.....39
3.2.1 Titration Methods.....42
3.2.2 Spectroscopic Methods.....43
3.2.3 Chromatographic Methods.....45
3.2.4. Electrochemical Methods.....46
3.2.4.1 The electrochemical analog of the methylene blue reaction.....49
3.2.5 Solid State Systems.....51
3.3 Conclusion.....51
3.4 Chapter 3 References.....52

Chapter 4: "Electrochemical Characterisation of Sulfide Tagging via its Reaction with Benzoquinone Derivatives".....56

4.1 Introduction.....57
4.2 Results and Discussion.....59
4.2.1 Reaction of p-Benzoquinone with Sulfide.....59
4.2.1.1 Square wave voltammetric response of p-benzoquinone to increasing additions of sulfide.....59
4.2.1.2 Effects of time on the voltammetric response of the p-benzoquinone sulfide solution.....60
4.2.1.3 Spectroscopic examination of the reaction process of p-benzoquinone with sulfide.....63
4.2.1.4 Voltammetric response of p-benzoquinone to increasing sulfide from pH 3 to 10.....65
4.2.2 Reaction of a Range of Sterically Hindered Benzoquinones with Sulfide.....67
4.3 Conclusion.....70
4.4 Chapter 4 References.....71

Chapter 5: "The Electrochemically Initiated Reaction of Sulfide with N,N'-Diethyl-p-phenylenediamine (DEPD) in N,N'-Dimethylformamide (DMF) Part I: a Mechanistic Study".....72

5.1 Introduction.....73

5.2 Theory.....75

5.3 Theoretical Results.....79

5.4 Experimental: "Hydrodynamic Cell Arrangement" 87

5.5 Results and Discussion.....88

5.5.1 Experimental Results.....88

5.5.2 Fitting Experimental Data to Theoretical Results.....94

5.6 Conclusion.....96

5.7 Chapter 5 References.....97

Chapter 6: "The Electrochemically Initiated Reaction of Sulfide with N,N'-Diethyl-p-phenylenediamine (DEPD) in N,N'-Dimethylformamide (DMF) Part II: Implications for Sensing Strategies".....99

6.1 Introduction.....100

6.2 Experimental.....101

6.2.1 Hydrogen Sulfide Delivery Assembly.....101

6.3 Results and Discussion.....102

6.4 Conclusion.....112

6.5 Chapter 6 References.....112

Chapter 7: "Detection of Sulfide at Nickel Modified Electrodes in Alkaline Media: a New Electrochemical Sensor".....114

7.1 The Electrochemistry of the Nickel Electrode in Alkaline Media.....115

7.2 Experimental.....119

7. 2.1 Manufacture of the Ag/AgCl Electrode.....119

7.2.2 Cell Design.....119

7.3 Results and Discussion.....120

7.3.1 Formation of the Nickel Hydroxide Layer.....120

7.3.2 Response of the Nickel Hydroxide Layer to Sulfide.....122

7.3.3 Comparison of the Electro-oxidation of Sulfide at a NHMN Electrode with other Electrode Substrates.....125

7.3.4 Sensor Response.....129

7.4 Conclusion.....130

7.5 Chapter 7 Reference.....131

Chapter 8 "Detection of Sulfide at Nickel Modified Electrodes in Acidic Media: the Development of a Reagentless Sensor".....133

8.1 Detection of Sulfide at Nickel Oxide Modified Nickel (NOMN) Electrodes in Acidic Media.....134

8.1.1 Experimental: Nickel Determination Protocol.....135

8.1.2 Results and Discussion.....136

8.1.2.1 Formation and stability of the nickel oxide layer.....136

8.1.2.2 Response of the NOMN electrode to H_2S.....138

8.1.2.3 Effect of the pH (3<pH<7) on the response of the NOMN electrode to H_2S.....140

8.1.2.4 UV/VIS spectroscopy.....143

8.1.2.5 Analytical performance.....144

8.1.3 Conclusion.....145

8.2 Detection of Sulfide at Nickel Modified Screen Printed Carbon (Ni-SPC) Electrodes in Acidic Media.....147

8.2.1 Experimental.....148

8.2.1.1 Manufacture of the Screen Carbon Printed (SCP) Electrode.....148

8.2.1.2 Nickel deposition protocol.....148

8.2.2 Results and Discussion.....149

8.2.2.1 Deposition of nickel on glassy carbon and passivation of the nickel oxide film.....149

8.2.2.2 In-situ response of H_2S at a passivated nickel oxide layer on glassy carbon.....150

8.2.2.3 Optimisation of the electro-deposition conditions.....151

8.2.2.4 Analysis of the surface morphology of nickel and nickel oxide films.....153

8.2.2.5 Response of sulfide at passivated nickel oxide layer at a SPE (in-situ).....155

8.2.2.6 Ex-situ determination of sulfide.....156

8.2.2.7 Increasing the sensitivity.....158

8.2.3 Conclusion.....160

8.3 Chapter 8 References.....160

Part 3: "Electrochemical Determination of Gaseous Ammonia".....162

Aim and Scope.....162

Chapter 9: "Determination of Ammonia based on the Electro-oxidation of Hydroquinone in N,N-Dimethylformamide or in the Room Temperature Ionic Liquid, 1-Ethyl-3-methylimidazolium bis(trifluoromethylsulfonyl)imide".....163

9.1 Introduction.....164

9.2 Experimental Section.....166

9.2.1 Chemical Reagents.....166

9.2.2. Instrumentation.....166

9.3 Results and Discussion.....168

9.3.1 Voltammetric Response of Hydroquinone in DMF in the Presence of Ammonia.....168

9.3.2 Elucidation of the Effect of Ammonia on the Voltammetric Response of Hydroquinone.....169

9.3.3 Reversibility of the Response of Hydroquinone to Ammonia in DMF...171

9.3.4 Analytical Utility.....172

9.3.5 Interference Studies.....174

9.3.6 Voltammetric Response of Hydroquinone in the Ionic Liquid [EMIM][$N(Tf)_2$] in the Absence and in the Presence of Ammonia.....176

9.4 Conclusion.....180

9.5 Chapter 9 References.....181

Chapter 10: "Elucidation of the Electrochemical Oxidation Pathway of Ammonia in Dimethylformamide and the Room Temperature Ionic Liquid, 1-Ethyl-3-methylimidazolium bis(trifluoromethylsulfonyl)imide and Application to Ammonia Sensing".....182

10.1 Introduction.....183

10.2 Experimental.....184

10.3 Results and Discussion.....184

10.3.1 Voltammetric Response of Ammonia in DMF.....185

10.3.1.2 Oxidation of ammonia in DMF at different electrode substrates.....185

10.3.1.3 Steady state linear sweep voltammetry for the oxidation of ammonia in DMF at platinum microdisk electrodes.....187

10.3.1.4 Cyclic voltammetry at platinum microdisk electrodes.....189

10.3.2 Voltammetric Response of Ammonia in [EMIM][$N(Tf)_2$].....190

10.3.2.1. Oxidation of ammonia in [EMIM][$N(Tf)_2$].....190

10.3.2.2 Elucidation of the oxidative process.....193
10.3.2.3 Reduction of ammonium hexafluorophosphate in [EMIM][$N(Tf)_2$] and in DMF.....194
10.4 Conclusion.....196
10.5 Chapter 10 References.....197

Part 4: Halothane Sensing Based on Photo-electrochemical Processes in Microdroplets Containing p-Chloranil.....198
Aim and Scope.....198

Chapter 11: "Voltammetry of Immobilised Microdroplets Containing p-Chloranil on Basal Plane Pyrolytic Graphite Electrodes".....199
11.1 Introduction.....200
11.2 Experimental.....202
11.2.1 Chemical Reagents.....202
11.2.2 Electrochemical Assembly.....203
11.2.4 Computation.....204
11.3 Results and Discussion.....204
11.3.1 Homogeneous Voltammetry.....204
11.3.1.1. Electrochemical reduction of TCBQ in benzonitrile (BN) at glassy carbon (GC) and basal plane pyrolytic graphite (bppg) electrodes.....204
11.3.1.2 Comparison of the electrochemical reduction of TCBQ at GC in BN with other aprotic solvents (DMF, DMSO and PrCN).....207
11.3.2 Heterogeneous Voltammetry.....209
11.3.2.1. Determination of the average size of microdroplets deposited on a bppg electrode.....209
11.3.2.2 Voltammetry of unsupported microdroplets of TCBQ deposited on a bppg electrode immersed in aqueous 0.1 M Y^+Cl^- ($Y = Li^+$, K^+, Rb^+, $TMeA^+$, $TPrA^+$, $TBuA^+$ or $TPeA^+$).....213
11.3.2.3 Effect of increasing the aqueous phase proton concentration on the voltammetry of TCBQ microdroplets.....222
11.3.2.4 Voltammetry of purposely supported microdroplets of TCBQ deposited on a bppg electrode immersed in aqueous 0.1 M Y^+Cl^- ($Y = Li^+$, $TPeA^+$ or $TBuA^+$).....225
11.4 Photochemically Induced Electrocatalytic Processes.....229
11.4.1 Photochemical Reduction of the Anaesthetic Gas Halothane within Femtolitres Droplets Containing TCBQ Deposit.....230
11.5 Conclusion.....232

11.6 Chapter 11 References.....234

Part 5: "Electrochemistry at High Temperatures and Pressures"...236

Aim and Scope.....236

Chapter 12: "High Temperature Electrochemistry: a Review".....237

12.1. Introduction.....238

12.2. Heating Methodologies.....239

12.2.1 Isothermal Heating Methods.....240

13.2.2 Non-isothermal Heating Methods.....245

12.3. Reference Electrodes.....252

12.4 Kinetic and Analytical Applications.....257

12.4.1 Temperature Effects on Mass Transport Phenomena.....257

12.4.2 Effect of Temperature on Reaction Kinetics.....257

12.4.3 Application of Temperature Effects to Electrochemical Analysis.....260

12.5 Conclusion.....263

12.6 Chapter 12 References.....264

Chapter 13: "High Pressure Electrochemistry: a Review".....267

13.1 Introduction.....268

13.2 High Pressure Experimental Setup.....270

13.2.1 Pressurisation Methodologies.....271

13.2.1.1 Thermal expansion of the material.....272

13.2.1.2 Pressure generation by the intrusion of a piston into a cylinder.....272

13.2.2 Electrochemical Cells.....274

13.2.2.1 Conductivity cells.....275

13.2.2.2 EMF cells.....276

13.2.2.3 Three electrode cells.....277

13.2.2.4 Polarography measurements at high pressure.....285

13.3 High Pressure Electrochemical Measurements.....285

13.3.1 Conductance Measurements.....285

13.3.2 EMF Measurements.....288

13.3.3 Electrode Processes.....289

13.3.3.1 Diffusion-controlled electrode processes.....289

13.3.3.2 Effects of pressure on electrodeposition and stripping analysis.....293

13.4 Volumes of Activation and Electrode Potentials.....294

13.4.1 Theory.....294

13.4.2 Pressure Effects on the Redox Potential of Metal Complexes.....295
13.4.3 Pressure Effects on the Kinetics of Electrode Reactions of Metal Complexes.....300
13.4.4 Effects of Solvents Dynamics at Elevated Pressures.....302
13.4.5 Effects of Pressure on the Electrochemistry of Proteins.....303
13.4.6 Effect of Pressure on the Electrochemistry of Self-Assembled Monolayer (SAMs) and Quaternised Poly-4-VinylPyridine (QPVP) films.....304
13.5 Application of Pressure to Specific Electrochemical Systems.....305
13.5.1 Electrochemistry of Superoxide at Elevated Pressures (up to 10 atm)...305
13.5.2 High Pressure Electrochemical Promotion of Ammonia Synthesis over an Industrial Iron Catalyst.....306
13.5.3 High Pressure Sono-Electrochemistry.....307
13.6 Voltammetry at High Temperatures and High Pressures.....308
13.7 Conclusions.....311
13.8 Chapter 13 References.....312
Chapter 14: "Electrochemical Determination of Sulfide at High Temperatures via Its Electrochemically Initiated Reaction with diethyl-p-phenylenediamine (DEPD) in N,N',-dimethylformamide (DMF)".....316
14.1 Introduction.....317
14.2 Experimental.....318
14.2.1 Electrochemical Equipment.....318
14.2.2 Uniformly Heated Cell.....318
14.2.3 Heated Microdisc Set-Up.....318
14.3 Results and Discussion.....319
14.3.1 Electrochemical Oxidation of DEPD in DMF at Elevated Temperatures.....319
14.3.2 Electrochemically Initiated Reaction of Sulfide in DMF at Elevated Temperatures.....326
14.4 Conclusion.....327
14.5 Chapter 14 References.....328
Chapter 15: "Elevated Temperature Electrochemical Studies of Nickel Oxide Modified Nickel (NOMN) Electrodes in Acidic Media in the Presence of Sulfide".....329
15.1 Introduction.....330
15.2 Experimental.....330

15.3 Results and Discussion.....330

15.4 Conclusion.....337

15.5 Chapter 15 References.....337

Appendix 1: "Derivation of Fick's Laws".....338

Appendix 2: "Chemicals and Suppliers".....341

Appendix 3: "The Wilke-Chang Expression".....342

Part 1: "Introduction and Experimental"

Aims and Scope:

This thesis is divided into five parts and each part is sub-sectioned into individual chapters. Part 2 examines various methodologies for monitoring hydrogen sulfide. Part 3 illustrates two strategies for determining gaseous ammonia in organic solvent and in room temperature ionic liquids (RTILs). Part 4 looks at the possibility of photochemically induced electrocatalytic processes within microdroplets containing p-chloranil (2,3,5,6-tetrachloro-1,4-benzoquinone, TCBQ) as a mean of detecting the anaesthetic gas halothane. Finally, Part 5 discusses the application of high temperature at two of the more promising routes for sulfide detection identified in Part 2. First, in Part 1 the background to the electrochemistry and the experimental techniques utilised in the results section is discussed.

Chapter 1: "Electrochemical Background"

The work presented in this thesis deals primarily with electrochemical measurements carried out away from equilibrium (that is there is passage of current) with amperometric sensors as a means of measuring the concentration of the gases hydrogen sulfide, ammonia and halothane. The techniques used are mainly potential sweep methods (Section 1.5). These consist in the application of a continuously time-varying potential to the working electrode to drive oxidative or reductive processes at the electrode-solution interface. Concentration changes occur in response to redox reactions at the electrode of interest. These changes in concentration follow Faraday's laws, so the analytical variable during measurements is current, where:

$$I \propto c_{analyte}$$

This chapter aims to provide an overview of the fundamental electrochemical principles and of the electrochemical techniques utilised to carry out the experimental work described in the result sections; wider discussions can be readily found in various textbooks [1-9].

1.1 Dynamic Electrochemistry

This section discusses electrochemical systems which are not in equilibrium.

1.2 The Electrical Double Layer

In dynamic electrochemistry a potential difference is applied between an electrode and a solution containing an electrolyte. The electrode|solution interface has been shown experimentally to behave like a capacitor. The metal possesses a charge density (q^M) which arises from an excess (q^M negative) or deficiency (q^M positive) of electrons at the electrode surface and resides in a very thin layer (0.1 Å, [1]). In order for the interface as a whole to maintain electrical neutrality however, at all the times, $q^M = -q^S$

(where q^S is the charge in solution made up of an excess of either cations or anions in the vicinity of the electrode surface). The charges q^M and $-q^S$ are often divided by the electrode area and expressed as *charge densities*, such as, $\sigma_M = q^M / A$. The whole array of charged species and oriented dipoles of ions in the proximity of the metal|solution interface is called the *electrical double layer.* Several double layer models have been described. In 1879 Helmholtz [10,11] proposed the first simple model where positive and negative charges were ordered in a rigid fashion on the two sides of the interface, comparing the problem to that of a parallel-plate capacitor. The potential drop between the two charged layers is linear.

There are two main limitations in this model. Firstly it neglects interactions that occur further from the electrode than the first layer of adsorbed species (the so called Outer Helmholtz Plane, OHP) and secondly, it does not take into account any dependence on electrolyte concentration.

At the beginning of the 20th century, an improved model was independently suggested by Gouy [12] and Chapman [13], in which the electrostatic attraction forces attracting or repelling ions from the electrode are counteracted by Brownian motion in solution which tends to disperse the ions. Hence the excess charge density in solution is not exclusively situated at the OHP and the double layer would not be compact as in Helmholtz's description but of variable thickness. This is called the *diffuse double layer.* In this diffuse double layer the net charge density decreases with distance away from the electrode|solution interface and the potential drop is shared across the whole region.

In 1949 Stern combined the Helmholtz, Gouy and Chapman models and described a double layer formed by a compact layer of ions next to the electrode followed by a diffuse layer extending into bulk solution. In terms of the potential distribution across

the interface, a sharp drop exists between electrode (ϕ_m) and OHP (ϕ_{OHP}) beyond which the potential gradually falls to a value characteristic of the bulk solution.

In 1947 Grahame [14] proposed the existence of specific adsorption: ions may discard their solvation shell and adsorb onto the electrode surface forming a new (closer) plane of minimum approach termed the Inner Helmholtz Plane (IHP).

More recently (1963) Bockris, Devanathan and Muller [15] have take in account the physical nature of the interfacial region. A schematic of their model is given in figure 1.1 (adapted from ref. [1]).

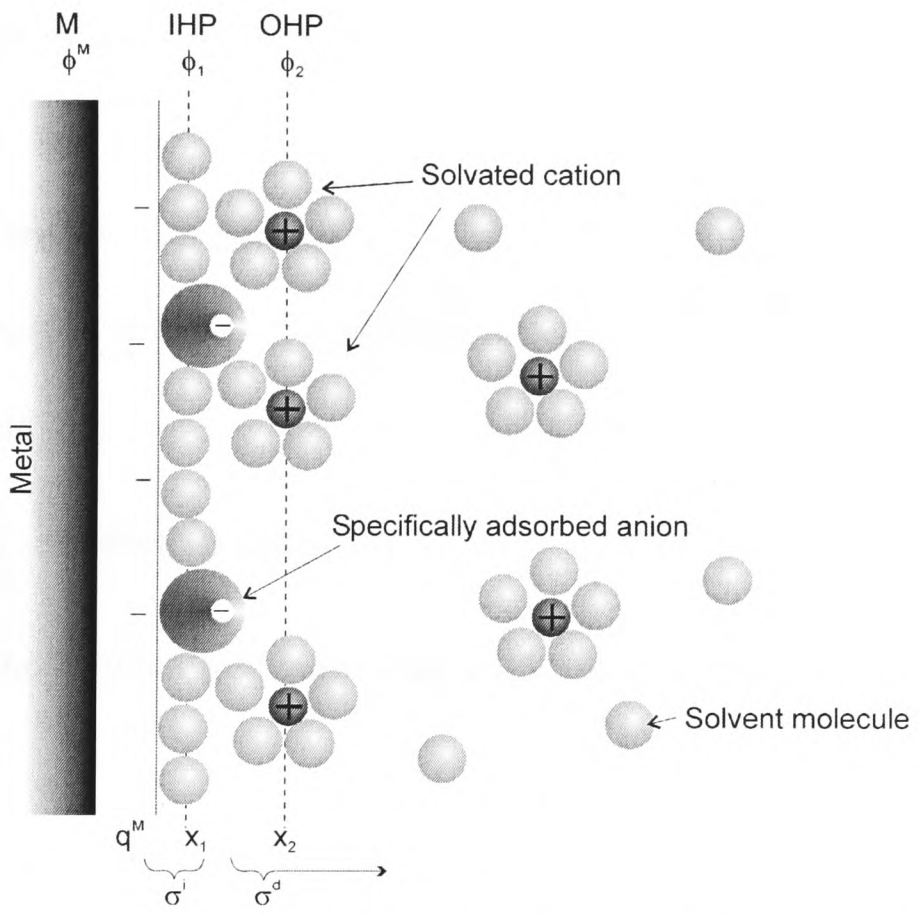


Figure 1.1: Proposed model of double layer region showing specifically adsorbed anions and solvated cations (adapted from ref. [1]).

The double layer region is thought to consist of several layers. The inner layer (i.e., the closest layer to the electrode, also called the compact, Helmholtz or Stern layer) contains solvent molecules and sometimes other species (ions or molecules) that are said to be specifically adsorbed. At a distance x_1, resides the locus of the electrical centres of the specifically adsorbed ions, also termed inner Helmholtz plane (IHP). At a distance x_2 resides the locus of centres of the nearest solvated (referred as "nonspecifically adsorbed") ions which is called outer Helmholtz plane (OHP). Due to

thermal agitation nonspecifically adsorbed ions are distributed in a three-dimensional region called diffuse layer, extending from the OHP to bulk solution. The sum of charge density accumulated between the region of the metal and IHP (σ^i) and charge density accumulated between the IHP extending to the diffuse layer (σ^d), is termed σ^S and is equal in magnitude, but opposite in sign, to the charge density on the metal σ^M as expressed by:

$$\sigma^S = \sigma^i + \sigma^d = -\sigma^M \qquad (1.1)$$

The thickness of the diffuse layer depends on the total ionic concentration in solution and for concentration greater than 0.01 M is less than ~ 100 Å.

1.3 Electron Transfer Kinetics

Consider the electron transfer at a metallic electrode (m) accompanying the simple, general reaction [9]:

$$O\ (aq) + e^-\ (m) \underset{k_{ox}}{\overset{k_{red}}{\rightleftharpoons}} R\ (aq) \qquad (1.2)$$

The current for the forward (reductive), I_c, and reverse (oxidative), I_a, processes can be written as:

$$I_c = FAk_{red}[O]_o \qquad (1.3)$$

$$I_a = FAk_{ox}[R]_o \qquad (1.4)$$

where A is the electrode area, *F* is the Faraday constant (96485 C mol^{-1}), k_{red} and k_{ox} are the rate constants for the electron transfer and finally $[O]_o$ and $[R]_o$ are the concentrations of species O and R at the electrode surface. For the reaction, the net current flowing (I) is a sum of the anodic and cathodic contributions, hence:

$$I = I_a + I_c \quad \text{thus} \quad I = FA(k_{ox}[R]_o - k_{red}[O]_o) \qquad (1.5)$$

By transition state theory, TST, the species O, equation (1.2), which gain an electron go through a transition date as shown in figure 1.2. The energy barrier to forming R is called $\Delta G^{\pm}_{red}$.

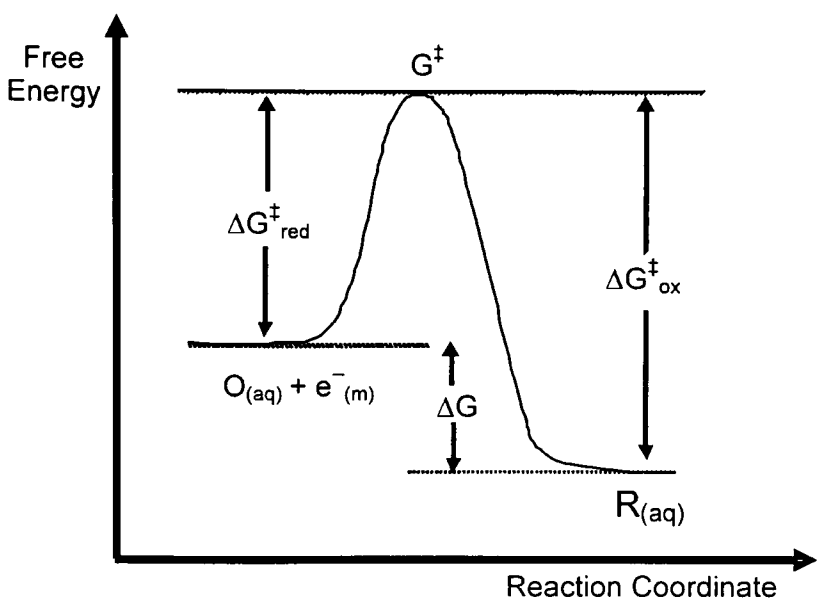


Figure 1.2: Free energy *vs.* reaction coordinate diagram for one electron process illustrated in equation (1.2).

We can write the Arrhenius equation for the rate of reduction and oxidation (ν_c and ν_a respectively):

$$\nu_c = k_{red}[O]_o e^{\frac{-\Delta G^{\mp}_{red}}{RT}} \quad \text{and} \quad \nu_a = k_{ox}[R]_o e^{\frac{-\Delta G^{\mp}_{ox}}{RT}} \tag{1.6}$$

where R is the gas constant (8.315 J K^{-1} mol^{-1}), T is the temperature and the quantity $k_{red}[O]_o$ or $k_{ox}[R]_o$ is the pre-exponential factor and accounts for the rate of collision between the species with the electrode surface. At equilibrium, the rate of reduction and oxidation are equal, hence:

$$\nu_c = \nu_a \quad \text{and} \quad k_{red}[O]_o e^{\frac{-\Delta G^{\mp}_{red}}{RT}} = k_{ox}[R]_o e^{\frac{-\Delta G^{\mp}_{ox}}{RT}} \tag{1.7}$$

which can be rearranged as:

$$\frac{k_{red}[O]_o}{k_{ox}[R]_o} = \frac{e^{\frac{-\Delta G^{\mp}_{ox}}{RT}}}{e^{\frac{-\Delta G^{\mp}_{red}}{RT}}} \tag{1.8}$$

and taking logarithms of both sides:

$$\ln \frac{k_{red}[O]_o}{k_{ox}[R]_o} = -\frac{\Delta G_{ox}^{\mp}}{RT} + \frac{\Delta G_{red}^{\mp}}{RT} \qquad (1.9)$$

From figure 1.2, it can be seen that:

$$\Delta G = \Delta G_{ox}^{\mp} - \Delta G_{red}^{\mp} \qquad (1.10)$$

hence:

$$\ln \frac{k_{red}[O]_o}{k_{ox}[R]_o} = -\frac{\Delta G}{RT} \qquad (1.11)$$

Finally, substituting the relation $\Delta G = -nFE$:

$$\ln \frac{k_{red}}{k_{ox}} - \ln \frac{[O]_o}{[R]_o} = \frac{nFE}{RT} \qquad (1.12)$$

which can be rearranged to form:

$$E = \frac{RT}{nF} \ln \frac{k_{red}}{k_{ox}} + \frac{RT}{nF} \ln \frac{[O]_o}{[R]_o} \qquad (1.13)$$

and at equilibrium, this gives:

$$E = E^O + \frac{RT}{nF} \ln \frac{[O]_o}{[R]_o} \qquad (1.14)$$

Equation (1.14) is the Nernst equation derived using a kinetic consideration [8].

We will now look at the variation of the free energy barrier as a function of applied potential, E. In irreversible systems, no appreciable currents flow when the potential is set to E° (where E° is the standard electrode potential, measured relative to the normal hydrogen electrode with all species at unit activity). Therefore to effect the flow of additional current from the reduction of $O_{(aq)}$, an overpotential (η) must be applied where:

$$\eta = E - E^{\circ} \qquad (1.15)$$

In such cases, the magnitudes of $\Delta G^{\ddagger}_{red}$ and $\Delta G^{\ddagger}_{ox}$ are modified as a result (for $n = 1$), giving:

$$\Delta G_{red}^{\mp} = (\Delta G_{red}^{O})^{\mp} + \alpha F\eta \quad \text{and} \quad \Delta G_{ox}^{\mp} = (\Delta G_{ox}^{O})^{\mp} - (1-\alpha)F\eta \qquad (1.16)$$

where ΔG°_{red} and ΔG°_{ox} are the free energy changes when the applied potential is equal to E° and the quantity α is known as the transfer coefficient which relates to the symmetry of the energy barrier and has a value between 0 and 1, but is often taken to be 0.5. The effect of the applied η is two-fold: it is used to assist the cathodic process and the remainder is used to retard the anodic process. This can be seen more clearly in the diagram below (Figure 1.3). The whole (dark lines) show the energy barrier when the system is at equilibrium as no potential has been applied (this is the situation depicted in figure 1.2). When an overpotential is applied, the free energy of reactants ($O + ne^{-}$) is raised by an amount $\alpha F\eta$ where η is the applied overpotential. The reaction coordinate changes to the dotted line and it can be seen that the energy required to reach the transition state is lowered. Overall this has the effect of increasing the magnitude of ΔG and therefore to promote the formation of products.

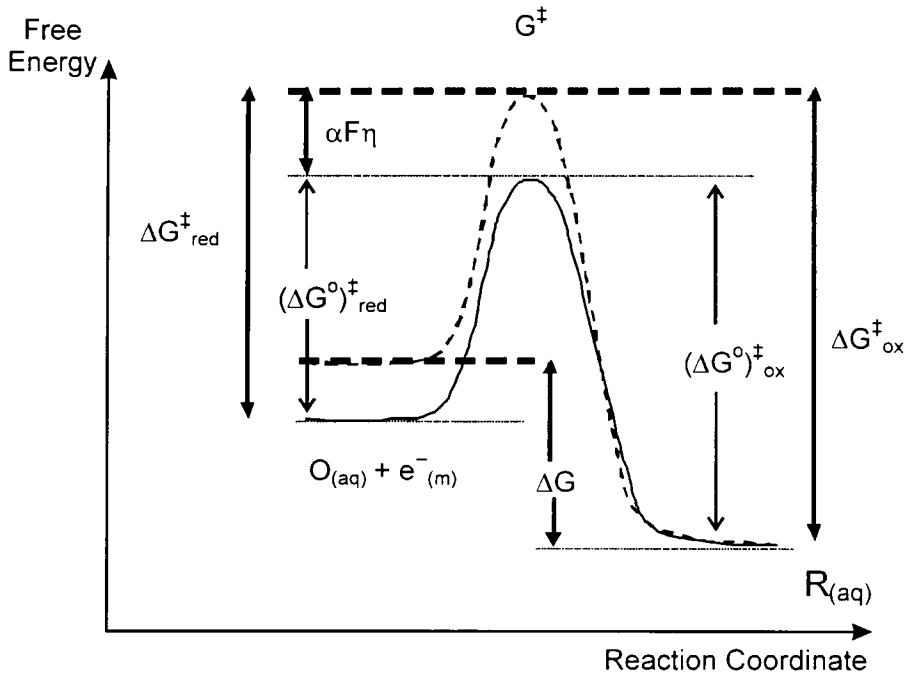


Figure 1.3: Change in the free energy ($\Delta G^{\ddagger}_{red}$ and $\Delta G^{\ddagger}_{ox}$) through application of a cathodic overpotential, η.

The modified values for $\Delta G^{\pm}_{red}$ and $\Delta G^{\pm}_{ox}$ can be again written in terms of the Arrhenius expression, leading to equations (1.17) and (1.18):

$$\nu_c' = k_{red}[O]_o e^{\left[-\frac{(\Delta G^{O}_{red})^{\mp} + \alpha F\eta}{RT}\right]} \qquad (1.17)$$

$$v_a' = k_{ox}[R]_o e^{\left[-\frac{(\Delta G_{ox}^{O})^{\ddagger} - (1-\alpha)F\eta}{RT}\right]} \tag{1.18}$$

In this case, the rates of the cathodic and anodic reactions are not equal, we therefore have a net current flowing. The rate can be expressed in terms of current flow using the form:

$$v_c' = \frac{I_c}{F} \quad \text{and} \quad v_a' = \frac{I_a}{F} \tag{1.19}$$

and substituting into equations (1.17) and (1.18):

$$I_c = Fk_{red}[O]_o e^{\left[-\frac{(\Delta G_{red}^{O})^{\ddagger} + \alpha F\eta}{RT}\right]} \tag{1.20}$$

$$I_a = Fk_{ox}[R]_o e^{\left[-\frac{(\Delta G_{ox}^{O})^{\ddagger} - (1-\alpha)F\eta}{RT}\right]} \tag{1.21}$$

and by expanding the exponent gives:

$$I_c = Fk_{red}[O]_o e^{\left[-\frac{(\Delta G_{red}^{O})^{\ddagger}}{RT}\right]} e^{\left[-\frac{\alpha F\eta}{RT}\right]} \tag{1.22}$$

$$I_a = Fk_{ox}[R]_o e^{\left[-\frac{(\Delta G_{ox}^{O})^{\ddagger}}{RT}\right]} e^{\left[\frac{(1-\alpha)F\eta}{RT}\right]} \tag{1.23}$$

Equations (1.22) and (1.23) can be simplified to:

$$I_c = I_o e^{\left[-\frac{\alpha F\eta}{RT}\right]} \quad \text{and} \quad I_a = I_o e^{\left[\frac{(1-\alpha)F\eta}{RT}\right]} \tag{1.24}$$

where I_o is known as the exchange current. For the reaction scheme posed in equation (1.2), when an overpotential is applied, the net reductive current will be $I = I_c - I_a$ hence,

$$I = I_o \left\{ e^{\left[-\frac{\alpha F\eta}{RT}\right]} - e^{\left[\frac{(1-\alpha)F\eta}{RT}\right]} \right\} \tag{1.25}$$

Equation (1.25) is known as the Butler-Volmer equation, named after the two electrochemists who contributed to its formation [16] and experimental test [17] respectively, and very important in understanding electrode kinetics.

1.4 Mass Transport

In the previous section we have considered the effect of the electrode potential on the rate of an electron transfer reaction taking place at the electrode|solution interface. Clearly, other physically processes may contribute to the overall kinetics of any particular reaction. In this section we will consider the mass transport of electroactive species to the electrode from bulk solution, and vice-versa. Mass transport is defined as the movement of material from one location in solution to another which arises either from differences in electrical or chemical potential at the two locations or from movement of a volume element in solution. The modes of mass transport are diffusion, convection and migration as pictured in figure 1.4 and discussed in this section.

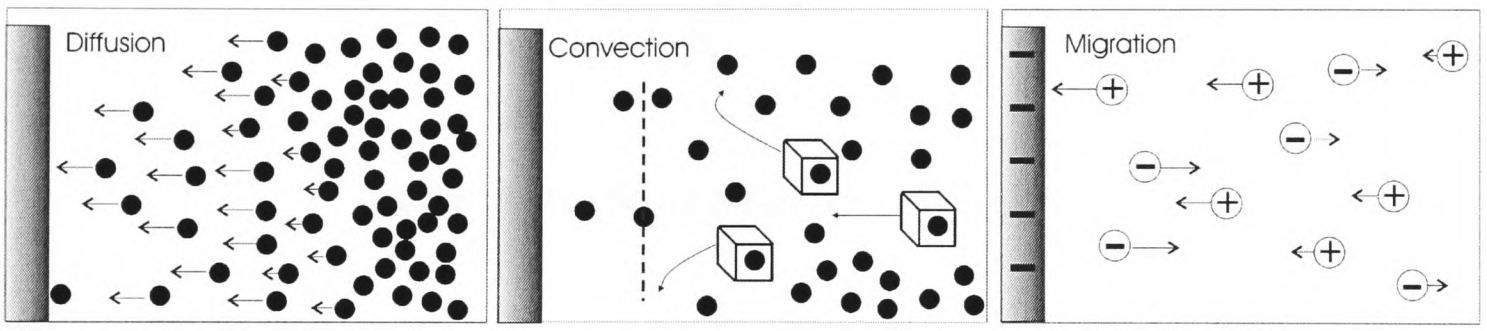


Figure 1.4: The three modes of mass transport (adapted from ref. [6]).

1.4.1. Diffusion

Diffusion is the natural movement of both neutral and charged species in solution under the influence of a concentration gradient. It leads to an effective homogenization of the mixture that can be thought of as a "random walk" process [1]. The rate of diffusion is entirely dependent of the presence of a concentration gradient, as illustrated by Fick's laws of diffusion ([18,19], Appendix 1). These laws are differential equations that describe the flux and concentration of a species as a function of position and time and have been derived on the basis of the random walk model. Fick's first law states that, for a planar geometry, the diffusional flux of a species is proportional to the concentration gradient:

$$J_{d,O}(x,t) = -D_O \frac{\partial C_O(x,t)}{\partial x} \qquad (1.26)$$

where $J_{d,O}$ /mol cm^{-2} s^{-1} is the diffusional flux of species O, $\partial C_O/\partial x$ is the concentration gradient in the x-direction and D_O /cm^2 s^{-1} is the diffusion coefficient. The diffusion coefficient is an intrinsic property of the species and can take values between 10^{-5} and 10^{-6} cm^2 s^{-1} in aqueous solution. Figure 1.5 shows the concentration gradient profile which derives from the depletion or production of species at the electrode surface.

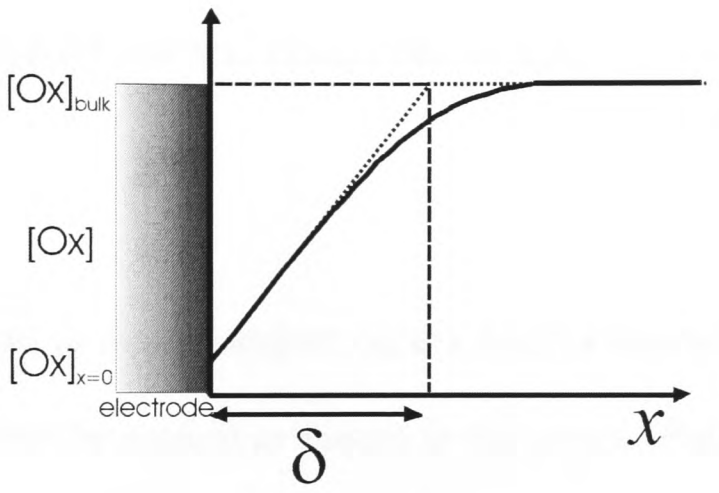


Figure 1.5: The Nernst diffusion layer for a reduction

The area between the electrode and the bulk solution where there is a concentration gradient is called the diffusion layer. Nernst [20] estimated the size of the diffusion layer thickness, δ, by extrapolation of the linear region in figure 1.5 to a concentration corresponding to that in bulk solution. Knowledge of the diffusion layer thickness can be used to estimate the flux at the electrode surface according to:

$$J_{d,O} = \frac{\partial [Ox]_{x=0}}{\partial x} = D_O \frac{[Ox]_{x=0} - [Ox]}{\delta} \qquad (1.27)$$

and the current using the expression which relates the flux, J, to the electrode current, I, as illustrated by [21]:

$$I = nAFJ \qquad (1.28)$$

where n is the number of electrons transferred, F is the Faraday constant (96485 C mol^{-1}) and A/cm^2 is the area of the electrode.

Fick's second law describes the variation of the concentration of a substance as a function of time:

$$\frac{\partial C_O(x,t)}{\partial t} = D_O\left(\frac{\partial^2 C_O(x,t)}{\partial x^2}\right) \tag{1.29}$$

The derivation of Fick's laws are included in Appendix 1.

The magnitude of electrolytic current will be dependent on the diffusion coefficient of the species D, which is itself dependent on the solvent medium, composition, temperature and the physical characteristics (size, weight) of the electroactive species.

1.4.2 Convection

A convective component to mass transport occurs when a mechanical force acts on the solution, which can either be natural or forced in its origin. Natural convection arises from the presence of local thermal/density gradients. Thermal gradients can be set up if the electrochemical reactions involve exo- or endothermic processes whereas density differences can occur if a species is produced at the electrode with a density different to that of bulk reagent. The effects of natural convection are difficult to predict and undesirable. However, more important in the present context is forced convection which is the deliberate movement of solution normally achieved through pumping, bubbling, stirring or through hydrodynamic flow. This has the effect of effectively swamping out the convective transport that is occurring naturally. Usually the forced convection is set up so that it operates with well-defined hydrodynamic behaviour. It can be useful applied in some electrochemical experiments such as the channel flow cell, where solution is forced over stationary electrode, and the rotating disc electrode, where the electrode is moved relative to the solution (Section 1.8). This facilitates a quantitative model of the solution flow, permitting the mass transport to the electrode

to be accurately predicted. Mathematically, the one-dimensional convective flux is given by:

$$J_{c,O}(x,t) = C_O(x,t)\,\nu_x \tag{1.30}$$

where $J_{c,O}$ is the convective flux and ν is the velocity of solution.

The convective analogue of Fick's second law can be therefore written as:

$$\frac{\partial C_O}{\partial t} = -\left(\nu_x \frac{\partial C_O}{\partial x}\right) \tag{1.31}$$

1.4.3 Migration

When a potential is applied to a solution, an electric field, $d\phi/dx$, is set up at the electrode-solution interface and results in a potential drop across the phase boundary. This has the effect of exerting an electrostatic force on charged species and induces movement of ions from the bulk solution to the electrode surface, and vice-versa. The magnitude of flux due to migration is directly proportional to the electric field gradient as illustrated below:

$$J_{m,O}(x,t) = -\frac{zF}{RT} D_O C_O(x,t) \frac{\partial \phi}{dx} \tag{1.32}$$

where J_m is the migratory flux in the x-direction and z is the charge on the ion.

The coupling of migratory processes with electrolysis experiments gives rise to complex mass transport properties in the solution which can be difficult to interpret. In order to minimise such problems, experiments are often conducted in conditions where the migrational component to the flux of the electroactive substance is made negligible. This is achieved through the addition of an excess of "background electrolyte", a chemically and electrochemically inert substance, usually an alkali metal salt such as KCl or $NaNO_3$ in aqueous solution, added in concentrations of 0.1 - 1 M [22,23]. Excess is broadly defined as the quantity of electrolyte that is required to ensure the migratory flux is 100 times smaller in magnitude than the

diffusional flux, and values of 33-fold excesses are commonly used [22]. The abundance of conducting ions at the electrode interface will effectively prevent the build up of localized electric field and hence eliminate the migratory transport effects. Background electrolyte provides further benefits. First, added background electrolyte increases the conductivity of the solution allowing charge transfer processes to be limited by electrode kinetics rather than the solution's resistance to the passage of current. Secondly, the size of the double layer (section 1.2) is reduced so that the change in potential (ϕ_m-ϕ_s) occurs in a very small region (typically of 10-20 Å for *ca.* 0.1 M concentration). This distance allows charge transfer via quantum mechanical tunneling between the metal and the electroactive species in solution [8]. Thirdly, as the ionic strength of the solution remains effectively constant due to the high concentration of electrolyte with respect to the reactants and products in solution, the activity coefficients (γ) of all species similarly remain constant throughout electrolysis, allowing the Formal Potential (E^{o}_{f}) to be related to the Standard Electrode Potential E^{o} by the following equation:

$$E_f^o = E^o + \frac{RT}{nF} \ln \left[\frac{a_{ox}}{a_{red}} \right] \qquad (1.33)$$

where γ_{ox} and γ_{red} are the activity coefficients of the oxidised and reduced species, respectively.

1.5 Potential Sweep Methods

This section describes the electrochemical techniques used to carry out the experimental work presented in this thesis. It is assumed that the analyte solution is unstirred, in order to ensure that mass transport by convection is absent, and that an excess of ionic electrolyte has been added to the solution so that the migratory

transport effects can also be ignored and the only mass transport remaining is diffusion.

1.5.1 Linear Sweep Voltammetry (LSV)

The potential of the working electrode is ramped from an initial potential E_1 (where no redox process takes place) to a final potential E_2 (where the kinetics of redox processes are rapid) usually in a linear fashion with time, using sweep rates, ν_s, ranging from 1 mV s^{-1} to about 1000 V s^{-1} at conventional electrodes, as shown below in figure 1.6 (a).

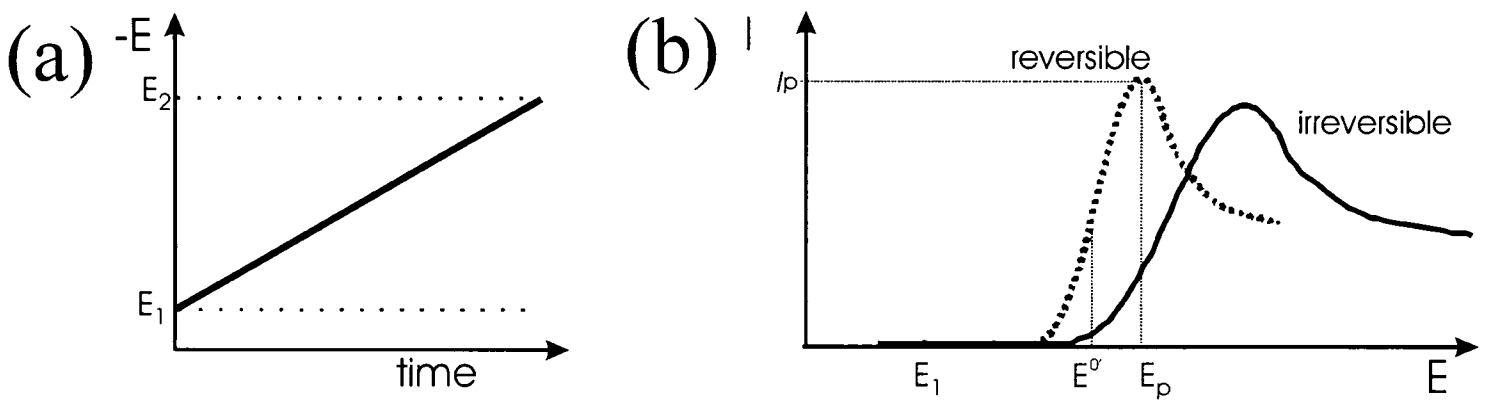


Figure 1.6: (a) The potential sweep employed in linear sweep voltammetry (LSV) starting at E_1. The gradient of the graph is equal to the scan rate, ν_s. (b) Linear sweep voltammogram for a reversible and irreversible one-electron system.

The potential at any time, t, is given by:

$$E_t = E_1 - \nu_s t \qquad (1.34)$$

The resulting voltammogram, plot of current against potential, for a reversible one-electron process is illustrated in figure 1.6 (b). Initially no current flows since the applied potential is not sufficient to induce an electron transfer. As the potential is swept more positive, towards more oxidizing potentials, the oxidation becomes more favorable and significant reductive currents begin to flow. When the potential is swept past $E^{o'}$, the surface concentration of the electroactive species begins to drop rapidly, increasing the flux of fresh material to the electrode surface. Here the current flow increases exponentially as predicted by the Butler-Volmer equation (1.25). Eventually

the surface concentration drops effectively to zero, and therefore the mass transport to the electrode surface reaches a maximum rate. The current is a balance of electrode kinetics and mass transport to the electrode. The flux of fresh material to the electrode surface is eventually compromised by gradual depletion of available species within the diffusion layer resulting in a decline in the observed current. These effects can explain the presence of a peak current response observed in the current-potential profile (figure 1.6 (b)).

Randles and Ševčik were the first to consider the diffusion equations for the reversible system and the peak current, I_p, for a reversible system, is given by the Randles-Sevčik equation [1]:

$$I_p = 0.4463\left(\frac{F^3}{RT}\right)^{1/2} n^{3/2} A D_O^{1/2} C_{bulk} \nu_s^{1/2} \qquad (1.35)$$

where n, A, F, D, R and T are as described previously, C_{bulk} / mol cm^{-3} is the bulk concentration of the electroactive species and ν_s is the scan rate. Similarly, the difference between the peak potential, E_p, and half-peak potential, $E_{p/2}$, (i.e., the potential at $I_{p/2}$) is derived using:

$$\left|E_P - E_{p/2}\right| = 2.20\frac{RT}{nF} = 56.5/n\ mV \quad at\ 25^oC \qquad (1.36)$$

Thus, for a reversible process operating under diffusion control, I_p is proportional to $\nu_s^{1/2}$ and E_p is independent of scan rate. For potentials less than E_p the system is said to be under the direct influence of the electrode kinetics, however, at potentials greater than E_p, the processes are limited by the rate of diffusion of the electroactive species.

Also overlaid in figure 1.6 (b) is the voltammogram for the case of an irreversible system. It can be seen that an overpotential has to be applied to drive the oxidation reaction. Hence E_p occurs at more negative potentials in irreversible systems. The corresponding equations are:

$$I_p = (2.99\times10^5)\alpha^{1/2} A D_O^{1/2} C_{bulk} v_s^{1/2} \qquad (1.37)$$

$$\left|E_P - E_{p/2}\right| = 1.857\frac{RT}{\alpha F} = 47.7/\alpha\, mV \quad at\ 25^oC \qquad (1.38)$$

From the above equations two points of comparison between the electrode kinetics of reversible and irreversible systems can be made. First, in the case of a reversible process, at potentials near E^o we observe large values for the heterogeneous rate constant k_{red} and k_{ox}. As a result, the concentrations of O and R *at the electrode surface* are effectively in equilibrium, with their ratio predicted by the Nernst equation. In contrast, in an irreversible systems electrolysis proceeds with negligible back reaction. Secondly, in the reversible case, the peak potential E_p is constant and independent of sweep rate, whereas for an irreversible system the E_p, shifts to more positive potentials (in the case of an oxidation reaction) at faster scan rates.

In both systems, however, it is seen that I_p increases linearly with $v_s^{½}$ and this can be interpreted as follows. At potentials close to E_p, the system is under the control of diffusion and Fick's first law states that I_p is a direct measure of the concentration gradient of O near the electrode, which in turn is controlled by diffusion layer thickness. If the scan rate is increased there is relatively less time for electrolysis to occur and subsequently a thinner diffusion layer is present. This gives rise to a steeper concentration gradient and hence increased flux. As a consequence, larger currents are observed. Thus in equation (1.35) and equation (1.37) the value of I_p is related to the scan rate.

1.5.2 Cyclic Voltammetry (CV)

Cyclic voltammetry is the most widely used technique in electrochemistry and is especially popular for the initial characterization of new systems. It is relatively

simple to carry out and results are highly informative. It was used extensively throughout the experimental work presented in this thesis.

In this case the linear sweep voltammogram is extended back to the potential of origin, E_1, which, as shown in figure 1.7 (a) results in a triangular potential wave-shape with time.

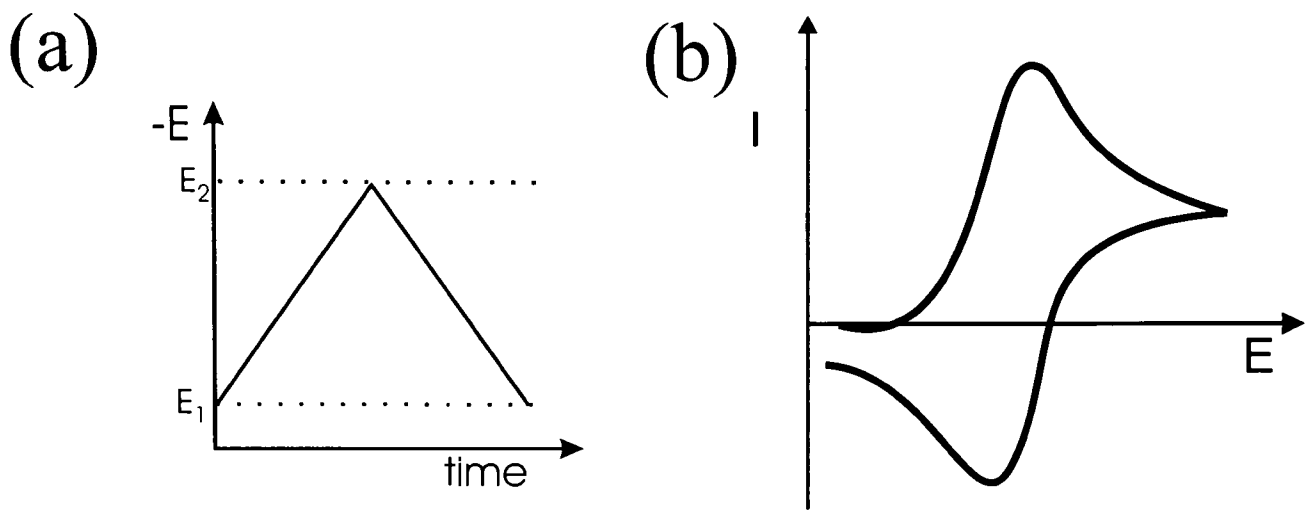


Figure 1.7: (a) Cyclic potential sweep starting at E_1. (b) Cyclic voltammograms for a reversible one-electron system as outlined in equation (1.2).

The scan rates used may range from 10 to 1000 mV s^{-1}, however with microelectrode rates up to 10^6 V s^{-1} have been achieved [1,24]. The lower scan rate limit is restricted by the onset of significant natural convection which leads to non-reproducible mass transport. Capacitative charging restricts the upper scan rate limit as it can mask the Faradaic current of interest.

Figure 1.7 (b) shows the voltammogram obtained for the one-electrode reaction detailed in equation (1.2). The forward scan is essential identical to that recorded using linear sweep voltammetry (*vide supra*), with the interplay of electrode kinetics and diffusion properties of the electroactive species O. Once E_2 is attained, the potential is swept back resulting in the re-oxidation of species R formed from the forward scan. The anodic current increases as the potential moves steadily past E^o as seen previously, increasing the kinetics for the oxidation of R present in the diffusion layer. The current then drops to zero as the concentration of R depletes.

The shape of the CV will depend mainly on the reversibility of the O/R redox couple. Figure 1.8 details the cyclic voltammetric response for electrochemically A) reversible, B) irreversible and C) quasi-irreversible systems.

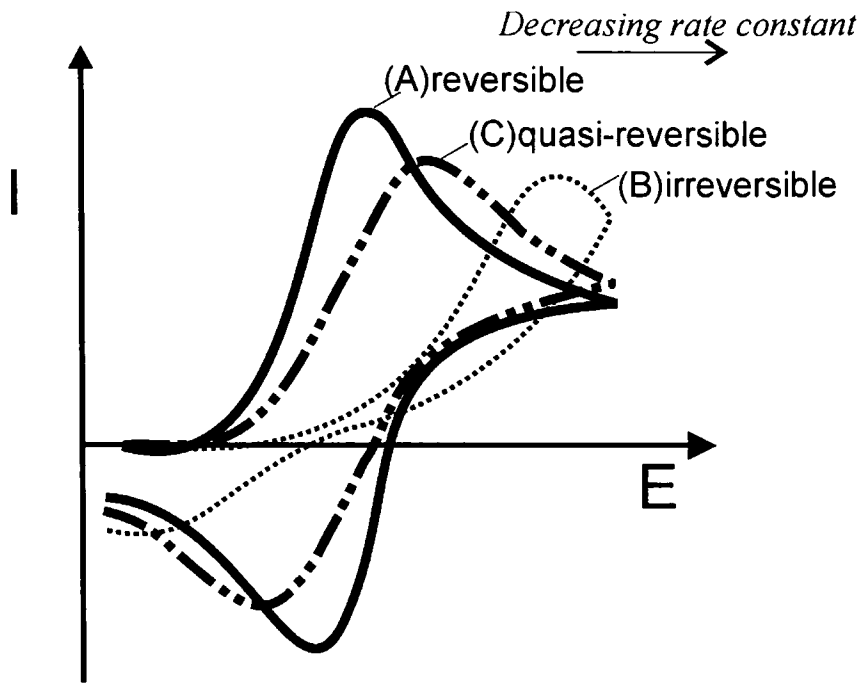


Figure 1.8: Cyclic voltammograms showing a (A) reversible, (B) irreversible and (C) quasi-reversible electron transfer reaction.

For a process to be reversible it requires fast electrode kinetics compared to the rate of mass transport. An example of this type of process is the oxidation of ferrocene to the ferricenium cation in acetonitrile solution containing 0.1 M tetrabutylammonium perchlorate, $(C_4H_9)_4NClO_4$, as supporting electrolyte [25,26]. In this type of process, the oxidative, I_p^{ox}, and reductive, I_p^{red}, peak heights are identical (deviation of the ratio of peak currents from unity is indicative of homogeneous kinetics or other complications in the electrode process, Section 1.6) and are separated by a potential of $59/n$ mV (at 25 °C) (equation (1.36)) and are independent of scan rate [8].

Irreversible systems (figure 1.8, curve (B)) have slow kinetics compared to the mass transport. An appreciable overpotential is required to reduce species O on the forward scan and on the reverse scan the absence of any current due to the re-oxidation of species R is noted because the electrode process does not occur at a measurable rate in the potential range of interest. Unlike the reversible case, the size and position of the reverse peak relative to the forward peak depends on the voltage sweep rate as seen in

the case with LSV (equation (1.37)). This is in direct contrast with the reversible system, whereby the peak potentials are scan rate independent.

Quasi-reversible systems (figure 1.8, curve (C)) are intermediate between the two extreme cases discussed above.

1.5.3 Square Wave Voltammetry (SWV)

Square wave voltammetry (SWV) was first developed in the 1950s by Barker [27] and transformed into a powerful analytical tool through the work of Ramaley and Krause [28] and Osteryoung *et al.* [29-31].

Square wave voltammetry is normally performed at a stationary electrode and involves the superimposition of a square wave pulse upon a slowly varying stepwise ramp (figure 1.9).

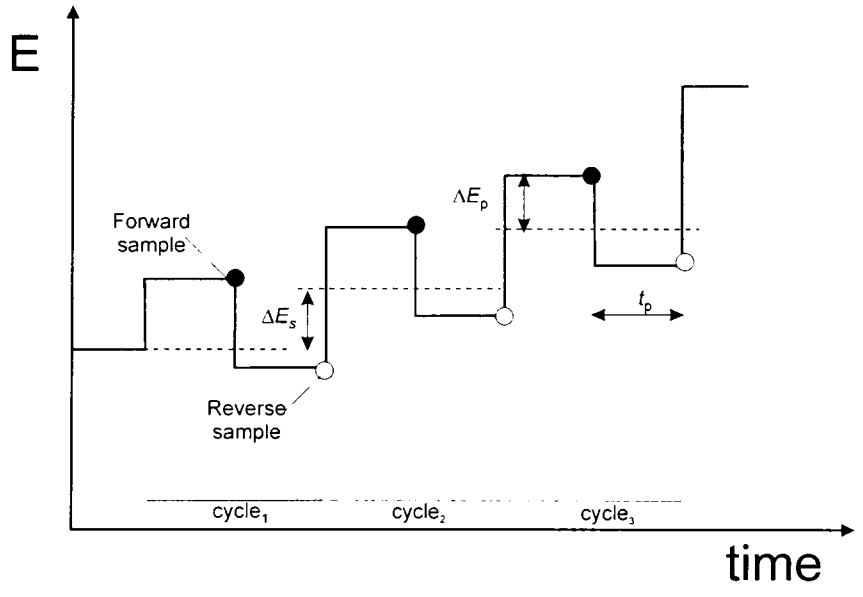


Figure 1.9: The time-potential profile for SWV (adapted from reference [1]).

The key features of the square wave are defined by the pulse height, ΔE_p, measured with respect to the corresponding potential staircase (ΔE_s), and by the pulse width t_p. In turn, the pulse width is defined by the frequency of the square wave, f,:

$$f = \frac{1}{2t_p} \tag{1.39}$$

The staircase increases by ΔE_s at the start of each cycle and the scan rate, ν, is therefore equal to

$$\nu = \frac{\Delta E_s}{2t_p} = f \Delta E_s \qquad (1.40)$$

The current is monitored twice per cycle at the end of each pulse and is attributed to either the forward sample (I_f), which is the first pulse and in the direction of the staircase scan, and the reverse sample (I_r), which is the second pulse and in the opposite direction. The difference between the currents obtained at the forward and reverse samples, as shown in equation (1.41) given below, is normally recorded as a function of potential.

$$\Delta I = I_f - I_r \qquad (1.41)$$

A typical response of square wave voltammetry is shown in figure 1.10, where the forward current, I_f, the reverse current, I_r, and their difference, ΔI, are plotted as a function of potential.

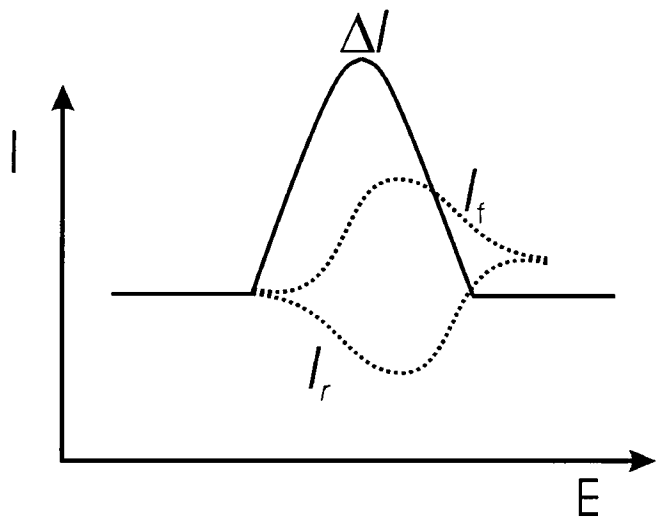


Figure 1.10: Typical current response following the application of SWV.

SWV affords several advantages. First, ΔI is larger than either I_f or I_r so the height of the voltammetric peak is usually quite easy to read, thereby increasing the accuracy. A detection limit of about 10^{-8} mol dm^{-3} is attainable under optimized conditions [32]. Second, the capacitive contributions are minimized so that scan rate up to 1 V s^{-1} are achievable, allowing faster analysis speed, lower consumption of the electroactive

species and increased sensitivity. Third, dissolved oxygen need not to be excluded from the analyte solution. Provided that the voltammetric peak of study is more cathodic than that for the reduction of oxygen, then the magnitude of both I_f or I_r will incorporate an equal current due to the reduction of oxygen. Since both $I_{f(oxygen,}$ and $I_{r(oxygen)}$ are equal, they cancel out and ΔI is seen to be independent of the oxygen concentration in the sample.

1.6 The Testa-Reinmuth Notation for Electrochemical Processes

In this section we considered heterogeneous electron transfer reactions which are followed or preceded by homogeneous reactions. This is the case, for example, of neutral organic molecules which when undergo a one-electron reduction form radical anions which are often unstable over the relevant time period. Testa and Reinmuth notation dictates that the letter "E" denotes the heterogeneous electron transfer step and the letter "C" the homogeneous chemical reaction step [33].

The following are examples of the Testa-Reinmuth notation for a range of important mechanisms.

1.6.1 CE Reaction

In this case the electroactive species is generated by a chemical reaction which precedes the heterogeneous electrochemical reaction as expressed by:

$$A \rightleftharpoons B \qquad\qquad C$$

$$B + e^- \rightleftharpoons C \qquad\qquad E$$

An example of the CE mechanism is the reduction of weak acids, for example acetic acid which has to release a proton, prior the proton being reduced at the electrode surface to hydrogen [34] as given in Scheme 1.1:

$$CH_3COOH \rightleftharpoons CH_3COO^- + H^+$$
$$H^+ + e^- \rightleftharpoons 1/2H_2$$

Scheme 1.1

Another example of the CE reaction process is the oxidation of hydroquinone in aprotic solvent which will be discussed in Part 3, Chapter 9.

1.6.2 EC Reaction

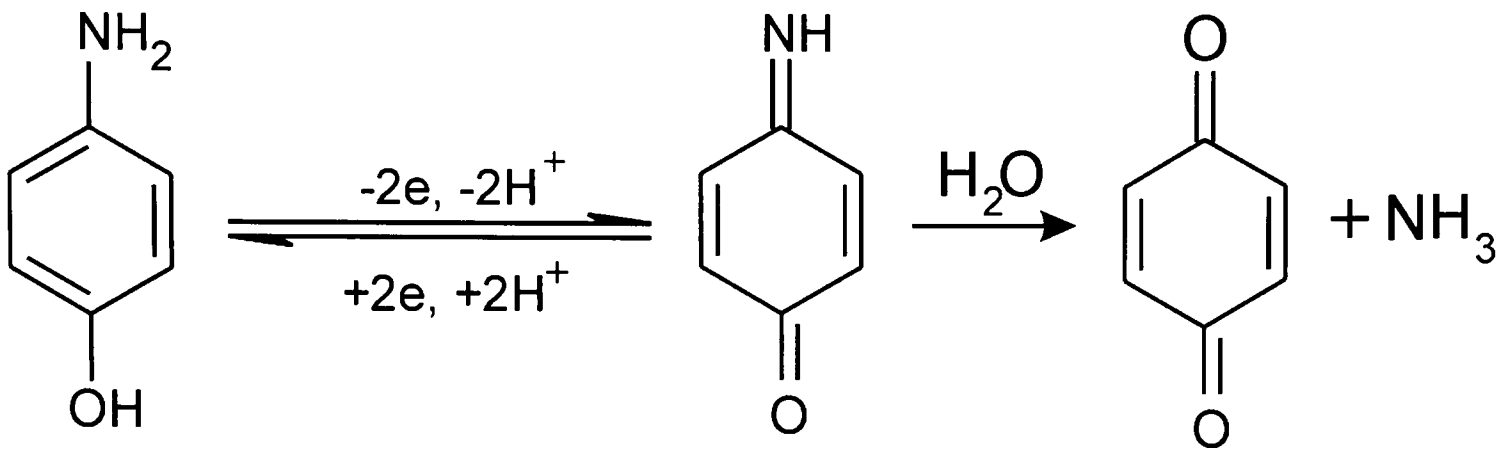
In this case the chemical reaction follows the electron transfer step and forms a product which can then react further in a homogeneous reaction:

$A - e^- \rightleftharpoons A^+$ E

$A^+ + X^- \rightleftharpoons AX$ C

It can be anticipated that in the case of a EC reaction, at fast scan rates the electrochemical reaction is reversible, with well-resolved oxidative and reductive waves, however at the slower scan rates the loss of the reduction peak suggests that the electrochemically generated species A^+ have undergone a chemical reaction (either with the solvent, the parent species or other species present in the solution media). A knowledge of the oxidative and reductive peak currents as a function of the scan rate may therefore aids in the determination of the chemical reaction rate.

The EC mechanism is very common as the electrochemical oxidation or reduction will often produce a very reactive species. An example of such mechanism is the oxidation of p-aminophenol at a platinum electrode in aqueous media [1]. The p-aminophenol is oxidised to the corresponding quinone-imine which can undergo hydrolysis to form benzoquinone, which is electrochemically inactive within the potential region for the oxidation of p-aminophenol (scheme 1.2).



Scheme 1.2

1.6.3 EC' Reaction

In this specific type of EC reaction the products of the chemical reaction step are the electrochemically active starting reactants. Because the starting material are regenerated through this type of mechanism, this is known as the catalytic reaction.

$A + e^- \rightleftharpoons A^+$ E

$A^+ + X \rightleftharpoons A + X^+$ C'

An example of EC' reaction is the electrochemically initiated reaction of ferricyanide with sulfide [35] which will be discussed in Chapter 7, Scheme 7.2. Ferrocyanide is oxidised at the electrode surface to ferricyanide which in the presence of sulfide is subsequently reduced back to ferrocyanide whilst the sulfide is oxidised.

1.6.4 ECE and $EC_{2x}E$ Reaction

The ECE and $EC_{2x}E$ mechanisms involves initially an electrochemical oxidation or reduction, to form a chemically active species, which is then capable of undergoing a homogeneous chemical reaction to form a new electroactive species. The latter can subsequently undergoe further electron transfer thus:

$A - e^- \rightleftharpoons A^+$ E

$A^+ - X^- \rightarrow AX$ C

$AX - e^- \rightleftharpoons AX^+$ E

An example of the $EC_{2x}E$ reaction process is the electrochemically initiated reaction of phenylediamine with sulfide in aqueous media (Chapter 3, Scheme 3.2, [36]). The resulting reaction mechanism is termed an $EC_{2x}E$ reaction due to the catalytic enhancement observed in the oxidative peak current when sulfide is introduce to the solution.

1.7 Microelectrodes

Microelectrodes (also referred to as ultramicroelectrodes) are electrodes which possess at least one dimension that is sufficiently small that the mass transport regime is a function of size. In practise, the upper limit of this small dimension is approximately 20 μm in size [1]. Such dimensions offer obvious analytical advantages (allowing, for example, *in vivo* analysis [37]) however, following the pioneering work by Wightman [38] and by Fleischmann *et al.* [39], the merits of these electrodes have also been recognised for the study of fast homogeneous and heterogeneous kinetic processes. The most common of such electrodes are disc microelectrodes, but spherical, hemispherical and ring geometries are all commonly used in electrochemical experiments.

Diffusion can occur in two dimensions, radially with respect to the axis of symmetry and normal to the plane of the electrode [40,41], as shown schematically below in figure 1.11.

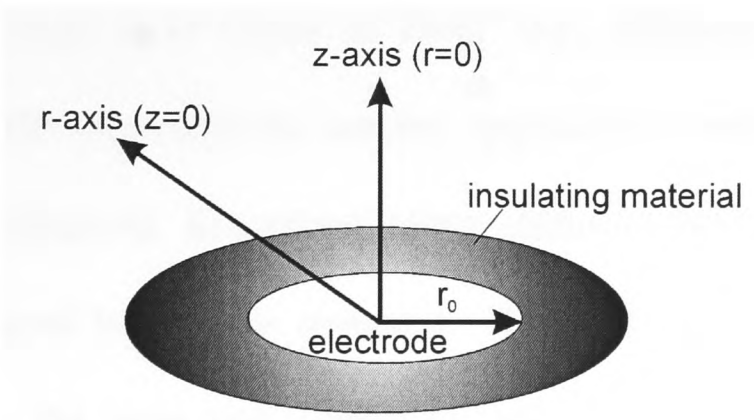


Figure 1.11 Schematic showing the geometry of a microelectrode.

As a consequence of such a diffusional system the current density at the microelectrode is non-uniformly accessible since the edges are more available to the diffusing electroactive species as shown in figure 1.12.

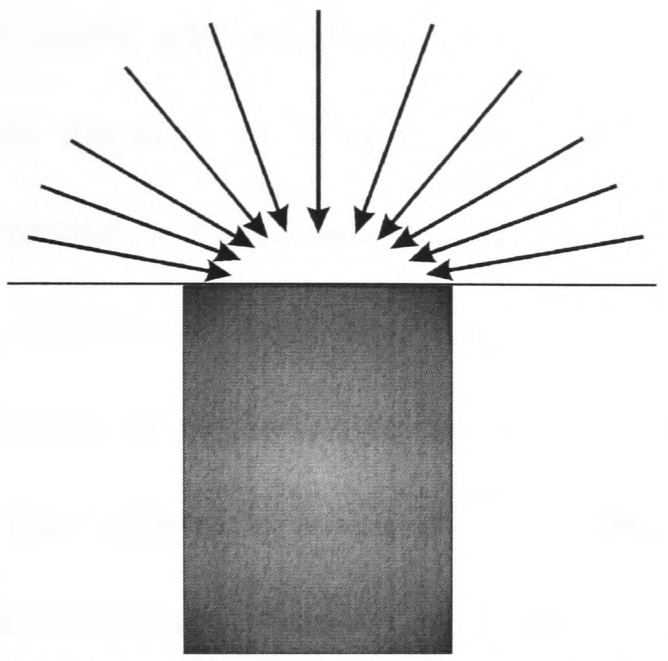


Figure 1.12: Diffusion to a microdisc electrode.

For disk, spherical, and hemispherical geometries the general expression for the radial diffusion component to the steady-state limiting current is given by:

$$I_{radial} = arnFDC \qquad (1.42)$$

where r is the radius of the electrode and a is a function of the electrode geometry (for disks, spheres, and hemispheres the a value are equal 4, 4π, and 2π, respectively). The extent to which the planar or radial component dominates depends on the relative dimensions of the electrode and the diffusion layer, as expressed by the dimensionless parameter Dt/r_0^2 where t is the electrolysis time and r_0 is the smallest dimension of the electrode [6]. For large (> 1) values of Dt/r_0^2 (i.e., diffusion layer thickness that exceeds the size of the electrode) the current approaches steady-state and sigmoidal voltammograms are observed. In contrast, planar diffusion dominates at small value of Dt/r_0^2 and a peak-shaped behavior is observed. Hence, depending on the timescale of the experiment (i.e., the scan rate), the same electrode may exhibit sigmoidal or peak-shaped current-potential profiles.

The design of the microelectrode is such that it has significant advantages over conventional macroelectrodes. Since the electrode area is small, significantly lower currents are passed resulting in negligible electrolysis of the solution. This manifests itself in thin diffusion layers and therefore steep concentration gradients which enhance the rate of mass transport in comparison to macroelectrodes. The greatly reduced double-layer capacitance of microelectrodes, associated with their small area, means that electrolysis currents are less distorted. As a consequence, high-speed voltammetric experiments can be performed on the microsecond timescale (scan rates higher than 10^6 V s^{-1}), thus allowing probing of the kinetics of very fast electron transfer and coupling-chemical reactions. The final benefit of microelectrodes comes in the form of reduced "ohmic drop", (iR), which permits electrochemical experiments to be conducted in highly resistive media. Thus microelectrode experiments have been reported in low-dielectric solvents (e.g., benzene, toluene), frozen acetonitrile, low-temperature glasses, gaseous and solid phases, supercritical carbon dioxide, ionically conductive polymers, oil-bases lubricants and milk [6]. In addition, more conventional electrochemical experiments can be carried out with little or no deliberately added background electrolyte, and with two-electrode systems. The absence of electrolyte allows wider electrochemical window of investigation, making possible studies of species with very high oxidation potentials.

1.8 Rotating Disk Electrode

The rotating disc electrode (RDE) consists of electrode material that has been embedded in a shaft of insulating material, typically Teflon or epoxy resin, as illustrated in figure 1.13. The electrode is rotated at a steady rate which allows a steady supply of electroactive material to the electrode to be sustained.

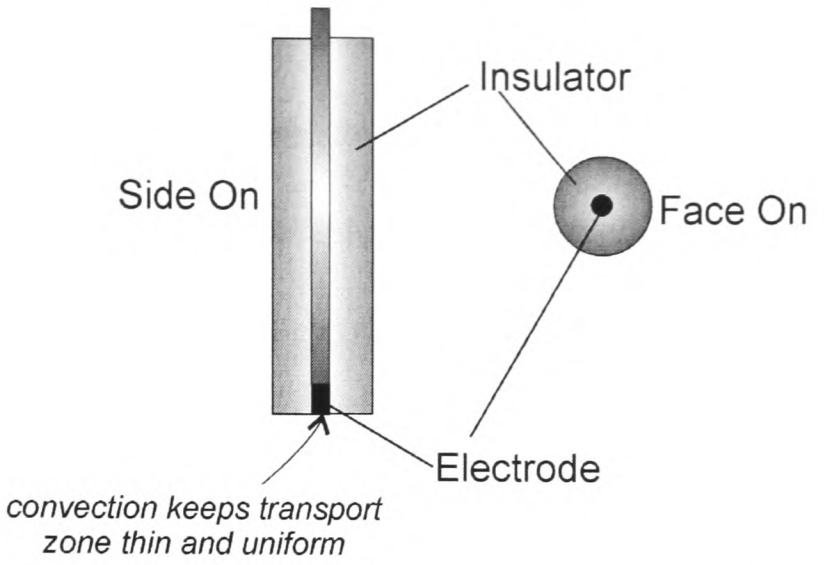


Figure 1.13: Schematic showing the rotating disc electrode (RDE).

The shaft is driven by a motor and is rotated at a determined frequency, f (revolutions per second). It is more common to describe an angular velocity, ω, measured in rad s^{-1} where:

$$\omega = 2\pi f \tag{1.43}$$

Through the solution of steady-state hydrodynamic equations, von Karman and Cochran first described the velocity profile of a fluid acting near a rotating disc [42] as illustrated below in figure 1.14.

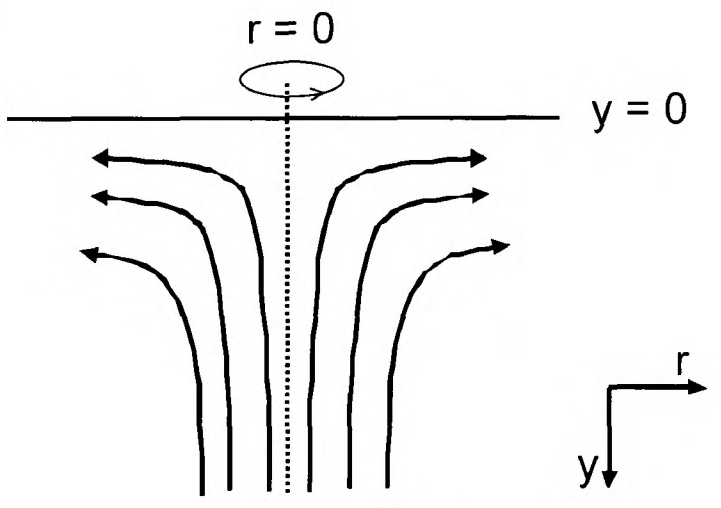


Figure 1.14: Flow velocities at a rotating disc electrode (RDE).

The velocity, v, of the flow normal to the electrode surface (y-direction) is given by:

$$v = -C_y^2 \quad \text{where} \quad C_y = 0.510\omega^{3/2}\nu^{1/2}D^{-1/3} \tag{1.44}$$

where ν/cm^2 s^{-1} is the kinematic viscosity of the solution, ω/rad s^{-1} is the rotation speed and D/cm^2s^{-1} is the diffusion coefficient. After application of the above velocity

profile to the convective-diffusion equations, the limiting current is described by the Levich equation [1] for laminar conditions:

$$I_{Lim} = 0.62nFAD_O^{2/3}\omega^{1/2}\nu^{-1/6}[O]_{bulk} \qquad (1.45)$$

This equation predicts that the mass-transport limited current should vary linearly with $\omega^{1/2}$. The current-potential profile obtained under hydrodynamic conditions are very different from those obtained under diffusion-only conditions in stagnant solutions due to the presence of a plateau or limiting current (I_{Lim}), predicted by equation (1.45), rather than a peak.

The convective flux of fresh material has the effect of shrinking the diffusion layer as expressed by the equation (1.46) below where the diffusion layer thickness is inversely proportional to $\omega^{1/2}$

$$\delta_O = \frac{1.61D_O^{1/3}\nu^{1/6}}{\omega^{1/2}} \qquad (1.46)$$

According to Fick's first law (Appendix 1,[18,19]) the flux to the electrode is greater when the diffusion layer is thinner and this is why greater currents are observed at higher rotation speed.

1.9 Standard Addition Plot and Detection Limits

The majority of the results described in this thesis are of analytical nature and plots of current response against analyte concentration are utilised to determine the analytical parameters of the system, such as linear ranges and limits of detection.

The unknown concentration of a sample can be inferred through the standard addition method. This method involves the analysis of a sample with unknown concentration through spiking with aliquots of a standard, building up a standard addition plot as shown in figure 1.15.

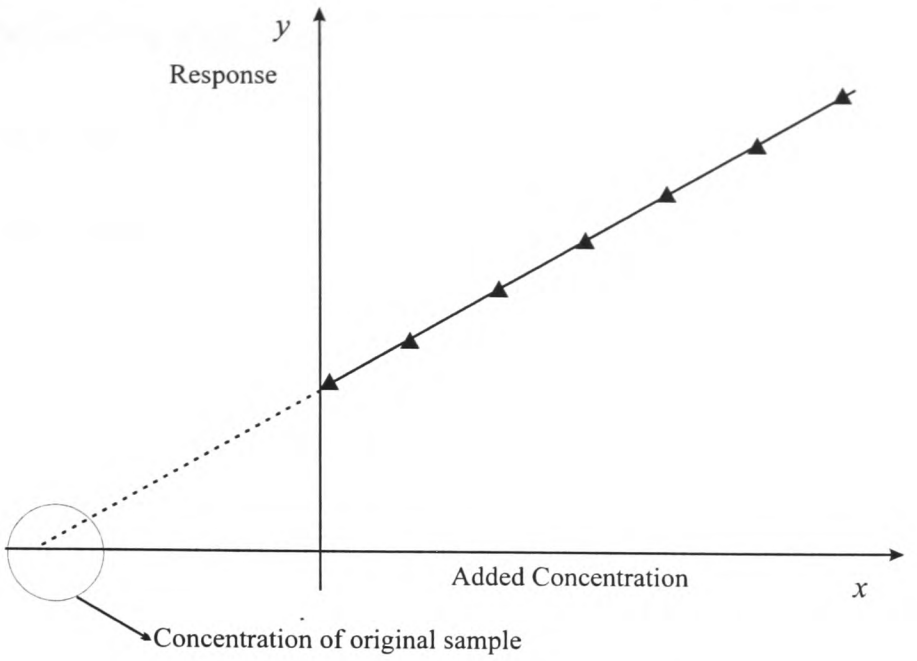


Figure 1.15: Standard addition method.

The concentration of the unknown is then determined through extrapolation to the intercept on the concentration axis. The accuracy of this techniques relies on a good linear response from standard additions and in practise is achieved from best fit lines with a correlation coefficient, r, (or more commonly quoted r^2) approaching unity.

Known concentration are plotted on the x-axis with the response on the y-axis, and it is generally assumed that all the errors are in the y-values, and that the magnitude of theses errors is independent of the analyte concentration although the statistical analysis can be adapted to take varying error magnitude into account.

The line of best fit is calculated by minimising the sum of the squares of the residuals from the line of best fit, giving a gradient and an intercept. This is known as the method of least squares. A good straight line is again indicated by the correlation coefficient r^2 approaching unity. Normally numerical values of at least 0.99 are necessary for a line that would visually be referred to as straight.

The limit of detection (DOL) is defined as the minimum value of the signal from the species being measured that is significantly different from the blank signal. This is normally open to discussion, however modern analytical techniques often quote detection limits based on three time the standard deviation of the y-residuals [3]. From the plot in figure 1.16, the intercept of the linear plot, $y = a + bx$, is the blank

value of the response ($y_B = a$), and the limit of detection (LOD) for x corresponds to the y-value $y = y_B + 3s_B$, where s_B is the standard deviation of the y-residuals from the line of best fit. The limit of detection is then ($3s_B$ / b) as shown in figure 1.16.

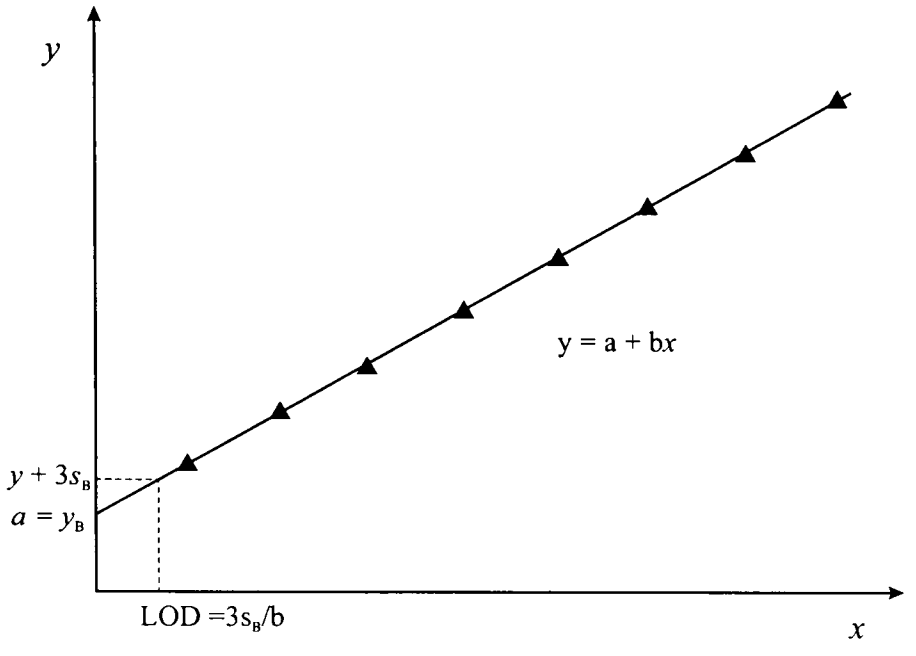


Figure 1.16: Determination of LOD from a linear calibration plot.

1.10 Chapter 1 References

[1] A. J. Bard, L. R. Faulkner, *Electrochemical Methods: Fundamentals and Applications*, 2nd Ed., John Wiley and Sons, New York, **2001**.

[2] C. M. A. Brett, A. M. O. Brett, *Electrochemistry Principles, Methods and Applications*, Oxford University Press, Oxford, **1993**.

[3] C. M. A. Brett, A. M. O. Brett, *Electroanalysis*, Oxford University Press, Oxford, **1998**.

[4] D. R. Crow, *Principles and Applications of Electrochemistry*, Blackie Academic and Professional, London, **1996**.

[5] A. M. Bond, *Broadening Electrochemical Horizons*, Oxford University Press, Oxford, **2002**.

[6] J. Wang, *Analytical Electrochemistry*, 2nd Ed., Wiley-VCH, New York, **2000**.

[7] R. G. Compton, G. H. W. Sanders, *Electrode Potentials*, Oxford University Press, Oxford, **1996**.

[8] A. C. Fisher, *Electrode Dynamics*, Oxford University Press, Oxford, **1996**.

[9] P. H. Rieger, *Electrochemistry*, Chapman & Hall, New York, **1994**.

[10] H. L. F. von Helmholtz, *Ann. Physik.* **1853**, *89*, 211.

[11] H. L. F. von Helmholtz, *Ann. Physik.* **1879**, *7*, 337.

[12] G. Gouy, *Compt. Rend.* **1910**, 654.

[13] D. L. Chapman, *Phil. Mag.* **1913**, *25*, 75.

[14] D. C. Grahame, *Chem. Rev.* **1947**, *41*, 441.

[15] J. O. M. Bockris, M. A. Devanathan, K. Muller, *Proc. R. Soc.* **1963**, *55*, A274.

[16] J. A. V. Butler, *Trans. Faraday Soc.* **1924**, *19*, 729 and 734.

[17] T. Erdey-Gruz, M. Volmer, *Z. Physik. Chem.* **1930**, *150A*, 203.

[18] A. Fick, *Philosophical Magazine and Journal of Science* **1855**, *10*, 30.

[19] A. Fick, *Pogendorff's Annel. Physik* **1855**, *94*, 9.

[20] W. Nernst, *Z. Physik. Chem.* **1904**, *47*, 52.

[21] J. C. Eklund, A. M. Bond, J. A. Alden, R. G. Compton, *Advances in Physical and Organic Chemistry* **1999**, *32*.

[22] K. B. Oldham, C. G. Zoski, *Comprehensive Chemical Kinetics* **1986**, *26*, 122.

[23] C. M. A. Brett, A. M. O. Brett, *Comprehensive Chemical Kinetics* **1986**, *26*, 355.

[24] C. A. Amatore, E. Maisonhaute, G. Simmonneau, *Electrochem. Commun.* **2000**, *2*, 81.

[25] M. Sharp, M. Peterson, K. Edstrom, *J. Electroanal. Chem.* **1980**, *109*, 271.

[26] K. M. Kadish, J. Q. Ding, T. Malinski, *Anal. Chem.* **1984**, *56*, 1741.

[27] G. C. Barker, J. L. Jenkins, *Analyst* **1952**, *77*, 685.

[28] L. Ramaley, M. S. Krause Jr., *Anal. Chem.* **1969**, *41*, 1362.

[29] J. Osteryoung, R. A. Osteryoung, *Phil. Trans. Roy. Soc. London, Ser. A* **1981**, *302*, 315.
[30] J. Osteryoung, J. J. O'Dea, *Electroanal. Chem.* **1986**, *14*, 209.
[31] J. Osteryoung, *Accts. Chem. Res.* **1993**, *26*, 77.
[32] P. M. S. Monk, *Fundamentals of Electroanalytical Chemistry*, Wiley & Sons., Chichester, **2001**.
[33] A. C. Testa, W. H. Reinmuth, *Anal. Chem.* **1961**, *33*, 1320.
[34] W. Vielstich, D. Jahn, *Advan. Polarog. Proc. Intern. Congr.* **1959**, *1*, 281.
[35] N. S. Lawrence, M. Thompson, C. Prado, L. Jiang, T. G. J. Jones, R. G. Compton, *Electroanalysis* **2002**, *14*, 499.
[36] N. S. Lawrence, J. Davis, L. Jiang, T. G. J. Jones, S. N. Davies, R. G. Compton, *Electroanalysis* **2000**, *12*, 1453.
[37] R. N. Adams, *Anal. Chem.* **1976**, *48*, 1126A.
[38] R. M. Wightman, *Anal. Chem.* **1981**, *53*, 1125A.
[39] M. Fleischmann, S. Pons, D. R. Rolison, P. P. Schmidt, *Ultramicroelectrodes*, Morganton, NC, **1987**.
[40] Y. Saito, *Rev. Polarog.* **1968**, *15*, 177.
[41] K. B. Oldham, *J. Electroanal. Chem.* **1981**, *122*, 1.
[42] V. G. Levich, *Physiochemical Hydrodynamics*, Prentice Hall, Englewood Cliffs, New York, **1962**.

Chapter 2: "Experimental"

2.1 Chemicals

A detailed list of all the chemicals used can be found in Appendix 2. All solutions and subsequent dilutions were prepared daily using deionised water from a Vivendi (Vivendi, UK) UHQ grade water system with a resistivity of not less than 18 MΩ cm. Solutions were prepared by dissolving the appropriate analyte in either 3, 4 or 5 acetate or Britton-Robinson (BR) buffer (comprising equimolar amounts of acetic, phosphoric and boric acids adjusted to the required pH with NaOH) or pH 4 and 6 phosphate buffer. In general, all the solutions were degassed and stored under nitrogen and used within 12 hours to minimise degradation. Phenylenediamine stock solutions were kept in the dark due to their photosensitivity. Stock sulfide solutions (0.05 M) were prepared by dissolving the sodium salt in deionised water and used within one hour of preparation to minimise losses due to aerial oxidation.

2.2 Electrochemical Equipment

Electrochemical measurements were conducted using a PG STAT 20 computer controlled potentiostat (Eco-Chemie BV, Utrecht, Netherlands) with a standard three electrode configuration. A platinum wire wound into a spiral provided the counter electrode and a saturated calomel reference electrode (SCE, Radiometer, Copenhagen) or a Ag/AgCl reference electrode completed the cell assembly. The reference electrode was connected through high impedance circuitry (~10 MΩ) which draws negligible current so that its potential would remain constant and essentially equal to its open circuit value. The working electrodes (see individual chapters) were polished

between experiments with diamond pastes of decreasing particle size (6 μm to 1 μm, Kemet, UK) or using 1.0 and 0.3 μm alumina (Buehler, USA) on soft pads.

All the microelectrodes were carefully polished prior to use, using 1.0 and 0.3 μm alumina (Buehler, USA) [1]. The microelectrodes were electrochemically calibrated prior to use to obtain an accurate measurement of electrode radius. This was carried out recording linear sweep voltammograms in solutions containing either various concentration of ferricyanide (0.25 to 2.0 mM, $D = 0.76 \times 10^{-5}$ cm^2 s^{-1} [2]) in 0.1M aqueous KCl or 2 mM Cp_2Fe in acetonitrile (0.1 M tetrabutylammonium perchlorate, $D = 2.3 \times 10^{-5}$ cm^2 s^{-1} at 20 °C [3]).

2.3 Rotating Disk Electrodes

Rotating disk analysis was conducted using an Oxford electrode motor controller with the three-electrode arrangement described above. The working electrode used was sheathed in Teflon TM with a brass thread to allow connection to the motor. The electrode was rotated at different speeds (2.5 – 40 Hz).

2.4 Atomic Force Microscopy (AFM)

Atomic Force Microscopy (AFM) images were obtained using a Park Scientific Instruments Autoprobe cp atomic force microscope operating in contact mode with 100 μm scanner. These experiments were performed by Dr. Shelley Wilkins.

2.5 Scanning Electron Microscopy (SEM)

Scanning Electron Microscopy (SEM) images were obtained using a Jeol JSM6300 microscope. These images were recorded by Dr. Shelley Wilkins.

2.6 UV / Visible Spectrometry

UV / Visible spectroscopy was carried out using a Unicam UV / Vis spectrometer U/V 2, with a clear quartz cuvette of path length 1 cm.

2.7 Chapter 2 References

[1] T. J. Cardwell, J. Mocak, J. H. Santos, A. M. Bond, *Analyst* **1996**, *121*, 357.
[2] R. N. Adams, *Electrochemistry at Solid Electrodes*, Marcel Dekker, New York, **1969**.
[3] P. Sharp, *Elecrochim. Acta* **1983**, *28*, 301.

Part 2: "Electrochemical Detection of Hydrogen Sulfide"

Aims and Scope:

The aim of the work reported in this section is to explore various amperometric possibilities for the detection of hydrogen sulfide and to identify the more promising routes for the realisation of practical prototype gas sensors that can be used under conditions akin to those to be encountered in the oilfield environment (notable high temperature and pressure). The latter will be discussed in Part 5.

Chapter 3: "A Review of the Analytical Detection Strategies for Sulfide"

This chapter is a brief overview of the toxicological effects of hydrogen sulfide and the methods available to the analytical community for its detection.

3.1 Introduction

Hydrogen sulfide (H_2S, S^{2-} pKa=14.15, HS^- pKa=6.88, T=20 °C, [1]) is a colourless gas with a characteristic offensive odour suggesting "rotten eggs" [1-3]. Natural sources account for about 90% of the total hydrogen sulfide in the atmosphere and include crude petroleum [4-7], natural gas, volcanic gases [8], sulfur springs and putrefying vegetable and animal matter. H_2S is also found in groundwater and it is emitted from stagnant or polluted waters and manure or coal pits with a low oxygen content.

Hydrogen sulfide may also be released into the environment as a by-product of a variety of industrial operations, such as petroleum refineries, natural gas plants, petrochemical plants, coke oven plants, viscose rayon manufacture, sulfur production, iron smelters, food processing plants and tanneries [9]. Another large potential source of H_2S is from kraft mills during the preparation of paper [10].

Comprehensive and excellent reviews on the toxicity of H_2S have been published [11-14]. Only some of the toxicological aspects of H_2S are dealt with in this section.

Humans may be exposed to H_2S both from exogenous sources and from its endogenous production, the latter resulting from the metabolism of compounds containing various forms of sulfur such as methionine, cysteine and glutathione by bacteria present both in the intestine and in the mouth [15]. Human accidental exposure to exogenous H_2S is *via* inhalation.

Typical symptoms which indicate H_2S exposure include dizziness, weakness, nausea, headache, loss of consciousness, confusion and somnolescence [16]. Adverse effects are caused in human even in low concentration (ca. 50 ppm) and at concentration greater than 140 mg m^{-3} (~ 100 ppm) olfactory paralysis occurs, making H_2S very dangerous because a few breath at 700 mg m^{-3} (= 500 ppm) can be fatal. Table 3.1 summarises the human health effects at various H_2S concentration as reported in ref. [11].

Table 3.1: Human health effects at various H_2S concentrations (reproduced from ref. [11]).

Exposure* / mg m^{-3}	/ ppm	**Effect / observation**
0.011	0.00781	Odour threshold
2.8	2.8	Bronchial constriction in asthmatic individuals
5.0	3.55	Increased eye complaints
7 - 14	4.97 – 9.94	Increased blood lactate concentration, decreased skeletal muscle citrate synthase activity, decreased oxygen uptake
5 - 29	3.55 – 20.59	Eye irritation
28	19.88	Fatigue, loss of appetite, headache, irritability, poor memory, dizziness
>140	> 99.4	Olfactory paralysis
>560	> 397.6	Respiratory distress
>700	> 497	Death

*The conversion factors for H_2S in air (20 °C, 101.3 kPa) are as follows: 1 mg m^{-3} = 0.71 ppm, 1 ppm = 1.4 mg m^{-3}.

The typical "rotten egg" odour of H_2S is detectable by olfaction at very low concentrations, between 0.2 and 0.13 ppm, and it is usually a safe and useful warning signal. However, olfactory fatigue or paralysis of the olfactory nerve which rapidly occurs where lethal concentrations of the gas are present can also occur gradually on exposures to small amounts of H_2S meaning that prolonged exposure even to low concentrations can impair the perception of the gas.

Two major effects of H_2S exposure in humans are known: (1) local inflammatory and irritative effects on moist membrane including the eyes and respiratory tract resulting from direct H_2S action on tissues and, (2) H_2S inhalated at sufficiently high concentrations causing systemic intoxication which often results in death.

The primary mechanism of H_2S toxicity has been show to be the inhibition of cytochrome oxidase (the final enzyme in the respiratory chain) in the mitochondria [11,12,17,18]. This disrupts the electron transport chain and impairs oxidative metabolism and thus affects the respiratory and central nervous systems and may ultimately result in death from respiratory arrest.

The gas is particularly hazard for workers in the oil drilling and refining industries, extruded rubber plants, sewage collection and treatment works, landfill sites and for farm workers near manure holding tanks and pits. The current limit for a 10 minutes exposure in the UK set by the government legislation is 10 ppm [19]. Ambient air concentration of H_2S are generally well below both the short-term (for exposure duration of 1-14 days) and medium-term (for exposure duration of up to 90 days) tolerable concentrations of 100 and 20 $\mu g\ m^{-3}$, respectively, set by the World Health Organization [11]. However, the general population may be exposed to H_2S by accidental release from natural gas wells during drilling operations near residential area.

As adverse toxicological effects of hydrogen sulfide in human are observed at very low concentration, there has been a constant requirement for H_2S sensors that are both sensitive and rapid in their response and inexpensive so that they can be widely deployed to protect the wellbeing of workers. Several methodologies for the detection of the toxic gas have been proposed and these will be briefly reviewed in the following section.

3.2 Analytical Detection Strategies for Sulfide

In two recent review articles, Lawrence *et al.* [20,21] have described the various methodologies available for sulfide detection and they conclude that the high reactivity of sulfide provides a plethora of detection strategies. In terms of number of

publications, the most popular approaches for sulfide analysis use spectrocopic methods [15,22-72] with electrochemical [21,73-115] and chromatographic [36,115-139] techniques in second and third places, respectively.

A number of approaches which are not included in the formerly mentioned categories include monitoring tapes [140], an elementar analyser [141], an electronic nose [142], mass spectroscopic probe [143] and luminescent sorbent tubes [144].

The different strategies available to the analytical community for sulfide detection in its different forms are shown in figure 3.1 (reproduced from reference [20]) and the analytical characteristics (i.e., reaction medium, matrix and lower and upper limit of detection) of the techniques discussed in this chapter are summarised in Table 3.2.

The use of the various methods employed in the detection of sulfide is next described.

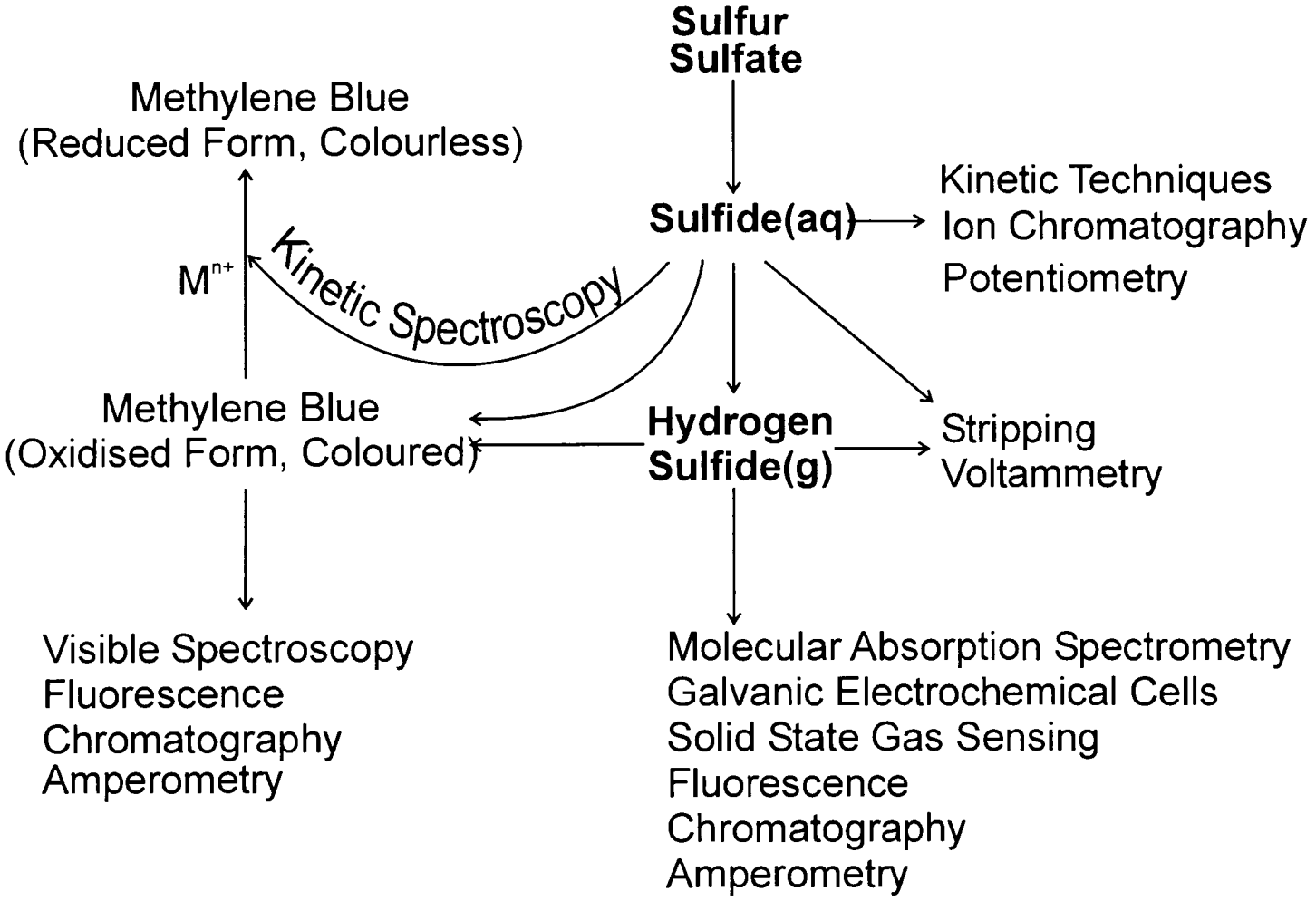


Figure 3.1: Analytical pathway for the determination of sulfide.

Table 3.2: *Analytical characteristics of the techniques discussed in this chapter for sulfide monitoring.*

Reaction medium	Matrix	Methodology	Detection Range / ppb		Ref.
			lower	upper	
Aq.	N/S	Classical	200	4000	[145]
Aq	Sediment	UV/Vis	N/S	N/S	[146]
Aq.	Waste water	UV/Vis	0.1	32	[34]
Aq.	Air extraction	U V/Vis	70	2000	[53]
Aq.	Natural water	UV/Vis	1	N/S	[33]
Air	Air extraction	Spectroscopic	0.3 mg	N/S	[32]
Aq.	Blood	Kinetic-UV/Vis	32	16 ppm	[3]
Aq.	Spring water	Kinetic-UV/Vis	50	2000	[147]
Aq.	Spring water	Kinetic-UV/Vis	0.015	6000	[44]
Aq.	Spring water	Kinetic-UV/Vis	0.04	25	[45]
Aq.	Spring water	Kinetic-UV/Vis	50	2000	[50]
Aq.	Spring water	Kinetic-UV/Vis	20	500	[132]
Air	Exhaled breath	Fluorescence	4 ppb / v	200 ppb / v	[15]
Air	N/S	Fluorescence	80	15 ppm	[35]
Air	N/S	Fluorescence	1.792	640	[55]
Air	N/S	Fluorescence	2.24	141	[148]
Air	N/S	Fluorescence	N/S	100 ppb / v	[57]
Air	Air Extraction	Fluorescence	N/S	25 ppm	[56]
Air	Air Extraction	Fluorescence	10^{-12}	N/S	[31]
Air	Mineral water	Mol. Absorption	50 ppm	700 ppm	[149]
Air	Natural water	Mol. Absorption	1 ppm	550 ppm	[58]
Air	Waste stream	Mol. Absorption	0.13 ppm	100 ppm	[60]
Air	N/S	Mol. Absorption	10 ppm	6000 ppm	[61]
Aq.	N/S	Potentiometric	N/S	N/S	[150]
Aq.	N/S	Potentiometric	3 ppm	32 ppm	[151]
Aq.	Steel	Potentiometric	2 ppm	N/S	[74]
Aq.	Sol gel processing	Potentiometric	1.92	640	[75]
Aq.	N/S	Potentiometric	32	320 ppm	[76]
Aq.	N/S	Potentiometric	0.13 ppm	24 ppm	[77]
Air	Air Extraction	Potentiometric	50	1000	[105]
Aq.	N/S	Potentiometric	0.1 $\mu g\ mL^{-1}$	30 $\mu g\ mL^{-1}$	[152]
Aq.	N/S	Galvanic (g)	0.1 ppm / v	300 ppm / v	[82]
GS	N/S	Galvanic (aq)	96	3000	[84]
GS	N/S	Galvanic (g)	30	100 ppm	[85]
Aq.	N/S	Amperometric	100	3000	[38]
Aq.	N/S	Amperometric	32	24 ppm	[83]
Air	N/S	Amperometric	N/S	N/S	[86]
Aq.	N/S	Amperometric	12 nM	N/S	[153]
Aq.	N/S	Amperometric	3 $\mu M\ L^{-1}$	150 $\mu M\ L^{-1}$	[94-96]
Aq.	Sewage water	Amperometric	24 $\mu M\ L^{-1}$	48 $\mu M\ L^{-1}$	[101]
Aq.	N/S	Amperometric	4 $\mu M\ L^{-1}$	100 $\mu M\ L^{-1}$	[98]
Aq.	N/S	Amperometric	20 $\mu M\ L^{-1}$	103 $\mu M\ L^{-1}$	[97]
Aq.	N/S	Amperometric	7.5 $\mu M\ L^{-1}$	165 $\mu M\ L^{-1}$	[99]
Aq.	N/S	Amperometric	13.4 $\mu M\ L^{-1}$	80 $\mu M\ L^{-1}$	[154]
Air	N/S	Cathodic stripping	0.07 ppm / v	113 ppm / v	[88]
Aq.	N/S	Cathodic stripping	0.32	3	[89]
Aq.	Amino acids prep.	Cathodic stripping	0.9	200	[90]
HS	Drug formulation	GC-chromatography	5	340	[117]
Aq.	Pore water/sediment	GC-chromatography	6.4×10^{-4}	0.004	[119]
Aq./HS	Aqueous effluent	GC-chromatography	0.49	4900	[120]
Aq.	Blood	GC-chromatography	0.01 $\mu g\ g$	N/S	[139]
Aq.	Blood	HPLC	0.32	96	[124]
Aq.	Sea water	HPLC	12.8	25.6 ppm	[125]
Aq.	Dairy farm effluent	Ion exchange	3.7 ppm	50 pppm	[129]
Aq.	Hot Spring water	Ion chromatography	0.14	16	[115]

Reaction medium	Matrix	Methodology	Detection Range / ppb		Ref.
			lower	upper	
Aq.	N/S	Ion chromatography	35	50	[130]
Aq.	Leather effluent	Capillary electrophoresis	0.5	10 ppm	[9]
Aq.	Paper processing effluent	Capillary electrophoresis	0.5	10 ppm	[10]
Aq.	Mining water	Capillary electrophoresis	15 ppm	50	[131]
Air	N/S	Solid State	0.01 ppm / v	10 ppm / v	[155]
Air/HS	N/S	Solid State	50 ppb / v	13.5 ppm / v	[156]
Air	N/S	Solid State	0.05 ppm / v	1000 ppm / v	[142]
Air	N/S	Solid State	0.2 ppm / v	12 ppm / v	[157]

3.2.1 Titration Methods

A classical approach to sulfide determination is represented by its titration with iodine [145,158]. An excess of iodine is normally added to the sulfide sample with the remaining back titrated with thiosulfate as expressed by the following reactions:

$$H_2S + I_2 \rightarrow 2HI + S \qquad (3.1)$$

$$2S_2O_3^{2-} + I_3^- \rightarrow S_4O_6^{-2} + 3I^- \qquad (3.2)$$

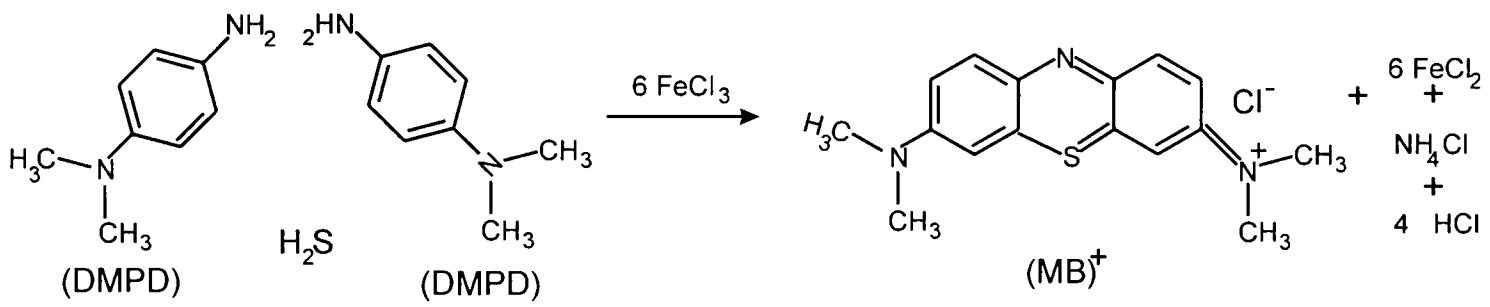
Direct titration with iodine is generally avoided due to loss of the sample through volatilisation and/or aerial oxidation.

This is a simple method which, however, has significant limitations in terms of sensitivity and selectivity when dealing with real world sample. It is however the preferred method for standardisation of sulfide calibration samples used in many of the other methodologies which are discussed further [9,45,50,53,55,61,76,77,83,115,125-130,147-149].

A titrimetric method for determination of sulfide and of sulfur in steels with chloranilic acid by biamperometric and automatic potentiometric end-point detection has also been reported [151]. The results obtained agree with those of the iodine-thiosulfate titration method.

3.2.2 Spectroscopic Methods

The methylene blue method has been widely [22-26,28-30,32,34,35,38-41,116,158] used since the original description in 1883 by Emil Fisher [22]. This involved the reaction of aqueous sulfide with N,N-dimethylphenyl-1,4,-diamine (DMPD) in the presence of a small quantity of ferric ions with gives rise to a characteristic blue coloration. This corresponds to the production of the phenothiazine dye methylene blue, MB, as shown in scheme 3.1:



Scheme 3.1

The blue colour of methylene blue is measured at 670 or 650 nm [24,34]. This method retains today significant value in term of simplicity, selectivity [24] and sensitivity (detection limit obtainable of 0.01 ppm). A possible problem associated with this method is however the presence of interfering coloured substances.

The methylene blue method has been applied to the determination of H_2S in air and in biological samples and in environmental studies [26,32].

Fluorescence [116] and high performance liquid chromatography, HPLC, [128] techniques have also been used to detect the resulting sulfur heterocycle adduct. HPLC of sulfide after conversion to methylene blue was found to be advantageous in situations where sample turbidity might hinder the spectroscopic analysis and showed to be very sensitive with a LoD = 0.8 ppb [128].

Under normal conditions the reduction of methylene blue by sulfide is a slow process with low analytical utility. However, the reductive capability of sulfide can be

significantly enhanced in the presence of trace quantities of certain metals. Several rapid and sensitive catalytic spectroscopic methods for the determination of trace amounts of sulfide based on its catalytic reduction of Methylene Blue (MB) in the presence of metals such as Te [147], Cu [44] and Se [43] have been reported. It was also shown that this type of reaction could be used for the detection of trace amount of the metal, particularly selenium, [42,43]. This approach has also been applied to a number of alternative chromogens (resazurin [44], aszurea [43], thionine [42], toluidine blue [46]).

An optode film, coated on an overhead transparency film, was recently employed as a sensing device for fluorometric detection of H_2S [56]. The H_2S-sensitive optode film was fabricated by immobilizing tetraoctylammonium fluorescein Hg(II) acetate (TOFMA) and tri-Bu phosphate in a poly(vinyl chloride) (PVC) matrix.

Others spectroscopic protocols based on the irreversible reaction of sulfide with chromogenic species leading to the production of a new absorption maximum or, more commonly, the diminution of the existing peak without the requirement for metal ion catalysis have also been reported [34,37,45,51-53,132]. Nitrosylpentacyanoferrate (II) gives rise to a transient red-violet coloration (detectable at 574 nm) [34,37] upon addition of sulfide, whereas the highly coloured Magenta (540 nm) [45] and Brillinat Green (625 nm) [50] dye reagents are converted to a colourless form. Iron-phenantroline [47], crystal violet [49] and para-rosaniline [51] have been investigated along similar lines.

Fluorescence-based detectors have been incorporated to some of the studies with methylene blue [35,52], thionine [52] and 2,7-dichlorofluorescein [53]. The reaction of sulfide with the mercuric complex of 2,2-pyridylbenzimidzole results in the formation of mercuric sulfide with the liberation of the fluorescent labels providing an increase in signal intensity [54]. The use of similar other fluorescent labels exploiting

the affinity for co-ordinated mercuric ions [55,57,148] have been studied and, the resulting protocols for sulfide detection were found to be sensitive but still prone to interferences when other thiols compounds are present.

Several spectroscopic quasi-direct methods for the determination of sulfide which use molecular absorption spectrometry have also been described [58-63]. Finally, the use of atomic spectroscopic [64,66], cheminulescent [67,68], infrared spectroscopic [70], diode lasers [71] and simplified optical transmittance [72] techniques also feature in the spectroscopic detection of sulfide.

Lawrence et al. [94-96] have recently devised an electrochemical analog of the MB test in which oxidation *via* ferric ions is replaced by electron transfer at a glassy carbon electrode. This will be discussed in more detail in section 3.2.4.1.

3.2.3 Chromatographic Methods

Gas chromatography [117-120,135,137-139,159-163] and HPLC [124,125,128] techniques have been applied to the determination of sulfide in a number of samples including pharmaceutical preparations [117], water samples [9,119,129,137,138], soil samples [118], paper processing water [120] and biological samples [124,125,135,137-139,159-163]. The separation capabilities of chromatographic techniques have proved particularly advantageous when dealing with complex matrices providing good selectivity between the different sulfur containing anions and thiol species.

End column detection has been utilised for conductivity [117], flame photometry [118-120] and fluorimetric systems [124-126]. Precolumn derivatisation procedures based on the methylene blue [52], thionine [120], [124] and the fluorescent label monobromobimabe [125] have also been implemented.

Ion chromatographic systems range from simple exchange columns [36,115,129,130] to gel base separation columns. Visible absorption spectrometry has been applied to

the ion chromatographic/ion exchange system. Solid lead (II) chromate loaded columns have also been utilised in sulfide ions removal and determination, however interferences from other metal ions (i.e., Ca, Mg, Fe) and hydroxyl ions were reported [129]. Gel based column [115] offered a more selective approach.

Inductively coupled plasma mass spectroscopy (ICP-MS) has been coupled to ion chromatographic procedure to increase the specificity of the end column detection [130].

With the advantages of less sample and solvent consumption compared to conventional liquid chromatograpy, short separation time, inexpensive and robust capillaries, capillary electrophoresis methods [9,10,131] have been recently employed for the determination of sulfide in the leather [9] and paper industry [10] with clear resolution of sulfide from other sulfur ions such as sulfite, thiosulfate and thiocyanate and more commonly encountered ions such as nitrate, nitrite and halides. UV and conductivity detectors are typically used as the end detection system [131].

3.2.4 Electrochemical Methods

Electrochemistry has been applied to the detection of sulfide for many years and as such a large number of analytical strategies have evolved. These include potentiometric [73-77,79-81,104-112,150-152,158], galvanic [82,84,85] coulometric [87] and amperometric [83,86,88-90] techniques.

The most commonly exploited potentiometric system involves silver sulfide as the main sensing element and have been successfully applied to a number of matrices. A sulfide ion-specific electrode has been use for the determination of sulfide in various biological samples [104-112]. The use of conventional sulfide electrodes has however been limited because problems such as long response times, deviation from ideal

Nernstian behaviour and poisoning of the reference electrode component by sulfide are often associated with their use.

Alternative potentiometric techniques involve the use of modified electrodes by the deposition of electropolymerised films such as binaphthyl-20-crown-6 [75], N,N',N",N'"-tetramethyltetra-3,4-pyridinoporphyrazinocobalt (I) [76] and tetraamino phthalocyanatocobalt (II) [77].

Kroll *et al.* [82] have described a galvanic sensor for H_2S sensing based on a modified Clark cell. The operation principle is oxidation of the gas molecules on a sensitive platinum electrode connected with a counter electrode based on macrocyclic or macrobicyclic polyaza cobalt(III) complexes as the catalysts. The sensor showed good linearity and selectivity, comparatively high sensitivity (0.1 ppm H_2S), perfect stability, and an extremely long operating life of up to several years. Similar systems utilising ferricyanide have also been employed for the development of galvanic devices for H_2S detection in the aqueous [84] and gas phase [85]. A gas porous membrane is used to ensure selectivity.

The ferricyanide/ferrocyanide ions redox mediator system has also been implemented in the design of an amperometric microsensor for detection of dissolved H_2S in aquatic environments [83,86]. The design of the microsensor is again based on the same principle as the Clark-type oxygen microsensor. The sensor is equipped with a glass-coated platinum working electrode and a platinum guard electrode positioned in an outer glass casing (tip diameter = 20 - 100 mm). Both working electrode and guard electrode are polarized at a fixed value in the range from +85 to + 150 mV with respect to a counter electrode. The outer casing is sealed with a thin silicone membrane and filled with a buffered electrolyte solution containing $K_3[Fe(CN)_6]$ as redox mediator. Hydrogen sulfide penetrates the silicone membrane and is oxidized by $K_3[Fe(CN)_6]$, resulting in the formation of elemental sulfur and ferrocyanide ($K_4[Fe(CN)_6]$). The

latter is electrochemically reoxidized at the exposed end of the platinum working electrode, thereby creating a current that is directly proportional to the dissolved H_2S concentration at the sensor tip. A wide dynamic working range of concentration from 1 to 750 $\mu mol\ L^{-1}$ H_2S was accessible [83]. This approach is readily applicable to portable sensing and can be used for continuous/remote monitoring application. A further advantage of this amperometric microsensor is that oxygen does not interfere with H_2S, such as with potentiometric Ag/Ag_2S sensors, because it does not react with ferricyanide.

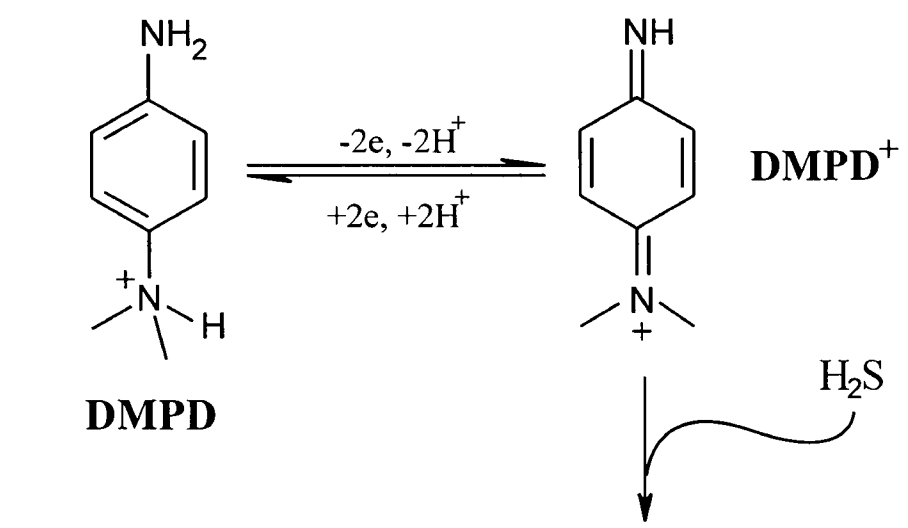
Lawrence *et al.* [101] have assessed the suitability of using boron doped diamond (BDD) electrode as a sulfide sensing substrate through examining the electrocatalytic oxidation of ferrocyanide to ferricyanide in the presence of sulfide using both cyclic voltammetry and chronoamperometry. The high oxidation potential for the direct oxidation of sulfide at a BDD electrode allows clear resolution of both the ferrocyanide wave and sulfide oxidation wave producing a distinct analytical signal at the oxidation peak potential of ferrocyanide. The procedure was applied to the recovery of a sulfide spike in sewage effluents with a recovery of $102 \pm 4.5\%$.

Silver [88] and mercury [89,90] modified electrode have also been investigated in amperometric systems. Sulfide reacts with the metal surface producing the corresponding metal sulfide, which is then reduced back to the metal by applying a sufficiently negative potential at the electrode surface. The reduction current can be related to the amount of sulfide initially present.

Modified screen printed carbon (SPC) electrodes with hexadecylpyridinium-bis(chloranilato)-antimonyl(V), $[Sb^{V}O(CHL)_2]Hex$ [103] and cinder/hexacyano cobaltate hybrid [153] have been recently applied to the determination of sulfide with good sensitivity and selectivity. The high stability, low cost and easy preparation route might offer scope for application in routine analysis.

3.2.4.1 The electrochemical analog of the methylene blue reaction

Lawrence *et al.* [94] have recently devised an electrochemical analog of the traditional spectroscopic methylene blue test (Section 3.2.2) in which oxidation *via* ferric ions is replaced by electron transfer at a glassy carbon electrode. The chemistry is aqueous-based (over a pH range of 3 - 6) and relies on the 1,4-Michael addition of sulfide to the electro-generated quinone-imine resulting in the formation of the corresponding thiol adduct which can be oxidised at the electrode surface to produce the analytical signal as shown in Scheme 3.2:



Scheme 3.2: Proposed reaction pathway for the electrochemically initiated reaction of DMPD and sulfide.

The increase in oxidative current was found to scale linearly with sulfide concentration within the range 3 μM to 150 μM (= 0.1 to 4.8 ppm) which compares favourably with detection range of other electrochemical techniques described in this chapter (Table 3.2). Methylene blue was not formed on the timescale of the voltammetric experiment but was detected spectroscopically at 460 nm only after prolonged electrochemical oxidation of DMPD in the presence of sulfide.

The reaction pathway has been shown to be generic in nature with a wide range of similarly structured molecules (catechol, dopamine, hydroquinone and p-aminophenol [96], diphenylamine (DPA), diphenylamine-4-sulfonic acid (DPS) and 4,4'-diaminophenylamine sulfate (DADPA) [95]) undergoing similar chemistry with sulfide. Each derivative was found capable of forming a quinoid intermediate upon oxidation and all responded to increasing concentration of sulfide in pH 4 buffer (typically over a range extending from 10 - 300 μM sulfide). The relative merits of each system are discussed and their analytical parameters (linear range, detection limits, redox potentials etc.) are tabulated for ease of comparison in Table 3.3.

Table 3.3: *Response of the different indicator species toward hydrogen sulfide* [95,96].

Compound[1]	**pH**	**Sensitivity**[2]	**N**[3]	**LoD**[4] **/ μM**	**Linear Range / μM**
DMPD	4	3.94×10^{-8} X	7	3	3 - 150
Hydroquinone	4	5.08×10^{-8} X	10	10	10 – 192
Hydroquinone	7	3.22×10^{-8} X	4	3	21 – 104
4-aminophenol	4	3.56×10^{-8} X	9	3	3 – 150
Cathecol	4	2.92×10^{-8} X	13	3	3 – 150
Dopamine	4	1.21×10^{-8} X	6	3	3 – 150
DADPA	4	7.94×10^{-8} X	8	3	3 - 150
DPS	4	1.60×10^{-8} X	8	3	3 - 150
DPA	4	N/A[5]	N/A[5]	N/A[5]	N/A[5]

[1]The concentration of each indicator species was 180 μM. [2]X = concentration of sulfide / μM, [3]N = number of data points on regression line, [4]LoD = calculated limit of detection based on $3s_b$, N/A[5] = non applicable with no calibration data obtained.

The electrochemical oxidation of phenylenediamine and its subsequent reaction with sulfide was employed as the main analytical signal in the realisation of a thin-layer Clark-type amperometric sensor [98] and in the application of a dual flow electrochemical cell [97] for the detection of the toxic gas.

The low solubility of a phenylenediamine derivative (N,N'-diphenyl-p-phenylenediamine, DPPD) was exploited as a means of developing reagentless and inexpensive sensors for sulfide in which DPPD is mechanically incorporated into carbon-epoxy [154,164] or screen printed carbon electrodes [99]. The voltammetric

response of the modified-screen printed electrodes was initially characterised in the absence of sulfide and a suitable pathway proposed consistent with the reaction occurring at the three-phase boundary between solid DPPD, C, and the aqueous solution. In the presence of sulfide a decrease in both the oxidative and reductive waves was observed, which was attributed to the sulfide effectively blocking the three-phase boundary. The response obtained at pH 4 produced a linear range from 20 to 165 μM, and a limit of detection of 7.5 μM for sulfide.

The electrochemical initiated reaction of sulfide with molecules with a quinoid-type structure was also successfully utilised for the quantification of thiols within biological matrices [93,165] .

3.2.5 Solid State Systems

Numerous works have described the implementation of solid state materials, usually involving metallic oxides, for the facile fabrication of sensors for detection of gaseous H_2S [155-157,166-168]. These systems are generally susceptible to temperature and humidity variations and offer less selectivity when compared with many of the methodologies described above. A more comprehensive assessment of their relative merit and limitations is discussed in ref. [158] and ref. [166].

3.3 Conclusion

A wide range of different methods are available to the analytical chemist for detection of hydrogen sulfide in both environmental samples, such as air, water sediment and sludge, and in biological samples such as human breath, biological tissues and fluids including blood and saliva. Most of these approaches provide adequate sensitivity and can be effectively moulded to suit a given application. However, interferences from other members of the sulfur family (anions or thiols) are still an issue in some

instances. Selectivity can be improved by the incorporation of column separation device or membrane systems. The latter approach has been successfully implemented in a number of electrochemical methods as a barrier against interferences.

In the recent years there has been a change in emphasis towards fast, inexpensive and on-site analysis. With the exception of some of the chromatographic techniques, many of the systems discussed in this chapter (in particularly the electrochemical approaches) hold significant promise for fulfilling such criteria.

In the next chapter we look at the electrochemically initiated reaction of sulfide with various benzoquinone derivatives as a means of detecting hydrogen sulfide in aqueous solution.

3.4 Chapter 3 References

[1] N. N. Greenwood, A. Earnshaw, *Chemistry of the Elements*, 2nd Ed., Butterworth Heinemann, Oxford, **1997**.

[2] P. Patnaik, *A Comprehensive Guide to the Hazardous Properties of Chemical Substances*, Wiley, New York, **1999**.

[3] R. P. Pohanish, S. A. Greene, *Hazardous Materials Handbook*, Van Nostrand Reinhold, New York, **1996**.

[4] W. L. Orr, J. S. Sinninghe Damste, in *Geochemistry of Sulphur in Fossil Fuels, ACS Symposium Serie 429* (Eds: W. L. Orr, C. M. White), American Chemical Society, Washington D.C. **1990**.

[5] A. C. Aplin, M. L. Coleman, in *The Geochemistry of Reservoirs* (Eds: J. M. Cubitt, W. A. England) London **1995**, pp. 303.

[6] R. D. Kane, R. J. Horvath, M. S. Cayard, *Wet H2S cracking of carbon steels and weldments*, NACE International, Houston, **1996**.

[7] M. R. Carlson, W. B. Cawston Obatining PVT data for very sour retrograde condensate gas and volatile oil reservoirs: a multi-disciplinary approach. *SPE Gas Tech. Conf.,*: Calgary, April-May 1996.

[8] G. Montegrossi, F. Tassi, O. Vaselli, A. Buccianti, K. Garofalo, *Anal. Chem.* **2001**, *73*, 3709.

[9] J. Font, J. Gutierrez, J. Lalueza, X. Perez, *J. Chromatogr., A* **1996**, *740*, 125.

[10] D. R. Salomon, J. P. Romano, *Process Control Qual.* **1992**, *3*, 219.

[11] C. H. S. J. Chou, *Concise International Chemical Assessment Document* **2003**, *53 (i-iv)*, 1.

[12] R. O. Beauchamp, Jr., J. S. Bus, J. A. Popp, C. J. Boreiko, D. A. Andjelkovich, *Crit. Rev. Toxicol.* **1984**, *13*, 25.

[13] R. J. Reiffenstein, W. C. Hulbert, S. H. Roth, *Annu. Rev. Pharm. Toxicol.* **1992**, *32*, 109.

[14] H. M. Ammann, *J. Hazardous Mat.* **1986**, *13*, 369.

[15] J. Rodriguez-Fernandez, J. M. Costa, R. Pereiro, A. Sanz-Medel, *Anal. Chim. Acta* **1999**, *398*, 23.

[16] D. C. Glass, *Annals of Occupational Hygiene* **1990**, *34*, 323.

[17] P. Nicholls, J. K. Kim, *Can. J. Biochem.* **1982**, *60*, 613.

[18] A. A. Khan, M. M. Schuler, M. G. Prior, S. Yong, R. W. Coppock, L. Z. Florence, L. E. Lillie, *Toxicol. Appl. Pharm.* **1990**, *103*, 482.

[19] *Health and Safety Executive: Occupational Exposure Limits* **2002**, *Publication: EH40/2002*, ISBN:07176220832.

[20] N. S. Lawrence, J. Davis, R. G. Compton, *Talanta* **2000**, *52*, 771.

[21] N. S. Lawrence, T. G. J. Jones, R. G. Compton, L. Jiang, *Chem. J. Chin. Uni* **2002**, *18*, 161.

[22] E. Fisher, *Ber. Dtsch. Chem. Ges.* **1883**, *16*, 2234.
[23] J. K. Fogo, M. Popowsky, *Anal. Chem.* **1949**, *21*, 732.
[24] L. M. Siegel, *Anal. Biochem.* **1965**, *11*, 126.
[25] N. Gilboa-Garber, *Anal. Biochem.* **1971**, *43*, 129.
[26] M. B. Jacobs, M. M. Braverman, S. Hochheiser, *Anal. Chem.* **1957**, *29*, 1349.
[27] W. L. Bamesberger, D. F. Adams, *Environ. Sci. Technol.* **1969**, *3*, 258.
[28] M. H. Stipanuk, P. W. Beck, *Biochem. J.* **1982**, *206*, 267.
[29] T. H. J. Florin, *Clin. Chim. Acta* **1991**, *196*, 127.
[30] H. Sakurai, S. Lien, A. San Pietro, *Anal. Biochem.* **1982**, *119*, 372.
[31] D. F. S. Natusch, H. B. Klonis, H. D. Axelrod, R. J. Teck, J. P. Lodge, Jr., *Anal. Chem.* **1972**, *44*, 2067.
[32] N. Balasubramanian, B. S. M. Kumar, *Analyst* **1990**, *115*, 859.
[33] E. A. Guenther, K. S. Johnson, K. H. Coale, *Anal. Chem.* **2001**, *73*, 3481.
[34] V. Kuban, P. K. Dasgupta, J. N. Marx, *Anal. Chem.* **1992**, *64*, 36.
[35] M. A. Spaziani, M. Tinani, M. K. Carroll, *Analyst* **1997**, *122*, 1555.
[36] M. Okumura, Y. Seike, K. Fujinaga, N. Yano, *Bunseki Kagaku* **1997**, *46*, 329.
[37] R. J. Cassella, R. E. Santelli, *Quim. Nova* **1995**, *18*, 536.
[38] R. J. Cassella, L. G. De Oliveira, R. E. Santelli, *Spectrosc. Letts.* **1999**, *32*, 469.
[39] T. D. Rees, A. B. Gyllenspetz, A. V. Docherty, *Analyst* **1971**, *96*, 201.
[40] F. A. Mohamed, M. A. AbdAllah, S. M. Shammat, *Talanta* **1997**, *44*, 61.
[41] H. Scharf, *Fres. J. Anal. Chem.* **1992**, *343*, 733.
[42] M. F. Mousavi, A. R. Ghiasvand, A. R. Jahanshahi, *Talanta* **1998**, *46*, 1011.
[43] A. Safavi, M. Mirzaee, *Anal. Letts.* **1999**, *32*, 971.
[44] A. Safavi, A. Rahmani, V. Naeemie Hosseini, *Fres. J. Anal. Chem.* **1996**, *354*, 502.
[45] A. Safavi, Z. Ramezani, *Talanta* **1997**, *44*, 1225.
[46] M. F. Mousavi, M. Shamsipur, *Bull. Chem. Soc. Japan* **1992**, *65*, 2770.
[47] M. Yaqoob, A. Nabi, A. Wahab, A. Bano, S. H. Shah, A. K. K. Achakzai, *J. Chem. Soc. Pakistan* **1998**, *20*, 214.
[48] M. Pandurangappa, N. Balasubramanian, *Environ. Poll.* **1997**, *94*, 255.
[49] A. K. Verma, V. K. Gupta, *Chemia Analityczna (Warsaw)* **1996**, *41*, 999.
[50] A. A. Ensafi, *Anal. Letts.* **1992**, *25*, 1525.
[51] K. Shanthi, N. Balasubramanian, *Microchemical J.* **1996**, *53*, 168.
[52] Y. Yamamoto, M. Umeda, K. Morishige, Y. Nishikawa, *Bunseki Kagaku* **1988**, *37*, 421.
[53] K. Shanthi, N. Balasubramanian, *Analyst* **1996**, *121*, 647.
[54] S. Bottrell, D. Banks, D. Bird, R. Raiswell, *Environ. Tech.* **1997**, *12*, 393.
[55] M. M. F. Choi, P. Hawkins, *Anal. Chim. Acta* **1997**, *344*, 105.
[56] M. M. F. Choi, P. Hawkins, *Sens. and Actuators, B* **2003**, *B90*, 211.
[57] A. A. Cardoso, H. Liu, P. K. Dasgupta, *Talanta* **1997**, *44*, 1099.
[58] J. Sanz, S. Cabredo, J. Galban, *Anal. Letts.* **1992**, *25*, 2095.
[59] S. C. Pinillos, I. S. Vicente, J. S. Asensio, *Talanta* **1995**, *42*, 937.
[60] L. Ebdon, S. J. Hill, M. Jameel, W. T. Corns, P. B. Stockwell, *Analyst* **1997**, *122*, 689.
[61] Q. Jin, H. Zhang, Y. Duan, A. Yu, X. Liu, L. Wang, *Talanta* **1992**, *39*, 967.
[62] P. Parvinen, L. H. J. Lajunen, *At. Spectrosc.* **1994**, *15*, 83.
[63] T. A. Arowolo, M. S. Cresser, *Talanta* **1992**, *39*, 1471.
[64] E. Guadagnino, O. Corumluoglu, *Glass Technol.* **1997**, *38*, 179.
[65] A. G. Howard, C. Y. Yeh, *Anal. Chem.* **1998**, *70*, 4868.
[66] K. Hoppstock, H. Lippert, *At. Spectrosc.* **1997**, *18*, 35.
[67] I. L. Garcia, P. Vinas, J. A. M. Gil, *Fres. J. Anal. Chem.* **1993**, *345*, 723.
[68] M. Ishii, M. Miura, J. Sato, *Bunseki Kagaku* **1992**, *41*, 157.
[69] S. C. Jain, N. Singh, M. Singla, A. K. Aggarwal, *J. Sci. Indust. Res.* **1999**, *58*, 355.
[70] E. S. Larsen, M. L. Spartz, *Mikrochimica Acta, Supplement* **1997**, *14*, 555.
[71] G. Modugno, C. Corsi, M. Gabrysch, M. Inguscio, *Opt. Commun.* **1998**, *145*, 76.
[72] L. A. Shelef, W. Tan, *J. Food Prot.* **1998**, *61*, 620.
[73] Orion, *9614A Sulphide Ion Selective Electrode*, Orion Research Inc., Beverly, MA, USA,
[74] V. Stanic, T. H. Etsell, A. C. Pierre, R. J. Mikula, *Electrochim. Acta* **1998**, *43*, 2639.
[75] Y. L. Ma, A. Galal, H. Zimmer, H. B. Mark, Jr., Z. F. Huang, P. L. Bishop, *Anal. Chim. Acta* **1994**, *289*, 21.
[76] Y. H. Tse, P. Janda, A. B. P. Lever, *Anal. Chem.* **1994**, *66*, 384.
[77] Y.-H. Tse, P. Janda, H. Lam, A. B. P. Lever, *Anal. Chem.* **1995**, *67*, 981.
[78] S. I. Krichmar, V. M. Bezpalchenko, *Industr. Labor.* **1995**, *61*, 621.
[79] S. I. Krichmar, A. Y. Shepel, *J. An. Chem.* **1996**, *51*, 277.
[80] X. Hu, Z. Leng, *Anal. Commun.* **1996**, *33*, 297.
[81] B. Muller, R. Stierli, *Anal. Chim. Acta* **1999**, *401*, 257.

[82] A. V. Kroll, V. I. Smorchkov, A. Y. Nazarenko, *Sens. and Actuators, B* **1994**, *B21*, 97.
[83] P. Jeroschewski, S. Braun, *Fres. J. Anal. Chem.* **1996**, *354*, 169.
[84] P. Jeroschewski, K. Haase, A. Trommer, P. Gruendler, *Fres. J. Anal. Chem.* **1993**, *346*, 930.
[85] P. Jeroschewski, K. Haase, A. Trommer, P. Gruendler, *Electroanalysis* **1994**, *6*, 769.
[86] P. Jeroschewski, C. Steuckart, M. Kuehl, *Anal. Chem.* **1996**, *68*, 4351.
[87] M. Becker, M. Martienssen, B. Fuhrmann, U. Spohn, *Acta Biotech.* **1997**, 39.
[88] G. Schiavon, G. Zotti, R. Toniolo, G. Bontempelli, *Anal. Chem.* **1995**, *67*, 318.
[89] N. Batina, I. Ciglenecki, B. Cosovic, *Anal. Chim. Acta* **1992**, *267*, 157.
[90] P. C. Do Nascimento, D. Bohrer, J. Tramontina, *Analyst* **1997**, *122*, 835.
[91] R. Al-Farawati, C. M. G. van den Berg, *Marine Chemistry* **1997**, *57*, 277.
[92] J. S. Redinha, C. Paliteiro, J. L. C. Pereira, *Anal. Chim. Acta* **1997**, *351*, 115.
[93] N. S. Lawrence, J. Davis, R. G. Compton, L. Jiang, T. G. J. Jones, S. N. Davis, *Analyst* **2000**, *125*, 661.
[94] N. S. Lawrence, J. Davis, L. Jiang, T. G. J. Jones, S. N. Davies, R. G. Compton, *Electroanalysis* **2000**, *12*, 1453.
[95] N. S. Lawrence, J. Davis, L. Jiang, T. G. J. Jones, S. N. Davies, R. G. Compton, *Electroanalysis* **2001**, *13*, 143.
[96] N. S. Lawrence, J. Davis, L. Jiang, T. G. J. Jones, S. N. Davies, R. G. Compton, *Electroanalysis* **2001**, *13*, 432.
[97] N. S. Lawrence, J. Davis, F. Marken, L. Jiang, T. G. J. Jones, S. N. Davies, R. G. Compton, *Sens. and Actuators, B* **2000**, *B69*, 189.
[98] N. S. Lawrence, L. Jiang, T. G. J. Jones, R. G. Compton, *Anal. Chem.* **2003**, *75*, 2499.
[99] N. S. Lawrence, L. Jiang, T. G. J. Jones, R. G. Compton, *Anal. Chem.* **2003**, *75*, 2054.
[100] N. S. Lawrence, M. Thompson, J. Davis, L. Jiang, T. G. J. Jones, R. G. Compton, *Mikrochimica Acta* **2001**, *137*, 105.
[101] N. S. Lawrence, M. Thompson, C. Prado, L. Jiang, T. G. J. Jones, R. G. Compton, *Electroanalysis* **2002**, *14*, 499.
[102] F. Marken, A. Blythe, R. G. Compton, S. D. Bull, S. G. Davies, *Chem. Commun.* **1999**, 1823.
[103] M. I. Prodromidis, P. G. Veltsistas, M. I. Karayannis, *Anal. Chem.* **2000**, *72*, 3995.
[104] D. W. Gruenwedel, R. K. Patnaik, *J. Agricult. Food Chem.* **1971**, *19*, 775.
[105] D. L. Ehman, *Anal. Chem.* **1976**, *48*, 918.
[106] P. F. Cook, R. T. Wedding, *J. Biol. Chem.* **1976**, *251*, 2023.
[107] B. H. McAnalley, W. T. Lowry, R. D. Oliver, J. C. Garriott, *J. Anal. Toxicol.* **1979**, *3*, 111.
[108] S. U. Khan, G. F. Morris, M. Hidiroglou, *Microchemical J.* **1980**, *25*, 388.
[109] R. T. Wedding, *Methods Enzymol.* **1987**, *143*, 29.
[110] H. Lindell, P. Jappinen, H. Savolainen, *Analyst* **1988**, *113*, 839.
[111] P. Jappinen, R. Tenhunen, *Brit. J. Ind. Med., 47*, 283.
[112] W. Puacz, W. Szahun, K. Linke, *Analyst* **1995**, *120*, 939.
[113] T.-M. Hseu, G. A. Rechnitz, *Anal. Chem.* **1968**, *40*, 1054.
[114] Y. Wang, g. Fangqiu, H. Lanfang, Z. Minghao, *Huangjin* **2003**, *24*, 44.
[115] M. Miura, K. Fukasawa, T. Koh, *J. Chromatogr. A* **1998**, *804*, 143.
[116] M. Okumura, N. Yano, K. Fujinaga, Y. Seike, S. Matsuo, *Anal. Sci.* **1999**, *15*, 427.
[117] T. Ramstad, A. H. Bates, T. J. Yellig, S. J. Borchert, K. A. Mills, *Analyst* **1995**, *120*, 2775.
[118] R. Simo, J. O. Grimalt, *J. Chromatogr., A* **1996**, *726*, 161.
[119] J. Radford-Knoery, G. A. Cutter, *Anal. Chem.* **1993**, *65*, 976.
[120] P. R. Berube, P. D. Parkinson, E. R. Hall, *J. Chromatogr., A* **1999**, *830*, 485.
[121] J. B. Laurens, E. R. Rohwer, *J. High Res. Chromatogr.* **1996**, *19*, 217.
[122] I. Devai, R. D. DeLaune, *Field Anal. Chem. Tech.* **1997**, *1*, 145.
[123] U. Brunner, T. G. Chasteen, P. Ferloni, R. Bachofen, *Chromatographia* **1995**, *40*, 399.
[124] Y. Ogasawara, K. Ishii, T. Togawa, S. Tanabe, *Analyst* **1991**, *116*, 1359.
[125] C. Gru, P. M. Sarradin, H. Legoff, S. Narcon, J. C. Caprais, F. H. Lallier, *Analyst* **1998**, *123*, 1289.
[126] T. W. Mitchell, J. C. Savage, D. H. Gould, *J. Appl. Toxicol.* **1993**, *13*, 389.
[127] K. Nagashima, K. Fukushima, M. Kamaya, *J. Liq. Chromatogr.* **1995**, *18*, 515.
[128] P. R. Haddad, A. L. Heckenberg, *J. Chromatogr.* **1988**, *447*, 415.
[129] J. F. van Staden, L. G. Kluever, *Anal. Chim. Acta* **1998**, *369*, 157.
[130] B. Divjak, W. Goessler, *J. Chromatogr., A* **1999**, *844*, 161.
[131] F. Hissner, J. Mattusch, K. Heinig, *J. Chromatogr., A* **1999**, *848*, 503.
[132] A. A. Ensafi, M. Samimifar, *Anal. Letts.* **1994**, *27*, 153.
[133] R. D. Rocklin, E. L. Johnson, *Anal. Chem.* **1983**, *55*, 4.
[134] M. W. Warenycia, L. R. Goodwin, C. G. Benishin, R. J. Reiffenstein, D. M. Francom, J. D. Taylor, F. P. Dieken, *Biochem. Pharm.* **1989**, *38*, 973.
[135] T. Ubuka, T. Abe, R. Kajikawa, K. Morino, *J. Chromatogr., B: Biomed. Appl.* **2001**, *757*, 31.

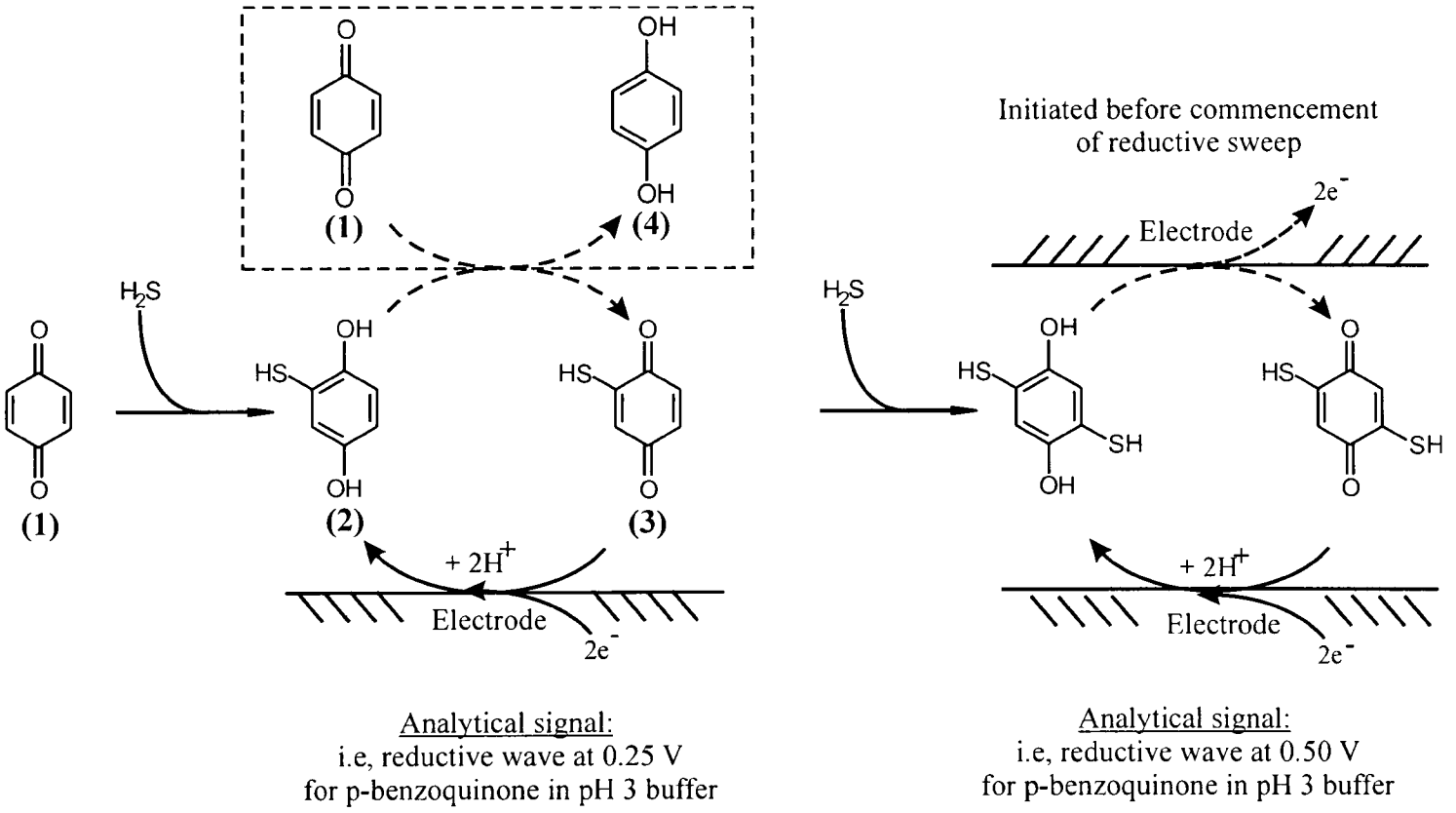
[136] S. S. Brody, J. E. Chaney, *J. Gas Chromatogr.* **1966**, *4*, 42.
[137] N. Ichinose, C. Shimizu, K. Okamoto, T. Inui, K. Adachi, *Anal. Sci.* **1987**, *3*, 131.
[138] G. A. Cutter, T. J. Oatts, *Anal. Chem.* **1987**, *59*, 717.
[139] S. Kage, T. Nagata, K. Kimura, K. Kudo, *J. Forensic Sci.* **1988**, *33*, 217.
[140] N. Nakano, A. Yamamoto, Y. Kobayashi, K. Nagashima, *Bunseki Kagaku* **1994**, *43*, 645.
[141] H. D. Fiedler, R. Rubio, G. Rauret, I. Casals, *Talanta* **1999**, *48*, 403.
[142] D. H. Dawson, G. S. Henshaw, D. E. Williams, *Sens. and Actuators, B* **1995**, *26*, 76.
[143] T. Meyer-Jens, G. Matz, H. Maerkl, *Appl. Microbiol. Biotech.* **1995**, *43*, 341.
[144] M. Volkan, T. Eroglu, A. E. Eroglu, O. Y. Ataman, H. B. Mark, Jr., *Talanta* **1998**, *47*, 585.
[145] Z. Pawlak, A. S. Pawlak, *Talanta* **1999**, *48*, 347.
[146] J. Wall, B. Chiswell, B. Hamilton, C. Dieckmann, K. O'Halloran, *Talanta* **1997**, *45*, 85.
[147] M. F. Mousavi, N. Sarlack, *Anal. Letts.* **1997**, *30*, 1567.
[148] M. M. F. Choi, *Analyst* **1998**, *123*, 1631.
[149] A. Lopez-Molinero, R. Batlle, A. Villareal, J. R. Castillo, *Talanta* **1996**, *43*, 1565.
[150] M. Garcia-Calzada, G. Marban, A. B. Fuertes, *Anal. Chim. Acta* **1999**, *380*, 39.
[151] J. Raba, M. A. Mallea, S. Quintar, V. A. Cortinez, *Talanta* **1992**, *39*, 1007.
[152] B. Vallejo, P. Richter, I. Toral, C. Tapia, M. D. Luque de Castro, *Anal. Chim. Acta* **2001**, *436*, 301.
[153] J.-M. Zen, P.-Y. Chen, A. S. Kumar, *Electroanalysis* **2002**, *14*, 513.
[154] M. Pandurangappa, N. S. Lawrence, L. Jiang, T. G. J. Jones, R. G. Compton, *Analyst* **2003**, *128*, 473.
[155] S. J. Hawkins, N. M. Ratcliffe, A. Sagastizabal, *Anal. Chim. Acta* **1998**, *359*, 125.
[156] T. L. Royster, D. Chatterjee, G. R. Paz-Pujalt, C. A. Marrese, *Sens. and Actuators, B* **1998**, *53*, 155.
[157] M. Miura, Y. Yan, G. Lu, N. Yamazoe, *Sens. and Actuators, B* **1996**, *34*, 367.
[158] D. E. Williams, *Sens. and Actuators, B* **1999**, *57*, 1.
[159] S. Persson, M. B. Edlund, R. Claesson, J. Carlsson, *Oral Microbiol. Immunol.* **1990**, *5*, 195.
[160] K. Yaegaki, K. Sanada, *J. Periodontal Res.* **1992**, *27*, 233.
[161] K. R. Christensen, G. A. Reineccius, *J. Dairy Sci.* **1992**, *75*, 2098.
[162] K. Kimura, M. Hasegawa, K. Matsubara, C. Maseda, M. Kagawa, S. Takahashi, K. Tanabe, *Forens. Sci., 66*, 111.
[163] J. Furne, J. Springfield, T. Koenig, E. DeMaster, M. D. Levitt, *Biochem. Pharm.* **2001**, *62*, 255.
[164] M. Thompson, N. S. Lawrence, J. Davis, L. Jiang, T. G. J. Jones, R. G. Compton, *Sens. and Actuators, B* **2002**, *B87*, 33.
[165] P. C. White, N. S. Lawrence, J. Davis, R. G. Compton, *Anal. Chim. Acta* **2001**, *447*, 1.
[166] P. T. Moseley, J. O. W. Norris, D. E. Williams, *Tecniques and Mechanisms in Gas Sensing*, **1991**.
[167] V. V. Malyshev, G. S. Pislyakov, *Sens. and Actuators, B* **1998**, *47*, 181.
[168] K. F. E. Pratt, D. E. Williams, *Sens. and Actuators, B* **1997**, *45*, 147.

Chapter 4: "Electrochemical Characterisation of Sulfide Tagging *via* its Reaction with Benzoquinone Derivatives"

In the previous chapter (Section 3.2.4.1) it was shown that several molecules with quinoid-type structure can undergo electrochemically initiated 1,4-Michael addition with sulfide to produce an analytical signal [1-6]. In this chapter the determination of sulfide is demonstrated by its electrochemically initiated reaction with a range of structurally diverse substituted benzoquinone species (p-benzoquinone, 2,3-dimethoxy-5-methyl-p-benzoquinone, 2,6-dimethoxy-p-benzoquinone and 3,5-ditert-butyl-o-benzoquinone). It is shown that by judicious choice of the pH of the solution analytical signals can be obtained for each species; the relative merits of each indicator are discussed and their corresponding analytical parameters are tabulated for ease of comparison. The results detailed have been subsequently published in Analytical Letters [7].

4.1 Introduction

Recent reports have utilised the chemical reaction of various thiol species with different benzoquinone derivatives as a means of producing an electrochemical label for the benzoquinone-thiol adduct [5,6,8] which is then used to determine the concentration of thiol present in the media under investigation. The addition of thiols to quinone moieties is well established, forming the basis of numerous spectroscopic [9-12] and pre-column chromatographic derivatisation protocols [13,14]. The basic reaction pathway exploited in the proposed protocol is shown in scheme 4.1 with the foundations of the approach relying on the ability of the electrochemical technique to primarily differentiate between the unreacted quinone 1 (scheme 4.1), and the consequent quinone-thiol adduct 2 and 3 (scheme 4.1).



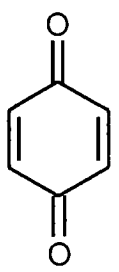
Scheme 4.1: Proposed tagging and detection pathway.

The generic nature of this reaction pathway has been demonstrated through the electrochemically initiated reaction of hydroquinone with thiols as a means of

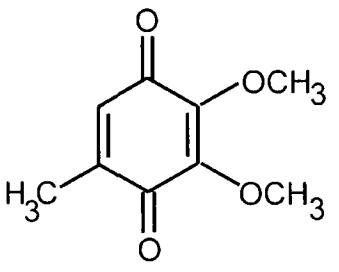
electrochemically tagging proteins in which the product is detected using mass spectrometry [15-17].

In the following report the generic nature of this reaction process is probed further and used as a means of determining hydrogen sulfide *via* its reaction with benzoquinone and its derivatives. Initial studies focus on the direct reaction of p-benzoquinone with sulfide and it is shown that multiple substitution reactions arise as a result of the adduct becoming re-oxidised by unmodified quinone 1 and 4 (scheme 4.1). As such a range of structurally diverse benzoquinone indicator species have been examined (scheme 4.2) in which blocking groups are placed around the benzene ring.

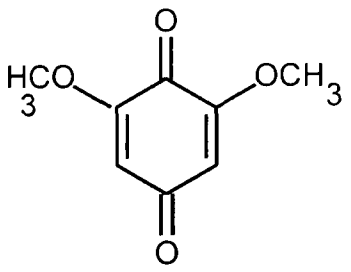
It can be foreseen the use of a low solubility benzoquinone species (i.e., 3,5-ditert-butyl-o-benzoquinone (3,5DTBQ)) that could be incorporated into a carbon based screen printed electrode [18-21] thereby allowing the development of a 'reagentless' sensor for sulfide.



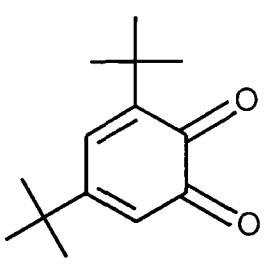
***p*-benzoquinone**
(BQ)



2,3-dimethoxy-5-methyl-p-benzoquinone
(2,3 DMBQ)



2,6-dimethoxy-p-benzoquinone
(2,6 DBQ)



3,5-di-tert-butyl-o-benzoquinone
(3,5 DTBQ)

Scheme 4.2: Structure of the various benzoquinone derivatives studied.

4.2 Results and Discussion

Initial analysis of the reaction of benzoquinone derivatives with sulfide centred upon understanding the reaction of p-benzoquinone with sulfide.

4.2.1 Reaction of p-Benzoquinone with Sulfide

4.2.1.1 Square wave voltammetric response of p-benzoquinone to increasing additions of sulfide

The possibility of providing sulfide with a redox label *via* its direct reaction with p-benzoquinone was first investigated using square wave voltammetry (frequency = 25 Hz, step potential = 2 mV, amplitude = 25 mV). The corresponding voltammetric responses obtained at a glassy carbon electrode for a solution (pH 3, 0.1 M acetate buffer) containing 0.5 mM p-benzoquinone to increasing additions of sulfide are depicted in figure 4.1 (a) and 4.1 (b). Figure 4.1 (a) shows the response when 0 to 0.18 mM sulfide is introduced to the solution and figure 4.1 (b) reveals the response when 0.2 to 0.5 mM sulfide is present in the solution.

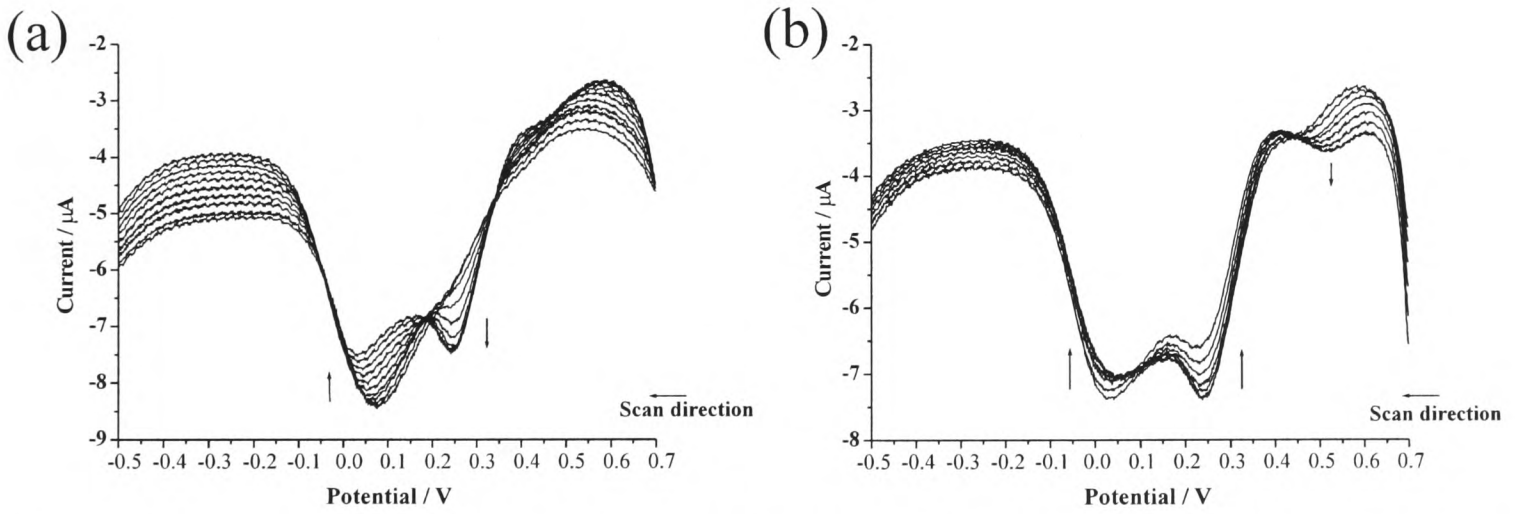


Figure 4.1: Square wave voltammetric response of a 0.5 mM solution of p-benzoquinone (pH 3, 0.1 M acetate buffer) to increasing concentration of sulfide from 0 to 0.18 mM (a) and from 0.2 to 0.50 mM (b), see text.

The voltammetric response obtained in the absence of any sulfide shown in figure 4.1(a) reveals a single broad reduction wave at +0.08 V which can be attributed to the

two-electron reduction of p-benzoquinone to its corresponding hydroquinone species as expressed by:

$$Q + 2e^- + 2H^+ \rightleftharpoons QH_2 \qquad (4.1)$$

Upon the addition of low concentrations of sulfide (giving aliquots of 0.02 mM sulfide up to 0.18 mM, figure 4.1(a)) to the solution a new voltammetric wave emerges at +0.25 V and the main reductive wave at +0.08 V due to the reduction of p-benzoquinone decreases. The wave at +0.25 V continues to enhance until 0.14 mM sulfide is present in solution after which the peak current stabilises. Upon subsequent additions of sulfide (0.20 to 0.5 mM, figure 4.1(b)) a second new redox wave emerges at +0.50 V, whilst the new wave at +0.25 V begins to decrease. Similar observations were made when cysteine was added to a p-benzoquinone solution [5]. The first wave to emerge at +0.25 V can be attributed to the reduction of the mono-substituted p-benzoquinone adduct (scheme 4.1) whereas the second wave to emerge at higher concentrations of sulfide can be attributed to the formation and reduction of di-substituted species (scheme 4.1). It is worth noticing that the second new wave at +0.50 V emerges when the concentration of sulfide is approximately half the concentration of p-benzoquinone, and it is to this observation that we next turn our attention.

4.2.1.2 Effects of time on the voltammetric response of the p-benzoquinone-sulfide solution

Figure 4.2 details the voltammetric responses obtained at a glassy carbon electrode when placed into a solution containing 0.5 mM p-benzoquinone and 0.25 mM sulfide (pH 3, 0.1 M acetate buffer). In this case the response is recorded every twenty seconds after the addition of sulfide. Also overlaid is the response of a solution containing only 0.5 mM p-benzoquinone.

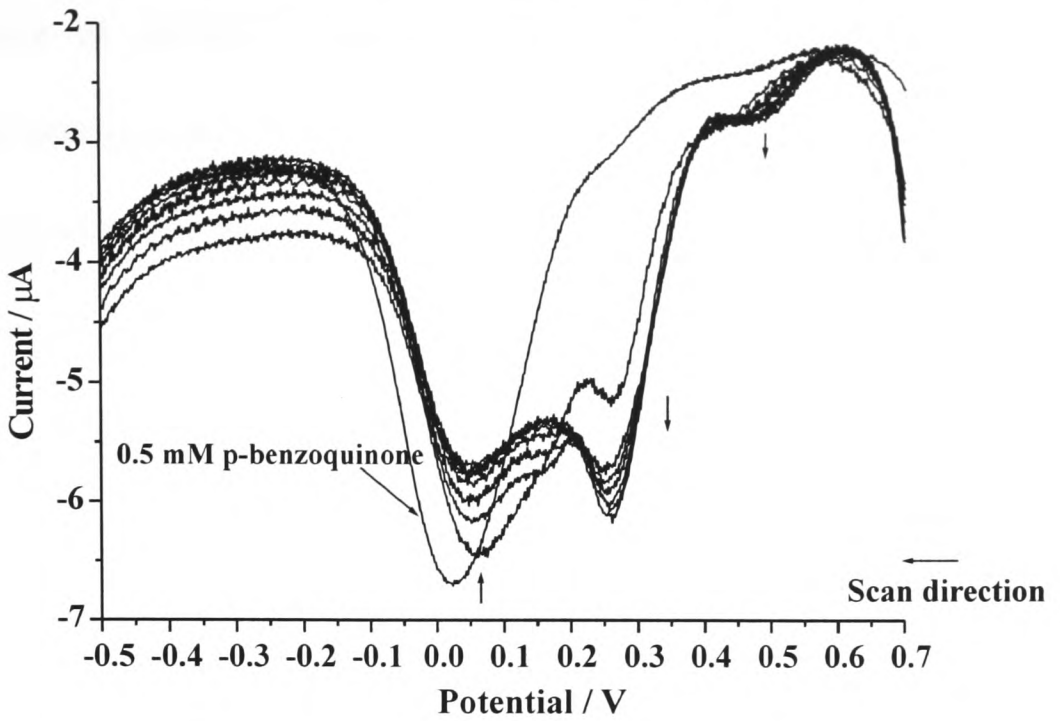


Figure 4.2: The voltammetric response of a solution containing 0.5 mM p-benzoquinone and 0.25 mM sulfide in which a scan is recorded every 20 seconds after the addition of sulfide.

In the absence of sulfide a single reduction wave is observed at +0.02 V consistent with that observed in figure 4.1 (a). Analysis of the responses obtained over the first minute after the addition of sulfide reveals that a new wave emerges at +0.26 V after twenty seconds. This wave continues to grow until a steady current is reached after sixty seconds. The occurrence of this wave coincides with a decrease in the reduction peak current at +0.02 V indicating the parent p-benzoquinone species is being consumed in a reaction. This wave is therefore attributed to the reduction of the oxidised mono-substituted benzoquinone-sulfide adduct (scheme 4.1). After the initial sixty seconds the magnitude of the new reduction peak at +0.25 V begins to decrease. This decrease is accompanied by the occurrence of a third reduction process at +0.48 V which continues to enhance with time. It was found that a stable voltammetric response was obtained after 140 seconds. In order to verify that the new reduction process can be attributed to a solution based moiety rather than an adsorbed species the electrode was taken from the experimental solution, placed into a fresh pH 3 buffer and the voltammetric response recorded. The corresponding response (not shown) revealed no reduction processes in the scan range studied. This suggests that

the new wave at +0.48 V corresponds to the reduction of the solution phase di-substituted benzoquinone-sulfide adduct.

In order to elucidate the reaction mechanism, the same experiment was repeated for a solution containing equimolar concentration of p-benzoquinone and sulfide (= 0.5 mM). The corresponding voltammetric responses were found to be analogous to those shown in figure 4.2. A new reduction wave was first observed at +0.25 V after which a second reduction process occurred at +0.48 V. However, in this case the time taken for the second wave to emerge at +0.48 V was found to be forty seconds rather than sixty seconds.

This can be rationalised as follows: at lower concentrations of sulfide the initial reaction to form the mono-substituted adduct will dominate and the rate of oxidation of this adduct to its quinone form (step 1) will be the rate determining step. Therefore the amount of di-substituted species will depend on this rate. However, when the concentration of sulfide is increased then the time taken to form the di-substituted will be decreased as there is more sulfide present in the solution to attack the oxidised mono-substituted adduct to form the di-substituted species (scheme 4.1).

It was also noted that during the standard addition experiment the solution was seen to physically change colour from colourless to yellow back to colourless at the higher concentrations of sulfide. This will be further discussed in the next section.

Unfortunately due to the overlapping nature of the electrochemical waves obtained for the benzoquinone species and the sulfide-benzoquinone adducts the kinetics of the reaction are not elucidated.

4.2.1.3 Spectroscopic examination of the reaction process of p-benzoquinone with sulfide

In order to characterise the reaction process further UV/Visible spectroscopy was next utilised. In these experiments six different solutions were analysed. Each solution (pH 3 acetate buffer) contained 0.5 mM p-benzoquinone and increasing additions of sulfide were introduced to each one (0 mM, 0.125 mM, 0.25 mM, 0.375 mM, 0.5 mM and 1.0 mM).

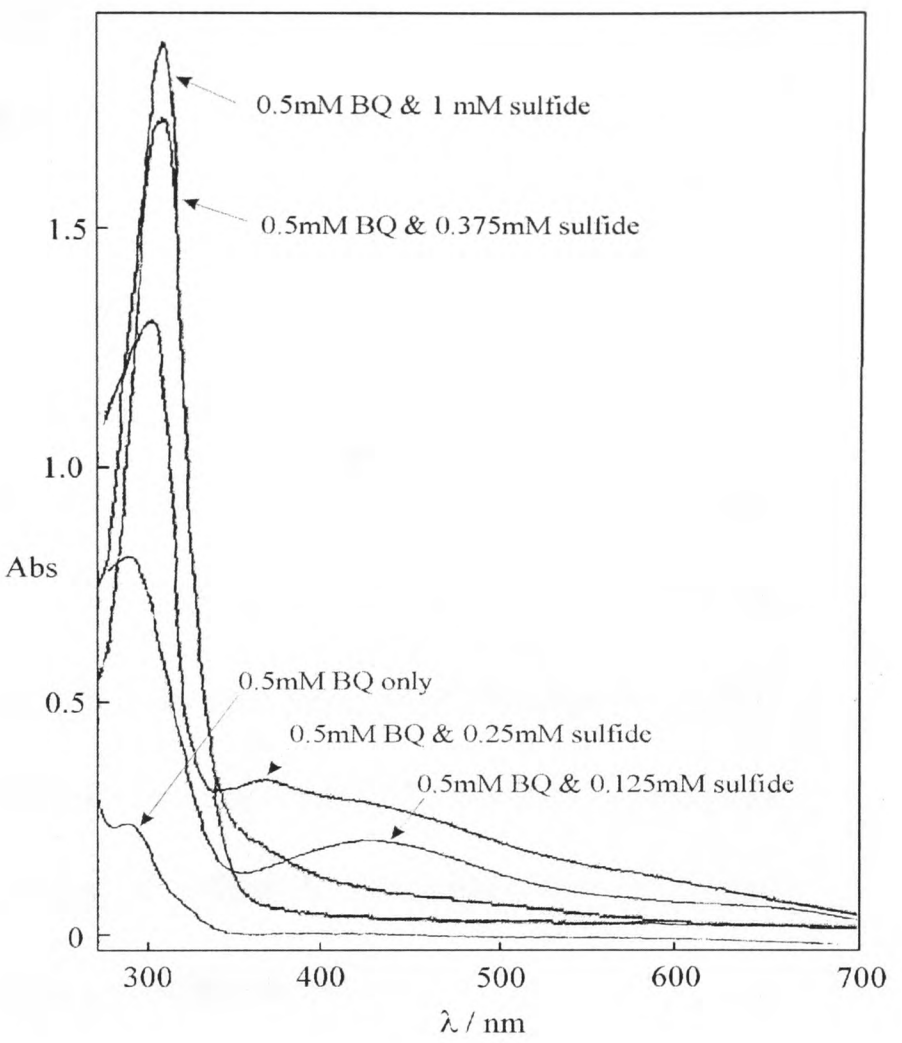


Figure 4.3: UV/Vis spectra obtained for five different solutions each containing 0.5 mM p-benzoquinone (pH 3, acetate buffer) to increasing additions of sulfide (0 mM, 0.125 mM, 0.25 mM, 0.375 mM and 1 mM).

The corresponding UV/Vis voltammograms obtained for each solution are overlaid in figure 4.3. The results show that in the absence of any sulfide a single absorbance wave is observed at 287 nm consistent with literature values [22]. Upon the first addition of sulfide (0.125 mM) to the solution the absorbance at 287 nm increases and a new wave emerges with an absorbance maximum at 416 nm. The next addition of sulfide (0.25 mM) shows a maximum absorbance at 293 nm and a second absorbance maximum at 373 nm occurs. It is worth noticing that when sulfide is added to a solution containing 0.5 mM p-benzoquinone as a 0.125 mM and 0.25 mM concentration, the resulting solution changes from a colourless to a yellow solution. The emergence of the new wave at 416 nm (for the solution containing 0.125 mM sulfide) and at 373 nm (for the solution containing 0.25 mM sulfide) can be tentatively

attributed to the formation of the oxidised and reduced forms of the mono-substituted p-benzoquinone-sulfide adduct (scheme 4.1) in the solution.

Upon subsequent additions of sulfide (from 0.375 to 1 mM) the solution returns to colourless and these waves diminishes and the spectra are characterised by a single new wave at 306 nm which can be attributed to the formation of the di-substituted p-benzoquinone-sulfide adduct (scheme 4.1).

It appears that when the sulfide concentration is equal to or less than half the concentration of p-benzoquinone present, the waves at 416 nm or 373 nm are present whereas at higher concentrations these diminish and the maximum at 306 nm enhances. This behaviour is analogous to that detailed above in figure 4.1 for the voltammetric response of p-benzoquinone to increasing sulfide concentrations. In this case it is shown that at sulfide concentrations less than half of the p-benzoquinone concentration present the voltammetric wave at +0.08 V dominates but at higher concentrations this diminishes and a new wave emerges at +0.25 V.

UV / Vis were also recorded over time (from 0 to 60 minutes) for solutions containing 0.5 mM p-benzoquinone (pH 3 acetate buffer) each and increasing additions of sulfide (0.25 mM, 0.5 mM and 1.0 mM). When the spectrum was recorded immediately after adding 0.25 M sulfide to the p-benzoquinone solution, a single maximum was observed at 303 nm. However, when the spectrum was recorded after 10 minutes the absorbance at 298 nm increased and a second absorbance maximum was seen at 373 nm, consistent with the observations above. The absorbance at 373 nm increased with time and finally stabilised after 30 minutes.

When the sulfide was present at concentration greater than a half that of p-benzoquinone, no absorbance maximum at 373 nm was observed and the spectra exhibited a single absorbance maximum at 306 nm, consistent with only the di-substituted p-benzoquinone being present in the solution.

This behaviour can be rationalised by the reaction mechanism detailed in scheme 4.1. Upon the initial addition of sulfide to the solution this reacts with p-benzoquinone to form the hydroquinone-sulfide adduct. In order for this to react further with any remaining sulfide, the hydroquinone-sulfide adduct has to be oxidised to the benzoquinone-sulfide adduct. To achieve this one molecule of benzoquinone has to be reduced for each molecule for the hydroquinone-sulfide adduct oxidised. Therefore the maximum concentration of mono-substituted p-benzoquinone adduct is half the concentration of the un-substituted p-benzoquinone.

When the ratio of sulfide to quinone is greater than 1:2, the sulfide immediately reacts with the mono-substituted p-benzoquinone to form the di-substituted p-benzoquinone. Unfortunately once again due to the overlapping nature of the spectroscopic signals obtained for the benzoquinone species and the sulfide-benzoquinone adducts the kinetics of the reaction are not readily elucidated. We next look at optimising the experimental conditions for the analytical determination of sulfide.

4.2.1.4 Voltammetric response of p-benzoquinone to increasing sulfide from pH 3 to 10

The square wave voltammetric response of p-benzoquinone to increasing additions of sulfide was examined over a wide pH range (from pH 3 to pH 10). The corresponding current-potential profiles obtained at pH 5 and pH 7 for solutions containing 0.5 mM p-benzoquinone and increasing additions of sulfide (0.02 - 0.2 mM) are detailed in figures 4.4 (a) and 4.4 (b), respectively. It should be noted that in these cases the sulfide concentration was kept low such that only the mono-substituted adduct should be present in the solution.

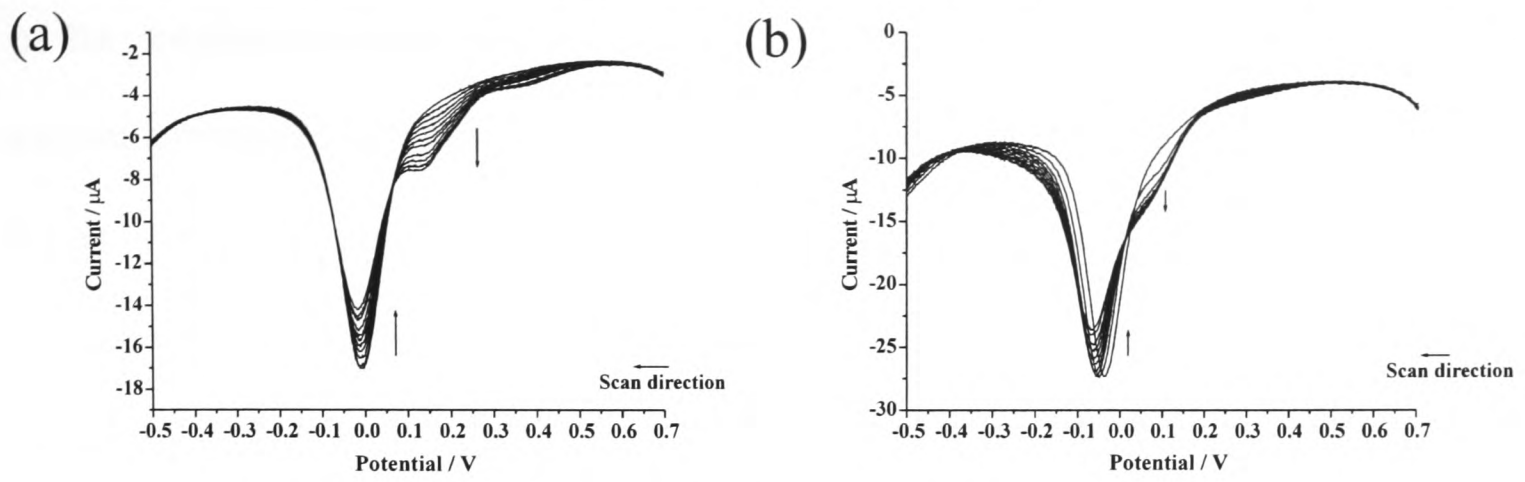


Figure 4.4: Square wave voltammetric responses obtained for solutions of 0.5m M p-benzoquinone to increasing additions of sulfide (0.02 - 0.2 mM) in (a) pH 5 acetate buffer and (b) pH 7 phosphate buffer.

In the absence of sulfide the response at pH 5 shows a single reduction wave at -0.01 V consistent with a two-electron reduction of benzoquinone to the hydroquinone structure as given in equation (4.1) (*vide supra*). Upon the addition of sulfide to the solution a new wave emerges at +0.15 V and this can be attributed to the reduction of the oxidised mono-substituted species.

Similarly the response obtained at pH 7 reveals a single reductive process at -0.03 V in the absence of sulfide and the emergence of a new wave at +0.10 V when sulfide is introduced to the solution, consistent with the voltammetric behaviour observed previously at the lower pHs. However, this new reduction wave at +0.10 V is not well resolved from the main reduction wave at -0.03 V attributed to the reduction of the parent benzoquinone species and as such its analytical utility is compromised.

It was also observed that the voltammetric responses obtained at higher concentrations of sulfide (not shown) produced a second new reductive wave (at +0.45 V and at +0.40 V at pH 5 and pH 7, respectively). A comparison of the voltammetric responses detailed in figures 4.1 and 4.4, reveals that as the pH increases the voltammetric waves attributed to the direct reduction of p-benzoquinone and the benzoquinone sulfide adduct begin to merge. In fact the response (not shown) at pH 10 revealed a slight shoulder when sulfide was added at potentials negative of the wave attributed to the reduction of p-benzoquinone. Overall these results suggest that by increasing the pH

of the solution the analytical utility of monitoring sulfide by examining the peak current attributed to the benzoquinone-sulfide adduct becomes compromised.

It can be predicted that the analytical capabilities of utilising benzoquinone as a redox indicator for sulfide even under the optimised pH conditions becomes hindered by the fact that p-benzoquinone can undergo multiple additions by sulfide (*vide supra*). This complicates the voltammetric signal and may decrease the sensitivity for sulfide detection. Therefore in order to overcome such problems the voltammetric response of a range of sterically hindered benzoquinones to sulfide was examined and it is this to which we turn next.

4.2.2 Reaction of a Range of Sterically Hindered Benzoquinones with Sulfide

The voltammetric response of three diverse benzoquinone structures (2,3-dimethoxy-5-methyl-p-benzoquinone (2,3DMBQ), 2,6-dimethoxy-p-benzoquinone (2,6DBQ) and the low solubility 3,5-ditert-butyl-o-benzoquinone (3,5DTBQ), (scheme 4.2)) to increasing sulfide concentrations was next examined over a wide range of pHs (from pH 3 to pH 7) as a means of optimising the experimental conditions for sulfide detection. These conditions occur when the voltammetric signal of the parent benzoquinone and the sulfide-benzoquinone adduct are well resolved in terms of peak potentials.

The corresponding data obtained for each of the three substituted benzoquinone species studied is detailed in table 4.1. This compares the peak potentials of the three benzoquinone waves at each pH studied along with the peak potentials of any new redox waves observed when sulfide was added to the solution. Also detailed for comparison are the peak potentials of the waves observed when p-benzoquinone is the indicator species. In this case only the reduction wave attributed to the mono-substituted benzoquinone-sulfide adduct is shown.

Table 4.1: *The various voltammetric waves attributed to both benzoquinone and to the benzoquinone-sulfide adduct when sulfide (0.02 - 0.2 mM) was introduced to solutions containing different benzoquinones at different pHs.*

	pH 3		pH 5		pH 7	
Compound	**BQ**	**BQ-Su**	**BQ**	**BQ-Su**	**BQ**	**BQ-Su**
2,3DMBQ	-0.13 V	N/A	-0.16 V	-0.07 V	-0.22 V	-0.10 V
2,6DBQ	+0.05 V	N/A	-0.12 V	N/A	-0.22 V	-0.09 V
3,5DTBQ	+0.08 V	+0.45	+0.02 V	+0.35 V	-0.05 V	+0.25 V
p-BQ	+0.08 V	+0.25	-0.01 V	+0.15 V	-0.03 V	+0.10 V

BQ = peak potential attributed to the reduction of the benzoquinone, BQ-Su = peak potential attributed to the reduction of the benzoquinone-sulfide adduct. 0.5 mM 2,3DMBQ = 2,3-Dimethoxy-5-methyl-p-benzoquinone, 0.5 mM 2,6DBQ = 2,6-Dimethoxy-p-benzoquinone, 0.25 mM 3,5DTBQ = 3,5-Di-tert-butyl-1,2-o-benzoquinone, 0.5 mM p-BQ = p-benzoquinone.

Analysis of the data reveals that for each benzoquinone studied there is at least one pH in which a benzoquinone-sulfide adduct wave is observed.

The corresponding square wave voltammogram obtained for each quinone structure to increasing additions of sulfide under their optimised pH conditions are detailed in figure 4.5. Figure 4.5 (a) depicts the voltammetric response of 0.5 mM 2,3DMBQ in pH 7 phosphate buffer to increasing additions of sulfide (0.02 - 0.20 mM). These show that in the absence of sulfide a single reduction wave at -0.22 V is observed consistent with the two-electron reduction of the parent species to its hydroquinone structure (equation (4.1)). Upon the addition of sulfide to the solution a shoulder emerges at -0.10 V and continues to grow with increasing additions of sulfide, whilst the reduction wave at -0.22 V begins to decrease in current. This voltammetric behaviour is consistent with the sulfide reacting with the parent 2,3DMBQ to form the mono-substituted sulfide-hydroquinone adduct. This is oxidised homogeneously in the solution to the corresponding benzoquinone species which is then reduced at the electrode to produce the analytical signal. It was observed that, in contrast to the benzoquinone system discussed in section 4.2.1, only a single reduction wave emerges when sulfide is present in the solution due to the loss in reaction sites of the 2,3DMBQ compared to p-benzoquinone.

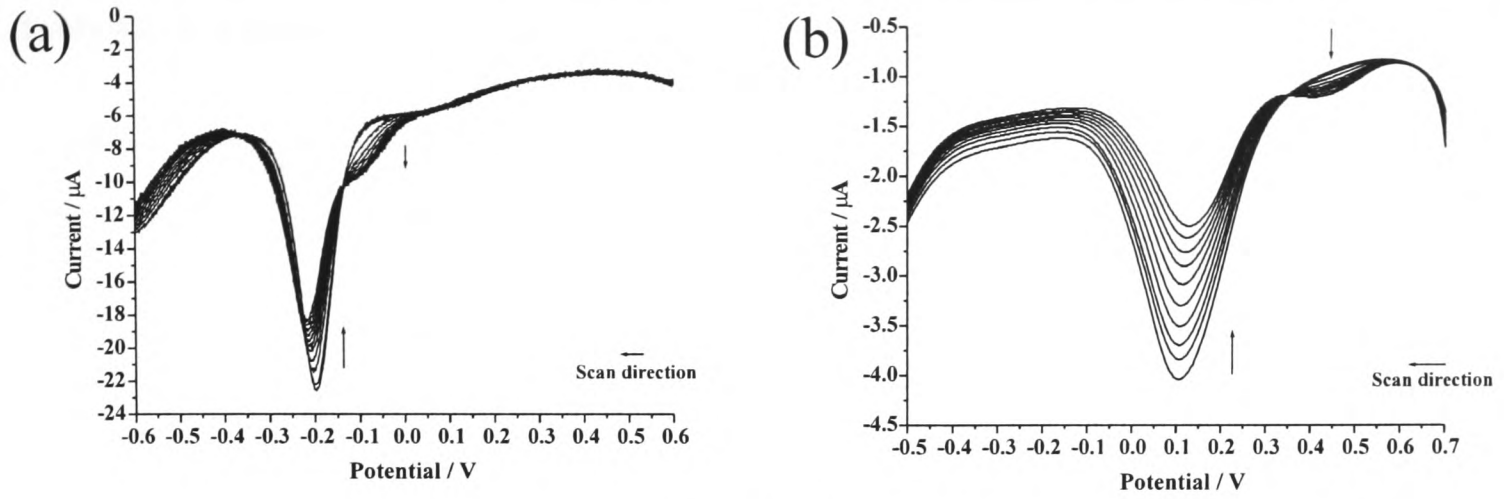


Figure 4.5: The voltammetric response of: (a) 0.5 mM 2,3DMBQ in pH 7 phosphate buffer to increasing additions of sulfide (0.02 - 0.2 mM) and (b) 0.25 mM 3,5DTBQ in pH 3 acetate buffer to increasing additions of sulfide (0.02 - 0.2 mM).

The resulting voltammetric responses of solutions containing 0.25 mM 3,5DTBQ (pH 3) to increasing additions of sulfide (0.02 - 0.20 mM) are depicted in figures 4.5 (b). These reveal that in the absence of sulfide only a single reduction wave is observed at +0.08 V for 3,5DTBQ, corresponding to the two-electron reduction from their benzoquinone structure to the corresponding hydroquinone species. Once again, as detailed above for p-benzoquinone and 2,3DMBQ, upon the addition of sulfide a new voltammetric reduction wave is observed at +0.45 V for 3,5DTBQ. The emergence of this new wave is accompanied by a decrease in the reduction current of the main benzoquinone species thereby showing a reaction process is occurring analogous to that detailed in scheme 4.1, suggesting the generic nature of the reaction process. Analogous results were obtained for 2,6DBQ in a pH 7 phosphate buffer solution whereby a new wave was observed at -0.09 V.

The analytical utility of each indicator species was assessed by examination of sensitivity, dynamic range and detection limits achievable for sulfide by monitoring the increase in the new reduction wave attributed to the production of the mono-substituted benzoquinone-sulfide adduct. The results are detailed in table 4.2. These show that for each indicator species studied the linear ranges and limits of detection for sulfide are comparable.

Table 4.2: The analytical parameters obtained for sulfide detection when each benzoquinone derivative was utilised at optimum pH conditions.

Compound	Optimum pH	Linear Range / μM	Sensitivity A M^{-1}	r^2	LoD / μM
p-BQ	3	20 - 120	0.0198	0.99	12
2,3DMBQ	7	40 - 120	0.0178	0.99	12
2,6DBQ	7	40 - 180	0.0025	0.99	15
3,5DTBQ	3	60 - 180	0.0013	0.99	16

LoD = Limit of detection based on $3s_b$. 0.5 mM p-BQ = p-benzoquinone, 0.5mM 2,3DMBQ = 2,3-Dimethoxy-5-methyl-p-benzoquinone, 0.5 mM 2,6DBQ = 2,6-Dimethoxy-p-benzoquinone, 0.25 mM 3,5DTBQ = 3,5-Di-tert-butyl-1,2-o-benzoquinone.

4.3 Conclusion

The chemical tagging of sulfide by various benzoquinone species has been studied and the analytical utility of each species has been appraised. The results show that when p-benzoquinone is used multiple substitution reactions can occur and as such compromises its analytical utility. The reaction process has been studied using both electrochemistry and UV / Vis spectroscopy and a suitable pathway for the reaction of sulfide with p-benzoquinone has been suggested (scheme 4.1).

To enhance the analytical utility of the approach the effects of increasing the substituents on the benzene ring has been assessed. It was found that by blocking the various reaction sites around the benzene ring the possibility of forming a di-substituted benzoquinone-sulfide adduct decreased. The voltammetric responses have been studied over a wide range of pHs (from pH 2 to pH 10) and the optimum conditions for sulfide sensing for each species studied have been identified. The low solubility of the 3,5DTBQ species promises the development of a screen printed electrode (SPE) in which 3,5DTBQ is incorporated into the carbon working electrode. This could then form the basis of a reagentless sensor to determine sulfide in aqueous media in which a gas permeable membrane could be incorporated to remove possible environment interferents.

4.4 Chapter 4 References

[1] N. S. Lawrence, J. Davis, L. Jiang, T. G. J. Jones, S. N. Davies, R. G. Compton, *Electroanalysis* **2000**, *12*, 1453.

[2] N. S. Lawrence, J. Davis, L. Jiang, T. G. J. Jones, S. N. Davies, R. G. Compton, *Electroanalysis* **2001**, *13*, 143.

[3] N. S. Lawrence, J. Davis, L. Jiang, T. G. J. Jones, S. N. Davies, R. G. Compton, *Electroanalysis* **2001**, *13*, 432.

[4] N. S. Lawrence, M. Thompson, J. Davis, L. Jiang, T. G. J. Jones, R. G. Compton, *Mikrochimica Acta* **2001**, *137*, 105.

[5] G. Hignett, S. Threlfell, A. J. Wain, N. S. Lawrence, S. J. Wilkins, J. Davis, R. G. Compton, M. F. Cardosi, *Analyst* **2001**, *126*, 353.

[6] P. C. White, N. S. Lawrence, J. Davis, R. G. Compton, *Anal. Chim. Acta* **2001**, *447*, 1.

[7] D. Giovanelli, N. S. Lawrence, J. Li, T. G. J. Jones, R. G. Compton, *Anal. Letts.* **2003**, *36*, 2941.

[8] O. Nekrassova, N. S. Lawrence, R. G. Compton, *Electroanalysis* **2003**.

[9] D. A. M. Zaia, K. C. L. Ribas, C. T. B. V. Zaia, *Talanta* **1999**, *50*, 1003.

[10] M. K. Tummuru, T. E. Divakar, C. S. Sastry, *Analyst* **1984**, *109*, 1105.

[11] J. Chrastil, *Analyst* **1990**, *115*, 1383.

[12] C. S. Sastry, P. Satyanarayana, M. K. Tummuru, *Analyst* **1985**, *110*, 189.

[13] K. Shimada, K. Mitamura, *J. Chromatography B* **1994**, *659*, 227.

[14] Y. Imai, S. Ito, K. Fujita, *J. Chromatography* **1987**, *420*, 404.

[15] T. C. Rohner, J. S. Rossier, H. H. Girault, *Electrochem. Commun.* **2002**, *4*, 695.

[16] T. C. Rohner, J. Josser, H. Jensen, H. H. Girault, *Anal. Chem.* **2003**, *75*, 2065.

[17] C. Roussel, T. C. Rohner, H. Jensen, H. H. Girault, *Chem. Phys. Chem.* **2003**, *4*, 200.

[18] J.-M. Zen, P.-Y. Chen, A. S. Kumar, *Electroanalysis* **2002**, *14*, 513.

[19] N. S. Lawrence, L. Jiang, T. G. J. Jones, R. G. Compton, *Anal. Chem.* **2003**, *75*, 2054.

[20] J. P. Hart, A. K. Abass, *Anal. Chim. Acta* **1997**, *342*, 199.

[21] M. I. Prodromidis, P. G. Veltsistas, M. I. Karayannis, *Anal. Chem.* **2000**, *72*, 3995.

[22] S. Berger, P. Hertl, A. Rieker, in *The Chemistry of Quinonoid Compouds* (Eds: S. Patai, Z. Rappoport), Wiley & Sons, London **1988**, pp. 29-86.

Chapter 5: "The Electrochemically Initiated Reaction of Sulfide with N,N-Diethyl-p-phenylenediamine (DEPD) in N,N-Dimethylformamide (DMF) Part I: a Mechanistic Study"

As discussed in Chapter 3, Lawrence *et al.* have recently devised an electrochemical analog of the traditional spectroscopic methylene blue test (Chapter 3, section 3.2.4.1) in which oxidation *via* ferric ions is replaced by electron transfer at a glassy carbon electrode [1]. The chemistry is aqueous-based and relies on the 1,4-Michael addition of sulfide to the electro-generated quinone-imine resulting in the formation of the corresponding thiol adduct which can be oxidised at the electrode surface to produce the analytical signal (Chapter 3, Scheme 3.2). It was desired to adapt this protocol in non-aqueous media with a view to detect hydrogen sulfide in adverse conditions of high temperature, as typically found in the oilfield industry. In this chapter the mechanism of the electrochemical oxidation of N,N-diethyl-p-phenylenediamine (DEPD) in organic solvents (i.e., DMF) is elucidated. The next chapter discusses the response of DEPD in the presence of sulfide. Finally, exploration of the DEPD and sulfide system at elevated temperature will be detailed in Chapter 14.

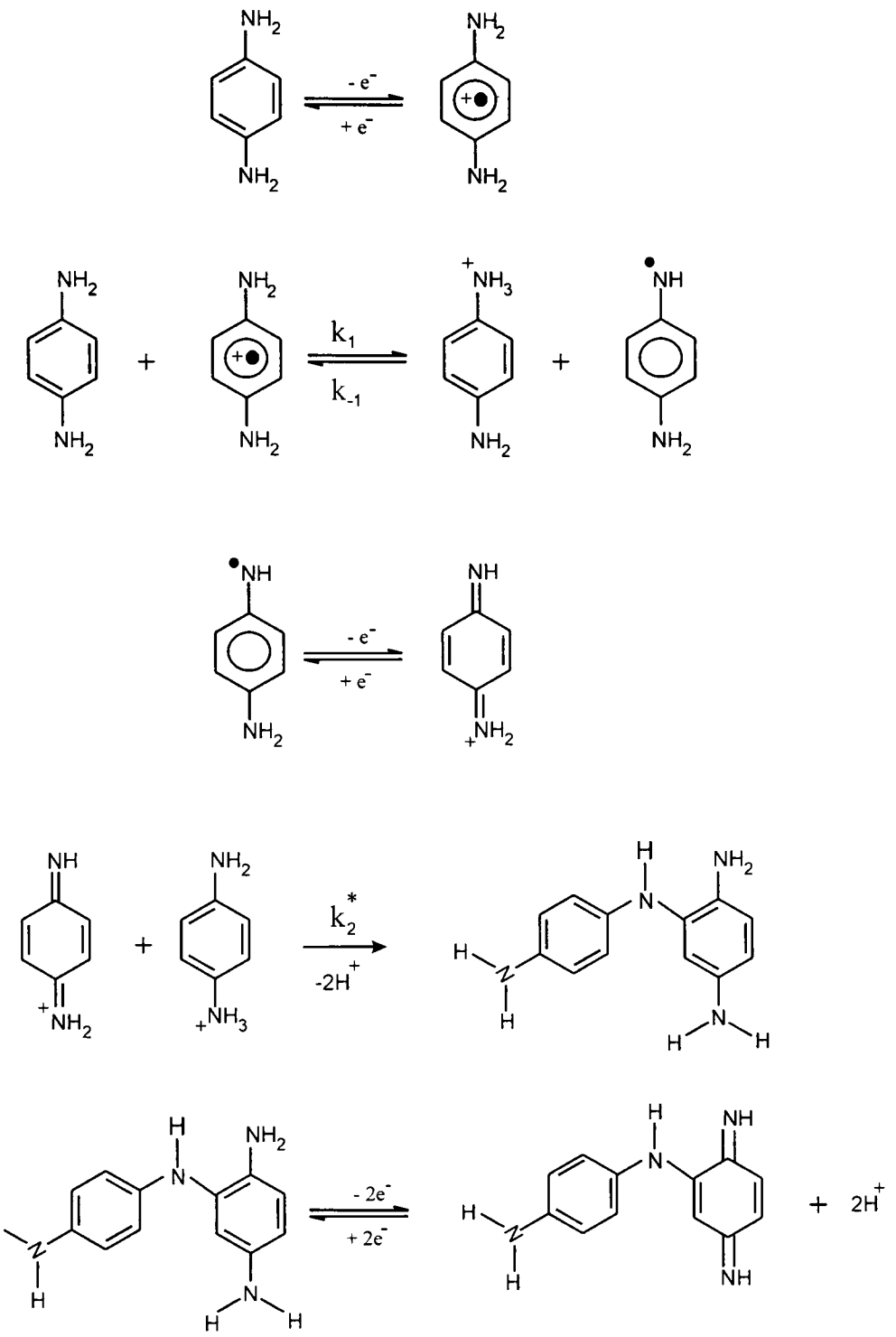
The results detailed below have been subsequently published in Electroanalysis [2]. The mathematical modelling for the simulation study was carried out by Oleksiy V. Klymenko and the high-speed channel electrode experiments by Neil V. Rees.

5.1 Introduction

The electrochemical oxidation of phenylenediamines in aqueous solutions has been recently studied as a means of detecting hydrogen sulfide [1,3,4] and thiols [5,6] (Chapter 3, section 3.2.4.1). The oxidative voltammetric response of N,N-diethyl-p-phenylenediamine (DEPD) in aqueous media is thought to be two overlapping electrochemical reversible processes and this has served as the basis for the detection of sulfide, cysteine, homocysteine and glutathione as a result of the extra current flow when these species react with the two electron oxidation product [5,6]. The transfer of this amperometric approach into non-aqueous solvents could have significant advantages in the detection of hydrogen sulfide under conditions of high temperature as encountered in the oilfield industry [7]; by selectively choosing the solvent in which to detect sulfide the temperature range can be significantly extended due to the enhancement in the boiling point. The literature reveals that N,N-dimethylformamide (DMF) produces good temperature versatility due to its relatively high boiling point of 153 ^{o}C [8], hence DMF was our solvent of choice. A second advantage will be shown to be the increased solubility of hydrogen sulfide and of the phenylenediamine species in the organic solvent; in aqueous media the linear range for sulfide detection was found to be dependent on the concentration of the indicator species. By having a higher solubility the concentration of phenylenediamine can be easily increased and therefore a larger linear range can be achieved.

First however, the electrochemical oxidation of DEPD in DMF has to be studied. The literature reports that this process is more complex than two sequential simple one-electron oxidations. Several papers have speculated, on the basis of potential step chronoamperometry and UV/Visible spectrometry, that the oxidation of p-phenylenediamine (PPD) in acetonitile *may* undergo the reaction mechanism detailed in scheme 5.1; PPD first undergoes a one electron loss to give the radical cation

species $PPD^{+\bullet}$, this species then undergoes a proton exchange with the parent (PPD) [9,10] (or possibly with the solvent [11]) to give the neutral radical species $PPD^{\bullet}$, which then undergoes further oxidation to the di-imine [9,10]. Coupling reactions then ensue and the scope for the formation of oligomeric or polymeric products is evident.



Scheme 5.1: Proposed reaction pathway for the oxidation of p-phenylenediamine (PPD) in DMF. $*k_2$ may undergo proton loss to other bases within the scheme or the protons may be returned by the products. A similar comment applies to the final step of the mechanism.

In this chapter the electrochemical oxidation of DEPD is studied at microdisc electrodes of different radii as a means of understanding the complex oxidative reaction process proposed in scheme 5.1. The ability of microdisc electrodes to interrogate fast electrochemical reactions has resulted in a wide range of analytical,

[12-17], semi-analytical [18] and numerical methods [19-34] to solve predominantly first-order mechanisms (E, CE, EC, EC' ECE, DISP1, DISP2, EC_2E and $EC_{2X}E$). The voltammetric responses of DEPD at different sized microelectrodes are examined and the corresponding voltammetric wave shapes have been analysed. The level of mechanistic detail of scheme 5.1 with three unknown rate constants and three different redox events represents a previously unexamined level of complexity for steady state microelectrode experiments. The following will show that the finite difference modelling via the alternating direction implicit (ADI) method allows the prediction of the voltammetric behaviour. Application of the theory to the experimental data for the DEPD oxidation in DMF shows the reactions mechanism to be not inconsistent with that suggested in scheme 5.1.

5.2 Theory

In this section we solve the problem of linear sweep voltammetry at a microdisc electrode for the mechanism introduced in the previous section (see Scheme 5.1). The latter can be summarised as:

$$\begin{aligned} A - e^- &\rightleftharpoons B \\ A + B &\underset{k_{-1}}{\overset{k_1}{\rightleftharpoons}} C + D \\ C - e^- &\rightleftharpoons E \\ E + D &\xrightarrow{k_2} F \\ F - 2e^- &\longrightarrow G \end{aligned} \qquad (5.1)$$

The time dependent equations for the mass transport of all the species to a microdisc electrode of radius r_d written in cylindrical coordinates are

$$\frac{\partial[A]}{\partial t} = D_A\left(\frac{\partial^2[A]}{\partial r^2} + \frac{1}{r}\frac{\partial[A]}{\partial r} + \frac{\partial^2[A]}{\partial z^2}\right) - k_1[A][B] + k_{-1}[C][D]$$

$$\frac{\partial[B]}{\partial t} = D_B\left(\frac{\partial^2[B]}{\partial r^2} + \frac{1}{r}\frac{\partial[B]}{\partial r} + \frac{\partial^2[B]}{\partial z^2}\right) - k_1[A][B] + k_{-1}[C][D]$$

$$\frac{\partial[C]}{\partial t} = D_C\left(\frac{\partial^2[C]}{\partial r^2} + \frac{1}{r}\frac{\partial[C]}{\partial r} + \frac{\partial^2[C]}{\partial z^2}\right) + k_1[A][B] - k_{-1}[C][D]$$

$$\frac{\partial[D]}{\partial t} = D_D\left(\frac{\partial^2[D]}{\partial r^2} + \frac{1}{r}\frac{\partial[D]}{\partial r} + \frac{\partial^2[D]}{\partial z^2}\right) + k_1[A][B] - k_{-1}[C][D] - k_2[D][E]$$

$$\frac{\partial[E]}{\partial t} = D_E\left(\frac{\partial^2[E]}{\partial r^2} + \frac{1}{r}\frac{\partial[E]}{\partial r} + \frac{\partial^2[E]}{\partial z^2}\right) - k_2[D][E]$$

$$\frac{\partial[F]}{\partial t} = D_F\left(\frac{\partial^2[F]}{\partial r^2} + \frac{1}{r}\frac{\partial[F]}{\partial r} + \frac{\partial^2[F]}{\partial z^2}\right) + k_2[D][E] \qquad (5.2)$$

where $D_A, D_B, \ldots$ are the diffusion coefficients of species $A, B, \ldots$; r is the radial coordinate, and z is the coordinate normal to the surface of the disc.

Boundary conditions for this model are shown in the Table 5.1, where k_f', k_b', k_f'' and k_b'' denote forward and reverse rate constants for E-steps in the kinetic mechanism:

$$k_f' = k_0' \exp\left(\frac{(1-\alpha')F}{RT}\left(E - E^{0'}\right)\right)$$

$$k_b' = k_0' \exp\left(-\frac{\alpha' F}{RT}\left(E - E^{0'}\right)\right)$$

$$k_f'' = k_0'' \exp\left(\frac{(1-\alpha'')F}{RT}\left(E - E^{0''}\right)\right)$$

$$k_b'' = k_0'' \exp\left(-\frac{\alpha'' F}{RT}\left(E - E^{0''}\right)\right) \qquad (5.3)$$

where k_0' and k_0'' are standard rate constants for the *A/B* and *C/E* couples and correspondingly α' and α'' are the transfer coefficients, and $E^{0'}$ and $E^{0''}$ the formal potentials. The oxidation of F in the reaction scheme 5.1 is thought to possess diffusion-controlled conditions under linear sweep voltammetry, because oxidation of the species F takes place at more negative potentials than required for the oxidation of C [9,10]; this will be assumed throughout the following, both in the theory and in the assessment of the DEPD system.

Table 5. 1. *Boundary conditions for the mathematical model of $EC_{REV}ECE$ process at microdisc.*

Boundary region	Equations
$z=0,\ 0\le r\le r_d$	$D_A\left.\frac{\partial[A]}{\partial z}\right\|_{z=0}=\left(k_f'[A]-k_b'[B]\right)_{z=0};\ D_B\left.\frac{\partial[B]}{\partial z}\right\|_{z=0}=-D_A\left.\frac{\partial[A]}{\partial z}\right\|_{z=0};$ $D_C\left.\frac{\partial[C]}{\partial z}\right\|_{z=0}=\left(k_f''[C]-k_b''[E]\right)_{z=0};\ D_E\left.\frac{\partial[E]}{\partial z}\right\|_{z=0}=-D_C\left.\frac{\partial[C]}{\partial z}\right\|_{z=0};$ $\left.\frac{\partial[D]}{\partial z}\right\|_{z=0}=0;\ [F]_{z=0}=0$
$z=0,\ r>r_d$	$\left.\frac{\partial[A]}{\partial z}\right\|_{z=0}=\left.\frac{\partial[B]}{\partial z}\right\|_{z=0}=\left.\frac{\partial[C]}{\partial z}\right\|_{z=0}=\left.\frac{\partial[D]}{\partial z}\right\|_{z=0}=\left.\frac{\partial[E]}{\partial z}\right\|_{z=0}=\left.\frac{\partial[F]}{\partial z}\right\|_{z=0}=0$
all $z,\ r=0$	$\left.\frac{\partial[A]}{\partial r}\right\|_{r=0}=\left.\frac{\partial[B]}{\partial r}\right\|_{r=0}=\left.\frac{\partial[C]}{\partial r}\right\|_{r=0}=\left.\frac{\partial[D]}{\partial r}\right\|_{r=0}=\left.\frac{\partial[E]}{\partial r}\right\|_{r=0}=\left.\frac{\partial[F]}{\partial r}\right\|_{r=0}=0$
$z,\ r\to\infty$	$[A]\to[A]_{bulk};\ [B]\to 0;\ [C]\to 0;\ [D]\to 0;\ [E]\to 0;\ [F]\to 0$

The current flowing at the electrode surface was calculated using the following expression:

$$i=2\pi F\int_0^{r_d}\left(D_A\frac{\partial[A]}{\partial z}+D_C\frac{\partial[C]}{\partial z}+2D_F\frac{\partial[F]}{\partial z}\right)_{z=0}r\,\mathrm{d}r \tag{5.4}$$

The coordinate transformation developed by Amatore and Fosset [27] was used to map an infinite area $[0,\infty)\times[0,\infty)$ in cylindrical coordinates r, z into a closed square $[0,1]\times[0,1]$ in the transformed θ, Γ-space:

$$R=\frac{\sqrt{1-\theta^2}}{\cos\left(\frac{\pi}{2}\Gamma\right)};\ Z=\theta\tan\left(\frac{\pi}{2}\Gamma\right) \tag{5.5}$$

where $R=\frac{r}{r_d}$ and $Z=\frac{z}{r_d}$. This transformation allows one to remove the edge singularity arising from the discontinuous boundary conditions and to improve simulation efficiency due to the less number of the mesh nodes required to obtain the desired level of accuracy.

The ADI method [23,34,35] was used to solve the mass transport equations (5.2) in two-dimensional domain. Newton's method [36] was used to solve systems of non-

linear algebraic equations arising from the discretisation of the PDEs (5.2) [37]. The generalised Thomas algorithm for banded matrices was used to solve linear systems. All the programs for the simulations were written by Oleksiy V. Klymenko in Delphi 6 Professional Edition (Borland Software Corporation, Scotts Valley, California, USA) and executed on a PC with Pentium III 1GHz processor and 256 MB of RAM.

In the following Oleksiy V. Klymenko investigated steady-state linear sweep voltammetry corresponding to the case when $E^{0'} < E^{0''}$ so that when the current-potential curve has two waves as shown in Figure 5.1.

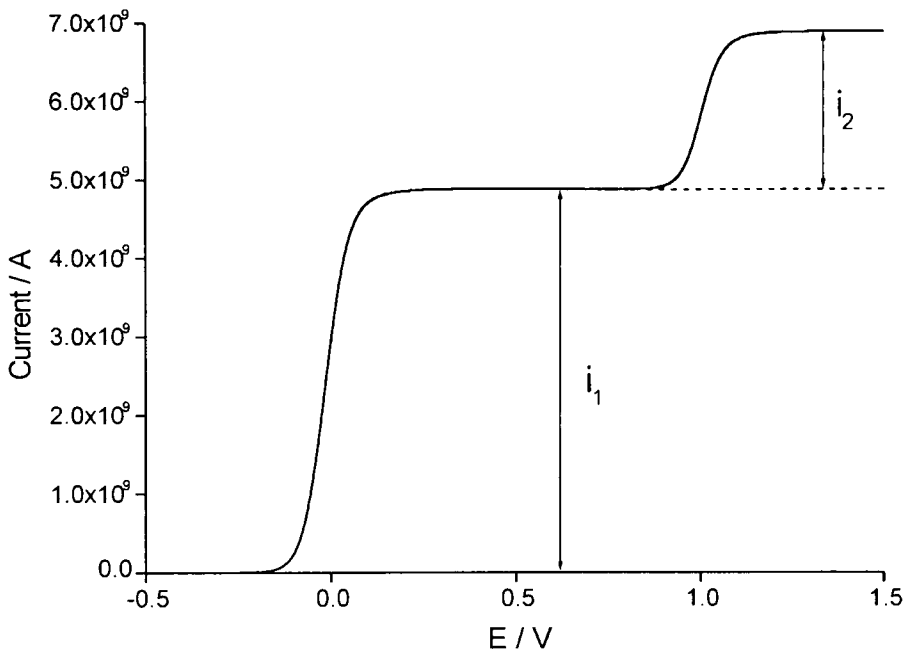


Figure 5.1: A schematic of a typical linear sweep voltammograms.

In order to check the accuracy of the numerical approximation of the current passed (5.4), we performed a series of simulations with increasing grid size. Figure 5.2 shows the convergence of the second wave current (see Figure 5.1) to the limiting value versus the grid step size, shown as a logarithmic plot of the relative error $|i\text{-}i_{\text{lim}}|/i_{\text{lim}}$ versus the grid step size $h = 1/N\theta = 1/N\Gamma$, calculated for "typical" ranges of rate constants as indicated in the figure legend. The exact value of the second wave current (i_{lim}) was found by running simulations for a range of grid sizes and extrapolating the data for the second wave current corresponding to the oxidation of C to the asymptotic value corresponding to a fully converged simulation.

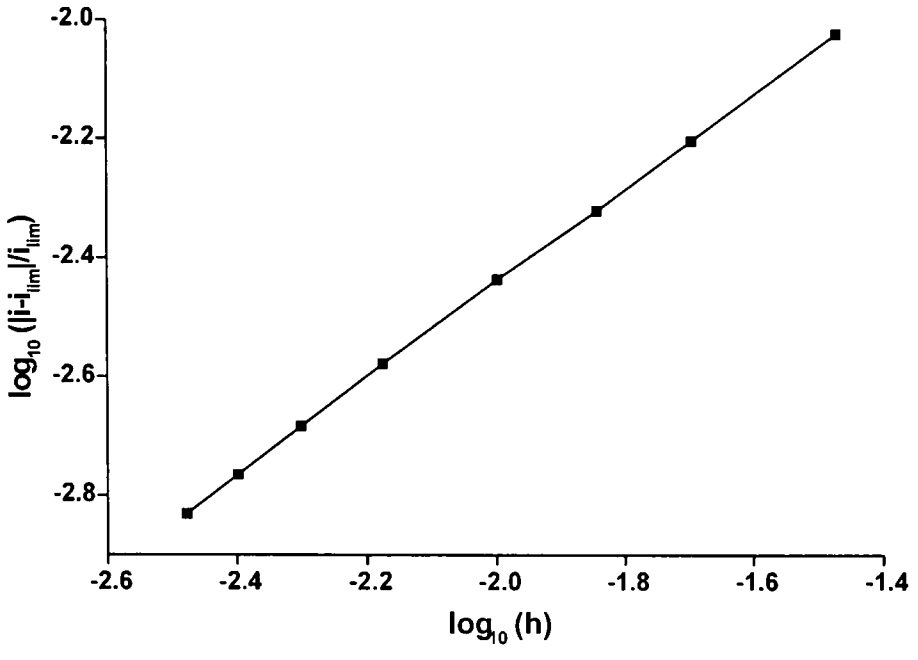


Figure 5.2: Convergence plot for the second wave current calculated for the parameter values $r_d = 17\,\mu m$, $[A]_{bulk} = 1mM$, $D_A = D_B = D_C = D_D = D_E = 9.5\times10^{-6}\,cm^2 s^{-1}$, $D_F = 6\times10^{-6}\,cm^2 s^{-1}$, $k_0' = k_0'' = 0.1\,cm\,s^{-1}$, $\alpha' = \alpha'' = 0.5$, $0 \le k_1 / mol^{-1}\,cm^3\,s^{-1} \le 10^{10}$, $0 \le k_1/k_{-1} \le 10^3$, $0 \le k_2 / mol^{-1}\,cm^3\,s^{-1} \le 10^{10}$.

The rate of convergence was found from Figure 5.2 to be of the order $O(h^{0.8})$, which is fast for a strongly non-linear system of PDEs when compared to similar systems in the literature [30,38]. It was also found that the grid of the size 50x50x3000 ($N\theta \times N\Gamma \times NT$) gives the value of convergence of less than 0.65% within 5 minutes of CPU time.

5.3 Theoretical Results

To verify his mathematical model and the computer program written to solve it Oleksiy V. Klymenko investigated several limiting cases. The first corresponds to the absence of homogeneous kinetics in the mechanism by setting $k_1 = 0$. In this case the simulation results should be the same as these for an E-reaction only. In order to test the results for this case, Oleksiy V. Klymenko simulated a linear sweep voltammogram with a slow scan rate to obtain a steady-state response. The results of this simulation were then compared with the limiting current expected from analytical theory and published independently simulated results for a simple E-reaction [34]. Figure 5.3

shows this comparison where the solid line represents the simulated linear sweep voltammogram for $EC_{rev}ECE$ mechanism with $k_1 = 0$ normalised with respect to the predicted limiting current [39] and the dots correspond to the literature data for a simple E reaction [34]. The error bars shown for the literature data points reflect inaccuracies in reading the data values from the published paper. The agreement of these voltammograms suggests that the first E-step in the mechanism is simulated correctly.

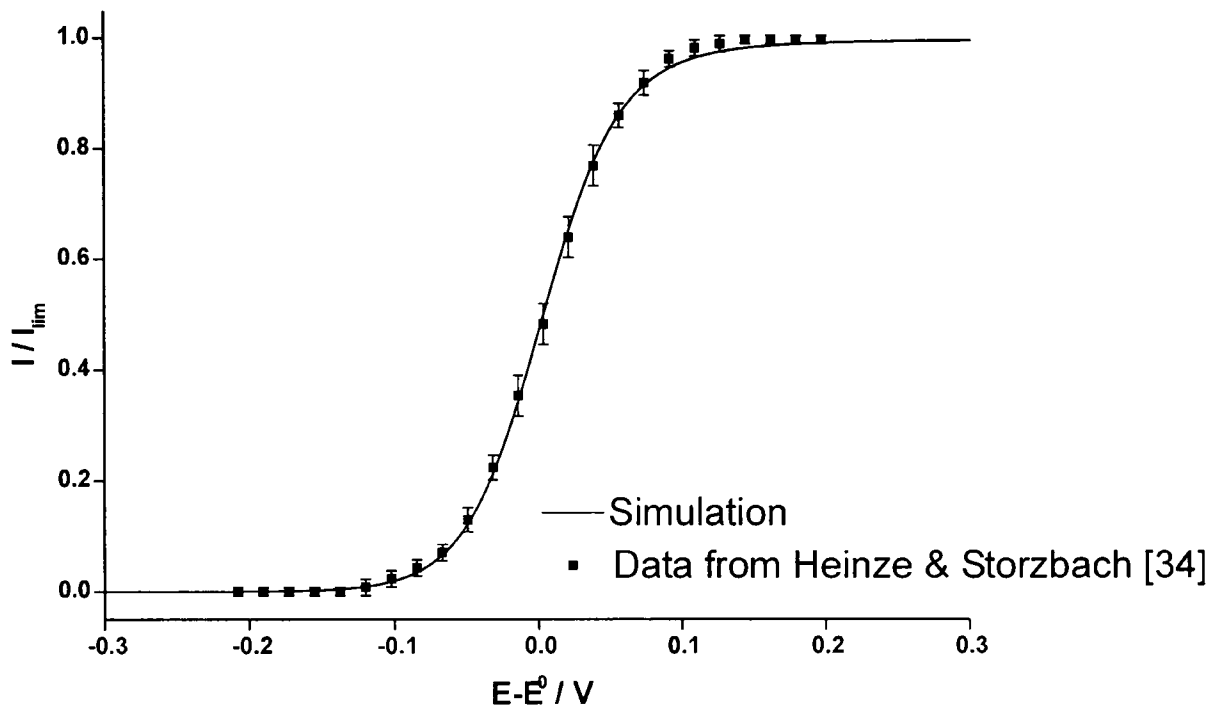


Figure 5.3: Linear sweep voltammogram calculated for $k_1 = 0$. The dots represent published results for the simulation of an E reaction at a microdisc electrode.

Second, we investigated the behaviour of the homogeneous kinetics by setting $k_1 > 0$. The three cases considered for the first homogeneous step were $K_{eq} = k_1/k_{-1} \to 0$, $K_{eq} \to \infty$ and $K_{eq} \approx 1$. The simulation was found to behave as expected in each case, which we shall examine in turn. When $K_{eq} \to 0$ we remove all homogeneous kinetics and the case is a simple E-reaction, which has already been considered above as the first limiting case (Figure 5.4 (a)). Simulations for $K_{eq} \to \infty$ have three most informative limits when (i) $k_1 \to \infty$ and $k_0'' = 0$, that is an EC mechanism with a fast irreversible C-step, (ii) $k_1 \to \infty$, $k_0'' \neq 0$ and $k_2 = 0$ corresponding to an ECE reaction

scheme and (iii) $k_1 \rightarrow \infty$ and $k_2 \rightarrow \infty$, which corresponds to fast irreversible chemical steps, i.e. to ECECE mechanism. Figure 5.4 shows the simulated voltammograms for all of these cases.

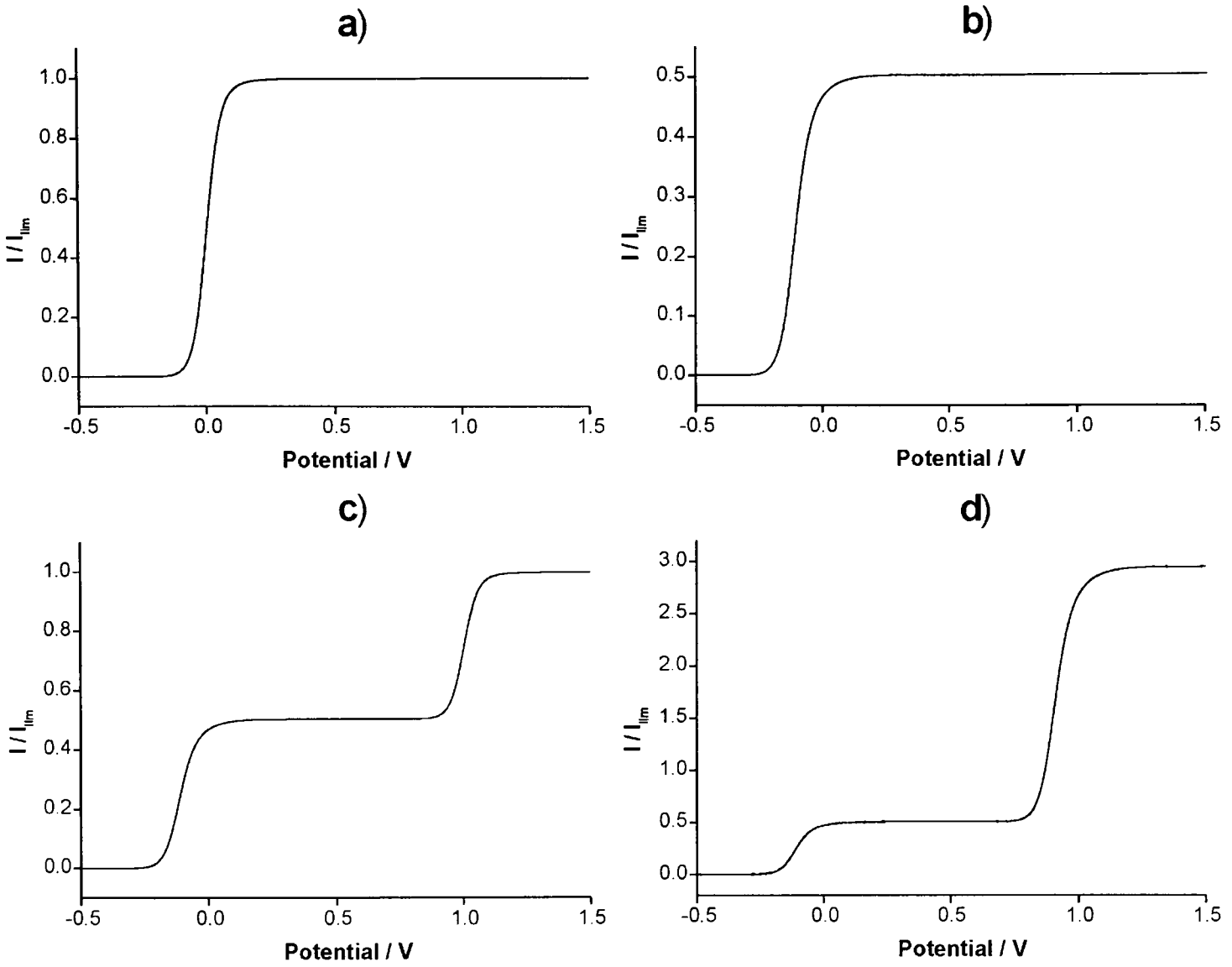


Figure 5.4: Linear sweep voltammograms for the four limiting cases identified in the text: (a) E reaction, (b) EC mechanism with fast irreversible C-step, (c) ECE mechanism with fast irreversible chemical step, and (d) ECECE mechanism with fast irreversible chemical steps.

For case (i), the simulated limiting current of linear sweep voltammogram is a half of that expected for an E reaction (Figure 5.4 (b)). The linear sweep voltammogram for (ii) has two waves (Figure 5.4 (c)) corresponding to the assumed formal potentials of $E^{0'} = 0\ \text{V}$ and $E^{0''} = 1\ \text{V}$. The height of the first wave is a half of the pure one-electron wave as well as the height of the second wave, which gives the total limiting current corresponding to one electron transferred. This is as expected. Simulation of a linear-sweep voltammetry for case (iii) gives the current-potential response with two waves (Figure 5.4 (d)), first of which corresponds to a half-electron transfer resulting

from the first two steps of the mechanism and the height of the second wave is 2.5 of that for one-electron transfer at a microdisc. Again this was as anticipated.

Simulations with the value of K_{eq} around 1 give intermediate results. Figure 5.5 shows a three-dimensional plot ("working surface") of a normalised first-wave current $\tilde{i}_1 = \frac{i_1}{4FD_A[A]_{bulk} r_d}$ versus normalised homogeneous rate constant $\tilde{k}_1 = \frac{k_1[A]_{bulk} r_d^2}{D_A}$ and equilibrium constant K_{eq}.

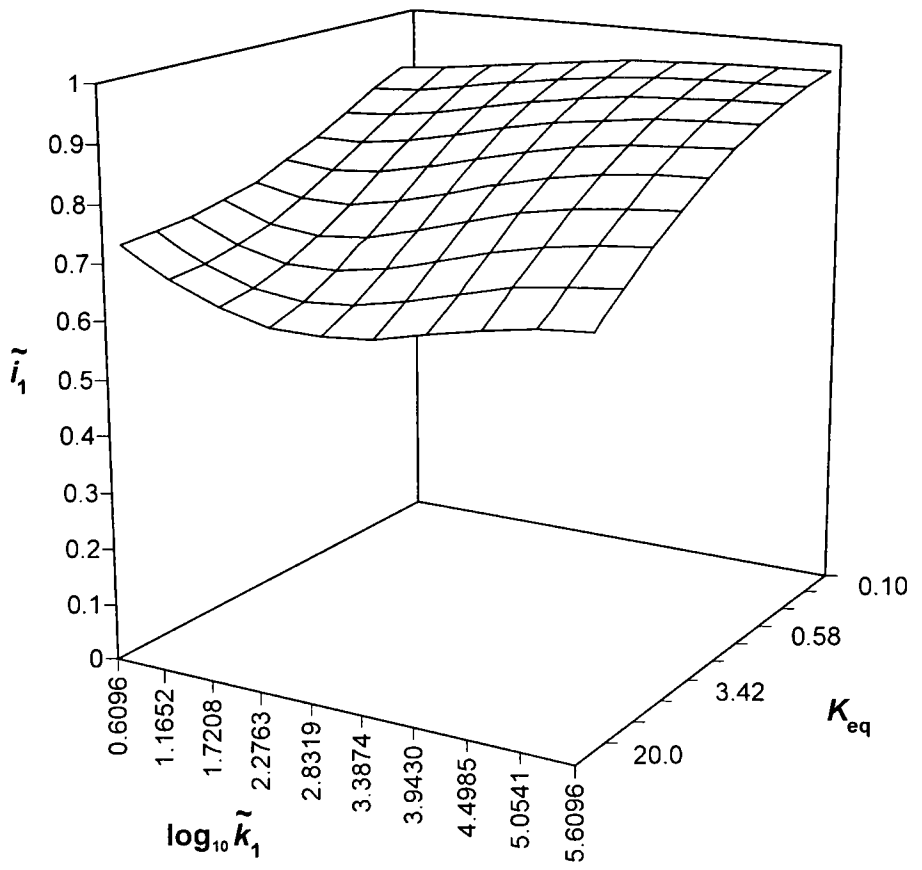
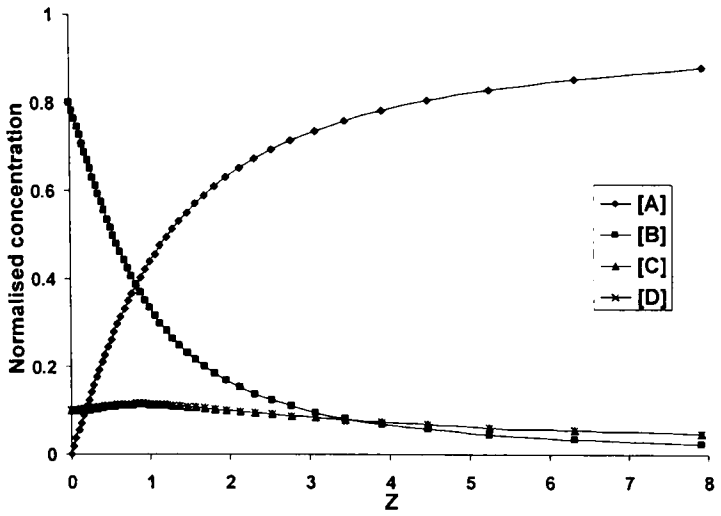


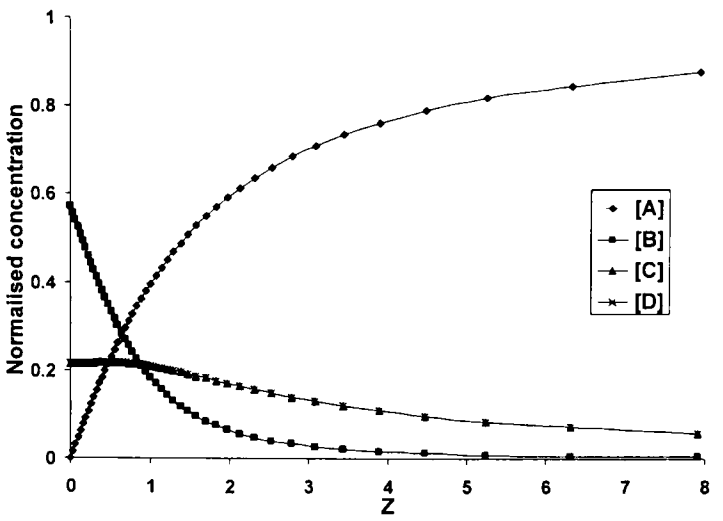
Figure 5.5: Simulated working surface for the first wave current.

The plots shown in Figure 5.6 represent concentration distributions of species *A*, *B*, *C* and *D* at the centre of the microdisc in the direction normal to the electrode surface ($Z = \frac{z}{r_d}$ is the normalised distance from the electrode) during the steady state electrolysis when $\tilde{k}_2 = \frac{k_2[A]_{bulk} r_d^2}{D_A} = 0$ (corresponding to the top of the first wave of the linear sweep voltammogram). It can be seen from the graphs 5.6 (a), 5.6 (b) and 5.6 (c) that increasing the K_{eq} value while holding $\tilde{k}_1$ constant (increasing the

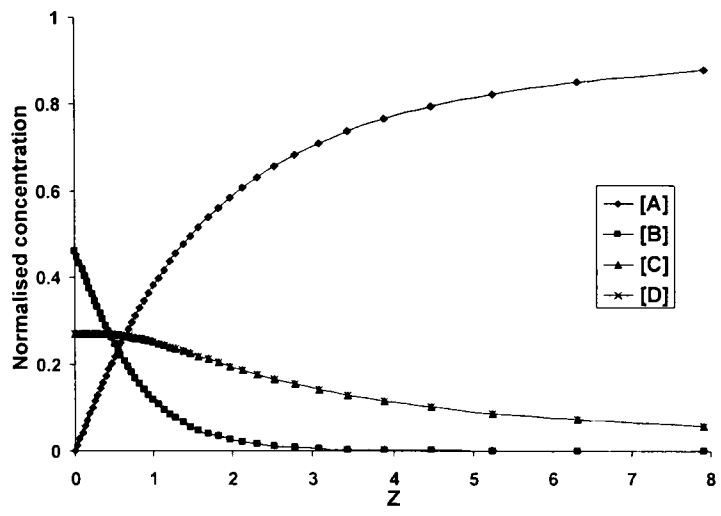
irreversibility of the first chemical step in the mechanism) leads to a decreasing gradient of concentration of species *A* and therefore to decreasing current. The first wave current shows similar behaviour for all values of $\tilde{k}_1$ (Figure 5.5). Next, we keep the value of K_{eq} constant and change the value of $\tilde{k}_1$ (Figure 5.6 (b), (d), (e)). When $\tilde{k}_1$ is small (Figure 5.6 (d)) the rate of the reaction between species *A* and *B* is not sufficient to change the concentration gradients significantly and the value of $\tilde{i}_1$ is close to 1. Increasing the value of $\tilde{k}_1$ results in the increasing rate of interaction between *A* and *B* leading to lower concentration gradient of species *A* and lower value of the current (Figure 5.6 (b)). With further increase of $\tilde{k}_1$ (for fixed K_{eq}) the back chemical reaction (of *C* with *D*) becomes crucial for the current behaviour. The rate with which species *C* and *D* react with each other in this area is sufficient to build up the concentration of *A* for values of $\tilde{k}_1$ beyond a critical threshold. Thus the concentration gradient of *A* increases due to the zero boundary condition at the electrode surface (Figure 5.6 (e)), which results in an increasing current. Hence the working curve corresponding to a certain value of the equilibrium constant K_{eq} has a minimum, which moves to higher values of the normalised rate constant $\tilde{k}_1$ as K_{eq} increases. Note that for all the cases shown in Figure 5.6 the concentration distributions of species *C* and *D* are the same because of the absence of any further kinetics.



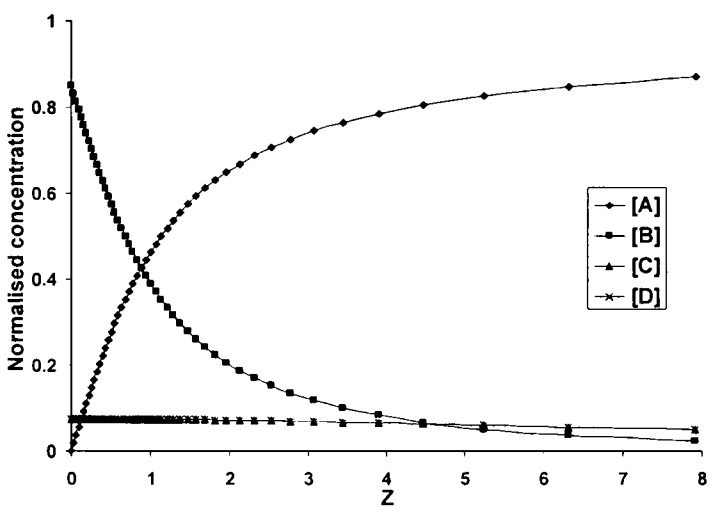
a) $\tilde{k}_1 = 3,\ K_{eq} = 0.1$



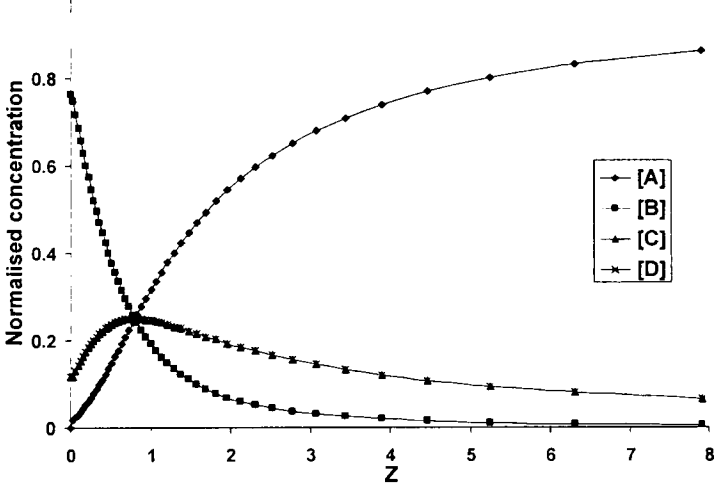
b) $\tilde{k}_1 = 3,\ K_{eq} = 1$



c) $\tilde{k}_1 = 3,\ K_{eq} = 10$



d) $\tilde{k}_1 = 0.03,\ K_{eq} = 1$



e) $\tilde{k}_1 = 3{\cdot}10^4,\ K_{eq} = 1$

Figure 5.6: Simulated concentration profiles for steady state conditions when $\tilde{k}_2 = 0$.

Finally we examine the behaviour of the second wave current. Figure 5.7 shows a working surface for $\tilde{i}_2 = \dfrac{i_2}{4FD_A[A]_{bulk}\, r_d}$ as a function of the logarithms of the normalised rate constants $\tilde{k}_1$ and $\tilde{k}_2$ simulated for the fixed value of $K_{eq} = 0.75$. When $\tilde{k}_2$ is small the value of the second wave current first increases with increasing

$\log_{10}\tilde{k}_1$, passes through a maximum and then decreases. It can be explained by the fact that $\tilde{i}_2$ in this case is formed only by oxidation of species *C* (see third step of the reaction mechanism). While $\log_{10}\tilde{k}_1$ is smaller than 1.07 concentrations of species *C* and *D* near the electrode surface increase which results in the increasing current. But when $\log_{10}\tilde{k}_1$>1.07 concentrations of *C* and *D* near the electrode decrease due to increasing reverse rate constant of the second step (Figure 5.6 (e)). Decreasing concentration leads to decreasing current, which is proportional to the concentration gradient. For large values of $\tilde{k}_2$ the value of the second wave current increases monotonically with increasing $\tilde{k}_1$. This occurs due to increasing contribution of the last oxidative step of the $EC_{rev}ECE$ mechanism into the second wave current. For all values of $\tilde{k}_1$ the second wave current increases with increasing rate constant $\tilde{k}_2$.

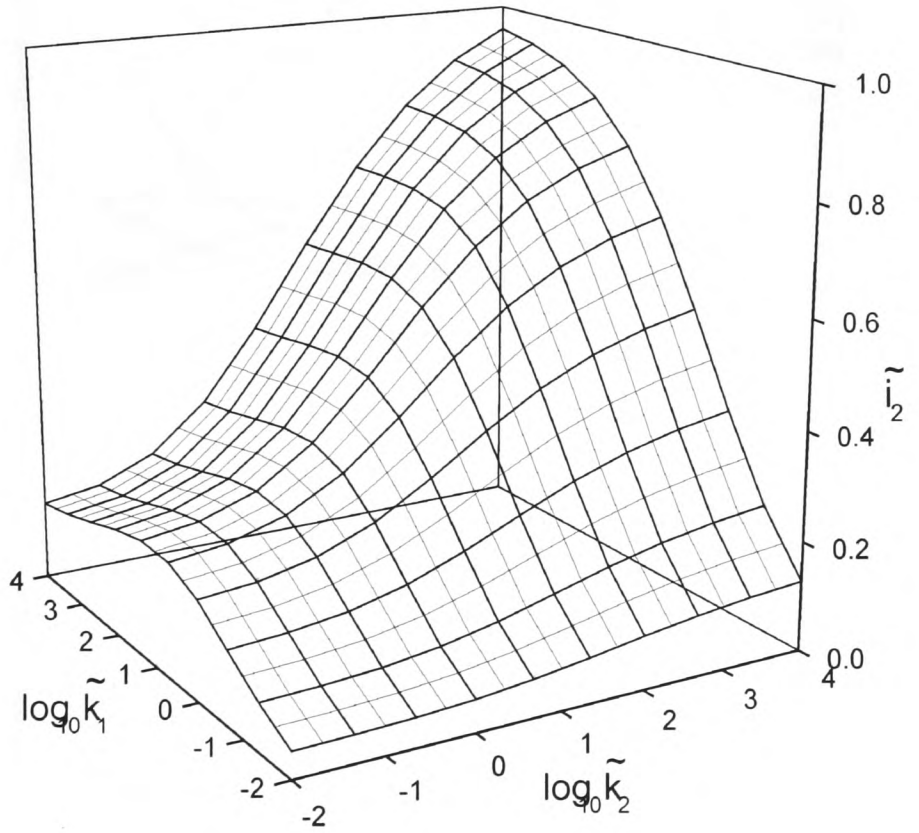


Figure 5.7: Working surface for the second wave current simulated for fixed value of $K_{eq} = 0.75$.

Figure 5.8 represents simulated concentration profiles corresponding to different values of $\tilde{k}_2$. It can be seen from these profiles that the concentration profile of

species C does not change significantly while the concentration gradient of species F increases with increasing $\tilde{k}_2$ which causes the substantial rise of the current.

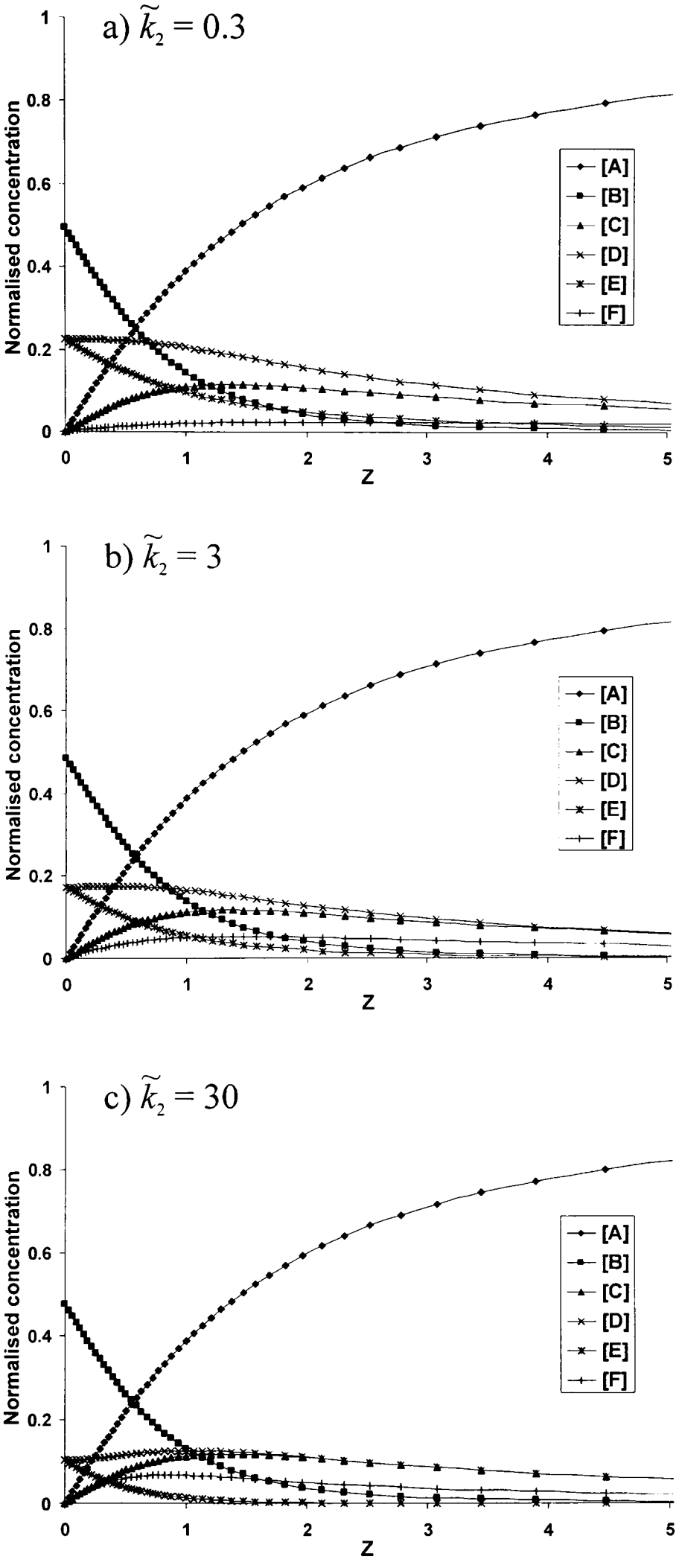


Figure 5.8: Concentration profiles for steady state conditions corresponding to the second wave of the current-potential curve simulated for the fixed values of $\tilde{k}_1 = 3$ and $K_{eq} = 0.75$.

5.4 Experimental: "Hydrodynamic Cell Arrangement"

The high-speed channel electrode (HSChE) flow-cell and pressurized apparatus are described in refs [40-43]. Only some details are given in this section. Extremely high flow rates across a microband electrode are achieved by pressurising a chamber containing the solution and electrode assembly up to 1.5 atmospheres. The solution flows through a specially designed flow-cell (of fixed width, $d = 2$ mm and height, $2h$) and out through one of three capillaries, to the exit at atmospheric pressure. The flow-cell is constructed of fused blocks of silica (Optiglass Ltd, Hainault, Essex, UK), and is shown in figure 5.9. It has been designed to minimise flow resistance and to maintain a smooth flow from the cell inlet to the start of the channel by using wide bore connection tubes with low flow velocities; this flow is then accelerated by a factor of 35 as it enters the channel through a short taper section. The length of the channel is 2 mm to establish a stable flow pattern and allow space for the electrode assembly, whilst keeping the pressure drop required within practicable values of 150 – 200 kPa.

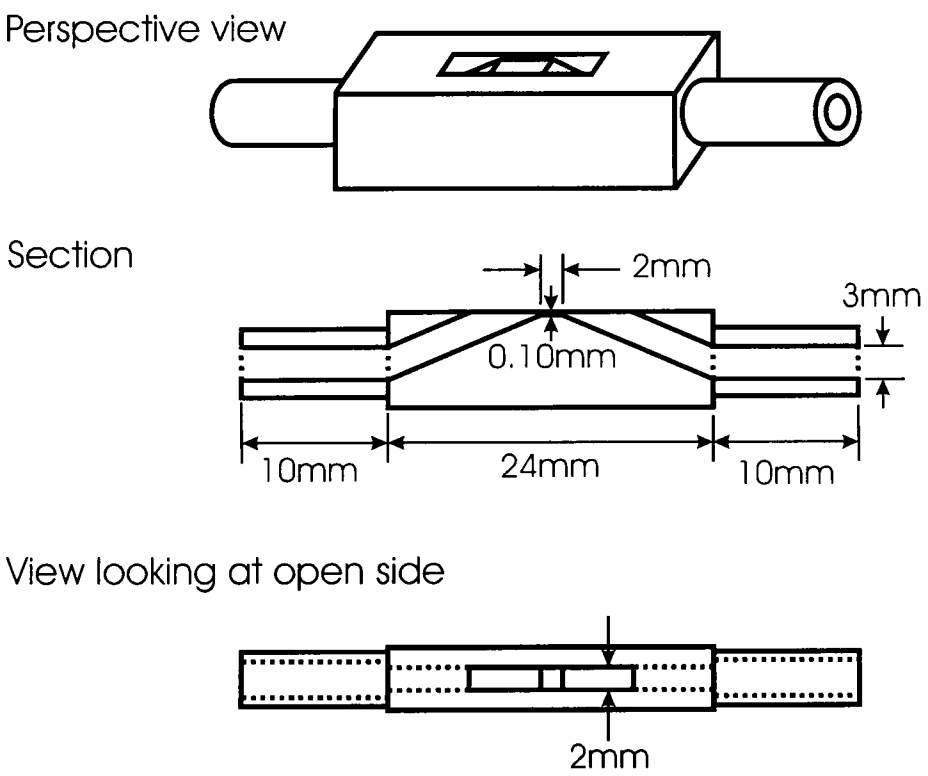


Figure 5.9: The high-speed channel flow-cell.

In this way, volume flow rates of up to 2.5 $cm^3 s^{-1}$ can be achieved with DMF as solvent, corresponding to centre line velocities in the channel approaching 20 $m s^{-1}$.

The chamber is pressurised by cylinder Argon ("Pureshield", BOC Gases Ltd., UK) under computer control using two fast-acting electromagnetic valves (Clippard Inc., Cinncinnati, Ohio, USA), with pressure being measured by a silicon diaphragm pressure sensor (Entran Ltd., Watford, UK). Oxygen may be removed from the chamber by repeated cycles of pressurising and venting. A separate valve controls deoxygenation of the solution by bubbling, which is carried out with the chamber at atmospheric pressure to avoid super-saturation with argon.

A microband electrode of length 2.5 μm was fabricated by sealing a strip of platinum foil (99.95%, Johnson Matthey plc, London UK) into soda glass according to a reported method [43]. The electrode size was measured using the electrochemical calibration described in the Experimental section. The limiting currents were obtained and the corresponding electrode size determined. The microband working electrode was polished in-between experiments using alumina lapping compounds (BDH) of decreasing size from 3 μm down to 0.25 μm on glass and soft lapping pads (Kemet Ltd, UK). The counter electrode was a smooth, bright platinum wire mesh, and a silver wire (99.95%, Johnson Matthey plc, London UK) used as a pseudo-reference electrode.

5.5 Results and Discussion

5.5.1 Experimental Results

We first consider the use of the high-speed channel electrode to measure the diffusion coefficient of DEPD in DMF from investigation of the first oxidation wave. This set of experiments was carried out by Neil V. Rees. The aim of using this approach was to obtain data under conditions where the first electron transfer was largely, free of homogeneous kinetic complications, so allowing an estimate to be made of the diffusion coefficient of DEPD in DMF.

A solution containing 1.26 mM DEPD and 0.1 M TBAP in DMF was introduced into the pressure chamber of the apparatus used with a 2.5 μm platinum microband electrode, and an initial pressure set. A linear sweep voltammogram was then recorded under effectively steady-state conditions [44] enabling a limiting current to be measured for the first oxidation wave. This was repeated at a range of chamber pressures from 30 - 150 kPa, using a combination of chamber pressure and choice of one of three capillaries of different internal bores to obtain a range of volume flow rates (from 0.34 - 2.30 $cm^3\ s^{-1}$). Next, a plot was made of measured limiting currents against $V_f^{1/3}$ according to the Levich equation for channel flow-cells:

$$i_{\lim} = 0.925nFw[A]_{bulk}\left(x_e D\right)^{2/3}\left(V_f / h^2 d\right)^{1/3} \qquad (5.6)$$

and a straight line with zero y-intercept was obtained. The gradient of this plot was used to obtain a value for the diffusion coefficient of DEPD in DMF to be $(7.2 \pm 1.0) \times 10^{-6}\ cm^2\ s^{-1}$. This value compares with the value of $8.4 \times 10^{-6}\ cm^2\ s^{-1}$ deduced from the Wilke-Chang method for estimating diffusion coefficients (Appendix 3). This suggests that under the experimental conditions employed the homogeneous kinetics might not be completely outrun. Nevertheless the obtained value of the diffusion coefficient can be used as a lower boundary for further consideration.

In order to find a possible range for the rate constant k_1 (see Scheme 5.1) it was necessary to estimate an impact of the second and third E-steps of the mechanism on the overall current. In the channel electrode geometry it is not necessary to explicitly consider the $EC_{rev}ECE$ mechanism to do this, as there is a convenient analogy that can be drawn to the simpler, first-order ECE mechanism which incorporates a large "safety factor" in the calculation.

The rate of change in the concentration of C at any point in the bulk of the solution is given by the second order expression:

$$\frac{d[C]}{dt} = k_1[A][B] - k_{-1}[C][D]$$

But we can introduce the following upper estimation for the derivative in time:

$$\frac{d[C]}{dt} < k_1[A][B] < k_1[A]_{bulk}[B] = k_1'[B], \text{ where } k' = k_1[A]_{bulk}$$

This reduces the problem to a pseudo-first order ECE reaction, with an over-estimated rate constant (as [A] is clearly less than $[A]_{bulk}$). Thus, we consider the following mechanism:

$$A - e^- \rightarrow B$$

$$B \xrightarrow{k_1'} C$$

$$C - e^- \rightarrow E$$

which "produces" more E than the original mechanism. The second wave current due to the oxidation of C is a measure of the kinetic impact on the current-voltage response.

Using a simulated working curve of N_{eff} versus K_{ECE} (the normalised first order rate constant for the ECE reaction) [45] yields the condition that for $N_{eff} > 1.01$ (i.e., the impact of chemical kinetics on the current is more than 1% {E-step only, with no ensuing kinetics}), $K_{ECE} \geq 10^{-3/2}$. This condition can then be interpreted in terms of a maximum flow-rate required for a given value of k_1 for homogeneous kinetics to be not outrun:

$$V_f \leq 10^{2.25}\left(\frac{2dh^2 x_e [A]_{bulk}^{3/2}}{3D^{1/2}}\right)k_1^{3/2} \qquad (5.7)$$

Figure 5.10 shows the dependence of the flow rate on the homogeneous rate constant k_1 for the experimental conditions employed and an estimated diffusion coefficient of

8×10^{-6} cm^2 s^{-1}. It was found from this figure that for the maximum experimental flow rate of 2.3 cm^3 s^{-1} the corresponding value of k_1 is 7×10^8 cm^3 mol^{-1} s^{-1}.

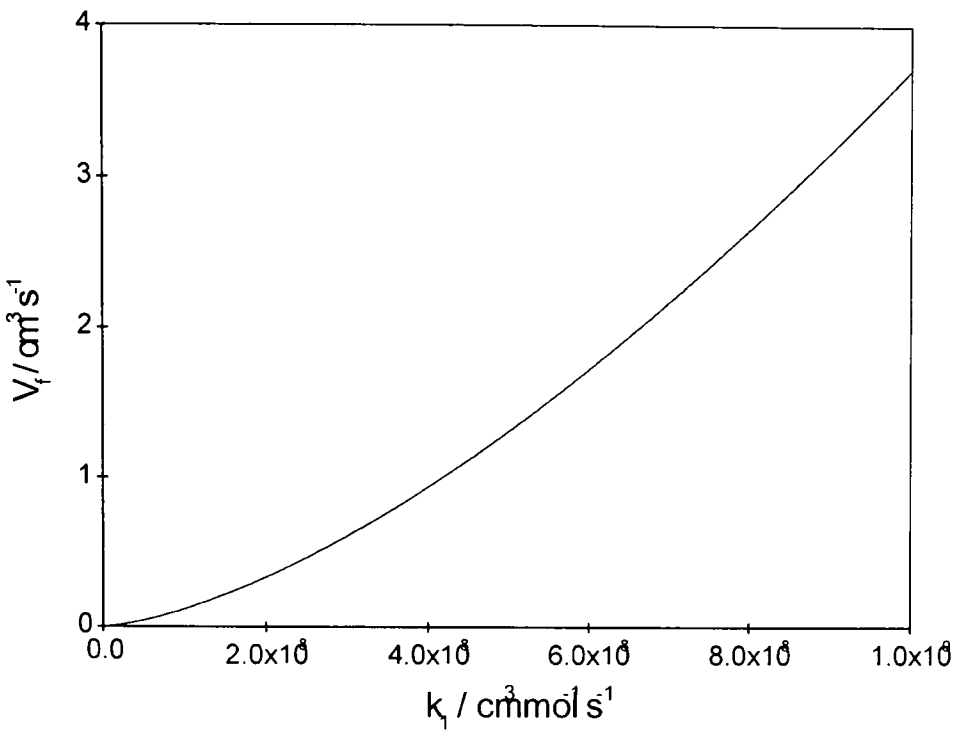


Figure 5.10: The threshold for the onset of "visible" kinetics.

The electrochemical response of DEPD in DMF was next examined at microdisc electrodes. Typical voltammetric responses obtained at a 17 μm radius platinum electrode to various concentrations of DEPD (0.6 – 6 mM) are detailed in figure 5.11.

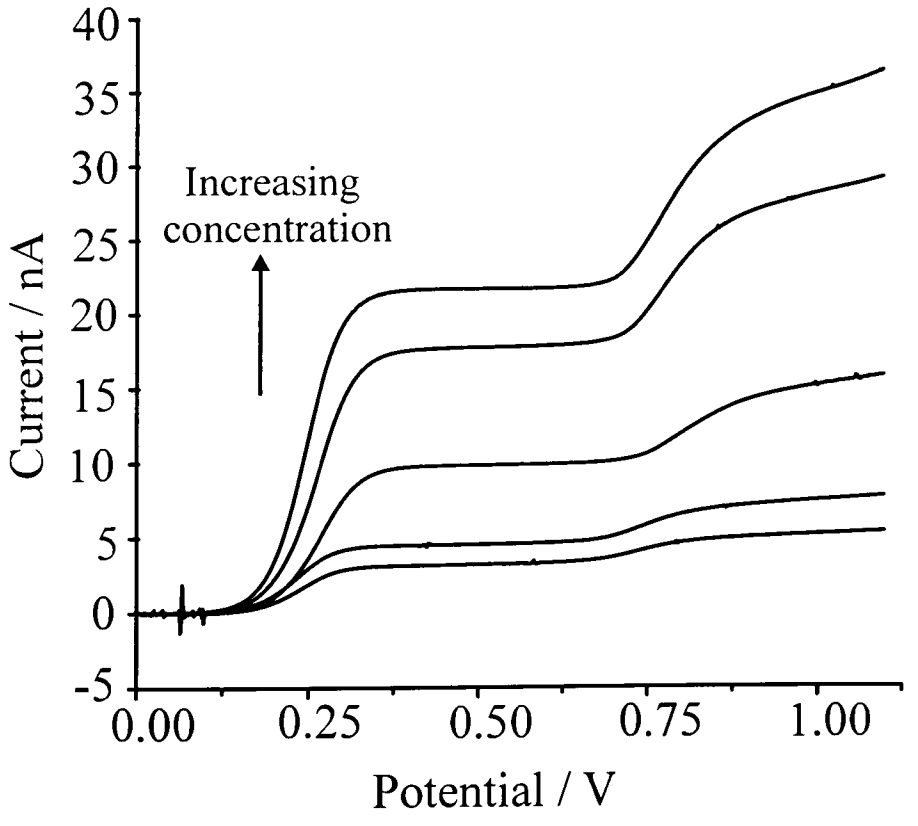


Figure 5.11: Linear sweep voltammetric response obtained at a 17 μm radius Pt electrode for the oxidation of DEPD (0.6 – 6 mM) in DMF.

These show two apparently electrochemically reversible redox processes occurring, with half potentials of +0.28 V (*vs.* Pt) and +0.79 V (*vs.* Pt) respectively. Figure 5.12 shows the magnitude of the limiting current for the first oxidation wave as a function of $r_d^2[DEPD]/D_A$; notice both the logarithmic scale of the x-axis and the considerable scatter in the experimental data. The current scale has been normalised with respect to steady state equation for microdisc electrodes [45] taking the diffusion coefficient of DEPD as 8.8×10^{-6} $cm^2\ s^{-1}$ (*vide infra*) so that the y-axis of figure 5.12 shows the effective number of electrons passed in the first oxidation wave.

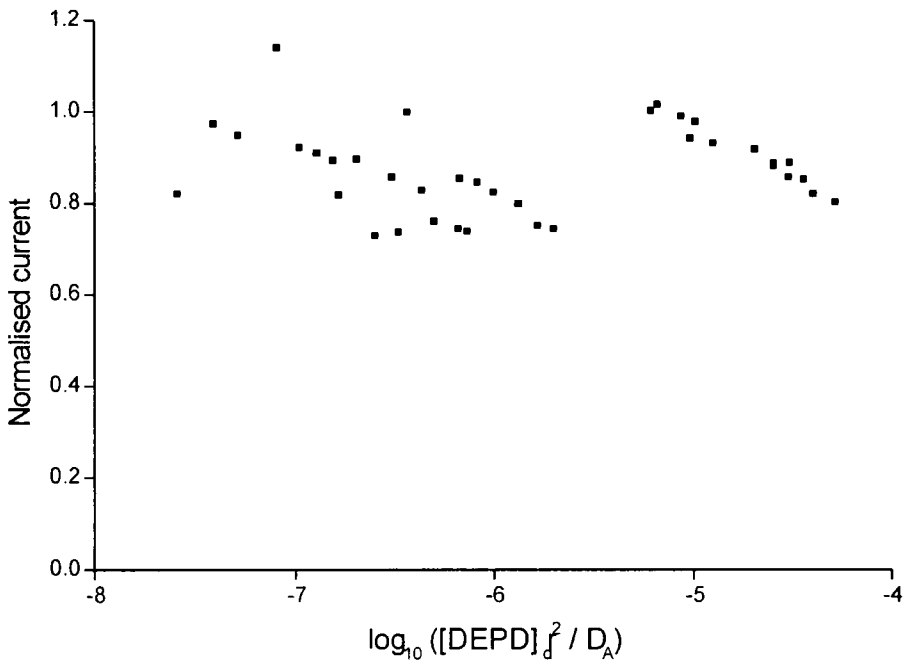


Figure 5.12: Normalised first wave current against $\log_{10}\frac{[DEPD]r_d^2}{D_A}$.

The scatter arises from the observed high probability of electrode fouling in this system, which arises from the formation of oligomeric products noted above. Analysis of the second oxidation wave shows that for the low concentrations of DEPD the second oxidation wave has limiting currents significantly smaller than that of the first oxidation wave. However, as the concentration increases the second limiting current increases to above half the value of the first.

In order to probe the results further analogous experiments were carried out at microdiscs of radius 6.7 μm, 32.4 μm and 66 μm respectively over the same

concentration range of DEPD. Figures 5.13 (a) and 5.13 (b) detail four voltammetric responses which depict the extreme cases studied. The linear sweep voltammetric responses observed at the smallest electrode studied (6.7 μm Pt) electrode for the highest and lowest concentrations (0.5 mM and 3 mM) DEPD used are shown in figure 5.12 (a), while the corresponding voltammograms obtained at the largest (66 μm Pt) electrode used for the highest and lowest concentrations (0.6 mM and 4 mM) DEPD are detailed in figure 5.13 (b).

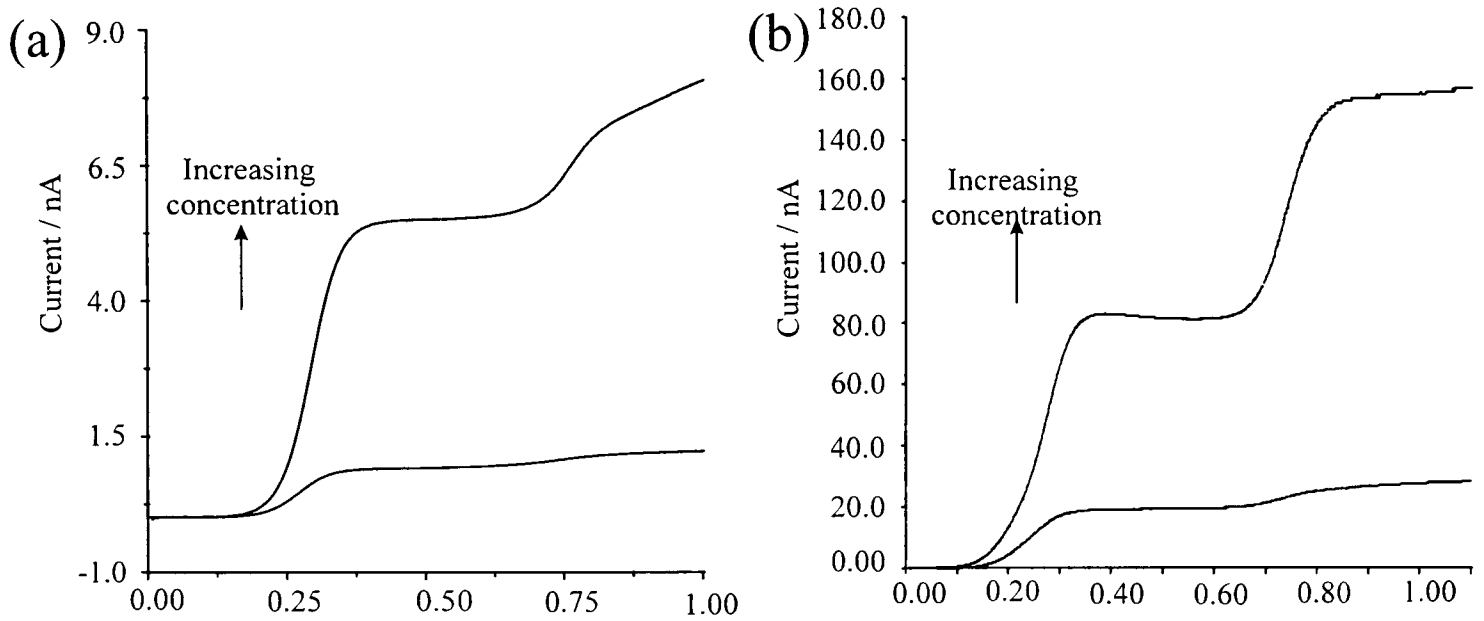


Figure 5.13: Linear sweep voltammmetry (3 mV s^{-1}), detailing the response at a (a) 6.7 μm electrode with 0.5 and 3 mM DEPD and (b) a 66 μm electrode with 0.6 and 4 mM DEPD.

These voltammograms show how at low concentrations the second oxidation wave is less than half that of the first oxidation wave and on the smallest electrode the second wave is immeasurably small. However, at the higher concentrations the second wave becomes far more pronounced at both electrode sizes. These results reveal that a reaction process is occurring after the first electron transfer, which is likely to involve a second order kinetic process. This can be tentatively attributed to a proton transfer step from the newly formed $DEPD^{+\bullet}$ to the parent DEPD species as outlined in scheme 5.1 by analogy with for the case of p-phenylenediamine (PPD) as advocated by Solis and Giordano [9,10]. We therefore apply the kinetic scheme developed earlier to the analysis of the microdisc data.

5.5.2 Fitting Experimental Data to Theoretical Results

All the experimental data for the first wave current $\tilde{i}_1$ obtained for different concentrations and electrode radii was plotted on the same graph as a function of $x = \log_{10}\left(\frac{[A]_{bulk}\, r_d^2}{D_A}\right)$. This scale is the same as in Figure 5.5 but shifted by a quantity $\log_{10} k_1$. Therefore in order to find the values of k_1 and K_{eq} corresponding to experimental conditions it was necessary to solve the following minimization problem:

$$\min_{K_{eq}} \min_{k_1} \sum_{i=1}^{N} \left| \tilde{i}_1^{\,\exp}(x_i) - \tilde{i}_1^{\,\mathrm{th}}\left(x_i + \log_{10} k_1,\, K_{eq}\right) \right| \tag{5.8}$$

where $\tilde{i}_1^{\,\exp}(x)$ are the experimental values of the first wave current related to values of x calculated from the conditions of experiment and $\tilde{i}_1^{\,\mathrm{th}}\left(\log_{10}\tilde{k}_1,\, K_{eq}\right)$ is a theoretical dependence of $\tilde{i}_1$ on the normalised rate constant of the C_{rev} step of the mechanism and the equilibrium constant K_{eq}.

As we have shown earlier (Figure 5.7) the second wave current depends on both normalised rate constants of the chemical steps of the kinetic mechanism (the equilibrium constant is known). Logarithms of these rate constants can be represented as $\log_{10}\tilde{k}_1 = x + \log_{10} k_1$ and $\log_{10}\tilde{k}_2 = x + \log_{10} k_2$. Since both $\log_{10}\tilde{k}_1$ and $\log_{10}\tilde{k}_2$ linearly depend on x we can deduce the following relation between the normalised rate constants corresponding to the experimental conditions (the values of the real rate constants do not change):

$$\log_{10}\tilde{k}_2 = \log_{10}\tilde{k}_1 + \log_{10}\frac{k_2}{k_1}. \tag{5.9}$$

It follows from the last expression that we shall examine the cross-sections through the working surface shown in Figure 5.7 along the lines parallel to the main diagonal (Figure 5.14).

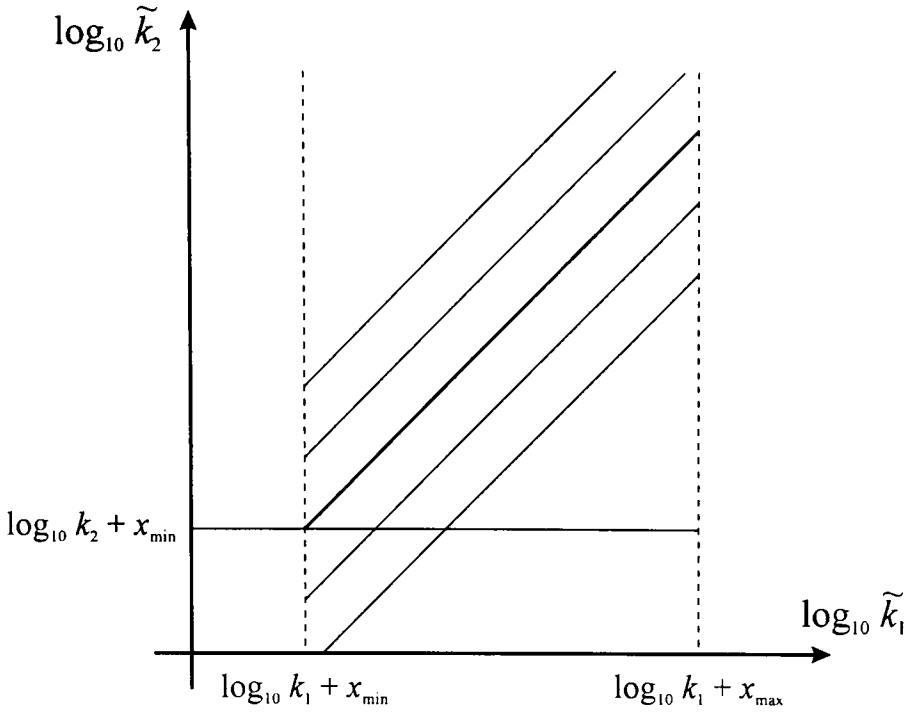


Figure 5.14: Relationship between the normalised rate constants of the chemical steps.

The current profiles obtained in this way can then be projected onto the $\log_{10} \tilde{k}_2$ axis and compared to the experimental data. In order to find the value of k_2 the values of the normalised second wave current $\tilde{i}_2$ were plotted against x as in the case of the first wave current and the next minimisation problem was formulated:

$$\min_{k_2} \sum_{i=1}^{N} \left| \tilde{i}_2^{\,\mathrm{exp}}(x_i) - \tilde{i}_2^{\,\mathrm{th}}(x_i + \log_{10} k_1,\, x_i + \log_{10} k_2) \right| \qquad (5.10)$$

where $\tilde{i}_2^{\,\mathrm{exp}}(x)$ are the experimental values of the second wave current and $\tilde{i}_2^{\,\mathrm{th}}(\log_{10} \tilde{k}_1, \log_{10} \tilde{k}_2)$ is a theoretical dependence of the second wave current on the logarithms of the normalised rate constants.

As the value of the diffusion coefficient of DEPD is not known we need to repeat the described fitting procedure for both $\tilde{i}_1$ and $\tilde{i}_2$ with increasing diffusion coefficient starting with the value obtained from the high-speed channel experiment. The best fit to both the first and second wave currents was reached at the value of diffusion coefficient $D = 8.8 \times 10^{-6}$ cm^2 s^{-1}.

The result of the minimisation process for the first wave current is shown in Figure 5.15 (a). The solid line corresponds to theoretical working curve for $\tilde{i}_1$ which is a

cross-section of the working surface from Figure 5.5 at $K_{eq} = 1$ that corresponds to the value of the equilibrium constant observed in the experiment. In the Figure 5.15 (a) the dots represent the experimental data obtained for a wide range of bulk concentrations of DEPD and electrode radii. The second step in the $EC_{rev}ECE$ mechanism was found to be effectively diffusion controlled, i.e. the value of k_1 found as a result of a minimisation procedure (5.8) is of order 10^{12} - 10^{13} cm^3 mol^{-1} s^{-1}.

The best fit to second wave current data is shown in Figure 5.15 (b) and the corresponding value of the rate constant is $k_2 = 1.2 \times 10^7$ cm^3 mol^{-1} s^{-1}.

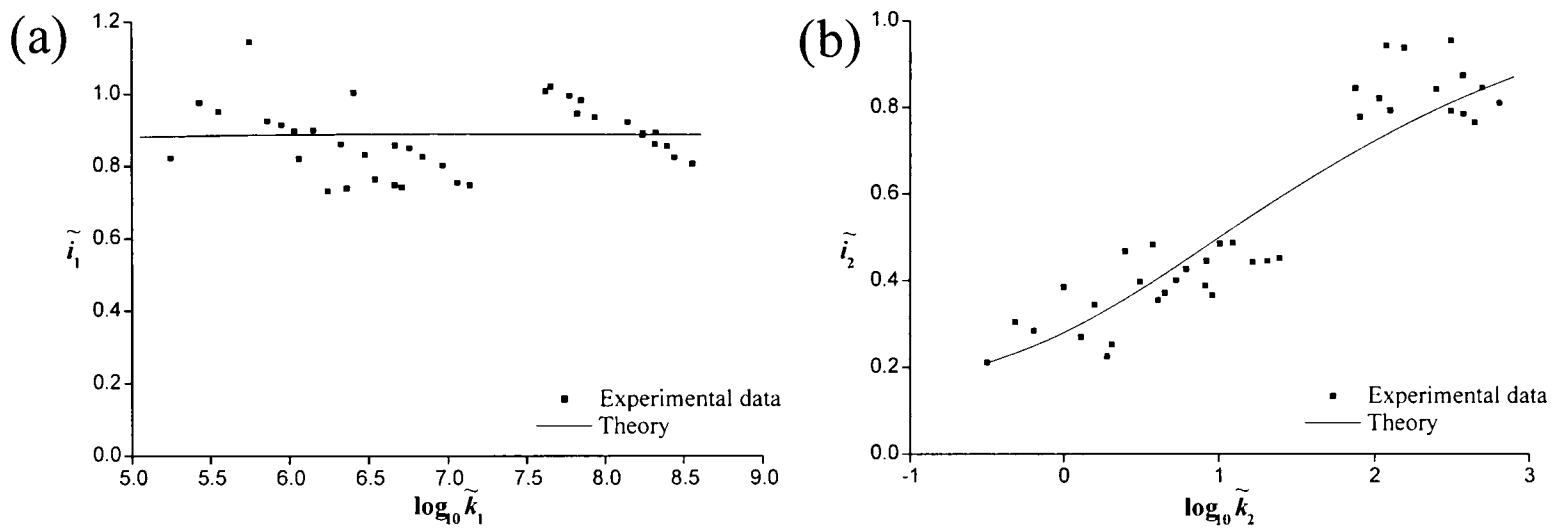


Figure 5.15: The best fit to: (a) the first wave current and (b) the second wave current.

5.6 Conclusion

A general method for modelling the $EC_{rev}ECE$ reaction at microdisc electrodes has been illustrated. The results of the simulations have been utilised and examined against the experimental results obtained for the oxidation of DEPD in organic solvents. The results have been compared with good agreement shown between experimental and theoretically predicted limiting currents for both the first and second oxidation waves.

Having elucidated the reactions mechanism of DEPD in DMF, we next turn our attention to its response in the presence of sulfide.

5.7 Chapter 5 References

[1] N. S. Lawrence, J. Davis, L. Jiang, T. G. J. Jones, S. N. Davies, R. G. Compton, *Electroanalysis* **2000**, *12*, 1453.

[2] O. V. Klymenko, D. Giovanelli, N. S. Lawrence, N. V. Rees, L. Jiang, T. G. J. Jones, R. G. Compton, *Electroanalysis* **2003**, *15*, 949.

[3] N. S. Lawrence, J. Davis, L. Jiang, T. G. J. Jones, S. N. Davies, R. G. Compton, *Electroanalysis* **2001**, *13*, 432.

[4] N. S. Lawrence, M. Thompson, J. Davis, L. Jiang, T. G. J. Jones, R. G. Compton, *Mikrochimica Acta* **2001**, *137*, 105.

[5] N. S. Lawrence, J. Davis, R. G. Compton, L. Jiang, T. G. J. Jones, S. N. Davis, *Analyst* **2000**, *125*, 661.

[6] P. C. White, N. S. Lawrence, J. Davis, R. G. Compton, *Anal. Chim. Acta* **2001**, *447*, 1.

[7] W. L. Orr, J. S. Sinninghe Damste, in *Geochemistry of Sulphur in Fossil Fuels, ACS Symposium Serie 429* (Eds: W. L. Orr, C. M. White), American Chemical Society, Washington D.C. **1990**.

[8] D. R. Lide, *CRC Handbook of Chemistry and Physics*, 74th Ed., CRC Press, Florida, US, **1993**.

[9] M. C. Giordano, V. M. Solis, *Anales de la Asociacion Quimica Argentina* **1982**, *70*, 69.

[10] V. Solis, T. Iwasita, M. C. Giordano, *J. Electroanal. Chem.* **1976**, *73*, 91.

[11] O. Fischer, V. Komarek, *Coll. Czech. Chem. Commun.* **1976**, *41*, 2320.

[12] C. G. Phillips, *J. Electroanal. Chem.* **1990**, *296*, 255.

[13] L. Rajendran, M. V. Sangaranarayanan, *J. Electroanal. Chem.* **1996**, *415*, 1.

[14] K. Aoki, J. Osteryoung, *J. Electroanal. Chem.* **1981**, *122*, 19.

[15] D. Shoup, A. Szabo, *J. Electroanal. Chem.* **1982**, *140*, 237.

[16] M. Fleischmann, D. Pletcher, G. Denuault, J. Daschbach, S. Pons, *J. Electroanal. Chem.* **1989**, *263*, 225.

[17] L. Rajendran, M. V. Sangaranarayanan, *J. Phys. Chem. B* **1999**, *103*, 1518.

[18] M. V. Mirkin, A. J. Bard, *J. Electroanal. Chem.* **1992**, *323*, 1.

[19] A. C. Michael, R. M. Wightman, C. A. Amatore, *J. Electroanal. Chem.* **1989**, *267*, 33.

[20] G. Taylor, H. H. Girault, J. McAleer, *J. Electroanal. Chem.* **1990**, *293*, 19.

[21] D. J. Gavaghan, *J. Electroanal. Chem.* **1998**, *456*, 1.

[22] J. Heinze, *J. Electroanal. Chem.* **1989**, *124*, 73.

[23] J. Heinze, *Berichte der Bunsen-Gesellschaft* **1981**, *85*, 1096.

[24] I. Lavagini, P. Pastre, F. Magno, C. A. Amatore, *J. Electroanal. Chem.* **1991**, *316*, 37.

[25] J. A. Alden, R. G. Compton, *J. Phys. Chem. B* **1997**, *101*, 8941.

[26] J. A. Alden, R. G. Compton, *J. Phys. Chem. B* **1997**, *101*, 9606.

[27] C. A. Amatore, B. Fosset, *J. Electroanal. Chem.* **1992**, *328*, 21.

[28] M. W. Verbrugge, D. R. Baker, *J. Phys. Chem.* **1992**, *96*, 4572.

[29] R. Ferringo, P. F. Brevet, H. H. Girault, *Electrochim. Acta* **1997**, *42*, 1895.

[30] K. Harriman, D. J. Gavaghan, P. Houston, E. Suli, *Electrochem. Commun.* **2000**, *2*, 150.

[31] T. Nann, J. Heinze, *Electrochem. Commun.* **1999**, *1*, 289.

[32] J. Galceran, D. J. Gavaghan, J. S. Rollett, *J. Electroanal. Chem.* **1995**, *394*, 17.

[33] D. J. Gavaghan, *J. Electroanal. Chem.* **1997**, *420*, 147.

[34] J. Heinze, M. Stoerzbach, *Berichte der Bunsen-Gesellschaft* **1986**, *90*, 1043.

[35] I. B. Svir, O. V. Klimenko, R. G. Compton, *Radiorekhnika* **2001**, *118*, 92.

[36] G. Stephenson, *Mathematical Methods for Science Students*, Prentice Hall, New York, **1973**.

[37] K. Eriksson, D. Estep, P. Hansbo, C. Jonhnson, *Computational Differential Equations*, Cambridge University Press, Cambridge, **1996**.

[38] N. V. Rees, O. V. Klymenko, R. G. Compton, M. Oyama, *J. Electroanal. Chem.* **2002**, *531*, 33.

[39] A. J. Bard, L. R. Faulkner, *Electrochemical Methods: Fundamentals and Applications*, 2nd Ed., John Wiley and Sons, New York, **2001**.

[40] N. V. Rees, R. A. W. Dryfe, J. A. Cooper, B. A. Coles, R. G. Compton, S. G. Davies, T. D. McCarthy, *J. Phys. Chem.* **1995**, *99*, 7096.

[41] N. V. Rees, J. A. Alden, R. A. W. Dryfe, B. A. Coles, R. G. Compton, *J. Phys. Chem.* **1995**, *99*, 14813.

[42] B. A. Coles, R. A. W. Dryfe, N. V. Rees, R. G. Compton, S. G. Davies, T. D. McCarthy, *J. Electroanal. Chem.* **1996**, *411*, 121.

[43] N. V. Rees, O. V. Klymenko, B. A. Coles, R. G. Compton, *J. Electroanal. Chem.* **2002**, *534*, 151.

[44] R. G. Compton, P. R. Unwin, *J. Electroanal. Chem.* **1986**, *205*, 1.

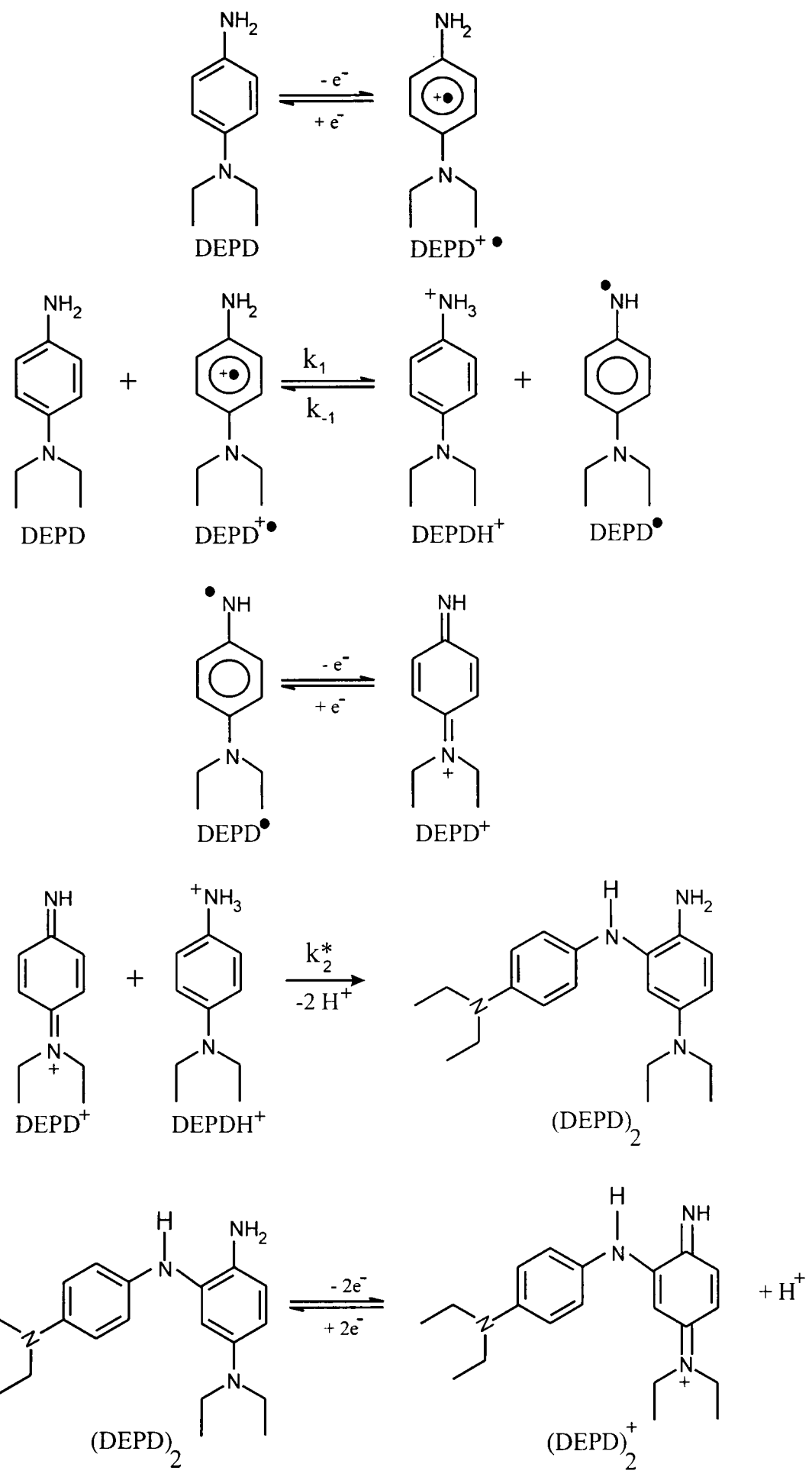
[45] J. A. Alden. *Dphil. Thesis, Physical and Theoretical Chemistry Laboratory*; University of Oxford: Oxford, 1998.

Chapter 6: "The Electrochemically Initiated Reaction of Sulfide with N,N-Diethyl-p-phenylenediamine (DEPD) in N,N-Dimethylformamide (DMF) Part II: Implications for Sensing Strategies"

In the previous chapter the voltammetric response of DEPD in DMF has been characterized as undergoing an $EC_{rev}ECE$ reaction process. In this chapter the electrochemically initiated reaction of N,N-diethyl-p-phenylenediamine (DEPD) with sulfide in N,N-dimethylformamide (DMF) is examined at both macro and platinum microdisc electrodes with quantitative detection of sulfide produced by means of the enhanced currents observed upon its addition. The linear detection range for sulfide is dependent on the concentration of DEPD present with a linear range from 28 – 3290 μM and a limit of detection of 22 μM achievable. This represents a large increase compared to that formed previously in aqueous media (Chapter 3, Section 3.2.4.1) and offers the prospect of more ready applications in high temperature systems (Chapter 14). The results obtained have been published in Electroanalysis [1].

6.1 Introduction

The voltammetric response of DEPD in DMF (0.1 M TBAP) has been previously characterized as undergoing an $EC_{rev}ECE$ reaction process as depicted in scheme 6.1 [2].



Scheme 6.1: Electrochemical oxidation mechanism of N,N-diethyl-p-phenylenediamine (DEPD) in N,N-dimethylformamide (DMF) [2].

We now report the electrochemically initiated reaction of DEPD with sulfide in DMF, under both macro and microdisc conditions and a possible reaction scheme is suggested (scheme 6.2, *vide infra*). The nature of the electrode process in the absence of sulfide is such that for small electrode radii of less than 100 μm and low DEPD concentrations the second oxidation wave disappears. Accordingly we identify the conditions under which useful analytical measurements can be made using the proposed strategy under the microdisc regime. The results illustrate that by using a 66 μm radius Pt disc electrode with 0.5 mM DEPD quantitative detection of sulfide is achieved.

6.2 Experimental

6.2.1 Hydrogen Sulfide Delivery Assembly

Sulfide additions were prepared by utilizing the cell arrangement detailed in figure 6.1 which can be constructed from readily available standard glassware [3]. The cell was used principally to liberate hydrogen sulfide gas from a sample injected into the acidified solution (3 mL, 0.1 M H_2SO_4) contained within compartment A. The gas passes into the adjoining chamber (B, figure 6.1) through a gas permeable membrane (in order to avoid passing water into the organic solution) where it is bubbled through a solution containing a known quantity of the indicator species (DEPD) dissolved in DMF and 0.1 M TBAP.

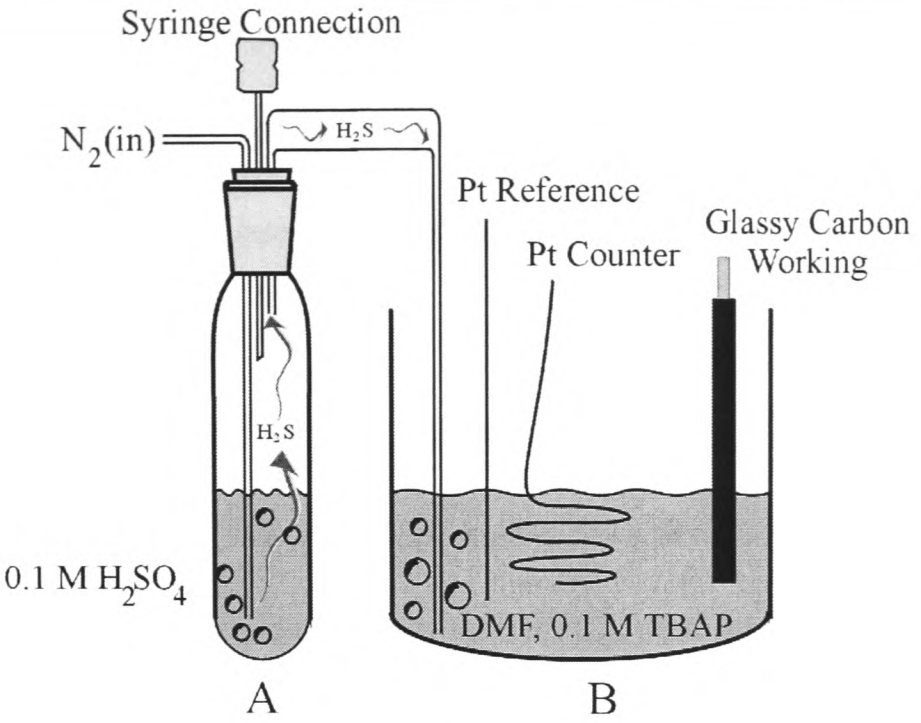


Figure 6.1: Hydrogen Sulfide Delivery Assembly.

6.3 Results and Discussion

Preliminary investigation of the detection process involved the use of cyclic voltammetry at a 3 mm glassy carbon working electrode as a means of probing the electrochemical behavior of N,N-diethyl-p-phenylenediamine (DEPD) with sulfide in DMF. The corresponding cyclic voltammetry (100 mV s^{-1}) for a solution containing 0.25 mM DEPD in DMF (0.1 M TBAP) are detailed in figure 6.2.

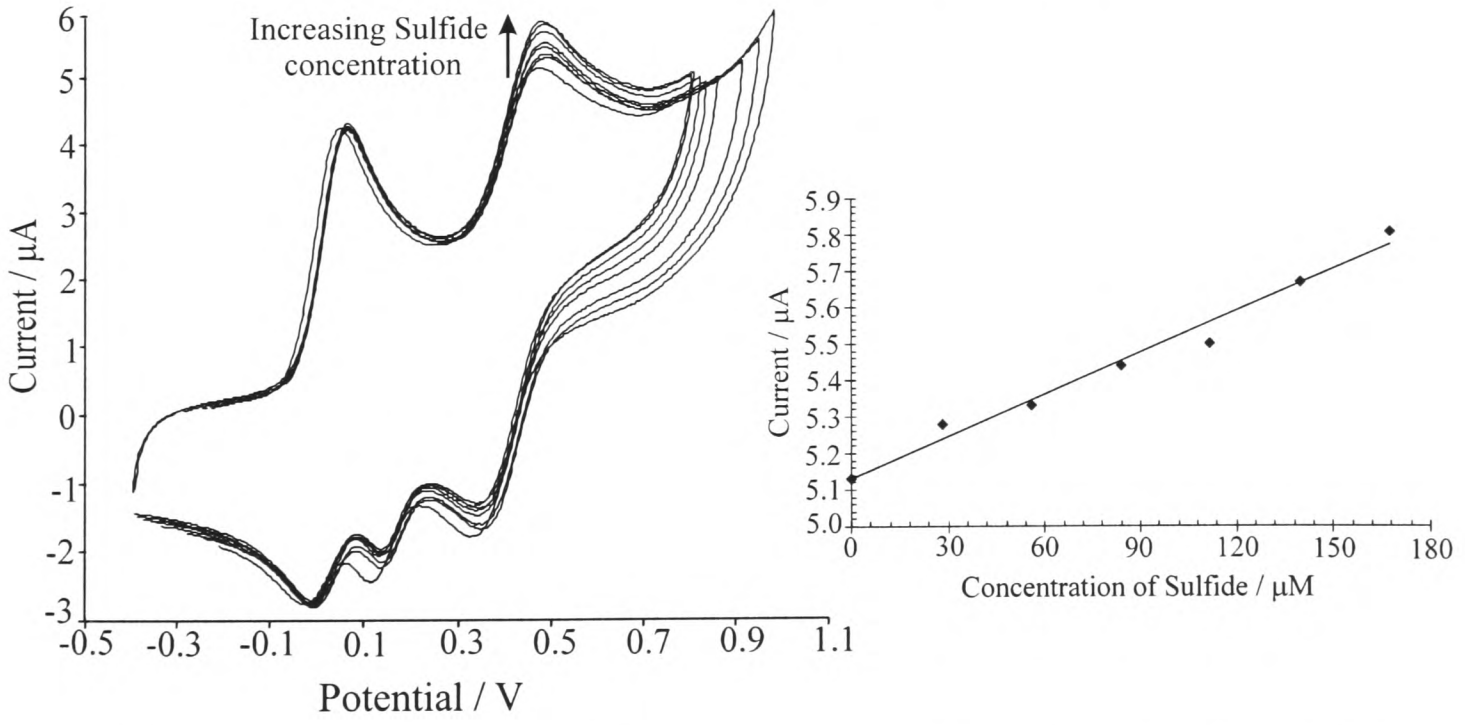


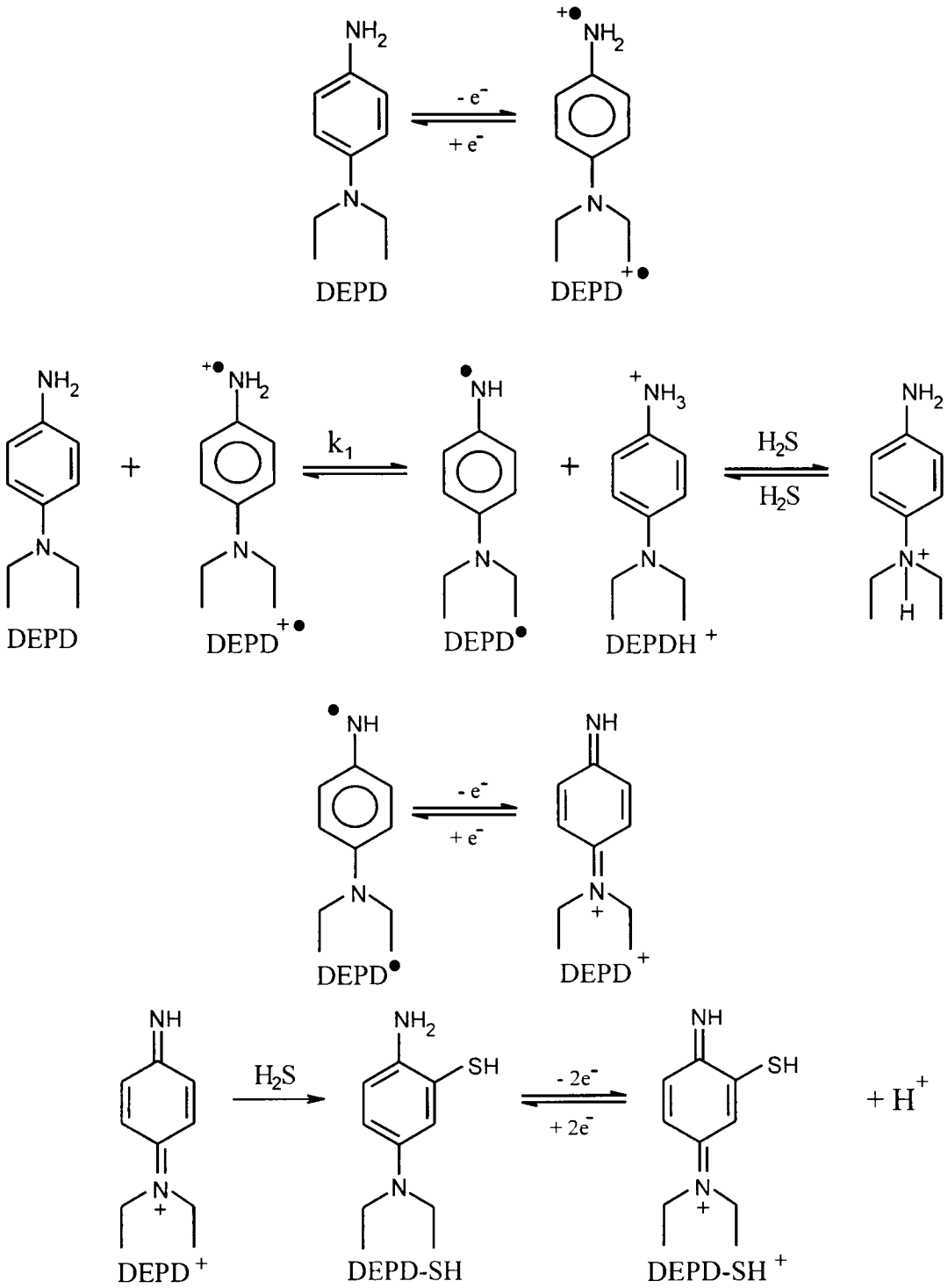
Figure 6.2: Cyclic voltammetric (100 mV s^{-1}) response for the oxidation of 0.25 mM DEPD in DMF (0.1 M TBAP) in the presence of additions of sulfide (28 – 196 µM). Insert: A plot of oxidation peak current at +0.48 V against concentration of sulfide.

This reveals two oxidative waves at +0.06 V and +0.48 V (*vs.* Pt) corresponding to the oxidation of the parent DEPD species to the radical cation followed by further reactions including a second heterogeneous electron transfer as deduced previously ($EC_{rev}ECE$, scheme 6.1) [2].

Upon reversal of the scan three reductive waves are observed at +0.40 V, +0.12 V and -0.02 V (*vs.* Pt). The first wave at +0.40 V can be attributed to the reduction of the doubly oxidised $DEPD^{+}$ cation species to the $DEPD^{\bullet}$ radical species (see scheme 6.1). The second (+0.12 V) can be tentatively assigned to the reduction of the newly formed oligomeric or polymeric species [2] and the final reduction wave at -0.02 V corresponds to the reduction of the electrochemically generated radical cation species back to the parent DEPD species (scheme 6.1).

The voltammetric responses to the increasing additions of sulfide (28 μM) are also detailed in figure 6.2. First, it should be noted that upon the addition of sulfide there was a shift in the oxidation potentials of the DEPD species which is likely due to sulfide contaminating the Pt pseudo-reference electrode. Therefore all the current-potential traces shown in this work have been superimposed by matching the oxidation peak potential of the first wave for each voltammetric response. The voltammograms reveal that upon the introduction of sulfide to the cell no change is observed in the voltammetric signal of the first oxidation wave other than the shift attributed to the poisoning of the reference electrode. However, the second wave peak current is seen to increase in size with increasing sulfide additions. This increase can be attributed to the sulfide species attacking the $DEPD^{+}$ species in a 1,4-Michael addition (scheme 6.2). The resulting product (DEPD-SH, scheme 6.2) can be subsequently re-oxidised at the electrode surface to produce the enhancement in the current signal in an analogous manner to that observed with the electrochemically initiated reaction of phenylenediamines with sulfide [3-6] or thiols [7,8] in aqueous

media (Chapter 3, scheme 3.2). Analysis of this increase by means of a standard addition plot is also illustrated in figure 6.2. This produces a linear range from 28 to 168 μM with a corresponding limit of detection of 22 μM sulfide. It was shown that an analogous response whereby the second oxidation wave increased in the presence of sulfide was observed over a range of scan rates (50 - 200 mV s^{-1}).



Scheme 6.2: The proposed electrochemically initiated reaction of sulfide with DEPD in DMF.

In order to provide evidence that the sulfide is attacking the doubly oxidised $DEPD^{+}$ species, cyclic voltammograms at 100 mV s^{-1} were recorded with the potential sweep range limited so that only oxidation of the parent to the radical cation ($DEPD^{+\bullet}$) species took place. The voltammetric response showed no change in signal upon the

addition of sulfide (up to 174 μM) to the solution and this suggests that sulfide does not attack the cation radical $DEPD^{+\bullet}$ under these conditions.

In order to increase the linear range of sulfide detection and to improve the limit of detection for sulfide, the concentration of DEPD was varied. Analysis of the resulting data shows that by increasing the concentration of DEPD to 0.50 mM the linear range can be usefully increased up to 3.3 mM sulfide.

The generic nature of the detection process was also investigated by examining the electrochemical response of p-phenylenediamine (PPD) and N,N-dimethyl-p-phenylenediamine (DMPD) both in the absence and presence of sulfide. Examination of the cyclic voltammetric response in the absence of sulfide again shows two oxidative waves for both DMPD and PPD oxidation. Upon addition of sulfide, similarly to what seen when DEPD was used as indicator species, an enhancement in the second oxidation wave was observed. This gave a linear range from 109 μM to 654 μM sulfide for PPD and from 80 μM to 480 μM sulfide for DMPD.

In order to develop the analytical protocol outlined above towards a sensing device, the reaction was next studied at microelectrodes. The advantages of utilising microelectrodes in sensors are that they allow enhanced mass transport due to the small diffusion layer with convergent diffusion. Moreover a current signal can be obtained without significantly depleting the indicator solution. This is a vital asset given the need to develop small cell configurations with a static pool of indicator. As mentioned above the voltammetric response of DEPD has been previously characterised as undergoing an $EC_{rev}ECE$ [2] reaction mechanism detailed in scheme 6.1. The DEPD species is first oxidised to the radical cation species $DEPD^{+\bullet}$; this then undergoes proton transfer to form $DEPD^{\bullet}$ which can then undergo further oxidation and reaction to ultimately form the dimeric species [2]. As shown earlier the cyclic voltammetric response of DEPD with sulfide revealed an increase in the second oxidation wave. It

was expected an analogous response might be observed under the regime of convergent diffusion.

First however, the optimum experimental conditions have to be determined. As shown in the previous chapter [2] under certain conditions (small electrode radii and low concentrations of DEPD) the voltammetric response of DEPD fails to produce a notable second oxidation limiting current. This is due to the fact that the rate of diffusion of $DEPD^{+\bullet}$ away from the electrode outruns the kinetics of the proton transfer such that only a small concentration of $DEPD^{\bullet}$ is formed. Therefore the question is for a certain size of electrode what concentration of DEPD is required in order to produce a second limiting current with a magnitude say at least half that of the first limiting current. In order to answer this question the theory for the $EC_{rev}ECE$ reaction occurring for the electrochemical oxidation of DEPD in DMF at a microdisc electrode has to be developed. Using the model reported in the previous chapter a zone diagram with concentration and electrode radius as axes was deduced and is shown in figure 6.3.

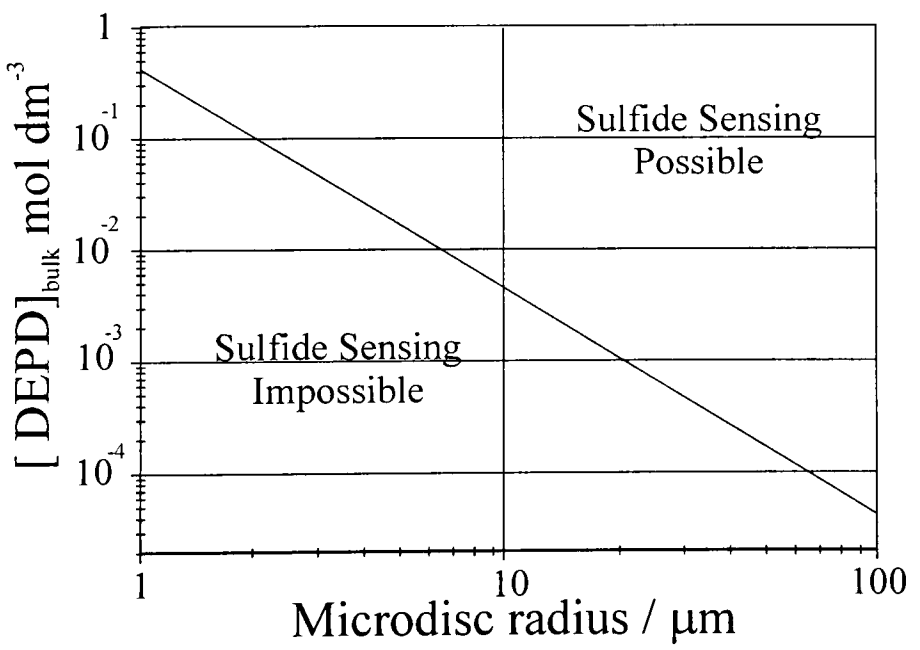


Figure 6.3: A zone diagram with concentration and electrode radius as axes (deduced using the model described in Chapter 5, [2]) showing the boundary. Above the latter is where the second limiting current will be greater than a half that of the first.

This shows a boundary: the region above is where the second limiting current will be greater than a half that of the first. The area below the boundary is where the second

limiting current is less than half that of the first. Therefore, by using this plot the concentration of DEPD required to produce a second limiting current half the magnitude of the first can be determined for any electrode radius. In the work outlined below the voltammetric response of a 66 μm electrode in 0.5 mM DEPD solution to increasing additions of sulfide is examined. Theory reveals that these conditions are such that the second wave is 96 % of the first and that the operating conditions are in the 'safe' zone.

Linear sweep voltammetry (3 mV s^{-1}) was carried out. The corresponding voltammetric response for a solution containing 0.5 mM DEPD to increasing additions of 37 μM sulfide is detailed in figure 6.4 (a). In the absence of sulfide this produced two oxidation waves with half potentials of +0.60 V (*vs.* Pt) and +1.05 V (*vs.* Pt) respectively in agreement with previous observations (Chapter 5). Upon addition of sulfide to the solution the voltammetric signal changes. The second limiting current begins to increase, whilst the first limiting current remains constant. This is consistent with that observed at macro electrodes as reported above.

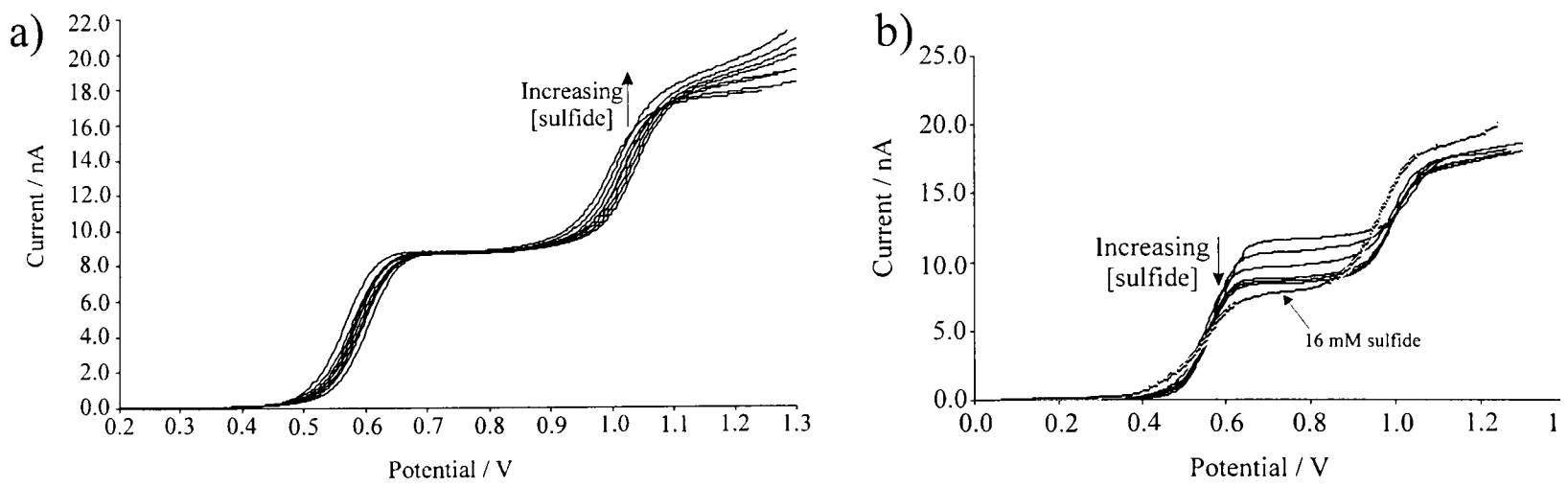


Figure 6.4: Linear sweep voltammetry (3 mV s^{-1}) obtained at a 66 μm radius microelectrode of 0.50 mM DEPD to increasing additions of sulfide in aliquots of (a) 37 μM and (b) 452 μM (see text).

However, as shown in Figure 6.4 (b), when sulfide is added in higher concentrations (i.e, aliquots of 450 μM sulfide), the first limiting current decreases whilst the second limiting current stays constant. This decrease of the first wave is shown to limit at

7.8 nA and never decreases to zero. This was confirmed by examining the current-potential profile of an extreme case, for a solution containing 0.50 mM DEPD and 16 mM sulfide. This is also overlaid on figure 6.4 (b). As is shown here the first limiting current has not decreased to zero, whilst the second limiting current remains the same as for a solution containing no sulfide. This behaviour can be rationalized by examination of scheme 6.1. This reveals that the proton transfer step is in fact likely to be an equilibrium process. If this equilibrium is adjusted such that either $DEPD^{\bullet}$ or $DEPDH^{+}$ is removed from the solution, this causes a depletion in the concentration of DEPD at the electrode surface and therefore causes a decrease in the limiting current of the first oxidation step. The fact that the second oxidation wave increases or remains at a single value when sulfide is present in great excess concurs with the macro electrode data as there is an enhancement in the oxidation wave with respect to the first limiting current so it can be concluded that the sulfide again attacks the $DEPD^{+}$ species in a 1,4-Michael addition as detailed earlier.

A consideration of the possible reaction processes which can occur suggests at first sight that sulfide might interact with the $DEPD^{+\bullet}$ species in a manner analogous to that observed in aqueous solutions where the homogeneous one electron oxidising agent Fe(III) reacts with DEPD [9]. However, this possibility can be ignored in the light of the fact that at macroelectrodes, sulfide had no effect on the voltammetric response when only the first oxidation process was allowed to occur (*vide supra*). This reaction of sulfide with $DEPD^{+\bullet}$ can be therefore discounted. In addition the interaction of sulfide with the $DEPD^{\bullet}$ species can be dismissed, as there appears to be no mechanistically plausible pathway available. It is most likely that the sulfide is reacting with the $DEPDH^{+}$ species.

Scheme 6.1 shows that in the proton transfer step, a proton from the $DEPD^{+\bullet}$ species likely adds to the primary amine end of the parent DEPD molecule, as this might be a

faster reaction than addition to the other nitrogen. However the different basicity of the two amine substituents [10] attached to either end of the benzene ring suggests that the tertiary amine species would likely be a stronger base due to the electron donating effects of the ethyl moieties. Therefore it is tentatively proposed that the hydrogen sulfide effectively catalyses the transfer of the proton from the primary amine substituent to the tertiary amine moiety as illustrated in scheme 6.2 and expressed by:

$$\text{-}NH_3^+ + H_2S \rightarrow \text{-}NH_2 + H_3S^+ \qquad (6.1)$$

$$H_3S^+ + \text{-}NR_2 \rightarrow + \text{-}NR_2H^+ + H_2S \qquad (6.2)$$

This would have the effect of depleting $DEPDH^+$ molecules from the reaction mixture, hence pushing the equilibrium across to the right, thereby causing more of the parent DEPD to be removed from the solution and so allowing for the decrease in the first limiting current (scheme 6.2). The fact that the decrease of the latter is only noticed when sulfide is added in considerable excess further supports this interpretation.

This suggestion of H_2S catalysed proton transfer was further partially verified by examining the voltammetry of the N,N-diethyl-p-phenylenediamine sulfate salt ($DEPDH^+HSO_4^-$) in DMF (0.1 M TBAP). In this case the salt is dissolved into the solution forming the $H_2NC_6H_6N(C_2H_5)H^+$ and HSO_4^- ($DEPDH^+HSO_4^-$) ions, in which the proton is complexed to the tertiary amine (thermodynamically the most stable site). The cyclic voltammetric (100 mV s^{-1}) response of 0.5 mM $DEPDH^+HSO_4^-$ is detailed in figure 6.5.

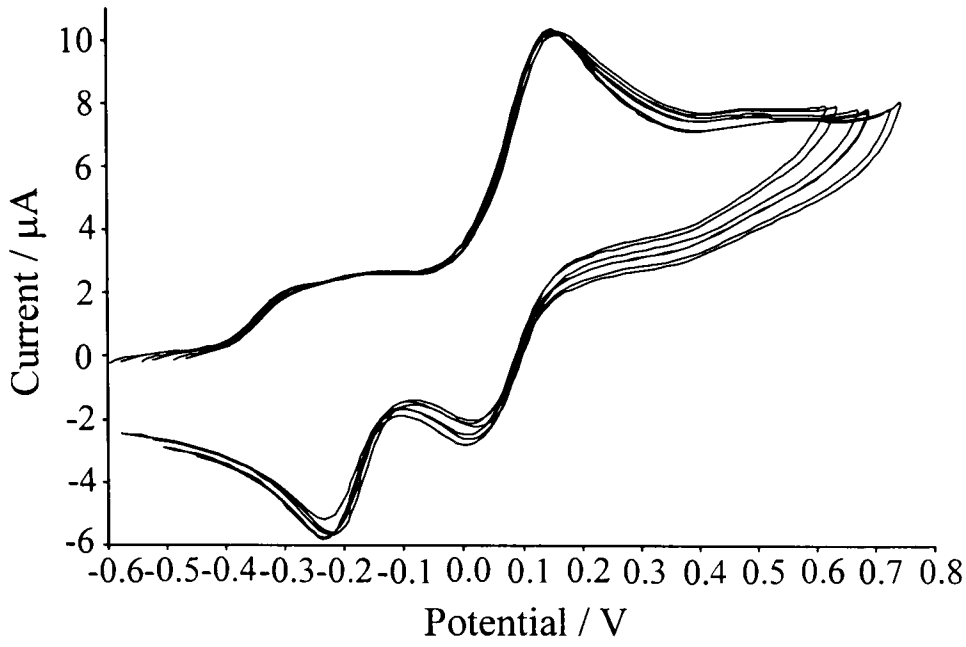
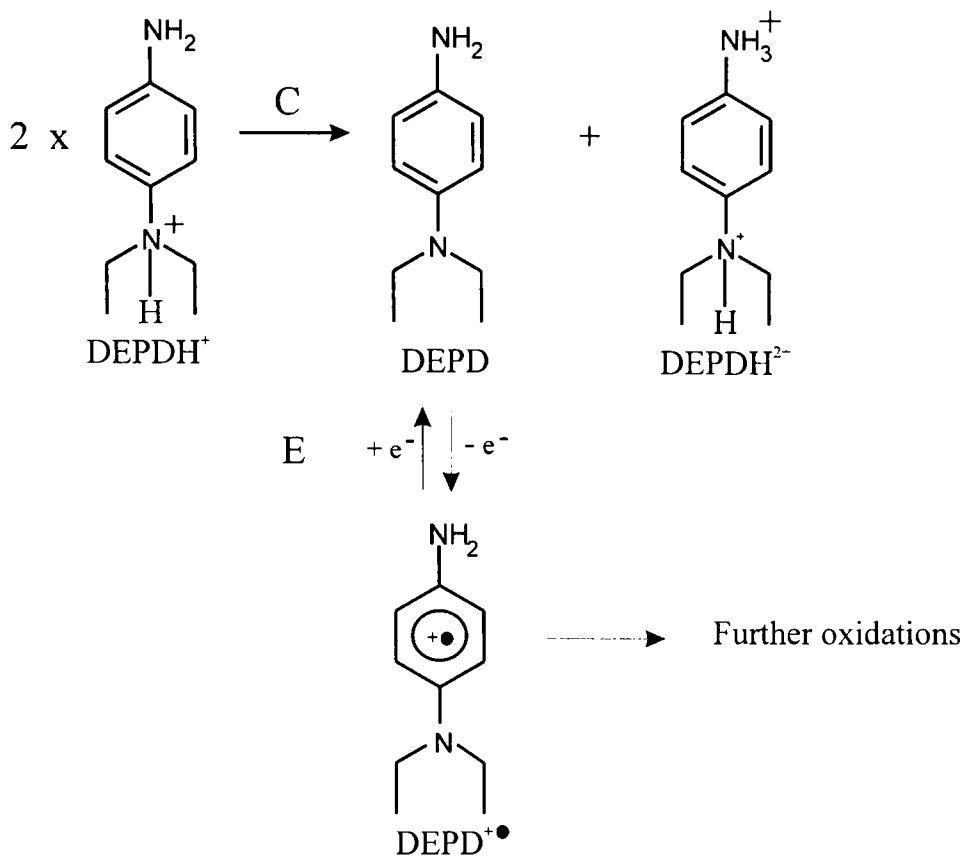


Figure 6.5: Cyclic voltammetric (100 mV s^{-1}) response for the oxidation of 0.5 mM protonated N,N-diethyl-p-phenylenediamine in DMF (0.1 M TBAP) in the presence of additions of sulfide (174 – 2,046 µM).

As can be seen from the figure the first oxidation wave at -0.20 V shows a broad oxidation signal, whereas the second oxidation wave at +0.13 V displays more reversible behaviour analogous to that observed earlier with the deprotonated DEPD species (figure 6.2). Upon reversal of the scan two electrochemically reversible waves are observed consistent with that seen above. The broad first oxidation wave can be attributed to the protonated parent DEPD species: the $DEPDH^+$ ion has to lose protons before oxidation can occur in a CE type mechanism and this leads to a perceived broadening of the wave (scheme 6.3). It was therefore anticipated that if hydrogen sulfide was a stronger base in DMF than the tertiary amine substituent of DEPD then upon the addition of sulfide to the system the broad oxidation wave would sharpen to give a response similar to that observed in figure 6.2, due to the fact that the hydrogen sulfide would effectively "pull" the protons from the $DEPDH^+$ ion producing the deprotonated DEPD species. As can be seen from figure 6.5 upon the addition of sulfide (170 - 2046 µM) there is no change in the voltammetric response. This therefore reveals that the hydrogen sulfide is a weaker base than the tertiary amine species but allows the inference to be drawn that the sulfide might remove the proton from the protonated primary amine species $DEPDH^+$ which could then be removed

from the sulfide by the tertiary amine moiety of DEPD (scheme 6.2), so catalysing the formation of the intramolecular proton transfer reaction.



Scheme 6.3: The proposed CE reaction of protonated N,N-diethyl-p-phenylenediamine in DMF.

Analytical Utility

In order to provide an analytical response from the microelectrode data, the limiting current data was analysed by examining the response of the ratio of limiting currents (I_2/I_1 = second limiting current/first limiting current) as a function of concentration of sulfide added. The corresponding plot of I_2/I_1 against concentration of sulfide is detailed in figure 6.6. The plot reveals a linear increase from 37 - 185 μM sulfide with a corresponding limit of detection of 6 μM sulfide. Once again this analytical range could be easily extended by varying the concentration of DEPD in the solution as shown earlier with the cyclic voltammetric data.

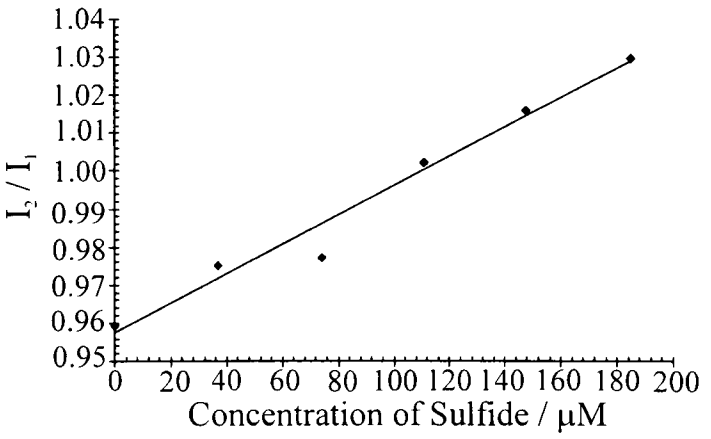


Figure 6.6: A plot of the ratio of the second to the first limiting current against concentration of sulfide for the microdisc data.

6.4 Conclusion

The electrochemically initiated reaction of DEPD with sulfide in DMF at both macro and microdisc electrodes has been examined. The response at macroelectrode was shown to produce an increase in the second oxidation wave consistent with the sulfide attacking the doubly oxidised $DEPD^+$ species in a 1,4-Michael addition similarly to the behavior observed in aqueous solutions (Chapter 3, Section 3.2.4.1, [3]). This response was found to be dependent on the concentration of DEPD present and produced a linear range from 28 - 3290 μM sulfide and a limit of detection of 22 μM at a macro electrode. This linear range provides a significant increase compared to that observed in aqueous solutions (Chapter 3, Section 3.2.4.1 [3]) .

Further probing of the reaction process at microdisc electrodes were carried out as a means of studying the reaction for sensor implications. The results have been rationalized fully as detailed in scheme 6.2. The response at a 66 μm radius microdisc electrode produces a linear range for 0.5 mM DEPD of 37 to 3160 μM sulfide and a limit of detection of 6 μM once again showing the analytical utility of the technique.

In order to relieve the constrains on the sensing system (namely the electrode radii and the indicator specie DEPD concentration), the effect of temperature on the reaction of sulfide with DEPD was next studied. It was anticipated that both the equilibrium constant for the proton transfer step and the rate of dimerisation would be affected by increasing the temperature, thereby enhancing the second limiting current. The results obtained are detailed in Chapter 14.

6.5 Chapter 6 References

[1] D. Giovanelli, N. S. Lawrence, O. V. Klymenko, L. Jiang, T. G. J. Jones, R. G. Compton, *Electroanalysis* **2003**, *15*, 961.

[2] O. V. Klymenko, D. Giovanelli, N. S. Lawrence, N. V. Rees, L. Jiang, T. G. J. Jones, R. G. Compton, *Electroanalysis* **2003**, *15*, 949.

[3] N. S. Lawrence, M. Thompson, J. Davis, L. Jiang, T. G. J. Jones, R. G. Compton, *Mikrochimica Acta* **2001**, *137*, 105.

[4] N. S. Lawrence, J. Davis, L. Jiang, T. G. J. Jones, S. N. Davies, R. G. Compton, *Electroanalysis* **2000**, *12*, 1453.
[5] N. S. Lawrence, J. Davis, L. Jiang, T. G. J. Jones, S. N. Davies, R. G. Compton, *Electroanalysis* **2001**, *13*, 143.
[6] N. S. Lawrence, J. Davis, L. Jiang, T. G. J. Jones, S. N. Davies, R. G. Compton, *Electroanalysis* **2001**, *13*, 432.
[7] N. S. Lawrence, J. Davis, R. G. Compton, L. Jiang, T. G. J. Jones, S. N. Davis, *Analyst* **2000**, *125*, 661.
[8] P. C. White, N. S. Lawrence, J. Davis, R. G. Compton, *Anal. Chim. Acta* **2001**, *447*, 1.
[9] V. Kuban, P. K. Dasgupta, J. N. Marx, *Anal. Chem.* **1992**, *64*, 36.
[10] J. March, *Advanced Organic Chemistry*, 4th Ed., Wiley, New York, **1992**.

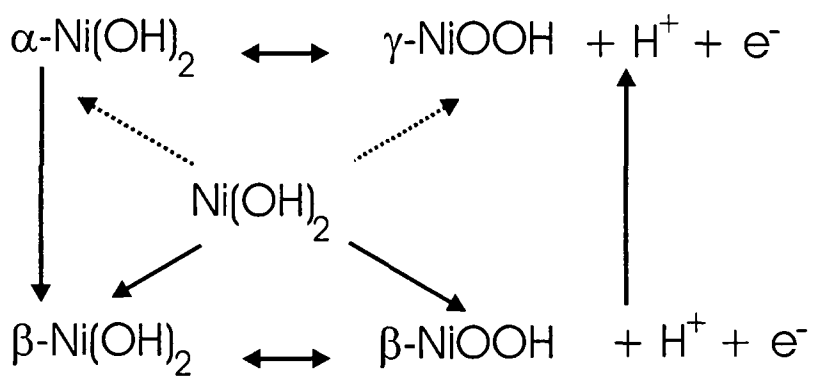
Chapter 7: "Detection of Sulfide at Nickel Modified Electrodes in Alkaline Media: a New Electrochemical Sensor"

This chapter outlines an amperometric detection strategy for sensing sulfide at a nickel hydroxide film developed on a nickel electrode by repetitive potential cycling in sodium hydroxide solutions. The results have provided the basis for the design of a simple, inexpensive and easily constructed sensing device for the toxic gas and have been published in Sensors and Actuators B [1].

7.1 The Electrochemistry of the Nickel Electrode in Alkaline Media

A survey of the literature reveals that nickel behaviour, nickel oxide formation, the nature, the structure and properties of the surface layers formed under different conditions and passivation phenomena have been widely investigated for a long time. This is not surprising as nickel and nickel based oxides are important electrode materials in nickel-based batteries and in a wide range of technological applications of batteries, electrochromic devise, water electrolysis, electrosynthesis and fuel cell [2,3]. Many articles have been devoted to the passivation phenomena and to the study of composition of the oxidation films of nickel in neutral [4,5] and acidic [2,6-18] conditions. These will be discussed further in the next chapter. In this chapter we describe the electrochemical properties of nickel hydroxide modified nickel (NHMN) electrodes in alkaline media.

The formation of nickel hydroxide in alkaline conditions have been achieved in different ways: potentiostatic [19,20], potentiodynamic [21-27], and galvanostatic [21,22,28] anodic sweeps as well as by the cathodic electrochemical deposition of a pH controlled salt of Ni in alkaline solution [29]. Under potentiodynamic conditions [27] a relative complex kinetic response due to the non-equilibrium states of both reactants and products has been reported. At least two reduced and two oxidised states were detected and the following square reaction scheme was proposed to illustrate chemical and electrochemical crossed reaction between different transient species involved in the formation of nickel hydroxide:



Scheme 7.1: A model representing the Ni(II)/Ni(III) transition as reported in reference [25].

However when considering nickel hydroxide films developed on a nickel metal electrode by repetitive potential cycling in sodium hydroxide solution, there is a general agreement that when nickel is immersed in the alkaline solution spontaneous dissolution of the metal occurs followed by the formation of a $Ni(OH)_2$ film [9,21-28,30-38] which initially has a thickness of ca. 10 atomic layers corresponding to 40-55 Å [23,24].

Furthermore, ellipsometric measurements carried out by Hopper [28] and, more recently by Vissher and Barendrecht [39] and by de Souza [40], have shown that the electro-oxidation of a nickel electrode in alkaline media leads to the formation of a first layer of NiO which is covered after the positive scan with a thick film of $Ni(OH)_2$. It has been reported [41,42] that, at the initial stages of the oxidation, α-$Ni(OH)_2$ forms and this is then further slowly converted to the β-$Ni(OH)_2$ form. At potentials above a critical value, the films converts [2,21,22,28] to a Ni (III) oxide phase and additional oxidation of Ni to Ni (II) and /or Ni (III) may also occur [22]. Upon reversal of the potential, β-NiO(OH) is reduced back to β-$Ni(OH)_2$. Both the nickel hydroxide and nickel oxy-hydroxyde phases are believed to be un-stoichiometric [34,43]. The chemical and electrochemical reactions of nickel in alkaline condition have been summarised by means of the following reactions [2]:

$$Ni_{(metal)} + H_2O \rightleftharpoons (NiOH)_{ad} + H^+ + e^- \quad (7.1)$$

$$(NiOH)_{ad} + H_2O \rightleftharpoons (NiOH \bullet H_2O)_{ad} \quad (7.2)$$

$$(NiOH \bullet H_2O)_{ad} \rightleftharpoons Ni(OH)_2 + H^+ + e^- \quad (7.3)$$

$$Ni(OH)_2 \rightleftharpoons HNiO_2^- + H^+ \quad (7.4)$$

$$Ni(OH)_2 \rightleftharpoons NiO(OH) + H^+ + e^- \quad (7.5)$$

Nickel hydroxide modified nickel (NHMN) electrodes formed in alkaline solutions have been exploited for the electro-oxidation of a large number of compounds [30,44-

50]. Pletcher and co-workers [30,45,46] showed that primary alcohols, secondary alcohols and primary amines can be oxidized in aqueous alkaline solution to carboxylic acids, ketones and nitriles, respectively, at the potential at which the surface of the Ni anode becomes oxidized [30]. They concluded that the oxidation of organic compounds is mediated by the nickel hydroxide layer as expressed by the following equations:

$$Ni(OH)_2 \xrightarrow{fast} NiO(OH) + H^+ + e^- \quad (7.6)$$

$$NiOOH + \text{organic compound} \xrightarrow{slow} Ni(OH)_2 + \text{product} \quad (7.7)$$

Similarly Lan *et al.* [48] showed that the regeneration of MnO_4^- from MnO_4^{2-} on a nickel electrode was significant improved when the nickel electrode was pre-treated with KOH solution for 30 minutes and suggested a similar mechanism to that proposed by Pletcher [30,46] involving a two-step reaction as given by:

$$Ni(OH)_2 + OH^- \rightleftharpoons NiOOH + H_2O + e^- \quad (7.8)$$

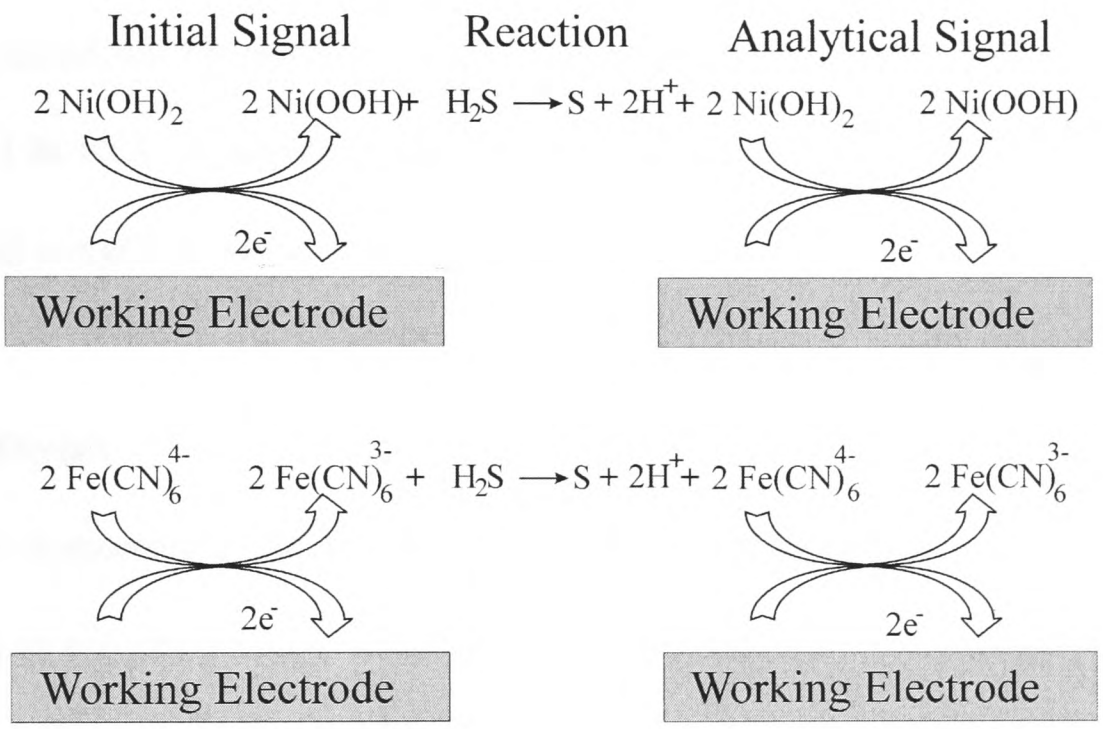
$$NiOOH + MnO_4^{2-} + H_2O \rightarrow Ni(OH)_2 + MnO_4^- + OH^- \quad (7.9)$$

Some amino acids (i.e., cysteine, asparagine and alanine) [49] were also found to undergo a catalytic electro-oxidation with nickel hydroxide formed on the surface of anodically polarised nickel electrode immersed in 0.5 M NaOH. Finally, NHMN electrodes were found to exhibit electrocatalytic activity for the oxidation of methane [51].

Further to Ni and nickel hydroxide, considerable attention has been given to the preparation of Ni-containing modifier electrodes and to its application in a variety of electrocatalytic oxidation [52-64] and reduction [65,66] processes.

The work presented in this chapter was initially undertaken to study the possible mediated oxidation of sulfide by the nickel hydroxide film formed by cycling the potential of a nickel electrode in sodium hydroxide solutions. It was proposed that

$Ni(OH)_2$ might be oxidised at the electrode surface to NiO(OH). NiO(OH) would then undergo a catalytic reduction by the sulfide ions back to $Ni(OH)_2$, which would be then electrochemically reoxidised to produce the analytical signal. This is illustrated schematically in Scheme 7.2 and it would be analogous to the electrocatalytic oxidation of ferrocyanide to ferricyanide in the presence of sulfide, also illustrated in Scheme 7.2 [67].



Scheme 7.2

However, the findings presented herein reveal that any EC' reaction is inhibited due to the direct oxidation of sulfide occurring prior to the oxidation of the nickel hydroxide layer. Nevertheless, nickel hydroxides were found to manifest catalytical activity in the oxidation of sulfide ions and the direct oxidation of sulfide on the NHMN electrode surface at +0.3 V (*vs.* SCE) provided an analytically relevant and readily accessible methodology for the determination of sulfide. The response of NHMN electrodes to sulfide was studied at both macro and microdisc nickel electrodes with the results providing the basis for the design of a simple, cheap and easily constructed reagentless sensing device.

7.2 Experimental

7.2.1 Manufacture of the Ag/AgCl Electrode

The Ag/AgCl reference electrode was made from a 0.5 mm diameter wire of silver, purity 99.99%, supplied by Advent Research Materials, UK. The silver wire was electrolytically coated with a porous, black silver chloride layer according to the reaction:

$$Ag(s) + Cl^-(aq) - e^-(metal) \rightarrow AgCl(s) \qquad (7.10)$$

This was carried out by poising the potential at +0.23 V (*vs.* SCE) for 30 minutes in aqueous 0.1 M KCl. Analysis of the amount of charge passed (= 2.22 C) suggests the formation of a AgCl layer ca. 60 μm thick.

7.2.2 Cell Design

In order to demonstrate the analytical viability of the proposed protocol for sulfide monitoring an electrochemical sensing cell was constructed. A schematic diagram of it is detailed in figure 7.1.

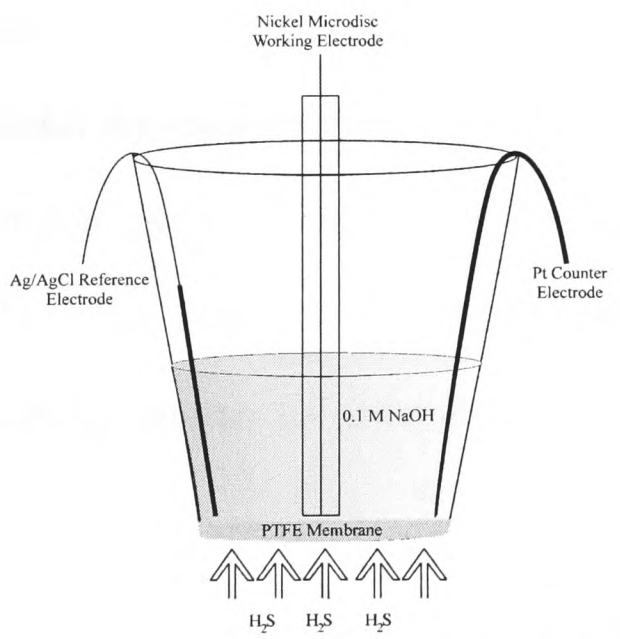


Figure 7.1: A schematic diagram of the electrochemical sensing cell.

It consists of a plastic casing made from a 1-5 mL pipette tip (Fisher, UK) in which a nickel microelectrode, a platinum counter electrode and a Ag/AgCl reference electrode

are immersed in 0.1 M NaOH (2 mL). One end of the pipette is sealed with a microporous PTFE membrane (0.085 mm thickness, 50 % porosity, 0.02 μm pore size, Goodfellow Advanced Materials, Cambridge, UK). The electrochemical cell was assembled by first fixing the platinum counter electrode and Ag/AgCl reference electrode inside the pipette after which the nickel microdisc electrode was inserted. This was positioned such that the microdisc was approximately 2 mm from the PTFE membrane.

During the determination of sulfide the electrochemical cell was placed into a sealed glass vial containing a static acidic solution (25 mL, 0.1 M H_2SO_4). Hydrogen sulfide gas was generated by injecting a known amount of sodium sulfide solution into the acidic solution through a syringe. Once liberated, the gas passes through the membrane into the alkaline sensor solution contained into the electrochemical cell. The purpose of the membrane is to prevent mixing of the two solutions whilst hydrogen sulfide gas is allowed to diffuse through it toward the electrode surface.

7.3 Results and Discussion

7.3.1 Formation of the Nickel Hydroxide Layer

The generation of the nickel hydroxide layer was first carried out using cyclic voltammetry (100 mV s^{-1}). The response of a nickel electrode (4 mm diameter) immersed in a 0.1 M NaOH solution to continuous redox cycling is detailed in figure 7.2.

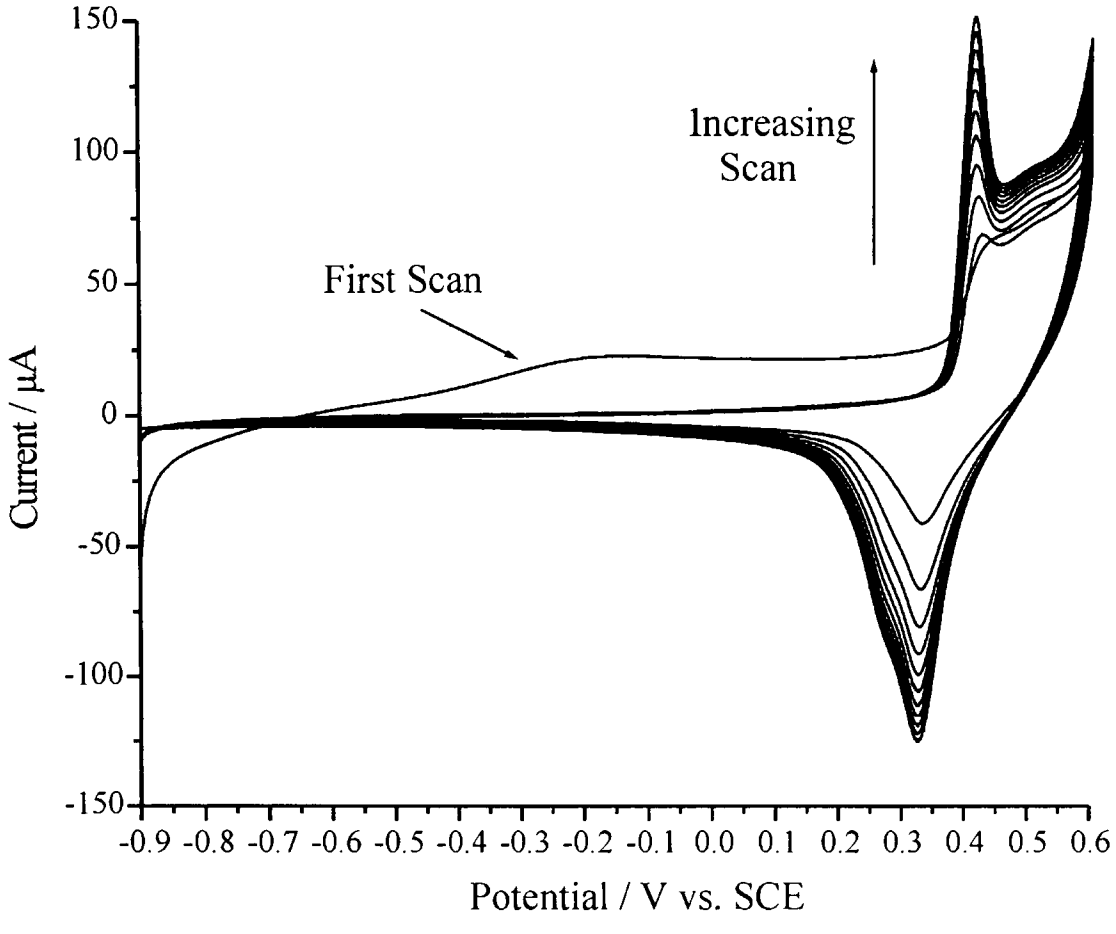


Figure 7.2: Repetitive cyclic voltammograms (100 mV s^{-1}) at a freshly polished nickel electrode (4 mm diameter) in 0.1 M NaOH.

As can be seen from the figure, the first cyclic voltammogram differs from the successive voltammograms. The first scan exhibits a broad oxidation peak at -0.2 V (*vs.* SCE) followed by an appreciable anodic current up to +0.4 V (*vs.* SCE) and a broad oxidative wave at +0.42 V with a corresponding reductive wave at +0.33 V observed on reversal of the scan. Neither the broad oxidation peak at -0.2 V nor the current plateau are observed on the following scans. However, the oxidative peak at +0.42 V continues to increase in magnitude along with the corresponding reductive wave at +0.33 V.

This type of electrochemical behaviour is in agreement with the published literature [2,9,21-24,26-28] and can be rationalised as follows. After nickel dissolution and oxide formation (broad peak at -0.2 V on first sweep), a nickel hydroxide layer is formed in the potential region corresponding to the plateau of the first cycle. The anodic peak at +0.42 V is then due to the oxidation of the β-$Ni(OH)_2$ to β-NiO(OH)

whilst the corresponding cathodic peak at +0.33 V represents the reduction of β-NiO(OH) back to β-$Ni(OH)_2$ as can be expressed by:

$$Ni(OH)_2 + OH^- \rightleftharpoons NiO(OH) + H_2O + e^- \qquad (7.11)$$

The changes of the shape and potential of the signal corresponding to the Ni(II)/Ni(III) couple (i.e., main peak at +0.42 V) are likely due to the changes in the crystal structure of the nickel hydroxide and nickel oxy-hydroxyde constituents during the growing and subsequent stabilisation of the nickel hydroxide film [21,22]. After approximately 50 cycles both the oxidative and reductive waves approach a current plateau and a stable voltammetric response is recorded.

A brief study into the effect of the scan rate (50 – 200 mV s^{-1}) on the peak potentials was also conducted. The peak potentials were found to be independent of the scan rate which is in agreement with the observations of Pletcher [30]. This indicates that the process observed correspond to a rapid conversion of a surface layer and not a diffusion or kinetically controlled reaction step.

The behaviour formerly depicted in figure 7.2 can be reproduced again after mechanically polishing the nickel electrode surface with 1 μm and 0.3 μm alumina (Bueheler, USA) as described in the Experimental Section , Chapter 2.

7.3.2 Response of the Nickel Hydroxide Layer to Sulfide

Next the voltammetric response of the nickel hydroxide modified nickel (NHMN) electrode to sulfide was investigated. The corresponding cyclic voltammograms obtained for the NHMN electrode immersed in 0.1 M NaOH to increasing additions (20 -200 μM) of sulfide are depicted in figure 7.3.

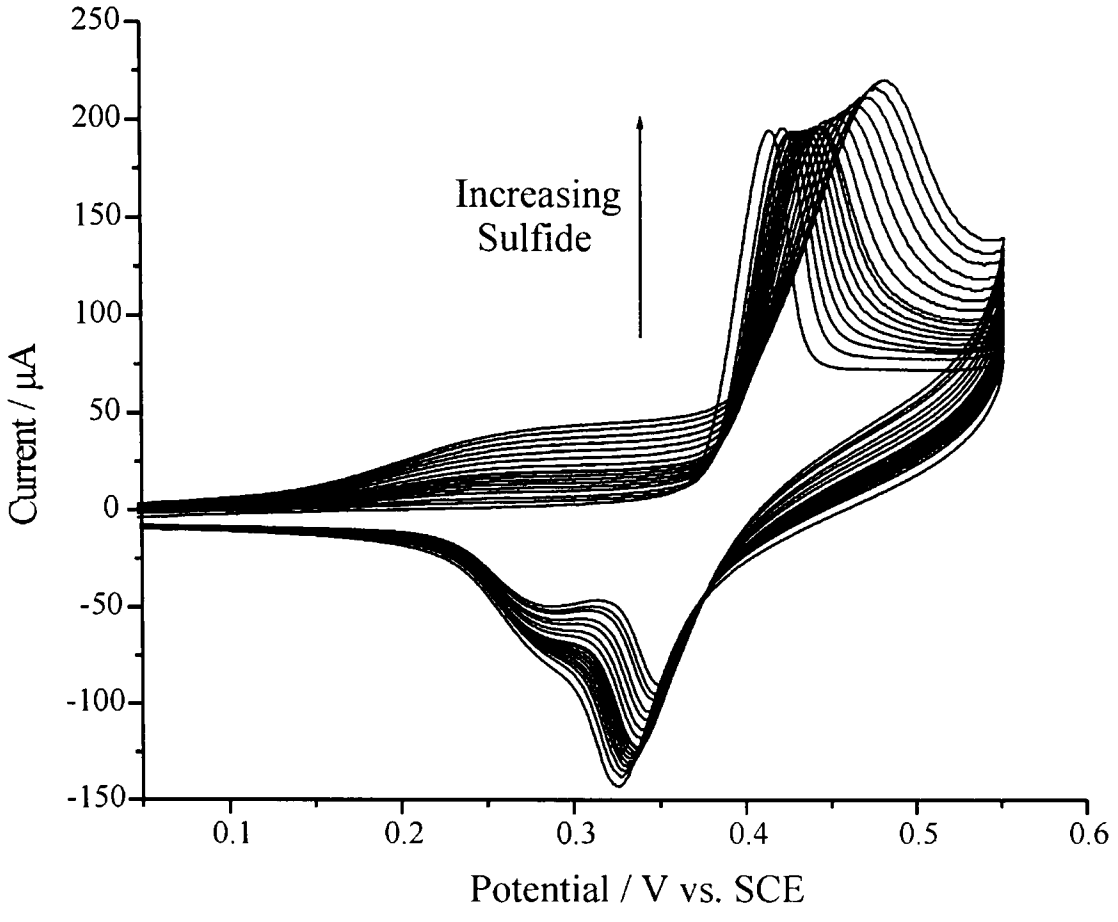


Figure 7.3: Cyclic voltammetric responses of the nickel hydroxide modified nickel (NHMN) electrode (4 mm diameter) to increasing additions of sulfide (20 - 200 μM).

In the absence of sulfide, a single oxidative wave appears at +0.42 V (*vs.* SCE) consistent with the reversible redox transfer between the active species Ni(II) and Ni(III) (equation (7.11)). However, upon the introduction of sulfide to the solution, a pre-oxidative wave at +0.25 V (*vs.* SCE) emerges and continues to grow with sulfide concentration. The potential of the anodic peak at +0.42 V shifts slightly toward more oxidizing potentials and shows also an apparent increase in current. The corresponding current-potential profiles were then analysed by means of standard additions. Figure 7.4 illustrates three different standard addition plots. The first, (a), shows how the current measured at +0.35 V varies with sulfide concentration, the second, (b), reveals how the peak current measured at +0.42 V varies with sulfide concentration, and the third, (c), shows the change in the peak current when the increase in the current at +0.35 V has been subtracted from the peak current at +0.42 V. This final plot reveals that there is little or no increase in the anodic peak at +0.42 V.

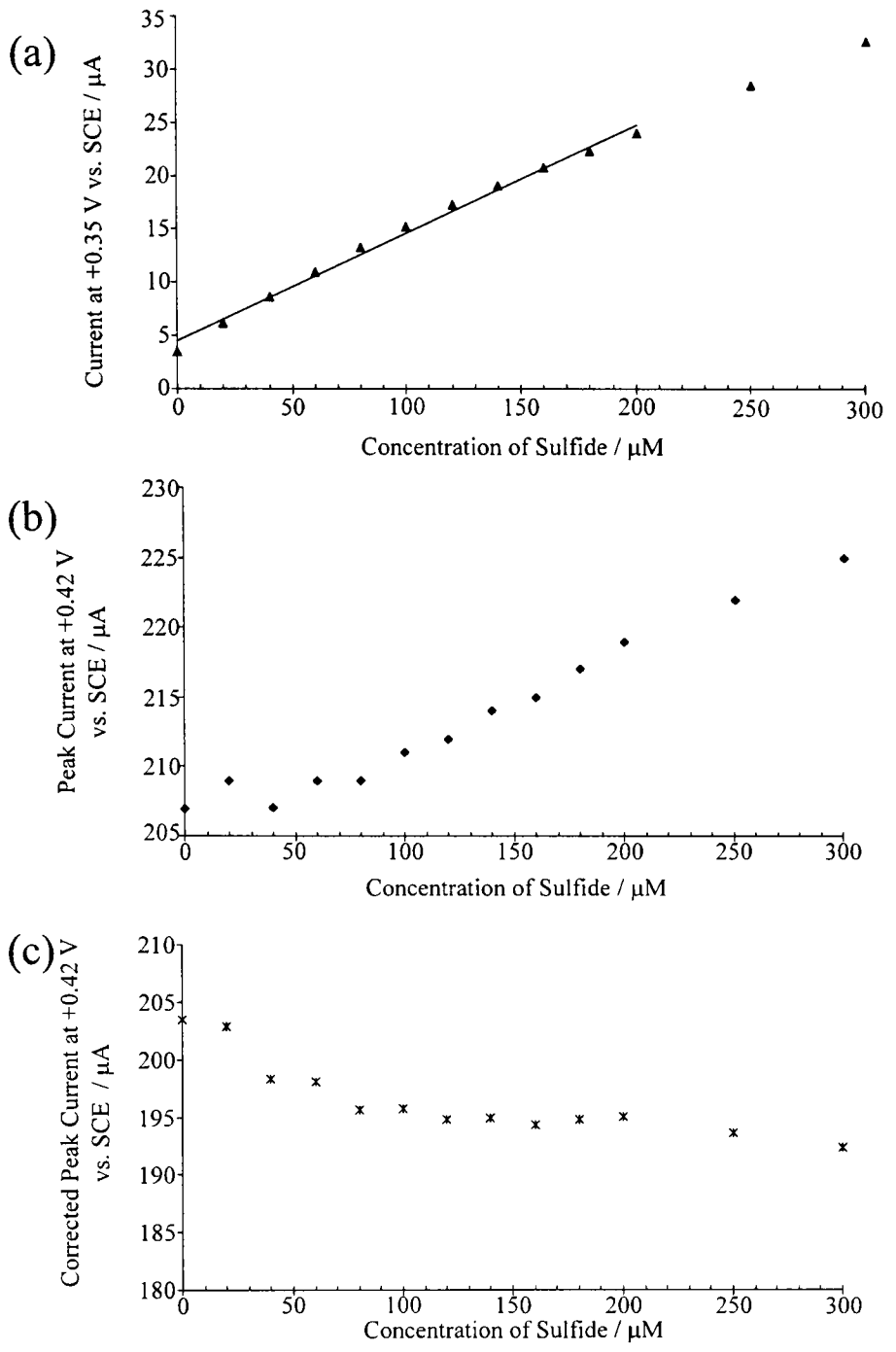


Figure 7.4: Plots of: (a) current measured at +0.35 V (*vs.* SCE), (b) peak current measured at +0.42 V and (c) the corrected peak current (peak current measured at +0.42 V minus the current measured at +0.35 V) against the concentration of sulfide (see text).

Analysis of the pre-wave current at + 0.35 V as a function of sulfide concentration (figure 7.4 (a)) provided a linear range from 20 μM to 200 μM sulfide with a calculated limit of detection (based on 3 S_b) of 19 μM. Given the work by Andreev and co-workers [68-70], the emergence of this pre-wave is tentatively attributed to the direct oxidation of the sulfide species, probably to elemental sulfur, at the nickel hydroxide layer. Andreev *et al.* [68-70] have measured the catalytic activity of a wide range of transition metal oxides in sulfide ions oxidation by oxygen in alkaline aqueous solutions through the monitoring of the volume of oxygen consumed. Nickel hydroxides were found to be promising catalysts for the sulfide oxidation with

important practical environmental application such as the removal of sulfide ions from industrial waters. The reaction mechanism proposed [70] envisages the activation of an oxygen molecule through electron transfer onto the oxygen species via the Ni^{2+}/Ni^{3+} transition involving the participation of OH^- groups as given by:

$$Ni^{2+}(OH)_2 + O_2 \rightarrow Ni^{3+}OOH + HO_2^- \quad (7.12)$$

$$2Ni^{3+}OOH + HS^- + H_2O \rightarrow 2Ni^{2+}(OH)_2 + S + OH^- \quad (7.13)$$

$$HS^- + HO_2^- \rightarrow S + 2OH^- \quad (7.14)$$

β-$Ni(OH)_2$ is isomorphous with brucite, $Mg(OH)_2$, and several other hydroxide with divalent metal cations such as Ca, Co and Cd [71]. It can be described as a layered structure consisting of parallel sheets of hexagonal close-packed OH^- ions between which nickel ions occupy the octahedral position of every second plane [72]. Trivalent nickel ions NiO(OH) are built in the plane of divalent nickel as defects [70] . The ability of nickel hydroxide to catalyse sulfide oxidation is thought to be due to the nickel hydroxide layered structure which allows sodium ions and water molecules to intercalate into the interlamellar space thus increasing the interlamellar distance and promoting a highly defective structure. The nickel ions which participate in catalysis are thought to be located on "edge sites" at the end of the lamellae [70].

7.3.3 Comparison of the Electro-oxidation of Sulfide at a NHMN Electrode with Other Electrode Substrates

In order to assess the analytical significant of the findings discussed hitherto, the voltammetric response of sulfide at the NHMN electrode was compared with that obtained at a platinum, Pt, and a glassy carbon, GC, electrode under analogous conditions (100 mV s^{-1}, 0.1 M NaOH). The cyclic voltammetric responses recorded at GC and Pt electrodes (not shown) in the presence of increasing amount of sulfide

(20 μM to 1 mM sulfide) revealed only a slight increase in the anodic current, within the potential window investigated (from -1.0 V to +0.6 V), suggesting that sulfide is difficult to oxidise at these electrode substrates. Figure 7.5 shows the current density at +0.35 V (*vs.* SCE) as a function of sulfide concentration for the three different electrode substrates.

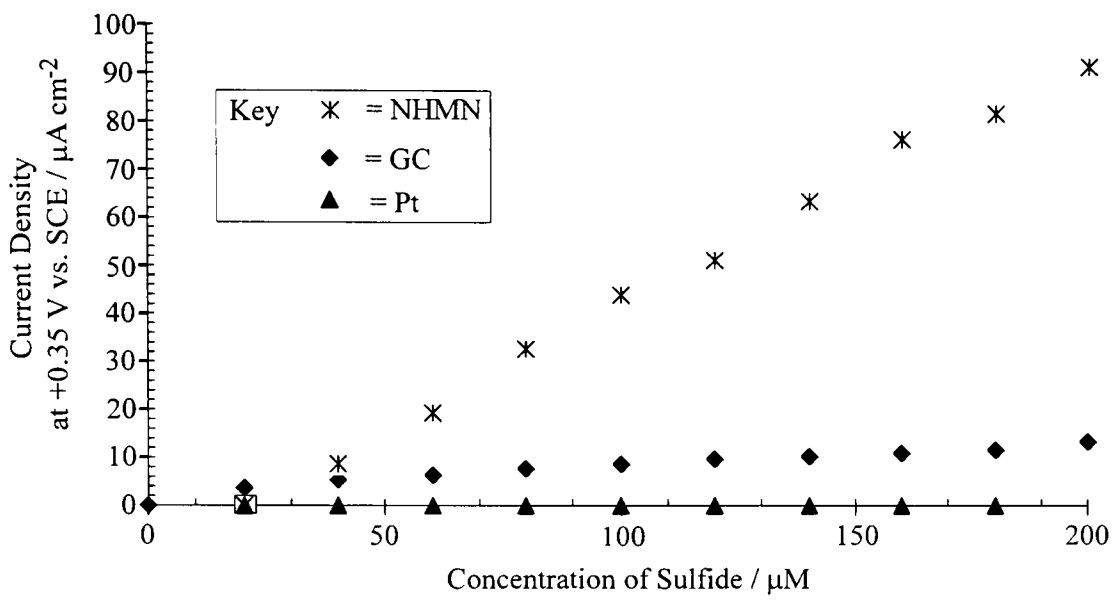


Figure 7.5: Plots of the current measured at +0.35 V against concentration of sulfide at a NHMN, GC and Pt electrode.

It can be seen that the oxidation of sulfide ions is significantly enhanced at a NHMN electrode in comparison with both GC and Pt electrodes. Several studies concerning the anodic oxidation of sulfide species at platinum [73], gold [74,75], and, more recently, at bare boron diamond doped electrodes [67] can be found in the literature and problems such as electrode fouling, high overpotential for the oxidation of sulfide and solvent decomposition masking the analytical signal are often reported. On the other hand, the use of the modified nickel electrode as a substrate for the direct electrochemical determination of sulfide is, to our knowledge, unexplored. The present investigation has shown that the direct oxidation of sulfide at a NHMN electrode is achievable at a low overpotential and provides good sensitivity for sulfide detection.

With the view of developing these results into the possible manufacture of a small sensor for sulfide, the response of a nickel microdisc electrode (50 μm diameter) was

next investigated. It should be noted that in all the experiments outlined below the Ag/AgCl reference electrode, constructed as described in the experimental section, was utilised in virtue of its small geometry which allows its incorporation into a small device.

Initially, a stable nickel hydroxide layer was formed on the nickel microelectrode by means of repetitive cyclic voltammetry (200 mV s^{-1}, 0.1 M NaOH) as shown previously for the macroelectrode studies. Then the voltammetric response of the NHMN microelectrode to increasing additions of sulfide (20 – 200 μM) was examined. As shown in figure 7.6, the response of sulfide at a NHMN microelectrode is similar to that obtained at the NHMN macroelectrode (figure 7.3).

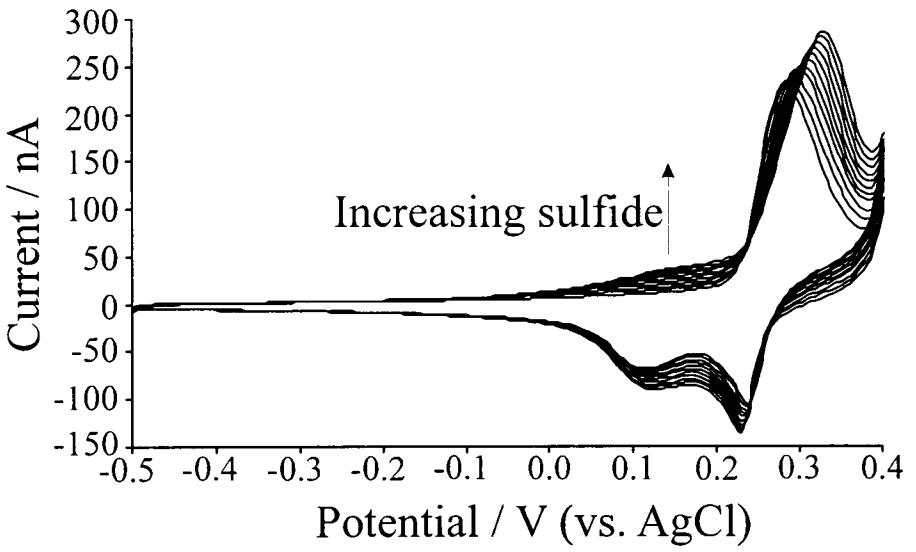


Figure 7.6: Cyclic voltammetric response of the NHMN microelectrode to increasing additions of sulfide (20 - 200 μM, 20 μM aliquots).

In the absence of sulfide, a single oxidation wave is observed at +0.29 V (*vs.* AgCl) with a corresponding reduction wave at +0.23 V (*vs.* AgCl). Upon addition of sulfide (20 μM) to the solution, a pre-wave emerges at +0.15 V (*vs.* AgCl) and continues to grow with sulfide along with the anodic peak at +0.29 V (*vs.* AgCl). The reduction wave at +0.23 V decreases with sulfide additions and a shoulder at +0.10 V appears and becomes well defined. Analysis of the two increasing anodic waves by means of standard addition plot against sulfide concentration is shown in figure 7.7.

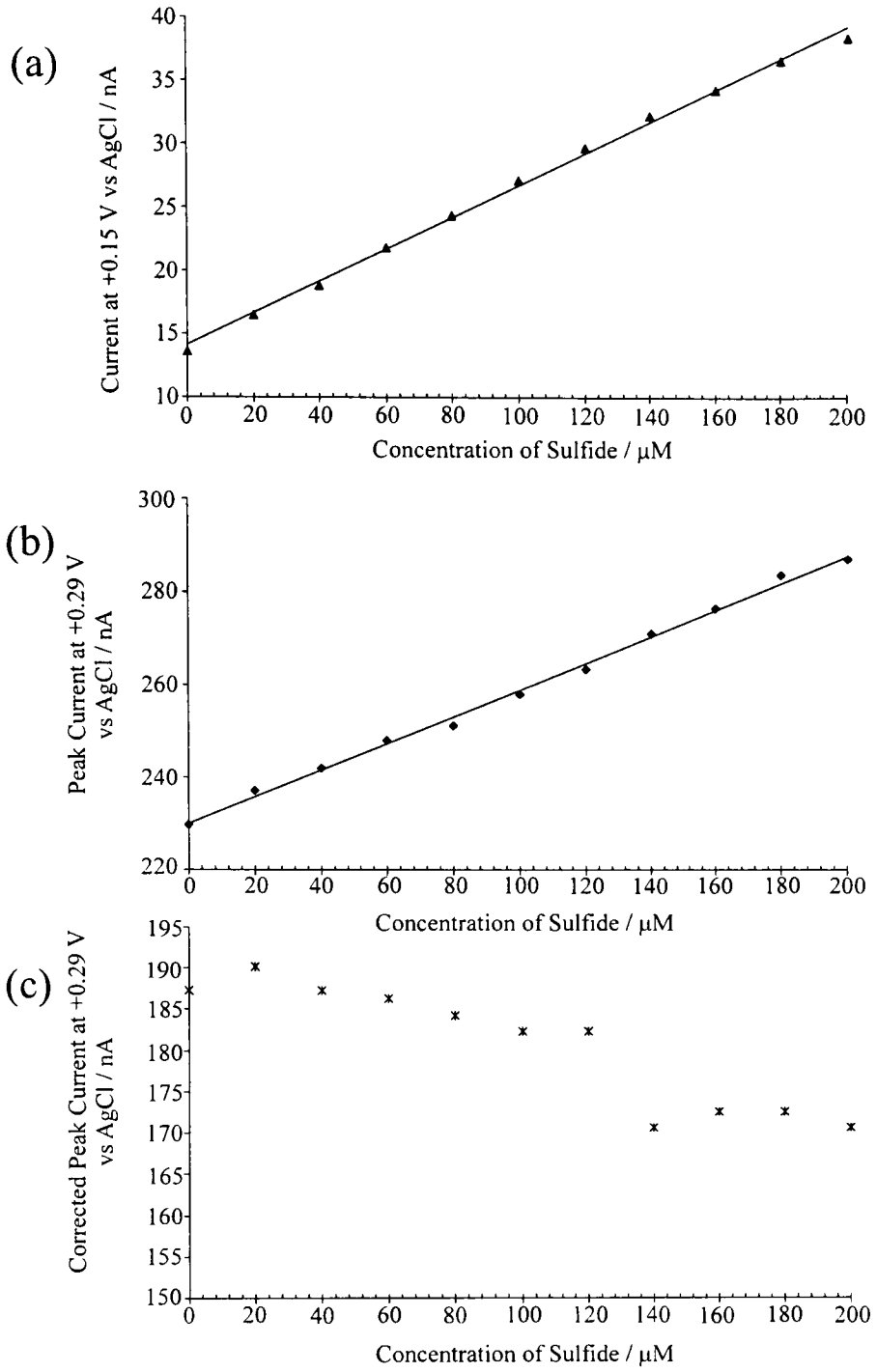


Figure 7.7: Plots of (a) current measured at +0.15 V (*vs.* AgCl), (b) peak current measured at +0.29 V and (c) the corrected peak current against the concentration of sulfide (see text).

In agreement with our observation at the NHMN macroelectrode (*vide supra*), the electro-oxidation of sulfide at +0.15 V provides a linear range between 20 and 200 μM sulfide and a limit of detection of 10 μM sulfide (figure 7.7, (a)). The analysis of the increase in the main oxidation peak current at +0.29 V with sulfide concentration as shown in figure 7.7 (b) reveals an apparent increase in the current with increasing sulfide concentration. However figure 7.7 (c) shows the corrected height peak current at +0.29 V (i.e, calculated by line extrapolation between the two current minima either side of the oxidation wave at +0.29 V) against the concentration of sulfide. It can be

seen that, in agreement with that observed at the NHMN macroelectrode, the increase in the peak current at +0.29 V with increasing sulfide concentration is insignificant.

7.3.4 Sensor Response

In order to demonstrate the analytical viability of the detection strategy proposed above for the determination of sulfide in alkaline aqueous solutions, a simple cell design was constructed. A description of the cell is given in the experimental section (*vide supra*) and a schematic diagram of the cell is shown in figure 7.1.

Preliminary characterisation of the sensor design focused on the response time for the determination of sulfide when it was placed inside a static acidic solution of sulfide. A stable nickel hydroxide layer was first formed on the nickel microdisc electrode by carrying out the pre-treatment detailed above. The amount of sodium sulfide required to liberate 20 μM of volatile hydrogen sulfide was then injected into the acidic solution within which the cell was placed. A scan was recorded every minute for a period of twenty minutes and figure 7.8 (a) shows the corresponding voltammetric responses recorded over the first five minutes.

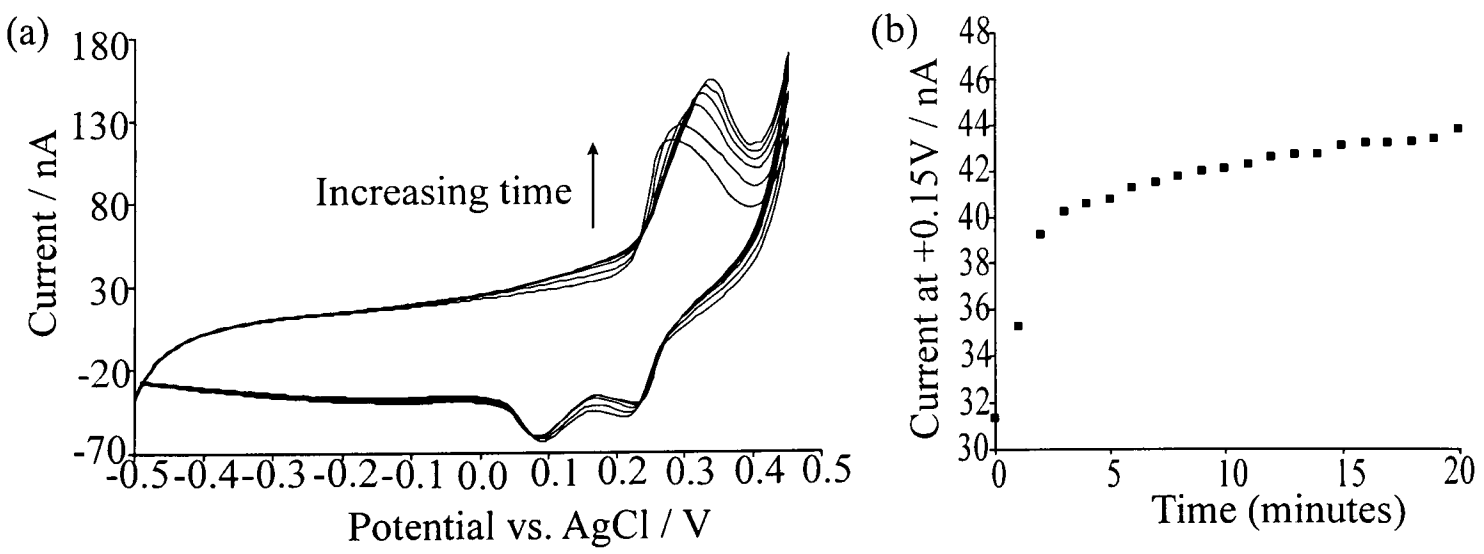


Figure 7.8: (a) Cyclic voltammetric responses of the NHMN microelectrode inside the cell to 20 μM sulfide over a period of five minues. (b) A plot of current measured at +0.15 V against time.

It can be seen that the response of sulfide is analogous to that described above for the NHMN microdisc electrode experiment with a new oxidative wave observed at

+0.15 V when sulfide is introduced to the acidic solution. Analysis of the increase of the current at +0.15 V as a function of time is detailed in figure 7.8 (b) and reveals a slight time delay before a steady current is reached after a period of five minutes. This time delay can be tentatively attributed to the diffusion of the sulfide through the acidic solution towards the membrane and then from the membrane to the electrode. This experiment was repeated for a range of sulfide concentrations and it was found that a linear range from 20 to 100 μM was achieved whereby the current was measured after a time period of 5 minutes to ensure a steady current was reached. The corresponding standard addition plot produced a calculated limit of detection (based on $3s_b$) of 10 μM.

7.4 Conclusion

The electrochemistry of a stable nickel hydroxide film electrode has been examined both in the presence and absence of sulfide at both microdisc and macro nickel electrodes. In the presence of sulfide a new oxidative wave is observed at +0.3 V (*vs.* SCE) which can attributed to the direct oxidation of sulfide at the nickel hydroxide surface. Analysis of this wave by means of a standard addition plot has allowed the determination of sulfide in an analytically relevant range from 20 to 200 μM with a corresponding limit of detection of 19 μM.

The use of the microdisc nickel electrode has allowed the development of a simple and cheap design for an electrochemical cell, whereby the electrode is placed in a pipette in a solution of 0.1 M NaOH behind a membrane. The response for the cell was found to be linear from 20 to 100 μM with a corresponding limit of detection of 10 μM. These results provide a simple methodology for the determination of volatile gaseous hydrogen sulfide which can foreseeably be transferred into a Clark type sensor to increase the response time.

7.5 Chapter 7 References

[1] D. Giovanelli, N. S. Lawrence, L. Jiang, T. G. J. Jones, R. G. Compton, *Sens. and Actuators, B* **2003**, *B88*, 320.
[2] A. J. Arvia, D. Posadas, in *Encyclopedia of electrochemistry of the elements* (Ed. A. J. Bard), Marcel Dekker, New York **1975**, pp. 211-421.
[3] C.-C. Hu, C.-Y. Cheng, *J. Power Sources* **2002**, *111*, 137.
[4] B. MacDougall, M. Cohen, *J. Electrochem. Soc.* **1974**, *121*, 1152.
[5] M. Okuyama, S. Haruyama, *Corros. Sci.* **1974**, *14*, 1.
[6] G. Cordeiro, O. R. Mattos, O. E. Barcia, L. Beaunier, C. Deslouis, B. Tribollet, *J. Appl. Electrochem.* **1996**, *26*, 1083.
[7] I. Epelboin, M. Keddam, *Electrochim. Acta* **1972**, *17*, 177.
[8] A. Jouanneau, M. Keddam, M. C. Petit, *Electrochim. Acta* **1976**, *21*, 287.
[9] J. R. Vilche, A. J. Arvia, *Lat. Am. J. Chem. Appl. Chem.* **1979**, *9*, 35.
[10] J. R. Vilche, A. J. Arvia, *Corros. Sci.* **1978**, *18*, 441.
[11] S. G. Real, J. R. Vilche, A. J. Arvia, *Corros. Sci.* **1980**, *20*, 563.
[12] M. R. Barbosa, S. G. Real, J. R. Vilche, A. J. Arvia, *J. Electrochem. Soc.* **1988**, *135*, 1077.
[13] S. G. Real, M. R. Barbosa, J. R. Vilche, A. J. Arvia, *J. Electrochem. Soc.* **1990**, *137*, 1696.
[14] B. MacDougall, *J. Electrochem. Soc.* **1980**, *127*, 789.
[15] B. MacDougall, M. J. Graham, *Electrochim. Acta* **1981**, *26*, 705.
[16] B. MacDougall, M. J. Graham, *Electrochim. Acta* **1982**, *27*, 1093.
[17] B. MacDougall, *Corros. Sci.* **1988**, *28*, 211.
[18] B. MacDougall, D. F. Mitchell, M. J. Graham, *J. Electrochem. Soc.* **1985**, *132*, 2895.
[19] L. D. Burke, T. A. M. Twomey, *J. Electroanal. Chem.* **1984**, *162*, 101.
[20] L. D. Burke, D. P. Whelan, *J. Electroanal. Chem.* **1980**, *109*, 85.
[21] J. F. Wolf, L. S. R. Yeh, A. Damjanovic, *Electrochim. Acta* **1981**, *26*, 409.
[22] J. F. Wolf, L. S. R. Yeh, A. Damjanovic, *Electrochim. Acta* **1981**, *26*, 811.
[23] J. L. Weininger, M. W. Breiter, *J. Electrochem. Soc.* **1964**, *111*, 707.
[24] J. L. Weininger, M. W. Breiter, *J. Electroanal. Chem.* **1963**, *110*, 484.
[25] R. S. Schrebler Guzman, J. R. Vilche, A. J. Arvia, *J. Appl. Electrochem.* **1978**, *8*, 67.
[26] R. S. Schrebler Guzman, J. R. Vilche, A. J. Arvia, *J. Appl. Electrochem.* **1979**, *9*, 183.
[27] R. S. Schrebler Guzman, J. R. Vilche, A. J. Arvia, *J. Appl. Electrochem.* **1979**, *9*, 321.
[28] M. A. Hopper, J. L. Ord, *J. Electrochem. Soc.* **1973**, *120*, 183.
[29] M. Wohlfahrt-Mehrens, R. Oesten, P. Wilde, R. A. Huggins, *Solid State Ionics* **1996**, *86-88*, 841.
[30] M. Fleischmann, K. Korinek, D. Pletcher, *J. Electroanal. Chem.* **1971**, *31*, 39.
[31] A. E. Bohe, J. R. Vilche, A. J. Arvia, *Corros. Sci.* **1993**, *43*, 151.
[32] R. Barnard, C. F. Randell, *J. Power Sources* **1983**, *9*, 185.
[33] R. Barnard, C. F. Randell, *J. Appl. Electrochem.* **1983**, *13*, 27.
[34] R. Barnard, C. F. Randell, *J. Appl. Electrochem.* **1983**, *13*, 89.
[35] A. Seghiouer, J. Chevalet, A. Barhoun, F. Lantelme, *J. Electroanal. Chem.* **1998**, *442*, 113.
[36] R. J. Smith, R. E. Hummel, J. R. Ambrose, *Corros. Sci.* **1987**, *27*, 815.
[37] R. E. Hummel, R. J. Smith, E. D. Verink, Jr., *Corros. Sci.* **1987**, *27*, 803.
[38] A. C. Makrides, *J. Electrochem. Soc.* **1966**, *113*, 1158.
[39] W. Visscher, E. Barendrecht, *Surf. Sci,* **1983**, *135*, 436.
[40] L. M. M. de Souza, F. P. Kong, F. R. McLarnon, R. H. Muller, *Electrochim. Acta* **1997**, *42*, 1253.
[41] G. W. D. Briggs, P. R. Snodin, *Electrochim. Acta* **1982**, *27*, 565.
[42] F. Hahn, B. Beden, M. J. Croissant, C. Lamy, *Electrochim. Acta* **1986**, *31*, 335.
[43] J. Desilvestro, D. A. Corrigan, M. J. Weaver, *J. Electrochem. Soc.* **1988**, *135*, 885.
[44] G. W. D. Briggs, W. F. K. Wynne-Jones, *Trans. Faraday Soc.* **1956**, *52*, 1272.
[45] M. Amjad, D. Pletcher, C. Smith, *J. Electrochem. Soc.* **1977**, *124*, 203.
[46] M. Fleischmann, K. Korinek, D. Pletcher, *J. Chem. Soc. Perkin Trans.* **1971**, *2*, 1396.
[47] P. M. Robertson, *J. Electroanal. Chem.* **1980**, *111*, 97.
[48] S. M. Lan, Y. Y. Wang, C. C. Wan, J. C. Chang, *Wat. Res.* **1994**, *28*, 909.
[49] Y. N. Bakanina, E. A. Zhukova, I. F. Abdullin, E. H. Turova, G. K. Budnikov, *Russian Journal of General Chemistry* **2000**, *70*, 837.
[50] A. Kowal, S. N. Port, R. J. Nichols, *Catalysis Today* **1997**, *38*, 483.
[51] M. Jafarian, M. G. Mahjani, H. Heli, F. Gobal, M. Heydarpoor, *Electrochem. Commun.* **2003**, *5*, 184.
[52] S. M. Golabi, A. Nozad, *Electroanalysis* **2004**, *16*, 199.

[53] J. Mohan, S. Joshi, R. Prakash, R. C. Srivastava, *Electroanalysis* **2004**, *16*, 572.
[54] A. Ciszewski, *Electroanalysis* **1995**, *7*, 1132.
[55] A. Ciszewski, G. Milczarek, *J. Electroanal. Chem.* **1999**, *469*, 18.
[56] A. Ciszewski, G. Milczarek, *J. Electroanal. Chem.* **1997**, *26*, 125.
[57] G. Roslonek, J. Taraszewska, *J. Electroanal. Chem.* **1992**, *325*, 285.
[58] Z. U. Bae, J. H. Park, S. H. Lee, H. Y. Chang, *J. Electroanal. Chem.* **1998**, *468*, 85.
[59] T. R. I. Cataldi, A. Centonze, G. Ricciardi, *Electroanalysis* **1995**, *7*, 312.
[60] T. Malinski, A. Ciszewski, J. Bennet, J. R. Fish, L. Czuchajoski, *J. Electrochem. Soc.* **1991**, *138*, 2008.
[61] A. Ciszewski, G. Milczarek, *J. Electroanal. Chem.* **1996**, *413*, 137.
[62] S. Trevin, F. Bedioui, J. Devynck, *J. Electroanal. Chem.* **1996**, *408*, 261.
[63] S. Trevin, F. Bedioui, M. G. G. Villegas, C. Bied-Charreton, *Mater. Chem.* **1997**, *7*, 923.
[64] I. G. Casella, T. R. I. Cataldi, A. M. Salvi, E. Desimoni, *Anal. Chem.* **1993**, *65*, 3143.
[65] B. k. Simpson, D. C. Johnson, *Electroanalysis* **2003**.
[66] J. Losada, I. del Peso, L. Beyer, *J. Electroanal. Chem.* **1998**, *447*, 147.
[67] N. S. Lawrence, M. Thompson, C. Prado, L. Jiang, T. G. J. Jones, R. G. Compton, *Electroanalysis* **2002**, *14*, 499.
[68] A. Andreev, V. Ivanova, K. Kirilov, G. Passage, *Appl. Catalysis A* **1993**, *107*, 189.
[69] A. Andreev, L. Prahov, M. Gabrovska, A. Eliyas, V. Ivanova, *Appl. Catalysis B* **1996**, *8*, 365.
[70] A. Andreev, P. Khristov, A. Losev, *Appl. Catalysis B* **1996**, *7*, 225.
[71] A. Szytula, A. Murasik, m. Balanda, *Phys. Status Solidi B* **1971**, *43*, 125.
[72] P. Oliva, J. Leonardi, J. F. Laurent, D. C., J. J. Braconnier, M. Figlarz, F. Fievet, A. de Guibert, *J. Power Sources* **1982**, *8*, 229.
[73] S. Kapusta, A. Viehbeck, S. M. Wilhelm, N. Hackerman, *J. Electroanal. Chem.* **1983**, *153*, 157.
[74] I. C. Hamilton, R. Woods, *J. Appl. Electrochem.* **1983**, *13*, 783.
[75] D. G. Wierse, M. M. Lohrengel, J. W. Schultze, *J. Electroanal. Chem.* **1978**, *92*, 121.

Chapter 8: "Detection of Sulfide at Nickel Modified Electrodes in Acidic Media: the Development of a Reagentless Sensor"

In the previous chapter we have shown that a quantitative measurement of sulfide can be obtained at a nickel hydroxide modified nickel (NHMN) electrode in alkaline conditions. We now examine the response of sulfide at a nickel oxide layer formed electrochemically when the nickel electrode is immersed in acidic media. This chapter is divided into two sections: the first part discusses the formation of a nickel oxide layer at a nickel electrode immersed in acetate buffered solutions covering a pH range $2 < pH < 5$ and its response in the presence of sulfide. It will be shown that sulfide can be stripped from the nickel oxide layer to produce an analytical signal. The second part examines the possibility of developing this approach further into the use of nickel modified screen printed carbon (Ni-SPC) electrodes as economical and disposable sensors for sulfide. The results detailed in section 8.1 and section 8.2 have been published in The Analyst [1] and in Talanta [2], respectively.

8.1 Detection of Sulfide at Nickel Oxide Modified Nickel (NOMN) Electrodes in Acidic Media

In chapter 7 it was shown that the direct oxidation of sulfide at a nickel hydroxide modified (NHMN) nickel electrode in alkaline media provided a quantitative means of determining sulfide. The present study examines the possibility of sensing sulfide at a modified nickel electrode in acidic media. The electro-oxidation of nickel in acidic media has been previously studied and found to form a passivated nickel oxide layer which has little voltammetric behaviour within a certain potential window [3-19]. The electrochemical and chemical processes which take place at the nickel electrode in acid solutions have been explained by means of a complex scheme coupled with a precipitation/dissolution mechanism [3,7] and it has been suggested that in acid solution the passive film on the nickel is a mixed nickel oxide film ($NiO(Ni_2O_3)$) [7]. It should be noted that in the pH range utilised in the studies detailed below for the interaction of sulfide with the nickel oxide film, both NiO and Ni_3O_4 are found to be stable species [20].

A rather complex reactions scheme for the anodic dissolution of nickel in sulfuric media was described [12] according to which the eletrochemical oxidation of nickel proceeds by two competitive processes: formation of a passive layer, equation (8.4a), and nickel dissolution, equation (8.4b), :

$$[Ni]_k + H_2O \Leftrightarrow [Ni]_k(H_2O)_{ad} \Leftrightarrow [Ni]_{k-1}Ni(OH)_{ad} + H^+_{aq} + e^- \qquad (8.1)$$

$$[Ni]_{k-1}Ni(OH)_{ad} \Leftrightarrow [Ni]_{k-1}Ni(OH^+)_{ad} + e^- \qquad (8.2)$$

$$[Ni]_{k-1}Ni(OH^+)_{ad} + H_2O \Rightarrow [Ni]_{k-1}Ni(OH)_2 + H^+_{aq} \qquad (8.3)$$

$$[Ni]_{k-1}Ni(OH)_2 \Leftrightarrow [Ni]_{k-1}[NiO] + H_2O \qquad (8.4a)$$

$$[Ni]_{k-1}Ni(OH^+)_{ad} + H_2O \Rightarrow [Ni]_{k-1}NiOH^+_{aq} + H^+ \Leftrightarrow [Ni]_k + H_2O + Ni^{2+} \qquad (8.4b)$$

The results detailed herein show that an electrochemically inactive nickel oxide film can be formed on the surface of a nickel electrode immersed in acidic buffered solutions. This has significant advantages over the previously studied nickel hydroxide film which showed a voltammetric signal due to the reversible redox transfer between the active species $Ni(OH)_2$ / NiO(OH) at higher oxidation potentials [21] and as such made it difficult to detect low concentrations (i.e.,< 10 μM) of sulfide due to the masking of the analytical signal by the oxidation of the nickel hydroxide layer.

The data reported in this chapter offer scope for the development of an amperometric sensor that can accurately monitor sulfide concentration in aqueous phase within the analytically relevant range between 1 and 200 μM.

8.1.1 Experimental: Nickel Determination Protocol

In order to provide evidence that nickel ions were being liberated from the electrode surface after the electrochemical experiments with sulfide had been completed (see Section 8.1.3.4), a standard UV/Vis protocol for nickel ions quantification based on the use of the dimethylglyoxime method was undertaken [22-24].

Nickel standards solutions (2 to 10 μM) for the calibration plot were prepared from a stock solution of 4 mM nickel sulfate salt dissolved in deionised water. Additions of 4 mM dimethylglyoxime to the nickel standards and to the sample were made from a 50 mM dimethylglyoxime stock solution in ethanol. These solutions were then left to stand for 24 hours to enhance sensitivity before an absorbance spectra was recorded. In order to show that the presence of sulfide would not interfere with the spectrophotometric measurement an analogous set of nickel solutions were prepared but each containing 50 μM sulfide. The absorbance spectra of the two sets of solutions

were then compared and it was shown that sulfide did not interfere with the analytical signal.

In order to quantify the amount of nickel ions released into the solution during the electrochemical experiment, first a known amount of sulfide (50 μM) was added to the electrochemical cell containing the passivated nickel oxide layer and was left to stand for 5 minutes such that the sulfide accumulated on the electrode surface. The voltammetric experiment was then conducted, and the pH of the solution was adjusted to pH 12. After which the sample was divided into two 2.5 cm^3 samples and 4 mM dimethylglyoxime was added to both of them while 4 μM nickel sulfate was added to one of the samples only. These solutions were then left to stand for 24 hours after which the absorbance spectrum was analysed and compared to a blank solution containing only 50 μM sulfide.

8.1.2 Results and Discussion

8.1.2.1 Formation and stability of the nickel oxide layer

The dissolution and passivation of the nickel electrode (4 mm diameter) in pH 4 acetate buffer solutions was first investigated by employing cyclic voltammetry. Figure 8.1 shows the first three, the 5^{th} and the 10^{th} corresponding cyclic voltammograms recorded when the potential was swept from from -0.5 V to +1.0 V at 100 mV s^{-1}.

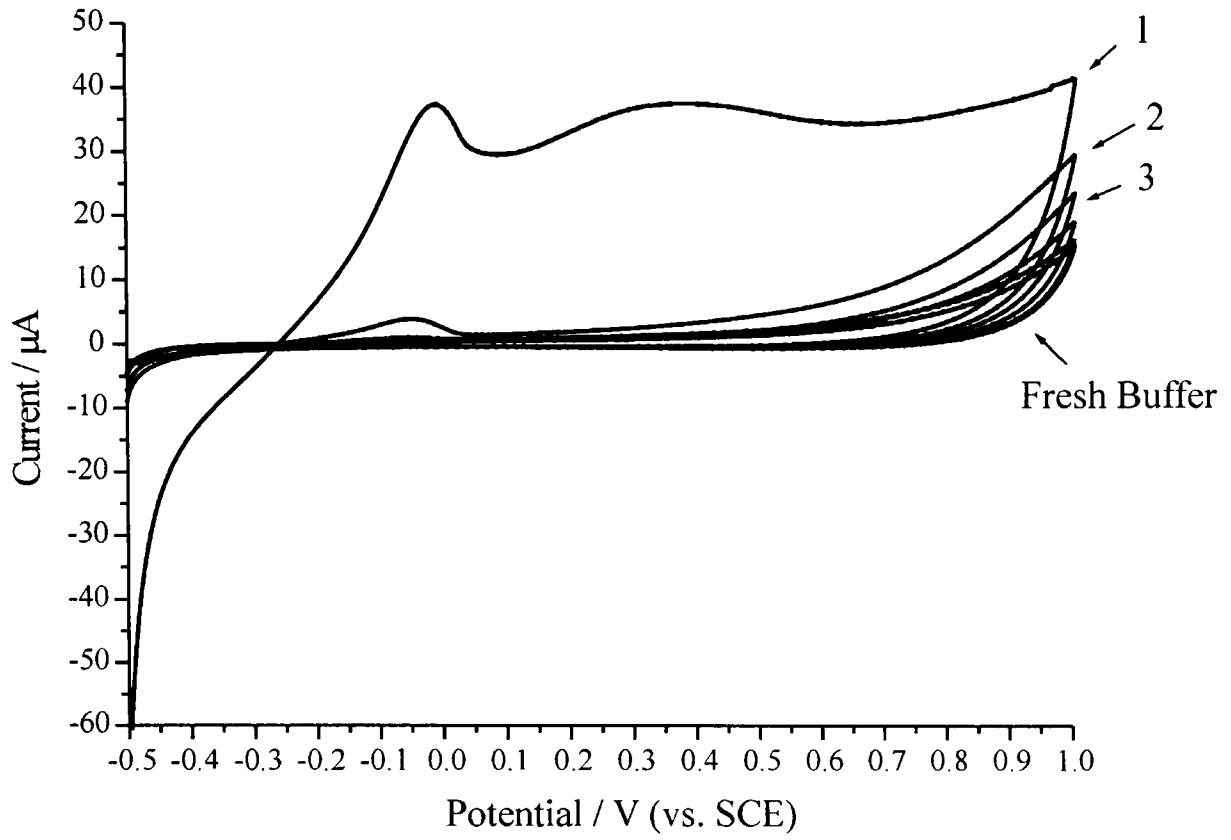


Figure 8.1: The first three, the fifth and the tenth cyclic voltammetric responses of the nickel electrode (4 mm diameter) immersed in a pH 4 acetate buffer solution. The voltammetric response after the electrode was placed in a fresh pH 4 solution is also overlaid (see text).

As can be seen from the figure, the first sweep reveals an oxidative wave at +0.0 V, followed by a current plateau from +0.1 V to +1.0 V. This initial voltammetric response is in good agreement with the literature [3-12] and can be rationalised as follows: the oxidative wave at low anodic potential corresponds to the active anodic dissolution of nickel and the anodic current is probably due to the presence of a protective film formed by oxide and hydroxide species which is known as an active-passive transition state [6,8-12]. Upon reversal of the potential no reduction wave is observed indicating that this passive state is retained.

The second voltammetric scan reveals only a little oxidative peak at +0.0 V and the third cycle exhibits a negligible anodic current occurring. The following sweeps clearly indicate the onset of passivity and, as the current-potential profile remains unchanged after the 3rd cycle, we can infer that the formation of an insoluble film which prevents further metal dissolution can be achieved within three cycles.

The amount of charged associated with the main oxidative process observed on the first scan was found to vary from 0.19 mC (= 1.68 mC cm^{-2}) to 0.75 mC (= 6.62

mC cm^{-2}), suggesting that several monolayers of nickel oxide are formed under these conditions. This calculation is based on the assumption that the nickel oxide layer is hexagonally closed packed.

The mechanically stability of the passive film was examined by recording a cyclic voltammogram of the nickel oxide modified nickel (NOMN) electrode when it was immersed in a fresh acetate buffered solution (pH 4). The corresponding current-potential profile is overlaid in figure 8.1 and it shows that no further dissolution of the metal is occurring and hence the passive nickel oxide layer formed is stable within the potential window of study.

Investigations into the effect of the increase of the applied potential range on the stability of the nickel oxide film were also conducted. Voltammetric responses recorded from -1.0 V to +1.0 V show a considerable flow of reductive current at -0.7 V which can be attributed to the breakdown of the passive layer. This suggests the films is sensitive to the initial potential and to the limits of both the anodic and cathodic potentials and that corrosion of the layer occurs if the applied overpotential exceed a certain threshold value. Hence all the experiments described below were conducted within the potential window of stability which was found to be between from -0.5 V to +1.0 V.

8.1.2.2 Response of the nickel oxide modified nickel (NOMN) electrode to H_2S

Next the voltammetric response of the NOMN electrode to increasing additions of sulfide was investigated as means of producing a quantitative analytical signal for sulfide detection. The corresponding current-potential profiles obtained at a NOMN electrode immersed in a pH 4 acetate buffered solution to increasing additions of sulfide (20 to 200 μM) are detailed in figure 8.2.

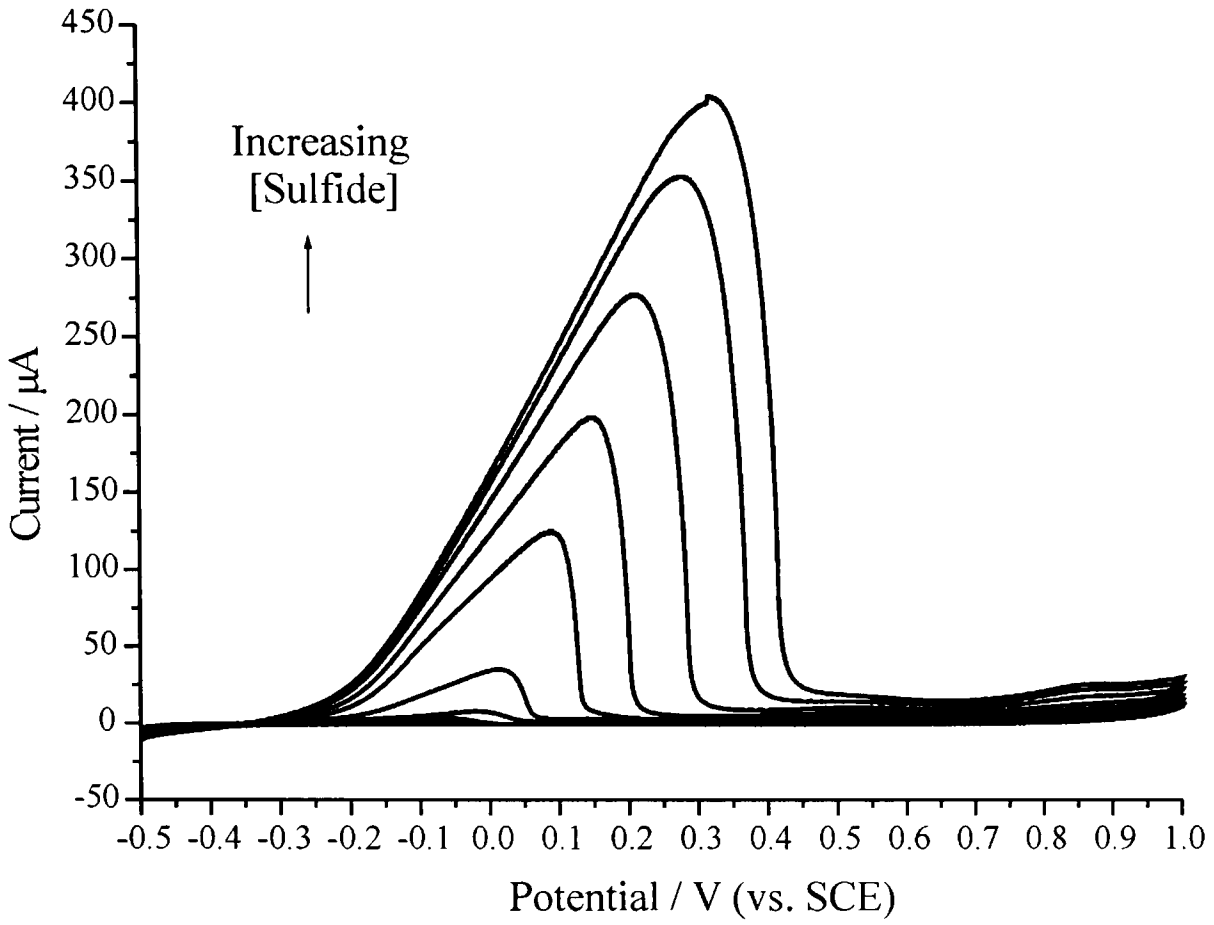


Figure 8.2: The voltammetric response (100 mV s^{-1}) of the NOMN electrode to increasing sulfide concentrations (20 to 140 μM, pH 4 acetate buffer) when 15 seconds accumulation time is allowed between the addition and the voltammetric scan.

Upon the addition of sulfide to the solution a new oxidative wave emerges at +0.1 V and continues to grow as sulfide concentration increases. Examination of the voltammetric waveshape reveals that the oxidative current rises sharply and drops off after a certain potential is reached. The resulting asymmetric shape resembles the stripping type response often observed in metal analysis [25]. This type of electrochemical behaviour can be therefore tentatively attributed to the formation and stripping of a nickel sulfide layer as expressed by Scheme 8.1 given below:

$$NiO + H_2S \rightleftharpoons NiS + H_2O \qquad (C, 1)$$

$$NiS \rightleftharpoons Ni^{2+} + S + 2e^- \qquad (E, 2)$$

Scheme 8.1

It is proposed that the anodic nickel oxide film undergoes a chemical reaction with H_2S leading the formation of NiS (Eq. C,1) which is then essentially 'stripped' from the electrode surface (Eq. E,2). The corresponding values for the standard heat and free energy of formation for the reactions detailed in scheme 8.1 were estimated to be -893

and -543 kJ mol^{-1}, respectively, thereby showing that the overall process is thermodynamically viable [26].

The coverage of nickel sulfide on the electrode surface can be calculated from the amount of charge passed during the oxidation process (i.e., integrated area of the oxidative peak). It can be estimated that if there was a monolayer of sulfur atoms present on the electrode surface then the charge passed would be equivalent to ca. 0.14 mC (= 1.3 mC cm^{-2}, based on atomic radius of sulfur 0.104 nm) and if there was a monolayer of S_8 rings present on the surface, analogous to that seen on gold [27], then the charge would be ca. 0.08 mC (= 0.73 mC cm^{-2}, based on a sulfur-sulfur bond length of 0.21 nm and assuming that S_8 forms a crown structure [27]). The amount of charge passed when 60 μM sulfide was added to the solution was 0.31 mC suggesting that a few monolayers of sulfur species are present on the electrode surface under these conditions.

Analysis of the oxidation wave by means of standard addition plot of anodic peak current against concentration of sulfide provides a linear range from 40 μM to 140 μM showing the analytical utility of the approach for sulfide determination. The next section discusses how the response of sulfide at a NOMN electrode can be improved with the view to developing a highly sensitive sulfide sensor.

8.1.2.3 Effect of the pH (3 < pH <7) on the response of the NOMN electrode to H_2S

As already discussed in the introduction, the electro-chemical dissolution of nickel and consequently the amount of nickel oxide formed at the nickel electrode, depends on the pH of the solution in which the electrode is immersed. According to the reactions pathway suggested in scheme 8.1, the stripping of sulfide is preceded by the homogeneous reaction of nickel oxide with H_2S (Eq. C,1). Therefore the response of sulfide is also likely to be pH dependent.

First, we investigated the influence of pH on the formation of the nickel oxide layer. This was done by examining the anodic oxidation of the nickel electrode in acetate buffered solution at pH 3, 4 and 5 and in phosphate buffered solutions at pH 4 and 7. Again, the nickel oxide layer formation was carried out in each different solution by means of cyclic voltammetry. The potential was swept from -0.5 V to +1.0 V at a scan rate of 100 mV s^{-1} and cycled 10 times.

The shape of the voltammetric profiles obtained in the acetate solutions at pH 3 and pH 5 were essentially analogous to those obtained in acetate solution at pH 4 already described in section 8.1.2.1 and a stable voltammetric response was recorded after the third consecutive scan. It was also observed that by changing the buffer solution at pH 4 from acetate to phosphate had no significant effects on the passivation procedure indicating both phosphate and acetate anions do not act as alternative cathodic reductant. However, when the pH was increased to pH 7 insufficient protons were available to achieve passivity of the nickel oxide layer in accordance with observations reported in the literature [7] and therefore no further voltammetric investigations were carried out at pH 7.

After having assessed that a stable nickel oxide layer could be electrochemically formed on the surface of the nickel electrode immersed in acetate buffer solutions in the pH range of $3 < pH < 5$, we next examined the influence of pH on the response of sulfide. The voltammetric responses of 50 μM sulfide at NOMN films formed at nickel electrodes immersed in pH 3, 4 and 5 are overlaid for comparison in figure 8.3.

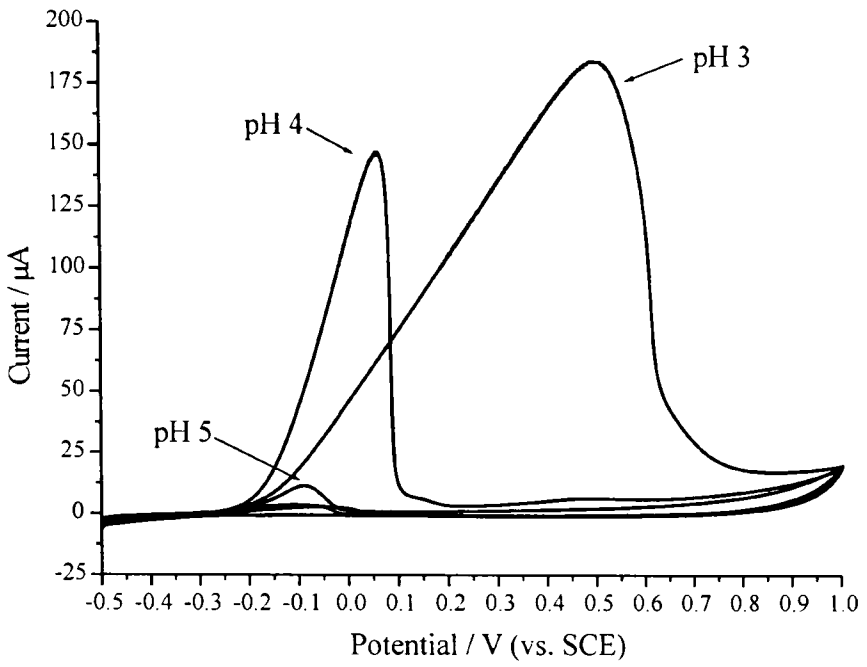


Figure 8.3: The effect of pH on the voltammetric signal of the nickel oxide layer in the presence of 50 μM sulfide with a 5 seconds accumulation time between the addition and the scan.

Upon addition of sulfide, a stripping-like oxidative wave is observed at all pH values. Visually it is evident that the signal is more enhanced as the acidity of the solution is increased. This is corroborated in table 8.1 which compares the oxidative peak current and charge of the oxidative wave at each pH examined, thereby confirming that the response of sulfide is pH dependent. The increase in response at lower pH can be tentatively attributed to catalysis of the NiO reaction with sulfide, possibly via protonation of the surface oxide.

Table 8.1: *The effect of acetate buffer pH on the peak current and oxidative charge for a solution containing 50 μM sulfide.*

	Oxidative Peak Height / mA	**Oxidative Charge / mC**	**Oxidative Charge Density / (mC cm^{-2})**
pH 3	0.173	0.789	6.97
pH 4	0.145	0.217	1.87
pH 5	0.011	0.014	0.12

The effect of changing the buffer solution from acetate to phosphate on the voltammetric signal of a solution containing 50 μM sulfide was examined and similar voltammetric responses were obtained suggesting that the process occurring is anion independent as expected from scheme 8.1.

Although decreasing the pH clearly improves the sensitivity of the response to sulfide, experiments carried out in pH 4 acetate buffer solutions offered the best compromise between sensitivity and reproducibility of the sulfide signal and therefore all the subsequent experiments were recorded at pH 4.

8.1.2.4 UV-VIS Spectroscopy

In order to produce corroborative evidence for the proposed reactions scheme detailed in Scheme 8.1, a spectrophotometric protocol was undertaken to quantity the concentration of Ni^{2+} ions released in the solution after the voltammetric experiment had been undertaken. The assay procedure is detailed in experimental section (*vide supra*) and it was based on the dimethylglyoxime method reported in the literature [22-24]. Absorbance spectra of the solutions in which a voltammetric experiment had been carried out revealed an enhancement in the absorbance at 460 nm (figure 8.4), providing qualitative evidence of the presence of Ni^{2+} in the solution. In order to quantify the amount of Ni^{2+} present, the sample was doped with 4 μM Ni^{2+} (figure 8.4, spectrum c) and the resulting spectra recorded and compared to that of un-doped sample (figure 8.4, spectrum b). A comparison of the absorbance at 460 nm of the two samples indicates the presence of 1.5 μM Ni^{2+}. This is in good agreement with the electrochemically estimated value of 1.5 μM which was calculated from the amount of charged associated with the oxidation process (= 1.4 mC).

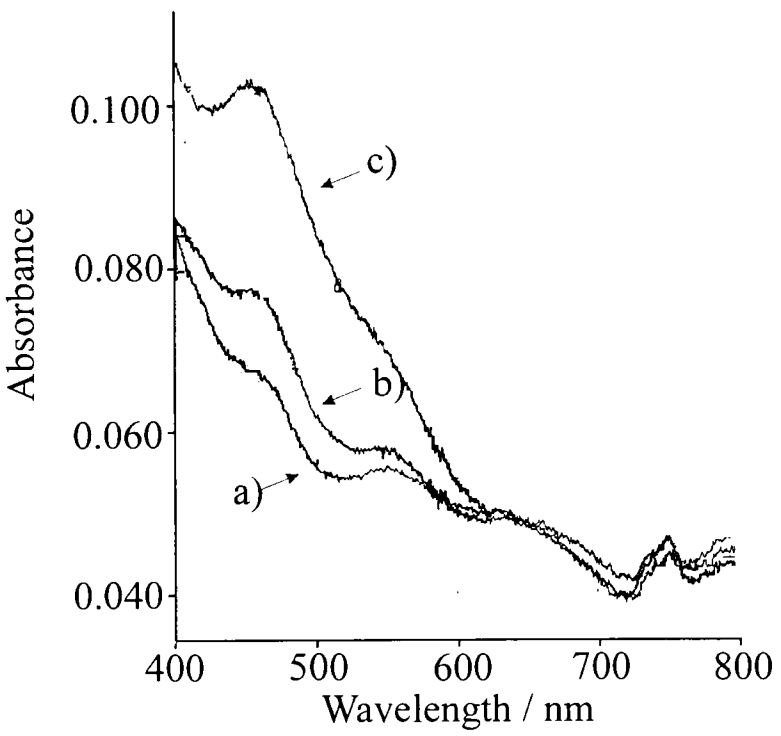


Figure 8.4: Absorbance spectra of: (a) a solution containing 4mM dimethylglyoxime and 50 μM sulfide, (b) a solution containing 4mM dimethylglyoxime and 50 μM sulfide in which an electrochemical experiment has been undertaken and (c) the same as solution b with 4 μM nickel sulfate added.

8.1.2.5 Analytical performance

We will now discuss the possibility of exploiting the stripping like response of sulfide at NOMN electrodes to determine low micromolar H_2S concentrations. According to the suggested reactions scheme (scheme 8.1), an increase in the stirring time of the solution following the addition of sulfide could cause an increase in the accumulation of NiS at the electrode surface. Consequently, when the electrochemical sweep is carried out a larger signal would be observed providing a more sensitive protocol. Initially, a stable nickel oxide passive layer was formed by means of repetitive cyclic voltammetry (100 mV s^{-1}, acetate buffer pH 4) as shown previously. Next the effect of increasing the stirring time on the response of 1 μM sulfide at a NOMN electrode was examined. The corresponding voltammograms for five different stirring times (from 1 to 5 minutes) are depicted in Figure 8.5. A gradual enhancement in the oxidative process with increasing accumulation time is observed suggesting that the limit of detection for sulfide can be significantly improved by allowing larger accumulation time.

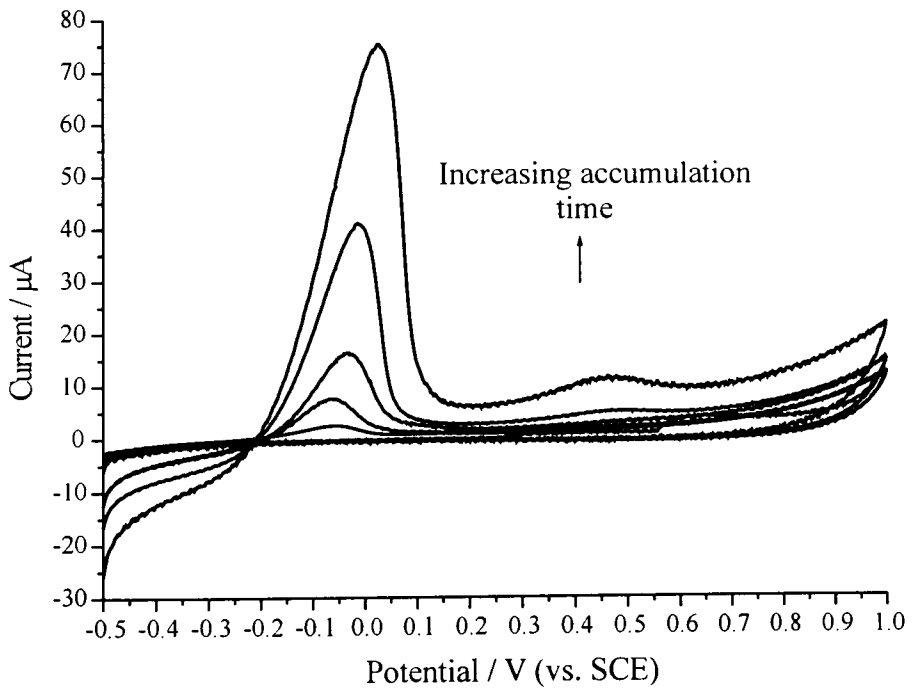


Figure 8.5: The effect of increasing the accumulation time (1 to 5 minutes) on the voltammetric signal (scan rate = 100 mV s^{-1}) of the NOMN electrode when placed in a pH 4 solution and in the presence of 1 μM sulfide.

Figure 8.6 depicts a set of current-potential responses recorded at a NOMN electrode immersed in a pH 4 acetate solution in which increasing additions of sulfide (1 to 7 μM) were made every two minutes. The corresponding voltammetric responses are analogous to those observed in the presence of higher concentrations of sulfide (figure 8.2), however the sensitivity towards sulfide detection is greatly enhanced producing a limit of detection of 0.8 μM (see insert plot figure 8.6).

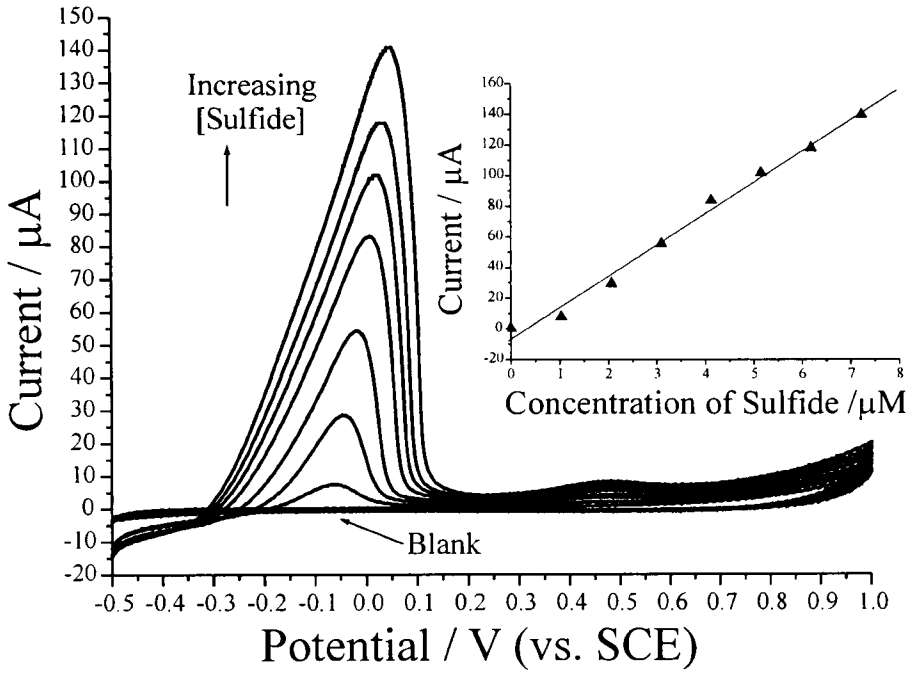


Figure 8.6: The voltammetric response (scan rate = 100 mVs^{-1}) of the NOMN electrode to increasing sulfide concentrations (1 to 7 μM, pH 4 acetate buffer) when a two minute accumulation time is allowed between the sulfide addition and the voltammetric scan.

8.1.3 Conclusion

The electrochemistry of a nickel electrode in acidic media has been studied and shown to form a passivated nickel oxide layer which exibits no voltammetric redox behaviour in the potential range studied. The response of the NOMN electrode to increasing additions of sulfide has been examined with the resulting voltammograms showing behaviour not inconsistent with that of stripping wave. A possible reactions pathway for the interaction of the sulfide species with the nickel oxide film is proposed whereby nickel sulfide is formed at the electrode providing the thermodynamic drive behind the mechanism. Spectroscopic corroborative evidence further confirm the viability of the suggested scheme of reactions. Finally, the analytical utility of the approach has been

appraised with a linear range from 40 to 140 μM if the measurement is recorded directly after the addition of sulfide and a limit of detection of 0.8 μM achieved by allowing the sulfide to accumulate at the electrode surface for a period of two minutes.

8.2 Detection of Sulfide at Nickel Modified Screen Printed Carbon (Ni-SPC) Electrodes in Acidic Media

In the section outlined below the nickel oxide films will be generated not on the surface of a nickel electrode as previously described but from metallic nickel electrodeposited on either a glassy carbon electrode or a carbon working electrode of a screen-printed strip. The interest in using a nickel oxide layer formed by electrodeposition of nickel metal stems from the possibility of forming a macroporous nickel which might likely have potential catalytic applications in the detection of sulfide. A macroporous structure could lead to an increase surface area resulting in an enhancement in the sensitivity of the sulfide response. In addition, the influence of the polishing of the nickel electrode to the response of sulfide is overcome as a controlled amount of metallic nickel can be deposited and hence a more reproducible response to sulfide obtained. Nickel metal nanoparticles supported on graphitised carbon have been shown to react with hydrogen sulfide to produce nanocrystals of the different phases of nickel sulfides thereby demonstrating the potential application in hydrodesulphurisation processes, in particular in the removal of sulfur and sulfur containing compounds from gas and oil [28]. However their analytical utility was neglected. Other studies have developed an anodic stripping voltammetric method for the sub-speciation of Ni_3S_2, NiS and NiS_2 in mixtures at carbon paste electrodes and in pH 5 acetate buffer [29]. In the present report nickel micro particles are first electrochemically deposited onto a carbon substrate and their analytical suitability for sulfide detection is appraised. The deposition of nickel was initially carried out onto glassy carbon (GC) to characterise the deposited metallic layer and its response to sulfide. After the initial characterisation process the deposition protocol was then extended to screen printed carbon (SPC) electrodes in view of developing economical, single shot disposable sensors. Modified screen printed electrodes for sulfide detection

have been reported previously with the majority consisting of an indicator placed into the carbon mix [30-33]. It will be shown that by using a nickel modified screen printed carbon electrodes (Ni-SPE) low micromolar sulfide can be detected.

8.2.1 Experimental

8.2.1.1 Manufacture of the Screen Carbon Printed Electrode (SCPE)

The ceramic screen printed (SPC) electrodes were manufactured by Gwent Electronic Materials Ltd (Monmouth House, Pontypool, Gwent). These comprised of a carbon working electrode (2 mm diameter, screen printed with an ink) a carbon counter electrode and a Ag/AgCl reference electrode (figure 8.7). For the experiments outlined below however a SCE was used as reference electrode.

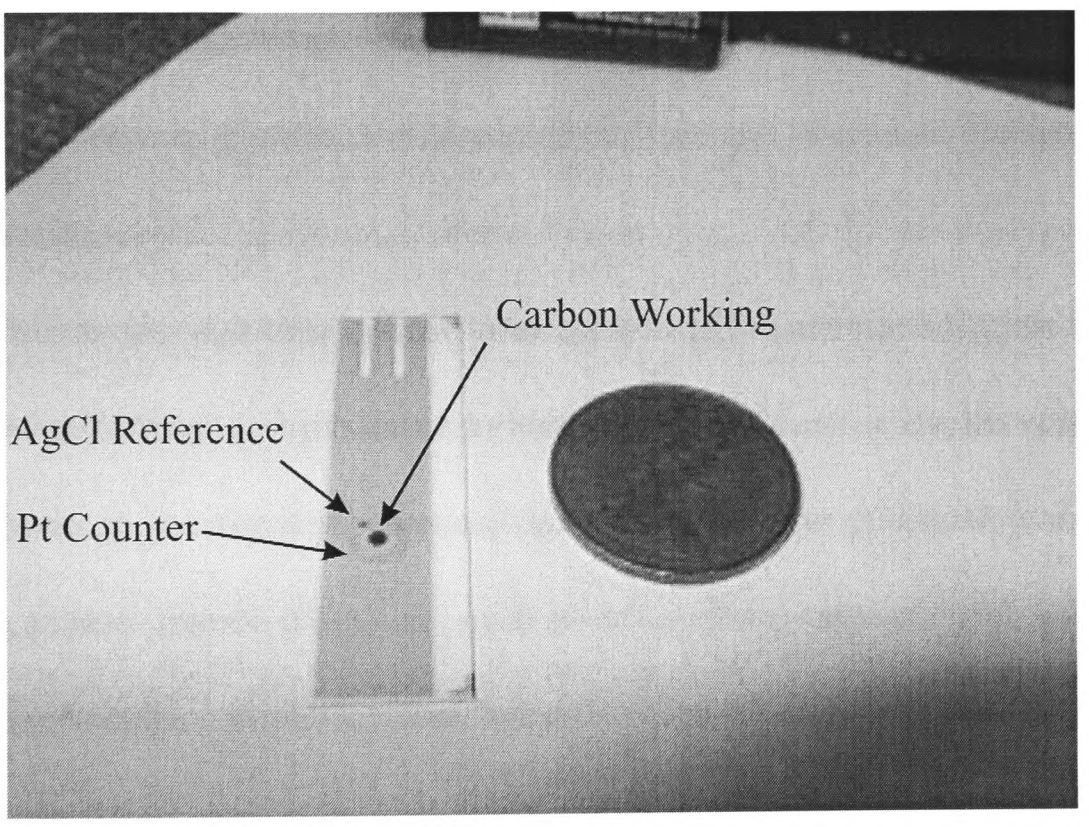


Figure 8.7: A screen printed carbon (SPC) electrode.

8.2.1.2 Nickel deposition protocol

The solution in which the nickel deposition was carried out typically consisted of 30 mL pH 4 acetate buffer. A blank measurement was recorded prior the addition of the appropriate concentration of nickel sulfate (*vide infra*) to check that the surface of

the glassy carbon (GC) or the screen printed carbon (SPC) electrodes were clean. The electrodeposition of metallic nickel was carried out using constant potential electrolysis for a set deposition time at a potential of -2.0 V in a solution containing a known concentration of nickel sulfate.

Quantification of the amount of nickel deposited was carried out by stripping nickel using linear sweep voltammetry (between -1.0 V and +1.0 V, 100 mV s^{-1}, not shown) in the same solution of nickel sulfate pH 4 acetate buffer. A sharp stripping peak was observed at -0.08 V corresponding to the oxidation of metallic nickel.

8.2.2 Results and Discussion

8.2.2.1 Deposition of nickel on glassy carbon and passivation of the nickel oxide film

Nickel was initially electrodeposited (-2.0 V, 3 minutes deposition time) on a glassy carbon (GC) electrode from a 5 mM nickel sulfate pH 4 acetate buffer solution as described in section 8.2.1.2.

The Ni-GC electrode was then placed into a fresh pH 4 acetate solution and a nickel oxide layer was formed and passivated electrochemically using cyclic voltammetry as described above in the previous section (*vide supra*). The potential was repetitively cycled (10 scans) from -0.5 V to +1.0 V at a scan rate of 100 mV s^{-1}. The corresponding anodic potentiostatic current-potential curves (not shown) were consistent with those shown previously at a nickel electrode and exhibit a region of active dissolution at low anodic potentials (i.e., an oxidative wave at +0.05 V on the first scan) and a passivation region due to the formation of insoluble substances on the surface at high anodic potentials. Subsequent scans clearly indicate the onset of passivity and reveal that a stable baseline is obtained after the 3rd cycle. Analysis of the amount of charge associated with the electro-dissolution process observed on the

first voltammetric scan suggest that ca.13 monolayers of nickel oxide are formed (Q_{oxi} = 8.0 mC cm^{-2}).

It was also shown that the nickel oxide layer was electrochemically inert over a wide range potential range from -0.5 V to +1.0 V, and was sufficiently mechanically stable to be transferred and placed into a fresh acetate solution, without any further metal dissolution in the fresh acidic buffer occurring.

8.2.2.2 In-situ response of H_2S at a passivated nickel oxide layer on glassy carbon (GC)

We next turn our attention to examining the voltammetric response of sulfide at a modified Ni-GC electrode as described above.

Figure 8.8 shows the voltammetric response (100 m Vs^{-1}) of the modified Ni-GC electrode to increasing additions of sulfide from 10 to 100 μM to the same buffer solution in which the passivation of the layer was carried out (designated as "in-situ" determination of sulfide).

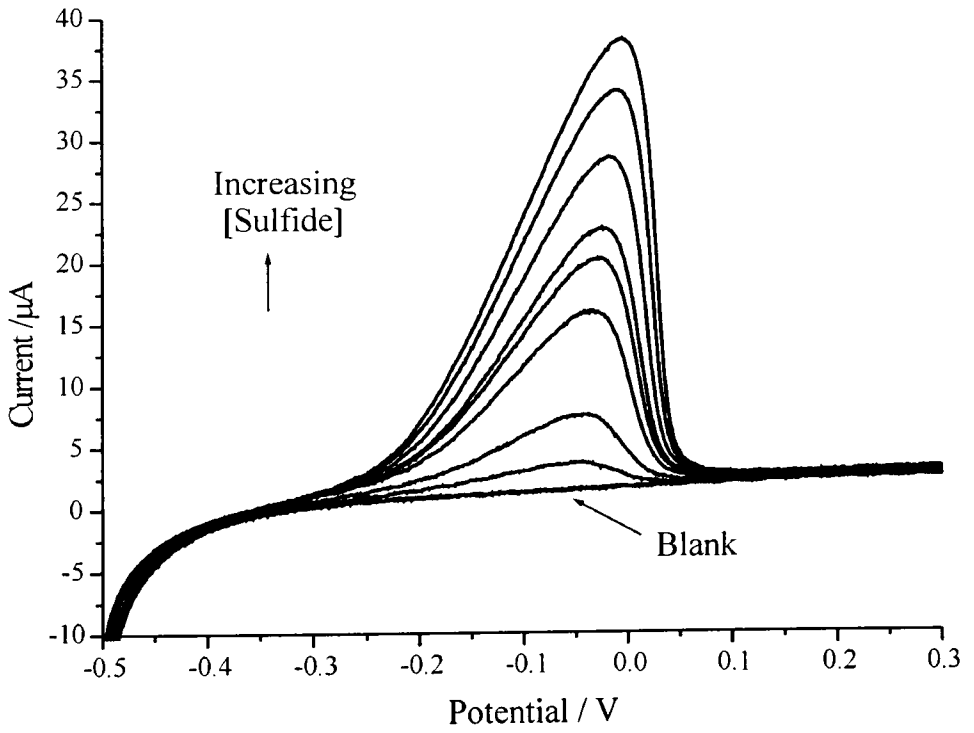


Figure 8.8: The voltammetric response (scan rate = 100 mVs^{-1}) of the passivated deposited nickel oxide film on a GC electrode to increasing sulfide concentrations (10 to 100 μM, pH 4 acetate buffer) when 15 seconds accumulation time is allowed between the addition and the voltammetric scan.

Upon the addition of sulfide a stripping-like oxidative wave is observed at -0.05 V which increases linearly with the sulfide concentration. This is in agreement with the response of sulfide observed previously at a NOMN electrode (Section 8.1, [1]) and is attributed to formation and stripping of a nickel sulfide layer formed by the homogeneous reaction of nickel oxide with sulfide prior to the electron transfer occurring as outlined in scheme 8.1 (*vide supra*).

Analysis of the stripping wave by means of a standard addition plot of peak area against concentration of sulfide showed a linear range from 20 to 90 μM sulfide (gradient= 0.7791 CM^{-1}, r^2= 0.9934). It can be seen that for concentration below 20 μM no signal was observed, thereby inhibiting the analytical utility of the approach. However solutions to overcome this drawback are detailed later in the text (section 8.2.2.7).

The optimisation of the nickel deposition procedure on the GC electrode was next investigated.

8.2.2.3 Optimisation of the electro-deposition conditions

According to Scheme 8.1, the response to sulfide depends on the amount of nickel oxide formed at the electrode surface (Eq. C,1). Quantification of the amount of nickel deposited on GC electrodes by anodic stripping voltammetry revealed a dependence of the former on both accumulation time and concentration of nickel (II) sulfate solution. Hence, before extending the analytical protocol outlined above to a disposable screen-printed sensing device, the optimum deposition conditions (i.e., nickel sulfate concentration and deposition time) needed to be determined.

First the influence of the deposition time during the electrodeposition step on the analytical signal for sulfide was examined. This was carried out by varying the deposition time from one to eight minutes of nickel onto the GC electrode from a

5 mM concentration of nickel (II) solution, after which the passivation of the nickel was carried out by means of cyclic voltammetry as described above. Finally, the voltammetric response (not shown, 100 mV s^{-1}) of the modified Ni-GC electrode to increasing additions of sulfide from 10 to 100 μM was examined.

Analysis of the voltammetric waves obtained for the sulfide standard addition experiments was carried out by plotting the peak current against the concentration of sulfide added. The resulting standard addition plots obtained for each different nickel deposition time are overlaid in figure 8.9 (a).

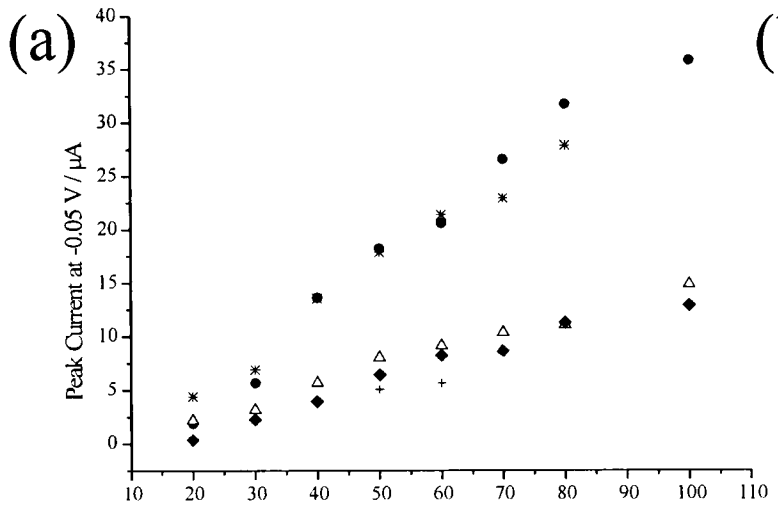


Figure 8.9 (a): The effect of changing the deposition time (1, 3, 4, 5 and 8 minutes) at a fixed nickel sulfate concentration (5 mM) on the voltammetric response (scan rate = 100 mVs^{-1}) of the deposited and passivated Ni-GC electrode to increasing sulfide concentrations (10 to 100 μM, pH 4 acetate buffer). Legend: 1 min (+), 3 min (•), 4 min (*), 5 min (△) and 8 min (♦).

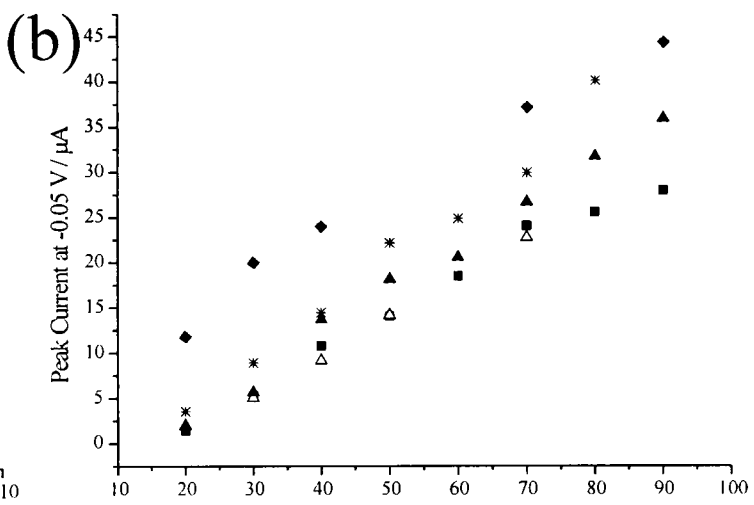


Figure 8.9 (b): The effect of changing the nickel sulfate concentration (3, 4, 5, 6 and 10 mM) at a fixed deposition time (3 minutes) on the voltammetric response (scan rate = 100 mVs^{-1}) of the deposited and passivated Ni-GC electrode to increasing sulfide concentrations (10 to 100 μM, pH 4 acetate buffer). Legend: 3 mM $NiSO_4$ (■), 4 mM $NiSO_4$ (△), 5 mM $NiSO_4$ (▲), 6 mM $NiSO_4$ (*) and 10 mM $NiSO_4$ (♦).

It can be seen from these plots that initially and for a typical concentration of nickel sulfate of 5 mM, the sensitivity increases with time. However, longer deposition time compromises both the sensitivity and the linearity of the response to sulfide. It can be envisaged that as the deposition time increases a larger nickel content will be present on the electrode surface; however above a certain threshold there may be some flaking or disruption of the layer might occur when it is placed into the fresh solution in which

the nickel oxide film is passivated. Overall the results reveal that the most sensitive response to sulfide occurs when the deposition time is set at three minutes.

Next, the effect of the concentration of the nickel sulfate solution during the electrodeposition step on the analytical response to sulfide was examined. In this case the nickel was deposited for a set time of three minutes, however the concentration of nickel (II) in the solution was varied from 1 to 10 mM. Once again after the electrodeposition of metallic nickel, a NiO film was formed and the voltammetric response to increasing additions of sulfide was examined. The corresponding standard addition plots obtained for the modified Ni-GC electrode to sulfide for each of the different deposition concentrations are detailed in figure 8.9 (b). As expected, the sensitivity of the response to sulfide slightly increases with the concentration of nickel (II) solution, as the amount of nickel deposited increases. However, when the concentration of nickel (II) is too high (i.e., 10 mM) then the linearity of the response is compromised possibly through the loss in stability of the nickel film.

Overall the results suggest that the optimum deposition time is three minutes in a solution containing 3 mM $NiSO_4$ and these are the conditions which will be deployed in the proceeding experiments.

8.2.2.4 Analysis of the surface morphology of nickel and nickel oxide films

In order to examine the surface morphology of the nickel and nickel oxide films atomic force microscopy imaging of the electrode surface was undertaken. The resulting AFM images are detailed in figure 8.10.

Figure 8.10 (a) details the AFM image of a freshly polished glassy carbon electrode, whilst 8.10 (b) is the AFM image of an electrode which has undergone a deposition step in the presence of 3 mM $NiSO_4$ for 3 minutes.



Figure 8.10: (a) AFM image of a polished GC electrode (x =10μm, y =10μm, z =300.1nm); (b) AFM image of a electrodeposited nickel layer on a GC electrode (-2.0 V, 3 minutes, 3 mM $NiSO_4$, pH 4 acetate buffer, (x =10μm, y =10μm, z =402.1nm).

Analysis of figure 8.10 (a) shows that the scratches on the GC electrode surface due to the 'polishing' procedure are clearly visible. However, the image detailed in figure 8.10 (b) for the deposited nickel on glassy carbon electrode shows the disappearance of the polishing scratches and indicates the formation of a clear and uniformly distributed film of nickel particles on the electrode surface. Examination of these particles reveals they have a mean diameter of 1 μm.

It was not possible to obtain AFM images of the modified Ni-GC electrode surface due to the fragile nature of the deposit on the electrode surface. Removal of the NiO layer by the tip during scanning occurred indicating a sticky nature of the deposit or, more probably, a poor adhesion of the film to the electrode surface. Topographical images of the NiO layer were thus obtained by SEM. Examination of the SEM image, figure 8.10 (c), reveals particulates on the electrode surface, corresponding to the

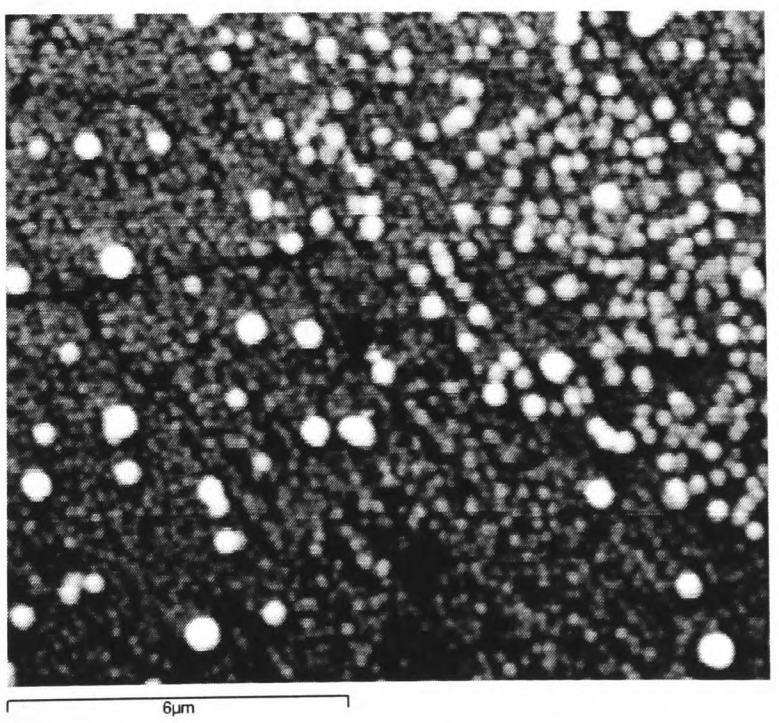


Figure 8.10 (c): SEM image electropassivated nickel oxide on GC (pH 4 acetate buffer, between -0.05 V and +1.0 V, 100 mV s^{-1}).

NiO film. These were found to be from 100 to 600 nm in diameter, suggesting that the NiO formation disrupts the nickel layer.

8.2.2.5 Response of sulfide at passivated nickel oxide layer at a SPE (in-situ)

Having assessed how the various deposition parameters can effect the analytical signal towards sulfide, the analytical assay was next extended to the detection of sulfide at a modified nickel screen printed carbon (Ni-SPC) electrode.

The initial deposition of metallic nickel and subsequent passivation of the nickel oxide film deposited on the SPC electrode was carried out as described for the GC electrode and an analogous electrochemical behaviour was observed to that seen previously. The voltammetric response of the modified Ni-SPE electrode to increasing additions of sulfide from 10 to 100 μM was then examined and the resulting responses are detailed in figure 8.11.

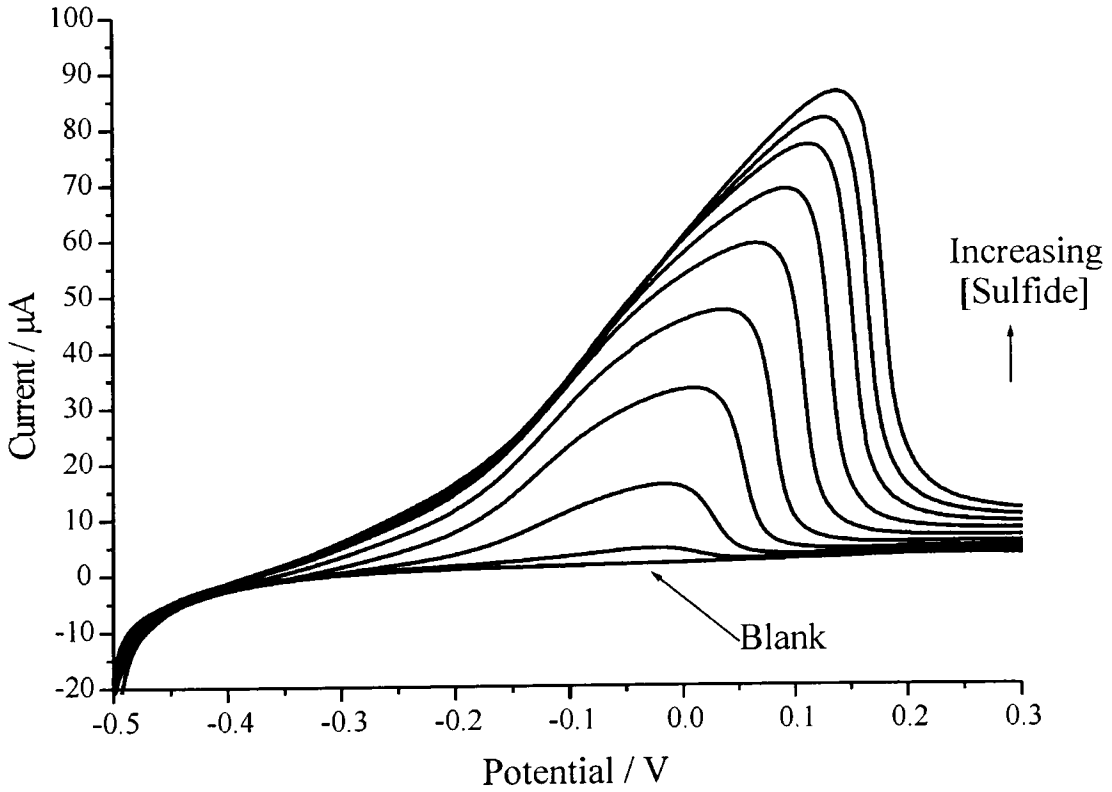


Figure 8.11: The voltammetric response (scan rate = 100 mVs^{-1}) of the nickel oxide film to increasing sulfide concentrations (10 to 100 μM, pH 4 acetate buffer) at a passivated deposited Ni-SPC electrode (In-Situ analysis, see text).

These reveal that the response at the passivated Ni-SPC electrode is similar to that observed at the passivated Ni-GC electrode as would be expected due to the formation of NiS on the electrode surface. A plot of the peak area against the concentration of

sulfide produced a linear range from 20 to 80 μM (gradient= 3.1501 C M^{-1}, r^2= 0.9919) and analogous to previous observations, no response was observed for sulfide concentration below 20 μM.

8.2.2.6 Ex-situ determination of sulfide

All the results to date have examined the response of modified Ni-GC or Ni-SPC electrodes to sulfide when the NiO layer was formed in the same solution to which the sulfide was added, however for a practical sensor to be constructed it would be desirable to form the NiO layer in a separate solution to the one in which the sulfide content is determined. Therefore the responses to increasing additions of sulfide (10-100 μM) at both the passivated Ni-GC electrode and the passivated Ni-SPC electrode when the electrode was removed from the solution in which the passivation was carried out and placed in a fresh buffer solution in which sulfide was added (designated as "ex-situ" determination of sulfide) was examined. The corresponding current-potential profiles are detailed in figures 8.12 (a) and 8.12 (b), respectively.

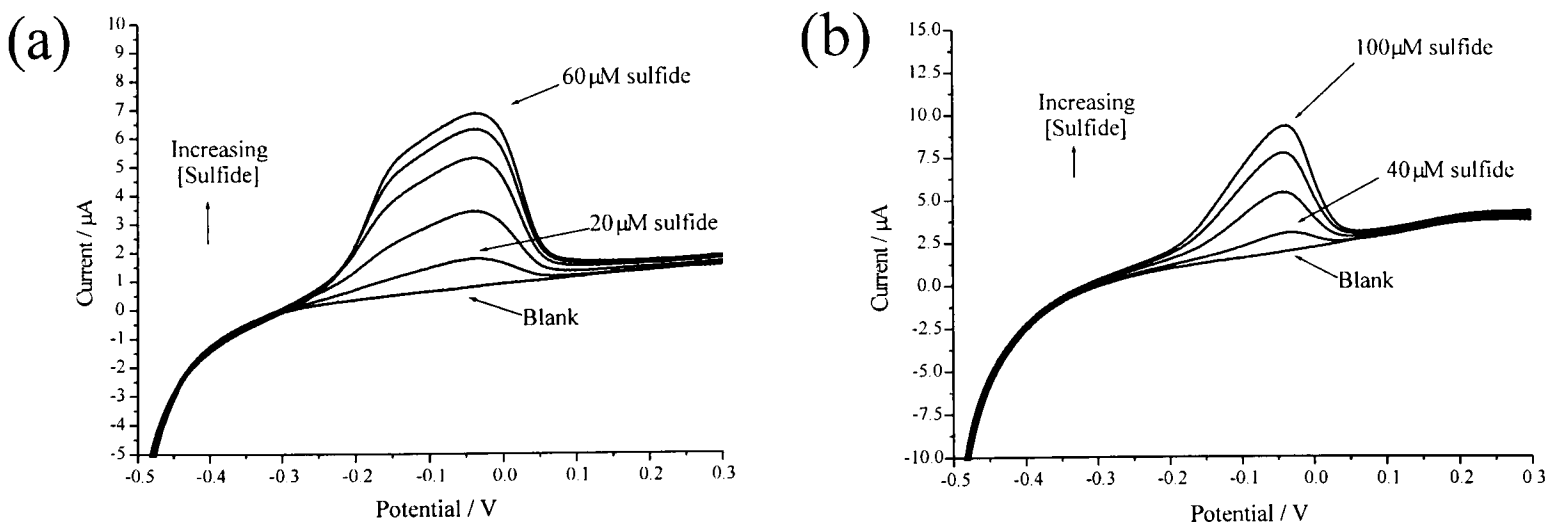


Figure 12: The voltammetric response (scan rate = 100 mV s^{-1}, pH 4 acetate buffer) of the nickel oxide film to increasing sulfide concentrations at a passivated deposited Ni-GC electrode from 20 to 60 μM (a), and at a passivated deposited Ni-SPC electrode from 40 to 100 μM (b). (Ex-Situ analysis, see text).

These responses show that the analytical signal for sulfide (i.e, the stripping wave at -0.05 V) is still observed at both modified electrodes. The ex-situ determination of

sulfide at either passivated Ni-SPC electrodes or at passivated Ni-GC electrodes was found to be comparable to the in-situ determination in regard to voltammetric characteristics and response linearity indicating that the passivated nickel layers deposited either on GC or SPC electrodes are mechanically stable. However, the major difference is that the ex-situ analysis is substantially less sensitive. This can be seen from Table 8.2 where the results obtained at the deposited Ni-GC electrode and analysed by means of a standard addition plot are compared to those typically obtained when the additions of sulfide were made in-situ. The results indicate a linear range for sulfide detection between 20 and 90 μM and between 20 and 60 μM, for in-situ and ex-situ experiments respectively, but a higher sensitivity (2.2 times) was observed for the in-situ analysis compared to that obtained for the ex-situ determination of sulfide. This can be attributed to a loss in coverage of the NiO layer when it is transferred from one solution to the next.

Table 8.2: *Comparison between In-Situ and Ex-Situ detection of sulfide at modified Ni-GC electrode.*

	Linear Range / μM	**Peak Charge Sensitivity / C M^{-1}**	**Peak Height Sensitivity / A M^{-1}**
In situ	20 - 90	0.66	0.39
Ex situ	20 - 60	0.29	0.13

An examination into the stability of the NiO layer on the screen printed electrode over a period of 27 hours was also investigated. In this case electrodeposition of nickel and passivation of the nickel oxide layer was carried out on a series of SPC electrodes as described earlier. The SPC electrodes were then removed from the solution and placed in the open air for a period of 27 hours and then the response to increasing addition of sulfide (10 – 100 μM) was recorded by means of cyclic voltammetry in a pH 4 acetate buffer solution.

The corresponding voltammograms (not shown) were found to be similar to those obtained when no time elapses between passivation of the nickel oxide layer and addition of sulfide indicating the stability of the modified Ni-SPC electrode to time. The resulting analytical parameters obtained for sulfide for a NiO electrode placed in the air for 27 hours and one in which no time elapsed before the sulfide was added are compared in table 8.3. Analysis of the values obtained reveal that they are similar thereby showing the stability of the nickel oxide film over time.

Table 8.3: *Stability of the sensor: effect of time on the quantitative measurement of sulfide at the electrodeposited nickel oxide layer on screen printed carbon electrode.*

Time / h	Linear Range / μM	Peak Charge Sensitivity / C M^{-1}	Peak Height Sensitivity / A M^{-1}
0	40 - 110	0.14	0.10
27	25 - 130	0.13	0.09

8.2.2.7 Increasing the sensitivity

To aid in the determination of lower concentrations of sulfide the effect of direct repetitive scanning and the effect of repetitive scan combined with a stirring time of 15 seconds between each addition of sulfide to the solution was investigated.

The deposition of nickel and the passivation of the nickel oxide film was carried out on a SPC electrode. Then the passivated Ni-SPC electrode was placed in a pH 4 acetate buffer solution containing 5 μM sulfide and stirred for 15 seconds. Finally, 14 repetitive/consecutive scans were recorded from -0.5 V to +1.0 V (100 mV s^{-1}). The corresponding potential-current profiles are shown in figure 8.13 (a). It can be seen that, the first scan gave an essentially flat base line. However, upon repetitive scans the amount of anodic current at -0.05 V increased considerably and after the eighth scan a distinctive anodic peak was observed.

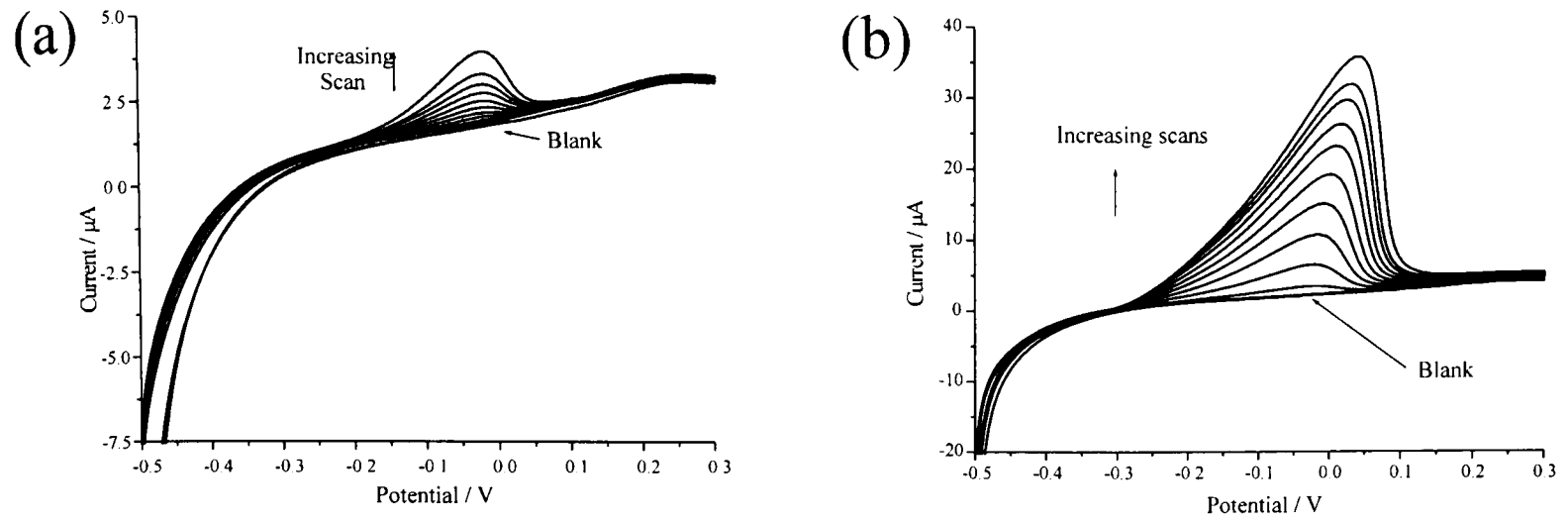


Figure 8.13: The effect of (a) repetitive scans and (b) repetitive scans with an accumulation time of 15 seconds between each scan on the sensitivity of the response of 5 µM sulfide at a passivated deposited Ni-SPC electrode (pH 4 acetate buffer, 100 mVs^{-1}).

In order to further enhance the signal towards the detection of sulfide the effect of repetitive scanning with a 15 seconds time delay between each scan was analysed. The resulting voltammetric responses recorded under these conditions are detailed in figure 8.13 (b). Once again, no analytical signal was observed on the first scan. However, the second scan already exhibited a considerable anodic peak at +0.05 V whose magnitude kept increasing with repetitive scanning thus showing that the detection of low concentration of sulfide is possible. It was further noted that a maximum current plateau was observed after 14 scans, indicating likely exhaustive formation of NiS at the electrode surface.

These results show that the sensitivity of the signal can be increased considerably by repetitive scanning. This effect can be tentatively attributed to the disruption of the nickel oxide layer by the initiation of the electrochemical sweep in the presence of sulfide. This then aids in the formation of NiS at the electrode surface (Scheme 8.1, Eq. C,1) thereby increasing the analytical signal for sulfide detection (Scheme 8.1, Eq. E,2). The observation that allowing 15 seconds stirring time between the scans results in a larger enhancement in the analytical signal for sulfide corresponding to an increase formation of NiS further supports this interpretation.

8.2.3 Conclusion

It has been shown that the amperometric detection of micromolar sulfide is possible at electrodeposited nickel films on GC and on SPC electrodes. In the absence of sulfide, the NiO layer was found to produce a stable and electrochemically inert response. In the presence of sulfide, a stripping-like wave was observed which produces a linear range to sulfide from 20 to 90 μM. The stability of the NiO film when it was placed into a fresh solution different to the one in which it was formed was examined. The corresponding response to sulfide in this fresh solution was found to have decreased in sensitivity compared to the response when sulfide was introduced directly into the solution in which the NiO layer was formed. Nevertheless, this loss of sensitivity for the ex-situ determination of sulfide was overcome by the means of repetitive voltammetric scanning of the electrode in presence of sulfide which produced an enhancement in the sensitivity and allowed the determination of low sulfide concentrations (5 μM). The use of modified Ni-SPC have been shown to provide a response to sulfide analogous to that seen with the Ni deposited GC electrode thereby demonstrating the possible development of inexpensive, and disposable sensors for sulfide.

8.3 Chapter 8 References

[1] D. Giovanelli, N. S. Lawrence, L. Jiang, T. G. J. Jones, R. G. Compton, *Analyst* **2003**, *128*, 173.
[2] D. Giovanelli, N. S. Lawrence, S. J. Wilkins, L. Jiang, T. G. J. Jones, R. G. Compton, *Talanta* **2003**, *61*, 211.
[3] A. J. Arvia, D. Posadas, in *Encyclopedia of electrochemistry of the elements* (Ed. A. J. Bard), Marcel Dekker, New York **1975**, pp. 211-421.
[4] G. Cordeiro, O. R. Mattos, O. E. Barcia, L. Beaunier, C. Deslouis, B. Tribollet, *J. Appl. Electrochem.* **1996**, *26*, 1083.
[5] I. Epelboin, M. Keddam, *Electrochim. Acta* **1972**, *17*, 177.
[6] A. Jouanneau, M. Keddam, M. C. Petit, *Electrochim. Acta* **1976**, *21*, 287.
[7] J. R. Vilche, A. J. Arvia, *Lat. Am. J. Chem. Appl. Chem.* **1979**, *9*, 35.
[8] J. R. Vilche, A. J. Arvia, *Corros. Sci.* **1978**, *18*, 441.
[9] S. G. Real, J. R. Vilche, A. J. Arvia, *Corros. Sci.* **1980**, *20*, 563.
[10] S. G. Real, M. R. Barbosa, J. R. Vilche, A. J. Arvia, *J. Electrochem. Soc.* **1990**, *137*, 1696.
[11] M. R. Barbosa, S. G. Real, J. R. Vilche, A. J. Arvia, *J. Electrochem. Soc.* **1988**, *135*, 1077.
[12] M. R. Barbosa, J. A. Bastos, J. J. Gracia-Jareno, F. Vicente, *Electrochim. Acta* **1998**, *44*, 957.

[13] J. V. Dobson, B. R. Chapman, *Electrochim. Acta* **1987**, *32*, 415.
[14] B. MacDougall, *J. Electrochem. Soc.* **1980**, *127*, 789.
[15] B. MacDougall, *Corros. Sci.* **1988**, *28*, 211.
[16] B. MacDougall, M. Cohen, *J. Electrochem. Soc.* **1974**, *121*, 1152.
[17] B. MacDougall, M. J. Graham, *Electrochim. Acta* **1981**, *26*, 705.
[18] B. MacDougall, M. J. Graham, *Electrochim. Acta* **1982**, *27*, 1093.
[19] B. MacDougall, D. F. Mitchell, M. J. Graham, *J. Electrochem. Soc.* **1985**, *132*, 2895.
[20] R. L. Cowan, R. W. Staehle, *J. Electrochem. Soc.* **1971**, *118*, 557.
[21] D. Giovanelli, N. S. Lawrence, L. Jiang, T. G. J. Jones, R. G. Compton, *Sens. and Actuators, B* **2003**, *B88*, 320.
[22] J. A. Dean, *Analytical Chemistry Handbook*, McGraw-Hill, New York, **1995**.
[23] A. Classen, L. Bastings, *Rec. Trav. Chim.* **1954**, *73*, 783.
[24] W. Oelschlager, *Z. Anal. Chem* **1955**, *118*, 557.
[25] R. P. Akkermans, J. C. Bal, O. Rebbit, F. Marken, R. G. Compton, *Electrochim. Acta* **1998**, *43*, 343.
[26] *CRC Handbook of Chemistry and Physics*, 74th Ed., CRC Press, Florida, USA, **1993**.
[27] X. Gao, Y. Zhang, M. J. Weaver, *J. Phys. Chem.* **1992**, *96*, 4156.
[28] R. D. Tilley, D. A. Jefferson, *J. Phys. Chem. B* **2002**, *106*, 10895.
[29] J. L. Wong, M. Tian, W. R. Jin, Y. N. He, *Electroanalysis* **2001**, *12*, 1355.
[30] N. S. Lawrence, L. Jiang, T. G. J. Jones, R. G. Compton, *Anal. Chem.* **2003**, *75*, 2054.
[31] J. P. Hart, A. K. Abass, *Anal. Chem.* **1997**, *342*, 199.
[32] J.-M. Zen, P.-Y. Chen, A. S. Kumar, *Electroanalysis* **2001**, *14*, 513.
[33] M. I. Prodromidis, P. G. Veltsistas, M. I. Karayannis, *Anal. Chem.* **2000**, *72*, 3995.

Part 3: "Electrochemical Determination of Gaseous Ammonia"

Aims and Scope:

This section consists of two chapters showing two different electrochemical strategies for sensing gaseous ammonia in aprotic solvents and in room temperature ionic liquids (RTILs). The first chapter details a new methodology for detecting ammonia based on its interaction with hydroquinone. The second chapter examines the electrochemical oxidation of ammonia in N,N-dimethylformamide, DMF, and in the RTIL, 1-ethyl-3-methylimidazolium bis(trifluoromethylsulfonyl)imide, [EMIM][$N(Tf)_2$].

Chapter 9: "Determination of Ammonia based on the Electro-oxidation of Hydroquinone in N,N-Dimethylformamide or in the Room Temperature Ionic Liquid, 1-Ethyl-3-methylimidazolium bis(trifluoromethylsulfonyl)imide"

The results in this chapter detail a novel methodology for the electrochemical determination of ammonia based on its interaction with hydroquinone, QH_2, in the aprotic solvent N,N-Dimethylformamide, DMF, and in the room temperature ionic liquid 1-ethyl-3-methylimidazoliumbis(trifluormethylsulfonyl)imide, [EMIM][$N(Tf)_2$]. The results detailed below have been published in Talanta [1].

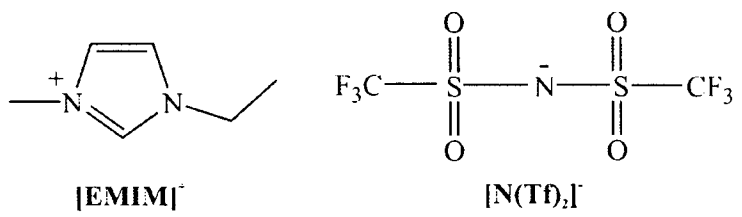
9.1 Introduction

Given its toxicity, the determination of ammonia is essential to a number of applications including clinical diagnosis, industrial hygiene, environmental protection and the monitoring of the leakage from refrigeration systems [2]. As ammonia is a commonly employed fertiliser, the ability to detect ammonia also holds great importance in the agriculture sector. Consequently, several ammonia sensors have been reported in the literature, the majority of which are based on a gas diffusion cell approach. In these systems ammonia gas diffuses through a gas permeable hydrophobic membrane (usually PTFE or Teflon) into a recipient solution where it can be detected by means of simple and inexpensive detection techniques such as a colorimetric pH indicator [3,4], a NH_4^+ selective electrode [5] or a pH sensor [6,7]. The use of the gas diffusion cell configuration allows the removal of potential interferents thus providing selectivity in complex media.

Devices containing a metal oxide or a polymer film have been reported. In metal oxide based sensors, monitoring of ammonia is based on the change in the electrical conductance caused by adsorption, desorption, or chemical reaction between ammonia gas and the surfaces [6]. A number of coatings have been investigated for the piezoelectric crystal in mass sensitive sensors for ammonia such as ascorbic acid, pyridoxine hydrochloride [6], L-glutamic acid hydrochloride [8], acrylic acid isooctylacrylate [9], TiN [10], and CuS [11]. The coating is deposited on the quartz crystal and, depending on its thickness, the analyte gas is adsorbed onto or into the surface coating. The corresponding change in frequency of oscillation of the quartz is then related to the amount of gas adsorbed. An amperometric sensor based on a polypyrrole-modified Pt electrode [12,13] where no gas diffusion cell was necessary has also been described. However, when used in clinical sample matrices, this sensor can suffer from interferences from ascorbic acid and uric acids, which are oxidised

within the working potential of the polypyrrole-based ammonia sensor. Permselective polymer films can however be used to prevent the access of interfering substances to the electrode [14,15].

This chapter describes a novel detection strategy for ammonia based on its interaction with hydroquinone in N,N-dimethylformamide (DMF) and in the room temperature ionic liquid 1-ethyl-3-methylimidazolium bis(trifluormethylsulfonyl)imide, [EMIM][$N(Tf)_2$] (Scheme 9.1).



Scheme 9.1: Structure of the room temperature ionic liquid 1-ethyl-3-methylimidazolium bis(trifluormethylsulfonyl)imide, [EMIM][$N(Tf)_2$].

The electrochemistry of the benzoquinone/hydroquinone redox reaction has been extensively studied in both aqueous and non-aqueous solvents [16]. The reduction of quinone derivatives in aprotic solvent has been investigated in the presence of acids and has provided the basis for the determination of biologically important acids [17].

We report the effect of ammonia as a proton acceptor species on the anodic oxidation of hydroquinone in the aprotic solvent DMF. The aim of this work was to investigate whether the acid-base equilibria between ammonia and hydroquinone could be used for ammonia sensing. Ammonia removes protons from the hydroquinone species, thus making the oxidative process easier, thereby shifting the oxidation potential of the hydroquinone/benzoquinone redox couple. In an attempt to overcome the sensitivity of the ammonia sensor to moisture and humidity, the investigation was extended to the hydrophobic room temperature ionic liquid, 1-ethyl-3-methylimidazolium bis(trifluormethylsulfonyl)imide, [EMIM][$N(Tf)_2$].

Room temperature ionic liquids (RTILs) are molten salts typically comprised of bulky cations and weakly coordinated anions, which are of great interest in electrochemical

studies because of their wide electrochemical windows (= 4.78 V for [EMIM][$N(Tf)_2$], [18]), extraordinarily high chemical and thermal stability, negligible vapour pressure and good conductivity [19-22]. We refer the reader to a review article recently published in ChemPhysChem [18] for a more comprehensive description of RTILs properties and uses. Careful selection of the cation/anion pair allows for control over several of the physical properties of these RTILs [23-25]. Given its hydrophobic nature, [EMIM][$N(Tf)_2$] was chosen as an alternate solvent to minimise water uptake and enable the realisation of a sensor which could tolerate atmospheric conditions. The hydrophobicity of [EMIM][$N(Tf)_2$] is attributed to the poor hydrogen bonding ability of the $[N(Tf)_2]^-$ anion due to the delocalisation of the negative charge over the trifluoromethylsulfonyl groups, resulting in typical water saturation levels of only 2 % [20].

9.2 Experimental Section

9.2.1 Chemical Reagents

1-Ethyl-3-methylimidazolium bis(trifluoromethylsulfonyl)imide, [EMIM][$N(Tf)_2$] was synthesized from the corresponding bromide salt via a metathesis reaction in aqueous lithium bis(trifluoromethylsulfonyl)imide, as described by Bonhôte *et al.* [20]. Impurity free nitrogen, oxygen and ammonia (BOC, Guildford, Surrey, UK) were used for electrochemical experiments as described below.

9.2.2. Instrumentation

For all electrochemical experiments carried out in DMF, 0.1 M tetrabutylammonium perchlorate (TBAP) was used as supporting electrolyte and a standard three electrode configuration was used within a five-arm electrochemical cell. A glassy carbon (GC, 3 mm diameter, BAS Technicol, UK) served as the working electrode, a platinum wire

wound into a spiral provided the counter electrode and a platinum pseudo-reference electrode completed the cell assembly. All the potential are quoted against Pt. DMF solutions were purged with nitrogen for 15 minutes prior each experiment to ensure the removal of any atmospheric oxygen.

For all electrochemical experiments involving the ionic liquid, a short piece (~ 2 cm long) of heat-shrink tubing was fitted around the glass surrounding the GC microdisk working electrode (5 μm diameter) to provide a casing, to which a typical volume of ~ 20 μL of ionic liquid was delivered by micropipette. A Pt wire was secured around the heat-shrink tubing, acting as a counter/reference electrode. A 20 μL aliquot of a stock solution of hydroquinone in acetonitrile, MeCN, was delivered directly to the ionic liquid sample. The solution was placed under vacuum (Edwards High Vacuum Pump, Model ES 50) for thirty minutes to allow for evaporation of MeCN and equilibrium of the hydroquinone with the ionic liquid, as well as removal of trace impurities such as water and atmospheric oxygen. An estimate of the concentration of the hydroquinone in the ionic liquids was determined under the assumption that all of the MeCN had evaporated in vacuo. All experiments were carried out in an electrochemical cell designed to sustain vacuum conditions at a temperature of 20 ± 3° C, as previously reported [26].

Ammonia was delivered directly from a cylinder containing a specified volume percentage (10, 20, 50 or 100 % vol.) or ppm concentration (95, 32 and 10 ppm). Nitrogen made up the remainder of all gas mixtures. Gas mixtures were passed through the cell for at least thirty minutes before final measurements were taken to ensure that equilibration of the gases and the solvent had been established.

9.3 Results and Discussion

9.3.1 Voltammetric Response of Hydroquinone in DMF in the Presence of Ammonia

The electrochemical behaviour of hydroquinone in the aprotic solvent DMF was characterised by employing cyclic voltammetry. Figure 9.1 (a) shows the cyclic voltammogram (100 mV s^{-1}) obtained at a glassy carbon electrode for a solution containing 0.5 mM hydroquinone in DMF (0.1 M TBAP).

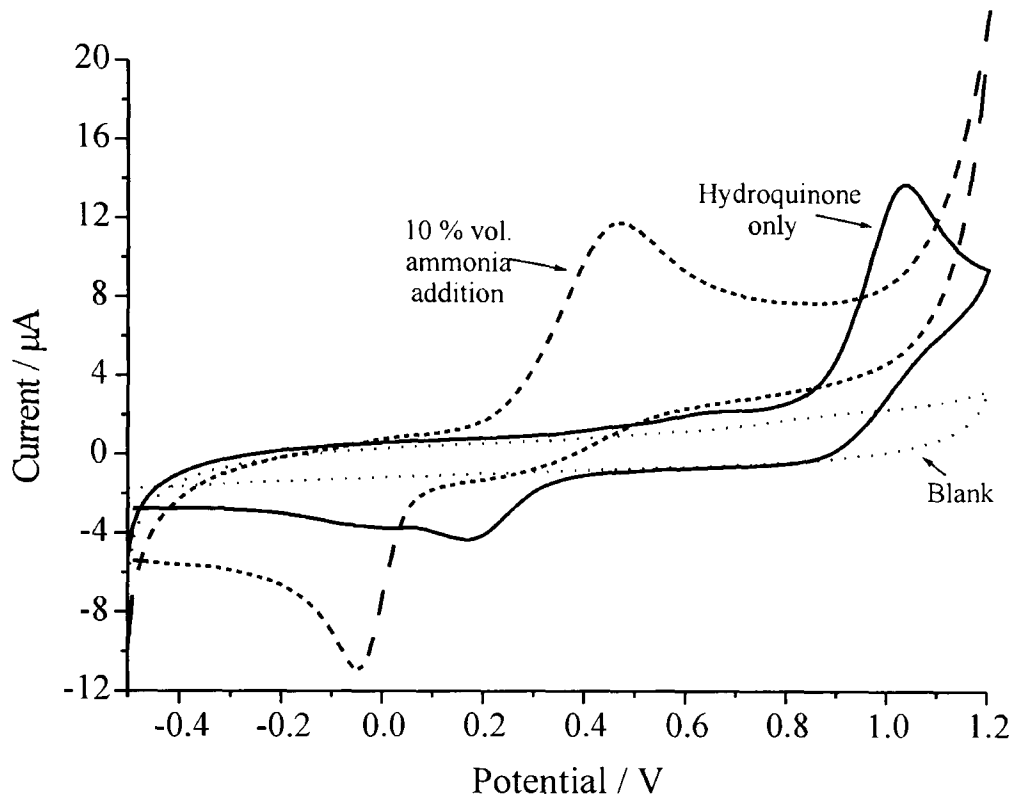


Figure 9.1 (a): The cyclic voltammetric response (GC, 100 mVs^{-1}) of 0.5 mM hydroquinone in DMF (0.1 M TBAP) in the absence and in the presence of 10 % vol. ammonia. Also overlaid is the corresponding blank voltammogram in DMF.

This reveals a single oxidative wave at +1.03 V (*vs.* Pt) and a corresponding reductive wave at +0.18 V (*vs.* Pt), producing a peak-to-peak separation of 0.85 V. This type of electrochemical behaviour is consistent with hydroquinone first undergoing a slow deprotonation step coupled to a two-electron process in a CE mechanism as expressed by [27-29]:

$$QH_2 \rightleftharpoons Q^{2-} + 2H^+ \qquad (9.1, C)$$

$$Q^{2-} \rightleftharpoons Q + 2e^- \qquad (9.2, E)$$

Also overlaid in figure 9.1 (a) is the voltammetric response of 0.5 mM hydroquinone when the DMF solution was saturated with 10 % vol. ammonia. Saturation of the DMF solution was achieved by bubbling ammonia from a cylinder containing 10 % vol. ammonia for thirty minutes. Upon addition of ammonia to the solution, the oxidation wave at +1.03 V (*vs.* Pt) is shown to shift to a less positive potential (+0.43 V). This is consistent with ammonia acting as a base, removing protons from the hydroquinone species and facilitating the deprotonation step which precedes the oxidation of hydroquinone, thus aiding the oxidation process. Similar behaviour was observed when ammonia was added in higher concentrations (20 and 50 % vol., figure 9.1 (b)).

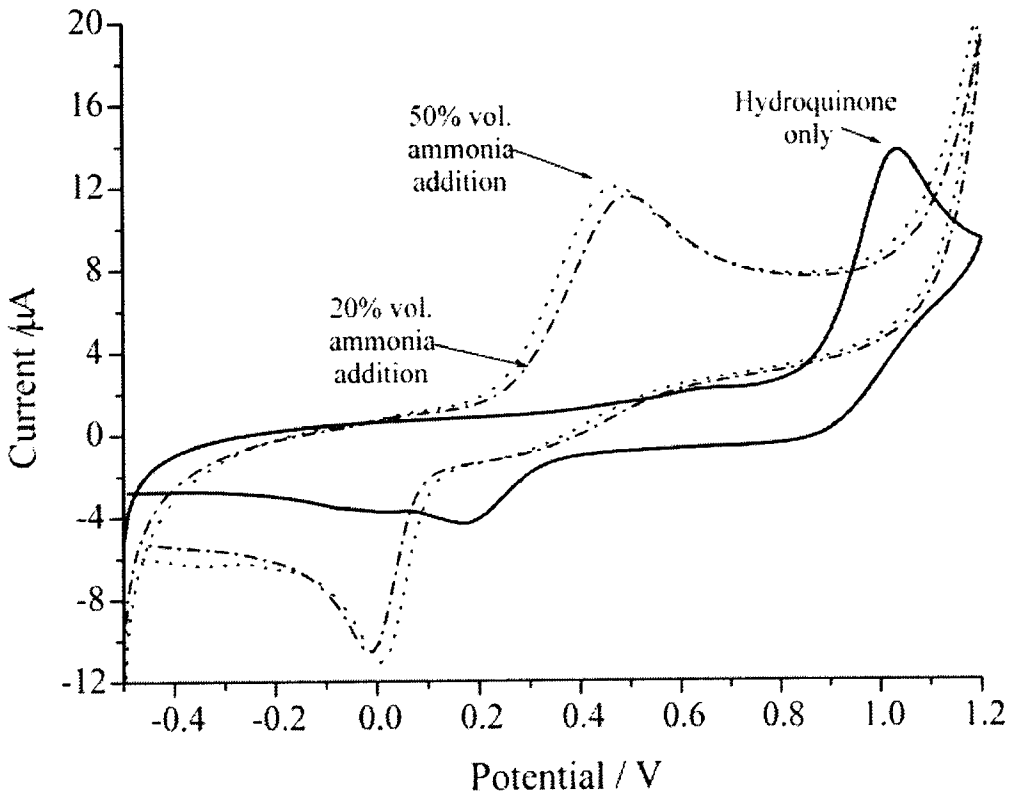


Figure 9.1 (b): The cyclic voltammetric response (GC, 100 mVs^{-1}) of 0.5 mM hydroquinone in DMF (0.1 M TBAP) in the absence and in the presence of 20 % and 50 % vol. ammonia.

9.3.2 Elucidation of the Effect of Ammonia on the Voltammetric Response of Hydroquinone

In order to elucidate the mechanism for the effect of ammonia on the oxidation of hydroquinone, 10 % vol. ammonia was bubbled into a solution containing 0.5 mM

hydroquinone for 2, 4 and 6 seconds and the response of hydroquinone was again investigated by means of cyclic voltammetry (figure 9.2).

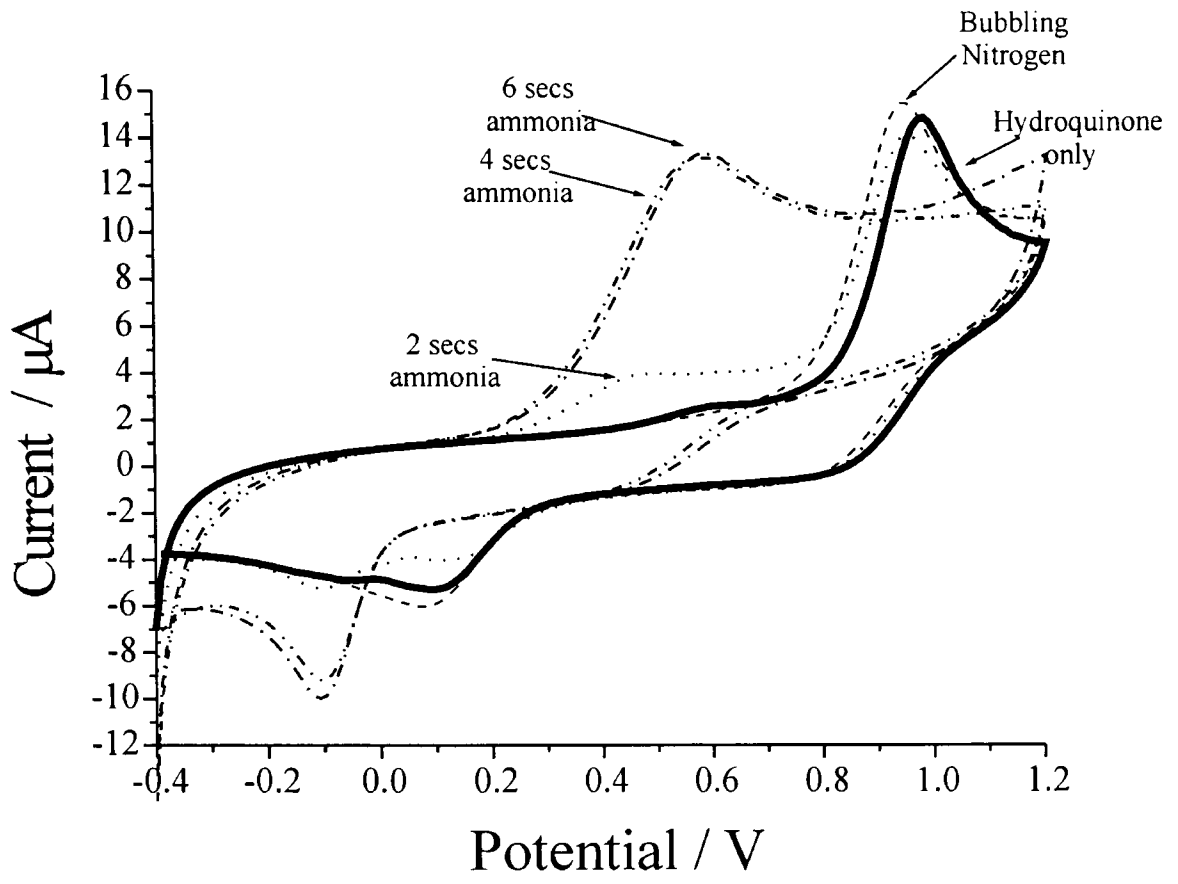


Figure 9.2: The cyclic voltammetric responses (GC, 100 mV s^{-1}) of 0.5 mM hydroquinone to increasing bubbling time (2, 4, and 6 seconds) from a 10 % vol. ammonia cylinder in DMF (0.1 M TBAP).

In this case, it can be seen that after two seconds of ammonia bubbling, a broad oxidative wave is observed at +0.50 V, while the magnitude of the main oxidative peak attributed to the oxidation of protonated hydroquinone (+0.98 V) has decreased slightly. On the reversal of the scan, the reductive peak at +0.10 V decreases in magnitude and a new reductive peak appears at more reducing potential (-0.10 V). Upon addition of more ammonia (4 seconds), the pre-wave at +0.50 V increases while the oxidative peak at +0.98 V decreases. After six seconds bubbling time, the voltammogram is characterised by a single oxidative wave at +0.58 V and a corresponding single reductive wave at -0.10 V.

This behaviour can be explained as follows: ammonia acts as a proton acceptor, drawing off protons from the hydroquinone molecules to form the more energetically favourable ammonium ions. This is the hydroquinone deprotonation reaction as expressed by equation (9.3, C) below:

$$QH_2 + 2NH_3 \rightleftharpoons 2NH_4^+ + Q^{2-} \qquad (9.3, C)$$

$$Q^{2-} \rightleftharpoons Q + 2e^- \qquad (9.4, E)$$

As this takes place, the concentration of deprotonated hydroquinone Q^{2-} increases and with it, the oxidative wave at +0.50 V. At sufficiently low ammonia concentration, only a fraction of the hydroquinone molecules will be deprotonated and so the resulting voltammogram shows 2 oxidative waves at +0.50 V and at +0.98 V corresponding to the oxidation of the deprotonated hydroquinone Q^{2-} and the protonated hydroquinone QH_2, respectively. However, at sufficiently high ammonia concentration (i.e, when ammonia is present in at least a 2:1 stoichiometric ratio to hydroquinone) all of the acidic protons of the hydroquinone molecules are removed. Therefore only a single oxidative wave is observed at +0.58 V which is attributed to the oxidation of Q^{2-}. This conclusion is further supported by the shape of the wave at +0.58 V which was found to be less sharp as compared to the original oxidative peak at +0.98V. This is consistent with the diffusing species now being the doubly charged dianion Q^{2-} which is expected to have a lower diffusion coefficient than the protonated hydroquinone QH_2 species.

9.3.3 Reversibility of the Response of Hydroquinone to Ammonia in DMF

According to equation (9.3, C) the deprotonation of the hydroquinone species in the aprotic solvent DMF is expected to be reversible under the admittance or removal of ammonia. In order to illustrate this effect, nitrogen was bubbled into the cell after completion of the experiment described above so as to remove any ammonia present in the solution and a cyclic voltammogram was recorded (overlaid in figure 9.2). The addition of nitrogen causes ammonium to decompose into NH_3 (which volatilises) and protons, which can add to the deprotonated hydroquinone molecules and thus restore the original form, QH_2. As it can be seen from figure 9.2, the voltammogram obtained

after addition of nitrogen to the solution is overlaid to that obtained prior the addition of ammonia showing that reversible ammonia effect on hydroquinone occurs. The reversibility of the deprotonation reaction encourages the possibility of the development of an hydroquinone based-sensor which can be regenerated by removal of ammonia from the solution and it is this to which we turn to next.

9.3.4 Analytical Utility

The voltammetric responses of 0.5 mM hydroquinone in DMF (0.1 M TBAP) in the absence of ammonia and after the DMF solution was saturated with 10, 32 and 95 ppm ammonia were recorded at a glassy carbon electrode by means of cyclic voltammetry and are shown in figure 9.3. In agreement with the observations discussed in section 9.3.1, in the absence of ammonia, the anodic oxidation of hydroquinone leads to the corresponding two-electron oxidation form of benzoquinone and exhibits a single oxidative wave at +0.98 V and a corresponding single reductive wave at +0.10 V. Upon addition of ammonia to the hydroquinone solution, a new wave emerges at +0.50 V and increases with ammonia concentration. This can be attributed to the oxidation of the deprotonated hydroquinone, Q^{2-} (equations (9.3) and (9.4)). The reductive wave initially observed at +0.10 V decreases with ammonia concentration, while a new reductive wave at -0.19 V emerges.

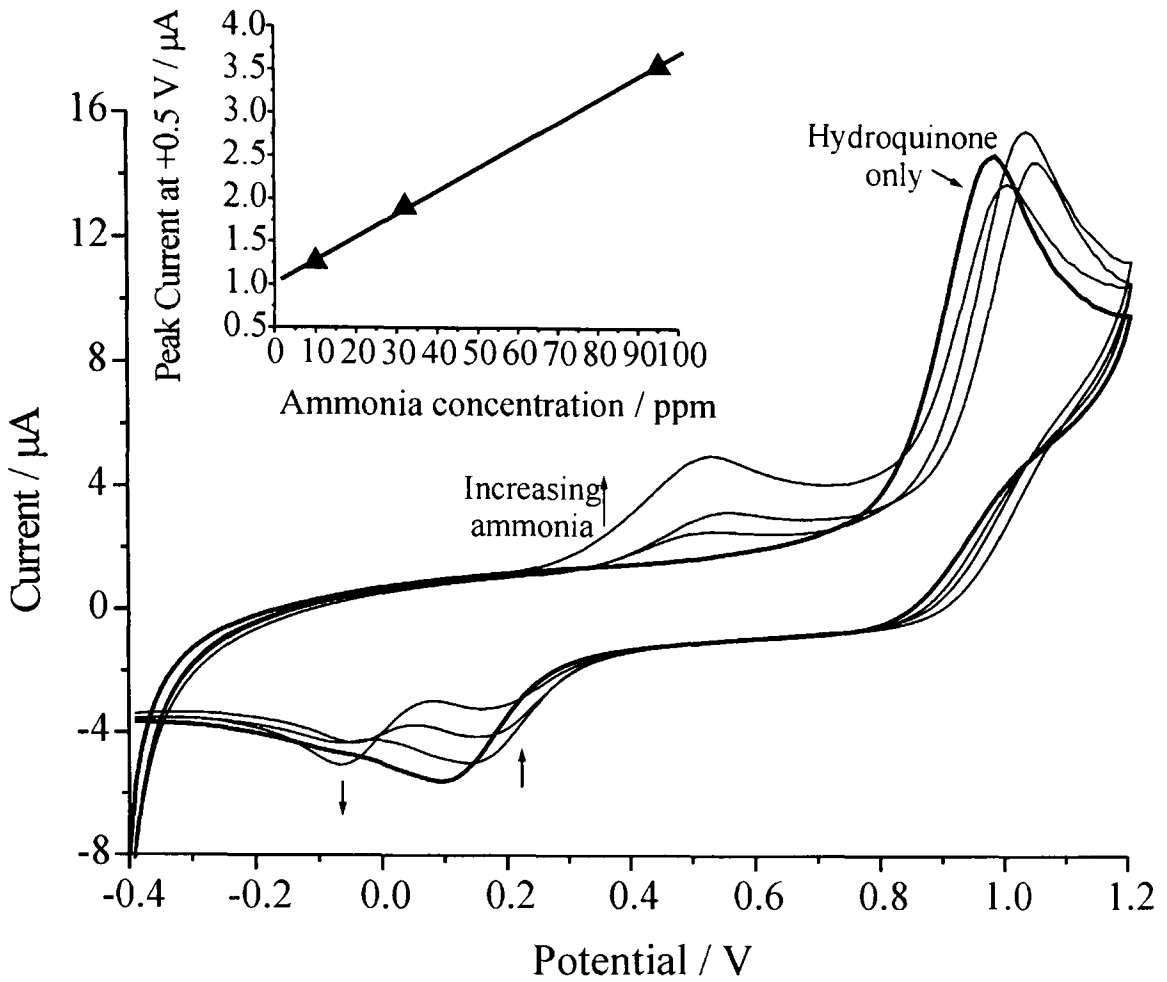


Figure 9.3: The cyclic voltammetric responses (GC, 100 mV s^{-1}) of 0.5 mM hydroquinone to increasing ammonia concentration (10, 32 and 95 ppm) in DMF (0.1 M TBAP). Insert graph: a plot of the anodic peak current at +0.50 V against concentration of ammonia / ppm.

Analysis of the increase of the oxidative wave at +0.50 V by means of a standard addition plot of peak current against concentration of ammonia (insert graph figure 9.3) revealed a linear response over the concentration range studied (sensitivity = 2.68 x 10^{-8} A ppm^{-1} and r^2= 0.995) and produced a limit of detection (based on $3s_b$) of 4.2 ppm ammonia, thereby demonstrating the analytical utility of the approach.

The response of hydroquinone was demonstrated to be reversible upon exposure to nitrogen for 15 minutes indicating the sensitive and reversible sensing properties of this method. In addition to cyclic voltammetry, square wave voltammetry was carried out. Although a similar qualitative response was observed, this technique did not offer further benefit as compared to CV.

9.3.5 Interference Studies

The effect of the presence of oxygen and trace amount of water on the analytical signal for ammonia sensing was next examined.

Initially oxygen was bubbled from a 100 % vol. cylinder for increasing times (5 - 30 minutes) into a DMF solution containing 0.5 mM hydroquinone. Cyclic voltammograms recorded (not shown) reveal that both the oxidative and the reductive peak potentials of hydroquinone are shifted as the oxygen concentration in solution increases. However, the resulting peak-to-peak separation is analogous to that observed in the absence of oxygen, suggesting a shift in the platinum pseudo-reference electrode is occurring. This was confirmed by monitoring the shift in the potential of the ferrocene/ferrocenium redox couple. It was found that both the hydroquinone and ferrocenium redox waves were shifted by similar potentials both in the presence and absence of oxygen, confirming a shift in the pseudo-reference electrode.

Next, the effect of a DMF solution containing 1 % vol. water on the analytical sensor was examined. The corresponding cyclic voltammogram of a solution containing 0.5 mM hydroquinone in the presence of 1 % water is compared to that obtained in pure DMF in figure 9.4 (a).

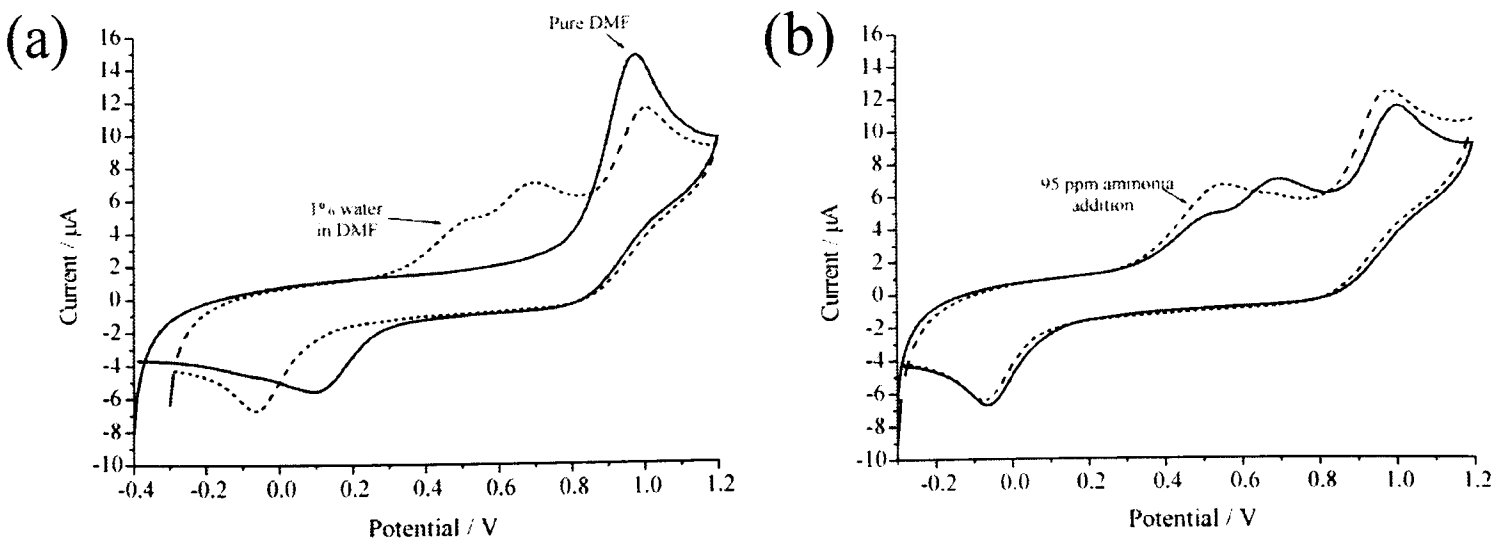


Figure 9.4: (a) The cyclic voltammetric responses (GC, 100 mV s^{-1}) of 0.5 mM hydroquinone in pure DMF (0.1 M TBAP) and when 1 % water is present in the DMF solution; (b) The cyclic voltammetric responses (GC, 100 mV s^{-1}) of 0.5 mM hydroquinone in a solution of 1 % water in DMF (0.1 M TBAP) in the absence and in the presence of 95 ppm ammonia (see text).

It can be seen that in the presence of water, three anodic waves at +0.41 V, +0.65 V and at +1.00 V are observed along with a single cathodic wave at -0.07 V showing that water facilitates the oxidation of hydroquinone. The stabilisation effect by proton transfer and the resulting dramatic change on the response of hydroquinone is not surprising considering the basic nature of water in the proton-deficient media DMF and the sensitivity of the oxidation of hydroquinone to protons (equation (9.1)). The ability of water to further stabilise both the mono-deprotonated anion (QH^-) and the dianion (Q^{2-}) by hydrogen bonding may account for the resulting more complex voltammogram obtained in the presence of water as compared to that obtained when ammonia is present. Hence, the new wave observed at +0.65 V can tentatively be attributed to the oxidation of QH^-, while the waves at +0.41 V and at +1.00 V correspond to the oxidation of Q^{2-} and QH_2, respectively.

The influence of water on the sensing signal of ammonia (i.e., the oxidative wave at +0.5 V) was also investigated. Figure 9.4 (b) shows the response of 0.5 mM hydroquinone in a DMF solution containing 1 % water in the presence and absence of 95 ppm ammonia. This shows that when ammonia is present at a 95 ppm concentration, the water interference does not suppress the ammonia signal (i.e, the wave at +0.5 V). However, masking of the sensor signal might be expected when ammonia is present in lower concentration, thereby compromising the feasibility of analytical application of this method.

The sensitivity of the ammonia sensor to humidity might however be overcome by the use of a gas-membrane such as PTFE that excludes the access of water to the test solutions. The use of the membrane should also remove any potential interferences from bases or redox species present in the matrix sample which may be electroactive in the potential window of investigation. While a membrane may minimise certain

complications, addition of such material to the system could also result in signal interference and increase in production cost.

Room temperature ionic liquids offer a promising alternative to conventional aprotic solvents and can reduce the extent of water contamination as the hydrophobicity of the salt can be controlled by careful selection of the anion. Therefore, we chose to employ the ionic liquid [EMIM][$N(Tf)_2$] for the investigation of the hydroquinone/ammonia system given the reported hydrophobic nature of the bis(trifluoromethylsulfonyl)imide anion [20].

9.3.6 Voltammetric Response of Hydroquinone in the Ionic Liquid [EMIM][$N(Tf)_2$] in the Absence and in the Presence of Ammonia

The electrochemical response of 0.4 M and 1.8 M hydroquinone in the ionic liquid [EMIM][$N(Tf)_2$] was first characterised at glassy carbon microdisk electrode (5 μm diameter) using cyclic voltammetry. The corresponding responses at various scan rates (0.1 to 1 V s^{-1}) for the two concentrations studied are depicted in figures 9.5 (a) and 9.5 (b), respectively.

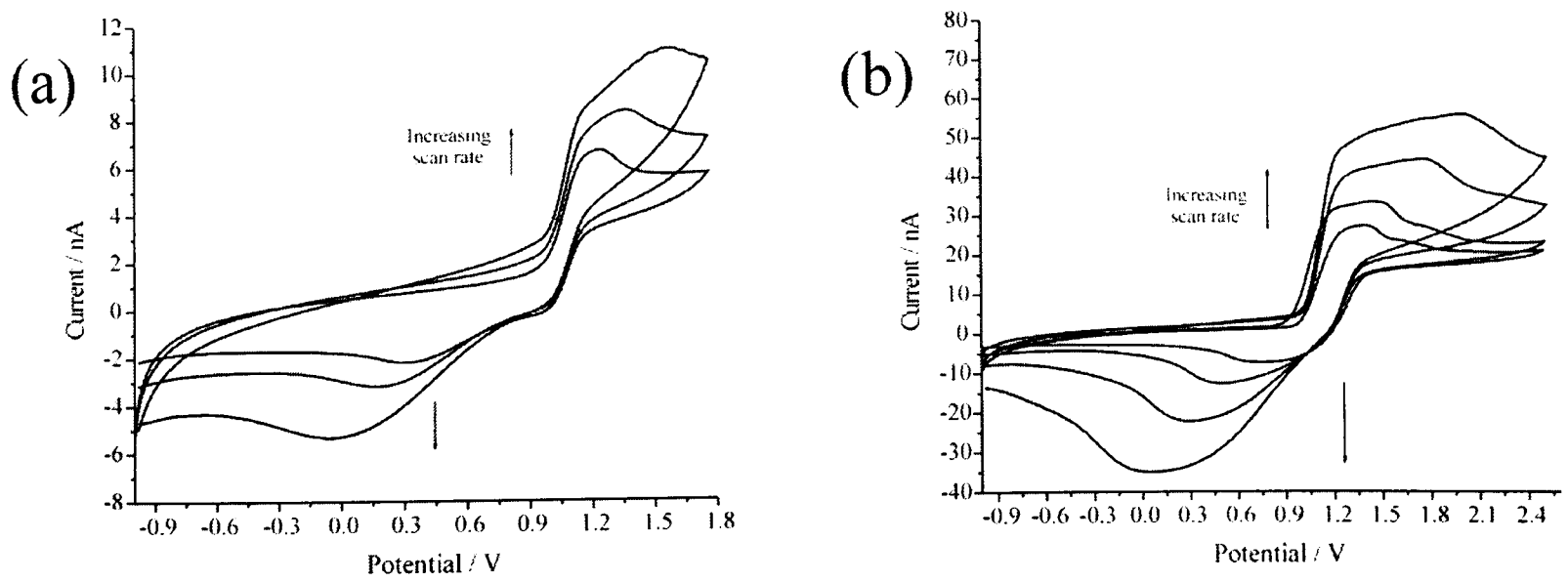


Figure 9.5: Cyclic voltammograms corresponding to the oxidation of: (a) 0.4 M and (b) 1.8 M hydroquinone in [EMIM][$N(Tf)_2$] to increasing scan rates at a 5 μm diameter glassy carbon electrode. The scan rates employed were (a) 0.1, 0.2 and 0.5 V s^{-1} and (b) 0.1, 0.2, 0.5 and 1 V s^{-1}.

The voltammogram obtained at 0.1 V s^{-1} for the 0.4 M hydroquinone sample, figure 9.5 (a), shows an oxidative peak at +1.22 V (*vs.* Pt) and a corresponding reductive peak at +0.34 V (*vs.* Pt), producing a peak to peak separation of 0.88 V, which is in good agreement with the observations in DMF. At higher scan rates, however, the shape of both the oxidative and the reductive peak is less defined and can be tentatively attributed to the higher viscosity of the ionic liquid, slowing the diffusion of the hydroquinone species to the electrode surface. All further voltammograms were recorded at 0.1 V s^{-1}.

Figure 9.6 (b) shows the voltammetric response (0.1 V s^{-1}) of 0.4 M hydroquinone when ammonia was bubbled into the sample from a 50 % vol. cylinder for 5 and 15 minute.

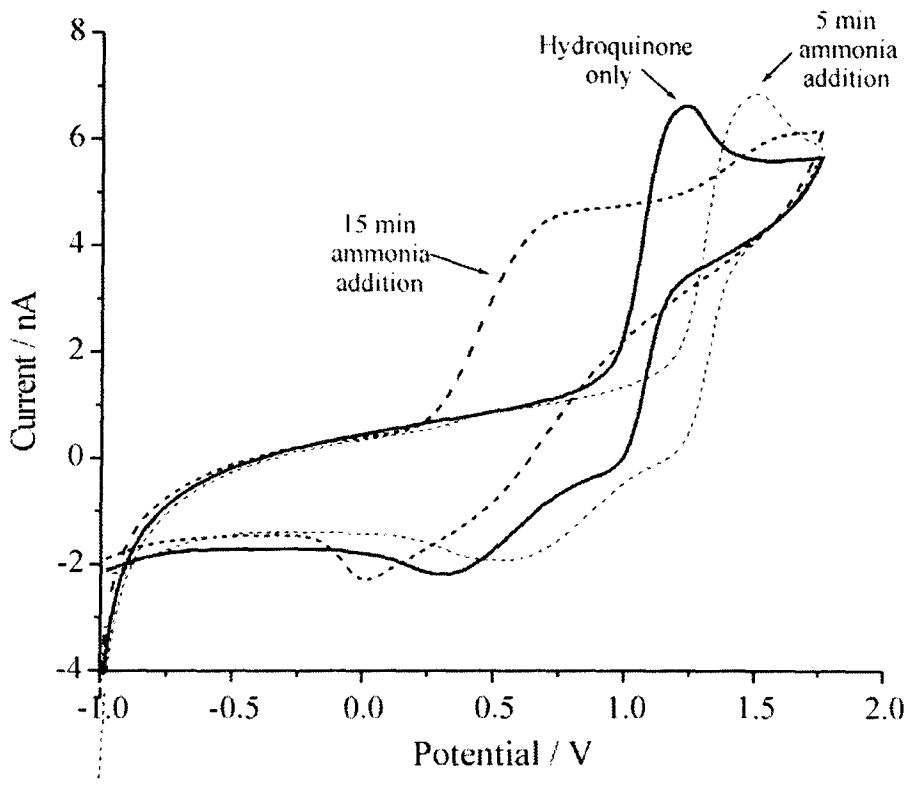


Figure 9.6: Cyclic voltammograms corresponding to the oxidation of 0.4 M hydroquinone in [EMIM][$N(Tf)_2$] when 50 % vol. ammonia was bubbled into the sample for 5 and 15 minutes.

In contrast with the observation in DMF, after ammonia was bubbled for 5 minutes, the peak potential of hydroquinone was shifted in the positive direction. However, after 15 minutes bubbling of ammonia, the oxidative peak potential is shifted to the negative direction by 0.7 V. This is in agreement with the findings in DMF and consistent with proton transfer from the hydroquinone molecules to NH_3, yielding the

dianion Q^{2-} which is then oxidised at the electrode surface at a less positive potential. A voltammogram (not shown) of the ionic liquid sample [EMIM][$N(Tf)_2$] saturated with 50 % vol. ammonia was also recorded. This reveals that direct oxidation of ammonia at the GC microdisk electrode occurs at + 2.0 V, showing that ammonia is not electrochemically active in the potential region of interest.

The initial shift in the positive direction suggests the acid-base equilibrium between hydroquinone and ammonia is sluggish in the ionic liquid as compared to the less viscous solvent DMF. This is not surprising considering that solvent effect can play a major role in the nature of solvation for both the dianion Q^{2-} and the ammonium cations NH_4^+. In the ionic liquid, the newly generated charges of the ammonium ions NH_4^+ and the divalent hydroquinone anion Q^{2-} have to redistribute throughout the highly viscous liquid. Additional binding of some Q^{2-} and NH_4^+ ions may take place, which may be responsible for the initially sluggish response. However, once equilibration is achieved, ammonia is found to affect the peak oxidation of hydroquinone in a similar fashion to that observed in DMF and expressed by equation (9.3).

The difference in magnitude of the potential shift (0.7 V in [EMIM][$N(Tf)_2$] and 0.6 V in DMF) can provide meaningful evidence for judging the extent of the contribution of the solvent to the ion pair interaction. A closer look at the shape of oxidative wave at +0.50 V reveals a far less sharp peak as compared to the oxidative wave of the protonated hydroquinone wave at +1.22 V, consistent with the diffusing species now being the doubly charged hydroquinone anion Q^{2-}, which has a lower diffusion coefficient. This effect was noted in DMF but it is shown to a greater extent in the more viscous ionic liquid medium.

Overall, these results corroborate the interpretation of the effect of ammonia on the oxidation of hydroquinone as described in the Section 9.3.2.

Figure 9.7 (a) shows the voltammograms corresponding to the oxidation of 0.4 M hydroquinone in [EMIM][$N(Tf)_2$] when 10 % vol. ammonia was bubbled into the sample for 5, 15, 30 and 45 minutes. The voltammetric responses obtained after 5 and 15 minutes are analogous to one another and show a single oxidative wave shifted at more positive potential (+1.40 V) as compared to the oxidative wave of hydroquinone in the absence of ammonia (+1.20 V). However, after 30 minutes of ammonia bubbling, a pre-wave at +0.50 V is observed, while the oxidative wave at +1.4 V decreases in magnitude. When the sample of ionic liquid is saturated with the 10 % vol. ammonia, the voltammogram exhibits a single broad oxidative wave at +0.50 V. Square wave voltammetry was carried out on the same sample (figure 9.7 (b)) and shows a wave at +0.48 V and a small oxidative wave at +1.3 V, suggesting that when the hydroquinone sample is saturated with 10 % vol. ammonia there is still a small amount of hydroquinone which is not deprotonated by ammonia and hence undergoes oxidation at +1.3 V.

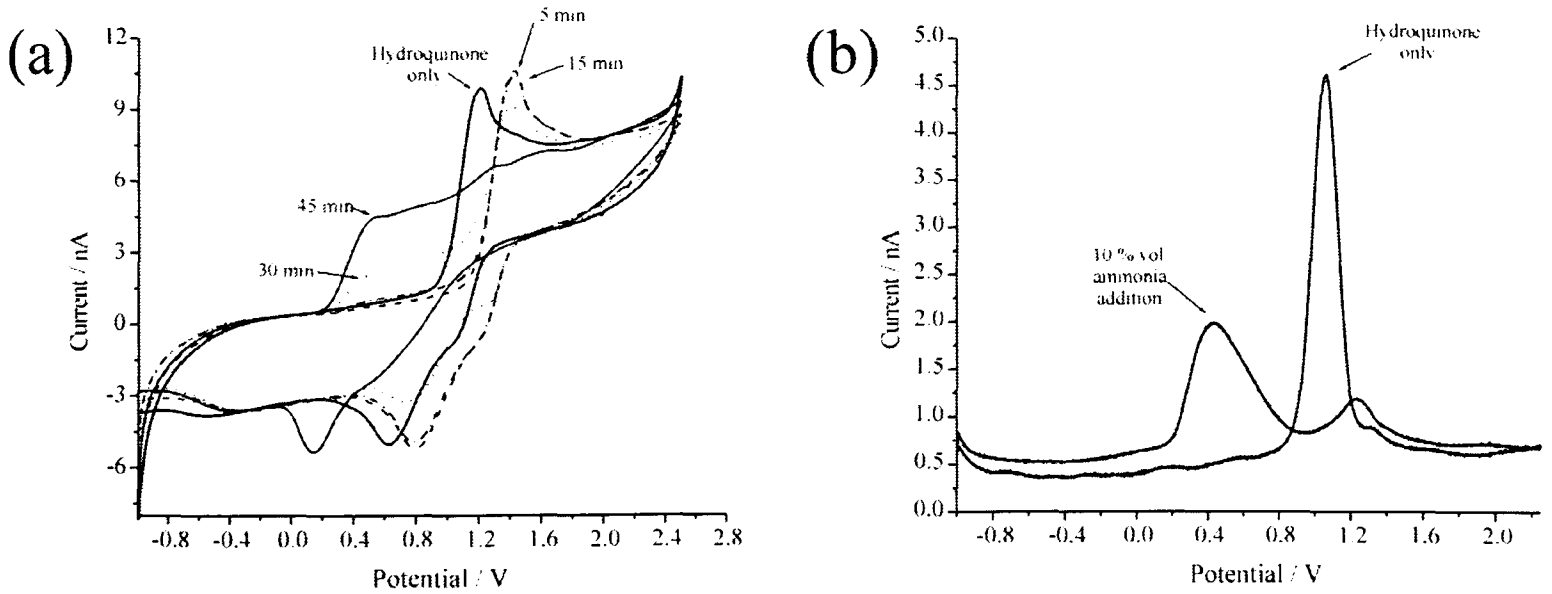


Figure 9.7: (a) Cyclic voltammograms corresponding to the oxidation of 0.4 M hydroquinone in [EMIM][$N(Tf)_2$] when 10 % vol. ammonia was bubbled into the sample for 5, 15, 30 and 45 minutes. (b) The square wave voltammograms corresponding to the oxidation of 0.4 M hydroquinone in [EMIM][$N(Tf)_2$] when the sample was saturated with 10 % vol. ammonia.

In order to provide further evidence, 10 % vol. ammonia was bubbled into an ionic liquid sample containing a higher concentration of hydroquinone (1.8 M). The corresponding voltammograms are detailed in figure 9.8. The increase in

hydroquinone concentration allows for clear observation of both a pre-wave (+0.40 V) due to oxidation of the deprotonated hydroquinone and a second wave (+1.30 V), owing to the oxidation of hydroquinone which has not been deprotonated by ammonia because of the stoichiometric deficiency.

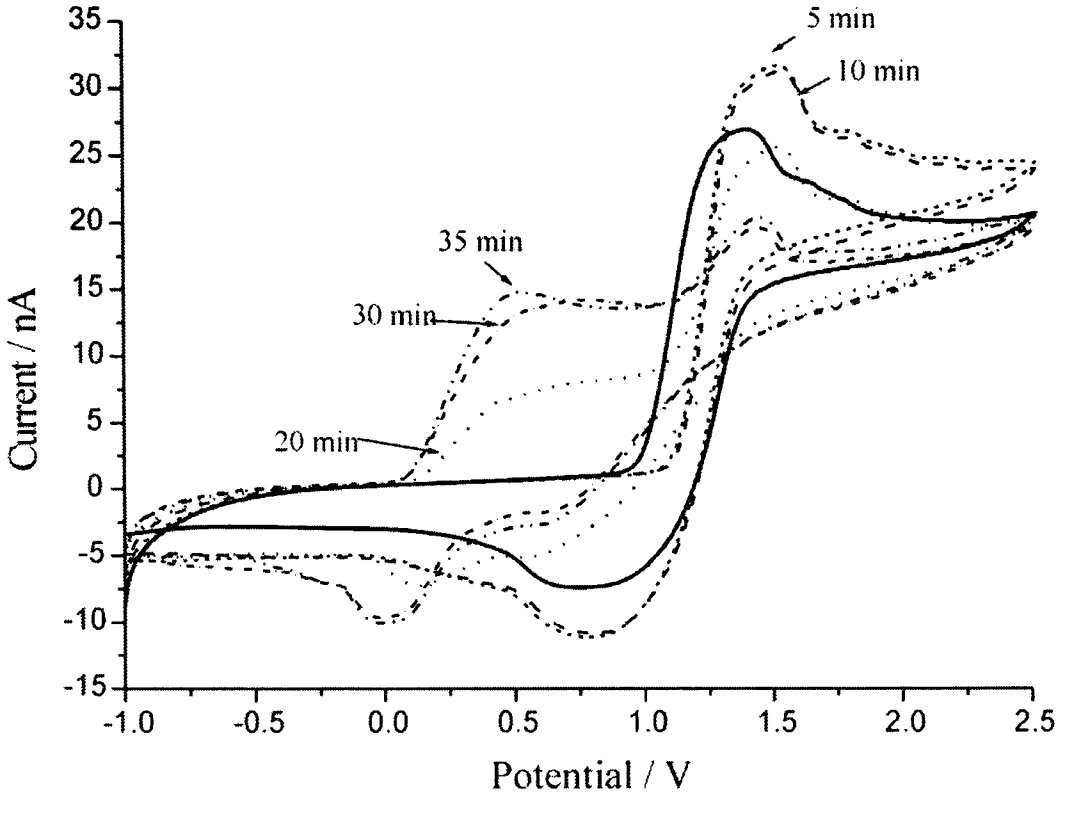


Figure 9.8: Cyclic voltammograms corresponding to the oxidation of 1.8 M hydroquinone in [EMIM][$N(Tf)_2$] when 10 % vol. ammonia was bubbled into the sample for 5, 15, 30 and 45 minutes.

9.4 Conclusion

The above results detail the effect of ammonia on the electrochemical oxidation of hydroquinone in aprotic solvents. It is shown that in the presence of ammonia a new wave at a less oxidising potential emerges and can be attributed to the basic ammonia removing protons from the hydroquinone species, thereby making the oxidation process easier. The voltammetric response has been examined both in DMF and in the ionic liquid 1-ethyl-3-methylimidazolium bis(trifluormethylsulfonyl)imide, [EMIM][$N(Tf)_2$], with analogous responses observed, thereby confirming the proposed reaction pathway. However, reversibility of the interaction between ammonia and hydroquinone was only observed in the less viscous solvent, DMF. Furthermore, the analytical utility of the system has been assessed by measuring the peak current of the pre-wave as a function of ammonia concentration in DMF with a linear range found

for ammonia detection from 10 to 95 ppm and an achievable detection limit of 4.2 ppm.

9.5 Chapter 9 References

[1] D. Giovanelli, M. Buzzeo, C. Hardacre, K. R. Seddon, R. G. Compton, *Talanta* **2004**, *62*, 904.
[2] N. N. Greenwood, A. Earnshaw, *Chemistry of the Elements*, 2nd Ed., Butterworth Heinemann, Oxford, **1997**.
[3] M. Van Son, R. C. Schothorst, G. Den Boef, *Anal. Chim. Acta* **1983**, *153*, 271.
[4] K. N. Andrew, P. J. Worsfold, M. Comber, *Anal. Chim. Acta* **1995**, *314*, 33.
[5] M. E. Meyerhoff, Y. M. Fraticelli, *Anal. Letters* **1981**, *14*, 415.
[6] R. W. Cattrall, *Chemical Sensors*, Oxford University Press, Oxford, **1997**.
[7] S. Alegret, J. Alonso, J. Bartroli, M. Del Valle, N. Jaffrezic-Renault, Y. Duvault-Herrera, *Anal. Chim. Acta* **1990**, *231*, 53.
[8] C.-Y. Shen, C.-P. Huang, H.-C. Chuo, *Sens. Actuators B.* **2002**, *B84*, 231.
[9] Q. Y. Cai, M. K. Jain, C. A. Grimes, *Sens. Actuators B.* **2001**, *B77*, 614.
[10] B. Ostrick, R. Pohle, M. Fleischer, H. Meixner, *Sens. Actuators B* **2000**, *B68*, 234.
[11] A. Setkus, A. Galdikas, A. Mironas, I. Simkiene, I. Ancutiene, V. Janickis, S. Kaciulis, G. Mattogno, G. M. Ingo, *Thin Solid Films* **2001**, *391*, 275.
[12] M. Trojanowicz, A. Lewenstam, T. Krawczynski Vel Krawczyk, I. Lahdesmaki, W. Szczepek, *Electroanalysis* **1996**, *8*, 233.
[13] I. Lahdesmaki, A. Lewenstam, A. Ivaska, *Talanta* **1996**, *43*, 125.
[14] W. W. Kubiak, J. Wang, *Anal. Chim. Acta* **1996**, *329*, 181.
[15] I. Lahdesmaki, W. W. Kubiak, A. Lewenstam, A. Ivaska, *Talanta* **2000**, *52*, 269.
[16] J. Q. Chambers, in *The Chemistry of the Quinonoid Compounds* (Eds: S. Patai, Z. Rappoport), John Wiley & Sons, Chichester **1988**, pp. 719-757.
[17] J. Kim, T. D. Chung, H. Kim, *J. Electroanal. Chem.* **2001**, *499*, 78.
[18] M. Buzzeo, R. G. Evans, R. G. Compton, *ChemPhysChem* **2004**, *5*, 1.
[19] P. Wasserscheid, T. Welton, *Ionic Liquids in Synthesis*, Wiley-VCH, Weinheim, **2003**.
[20] P. Bonhote, A.-P. Dias, N. Papageorgiou, K. Kalyanasundaram, M. Graetzel, *Inorg. Chem.* **1996**, *35*, 1168.
[21] J. Sun, M. Forsyth, D. R. MacFarlane, *J. Phys. Chem. B.* **1998**, *102*, 8858.
[22] J. Dupont, F. de Souza Roberto, A. Z. Suarez Paulo, *Chem. Rev.* **2002**, *102*, 3667.
[23] A. J. Carmichael, C. Hardacre, J. D. Holbrey, M. Nieuwenhuyzen, K. R. Seddon, *Anal. Chem.* **1999**, *71*, 4572.
[24] J. Dupont, P. A. Z. Suarez, R. F. De Souza, R. A. Burrow, J.-P. Kintzinger, *Chem. Eur. J.* **2000**, *6*, 2377.
[25] P. Wasserscheid, W. Keim, *Angew. Chemie, Int. Ed.* **2000**, *39*, 3772.
[26] M. C. Buzzeo, O. V. Klymenko, J. D. Wadhawan, C. Hardacre, K. R. Seddon, R. G. Compton, *J. Phys. Chem. A* **2003**, *107*, 8872.
[27] B. R. Eggins, *Chem. Comm.* **1969**, *21*, 1267.
[28] B. R. Eggins, J. Q. Chambers, *Chem. Comm.* **1969**, *5*, 232.
[29] B. R. Eggins, J. Q. Chambers, *J. Electrochem. Soc.* **1970**, *117*, 186.

Chapter 10: "Elucidation of the Electrochemical Oxidation Pathway of Ammonia in N,N-Dimethylformamide and in the Room Temperature Ionic Liquid, 1-Ethyl-3-methylimidazolium bis(trifluoromethylsulfonyl)imide and Application to Ammonia Sensing"

This chapter examines the direct electrochemical oxidation of ammonia in both the organic solvent N,N-dimethylformamide, DMF, and the room temperature ionic liquid 1-ethyl-3-methylimidazolium bis(trifluoromethylsulfonyl)imide [EMIM][$N(Tf)_2$] in view of its potential application for the detection of ammonia. The results discussed below have been published in Electroanalysis [1].

10.1 Introduction

The electrochemical oxidation of ammonia in alkaline solutions has been the subject of continuous investigations [2-12] and as a result, several protocols based on its determination via its direct oxidation have been developed [11,12]. Advances have been made in the development of amperometric sensors [11] and selected catalytic oxidation of ammonia to nitrogen has recently been explored as a possible method to reduce ammonia waste [13]. However, to our knowledge, very few studies have been reported in non-aqueous systems [14] and the analytical significance of the oxidation of ammonia has never been examined. The research presented in this chapter therefore examines the electrochemical oxidation of ammonia in N,N-dimethylformamide, DMF, and the room temperature ionic liquid, 1-ethyl-3-methylimidazolium bis(trifluoromethylsulfonyl)imide, [EMIM][$N(Tf)_2$].

The employment of non-aqueous solvents for electrochemical investigation offers several advantages. Traditionally aprotic polar organic solvents, such as DMF or dimethylsulfoxide, DMSO, have been utilised for electrochemical studies due to their wide potential window and great solubility of many organic species as compared to aqueous media. The use of these solvents has therefore provided a means of studying electrochemical reaction processes which would either be inhibited or not observed in aqueous media. Recently, however, room temperature ionic liquids (RTILs) have been employed as an alternative to such traditional organic solvents.

Room temperature ionic liquids offer an attractive alternate to conventional solvents and have shown to be versatile in their application. As already discussed in the previous chapter, their characteristically negligible vapour pressure, high thermal stability, good conductivity and wide potential window make them desirable solvents for the electrochemical investigation of a variety of electroactive species [15,16]. There have been few reports, however, on the dissolution and detection of gases in

ionic liquids [17-21]. The one-electron reduction of oxygen was first reported by Carter *et al.* [17] in the room temperature imidazolium chloride-aluminium chloride molten salts, although the generated superoxide species proved to be highly unstable in that medium. The electrochemical generation of superoxide has since been studied by cyclic voltammetry in 1-*n*-butyl-3-methylimidazolium hexafluorophosphate, ([BMIM][PF_6]) [18] hexyltriethylammonium bis(trifluoromethylsulfonyl)imide, [N_{6222}][$N(Tf)_2$] and [EMIM][$N(Tf)_2$] [21]. Reduction of oxygen in the presence of carbon dioxide has also been investigated in [BMIM][PF_6] [19]. More recently, an electrochemical sensor which comprises an ionic liquid as the electrolyte has been reported to detect sulfur dioxide gas at ppm concentration levels [20]. RTILs have shown to be an advantageous medium for the detection of gases with promising potential for application in sensor design.

In this chapter, we report the first study of the electrochemical oxidation of ammonia in DMF and [EMIM][$N(Tf)_2$] and the subsequent elucidation of the reaction pathway.

10.2 Experimental

All experiments were carried out using the experimental set-up and the conditions already detailed in the experimental section of Chapter 9.

For those experiments done with NH_4PF_6 in the ionic liquid, a 20 μL aliquot of a prepared 1 M NH_4PF_6/MeCN solution was added to a 40 μL sample of ionic liquid. The solution was placed under vacuum for sixty minutes to allow for evaporation of MeCN and equilibrium of the salt with the ionic liquid.

10.3 Results and Discussion

10.3.1 Voltammetric Response of Ammonia in DMF

10.3.1.2 Oxidation of ammonia in DMF at different electrode substrates

The electrochemical oxidation of ammonia in DMF in 0.1 M TBAP was first investigated at a platinum macroelectrode, using cyclic voltammetry. Figure 10.1 shows the cyclic voltammetric (100 mV s^{-1}) responses obtained at a platinum macroelectrode to increasing bubbling time (5 to 25 minutes) from a 100 % vol. ammonia cylinder in DMF (0.1M TBAP).

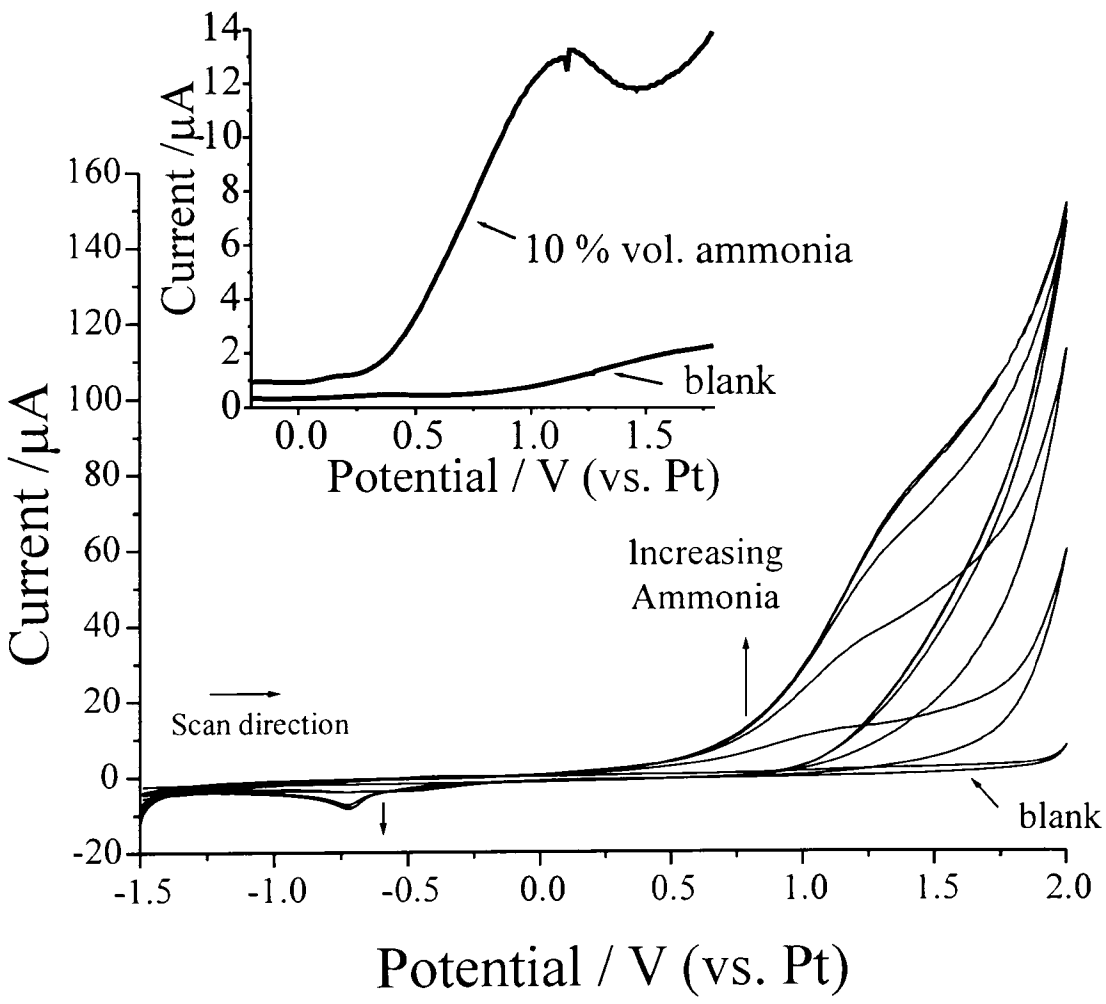


Figure 10.1: The cyclic voltammetric responses (100 mV s^{-1}) obtained at a platinum macroelectrode (1 mm diameter) to increasing bubbling time (5, 10, 15, 20 and 25 minutes) from a 100 % vol. ammonia cylinder in DMF (0.1 M TBAP). Insert graph: square wave voltammetric responses of a DMF solution saturated with 10 % vol. ammonia obtained at a platinum macroelectrode (1 mm diameter). Also overlaid are the corresponding responses of DMF in the absence of ammonia.

A blank cyclic voltammogram was also recorded prior to the addition of ammonia to examine the electrode response and the stability of DMF within the potential window of study (-1.50 V, +2.00 V *vs.* Pt) and the corresponding voltammogram is overlaid in figure 10.1. This reveals no significant voltammetric processes are observed in the

potential window investigated. Upon the introduction of ammonia to the DMF solution an increase in the anodic current at +1.10 V (*vs.* Pt) was observed and can be attributed to the direct oxidation of ammonia at the electrode surface. It was found that the anodic current at +1.10 V (*vs.* Pt) increases linearly as the ammonia concentration increases. The response obtained for a 25 minutes bubbling time is almost identical to the one obtained for 20 minutes bubbling (figure 10.1) showing that a current plateau is reached after 25 minutes. This suggests that saturation of the DMF solution with ammonia is achieved after 30 minutes bubbling. Hence all the experiments described here after were carried out in DMF solutions saturated with the specified volume percentage of ammonia by bubbling the gas into the cell for 30 minutes. Examination of the reductive wave after the addition of ammonia to the solution (figure 10.1) reveals the emergence of a new reductive wave at -0.75 V (*vs.* Pt), the significance of which will be discussed in the next section.

In order to verify that the ammonia was undergoing electrochemical oxidation, square wave voltammetry (frequency = 50 Hz, step potential = 3.5 mV, amplitude = 25 mV) was next carried out at the platinum electrode. The corresponding voltammograms recorded in the absence and after the DMF solution was saturated with 10 % vol. ammonia are detailed in the insert graph of figure 10.1. This shows that upon the introduction of ammonia to the solution, an oxidative wave is observed at +1.15 V (*vs.* Pt), consistent with the direct oxidation of ammonia at the electrode surface as observed above for the cyclic voltammetric response.

The investigation of the oxidation of ammonia was next extended to other electrode substrates, namely gold and glassy carbon electrodes. The cyclic voltammograms (not shown) obtained for a DMF solution in which 100 % vol. ammonia was bubbled for 5 minutes showed an oxidative wave at +1.20 V and at +1.60 V (*vs.* Pt) at gold and glassy carbon electrodes, respectively. Upon further addition of ammonia to the

solution, the oxidative wave was seen to begin to merge into solvent breakdown for both electrode substrates, unlike that observed at the platinum electrode.

Analysis of the reduction wave obtained at both electrode substrates reveals that no reductive waves were observed at the glassy carbon electrode, whereas at the gold electrode two reductive processes were observed at -0.10 V and -1.20 V (*vs.* Pt), respectively.

The above results reveal that the oxidation of ammonia in DMF occurs at +1.60 V (*vs.* Pt) at a GC electrode, +1.20 V (*vs.* Pt) at the Au electrode and +1.10 V (*vs.* Pt) at a Pt electrode. The lower (less positive) electrode potential at which the reaction takes place at platinum can be explained considering that, generally, noble transition metals such as platinum have higher adsorption energies for ammonia (hence stronger affinity for ammonia) [22] than coinage metals such as Au [23]. Furthermore, the better defined oxidation wave obtained at a platinum electrode as compared to GC and Au electrodes can be attributed to a change in the degree of adsorption of the starting material (NH_3), ammonia surface intermediates and the products.

These results reveal that platinum exhibits the best activity for the oxidation of ammonia and therefore subsequent studies reported below were carried out exclusively at platinum electrodes.

10.3.1.3 Steady state linear sweep voltammetry for the oxidation of ammonia in DMF at platinum microdisk electrodes

We next turn our attention to the response obtained at platinum microelectrodes under steady state conditions. Figures 10.2 (a) and 10.2 (b) depict the linear sweep voltammograms (10 mV s^{-1}) obtained, at a 25 μm and a 60 μm radius platinum microdisk electrode to increasing concentrations of ammonia (10, 20, 50 and 100 % vol.).

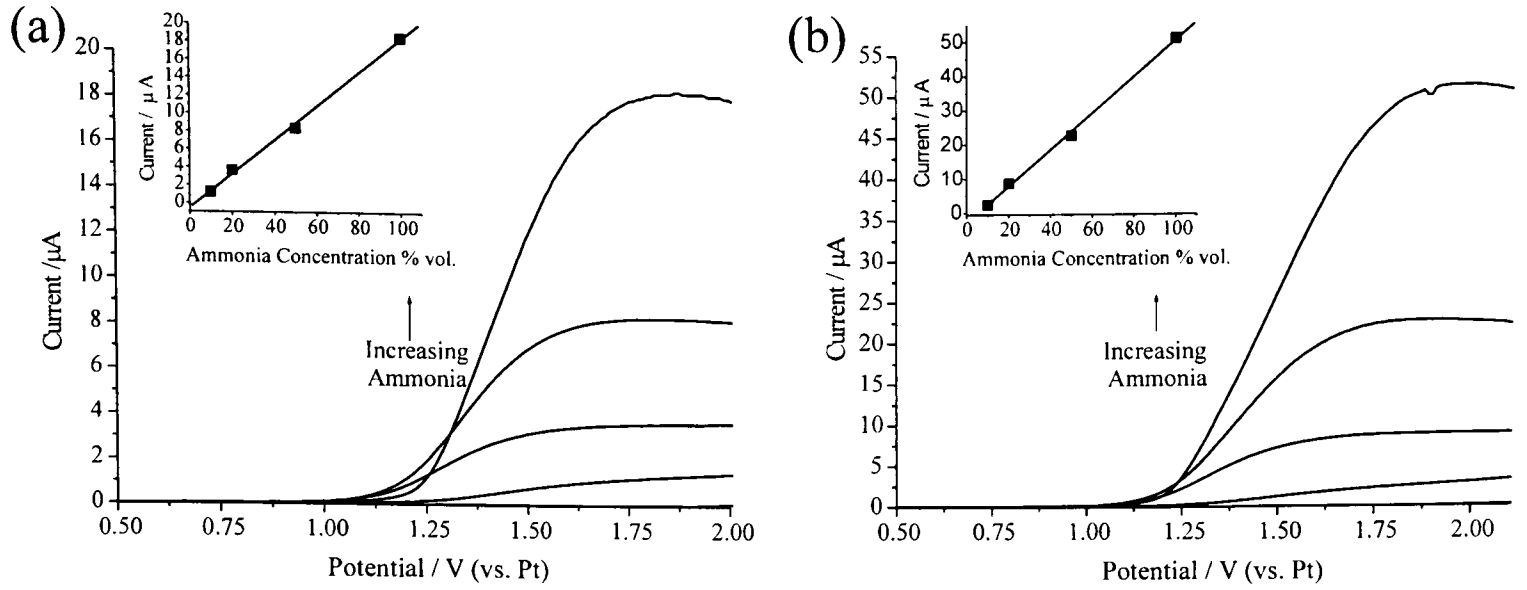


Figure 10.2: The linear sweep voltammetric responses (10 mV s^{-1}) to increasing concentration of ammonia (10, 20, 50 and 100 % vol.) obtained at a: (a) 25 µm (radius) platinum microdisk electrode and (b) 60 µm (radius) platinum microdisk electrode. Insert: a plot of limiting current against % vol. ammonia in DMF.

Analysis of the steady state linear sweep voltammograms reveals that upon the addition of ammonia to the solution an oxidative wave with a half potential of +1.40 V is observed consistent with that seen at macroelectrodes (figure 10.1). It can be seen that upon further additions of ammonia to the solution, the steady state limiting current increases at both microdisk electrodes. Analysis of this enhancement in the limiting current was carried out by means of a standard addition plot of limiting current against concentration of ammonia (see insert graph of figures 10.2 (a) and 10.2 (b)). These plots were found to be linear over the concentration range studied (sensitivity = 4.40×10^{-6} A M^{-1} and $r^2 = 0.997$ at the 25 µm microdisk and sensitivity = 1.24×10^{-5} A M^{-1} and $r^2 = 0.998$ at the 60 µm microdisk). The limit of detection (LOD) was found to be 7.8 % vol. at the 25 µm microdisk electrode and 6.4 % vol. at the 60 µm microdisk electrode [24]. This observed linear response offers some promise that the direct oxidation of ammonia in DMF may be exploited to develop an analytical sensor.

10.3.1.4 Cyclic voltammetry at platinum microdisk electrodes

Figure 10.3 details the cyclic voltammetric responses obtained at various scan rates from 40 V s^{-1} to 174 V s^{-1} at a platinum microdisk electrode (25 μm) when the DMF solution was saturated with 50 % vol. gaseous ammonia.

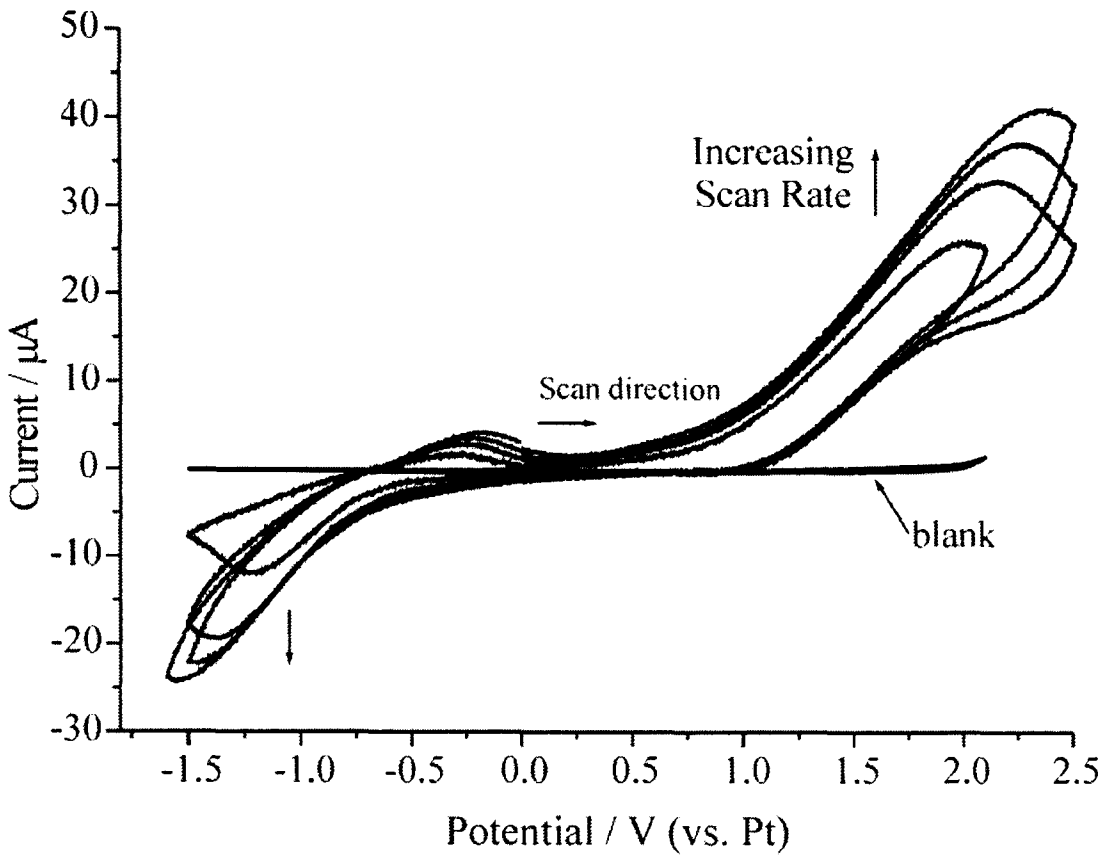


Figure 10.3: The cyclic voltammetric responses of a DMF solution saturated with 50 % vol. ammonia obtained at a 25 μm (radius) platinum microdisk electrode at increasing scan rates (from 40 to 174 V s^{-1}).

The potential was swept from +0.00 V to +2.40 V (*vs.* Pt), then negative to -1.50 V and back to +0.00 V. It can be seen that upon initiation of the voltammetric scan an oxidative wave is observed at +1.80 V (*vs.* Pt) consistent with the voltammetric responses detailed in figures 10.1 and 10.2. Upon reversal of the scan direction, a reductive peak emerges at -1.20 V (*vs.* Pt) with a corresponding oxidative wave at -0.30 V (*vs.* Pt). Analysis of the oxidative peak current at +1.80 V (*vs.* Pt) as a function of scan rate showed that the increase was found to be linear with the square root of scan rate, therefore suggesting a diffusion controlled process. It is worth noting that the oxidative and reductive peaks are shifted somewhat to more positive and

negative potentials, respectively, as the scan rate is increased consistent with the processes showing characteristics of an electrochemically irreversible process.

In order to understand the oxidative reaction process of ammonia, the electrochemical oxidation of ammonia was next studied in the ionic liquid, [EMIM][$N(Tf)_2$]. RTILs have some advantages over the use of DMF as they have a wide potential window, negligible vapour pressure and there is no need to add supporting electrolyte to the solution which may be beneficial in sensing devices.

10.3.2 Voltammetric Response of Ammonia in [EMIM][$N(Tf)_2$]

10.3.2.1 Oxidation of ammonia in [EMIM][$N(Tf)_2$]

The oxidation of ammonia gas was first investigated in [EMIM][$N(Tf)_2$] by linear sweep voltammetry at a platinum microdisk electrode (6 μm radius). Figure 10.4 shows the linear sweep voltammetric response obtained at 200 mV s^{-1} when [EMIM][$N(Tf)_2$] was saturated with increasing concentrations of gaseous ammonia (10 – 50 % vol.). As can be seen, upon the introduction of ammonia to the ionic liquid an oxidative wave occurs at +1.40 V (*vs.* Ag), and continues to increase as the concentration rises. The appearance of this oxidative wave is in good agreement with the behaviour observed at a platinum microdisk electrode in DMF in the presence of ammonia (figure 10.2). It was found that a plot of the limiting current versus the vol. % NH_3 showed a linear increase (r^2 = 0.999) with a limit of detection of 1.2 % vol., thereby demonstrating the possible analytical utility of the system.

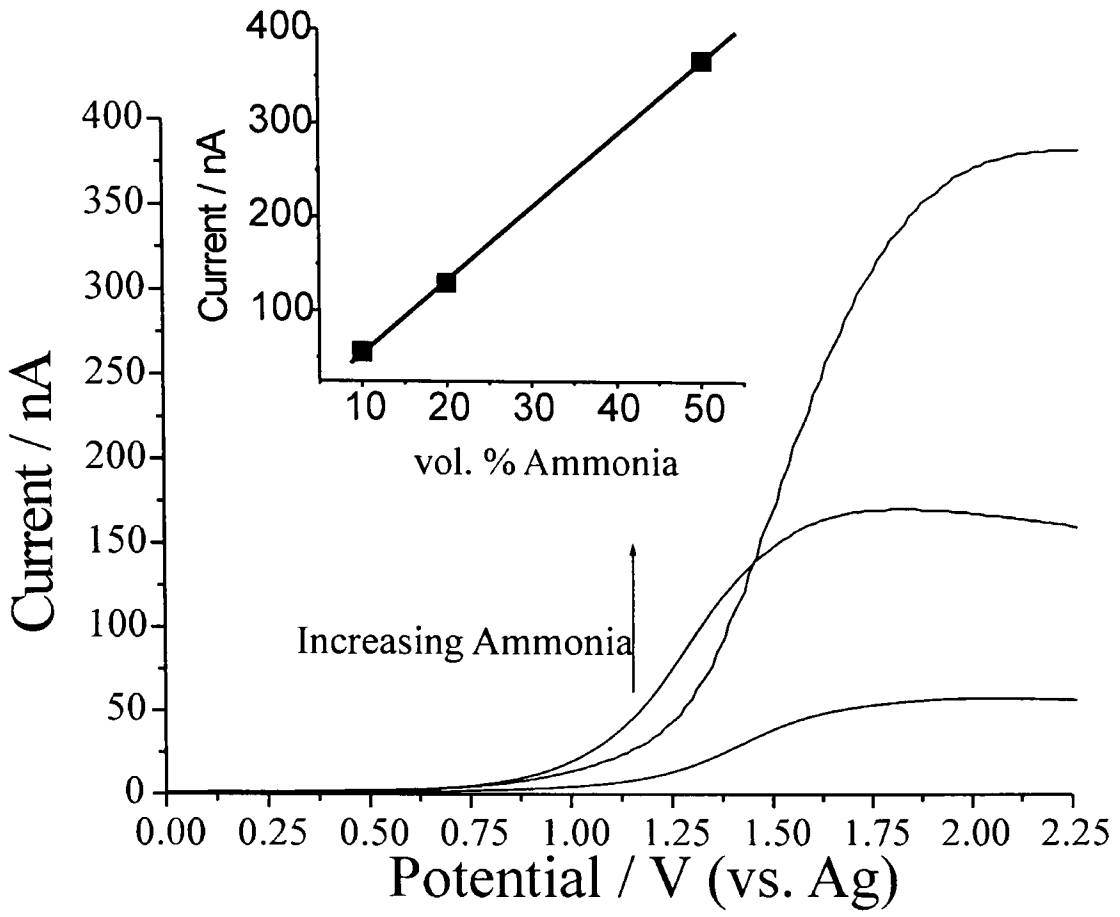


Figure 10.4: The linear sweep voltammetric responses of a sample of [EMIM][$N(Tf)_2$] saturated with increasing % vol. ammonia (10, 20 and 50 % vol.) obtained at a 6.2 μm (radius) platinum microdisk electrode at 200 mV s^{-1}. Insert: a plot of the limiting oxidative current against the % vol. ammonia.

In order to understand the oxidative reaction process further, cyclic voltammetric experiments were conducted in which the scan rate was varied from 20 to 116 V s^{-1}, for a fixed concentration of ammonia.

Figure 10.5 shows cyclic voltammograms for the oxidation of 10 vol. % ammonia at a platinum microdisk electrode in [EMIM][$N(Tf)_2$] at increasing scan rates. These results show an oxidative wave at +1.40 V (*vs.* Ag) which enhances as the scan rate is increased, the occurrence of this wave is consistent with the linear sweep voltammetric response observed at 200 mV s^{-1} (figure 10.4). Upon reversal of the scan direction, a reductive wave is observed at –0.70 V (*vs.* Ag) with its corresponding oxidative wave seen at -0.50 V (*vs.* Ag). It can also be observed that a slight pre-wave appears at -0.20 V (*vs.* Ag) on the reductive scan which can be tentatively attributed to the oxidation of surface bound products from the oxidation of ammonia (*vide infra*) on the electrode surface.

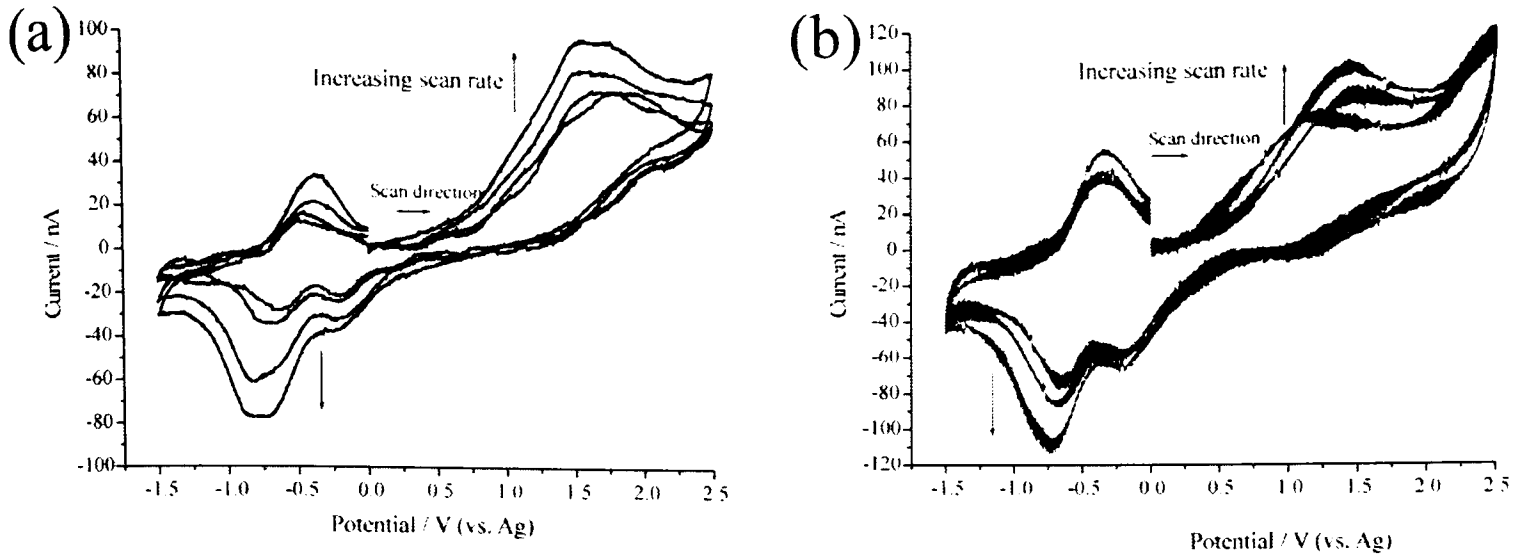


Figure 10.5: The cyclic voltammetric responses of a sample of [EMIM][$N(Tf)_2$] saturated with 10 % vol. ammonia obtained at a 6.2 μm (radius) platinum microdisk electrode at increasing scan rate (a) 20, 25, 45 and 60 V $s^{-1}$and (b) 84, 97 and 116 V s^{-1}.

Efforts to determine the diffusion coefficient of ammonia [EMIM][$N(Tf)_2$] by chronoamperometric methods proved to be inadequate for the mechanism under study due to the complexity arising from the coupled chemical reaction steps. The diffusion coefficient, *D*, in the ionic liquid, however, is expected to be at least an order of magnitude less than in DMF due to the higher viscosity in the former (0.78 cP *vs.* 32.1 cP) [25,26]. According to the Wilke-Chang equation (Appendix 3), the diffusion coefficient of ammonia in DMF is 3.75 x 10^{-9} m^2 s^{-1}, whereas a typical diffusion coefficient value in an ionic liquid is at least 1 x 10^{-10} m^2 s^{-1} [19].

Next we turn our attention to understanding the voltammetric response obtained for the oxidation of ammonia in both DMF and [EMIM][$N(Tf)_2$].

10.3.2.2 Elucidation of the oxidative process

Analysis of the voltammetric response obtained for the oxidation of ammonia in both DMF and [EMIM][$N(Tf)_2$] at a platinum microdisk electrode suggests that after ammonia is oxidised the products undergo a chemical reaction. The products of this chemical reaction can then be electrochemically reduced at the electrode surface consistent with the new reduction wave observed on the reductive scan. We therefore propose the following reaction mechanism: first the ammonia is oxidised to produce

ammonium ions and nitrogen, (eq. (10.1)), where three ammonium ions per every four ammonia molecules are formed in a three electron process. The ammonium ion can then under go a pre-equilibrium step to lose a proton and regenerate ammonia, (eq. (10.2)). The proton can then be electrochemically reduced to produce hydrogen (eq. (10.3)).

$$4NH_3\,(g) \rightarrow 3NH_4^+ + \tfrac{1}{2}N_2\,(g) + 3e^- \qquad (10.1)$$

$$NH_4^+ \rightleftharpoons NH_3\,(g) + H^+ \qquad (10.2)$$

$$H^+ + e^- \rightarrow \tfrac{1}{2}H_2\,(g) \qquad (10.3)$$

In order to support the proposed reaction pathway, the voltammetric response obtained at scan rates from 20 to 120 V s^{-1} for the oxidation of ammonia in [EMIM][$N(Tf)_2$] were examined. Integration of the area under the oxidative wave at +1.40 V (*vs.* Pt) and the reductive peaks at -0.50 V (*vs.* Pt) allowed the charge, Q passed during each process to be determined. Given the above reaction mechanism, it can be shown that the ratio of the charge due to the oxidation of ammonia (Q_{oxid}) to the charge due to the reduction of protons (Q_{red}) should reach a 4/3 ratio. A plot of the charge ratio of the oxidative wave over the reductive wave (Q_{oxid}/Q_{red}) versus the reciprocal of the scan rate ($1/\nu$) is detailed in figure 10.6. This illustrates a linear response over the scan rate studied and shows that when the scan rate is infinitely fast the ratio does indeed approach 1.33 as expected. It is believed that at slower scan rates, some of the products of the oxidative step are lost to bulk solution, resulting in less species available for reduction, justifying the higher ratio of charge Q_{oxid}/Q_{red} observed.

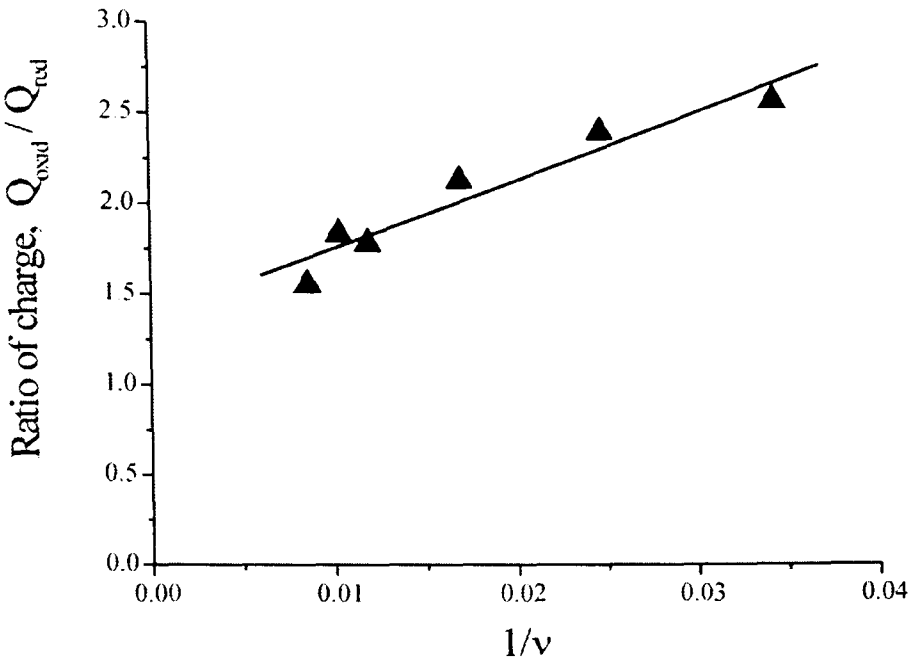


Figure 10.6: Plot of the ratio of charge, Q_{oxid}/Q_{red}, versus the reciprocal of scan rate, 1/v, for the oxidation of ammonia in [EMIM][$N(Tf)_2$].

10.3.2.3 Reduction of ammonium hexafluorophosphate in [EMIM][$N(Tf)_2$] and DMF

Further evidence of the reaction process detailed above was sought by examining the voltammetric response for the reduction of ammonium hexafluorophosphate, [NH_4][PF_6]. It can be envisaged that the ammonium would first lose a proton prior to the electrochemical reduction of the proton to hydrogen in a CE reaction (*vide infra*) thus enabling a potential means of "fingerprinting" the newly observed reduction wave after the oxidation of ammonia as detailed in figures 10.2 and 10.5.

$$NH_4^+ \rightleftharpoons NH_3\,(g) + H^+ \qquad (10.4, C)$$

$$H^+ + e^- \rightarrow \tfrac{1}{2} H_2\,(g) \qquad (10.5, E)$$

The reduction of [NH_4][PF_6] was carried out using cyclic voltammetry in both [EMIM][$N(Tf)_2$] and DMF at platinum electrodes at various scan rates. Figure 10.7 (a) shows the cyclic voltammograms for the reduction of [NH_4][PF_6] at a 6 μm Pt microdisk electrode in [EMIM][$N(Tf)_2$] to increasing scan rates from 30 to 250 V s^{-1}. These responses show a reductive peak at E = -1.10 V (*vs.* Ag), corresponding to the reduction of protons (equation 10.5, E) formed form the preceding dissociation of NH_4^+ ions as given in equation (10.4, C).

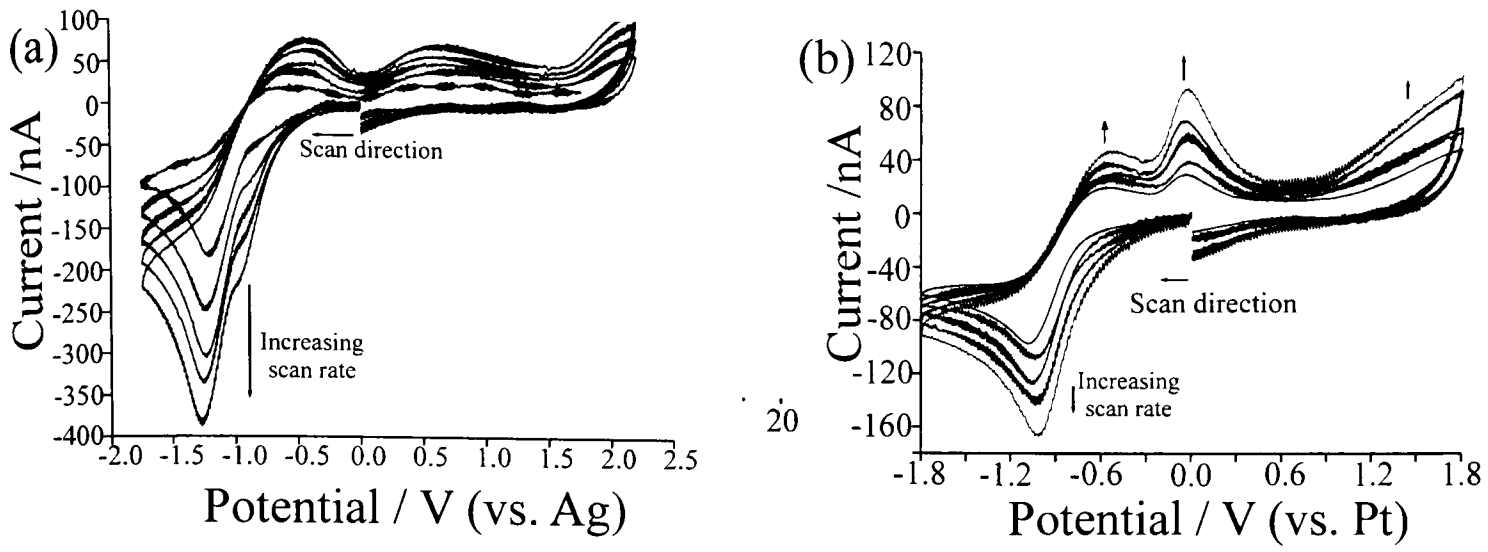


Figure 10.7: (a) The cyclic voltammetric responses of a sample of $[EMIM][N(Tf)_2]$ saturated with $[NH_4][PF_6]$ obtained at a 6 μm (radius) platinum microdisk electrode at increasing scan rates (from 30 to 250 V s^{-1}), (b) The voltammetric response for a solution containing 20 mM $[NH_4][PF_6]$ in DMF (0.1 M TBAP) to increasing scan rate (from 30 to 207 V s^{-1}) at a 5 μm (radius) platinum electrode.

Upon reversal of the scan direction it can be seen that two oxidative peaks are observed at -0.50 V and +0.90 V (*vs.* Pt). These can be tentatively attributed to the oxidation of hydrogen back to proton and the direct oxidation of ammonia, respectively. It can be seen that the half-wave potential corresponding to the reduction of ammonium is shifted to slightly negative potential compared to the potential of the reduction wave observed after the direct oxidation of ammonia. This is thought to be due to a possible double layer effect caused by the presence of PF_6^- anions.

In order to further corroborate this interpretation, the electrochemical reduction of $[NH_4][PF_6]$ was next evaluated in DMF. The corresponding voltammetric responses for a solution containing 20 mM $[NH_4][PF_6]$ in DMF (0.1 M TBAP) to increasing scan rates (from 30 to 207 V s^{-1}) at a platinum (5 μm) electrode are detailed in Figure 10.7 (b). These show a reductive wave at -1.00 V (*vs.* Pt) and two corresponding oxidative waves at -0.51 V and +0.00 V (*vs.* Pt). The presence of these waves can again be attributed to the initial dissociation of ammonium to form ammonia and protons, the protons are then reduced at the electrode surface to form hydrogen which

can be oxidised at the electrode surface along with the ammonia at higher potentials. These observations are consistent with that observed in $[EMIM][N(Tf)_2]$.

The voltammetric response of NH_4NO_3 was also evaluated in DMF and it was found to be in agreement with the literature [27] and analogous to the response observed for $[NH_4][PF_6]$. However, the reductive peak attributed to the reduction of protons was shifted slightly to a more negative potential (-1.06 V *vs.* Pt) as compared to that observed for $[NH_4][PF_6]$. This suggests that the reduction of ammonium is anion sensitive.

10.4 Conclusion

The results detailed have examined the direct electrochemical oxidation of ammonia in both the traditional electrochemical organic solvent DMF and the new electrochemical solvent $[EMIM][N(Tf)_2]$. The corresponding voltammetric responses have been shown to be similar in each solvent with a large oxidative wave seen initially and the appearance of a new reductive wave after the oxidation. The oxidative reaction process has been examined and a suitable reaction pathway has been proposed corresponding to the formation of NH_4^+ after oxidation. This newly formed ammonium cation can then undergo deprotonation to form ammonia and protons which can then be reduced at the electrode surface to produce the new reduction wave. The steady state linear sweep voltammetric response for the direct oxidation of ammonia in both DMF and $[EMIM][N(Tf)_2]$ was found to produce a linear response of limiting current against % vol. ammonia over the range studied, thereby demonstrating the possible analytical utility of the approach.

10.5 Chapter 10 References

[1] M. Buzzeo, D. Giovanelli, N. S. Lawrence, C. Hardacre, K. R. Seddon, R. G. Compton, *Electroanalysis* **2004**, *16*, 888.

[2] T. Katan, R. J. Galiotto, *J. Electrochem. Soc.*, **1963**, *110*, 1022.

[3] H. G. Oswin, M. Salomon, *Canad. J. Chem.*, **1963**, *41*, 1686.

[4] A. R. Despic, D. M. Drazic, P. M. Rakin, *Electrochim. Acta* **1966**, *11*, 997.

[5] D. W. McKee, A. J. Scarpellino, Jr., I. F. Danzig, M. S. Pak, *J. Electrochem. Soc.*, **1969**, *116*, 562.

[6] H. Gerischer, A. Mauerer, *J. Electroanal. Chem.*, **1970**, *25*, 421.

[7] K. Sasaki, Y. Hisatomi, *J. Electrochem. Soc.*, **1970**, *11*, 758.

[8] T. Pignet, L. D. Schmidt, *J. Catal.*, **1975**, *40*, 212.

[9] A. C. A. De Vooys, M. F. Mrozek, M. T. M. Koper, R. A. Van Santen, J. A. R. Van Veen, M. J. Weaver, *Electrochem. Comm.*, **2001**, *3*, 293.

[10] A. C. A. De Vooys, M. T. M. Koper, R. A. van Santen, J. A. R. van Veen, *J. Electroanal. Chem.*, **2001**, *506*, 127.

[11] B. A. Lopez de Mishima, D. Lescano, T. Molina Holgado, H. T. Mishima, *Electrochim. Acta* **1997**, *43*, 395.

[12] A. Spetz, M. Armgarth, I. Lundstroem, *J. App. Phys.*, **1988**, *64*, 1274.

[13] R. Q. Long, R. T. Yang, *J. Catal.*, **2002**, *207*, 158.

[14] K. K. Barnes, C. K. Mann, *J. Org. Chem.*, **1967**, *32*, 1474.

[15] J. Dupont, C. S. Consorti, J. Spencer, *J. Braz. Chem. Soc.*, **2000**, *11*, 337.

[16] T. Welton, *Chem. Rev.*, **1999**, *99*, 2071.

[17] M. T. Carter, C. L. Hussey, S. K. D. Strubinger, R. A. Osteryoung, *Inorg. Chem.*, **1991**, *30*, 1149.

[18] I. M. AlNashef, M. L. Leonard, M. C. Kittle, M. A. Matthews, J. W. Weidner, *Electrochem. Solid-State Lett.*, **2001**, *4*, D16.

[19] I. M. AlNashef, M. L. Leonard, M. A. Matthews, J. W. Weidner, *Ind. Eng. Chem. Res.*, **2002**, *41*, 4475.

[20] Q. Cai, Y. Xian, H. Li, T. Yang-ming, T. Jin, *Huadong Shifan Daxue Xuebao, Ziran Kexueban* **2001**, *3*, 57.

[21] M. Buzzeo, O. V. Klymenko, J. D. Wadhawan, C. Hardacre, K. R. Seddon, R. G. Compton, *J. Phys. Chem.*, **2003**, *107*, 8872.

[22] B. Ante, J. R. Reimers, N. S. Hush, J. Hafner, *J. Chem. Phys.*, **2002**, *116*, 8981.

[23] G. Papapolymerou, V. Bontozoglou, *J. Mol. Cat. A:Chem.*, **1997**, *120*, 165.

[24] C. M. A. Brett, A. M. O. Brett, *Electroanalysis*, Oxford University Press, New York, **1998**.

[25] A. J. Bard, L. R. Faulkner, *Electrochemical Methods: Fundamentals and Applications*, Second Ed., John Wiley and Sons, Inc., New York, **2001**.

[26] C. Hardacre, J. D. Holbrey, S. P. Katdare, K. R. Seddon, *Green Chem.*, **2002**, *4*, 143.

[27] D. A. Tkalenko, A. A. Rudnitskaya, I. E. Shpak, *Elektrokhimiya* **1978**, *14*, 993.

Part 4: Halothane Sensing Based on Photoelectrochemical Processes in Microdroplets Containing p-Chloranil

Aims and Scope:

In this part of the thesis we look at the possibility of photochemically induced electrocatalytic processes within microdroplets containing p-chloranil (2,3,5,6-tetrachloro-1,4-benzoquinone, TCBQ) as a mean of detecting the anaesthetic gas halothane. First however, the electron transfer properties of microdroplets containing TCBQ had to be investigated as the associated voltammetry is very sensitive to the nature and concentration of ions in the surrounding aqueous.

Chapter 11: "Voltammetry of Immobilised Microdroplets Containing p-Chloranil on Basal Plane Pyrolytic Graphite Electrodes"

This chapter examines the redox chemistry of TCBQ both in homogeneous and heterogeneous media. For the heterogeneous study, the voltammetry of TCBQ was studied in the form of microdroplets immobilized at a basal plane pyrolytic graphite electrode. The last section discusses the possibility of utilising this latter approach for sensing the anaesthetic gas halothane. Most of the results detailed in this chapter have been published in Physical Chemistry Chemical Physics [1].

11.1 Introduction

The investigation of electrochemically driven ion-transfer processes across liquid|liquid interfaces has been shown to be of fundamental interest [2-22] as well as of interest for specific ion sensing in aqueous media [23,24] and for the replication of redox chemistry occurring in both chemical (i.e, aqueous emulsion system, etc.) and natural systems [25-28]. Anson and co-workers modified macroscopic edge plane pyrolitic graphite (epg) electrodes with thin films (of average thickness ca. 30 μm) of nitrobenzene [7,9,11], tolunitrile [10] or benzonitrile [12] containing an electroactive, water-insoluble compound, such as decamethylferrocene [7] or a porphyrin-type molecule [8,9]. The modified electrodes were then inverted and immersed in aqueous supporting electrolytes allowing the determination of rates of redox reactions between reactants located on opposite sides of different liquid|liquid interface [7,9-11]. Scholz and co-workers described a method to attach droplets of polar and non polar aprotic solvents containing dissolved electroactive species to paraffin-impregnated graphite electrodes [18]. This electrode methodology compares favourably with the thin film technique developed by Anson *et al.* as it does not require the addition of a supporting electrolyte in the oil phase and it allows the determination of standard Gibbs energies of transfer of a large number of inorganic [22,29-31], and organic ions [22,29-37] across different liquid|liquid interfaces, such as water|nitrobenzene [18,22,29,30,32-34,36], water|octanol [31,37], water|menthol [35] and water|dichloroethane [18]. Other methods have been used to modify the surface of electrodes with oil droplets and we refer the reader to a recent review article by Banks *et al.* [38] for a more thorough description of the techniques used and the results obtained by different authors.

Based on the seminal work of Marken *et al.* [3-5] our group has, in the past six years, investigated the voltammetric processes of random arrays of unsupported electroactive microdroplets which are deposited on the surface of a basal plane pyrolytic graphite

electrode (bppg) *via* solvent evaporation of a solution of the electroactive oil [13-17,26,38]. This approach has provided a simple methodology to interrogate the electrochemistry at the liquid|liquid interface of several compounds that cannot be studied homogeneously in aqueous media due to their low solubility. Initial work was mainly focused on organic hydrophobic oils containing a phenylenediamine backbone [13-17,39], although recently the biphasic redox chemistry of n-butylferrocene [17], 4-nitrophenylnonylether [26], vitamin K_1 [27] and vitamin E [28] in the form of microdroplets has also been explored.

The voltammetry associated with microdroplets has been shown to be very sensitive to the nature and concentration of ions in the surrounding aqueous phase as, in order to preserve charge neutrality within the unsupported microdroplets oil environment, ion insertion into or expulsion from the oil phase must take place during the Faradaic current flow. When the transfer of the aqueous-based counterion from aqueous solutions into the oil droplet is thermodynamically more favourable than the transfer of the electrogenerated ion into the aqueous phase, electrochemically induced ion insertion leading to the formation of a novel ionic liquid was shown to occur at the triple phase boundary of electrode|oil|aqueous electrolyte [4,5,40]. However, when the transfer of the aqueous based counterion into the organic deposit is energetically unfavourable, expulsion of the electrogenerated charge species into the adjacent aqueous phase was observed. Dissolution processes of this sort have shown to take place at the liquid|liquid interface [40]. Finally, reactive chemistry between the electrogenerated and the inserted ions was also shown to occur on some occasions [40].

The research presented in this chapter falls into three sections. In the first part, the well-documented electrochemical reduction [41-45] of a hydrophobic benzoquinone derivative, p-chloranil (2,3,5,6-tetrachloro-1,4-benzoquinone, TCBQ), will be

examined in homogeneous solutions of various aprotic solvents (namely: benzonitrile (BN), N,N-dimethylformamide (DMF), propylcyanide (PrCN) and dimethylsulfoxide (DMSO)). In the second part, the redox chemistry of TCBQ will be further explored in the form of TCBQ/BN microdroplets immobilized at a bppg electrode surface immersed in various electrolyte solutions. The literature has many examples of anion insertion [3,13,15-17,23,24,38,40,46], however, much fewer examples of cation insertion have, so far, been reported [12,26]. It will be shown that, depending on the lipophilicity of the cation present in the aqueous phase, cation uptake into, or anion expulsion from, the organic deposit can take place to restore the electroneutrality within the microdroplet environment. Protonation across the liquid|liquid interface and the effect of the addition of a supporting electrolyte in the oil phase will also be examined. Finally, the last section examines photochemical redox catalysis at TCBQ microdroplets which hints at the possibility of using this ilk of modified electrode for the potential photoelectroanalytical detection of the anaesthetic gas halothane.

11.2 Experimental

11.2.1 Chemical Reagents

Buffered solutions were prepared using 0.05 M Na_2HPO_4/ NaH_2PO_4, 0.1 M NaH_2PO_4 and 0.1 M boric acid solutions, and adjusted to the required pH (pH = 4, 7 or 10) using NaOH (all Aldrich). Britton-Robinson buffer solutions made up using 0.04 M acetic, phosphoric (both BDH) and boric (Sigma) acids were used for the experiments carried out at pH 2.

Solutions were deoxygenated by outgassing with oxygen-free nitrogen (BOC Gases, Guildford, Surrey, UK) for at least 15 minutes prior experimentation and a nitrogen atmosphere was maintained over the solutions during each experimental run. All experiments were carried out at room temperature of 20 ± 2 °C.

11.2.2 Electrochemical Assembly

For the homogeneous electrochemistry section, a glassy carbon (GC, 3 mm diameter, BAS Technicol, UK) or a bare basal plane pyrolytic graphite (bppg, 5 mm diameter, Le Carbone Ltd., Sussex, UK) electrode acted as working electrode, a platinum wire wound into a spiral provided the counter electrode and a platinum pseudo reference electrode completed the cell assembly.

For the microdroplets study, the bppg electrode (*vide supra*) was used as working electrode with a platinum wire wound into a spiral (counter electrode) and a saturated calomel reference electrode (SCE, $Hg/HgCl_2$, Radiometer, Copenhagen, Denmark). All potentials are quoted with respect to the SCE, unless otherwise specified.

For the photoelectrochemical experiments described in the last section, a white lamp producing light of wavelenght in the range 300-700 nm was used for irradiation.

11.2.3 Procedures

Several methods in which the surface of a bppg electrode can be modified with oil droplets containing an electroactive compound have been reported [38]. In the present study, we investigated droplets of the electroactive hydrophobic yellow material TCBQ. An inert organic liquid was required to dissolve the solid TCBQ and benzonitrile (BN) was chosen as it was found to be electrochemically inert in the potential window of interest.

The bppg working electrode was modified with microdroplets of TCBQ dissolved in BN by solvent evaporation of a volatile solvent (MeCN) from an aliquot (typically 5μL) of TCBQ/BN stock solution of accurately known concentration that had been pipetted onto the electrode surface prior the immersion in aqueous solution. The concentration of TCBQ in the BN oil phase was ca. 35 mM (ca. 1 nmol of TCBQ in a typical volume of 2.7×10^{-8} L of BN). This technique of depositing the organic phase containing the electroactive species in the form of microdroplets rather than a

continuous film [12] gives the opportunity to omit supporting electrolytes in the organic phase as, due to the presence of the contact lines, electrode|BN|water, charge compensation during electrochemical reduction or oxidation can always be provided at the three-phase boundary [13]. However, a study of the behaviour of supported microdroplets was also conducted by preparing stock TCBQ/BN in MeCN solution containing the required amount of tetrabutylammonium perchlorate (TBuAP) so that the concentration of TBuAP in the microdroplets was either 0.1, 1 or 2 M (see Section 11.3.2.4).

In order to obtain reproducible results, careful bppg electrode preparation was found to be important. The bppg electrode was cleaned prior to each scan by rinsing with MeCN and water, and the surface was renewed by polishing on carborundum paper (P1000 grade, Acton and Bormans, Stevenage, UK) prior each experimental run. All the experiments were undertaken as soon as possible after immersion of the modified bppg electrode into the aqueous phase.

11.2.4 Computation

The voltammetric response of microdroplet partially blocked electrodes was simulated using the same method described in reference [15]. Simulations for naked electrodes were carried out with DigiSim 3.0© [47], a commercially available computer code, distributed by Bioanalytical systems, 2701 Kent Ave., West Lafayette, IN 47906.

11.3 Results and Discussion

11.3.1 Homogeneous Voltammetry

11.3.1.1. Electrochemical reduction of TCBQ in benzonitrile (BN) at glassy carbon (GC) and basal plane pyrolytic graphite (bppg) electrodes

First, we investigated the voltammetric reduction of TCBQ in a homogeneous solution of benzonitrile (BN) containing 0.1 M TBuAP as supporting electrolyte at a GC (3 mm

diameter) electrode. The corresponding cyclic voltammetric responses obtained at increasing scan rates (from 0.1 to 1 V s^{-1}) for the reduction of 1 mM TCBQ in BN are shown in figure 11.1 (a) and the potential data are summarised in Table 11.1.

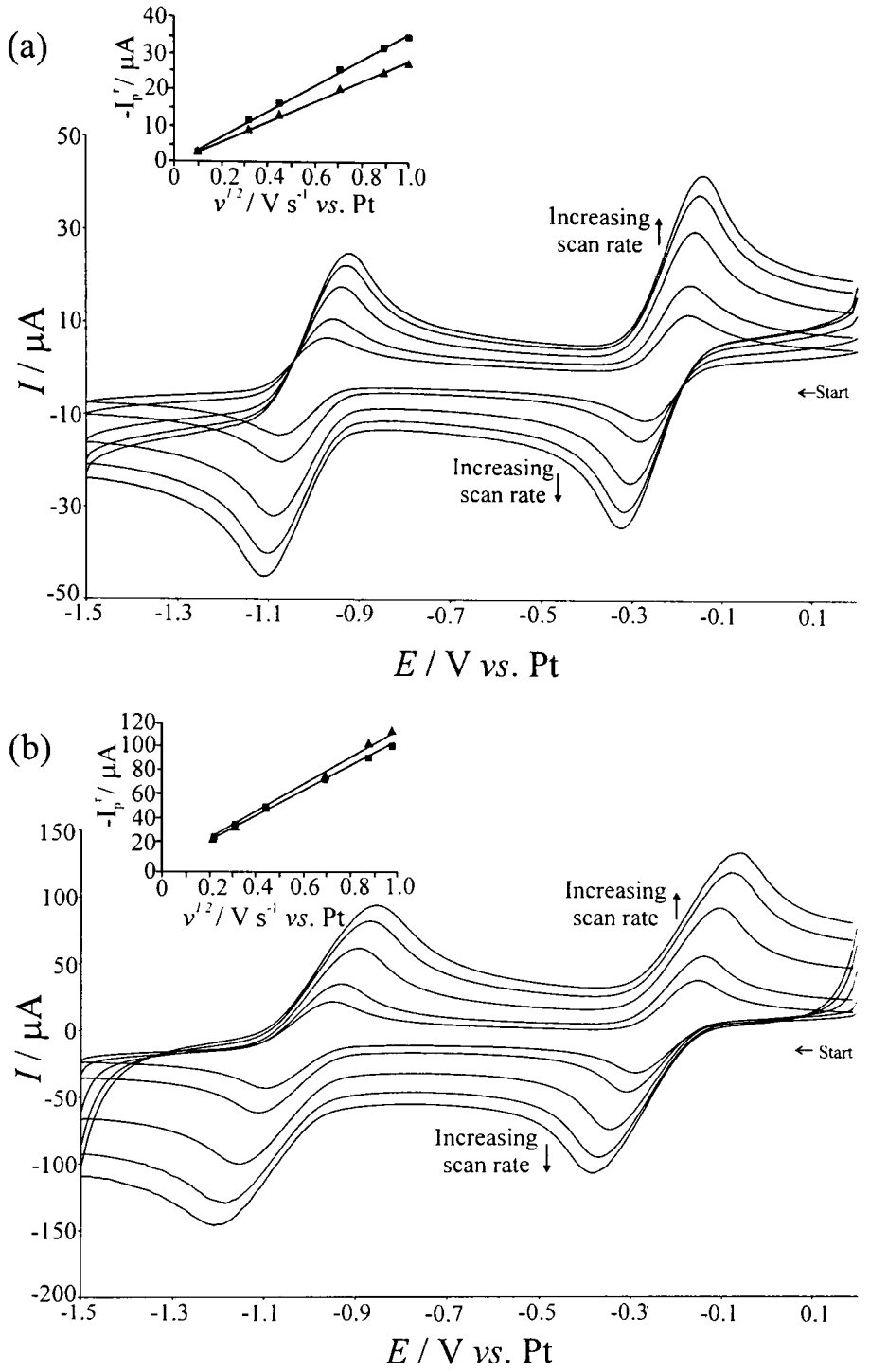


Figure 11.1: Cyclic voltammograms obtained at different scan rate (0.1, 0.2, 0.5, 0.8 and 1 V s^{-1}) corresponding to the reduction of 1 mM TCBQ in homogeneous solution of BN containing 0.1 M TBuAP at a (a) GC (3 mm diameter) electrode and (b) bppg (5 mm diameter) electrode. Insert graph in each figure: a plot of the first $-I_p^{r1}$ (■) and second $-I_p^{r2}$ (▲) reductive peak current against the square root of scan rate, $v^{1/2}$.

***Table 11.1**: Potential data (vs. Pt) for the reduction of 1mM TCBQ in BN (0.1 M TBuAP) at a GC (3mm diameter) electrode.*

Scan rate V s^{-1}	E_p^{r1} /V	E_p^{o1} /V	E_{mid}^{1} /V	ΔE_p^{1} /mV	E_p^{r2} /V	E_p^{o2} /V	E_{mid}^{2} /V	ΔE_p^{2} /mV
0.1	-0.273	-0.173	-0.233	100	-1.069	-0.968	-1.08	101
0.2	-0.283	-0.173	-0.228	110	-1.069	-0.958	-1.01	111
0.5	-0.303	-0.163	-0.233	140	-1.089	-0.938	-1.01	151
0.8	-0.314	-0.152	-0.233	162	-1.089	-0.928	-1.01	161
1.0	-0.324	-0.142	-0.233	182	-1.109	-0.928	-1.01	181

Two well-separated one-electron reduction processes were observed at -0.273 V (vs. Pt) and -1.069 V (vs. Pt), respectively. These can be attributed to the formation of the radical anion, $TCBQ^{-\bullet}$, which can be further reduced in a second one-electron transfer to the dianion, $TCBQ^{2-}$. The latter is re-oxidable in two successive one-electron transfers up to the quinone state. Therefore, the reduction mechanism can be denoted as a quasi-reversible process as expressed by the reactions:

$$TCBQ + e^- \underset{}{\overset{k_1^0}{\rightleftharpoons}} TCBQ^{-\bullet} \qquad (11.1)$$

$$TCBQ^{-\bullet} + e^- \underset{}{\overset{k_2^0}{\rightleftharpoons}} TCBQ^{2-} \qquad (11.2)$$

The ratio of the forward and backward peaks height of both signals were ca. 1 corroborating the formation of *a stable* radical anion capable of undergoing further reduction and then re-oxidation to the parent.

Both the reduction and re-oxidation peaks currents of both couples were found to increase with scan rate and a plot of the reduction current peaks ($I_p^{r1}$and I_p^{r2}) against the square root of scan rate ,$\nu^{1/2}$, (insert plot figure 11.1 (a)) was found to be linear suggesting diffusion-controlled processes. The peak potentials were found to be slightly dependent on the scan rate. With increasing scan rate, the first and the second reduction peaks ($E_p^{r1}$and E_p^{r2}) were shifted toward more negative potentials. In contrast, the first and the second re-oxidation peaks ($E_p^{o1}$and E_p^{o2}) moved towards more positive potentials. As a consequence, the potential separation ΔE_p ($=E_p^{o} - E_p^{r}$) increased with increasing scan rate (see Table 11.1), consistent with a quasi-reversible behaviour. Analysis of the peak currents using the Randles-Sevčik equation and the peak-to-peak separation data using the Nicholson's treatment [48] yielded a value for the diffusion coefficient D for the radical anion $TCBQ^{-\bullet}$ in BN of $D = 3.6 \times 10^{-6} \pm 0.2\ cm^2\ s^{-1}$.

The reduction of TCBQ was also studied at a bppg electrode (5 mm diameter) and the corresponding voltammograms obtained at increasing scan rate (0.1, 0.2, 05, 0.8 and 1 V s^{-1}) are shown in figure 11.1 (b) and the potential data are summarised in Table 11.2.

Table 11.2: *Potential data (vs. Pt) for the reduction of 1mM TCBQ in BN (0.1 M TBuAP) at a bppg (5 mm diameter) electrode*

Scan rate V s^{-1}	E_p^{r1} /V	E_p^{o1} /V	E_{mid}^{1} /V	ΔE_p^{1} mV	E_p^{r2} /V	E_p^{o2} /V	E_{mid}^{2} /V	ΔE_p^{2} /mV
0.1	-0.283	-0.152	-0.217	131	-1.089	-0.948	-1.02	141
0.2	-0.303	-0.142	-0.222	161	-1.109	-0.928	-1.02	171
0.5	-0.344	-0.112	-0.228	232	-1.149	-0.898	-1.02	251
0.8	-0.364	-0.082	-0.223	282	-1.180	-0.867	-1.02	313
1.0	-0.374	-0.072	-0.223	302	-1.190	-0.857	-1.02	333

Similar to that seen at the GC electrode, the electrochemical reduction of TCBQ revealed two successive one-electron transfer according to a quasi-reversible EE mechanism. However, ΔE_p at bppg electrode was larger than ΔE_p obtained at the GC electrode (Tables 11.1 and 11.2) suggesting more sluggish electron transfer kinetics operate at a bppg electrode as compared to a GC electrode. Furthermore, ΔE_p^{2} was found to be slightly larger than ΔE_p^{1} (Table 11.2) suggesting that the second electron transfer step is slower than the first one at a bppg electrode.

11.3.1.2 Comparison of the electrochemical reduction of TCBQ at GC in BN with other aprotic solvents (DMF, DMSO and PrCN)

The reduction of TCBQ was also carried out in other aprotic solvents, namely DMF, DMSO and PrCN in the presence of 0.1 M TBuAP as supporting electrolyte. The corresponding voltammograms (0.1 V s^{-1}) for the reduction of 0.5 mM TCBQ at GC electrode in each different solvent are overlaid in figure 11.2. The potential data are

summarised and compared to those obtained in BN in Table 11.3 along with the Gutmann donor number , DN, and the viscosity, η, of each solvent.

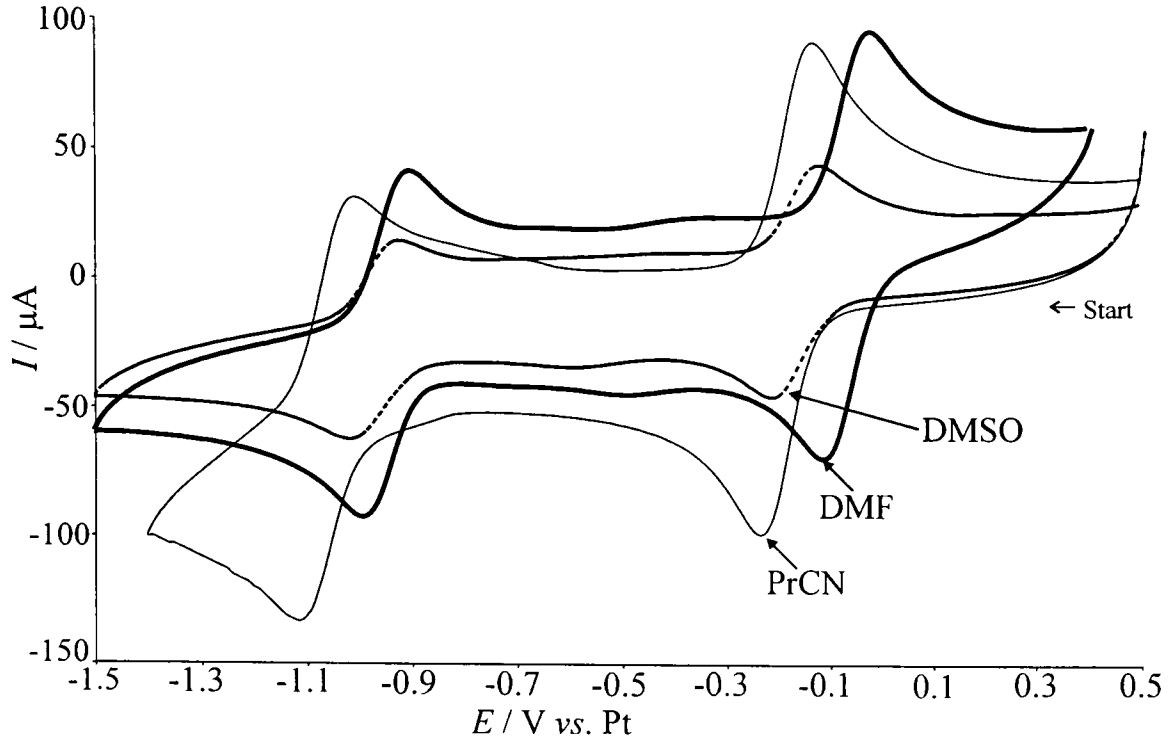


Figure 11.2: Cyclic voltammograms (0.1 V s^{-1}) recorded at a GC electrode (3 mm diameter) for the reduction of 0.5 mM TCBQ in homogeneous solutions of DMF, DMSO and PrCN all containing 0.1 M TBuAP as supporting electrolyte.

***Table 11.3**: Potentials (vs. Pt) for the reduction of 0.5 mM TCBQ in different aprotic solvents (0.1 M TBuAP) at a GC (3mm diameter) electrode and solvent donor number (DN, [49,50]) and viscosity (η, [51]).*

Solvent	η /cP	DN	E_p^{r1} /V	E_p^{o1} /V	E_{mid}^{1} /V	ΔE_p^{1} mV	E_p^{r2} /V	E_p^{o2} /V	E_{mid}^{2} /V	ΔE_p^{2} /mV
DMSO	2	29.8	-0.193	-0.123	-0.158	70	-1.02	-0.93	-0.97	90
DMF	0.796	27	-0.120	-0.023	-0.071	97	-0.99	-0.89	-0.93	100
PrCN	0.515	16.6	-0.214	-0.112	-0.179	71	-1.11	-1.02	-1.06	90
BN[a]	1.24	11.9	-0.273	-0.173	-0.233	100	-1.07	-0.97	-1.08	101

[a] Reduction of 1 mM TCBQ

In all the solvents, two peaks were observed corresponding to the reduction of TCBQ to the radical anion, followed by reduction to the dianion. However, variation in the peak potential for the reduction were seen and a comparison of the reduction peak potential observed for the first process reveals that E_p^r is less negative for DMF and DMSO as compared to BN and PrCN. Solvent effects in the electrochemical reduction of several p-quinones in aprotic solvents have been reported before [45] and can be interpreted in terms of increasing stabilisation of the electrode products (radical anion

and di-anion) with increasing donor number of the solvent. The relative order of donor number DN is [49,50]:

BN < PrCN < DMF ~DMSO

Indeed, a shift towards more positive potentials was found going from the higher electron donating solvents DMF and DMSO (DN=26.6 and 29.8, respectively [49]) to BN and PrCN (DN=11.9 and 16.6, respectively [49,50]).

The less magnitude of both signals obtained in DMSO, as compared to that obtained in the other aprotic solvents, might be accounted for the lower diffusion coefficient of TCBQ in DMSO [52] as a result of its higher viscosity (see Table 11.3, [51]).

11.3.2 Heterogeneous Voltammetry

The study of the redox chemistry of TCBQ was extended and its electron transfer properties were investigated at the liquid|liquid interface *via* immobilisation of electrically insulating microdroplets of TCBQ at a bppg electrode surface as described in the experimental section.

11.3.2.1. Determination of the average size of microdroplets deposited on a bppg electrode.

First, the average size of the microdroplets deposited on a bppg electrode surface was determined using a cyclic voltammetric method recently developed by our group [15] which is only briefly summarised in this section. Davies and co-workers [15] introduced a method to ascertain the cyclic voltammetric characteristics of a single diffusion domain, a circular inert disk of radius R_b situated at the bottom of a cylinder of radius R_0 for the simple redox couple:

$$A \underset{k_b}{\overset{k_f}{\rightleftharpoons}} B + e^-$$

The protocol allowed the calculation of the dimensionless peak current Ψ_{max}, from knowledge of the dimensionless scan rate, ν_{dl}, microscopic coverage, θ, and dimensionless rate constant, k^0_{dl}.:

$$\Psi_{max} = f(\nu_{dl}, \theta, k^0_{dl})$$

where:

$$\nu_{dl} = \frac{nFR_0^2}{DRT}\nu$$

$$\theta = \left(\frac{R_b}{R_0}\right)^2$$

$$k_{dl} = \frac{k^0 R_0}{D}$$

where n is the number of electrons transferred at the electrode surface, F is the Faraday constant, ν is the scan rate, D is the diffusion coefficient of the electroactive species, R is the molar gas constant, and k^0 is the heterogeneous rate constant for the redox reaction. By comparison with experimental data obtained for model electrodes, it was shown that partially blocked electrodes of high symmetry could be modelled as an ensemble of independent diffusion domains. Furthermore, to include the effects of a randomly distributed blocking systems and to identify explicitly the role played by blocking disk overlap three further models (models A, B1 and B2) were developed in which the assumptions of monodisperse blocking disks or microdroplets prevails.

For a particular redox couple, by measuring the decrease in peak current when the electrode is modified with inert microdroplets compared to when the electrode is naked, we can obtain an estimate of the microdroplet size and total coverage of the electrode surface [15]. Figure 11.3 illustrates cyclic voltammograms recorded at 0.2 V s^{-1} with a 5 mm diameter bppg electrode in 1.5 mM ferrocyanide/0.1 M KCl solution where the electrode is (a) naked and (b) partially covered with 2.7 x 10^{-5} cm^3 of benzonitrile, corresponding to 10 μL of 26 mM benzonitrile (BN) in MeCN.

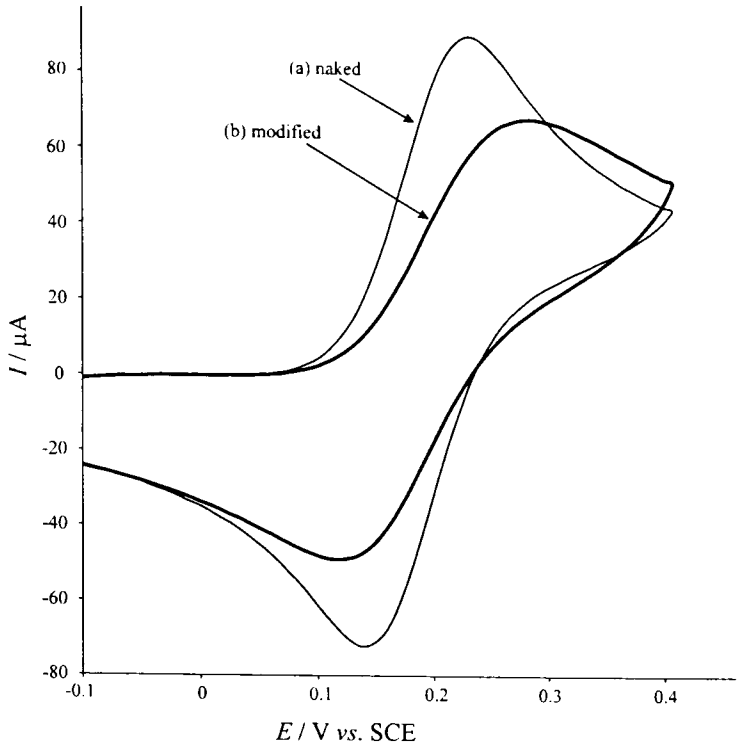


Figure 11.3: Cyclic voltammograms for the oxidation of 1.5 mM $Fe(CN)_6^{-4}$ in aqueous 0.1 M KCl where the 0.20 cm^2 bppg electrode surface is naked and partially covered with 2.7 x 10^5 cm^3 of BN microdroplets. The scan rate is 0.2 V s^{-1}.

The voltammogram for the modified electrode shows a clear decrease in peak current, I_p, and increase in peak to peak separation, ΔE_p, when compared to the response of the naked electrode. Both observations are consistent with an inertly partially blocked surface indicating the microdroplets are inert in this particular medium and potential window. Analysis of the naked electrode data (for a range of scan rates) with DigiSim 3.0© gave $D = 6.5 \times 10^{-6}$ cm^2 s^{-1} and $k^o = 0.01$ cm s^{-1} for the $Fe(CN)_6^{4-}$ / $Fe(CN)_6^{3-}$ redox couple, which agrees well with that determined previously for carbon electrodes [53].

We can model the microdroplet partially blocked electrode surface as a random array of overlapping hemispheres of the same radius [15]. This is based on the experimental observation that at low surface coverage when microdroplets are well spaced, their distribution is approximately monodisperse, whereas at high surface coverage there is a larger range of droplet radii [15]. Using the method described in ref. [15] we can simulate the dependence of peak current with droplet radii for a range of scan rates. This is illustrated in figure 11.4 for the modified electrode discussed above at scan rates of 0.1, 0.2, 0.5, 1.0 and 2.0 V s^{-1}. Overlaid as dashed horizontal lines are the

experimental peak currents recorded at each scan rate. The points where the dashed and solid lines cross are highlighted in the figure and represent the best agreement between theory and experiment.

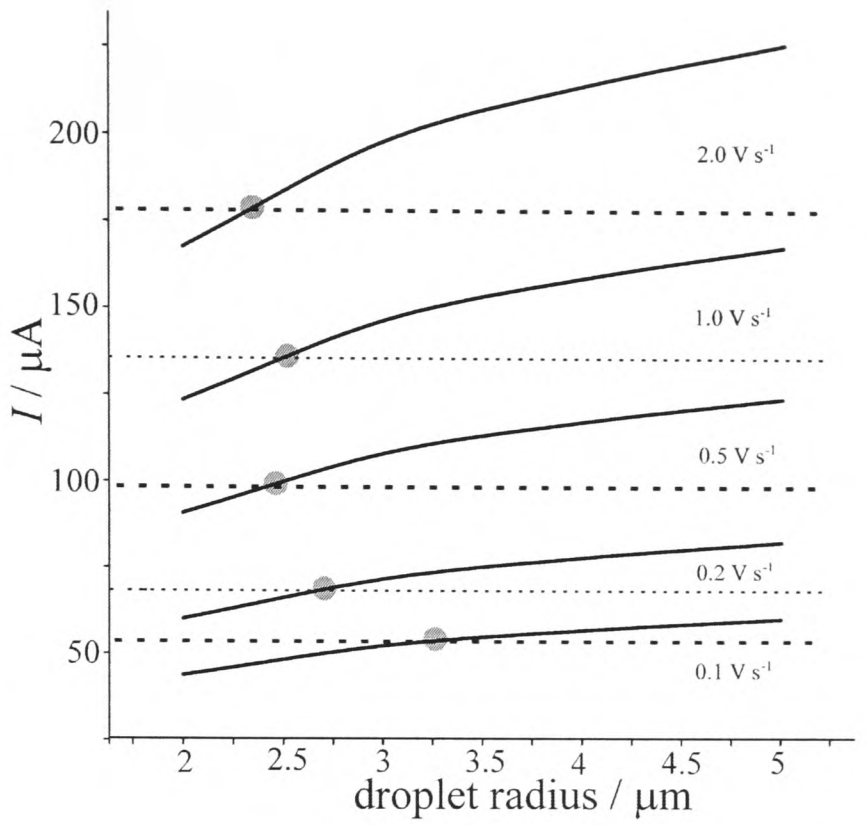


Figure 11.4: Simulated relationships between the peak current, I_p, and the droplet radius for the oxidation of 1.5 mM $Fe(CN)_6^{4-}$ in aqueous 0.1 M KCl at a 0.20 cm^2 bppg electrode modified with 2.7 x 10^{-5} cm^3 of benzonitrile at the scan rates indicated (0.1, 0.2, 0.5, 1.0 and 2.0 V s^{-1}). The dashed lines correspond to the recorded experimental peak currents and the grey circles highlight the best fit between theory and experiment.

As observed, the results suggest an average droplet radius of 2.5 μm (experiments where the benzonitrile droplets contained 0.1 M TBuAP gave a similar result).

Figure 11.5 illustrates a 100 x 100 μm section of the corresponding *model* electrode surface that best fits the experimental results, i.e. where the droplet radius is 2.5 μm. It should be noted that figure 11.5 corresponds to how the model perceives the electrode surface. In reality, overlapping droplets would coalesce, forming larger droplets of different radii. Our approach to modelling random arrays of droplets ignores the resulting geometry from hemisphere/droplet overlap allowing us to treat the surface as a random array of overlapping discs, which is far easier to simulate the voltammetry of [44]. Indeed, inclusion of droplet coalescence in the modelling process would result in a problem requiring far more computation time.

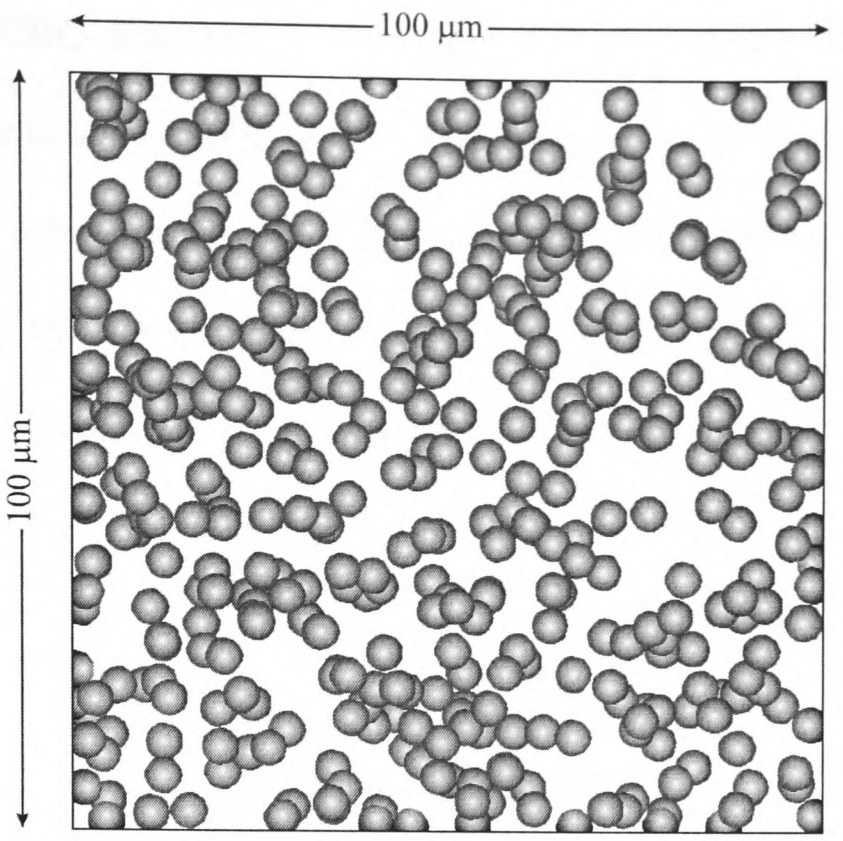


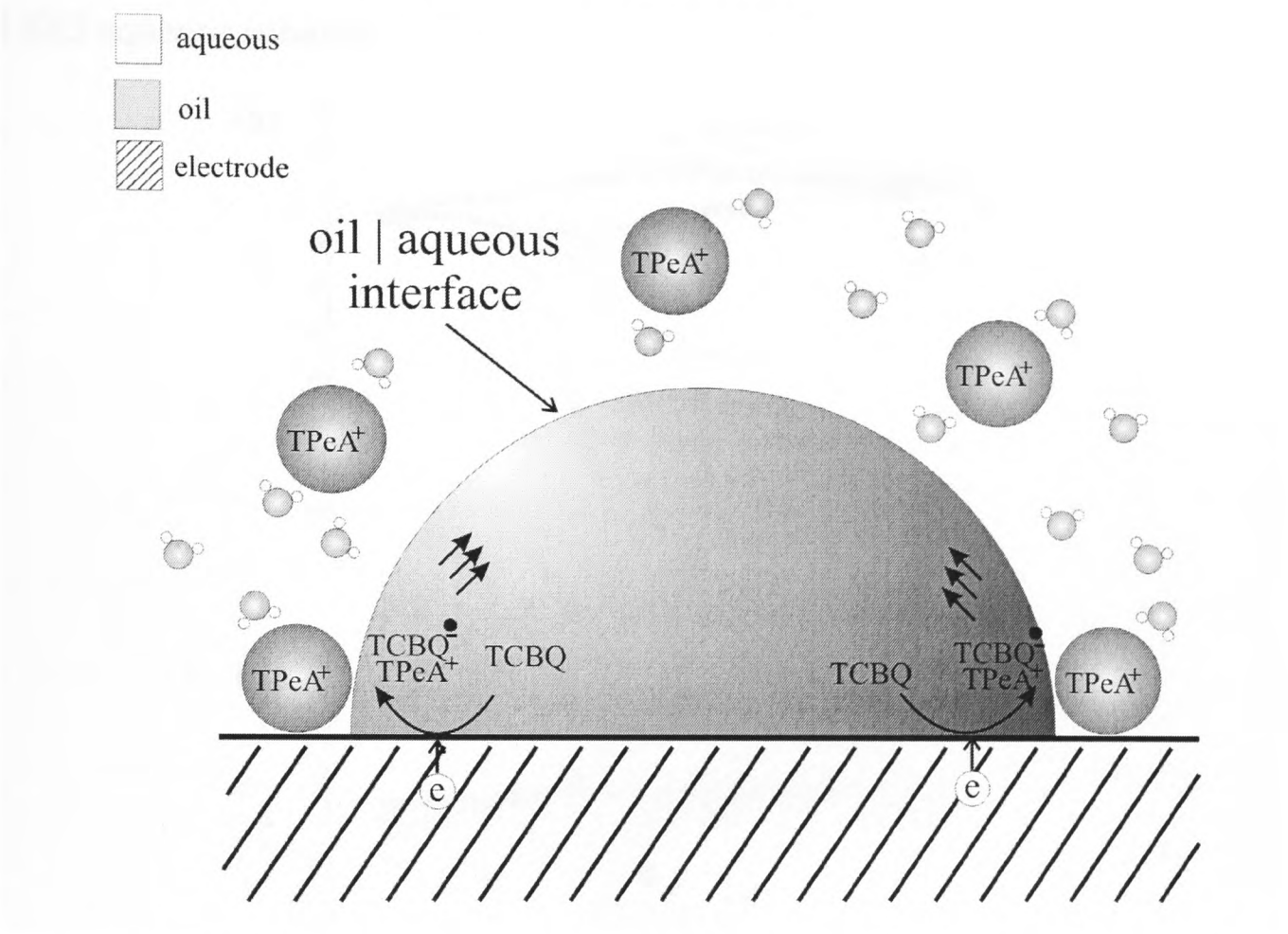
Figure 11.5: A 100 x 100 µm section of the model electrode surface made from overlapping hemispheres of radius 2.5 µm, the total volume of which equals 2.7 x 10^5 cm^3. This model electrode provides the best fit between theory and the experimental data in figure 11.4.

For this particular block volume there is a large amount of overlap resulting in a wide range of observable droplet radii. We can calculate the fraction of the uncovered electrode area to be $\Theta = \frac{\text{uncovered electrode area}}{\text{total electrode area}} = 0.44$. Note that only 44 % of the electrode is available for the electrochemical redox reaction yet the peak current of the modified electrode greatly exceeds 44 % of that for the naked electrode. Thus for redox reactions of this type, the uncovered surface area of the microdroplet modified electrode behaves more like an array of microelectrodes than a macro electrode of the same total area.

11.3.2.2 Voltammetry of unsupported microdroplets of TCBQ deposited on a bppg electrode immersed in aqueous 0.1 M Y^+Cl^- (Y = Li^+, K^+, Rb^+, $TMeA^+$, $TPrA^+$, $TBuA^+$ or $TPeA^+$).

In this section we discuss the voltammetric processes that occur at a bppg electrode (5 mm diameter) covered with a random arrays of purposely unsupported electroactive

microdroplets of TCBQ dissolved in BN (formed as described in Section 11.2.3) and immersed into an aqueous electrolyte where the droplet organic phase is insoluble and in which the SCE reference and the Pt counter electrodes are placed. A schematic diagram illustrating the electrochemical reduction of one TCBQ microdroplet in the presence of aqueous TPeACl is given in Scheme 11.1.



Scheme 11.1: Schematic diagram illustrating the electrochemical reduction of TCBQ in the form of microdroplets immobilised at a bppg electrode immersed in aqueous 0.1 M TPeACl. Only one TCBQ microdroplet is considered for simplicity.

In these experiments TCBQ is reduced to the respective anion radical $TCBQ^{\bullet-}$. Hence the electroneutrality of the oil environment can be retained by either the uptake of a cation from the aqueous phase or the expulsion of a newly generated anion into the aqueous phase. It can be anticipated that as the aqueous cation hydrophilicity increases, it becomes increasingly energetically more difficult to transfer the cation into the oil phase, until the cation can no longer thermodynamically transfer and the organic phase anion is expelled into the aqueous phase.

We have examined aqueous chloride solutions containing the hydrophilic alkaline metal cations Li^+, K^+ and Rb^+ and the less hydrophilic tetraalkylammonium cations NR_4^+ (R = Me, Pr, Bu and Pe). We first consider the response obtained in 0.1 M A^+Cl^- (A^+ = K^+, Li^+, Rb^+) aqueous solutions. Figure 11.6 (a) shows 5 successive scans (0.1 V s^{-1}) obtained at a bppg electrode modified with 1 nmol of TCBQ immersed in 0.1 M KCl aqueous solution.

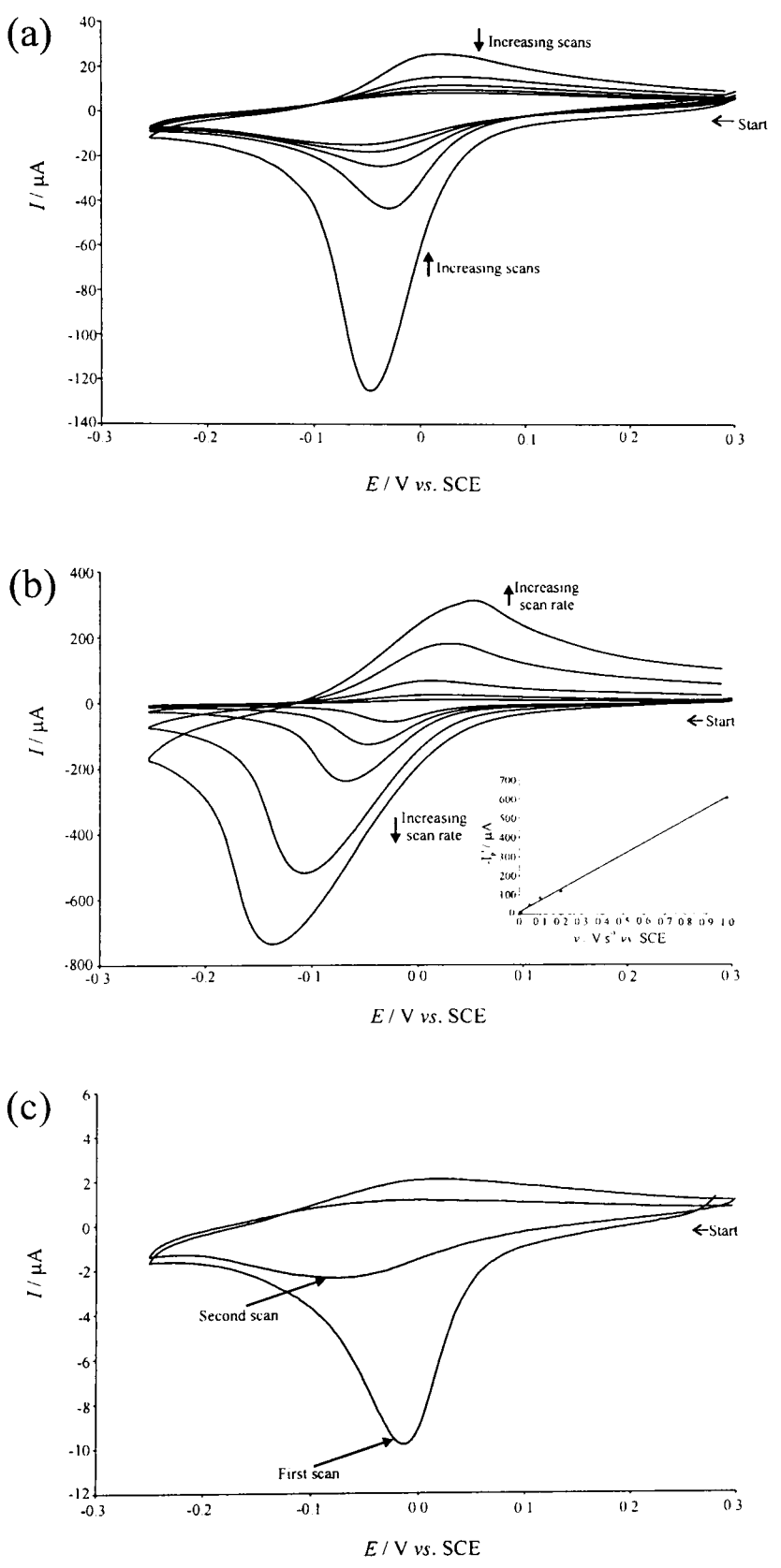


Figure 11.6: Cyclic voltammograms for the reduction of 1 nmol of TCBQ deposited onto a 5 mm diameter bppg electrode immersed in aqueous 0.1 M KCl: (a) showing the first five scans obtained at scan rate 0.1 V s^{-1}, (b) recorded at 0.05, 0.1, 0.2, 0.5 and 1.0 V s^{-1} and (c) showing the first and the second scan recorded at 0.01 V s^{-1}. Insert graph of figure 11.6 (b): a plot of the reductive peak current $-I_p^r$ versus scan rate.

The first cycle exhibits a single reduction peak at -0.052V (vs. SCE) and a small back oxidative peak at +0.008V (vs. SCE) (ratio of the anodic to cathodic charge $Q^o/Q^r = 0.26$) giving rise to a peak-to-peak-potential separation of 60 mV. With increasing potential redox cycling on the same electrode, the prominent reductive peak magnitude decreases and almost no anodic response remains. A slightly shift toward less negative reductive potential is observed on the second scan. This might be due to an electrochemically induced partitioning of the electrolyte into the droplets causing the electrical resistance of the droplets to diminish which in turn makes the reduction process easier or, more likely, to the reduction of the smaller size droplets. A scan rate dependence study was also carried out. The corresponding initial (first cycle) voltammograms recorded at different scan rate (0.05, 0.1, 0.2, 0.5 and 1.0 V s^{-1}) are shown in figure 11.6 (b) and the voltammetric data summarised in Table 11.4.

Table 11.4: *Voltammetric data (vs. SCE) for the reduction of 1 nmole of TCBQ deposited onto a 5 mm diameter bppg electrode immersed in aqueous 0.1 M KCl.*

ν/ V s^{-1}	E_p^r / V	E_{mid}^r / V	ΔE_p / V	Q^r x 10^5 / C	n^a	Q^o/Q^r
0.01	-0.011	-0.006	0.010	9.6	0.995	0.36
0.05	-0.022	-0.002	0.040	9.05	0.938	0.25
0.1	-0.052	-0.022	0.060	8.86	0.918	0.26
0.2	-0.052	-0.022	0.060	6.34	0.657	0.37
1.0	-0.133	-0.0543	0.181	8.57	0.89	0.53

[a] n = Number of electrons transferred for TCBQ molecule. Note the material is delivered to the electrode surface via a micropipette; a maximum error of 10% is estimated in this procedure which should be directly reflected in the values above for the number of electrons transferred.

A single reductive wave with a corresponding small oxidative wave is observed at all scan rates. The ratio anodic charge to cathodic charge, Q^o/Q^r, (see Table 11.4) increases slightly with increasing scan rate, however data obtained at scan rate larger that 0.2 V s^{-1} should be treated carefully since ohmic losses in the unsupported microdroplets are not negligible. A plot of the reductive peak current versus scan rate (insert plot of figure 11.6 (b)) is shown to be linear, consistent with an essentially complete electrolysis with a thin layer of deposited material.

Figure 11.6 (c) exhibits the voltammograms obtained when the potential was cycled twice at very slow scan rate (i.e, 10 mV s^{-1}). The first scan exhibits a reductive wave at -0.0011 V and no appreciable anodic counterpart. The second scan shows little further than resistive behaviour suggesting that complete reduction of the whole droplet has occurred during the first cycle. Analysis of the amount of charge passed (i.e, integrated area of the reductive peak) on the first reductive scan potential reveals the transfer of a single electron per TCBQ molecule (see Table 11.5).

Table 11.5: *Voltammetric data (vs. SCE) obtained at 0.1 V s^{-1} for the reduction of 1 nmole of TCBQ deposited onto a 5 mm diameter bppg electrode immersed in aqueous 0.1 or 1 M ACl (A= Li, K, Rb).*

	0.1M LiCl	1M LiCl	0.1M KCl	1M KCl	0.1M RbCl	1M RbCl
E_p^r /V	-0.052	-0.032	-0.052	-0.032	-0.042	-0.032
E_{mid}^r / V	-0.022	-0.007	-0.022	-0.012	-0.017	-0.012
ΔE_p / V	0.06	0.05	0.06	0.04	0.05	0.04
$Q^r \times 10^4$ /C	0.96	0.94	1.07	1.13	1.08	1.03
n^a	1.1	1.1	1.0	0.98	1.1	1.1
Q^o/Q^r	0.35	0.40	0.26	0.40	0.44	0.60

n^a = Number of electrons transferred for TCBQ molecule. Data obtained at 0.01 V s^{-1}. Note the material is delivered to the electrode surface via a micropipette; a maximum error of 10% is estimated in this procedure which should be directly reflected in the values above for the number of electrons transferred.

A similar response was observed for other very hydrophilic metal cations such as Li and Rb and the corresponding voltammograms obtained at 0.01 V s^{-1} are overlaid for comparison in figure 11.7 (a). A single reductive peak of similar magnitude is observed at ca. +0.0 V for all cations.

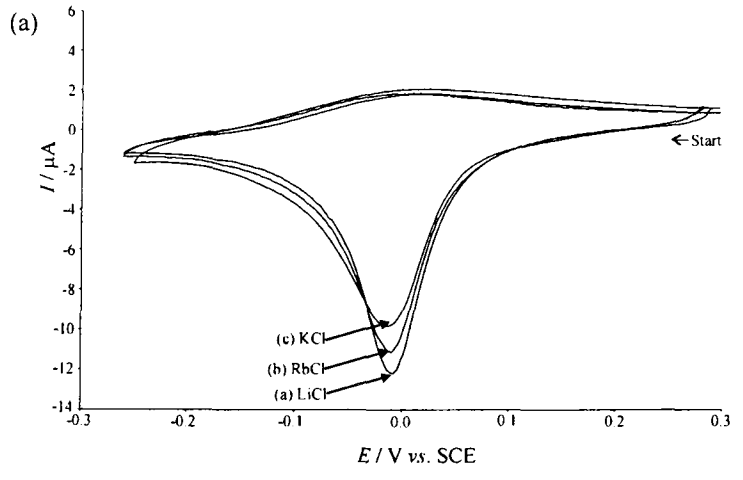


Figure 11.7 (a): Comparison of the voltammetric response (scan rate 0.01 V s^{-1}) for the reduction of 1 nmol of TCBQ deposited onto a 5 mm diameter bppg electrode immersed in aqueous 0.1 M (a) LiCl, (b) RbCl and (c) KCl.

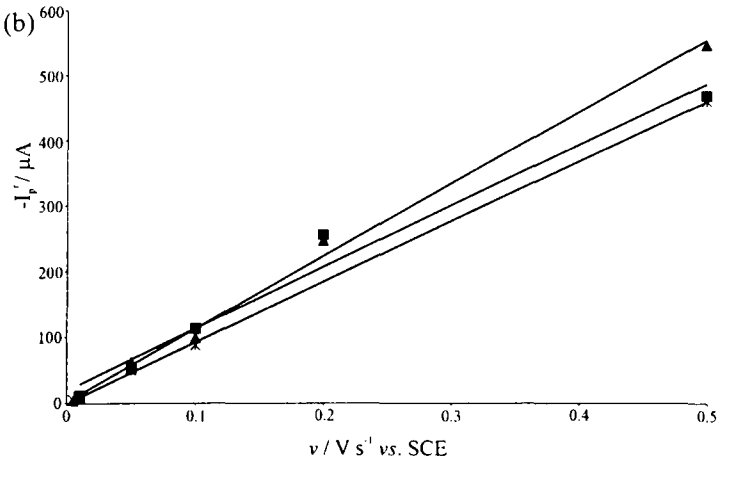


Figure 11.7 (b): A plot of the reductive peak current $-I_p^r$ versus scan rate for the single reductive peak obtained for the reduction of 1 nmol of TCBQ deposited onto a 5 mm diameter bppg electrode immersed in aqueous 0.1 M (■) LiCl, (▲) RbCl and (*) KCl.

Furthermore, plots of the reductive peak current against scan rate (figure 11.7 (b)) are linear for each different metal cation and the amount of charge passed suggested, in all cases, the discharge of one electron per molecule of TCBQ (Table 11.5). This type of electrochemical behaviour is somehow not surprisingly considering the high transfer free energy possessed by the alkali metal [54] which makes the insertion into the oil deposit a thermodynamically unfavourable process. Hence the electroneutrality of the organic phase is maintained by expulsion of the electro-generated radical anion into the aqueous phase as expressed by:

$$TCBQ(oil) + e^- \rightarrow TCBQ^{-\bullet}(aq) \qquad (11.3)$$

As the radical anion diffuses out of the diffusion layer during reduction, little radical anion remains to be oxidised and therefore little oxidative back peak is observed. Furthermore, this process causes depletion of TCBQ in the oil phase and hence, on successive scans, the peak height decreases as shown in figure 11.6 (a).

This has been described as the electrochemically induced anion dissolution mechanism [13]. It has been shown that, in the case of anion dissolution, the electron transfer might be initiated at the three phase boundary, but the dissolution may occur from the liquid|liquid interface. The large currents observed further support this interpretation.

We now turn to the voltammetric characteristics of the microdroplets in the presence of less hydrophilic cations, i.e the quaternary alkylammonium cations NR_4^+ (R= Me, Pr, Bu and Pe) in the aqueous phase.

Figure 11.8 (a), (b), (c) and (d) show the cyclic voltammograms obtained for the reduction of TCBQ deposited onto a bppg electrode and immersed in aqueous 0.1 M TMeACl, TPrACl, TBuACl and TPeACl, respectively. By increasing the length of the alkyl chain of the cation the hydrophobicity of the aqueous-based cation increases and this has profound effects on the electrochemical behaviour of the TCBQ microdroplets.

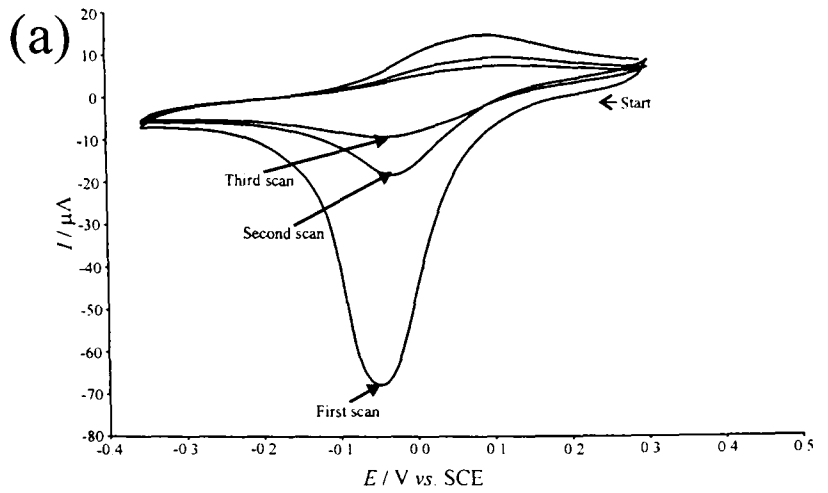


Figure 11.8: Cyclic voltammograms for the reduction of 1 nmol of TCBQ immobilised in the form of microdroplets at a bppg electrode immersed in various aqueous tetraalkylammonium chloride solutions: (a) showing the first three scans obtained at scan rate 0.1 V s^{-1} in aqueous 0.1 M TMeACl, (b) showing the first cycle obtained at scan rates (1) 0.01 V s^{-1}, (2) 0.05 V s^{-1} and (3) 0.1 V s^{-1} in aqueous 0.1 M TPrACl, (c) showing the first three scans obtained at scan rate 0.1 V s^{-1} in aqueous 0.1 M TBuACl and (d) showing the first cycle obtained at scan rate 0.05 V s^{-1} in aqueous 0.1 M TPeACl (see text).

In 0.1 M TMeACl solutions (figure 11.8 (a)) the response is qualitatively similar to that observed in aqueous alkali metal chloride solutions, with a single reductive peak at -0.05 V and a very little back oxidative peak. The signal was found to diminish on increasing redox cycling and charge integration at low scan rates (0.01 V s^{-1}) reveals the transfer of one electron per molecule of TCBQ suggesting that the dissolution of the electrogenerated radical anion is still a more favourable process than the insertion of $TMeA^+$.

Dissolution rather than cation insertion mechanism appears to be the pathway followed also in 0.1 M TPrACl aqueous solution. However, in this case, the associated voltammetry (figure 11.8 (b)) is more complex as it was found to be dependent on the scan rate. At low scan rate (0.01 V s^{-1}) a single reductive wave can be seen at -0.04 V, consistent with the dissolution of the radical anion. However, based on the charge under the peak, the number of electrons associated with this signal is only 0.5, suggesting that incomplete droplet conversion takes place under these conditions. Furthermore, voltammograms recorded at scan rate faster than 0.050 V s^{-1} (also overlaid in figure 11.8 (b)) exhibit two reductive peaks at +0.048V and at -0.1 V (vs. SCE), respectively. These could be tentatively attributed to the reduction of TCBQ to the radical anion and to the dianion, respectively, upon the uptake of $TPrA^+$ from the solution to balance the charge for TCBQ being reduced. However, the fact that the anodic to cathodic charge ratio is much less than one for both peaks, suggests that insertion pathway is only a minor contribution to the overall electrochemical process which is thought to proceed mainly via dissolution of the electrogenerated species.

Figure 11.8 (c) shows three successive redox cycles obtained in 0.1 M TBuACl solutions at 0.1 V s^{-1}. The first scan exhibits a single peak at +0.219 V (vs. SCE) with a corresponding oxidative peak at +0.289 V (vs. SCE) giving rise a peak-to-peak separation of 70 mV. The re-oxidative peak current is of the same magnitude of the

current associated with the reductive process and the anodic charge passed on the return of the scan is equal to the cathodic charge passed in the preceding negative going scan. Finally, analysis of the charge passed at 0.01 V s^{-1} suggests the transfer of 1 electron per molecule of TCBQ. All these observations are consistent with $TBuA^+$ insertion into the oil phase as expressed by:

$$TCBQ(oil) + TBuA^+(aq) + e^- \rightarrow [TCBQ^{-\bullet}TBuA^+](oil) \qquad (11.4)$$

As TCBQ is reduced to the radical anions $TCBQ^{-\bullet}$, $TBuA^+$ cations transfer across the liquid|liquid interface (specifically at the three phase boundary [4,5,40]) to preserve the electroneutrality of the electrically insulating oil microdroplets. A comparison of the reduction peak potential observed in aqueous TBuACl and in alkali metal chloride solutions reveals a shift versus less negative potential of ca. 0.27 V which further supports the assignment of the insertion mechanism. A slightly dissolution, probably *via* ion-pairs [43,55-58], is thought to be responsible for the diminished signal obtained upon continual redox cycling. The possibility of cation adsorption at the liquid|liquid interface and its slow transfer across it cannot be ruled out.

We finally turn our attention to the current|voltage characteristics of TCBQ microdroplets in 0.1 M TPeACl. The corresponding initial voltammogram recorded at 0.05 V s^{-1} (figure 11.8 (d)) reveals the appearance of a sharp reductive peak at +0.3 V (vs. SCE), a broad reductive peak at ca. -0.10 (vs. SCE) and a small third reductive wave at -0.245 V (vs. SCE). Upon reversal of the scan three corresponding oxidative back peaks are observed at +0.319 V, -0.215 V and -0.34 V, respectively.

As shown in figure 11.9, a stable response upon continual redox cycling is obtained (scan rate = 0.5 V s^{-1}).

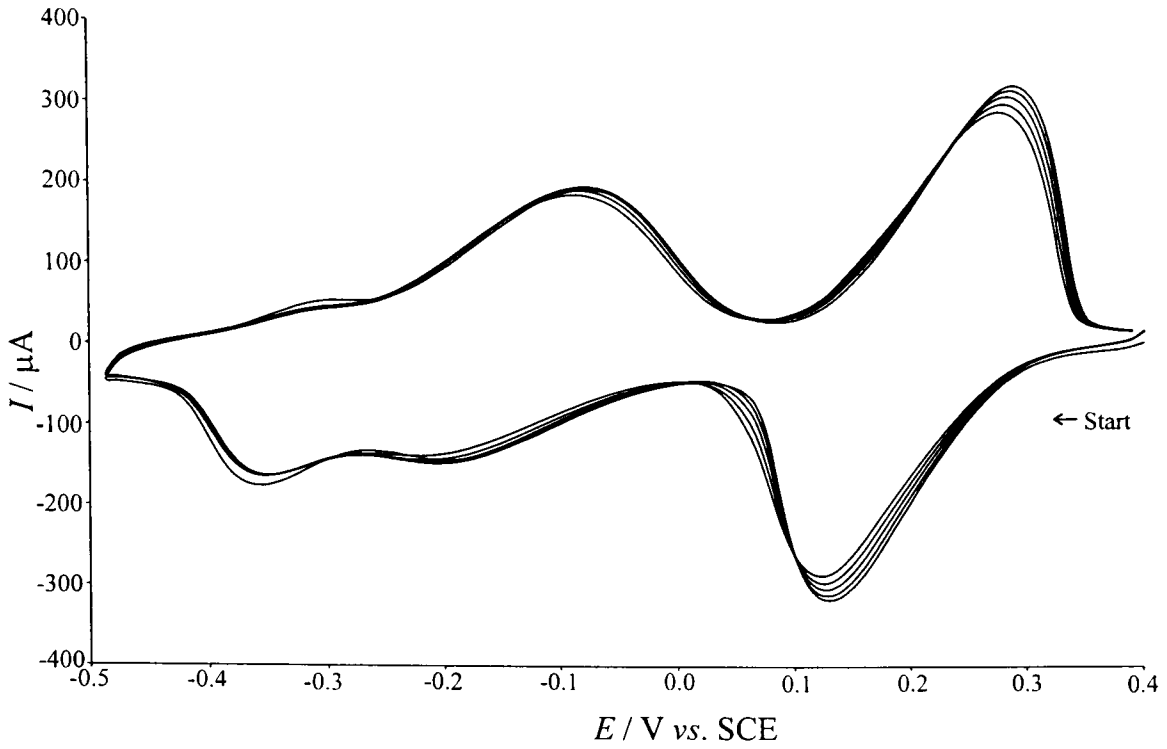


Figure 11.9: Cyclic voltammograms showing the first five scans obtained at scan rate 0.5 V s^{-1} for the reduction of 1 nmol of TCBQ deposited onto a bppg electrode immersed in aqueous 0.1 M TPeACl.

Therefore, we speculate the reversible $TPeA^+$ insertion and the assignment of the two reductive peaks as expressed by:

$$TCBQ(oil) + TPeA^+(aq) + e^- \rightarrow [TCBQ^{-\bullet}TPeA^+](oil) \quad (11.5)$$

$$[TCBQ^{-\bullet}TPeA^+](oil) + TPeA^+(aq) + e^- \rightarrow [TCBQ^{2-}(TPeA^+)_2](oil) \quad (11.6)$$

This response is analogous to that observed in homogeneous solution of BN (see section 11.3.1, Homogeneous Voltammetry). Voltammograms recorded when the droplets where purposely made conductive via the addition of TBuAP in the oil phase (see section 11.3.4) exhibited the same voltammetric characteristics of the unsupported droplets, which further suggests the insertion of $TPrA^+$ as given in equations (11.5) and (11.6).

11.3.2.3 Effect of increasing the aqueous phase proton concentration on the voltammetry of TCBQ microdroplets

The pH dependence on the reduction of unsupported microdroplets of TCBQ was examined in buffer solutions with pH values of 2, 4, 7 and 10 (see the Experimental section for a detailed specification of each buffer composition). Figure 11.10 exhibits

the corresponding cyclic voltammograms (scan rate 0.01 V s^{-1}) for the reduction of 1.1 nmoles of TCBQ immobilised on a bppg electrode immersed in each different buffer solution.

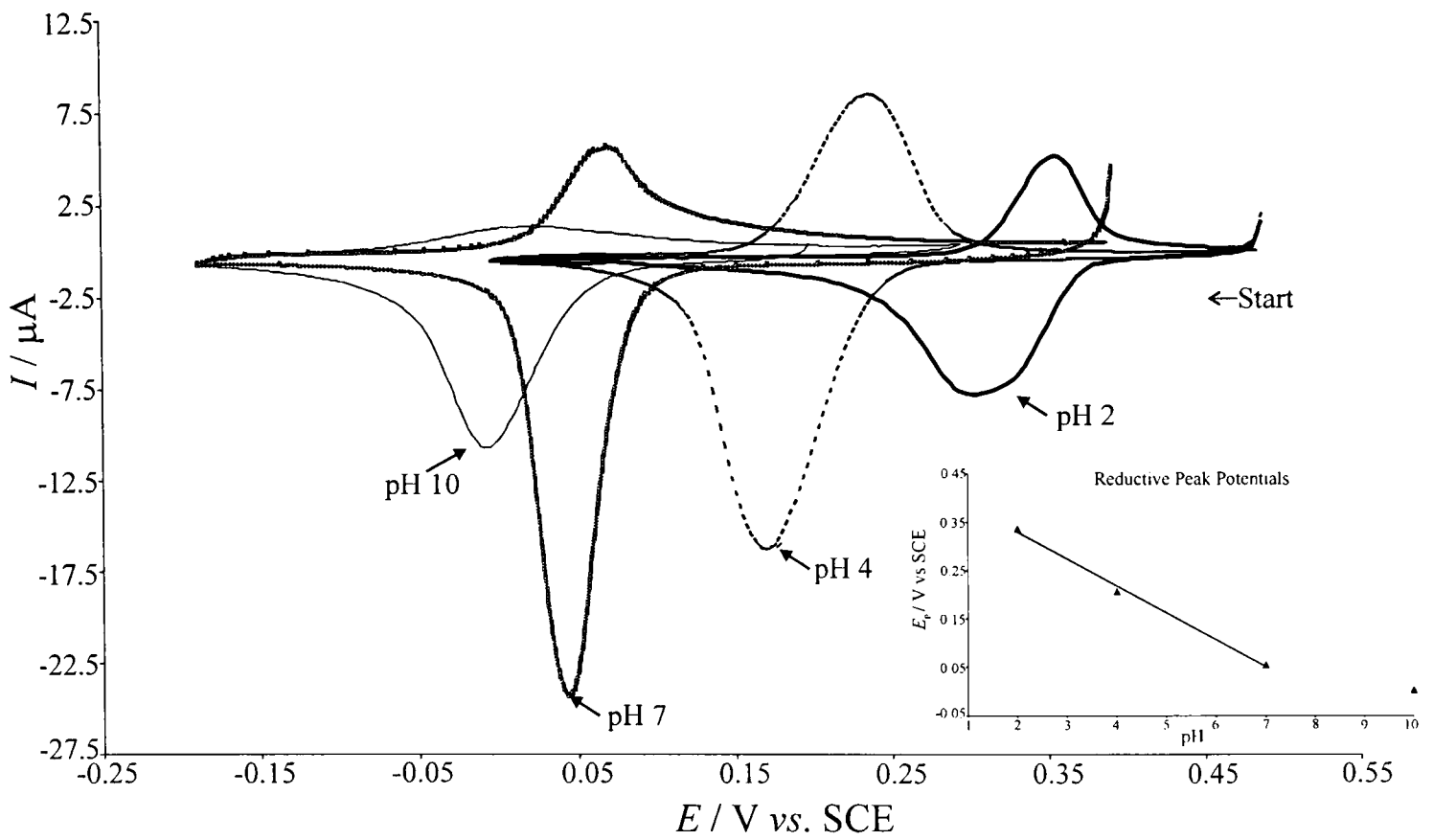


Figure 11.10: Cyclic voltammograms (0.01 V s^{-1}) for the reduction of 1 nmole of TCBQ deposited onto a bppg electrode immersed into buffer solutions with pH values of 2, 4, 7 and 10 (see Experimental section for details on the buffers composition). Insert graph: a plot of the reductive peak potential E_p^r versus scan rate.

It can be seen that the response obtained at pH 10 is similar to that obtained in 0.1 M alkali metal chloride solutions, with a single reductive peak at -0.013 V and almost negligible anodic counterpart. Analysis of the amount of charge passed at 0.01 V s^{-1} reveals the transfer of 1 electron per mole of TCBQ. This, together with a linear relationship of the magnitude of the reductive peak with scan rate, suggests that the radical anion $TCBQ^{-\bullet}$ dissolves out of the surface confined organic droplet phase.

However, as shown in figure 11.10, by increasing the concentration of protons in the aqueous phase, the reduction of TCBQ occurs at less negative potentials (the observed reductive peak potential were respectively, +0.042 V at pH 7, +0.173 V at pH 4, and +0.314 V at pH 2). A closer examination of this figure also reveals that, in the presence of a high proton concentration, the voltammetry is qualitatively different form that observed in the absence of protons. At lower pH values the signal shape is

more symmetric and the re-oxidative peak current is of the same magnitude of the forward going reductive peak current.

This pH dependence can be rationalised considering that protons are positively-charged species that are able to move into the oil phase to neutralise any negative charge that develops during the reduction of TCBQ. The liquid|liquid protonation process is well-documented in the literature [12,26] and protons are perhaps the most common type of electrolyte ions partitioning into an organic phase from an aqueous phase. The sensitivity of quinone species to protons is also well-known [59,60]. Thus, we might write for the reductive peak observed:

$$\mathrm{TCBQ(oil)} + m\mathrm{H^+(aq)} + n\mathrm{e^-} \rightarrow [\mathrm{TCBQ}^{n-}\mathrm{H}_m^+](\mathrm{oil}) \qquad (11.7)$$

We can then apply the Nernst equation to the proton insertion process described above in (11.7):

$$E = E^{\circ} + \frac{2.303RT}{nF}\lg\left(\frac{[\mathrm{TCBQ}](\mathrm{oil})}{[\mathrm{TCBQ}^{n-}\mathrm{H}_m^+](\mathrm{oil})}\right) - \frac{2.303mRT}{nF}\,\mathrm{pH} \qquad (11.8)$$

The identity of $[\mathrm{TCBQ}^{n-}\mathrm{H}_m^+](\mathrm{oil})$ species could, in principle, be inferred by the analysis of the variation of the reduction peak potential E_p^r with proton concentration together with the quantification of the amount of charged passed during the reductive process which should yield n for the process given in (11.6). In the range $2 \leq \mathrm{pH} \leq 7$, E_p^r for the single reductive peak observed varies as 56 mV per decadic change in proton concentration (see insert plot of figure 1.10), indicative (within the experimental error resulting from the analysis of distorted voltammograms associated with the resistive nature of the droplets) of $m = n$ in the process given in (11.7). Monitoring of the charge passed at low scan rate (0.01 $\mathrm{V\,s^{-1}}$) yields values of $n = 1.5 \pm 0.2$ at pH 2, $n = 1.2 \pm 0.2$ at pH 4 and $n = 1.15 \pm 0.2$ at pH 7. However, this data should be treated with caution as second scans on the same electrode reveals that exhaustive electrolysis did not occur at either pH 2, 4 or pH 7, under these conditions.

A quantitative analysis of this data is further complicated because of difference in the composition of the liquid|liquid interface determined by different identity and concentration of anions present in each different buffer solutions. Moreover, reactions between the semiquinone and the dianion of various quinone derivatives are well known [60] and thus, a cascade of follow-up chemistry via protonation can be anticipated. Nevertheless, the present results are qualitatively not inconsistent with either the transfer of one proton to the oil phase to protonate the electrogenerated radical anion $TCBQ^{-\bullet}$ (and produce a neutral free radical anion $TCBQH^{\bullet}$) or, more likely, the transfer of two protons and a two-electron reduction of TCBQ to the hydroquinone structure $TCBQH_2$.

This field-induced proton migration into and across the oil phase provides the ionic current required for the electron transfer to occur thereby ensuring electroneutrality within the microdroplets environment is maintained.

The observed selectivity towards proton insertion as compared to alkali metal cation insertion discussed above is contrary to thermodynamic considerations for which the free energy of transfer across the BN|water interface is least favourable for protons [54]. However, the higher efficiency of proton insertion, as compared with Group I cations insertion, reflects the basicity of the reduction products of TCBQ. Thus the proton phase is induced by the formation of strong O-H bonds within the hydroquinone molecules.

11.3.2.4 Voltammetry of purposely supported microdroplets of TCBQ deposited on a bppg electrode immersed in aqueous 0.1 M Y^+Cl^- ($Y = Li^+$, $TPeA^+$ or $TBuA^+$).

Having assessed the properties of unsupported TCBQ microdroplets, we now discuss the behaviour of microdroplets made conductive by addition of a hydrophobic, nonpartitioning supporting electrolyte such as TBuAP dissolved in the oil phase. As

the microdroplets are now supported, electron transfer may occur within the microdroplets or at the liquid|liquid interface.

We have studied the voltammetric characteristics of supported (with TBuAP) droplets of TCBQ immobilised on the bppg electrode immersed in three different aqueous chloride solutions containing the non-inserting cation Li^+ or the inserting $TBuA^+$ and $TPeA^+$.

We first examined the effect of the presence of TBuAP dissolved in the oil phase microdroplets on the reduction of 1 nmole TCBQ immobilised at a bppg electrode immersed in aqueous 0.1 M LiCl. Shown in figure 11.11 (a) is the effect of increasing the concentration of TBuAP in the oil phase (from 0 to 2 M) on the response of TCBQ microdroplets in 0.1 M LiCl solutions at 0.05 V s^{-1}.

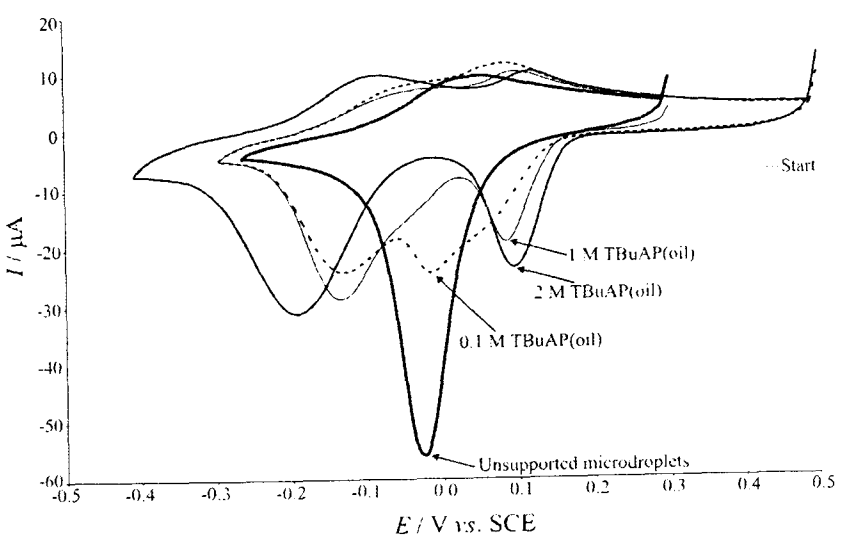


Figure 11.11 (a): The effect of increasing the concentration of TBuAP in the oil phase (from 0 to 2 M) on the response of TCBQ microdroplets in aqueous 0.1 M LiCl solution at 0.05 V s^{-1}.

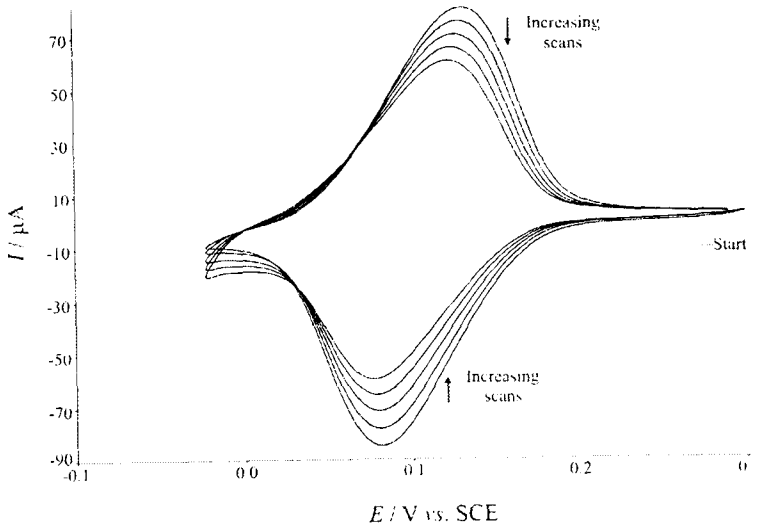


Figure 11.11 (b): Cyclic voltammograms showing the first five scans obtained for the reduction of 1 nmol TCBQ supported microdroplets ([TBuAP](oil) = 2M) deposited onto a bppg electrode immersed in aqueous 0.1 M LiCl solution. The potential was reversed after the first reductive process and the scan rate was 0.1 V s^{-1}.

It can be seen that the presence of a supporting electrolyte within the oil deposit has a profound effect on the resulting voltammetry of TCBQ. The current|voltage profiles are now characterised by two reductive peaks (as opposed to the single reductive peak observed in the case of unsupported droplets) and two small corresponding oxidative

back peaks. Furthermore, as the TBuAP concentration increases, the first reductive peak shifts versus less negative potential meanwhile the second reductive peak shifts versus more negative potential so that the potential separation between the two reductive peaks increases as the droplets are made more and more conductive.

Voltammograms were also recorded for the supported droplets (with 2 M TBuAP) when the potential was reversed after the first reductive process (figure 11.11 (b)). In this case, the ratio anodic to cathodic peak current was found to be ca. 1 and the signal was found to decrease only slightly upon continual redox cycling. Furthermore, a scan rate dependence study reveals that the first cathodic peak scales linearly with the scan rate and the peak-to-peak separation relative to the first reductive wave increases with scan rate, from 20 mV at 0.05 V s^{-1} to 200 mV at 1 V s^{-1}. Hence, the two reductive peaks can be attributed to the reduction of TCBQ to the radical anion $TCBQ^{-\bullet}$ and to the dianion $TCBQ^{2-}$, respectively, as observed in homogeneous solution of BN (*vide supra*).

Next we examine the electrochemical behaviour of supported TCBQ microdroplets immersed in an aqueous solution containing 0.1 M TPeACl. Overlaid in figure 11.12 are the responses obtained in the absence and in the presence of 2 M TBuAP in the oil phase.

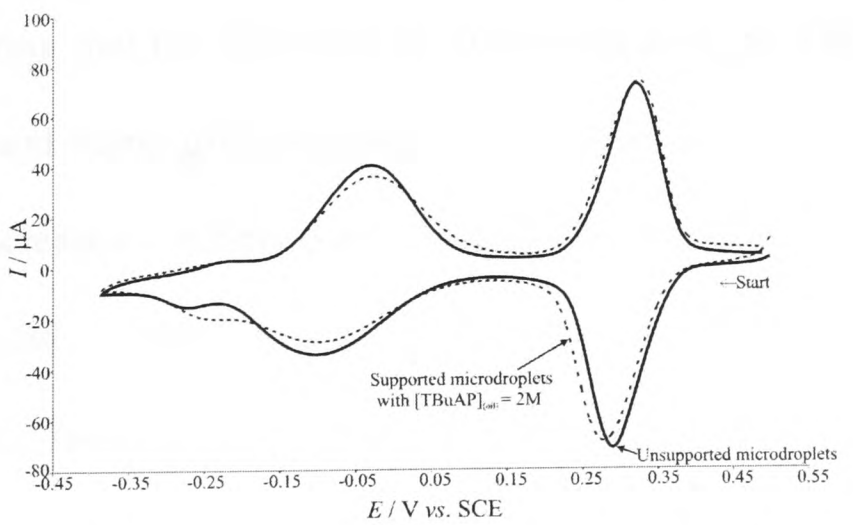


Figure 11.12: Cyclic voltammograms (0.1 V s^{-1}) for the reduction of 1 nmole unsupported microdroplets of TCBQ deposited onto a bppg electrode immersed in aqueous 0.1 M TPeACl. Also overlaid the corresponding voltammogram obtained when 2 M TBuAP supporting electrolyte is present in the organic phase.

No substantial change in the peaks appearance or in the peak shape are observed. Hence, addition of a nonpartitioning hydrophobic electrolyte such at TBuAP to the oil phase causes no change in the reduction of the immobilised microdroplets of TCBQ when 0.1M TPeACl is dissolved in the aqueous phase. Thus, it can be inferred that the insertion of the $TPeA^+$ cation is unaffected by the addition of an electrolyte in the oil phase.

However, when the supporting electrolyte dissolved in the aqueous phase still contains a more hydrophilic inserting cation than $TPeA^+$ the addition of a hydrophobic salt (i.e., TBuAP) to the oil phase microdroplets results in an anomalous and more difficult to explain voltammetric behaviour. In figure 11.13 (a), (b) and (c) are overlaid the first four current|voltage profiles obtained for the reduction of TCBQ microdroplets immersed in 0.1 M TBuACl in the absence and in the presence of 0.1, 1 and 2 M TBuAP, respectively, in the oil phase. It can be seen that, as the TBuAP concentration in the oil phase increases, the reductive peak moves versus more negative potential and the anodic counterpart of the voltammograms is almost lost as the droplets are made more conductive. The response from the $TCBQ/TCBQ^{-\bullet}$ couple is stable upon continual potential cycling. The fact that it is more difficult to reduce TCBQ as the resistance within the droplets decreases, is, at first, surprising. However, this might be explained considering that the reduction of TCBQ occurs upon $TBuA^+$ insertion, the latter being more and more difficult process to occur as the TBuAP concentration in the oil phase is increased. Alternatively, it might be suggested the electroneutrality within the oil deposit is maintained by expulsion of the perchlorate anion into the aqueous phase. The fact that perchlorate anion is toward the hydrophobic end of the Hofmeistrer scale, might account for the observed stretched voltammograms (i.e, perchlorate anion must be "dragged" out the oil phase into the aqueous phase).

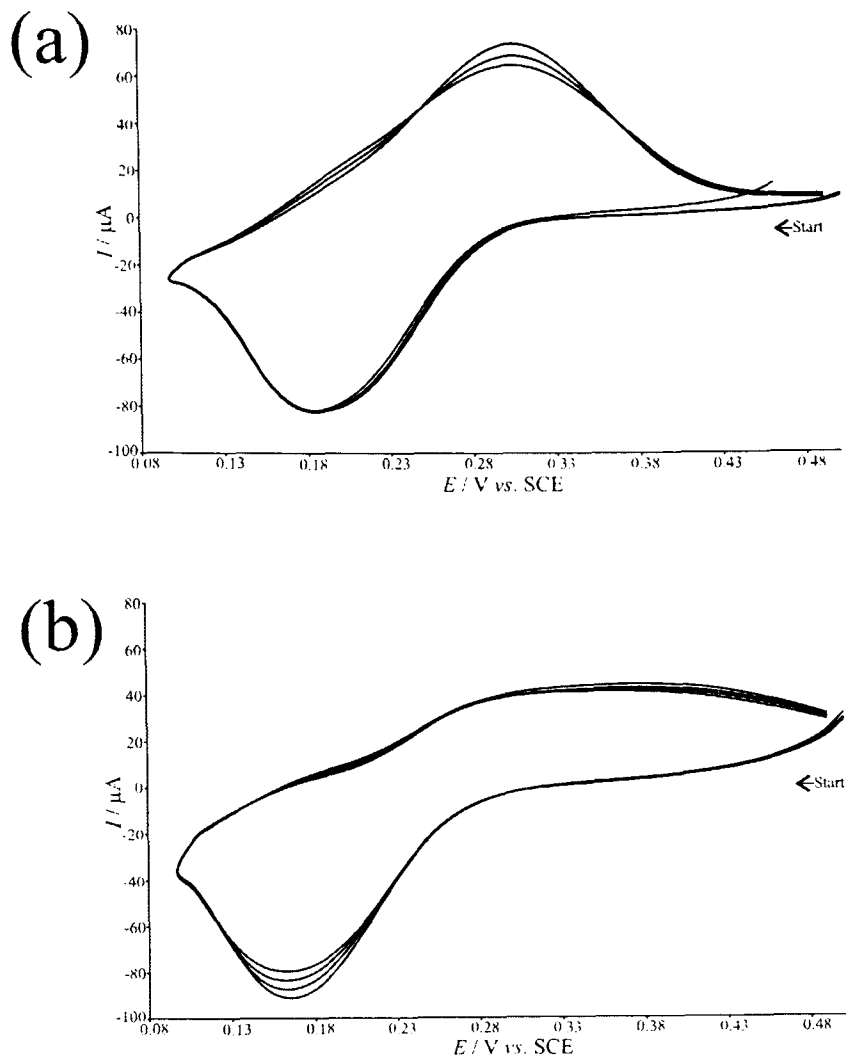


Figure 11.13: The effect of increasing the concentration of TBuAP in the oil phase on the response of TCBQ microdroplets in aqueous 0.1 M TBuACl solutions: (a) [TBuAP](oil) = 0.1 M, (b) [TBuAP](oil) = 1 M and (c) [TBuAP](oil) = 2 M. The scan rate is 0.1 V s^{-1} and overlaid in each figure are the first four scans obtained.

11.4 Photochemically Induced Electrocatalytic Processes

11.4.1 Photochemical Reduction of the Anaesthetic Gas Halothane within Femtolitres Droplets Containing TCBQ Deposit

Halothane (2-bromo-2-chloro-1,1,1-trifluoroethane, $CF_3CHClBr$) is a fluorinated hydrocarbon, liquid at room temperature and was the first satisfactory non-flammable inhalation anaesthetic agent introduced in the fifties [61]. Its use as an anaesthetic

rapidly spread worldwide because it proved to be effective and clinically safe. However, the use of halothane in clinical anaesthesia has nowadays declined due to the availability of alternative volatile anaesthetic agents (ie., isoflurane, $CHF_2OCHClCF_3$, enflurane, CHF_2OCF_2CHClF, sevoflurane, $[CH_2FOCH(CH_3)_2]$, and desflurane ($CHF_2OCHFCH_3$)) which have more desirable properties. These newer agents have significantly lower blood-gas solubilities, allowing greater control over induction and elimination of anaesthesia, lower metabolism and therefore reduced hepatic toxicity and also a reduction in undesirable cardiac effects [61]. Halothane is nevertheless still used in undeveloped countries because of its low cost and high anaesthetic potency.

This section examines the mediated reduction of halothane by the photochemical excited radical anion of TCBQ ($TCBQ^{\bullet -*}$) as a possible application of this type of modified electrode for the analytical detection of the anaesthetic gas.

It has been shown that TCBQ adsorbs UV light maximally at around 300 nm as a result of a π-π^* transition [62] and the corresponding anion radicals $TCBQ^{\bullet -}$ absorb light in both the UV and visible ranges [62,63], with a maximum at wavelengths around 325 nm.

We have considered the reduction of microdroplets of TCBQ immobilised on bppg electrode and immersed in aqueous solution containing 0.1 M TPeACl. The voltammograms recorded in the dark were consistent with the reversible insertion of the $TPeA^+$ as given in equation (11.5) above.

In the absence of halothane and when the electrode was potentiostated at +0.15 V (*vs.* SCE) only tiny reductive photocurrents [64] were observed on illumination at wavelengths in the range $300 < \lambda < 700$ nm at both the bppg naked and the TCBQ-modified bppg electrode. However, on the introduction of halothane to the aqueous phase, large reductive photocurrents were observed upon illumination. Figure 11.14 shows a typical reductive phototransient observed for 1 nmol TCBQ deposited

on a bppg electrode potentiostated at +0.15 V (*vs.* SCE) and immersed in 0.1 M TPeACl containing 10 mM halothane upon illumination.

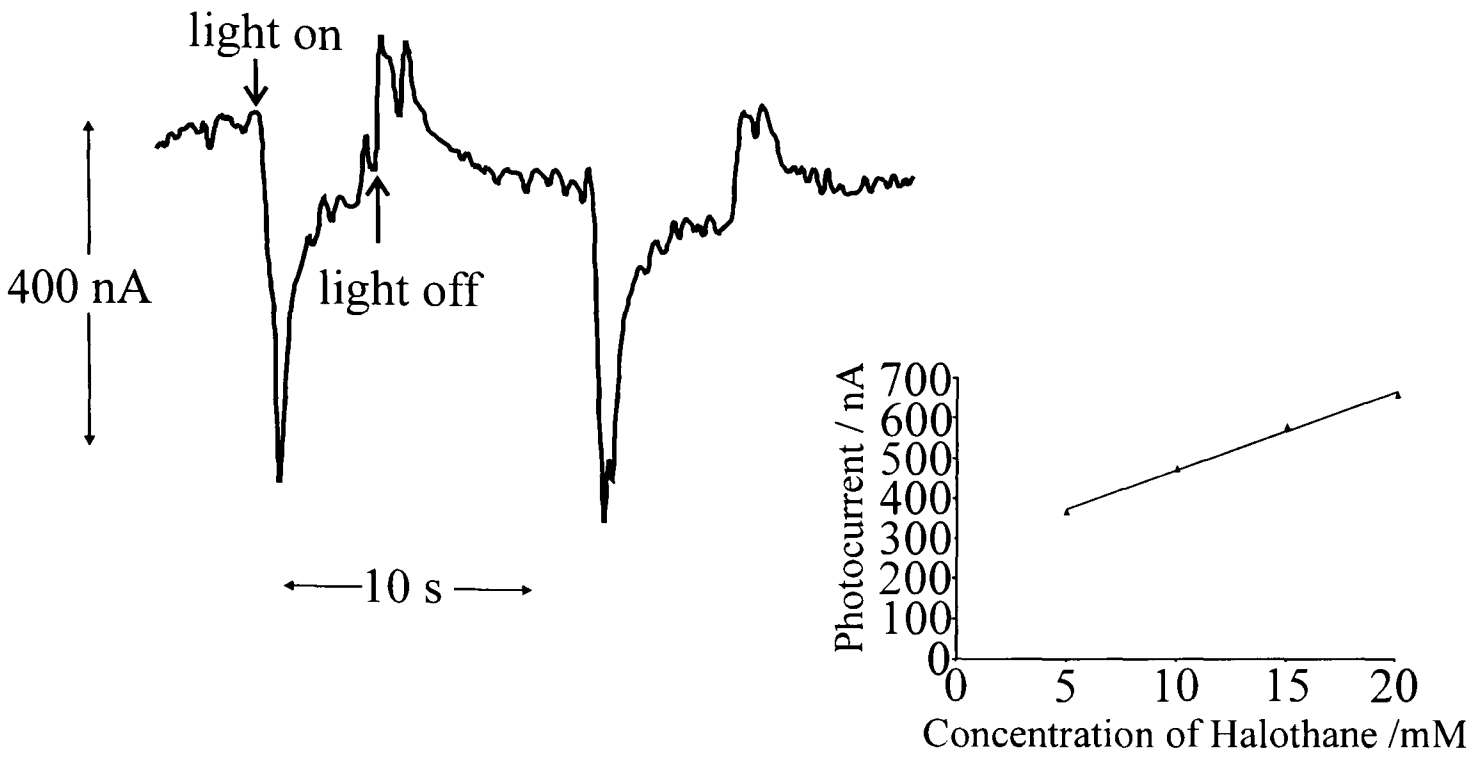


Figure 11.14: A typical reductive phototransient observed for 1 nmol TCBQ deposited on a bppg electrode potentiostated at +0.15 V (*vs.* SCE) and immersed in 0.1 M TPeACl containing 10 mM halothane with illumination by a white lamp with wavelengths in the range 300-700 nm.

The photocurrents recorded when halothane is added to the aqueous phase are much greater than in the TCBQ-only solution (typically ca. 400 nA for 1 nmol of TCBQ immobilised at the bppg, when 10 mM halothane is present in the aqueous phase) and a plot of reductive photocurrent against halothane concentration was found to be linear between 5 and 20 mM halothane (see insert graph figure 11.14). Given the earlier work of Compton *et al.* [16,63] and of Robertson *et al.* [65] and considering that the non-mediated photoelectrochemical reduction of halothane can be ruled out owing to the large negative potential required for halothane reduction in aqueous solution [66-68], the following reaction mechanism is proposed:

$$TCBQ(oil) + e^- \rightarrow TCBQ^{\bullet -}(oil) \qquad (11.9)$$

$$TCBQ^{\bullet -}(oil) + h\nu \rightarrow TCBQ^{\bullet -*}(oil) \qquad (11.10)$$

$$TCBQ^{\bullet -*}(oil) + CH_3CHClBr(aq) \rightarrow TCBQ + CH_3CHClBr^{\bullet -}(aq) \qquad (11.11)$$

$$CH_3CHClBr^{\bullet -}(aq) \rightarrow products \qquad (11.12)$$

Upon illumination, a charge–transfer process between photoexcited $TCBQ^{\bullet -*}$ and halothane equation (11.11) takes place to regenerate the parent TCBQ molecule, the discharge of which at the electrode surface gives rise to an increase in the reductive current. However, as the irradiation continues, the concentration of halothane present in the droplets at the three phase-boundary decreases leading to a fall of the current. The mediated electron transfer process given in equation (11.11) is likely irreversible owing to the reported ease of bromide loss from the halothane radical anion, $CH_3CHClBr^{\bullet -}$(equation (11.12)).

The donation of an electron from the photoexcited $TCBQ^{\bullet -*}$ molecules to those of halothane could either occurs at the interface between the two immiscible liquids (as suggested in the above scheme) or proceeds within the microdroplets deposit as a result of the liphophilicity of halothane, and hence its partitioning and possible diffusion within the microdroplets [39].

11.5 Conclusion

The electron transfer properties of TCBQ were investigated in both homogeneous and heterogeneous media. For the homogeneous study, the electrochemical reduction of TCBQ was carried out in different aprotic solvents (namely: benzonitrile (BN), N,N-dimethylformamide (DMF), propylcyanide (PrCN) and dimethylsulfoxide (DMSO)) and revealed two successive one-electron reductions according to a quasi-reversible EE mechanism. For the heterogeneous study, cyclic voltammetry with basal plane pyrolytic graphite electrodes modified with microdroplets of benzonitrile/TCBQ was employed. The droplets were found to be randomly dispersed with a degree of overlapping and average diameters of 5 μm giving the microdroplets individual volumes of ca. 33 fL. The redox processes within the electrically insulating microdroplets were shown to be very sensitive to the nature and concentration of ions

in the surrounding aqueous phase as, in order to retain electroneutrality within the unsupported oil phase, electric field-induced migration of ions likely occurs during the Faradaic current flow. Depending on the lipophilicity of the aqueous electrolyte cation uptake into or electrochemical generated anion expulsion from the organic phase containing the electroactive specie TCBQ was induced electrochemically. Alkali metal cation uptake into the microdroplet environment was not observed. However less hydrophilic tetraalkylammonium cations NR_4^+ (R^+= Bu and Pe) inserted. Proton insertion into the oil phase was also shown to occur as the current|voltage shifted to more positive potentials, making the reductive process more facile, as the pH of the buffer solution was decreased. The higher efficiency of proton insertion as compared with Group I cations insertion was explained in terms of the formation of strong O-H covalent bonds which outweighs the ion phase transfer thermodynamics.

The cross-phase electron transfer across the benzonitrile|water interface was examined when the TCBQ microdroplets were purposely made conductive by addition of a hydrophobic, nonpartitioning electrolyte in the oil phase. Again, the resulted voltammetry was found to change depending on the identity and concentration of the salt dissolved in the surrounding aqueous environment.

The method of immobilising microdroplets of TCBQ onto the surface of a bppg electrode and then investigating the electrochemical reduction when the electrode is placed in aqueous electrolyte solutions has given new insights into the redox chemistry of TCBQ because, in contrast to the case of its reduction in homogeneous media, the redox conversion of TCBQ in the form of microdroplets requires the uptake or expulsion of ions dictated by the requirements of electroneutrality. Hence, this study has provided new data on the nature of the processes occurring at the liquid|liquid interface involved in the reduction of microdroplets containing dissolved TCBQ.

Finally, the possibility of photochemical redox catalysis at TCBQ microdroplets was examined. On the introduction of halothane to the aqueous phase, large reductive photocurrent were observed on illumination at wavelength 300-700 nm, as a result of a charge–transfer process between photoexcited $TCBQ^{\bullet -*}$ molecules and those of halothane which hints at the possibility of using this type of modified electrode for potential photoelectroanalytical applications.

11.6 Chapter 11 References

[1] D. Giovanelli, T. J. Davies, Jiang Li, T. G. J. Jones, R. G. Compton, *PCCP* **2004**, *6*, 3889.
[2] A. M. Bond, J. B. Cooper, F. Marken, D. M. Way, *J. Electroanal. Chem.* **1995**, *396*, 407.
[3] F. Marken, R. D. Webster, S. D. Bull, S. G. Davies, *J. Electroanal. Chem.* **1997**, *437*, 209.
[4] Q. Fulian, J. C. Ball, F. Marken, R. G. Compton, A. C. Fisher, *Electroanalysis* **2000**, *12*, 1012.
[5] J. C. Ball, F. Marken, Q. Fulian, J. D. Wadhawan, A. N. Blythe, U. Schroder, R. G. Compton, S. D. Bull, S. G. Davies, *Electroanalysis* **2000**, *12*, 1017.
[6] N. Terui, K. Nakatani, N. Kitamura, *J. Electroanal. Chem.* **2000**, *494*, 41.
[7] C. Shi, F. C. Anson, *J. Phys. Chem. B* **1998**, *102*, 9850.
[8] C. Shi, F. C. Anson, *Anal. Chem.* **1998**, *70*, 3114.
[9] C. Shi, F. C. Anson, *J. Phys. Chem. B* **1999**, *103*, 6283.
[10] C. Shi, F. C. Anson, *J. Phys. Chem. B* **2001**, *105*, 8963.
[11] C. Shi, F. C. Anson, *J. Phys. Chem. B* **2001**, *105*, 1047.
[12] T. D. Chung, F. C. Anson, *Anal. Chem.* **2001**, *73*, 337.
[13] U. Schroeder, J. Wadhawan, R. G. Evans, R. G. Compton, B. Wood, D. J. Walton, R. R. France, F. Marken, P. C. B. Page, C. M. Hayman, *J. Phys. Chem. B* **2002**, *106*, 8697.
[14] B. A. Brookes, T. J. Davies, A. C. Fisher, R. G. Evans, S. J. Wilkins, K. Yunus, J. D. Wadhawan, R. G. Compton, *J. Phys. Chem. B* **2003**, *107*, 1616.
[15] T. J. Davies, B. A. Brookes, A. C. Fisher, K. Yunus, S. J. Wilkins, P. R. Greene, J. D. Wadhawan, R. G. Compton, *J. Phys. Chem. B* **2003**, *107*, 6431.
[16] J. D. Wadhawan, A. J. Wain, A. N. Kirkham, D. J. Walton, B. Wood, R. R. France, S. D. Bull, R. G. Compton, *J. Am. Chem. Soc.* **2003**, *125*, 11418.
[17] J. D. Wadhawan, R. G. Evans, R. G. Compton, *J. Electroanal. Chem.* **2002**, *533*, 71.
[18] F. Scholz, S. Komorsky-Lovric, M. Lovric, *Electrochem. Commun.* **2000**, *2*, 112.
[19] S. Komorsky-Lovric, M. Lovric, F. Scholz, *J. Electroanal. Chem.* **2001**, *508*, 129.
[20] S. Komorsky-Lovric, M. Lovric, F. Scholz, *Collect. Czech. Chem. Commun.* **2001**, *66*, 434.
[21] V. Mirceski, F. Scholz, *J. Electroanal. Chem.* **2002**, *522*, 189.
[22] F. Scholz, R. Gulaboski, K. Caban, *Electrochem. Commun.* **2003**, *5*, 929.
[23] F. Marken, R. G. Compton, C. H. Goeting, J. S. Foord, S. D. Bull, S. G. Davies, *Electroanalysis* **1998**, *10*, 821.
[24] F. Marken, A. Blythe, R. G. Compton, S. D. Bull, S. G. Davies, *Chem. Commun.* **1999**, 1823.
[25] T. J. Davies, C. E. Banks, B. Nuthakki, J. F. Rusling, R. R. France, J. D. Wadhawan, R. G. Compton, *Green Chem.* **2002**, *4*, 570.
[26] A. J. Wain, N. S. Lawrence, P. R. Greene, J. D. Wadhawan, R. G. Compton, *PCCP* **2003**, *5*, 1867.
[27] A. J. Wain, J. D. Wadhawan, R. G. Compton, *ChemPhysChem* **2003**, *4*, 974.
[28] A. J. Wain, J. D. Wadhawan, R. R. France, R. G. Compton, *PCCP* **2004**, *6*, 836.
[29] S. Komorsky-Lovric, K. Riedl, R. Gulaboski, V. Mirceski, F. Scholz, *Langmuir* **2002**, *18*, 8000.
[30] S. Komorsky-Lovric, K. Riedl, R. Gulaboski, V. Mirceski, F. Scholz, *Langmuir* **2003**, *19*, 3090.
[31] R. Gulaboski, V. Mirceski, F. Scholz, *Electrochem. Commun.* **2002**, *4*, 277.
[32] R. Gulaboski, K. Riedl, F. Scholz, *PCCP* **2003**, *5*, 1284.

[33] R. Gulaboski, F. Scholz, *J. Phys. Chem. B* **2003**, *107*, 5650.
[34] R. Gulaboski, V. Mirceski, F. Scholz, *Amino Acids* **2003**, *24*, 149.
[35] F. Scholz, R. Gulaboski, V. Mirceski, P. Langer, *Electrochem. Commun.* **2002**, *4*, 659.
[36] V. Mirceski, R. Gulaboski, F. Scholz, *Electrochem. Commun.* **2002**, *4*, 813.
[37] G. Bouchard, A. Galland, P.-A. Carrupt, R. Gulaboski, V. Mirceski, F. Scholz, *PCCP* **2003**, *5*, 3748.
[38] C. E. Banks, T. J. Davies, R. G. Evans, G. Hignett, A. J. Wain, N. S. Lawrence, J. D. Wadhawan, F. Marken, R. G. Compton, *PCCP* **2003**, *5*, 4053.
[39] J. D. Wadhawan, A. J. Wain, R. G. Compton, *ChemPhysChem* **2003**, *4*, 1211.
[40] J. D. Wadhawan, R. G. Evans, C. E. Banks, S. J. Wilkins, R. R. France, N. J. Oldham, A. J. Fairbanks, B. Wood, D. J. Walton, U. Schroeder, R. G. Compton, *J. Phys. Chem. B* **2002**, *106*, 9619.
[41] C. Ruessel, W. Jaenicke, *J. Electroanal. Chem.* **1984**, *180*, 205.
[42] C. Ruessel, W. Jaenicke, *J. Electroanal. Chem.* **1986**, *199*, 139.
[43] A. Desbene-Monvernay, P. C. Lacaze, J. E. Dubois, A. Cherigui, *J. Electroanal. Chem.* **1987**, *216*, 203.
[44] A. Desbene-Monvernay, P. C. Lacaze, A. Cherigui, *J. Electroanal. Chem.* **1989**, *260*, 75.
[45] K. Sasaki, T. Kashimura, M. Ohura, Y. Ohsaki, N. Ohta, *J. Electrochem. Soc.* **1990**, *137*, 2437.
[46] F. Marken, C. M. Hayman, P. C. Bulman Page, *Electrochem. Commun.* **2002**, *4*, 462.
[47] M. Rudolph, D. P. Reddy, S. W. Feldberg, *Anal. Chem.* **1994**, *66*, 589A.
[48] R. S. Nicholson, *Anal. Chem.* **1965**, *37*, 1351.
[49] W. R. Fawcett, *Langmuir* **1989**, *5*, 661.
[50] Y. Zhang, Y. Moriguchi, M. Hashimoto, K. Sakata, *Anal. Sci.* **2001**, *17*, 675.
[51] J. F. Coetzee, *Recommended Methods for Purification of Solvents and Tests for Impurities*, Pergamon Press, Oxford, **1982**.
[52] M. Gomez, I. Gonzalez, F. J. Gonzalez, R. Vargas, J. Garza, *Electrochem. Commun.* **2003**, *5*, 12.
[53] R. L. Mc Creery, in *Electroanalytical Chemistry* (Ed. A. J. Bard), Marcel Decker, New York **1990**, pp. 221-374.
[54] Y. Marcus, *Pure Appl. Chem.* **1983**, *55*, 977.
[55] M. Yamanuki, T. Hoshino, M. Oyama, S. Okazaki, *J. Electroanal. Chem.* **1998**, *458*, 191.
[56] T. Hoshino, M. Oyama, S. Okazaki, *J. Electroanal. Chem.* **1999**, *472*, 91.
[57] M. Oyama, R. D. Webster, M. Suarez, F. Marken, R. G. Compton, S. Okazaki, *J. Phys. Chem. B* **1998**, *102*, 6588.
[58] T. D. Chung, S. K. Kang, J. Kim, H.-s. Kim, H. Kim, *J. Electroanal. Chem.* **1997**, *438*, 71.
[59] N. Gupta, H. Linschitz, *J. Am. Chem. Soc.* **1997**, *119*, 6384.
[60] J. Q. Chambers, in *The Chemistry of the Quinonoid Compounds* (Eds: S. Patai, Z. Rappoport), John Wiley & Sons, Chichester **1988**, pp. 719-757.
[61] C. E. W. Hahn, *Analyst* **1998**, *123*, 57R.
[62] R. G. Compton, R. A. W. Dryfe, *Progress in Reaction Kinetics* **1995**, *20*, 293.
[63] R. G. Compton, J. C. Eklund, A. C. Fisher, A. M. Waller, *J. Chem. Soc. Faraday Trans.* **1990**, *86*, 2951.
[64] A. Modestov, O. Lev, G. Jenny, *J. Electroanal. Chem.* **1999**, *476*, 118.
[65] P. K. J. Robertson, B. R. Eggins, *J. Chem. Soc. Perkin Trans.* **1994**, 1829.
[66] W. J. Albery, C. E. W. Hahn, W. N. Brooks, *Brit. J. Anaesthesia* **1981**, *53*, 447.
[67] A. R. Mount, M. S. Appleton, W. J. Albery, D. Clark, C. E. W. Hahn, *J. Electroanal. Chem.* **1992**, *334*, 155.
[68] A. R. Mount, D. Clark, *J. Electroanal. Chem.* **1994**, *367*, 175.

Part 5: "Electrochemistry at High Temperatures and Pressures"

Aims and Scope:

As discussed in Part 1, Chapter 3, the determination of H_2S is of constant concern in many fields because of its release in a wide range of industrial processes. Awareness, detection and monitoring of H_2S are particularly important within the oilfield industry. H_2S can enter drilling muds from subsurface formations and can also be released by sulfate-reducing bacteria present in stored muds posing problems to the drilling crews on the rig.

In this last section of the thesis two of the analytical protocols for sulfide detection outlined in Part 1 will be studied at elevated temperatures with a view to developing a sensor for H_2S which could measure up to the adverse conditions of elevated temperatures typically found in the oilfield industry.

First however, a review of the literature was undertaken detailing the electrochemical experiments conducted at high temperature (Chapter 12) and high pressure (Chapter 13).

Chapter 12: "High-Temperature Electrochemistry: a Review"

High-temperature electrochemistry remains a relatively unexplored field of research, although in recent years significant developments have been made. This chapter details the main experimental methods and approaches to heating an electrochemical system under both isothermal and non-isothermal conditions, and gives an insight into the experimental and electroanalytical results obtainable under such conditions. It has been shown that the promotion of mass transport at high temperatures, through diffusion or convection, often results in increased current signals. This increase benefits electroanalytical measurements by lowering detection limits. High temperatures also usefully enhance the sensitivity of systems with sluggish kinetics. A review paper based on this chapter has been published in Electroanalysis [1].

12.1 Introduction

High-temperature electrochemistry is a relatively unexplored area of chemistry which has, however, in the past few years, seen renewed interest. Although the vast majority of electrochemical experiments are conducted at room temperatures (typically between 20 – 25 °C) there are both fundamental, analytical and technological reasons for wanting to extend this temperature range [2].

Technologically, the capital-intensive power generating industries such as nuclear, fossil-fueled and geothermal systems utilize high-temperature aqueous solutions and therefore knowledge of the corrosion kinetics and thermodynamic properties of high-temperature aqueous solutions in these environments is essential. An understanding of many geothermal processes also requires knowledge of high-temperature aqueous systems [3]. Development of thermodynamic properties of electrolytes at elevated temperatures offer advantages in the technologies of high-temperature fuel cells and high energy batteries [4,5].

Fundamentally, there are many reasons for studying systems at elevated temperatures. Accurate thermodynamic data is frequently derived from room temperature electrochemical measurements. Yet it is the temperature dependent electrode processes that are often of interest themselves, these include: standard electrode potentials, activity coefficients, Debye-Hückel equation (and its extensions) constants, conductance measurements, equilibrium constants, diffusion activation constants, the electrodeposition of metals and alloys, the variation of electrocapillary maxima and the points of zero charge [2]. Furthermore, detailed mechanistic studies have been reported in which dramatic changes in mechanisms can occur over a relatively small temperature range [6] and new reaction pathways, e.g intercalation processes, become accessible at elevated temperature [7].

Perhaps one of the reasons for the lack of previous interest in high-temperature electrochemistry is that it is an area fraught with experimental problems. The main issue when carrying out a high-temperature electrochemical experiment is how to heat the system. In aqueous solutions one cannot generally heat an electrolyte solution above 100 °C isothermally without the use of an autoclave; the latter has been predominantly used in corrosion studies and earlier works [2,6-24]. Other workers have developed alternative solutions to this problem. For instance, Goldfarb *et al.* developed a high-temperature and high-pressure cell made from titanium in which all the necessary electrodes and probes were housed to investigate the electrochemical properties of supercritical trifluoromethane [25]. For temperature ranges within the normal boiling point of the aqueous electrolyte simpler isothermal setups are possible, many of which involve adaptations of cell designs used at room temperature such as water-jacketed or double-walled cells used in conjunction with a water bath heated to the appropriate temperature [26-28]. Coles developed a novel cell design which is isothermally heated by an electronically controlled heat gun [29-31].

Isothermal systems are particularly important for measuring thermodynamic properties and, to a lesser extent, in kinetic studies. Gründler, Baranski and others have developed and utilized non-isothermal methods of heating electrodes; these include hot-wire techniques using AC heating [32-49], hot-microdisc techniques using very high frequency AC heating [50], microwave radiation [27,51-57] or radio frequency radiation [29,30,58]. The fundamental aspects of these heated electrodes are detailed in Section 12.4.1.

12.2 Heating Methodologies

There are two different approaches to heating a solution; isothermal and non-isothermal methods. A review of the literature reveals that autoclaves are the

most well developed isothermal strategy and are discussed next. Diverse strategies used in electrochemical studies to achieve non-isothermal heating methods are developed in later sections.

12.2.1 Isothermal Heating Methods

(a) Autoclaves

High-temperature studies create a number of problems for electrochemists, which have to be carefully considered and overcome. Experiments that use autoclaves require a design that utilizes materials that can safely withstand both the temperatures and pressures reached during an experiment. The nature of the vessel lining may be critical if the solutions are not to be contaminated by dissolution of the vessel walls. Furthermore, all electrical connections for electrodes and sensors must be sufficiently insulated so as to only measure the electrode processes under study. Specialist techniques for overcoming problems such as solution agitation, observation, pressure seals and electrical connections are discussed elsewhere [2]. Only a few aspects will be discussed in this chapter.

A number of vessel liners have been developed for use at high temperature and pressure. The most common materials are stainless steel and certain nickel alloys such as Nimonic, Hastelloy and Monel [2], but even these are susceptible to corrosion and cracking in hydroxide and chloride containing solutions. Ceramic, glass and plastic liners are also available, but they tend to be soluble in certain high-temperature solutions whilst plastics such as PTFE have been known to give off unidentified gases at temperatures between 200 °C and 300 °C [2,59]. All isothermal electrochemical measurements, particularly those of thermodynamic parameters, taken above the normal boiling point of the solvent of interest require pressure to prevent bubble formation on the electrode surface and subsequent boiling. Almost all of these

experiments utilize autoclaves to simultaneously provide controlled heating and pressure. A standard autoclave set-up is detailed in figure 12.1, which shows the basic features of the design.

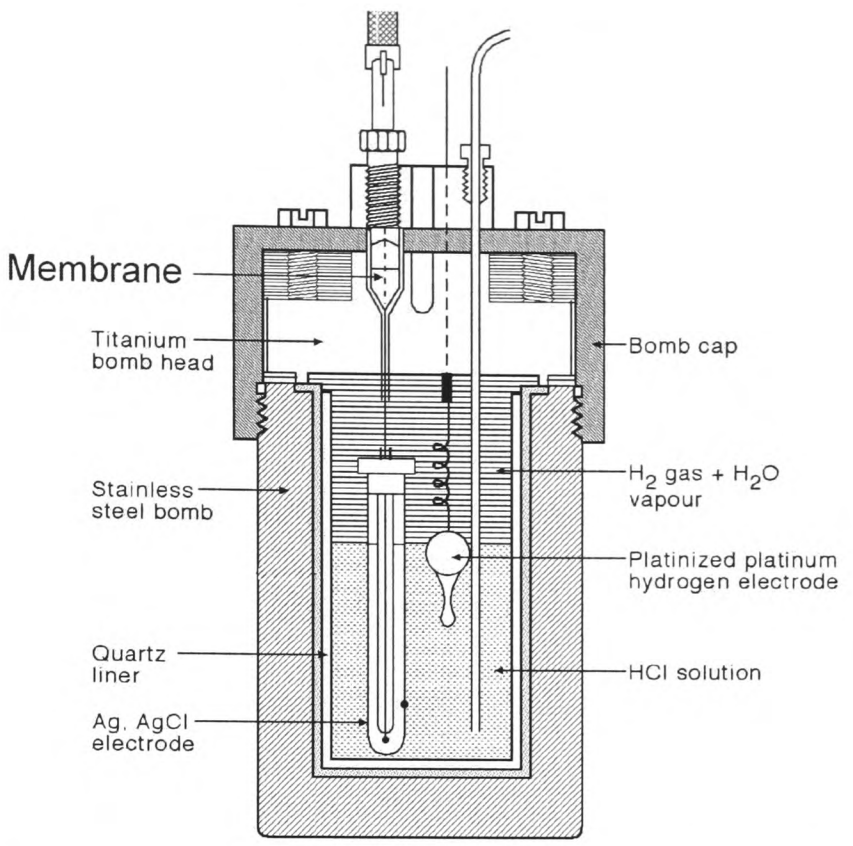


Figure 12.1: An early (1960) autoclave used by Lietzke showing all the main features of an autoclave (adapted from ref. [2]).

One field where autoclaves are heavily utilized concerns corrosion studies, especially in the power industry (nuclear and conventional). Such industries use boiling-water reactors (BWR) and the corrosion properties of the stainless steels and alloys that make up their reactor systems at the elevated temperatures are important. Autoclaves have therefore been used to study the effects on corrosion pitting and stress cracking of temperature, pH, dissolved oxygen and hydrogen concentrations on various stainless steels used in BWRs at temperatures up to 300°C [7,18,60,61].

Bard *et a.l* used autoclaves to study electrochemical systems in supercritical fluids such as water, acetonitrile and liquid ammonia, and spent a great deal of effort designing and perfecting cells capable of withstanding the extreme conditions used. They produced an extensive series of more than ten papers detailing their findings in supercritical fluids up to 345°C [62-71]. The solution to the problem of lining their

autoclaves has been to use passivated Titanium as most other metals, Pyrex, quartz and glass all dissolve in supercritical water [70].

Another pioneering group, which extensively uses autoclaves is that of Abbot *et al.* who produced a series of papers, focused on electrochemistry in supercritical non-polar solvents such as difluoromethane [72-75], carbon dioxide [76], and other assorted fluorinated hydrocarbons [77].

Autoclaves have been utilized to allow for the automated measurements of zeta-potential and point of zero charge of some transition metal oxides. This was done with the aim of understanding the products of corrosion after their decomposition in reactor systems [10]. Cowan and Kaznoff [17] have also developed a system for measuring high-temperature corrosion kinetics at temperatures greater than 932 ^{o}C in supercritical aqueous solutions.

A survey of the literature reveals that other applications of autoclave heating include: the development of ceramic membranes for high-temperature pH measurements [8], electrochemical measurements in liquid and super-critical CO_2 [78], the invention of an autoclave system that incorporates a scanning-tunneling microscope for use in high-temperature electrochemical STM experiments [12] and studying the electrochemistry of various molten salts [19,79,80]. The details of novel reference electrode designs [6,7,9,15,16,21,22,24,81] and the measurement of analytical data [81] will be discussed later in sections 12.3 and 12.4, respectively.

(b) Other isothermal heating methodologies

For high-temperature studies that do not exceed the boiling point of the solvent, or approach temperatures where bubble formation becomes a serious problem, the use of generic cell designs used for room temperature studies is widespread. The most common system of heating is using a water bath set at the specified temperature, and

either immersing the whole apparatus in the water bath, or using double-walled water jacketed cells through which water of the desired temperature circulates [2].

A second isothermal method of heating developed by Coles is the electronically controlled heat gun shown in figure 12.2 [29, 30].

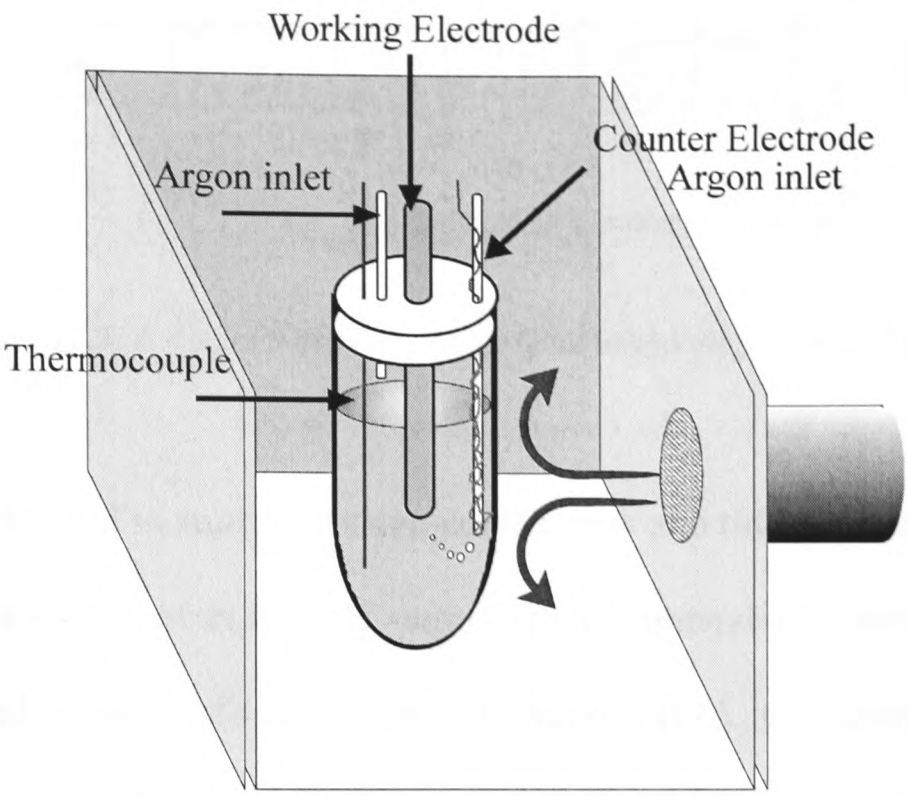


Figure 12.2: A diagram showing the heated air gun cell design [29].

This method allows for greater precision in controlling the temperature of the solution to within a tenth of a degree. The small cell volume, *ca.* 8 cm^3 is advantageous, although its use is limited to microelectrode studies. The heat gun is controlled electronically, the cell is placed in the path of the airflow inside an insulated box, through which all the necessary electrodes, and gas inlet and outlet ports are housed. A thermocouple positioned just in front of the cell wall nearest the heat gun is used to measure the air temperature and an independent digital thermometer can be placed directly in the solution prior to carrying out the experiment to calibrate the measured air temperature to the actual solution temperature [29,30,58].

A third isothermal heating method is a variable temperature flow cell design, which uses microdisc electrodes, is shown in figure 12.3 [82]. In this case, heat is supplied by means of a coiled manganin wire wrapped around the glass cell with a PID

control system. The tube-like design creates a large surface area allowing rapid and accurate heating of the cell to within 0.1 °C at 30 °C rising to 0.3 °C at 90 °C.

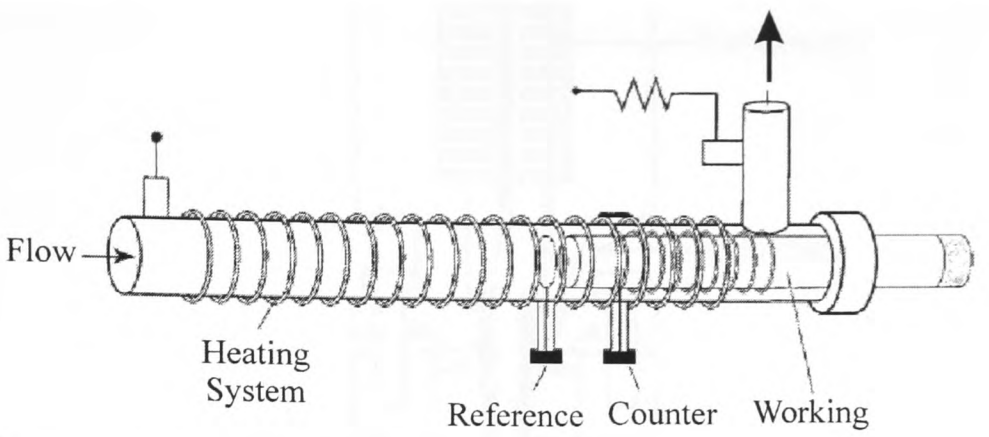


Figure 12.3: A diagram showing the variable temperature flow-cell design [82]

This set-up was used to study diffusion coefficients and diffusion activation energies at elevated temperatures of N,N,N',N'-tetramethyl-p-phenylenediamine ,TMPD, in both acetonitrile and water, tris(4-bromophenyl)amine, TBPA, in acetonitrile and ferrocene in both acetonitrile, MeCN, and N,N-dimethylformamide, DMF, [81]. The cell design allowed studies to be carried out on the electrochemistry of o-bromonitrobenzene in DMF and 9-chloroanthracene in acetonitrile where electron transfer is coupled with homogeneous reaction kinetics; both radical anions are known to undergo carbon-halide bond cleavage reactions.

Corti *et al.* have designed a novel high-temperature wall-jet cell containing a jet impinging on an electrode surface as shown in figure 12.4 [15]. Characterization of this cell was achieved by studying simple one-electron redox couples, namely $Fe(CN)_6^{3-/4-}$ and $Fe(H_2O)_6^{2+/3+}$ and two-electron, two-proton hydroquinone/quinone redox system. This design allowed diffusion coefficients of $Fe^{2+/3+}$ species to be measured, in sulfate solutions, at temperatures up to 142 °C. However, it was found that the diffusion coefficients were strongly affected by speciation, especially at higher temperatures.

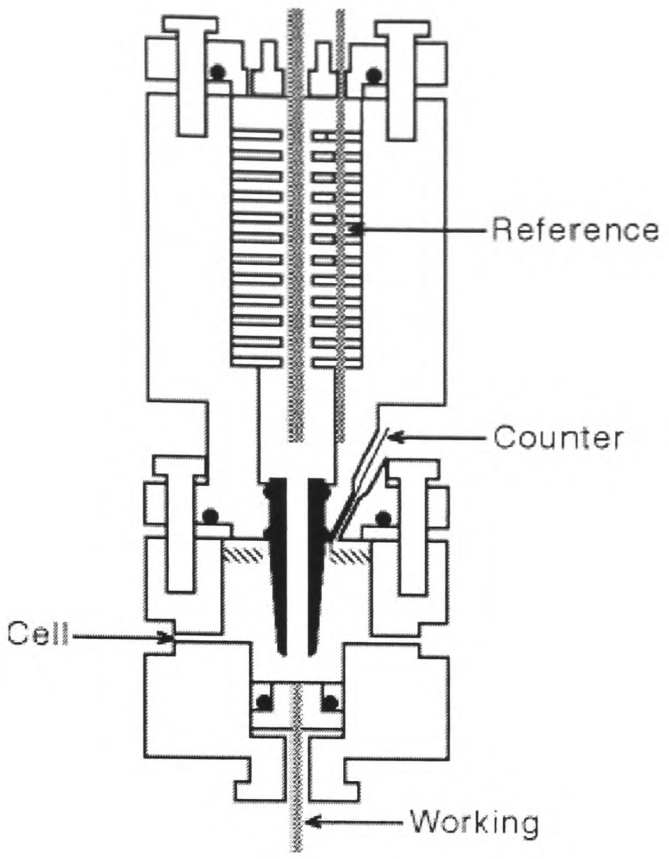


Figure 12.4: A diagram showing the high-temperature wall-jet cell used by Corti *et al* [15].

12.2.2Non-isothermal Heating Methods

(a) AC heating of wires

'Hot-Wire Electrochemistry' was first pioneered by Gründler and co-workers in 1993 and is based upon the use of AC heating to heat up thin wires or metallic layers [38] as shown in figure 12.5.

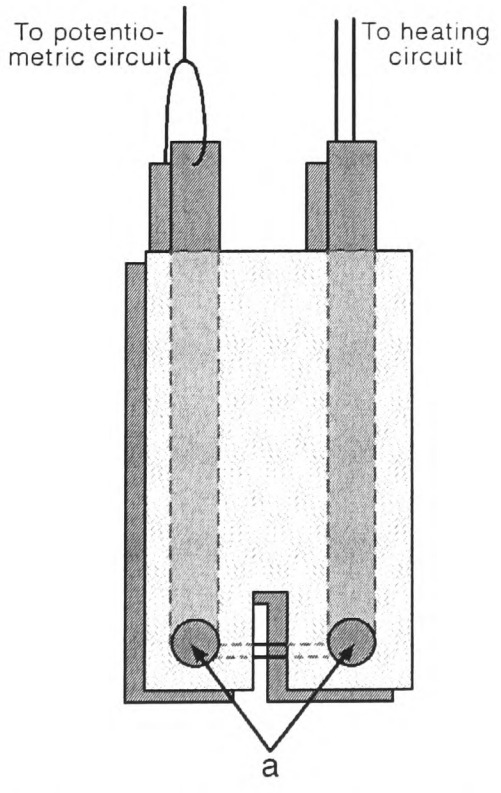


Figure 12.5: Schematic of the heated-wire electrode set-up [38].

Two different techniques were developed. The first method is continuous heating [32-39,42-49] of the electrode such that the temperature remained constant over a period of time. The second is known as Temperature Pulse Voltammetry (TPV) [40,41]. This is in essence analogous to Differential Pulse Voltammetry (DPV) but, unlike DPV, TPV utilizes pulsed temperature jumps to enhance signal-to-background ratios, and can be especially useful for redox systems with sluggish kinetics [38]. A second advantage of TPV is its ability to reach temperatures well above the normal boiling point of the solvent without the need for autoclaving. This is because a local hot spot is formed at the electrode surface (*vide infra*) and without the bulk solution being heated. This has allowed temperatures as high as 250 °C to be reached in aqueous solutions, whilst supercritical conditions for various other solvents are now being investigated [40,41]. AC heating has several advantages compared to other heating methods such as autoclaving or microwave irradiation (*vide infra*), as the instrumentation is not sophisticated, the energy demands are low and miniaturization is possible to the extent that the technique can easily be used outside of the laboratory.

The working electrode is heated using alternating current AC rather than direct current DC because when DC flows along a metal wire in solution iR drop occurs and acts as an additional polarization of the electrode and brings about unwanted Faradaic effects. This is analogous to that faced in conductance measurements where AC bridges are employed rather than DC bridges except that the iR drop in the case of DC heating could be of a few orders of Volts for metallic electrodes and tens of Volts for carbon fibre electrodes [38]. In order to overcome these Faradaic effects very high AC frequency (typically 100 kHz) is utilized.

A study into the temperature profiles for both the continuous heating and TPV techniques has been reported [33,38,40]. These were modeled at a continuously heated wire using a finite element simulation package (FIDAP^{TM}, version 8.52 Fluent Europe

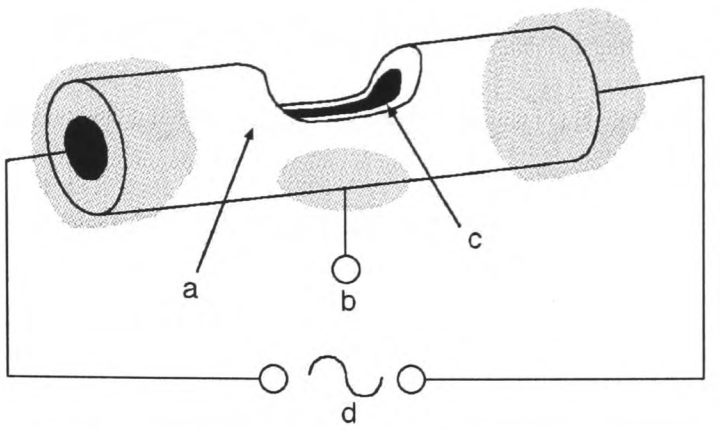
Ltd., Sheffield, UK, http://www.fluent.com) [33]. The results obtained showed that the temperature profile expands into the solution much faster and further than any concentration profile generated electrochemically. Therefore, temperature gradients inside any given diffusion layer are shallow and this implies that the electrochemical reactions proceed under almost uniform temperature conditions.

It was also shown that in aqueous solution the Nernst diffusion layer approaches a constant thickness when the temperature difference between the temperature of the bulk solution and the electrode surface temperature exceeds 30 K [38]. As a result, diffusion-limited current values of cyclic voltammetry and chronoamperometry can be evaluated directly. It was found that changing the solvent system led to an alteration in the value of the Nernst diffusion layer due to differences in viscosity and thermal conductivity. However, the fundamental result of a limiting fixed size diffusion layer still held true for both aqueous and non-aqueous solvent systems.

The use of TPV has allowed the study of near supercritical conditions in a variety of solvents [40]. In this case the heating pulses are generally of the order of milliseconds followed by rapid cooling process and therefore the heat transfer is modeled by conduction processes only, with no convective contributions [40]. The fact that the heating time is only a few milliseconds prevents bubble formation as this requires some form of nucleation process which occur at a restricted rate on the millisecond timescale. Boiling of the bulk solution is also avoided as only a region of solution *ca.* 0.15 mm from the electrode surface is heated.

These two AC heating methods have been successfully applied to a variety of situations including the reduction of dissolved oxygen on platinum electrodes [48], the oxidation of small organic molecules [49], and the development of stripping protocols for various systems, including arsenic (V) and hybridization of nucleic acids using a

carbon paste electrode shown in figure 12.6 [34,36,42,43,46,47]. The methods have been used in wide ranging fields such as bio-inorganic chemistry [44] to near-critical and super-critical fluids in electrochemical sensor technology [41].



(a) FEP plastic tube; (b) working electrode contact;
(c)Carbon paste; (d) a.c heating device.
Shadowed areas represent epoxy resin.

Figure 12.6: A cut-away diagram of a carbon paste heated-wire electrode design [34].

Baranski developed this technology further by applying it to heated microdisc electrodes [50]. Instead of using AC excitation waveforms with a frequency of 100 kHz, Baranski applied a waveform of much higher frequency (100 kHz - 2 MHz), which resulted in lower heating currents [50]. As the solution adjacent to the electrode generally has a much higher resistance than the electrode material itself, the heating effect is produced in a hot spot in front of the electrode surface. The size of the hot-spot is dependent on the size of the microelectrode itself and can be less than 1 μm in diameter [50]. Since the volume of the hot spot is so small, superheating of the solution is possible without the onset of bubble formation and boiling. A 25 μm disk electrode was reported to have been held at temperatures as high as 225 °C in an aqueous solution for greater than 15 minutes [50]. Baranski used this technique to investigate the effect of increased temperature on diffusion and mass transport processes for the model redox system $Ru(NH_3)_6^{2+/3+}$, including Soret diffusion contributions, using cyclic voltammetry, and linear sweep voltammetry under steady-state limiting current conditions [50].

(b) Microwave heating of microelectrodes

In the last two decades the interest and development in applying microwave technology to chemistry has grown, yet it was not until 1998 that it was applied to electrochemical systems. Marken *et al.* [27] pioneered the electrochemistry cell in which a high intensity microwave radiation is applied to platinum microelectrodes as illustrated in figure 12.7.

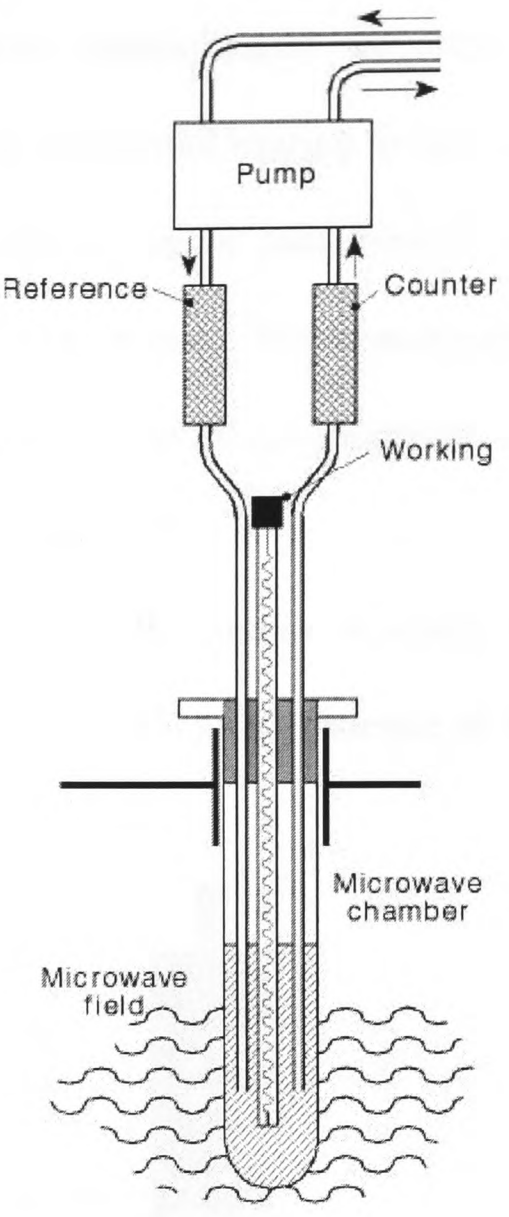


Figure 12.7: A schematic of the microwave heated cell design [27].

The resulting currents obtained were found to be enhanced during irradiation for the methylene green [27], ferrocyanide/ferricyanide and $Ru(NH_3)_6^{3+/2+}$ model redox systems. The enhanced currents were Faradaic in nature [51]. The redox potential of the ferrocyanide/ferricyanide couple was found to shift by of -1.53 mV K^{-1} [51]. This redox system was subsequently used as a model process to calibrate the local temperatures reached, at the electrode surface, for any given intensity of radiation for a specific electrode size and material [27,51-57].

It was found from pulsed microwave experiments that limiting current enhancement occurred only during the microwave pulse, but after the pulse the steady state limiting current very rapidly returned to that observed at room temperature. It was concluded that the effect of microwave heating was considerably more intense at the electrode solution interface compared to the effect upon the bulk solution [51]. Local temperatures can exceed the boiling point of the solvent, with temperatures of 150 °C reported in aqueous systems [53] and 118 °C in acetonitrile [57]. The heating process itself was investigated using the two-electron reduction of the methyl viologen

di-cation in aqueous solution [52]. It was shown that microwave activation achieves (i) high temperatures in the vicinity of the electrode, (ii) thermal desorption of deposits on the electrode surface and (iii) limiting currents approximately an order of magnitude higher than those achieved by conventional isothermal heating to the same temperature. To explain these results a simple physical picture of Joule heating was modeled using a finite element simulation (FIDAP^{TM}) procedure. This demonstrated the presence of a "hot-spot" in the diffusion layer just in front of the electrode with convective mass transport as shown schematically in figure 12.8.

The presence of this hot spot has been used in mechanistic studies in which the reaction process under investigation has an activation barrier [57]. An example of this type of reaction process is the ECE electrodehalogenation of p-bromonitrobenzene, o-bromonitrobenzene and m-iodonitrobenzene in DMF and acetonitrile [57].

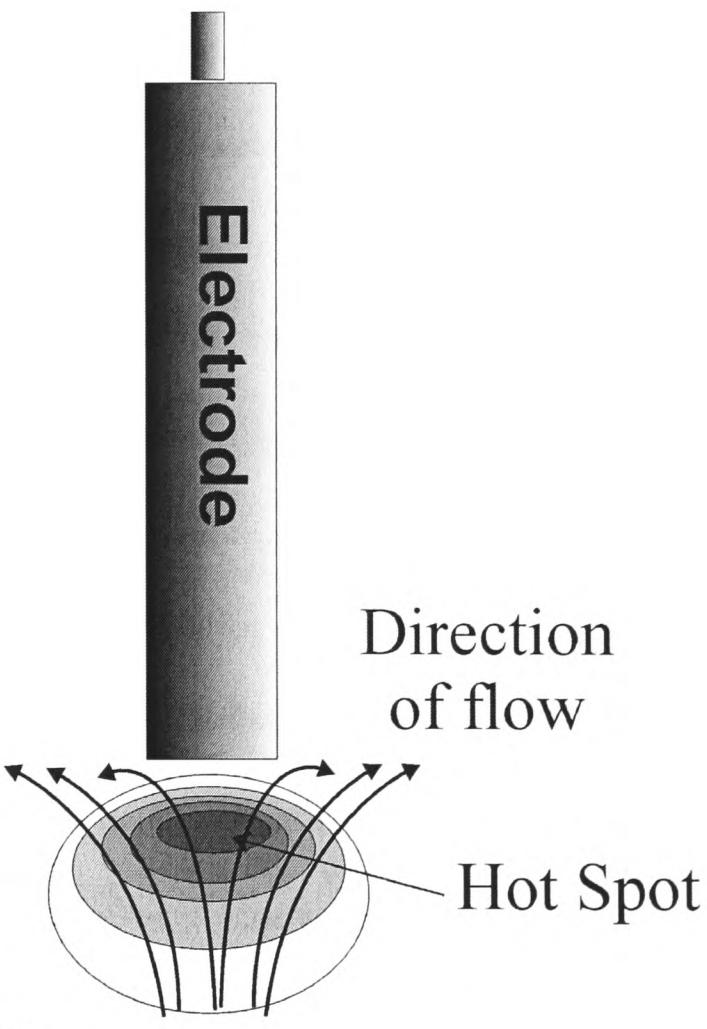


Figure 12.8: A schematic illustrating the hot-spot region formed under microwave irradiation [57].

Microwave radiation has also been applied for analytical purposes in the anodic stripping detection of cadmium both in the absence [53] and presence of surfactants [56]. The results showed that thermal activation by microwave irradiation strongly enhanced the accumulation process but not the stripping process thereby allowing lower detection limits to be achieved. Furthermore, the use of mercury deposited on platinum electrodes allowed temperatures greater than 150 °C to be achieved without the aqueous solution showing signs of boiling [53]. Other analytical systems which have been investigated using microwave activation include PbO_2 deposition and stripping on glassy carbon and boron doped

diamond electrodes [54] and Pb detection in river sediments [55]. In the former case, it was found that the deposition of PbO_2 at room temperature suffered from sluggish electro-kinetics, however this deposition process was greatly enhanced under thermal activation to the extent that they became almost diffusion controlled.

(c) Radio frequency heating

Radio frequency heating is a commonly used heating methodology in industry and is based on the induction of eddy currents within a metal slab causing the heating effect [58, 83]. The technique has since been adapted to form an electrochemical methodology for heating a solution the cell design of which is given in figure 12.9.

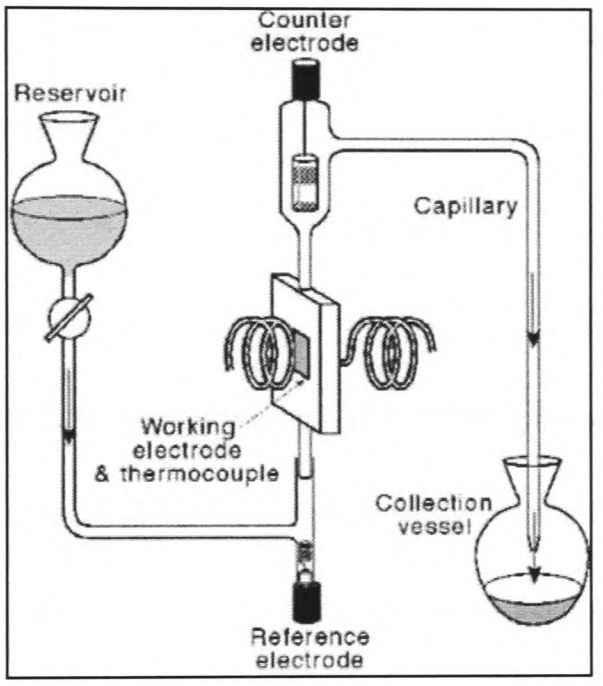


Figure 12.9: A diagram showing a channel flow-cell heated by radio-frequency radiation [26].

This consists of a 8 MHz radio frequency radiation generator for heating a 40 μm Pt foil working electrode. This is placed in a channel flow cell [58] with a reference electrode placed upstream and a counter electrode placed downstream.

It was shown that, to a good approximation, the electrochemical process occurs in a region where there is little significant temperature gradient in the solution phase adjacent to the electrode. However, along the electrode surface, there is a well-defined temperature profile [58] which is in contrast to the microwave radiation. Since the radio frequency channel operates under non-isothermal conditions the relationship

between the limiting current and the flow rate cannot be described by an analytical equation. Instead, a finite element program (FIDAP^{TM}) is used which takes into account the complex heat and mass flow, as well as subsequent differences in viscosity and diffusivity in the different regions of the flow-cell [29,30,58].

The RF-Cell to date was initially been used to investigate the simple one and two electron reactions in aqueous solutions of N,N,N',N'-tetramethyl-p-phenylenediamine (TMPD), N,N-dimethyl-p-phenylenediamine (DMPD), and hydroquinone [29] and diffusion activation parameters were determined from Arrhenius and Stokes-Einstein plots. It has since been utilized to study the diffusion activation parameters of similar compound along with the ECE reaction of m-iodonitrobenzene in acetonitrile [29].

12.3 Reference Electrodes

There are two main approaches to measuring electrode potential at high temperatures. The first is to use an *Internal Reference Electrode*. This is incorporated into the high-temperature cell and operates at the same temperature and pressure as the rest of the electrochemical cell. The second method is to use an *External Reference Electrode*. In this case, the electrode operates at room temperature and is linked to the cell by an electrolyte bridge, which can be set at the same pressure as the rest of the cell. Each method has its own drawbacks and advantages.

Internal reference electrodes suffer inconsistencies with stability due to problems of solubility and hydrolysis of the electrode material. Consequently, they must be carefully chosen to match the conditions being used in the cell. External reference electrodes do not have this problem and the choice of reference is less important as the temperature is maintained at 25 °C. However, if the external reference electrode is not pressure balanced, then pressure and thermal gradients form

across the thermal junction. These gradients give rise to irreversible streaming and thermal diffusion effects, both of which contribute to the measured potential difference and therefore means that external reference electrodes cannot be used as thermodynamic standards. They do however produce a stable, reproducible reference potential that can be calibrated using a suitable standard at various temperatures which can be related back to the thermodynamic scale [3,84].

Thermal liquid junction potentials (TLJP) have been investigated at temperatures greater than 300 °C by Lvov and MacDonald [81] in the development of their Flow-Through External Pressure Balanced Reference Electrode (*vide infra*). These liquid junction potentials are suppressed at room temperature by using a high concentration of KCl or another supporting electrolyte with roughly equal ionic transport numbers, which is only effective if the test solution is dilute. At high temperature, and especially in super-critical solutions phase, this is not the case and separation of highly concentrated solutions may occur. The transport numbers for Na^+ and Cl^- rapidly converge at temperatures greater than 300 °C and after the supercritical boundary and emulate those of KCl [81]. The dissociation constant for NaCl has been well documented over a temperature range up to 450 °C [81]. These two facts make the use of NaCl of considerable interest in high-temperature reference electrode internal solutions and allow theoretical calculations of the liquid junction potential (E_{TLJP}) using equation (12.1) below:

$$E_{TLJP} = \frac{-RT}{F} \sum_i \int \frac{t_i}{z_i} d \ln a_i \qquad (12.1)$$

where R, T and F have their usual meanings t is the transport number, a is the activity and z_i the valence of the i^{th} ion. The summation is taken over all ions and the integral is evaluated over the dimensions of the junction [81]. Lvov and MacDonald have used

this method and found that the magnitude of the TLJP is of the same order of magnitude as at room temperature [81].

High-temperature reference electrodes are described in more detail in reviews by D. de G. Jones and H. G. Masterson "Techniques for the Measurement of Electrode Processes" [2] and by Digby D. Macdonald "Electrochemistry of Metals in Aqueous Solution" [3].

The Standard Hydrogen Electrode (SHE) has been commonly used in fuel cell investigations [5]. However, the main drawback with using the SHE is that in some high-temperature aqueous solutions the platinum can dissolve [2].

Glass Electrodes (GE) used for high-temperature pH measurements have a limited life span at temperatures in the range of 180-200 °C [2] as GE is attacked on the glass membrane by the aqueous solution and therefore a loss in stability may occur.

The use of secondary electrodes has two general problems. The first is the solubility of the salt used as the reference. Under ideal conditions, this should be as low as possible. Unfortunately, the solubility tends to increase as the temperature of the cell is increased even for the sparingly soluble salts generally used in the secondary reference electrode. The second possible problem is hydrolysis of the salt at elevated temperatures, in particular for mercurous electrodes and metal/metal electrodes.

The main secondary electrode used is the Ag/AgCl electrode, which usually has a low solubility and is resistant to hydrolysis [2, 92, 93]. It is therefore extensively used as a high-temperature reference electrode even at temperatures as high as 225 °C [2]. However, when the Ag/AgCl electrode is used for the determination of thermodynamic data in hydroxide solutions at temperatures above about 160 °C the results should be treated with a degree of caution as significant hydrolysis of the AgX ($X= Cl^-$ or Br^-) to Ag_2O occurs under these conditions [3].

The Ag/AgCl/KCl reference system is also prevalent in corrosion studies [15-17] and several designs have been introduced. Figure 12.10 (a) shows a new internal reference electrode design for an autoclave system used to test steel corrosion in BWRs [7] whilst figure 12.10 (b) depicts another Ag/AgCl reference electrode based on a solid polymer electrode [9].

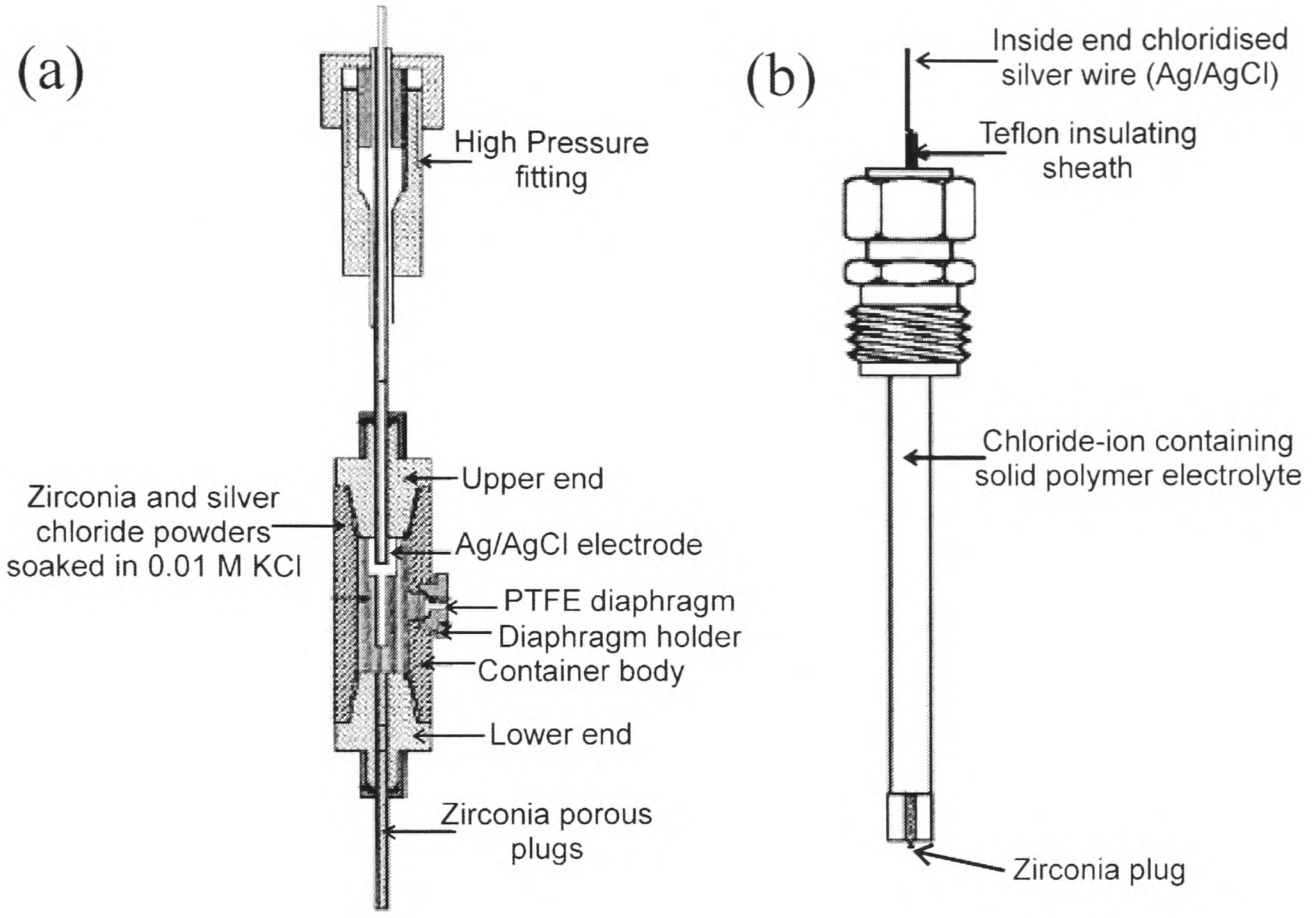


Figure 12.10: (a) An internal reference electrode design as used in an autoclave [7] and (b) a solid polymer internal reference electrode developed for use in corrosion studies [9].

Other applications of the Ag/AgCl reference electrode include studies into radio frequency heating of a flow cell [58], the measurement of the standard potentials of the Cl_2/Cl^- couple at temperatures up to 80 °C [94] and potentiometric studies of the thermodynamic properties of cadmium (II) chloride complexation [15].

The flow-through external pressure balanced reference electrode (FTEPBR) uses a Ag/AgCl system and was first characterized by Lvov and MacDonald to evaluate liquid junction potentials of high-temperature KCl from NaCl data and carry out pH measurements in sub and supercritical aqueous solvents up to 400 °C [22,24,81]. The same two authors also developed a novel reference system for assessing pH studies using three component systems such as [HCl + NaCl + H_2O] and

[$NaOH + NaCl + H_2O$] in varying densities against the FTEPBR Ag/AgCl electrode [21].

Despite the Ag/AgBr electrode having a lower solubility than the Ag/AgCl system at higher temperatures [93] and allowing thermodynamic data to be obtained up to 200 °C [2,93,95], the Ag/AgCl reference electrode is the most prevalent Ag/AgX reference electrode in the literature. This may be attributable to the fact that the Ag/AgBr electrode was reported to incur greater errors at higher temperatures than the Ag/AgCl electrode [2,96,97]. Ag/Ag_2SO_4 electrode have also been used in 0.05 - 0.5 M sulfuric acid at temperatures up to 250 °C [2, 98].

Mercury/Mercurous compound electrodes, such as the saturated calomel reference and the mercury/mercurous sulfate electrodes have an upper limit of about 100 °C [99] due to the onset of the disproportionation reaction:

$$Hg_2Cl_2 \rightleftharpoons Hg + HgCl_2 \qquad (12.2)$$

which is rapidly followed by hydrolysis to form HgO. To overcome this problem the Hg/Hg_2O electrode is used which has been shown to be thermodynamically valid up to 150 °C [3].

Metal electrodes, exemplified by the common use of the platinum pseudo reference electrode, have been used up to 300 °C [2,100] but they require a large surface area. Other metal/metal compound electrodes such as Sb/Sb_2O_3 have been used over the temperature range 100 – 300 °C [2,101]. $Pb/PbSO_4$ and (Pt)-$PbSO_4$ have also been shown to be good reference electrodes up to 250 °C [2,202].

A comprehensive review of the thermodynamic data required for accurate electrode cell potential measurements at high-temperatures was carried out by Lietzke, who showed the most common electrodes are Ag/Ag_2SO_4, Hg/Hg_2SO_4, Hg/Hg_2Cl_2, Ag/AgCl, Ag/AgBr and $PbO_2/PbSO_4$ [2,103,104].

12.4 Kinetic and Analytical Applications

In this section the effects of temperature on mass transport and kinetic phenomena along with its use in a number of electroanalytical procedures are discussed.

12.4.1 Temperature Effects on Mass Transport Phenomena

A major effect of elevated temperature is to increase mass transport to an electrode surface through diffusion and convection. Recent work has focused on the temperature dependence of diffusion coefficients, activation energies of diffusion and activation energies of coupled homogenous chemical reactions such as bond cleavage. The two most prevalent equations relating diffusion data to temperature changes are the Arrhenius (12.3) and the Stokes-Einstein equations (12.4):

$$\ln D = \ln D_o - \frac{E_A}{RT} \qquad (12.3)$$

$$D = \frac{k_B T}{6\pi\eta r} \qquad (12.4)$$

where D is the diffusion coefficent, E_A is the activation energy, R is the molar gas constant, T is the temperature, k_B is the Boltzmann constant, η is the solvent viscosity and r is the hydrodynamic radius. A plot of ln D against $1/T$ can be used to obtain the activation energy of diffusion for a given species, or a plot of D against T/η can be used to determine the effective radius of a species in solution.

Diffusion coefficients are readily obtained from steady state or transient current measurements. Theoretical expressions have been developed for most commonly used electrochemical methods from which diffusion data can be extracted. A popular methodology is to employ microelectrodes where the limiting current expression is given by equation (12.5) below (see Chapter 1):

$$I_{Lim} = 4nFDc_{\infty}r \qquad (12.5)$$

where n represents the number of electrons transferred, F is the Faraday constant/C mol^{-1}, D is the diffusion coefficient/cm^2 s^{-1}, c_∞ is the bulk concentration of the solution/mol cm^{-3} and r is the radius of the electrode/cm.

If the microelectrode is of a known radius, then limiting currents can be measured for various and known concentrations of the active species in solution at a given temperature. Under isothermal conditions plots of I_{lim} against c_∞ leads to a value for the diffusion coefficient at that temperature. The experiment can then be repeated at different temperatures and the resulting diffusion coefficients can be used to construct the Arrhenius plot.

However under non-isothermal conditions such at those employed by Coles *et al.* with the radio-frequency heating more complex modeling of the system is required to determine the diffusion activation parameters. In this case a finite difference modelling package (FIDAP™) capable of modeling the complex heat and mass flow, as well as taking into account the subsequent differences in viscosity and diffusivity in the different regions of the flow cell, was utilised. The modelling and diffusion coefficients were determined for $Ru(NH_3)_6^{3+}$, $Fe(CN)_6^{4-}$, N,N,N',N'-tetramethyl-p-phenylenediamine, N,N-dimethyl-p-phenylenediamine and hydroquinone in aqueous solution and N,N,N',N'-tetramethyl-p-phenylenediamine, ferrocene and tris(4-bromophenyl)amine in acetonitrile; the activation energy of diffusion of m-iodonitrobenzene in acetonitrile was measured as 7.4 kJ mol^{-1} [29,30,58].

Corti *et al.* used such procedures in the impinging wall-jet cell (Section 12.2.1) to determine the diffusion coefficients of $Fe^{2+/3+}$ species, in aqueous sulfate solutions, at temperatures up to 142°C [14]. In this case, equation (12.3) cannot be utilized due to the nature of the cell design in which a forced convection regime is applied.

Table 12.1 details the activation energies obtained for various redox systems under different heating regimes.

Table 12.1: *Comparison of diffusion constants at room temperature and activation energies of diffusion for redox systems under different heating methodologies. TMPD = N,N,N',N'-tetramethyl-p-phenylenediamine, $^{\S}Fe(Cp)_2$ = ferrocene/ferrocenium couple, E_A = Activation energy for diffusion.*

Redox couple and solvent	Heating Method	E_A / kJ mol^{-1}
$Fe(CN)_6^{4-}$/ H_20	Radio Frequency	13.0
$Fe(CN)_6^{4-}$/ H_20	Heat Gun	13.8
$Ru(NH_3)_6^{3+}$ / H_20	Radio Frequency	13.5
$Ru(NH_3)_6^{3+}$ / H_20	Heat Gun	13.8
TMPD/ H_20	Radio Frequency	18.0
TMPD / H_20	Heat Gun	16.1
TMPD/ H_20	Variable-Temperature Cell	19.0
TMPD/ Acetonitrile	Radio Frequency	9.0
TMPD/ Acetonitrile	Heat Gun	10.0
TMPD/ Acetonitrile	Variable-Temperature Cell	10.0
$^{\S}Fe(Cp)_2$ / Acetonitrile	Radio Frequency	7.0
$^{\S}Fe(Cp)_2$ Acetonitrile	Heat Gun	6.9
$^{\S}Fe(Cp)_2$ / Acetonitrile	Variable-Temperature Cell	6.9
$^{\S}Fe(Cp)_2$ / Acetonitrile	A.C. Heating	12.1

12.4.2 Effect of Temperature on Reaction Kinetics

The effects of temperature on heterogeneous electrode kinetic processes for both electron transfer reactions and ion transfer reactions are comprehensively reviewed by K. E. Heusler in "Influence of Temperature and Pressure on the Kinetics of Electrode Processes" [104] and are not discussed further here.

Coupled homogeneous chemical reactions, such as in an ECE reaction, are also dependant on temperature and this fact can be utilized to elucidate such information as the activation energy needed to drive the chemical step of the reaction. It can be foreseen that by increasing the temperature in cases where the chemical step is slow at room temperature would enhance the chemical step and as such provide a means of driving a reaction process through. This could have serious implications for both industrial and analytical processes. In order to obtain the activation energies of the chemical step, modeling of the system is required. Suitable programs for such analysis are Digisim^{TM} [106] or FIDAP^{TM} for isothermal or non-iosthermal calculations respectively and given known values of room temperature rate constants one can obtain a value for the activation energy of the chemical step.

Tsai *et al.* [57] applied microwave radiation to p-bromonitrobenzene, o-bromonitrobenzene and m-iodonitrobenzene in DMF in order to study the effect of temperature on electrodehalogenation process. Analysis of the voltammetric response at the elevated temperatures by FIDAP™ modeling allowed a value for the activation energy of C-I bond cleavage to be determined as 80 kJ mol^{-1} [57]. This reaction has also been studied using the radio-frequency radiation heating methodology. The results produced a reassuringly similar value of 80 ± 5 kJ mol^{-1} for the activation energy of the chemical step [30].

The use of microwave heating has been shown to help induce CE reaction type processes [53]. The detection of Cd^{2+} in an acetate buffer is impossible because of complexation of the Cd^{2+} by the acetate, so that Cd^{2+} can not be deposited at the electrode surface if anodic stripping voltammetry is attempted. The application of microwaves to the system has been found to dramatically aid in the determination of Cd^{2+} and can be attributed to the heating effects essentially labilising the Cd^{2+} acetate complex thereby liberating free Cd^{2+}, which can be detected at a mercury electrode [53].

12.4.3 Application of Temperature Effects to Electrochemical Analysis

The promotion of mass transport at high temperatures, through diffusion or convection, often results in increased current signals. If the level of background noise in the scan is not increased by the same magnitude as the current signal then this allows the benefits of using high-temperature electrochemistry in analysis, lowering detection limits and increasing the sensitivity of systems with sluggish kinetics.

In his hot-wire studies, Gründler found that the AC heating of the solution produced enhanced peak currents in the voltammograms which he applied to analytical problems such as the detection of heavy metals, including As (V) [36], Cd^{2+} and Pb^{2+}

[43] and mercury at a gold electrode [46]. In developing the hot-wire analytical technique Gründler looked at the effect of temperature on the kinetics of metal deposition on the surface of the electrode. He found that lead could be deposited anodically at the surface of a platinum electrode as lead dioxide and stripped cathodically [36]. In this case the deposit was insoluble in the electrode material and a nucleation overpotential was required [36]. It was found that the nucleation process was enhanced dramatically when heat was applied to the working electrode. In contrast, elemental arsenic is soluble in gold and a homogeneous alloy forms in the electrode [36]. A nucleation overpotential does not exist in this case, but even at room temperature, an underpotential deposition occurs. The effect of temperature on the kinetics of metal deposition and alloy formation was investigated, and for analytical detection methodologies where arsenate has to be reduced to its metallic state, enhanced redox kinetics and deposition were observed with increased temperature [36]. Not only is this useful for arsenic (V) detection, but the system can be considered as a model case for many other analytical problems. Many other important elements are soluble in gold, such as mercury, copper, bismuth and aluminium [36].

A comparison of the hot-wire technique with the rotating disc electrode was carried out with gold electrodes to further show the benefits of heating the electrode over the more conventional hydrodynamic systems. The study examined the deposition and stripping steps in the analysis and detection of Cu (II), Hg (II) and As (III) [34]. The reduction of these three analytes is fast and as such diffusion and/or convection should be rate determining. These experiments were carried out in order to determine whether convection is responsible for the increased mass transport, or whether the temperature dependence of the diffusion coefficient is the reason. It was found that heating during the stripping step for heavy metals actually decreased the analytical signal, on repetitive scans. This phenomenon was attributed to the fact that

at a heated electrode the material is deposited in different forms which can be oxidised more easily and as such an extremely enhanced diffusion process inside the electrode material would have a negative effect on the electrode behavior. However, due once again to enhanced deposition, the size of the peaks in the first scan increased at elevated temperatures and provided an enhancement in the analytical performance compared to that observed at a rotating disk electrode [34]. This is shown, for example, in the detection limit of Cu (II) which was 100 times lower at the heated wire electrode (10^{-9} mol L^{-1}) than for the rotating disc electrode (10^{-7} mol L^{-1}) [34].

Other examples of the heated microelectrode being utilised in analytical measurements have involved the examination of the effects of temperature on the structure of cytochrome *c* [44]. It was found that by increasing the temperature cytochrome *c* undergoes an unfolding of the protein structure. The technique has been further used in the detection of nucleic acids and in the control of DNA hybridization [47]. In the detection of trace amounts of nucleic acids, the application of higher temperatures during the deposition step again led to a 4-34 fold increase in the stripping signal, depending on the temperature applied to the microelectrode [47].

Current enhancement was also observed under microwave irradiation and the technique has been applied to the enhanced detection of lead in river sediment [55]. Detection limits of a mercury free method which utilises boron doped diamond electrodes, without microwave irradiation are reported as 1.0 μM and with microwave irradiation as 0.1 μM [55]. The detection of cadmium in the presence of surfactants such as Triton X is greatly enhanced by the application of microwave radiation [56].

A very recent application of high-temperature electrochemistry to solve an analytical problem is the development of a novel reagentless pH meter for use at temperatures as high as 70 °C [28]. In this methodology, carbon particles, chemically derivatized with anthraquinone, were immobilized on the surface of a basal plane

graphite electrode. The Nernstian response of the system to various pHs was observed in the voltammetry. Again, current enhancement was recorded in the voltammograms at high temperatures allowing accurate determination of the pH of aqueous solutions. It should be noted that there are difficulties in defining pH at elevated temperatures in different solutions and mixed solutions (organic/aqueous) due to the effects of temperature on the media. However these problems have been largely overcome with the measurement of pH according to the various IUPAC definitions which have been laid out over the years [107-111].

12.5 Conclusion

The above has shown that there is a variety of techniques available to the electrochemists wishing to carry out high-temperature electrochemical studies. These encompass cell designs from the simple thermally jacketed cells to the more advanced autoclave systems. Two conditions are used in electrochemical studies: isothermal conditions, where all three electrodes are maintained at a constant temperature, and non-isothermal conditions, where only the working electrode is heated. The non-isothermal conditions have utilized several diverse heating methodologies that include the use of radio frequency waves, microwaves and hot wire experiment. The merits of each technique have been assessed and the application of these methodologies to analytical problems has been discussed.

Finally, it has been shown that the enhanced mass transport at high temperatures, through diffusion or convection, often leads to increased current signals which benefit electroanalytical measurements by lowering detection limits.

In Chapter 14 it will be shown how the electrochemical oxidation of diethyl-p-phenylenediamine (DEPD) in DMF and its subsequent reaction with sulfide benefits from applying high temperatures to the solution. The effect of temperature on the

detection of sulfide at nickel oxide modified nickel (NOMN) electrodes in acidic media was also investigated and the results are detailed in Chapter 15.

12.6 Chapter 12 References

[1] G. G. Wildgoose, D. Giovanelli, N. S. Lawrence and R. G. Compton, *Electroanalysis*, **2004**, *16*, 421.

[2] D. D. G. Jones and H. G. Masterson, in *Advances in Corrosion Science and Technology*, Vol. 1, Plenum Press, **1970**.

[3] D. D. Macdonald, in *Modern Aspects of Electrochemistry*, Vol. 11, Plenum Press, **1975**.

[4] J. Barthel, R. Wachter, and H.-J. Gores, in *Modern Aspects of Electrochemistry*, Vol. 13, Plenum Press, **1979**.

[5] J. L. Sudworth, in *Electrochemical Power Sources: Primary and Secondary Batteries*, Peter Peregrinus, **1980**.

[6] B. E. Conway and D. P. Wilkinson, *Electrochim. Acta*, **1993**, *38*, 997.

[7] R. L. Cowan and A. I. Kaznoff, in *5th Int. Congr. Met. Corros.*, Natl. Assoc. Corros. Eng., Houston, Texas., USA, **1972**, p. 874.

[8] W. F. Bogaerts and A. A. Van Haute, *J. Electrochem. Soc.: Electrochem. Sci. Tech.* **1984**, *131*, 68.

[9] T. Fujii, J. C. Danko, Indig, M. E., J.-I. Takabayashi, Hishida, Mamoru., and K. Shimogori, Fukuzuka, T., Fujiwara, K., Tomari, H., in *Predictive methods for Assessing Corrosion Damage to BWR Piping and Steam Generators*, **1978**.

[10] S. Hettiarachchi and D. D. Macdonald, *J. Electrochem. Soc.*, **1984**, *131*, 2206.

[11] S. Hettiarachchi and D. D. Macdonald, *J. Electrochem. Soc.*, **1987**, *134*, 1307.

[12] P. Jayaweera, S. Hettiarachchi, and H. Ocken, *Colloids and Surfaces Physicochemical and Engineering Aspects*, **1994**, *85*, 19.

[13] S. N. Lvov, X. Y. Zhou, S. M. Ulyanov, and D. D. Macdonald, *Power Plant Chemistry*, **2000**, *2*, 5.

[14] Shkurankov, F. Endres, and W. Freyland, *Rev. Sci. Instr.*, **2002**, *73*, 102.

[15] L. N. Trevani, E. Calvo, and H. R. Corti, *Electrochem. Commun.*, **2000**, 2, 312.

[16] L. N. Trevani, E. Calvo, and H. R. Corti, *J. Chem. Soc. Faraday Trans.*, **1997**, *93*, 4319.

[17] D. A. Palmer, H. R. Corti, A. Grotewold, and K. E. Hyde, in *13th International Conference on the Properties of Water and Steam*, Toronto, **1999**, p. 736.

[18] R. L. Cowan and A. I. Kaznoff, *Corrosion, Houston*, **1973**, *29*, 123.

[19] V. Novoselova, V. A. Khokhlov, and V. Y. Shishkin, *Rasplavy*, **2000**, *200,* 16.

[20] S. N. Lvov and D. D. Macdonald, *Electrochem. Soc. Proc.*, **1997**, *39*, 746.

[21] S. N. Lvov, X. Y. Zhou, S. M. Ulyanov, and A. V. Bandura, *Chem. Geol.*, **2000**, *167,* 105.

[22] S. N. Lvov, X. Y. Zhou, and D. D. Macdonald, *J. Electroanal. Chem.*, **1999**, *463*, 146.

[23] G. R. Engelhardt, S. N. Lvov, and D. D. Macdonald, *J. Electroanal. Chem.*, **1997**, *429*, 193.

[24] S. N. Lvov and D. D. Macdonald, *J. Eectroanal. Chem.*, **1996**, *403*, 25.

[25] D. L. Goldfarb and H. R. Corti, *Electrochem. Commun.*, **2000**, *2,* 663.

[26] F. L. Qiu, R. G. Compton, F. Marken, S. J. Wilkins, C. H. Goeting, and J. S. Foord, *Anal. Chem.*, **2000**, *72*, 2362.

[27] R. P. Akkermans, S. L. Roberts, F. Marken, B. A. Coles, S. J. Wilkins, J. A. Cooper, K. E. Woodhouse, and R. G. Compton, *J. Phys. Chem. B.*, **1999**, *103*, 9987.

[28] G. G. Wildgoose, M. Pandurangappa, N. S. Lawrence, L. Jiang, T. G. J. Jones, and R. G. Compton, *Talanta,* **2003**, *60*, 887.

[29] M. J. Moorcroft, N. S. Lawrence, B. A. Coles, R. G. Compton, and L. N. Trevani, *J. Electroanal. Chem.*, **2001**, *506*, 28.

[30] B. A. Coles, M. J. Moorcroft, and R. G. Compton, *J. Electroanal. Chem.*, **2001**, *513*, 87.

[31] G. G. Wildgoose, D. Giovanelli, N. S. Lawrence, L. Jiang, T. G. J. Jones, and R. G. Compton, Electroanalysis, **2004**, 16, 337.

[32] A. Beckmann, A. Schneider, and P. Grundler, *Electrochem. Commun.*, **1999**, *1*, 46.

[33] A. Beckmann, B. A. Coles, R. G. Compton, P. Grundler, F. Marken, and A. Neudeck, *J. Phys. Chem. B*, **2000**, *104*, 764.

[34] G. U. Flechsig, O. Korbut, and P. Grundler, *Electroanalysis*, **2001**, *13*, 786.

[35] P. Grundler, T. Zerihun, A. Moller, and A. Kirbs, *J. Electroanal. Chem.*, **1993**, *360*, 309.

[36] P. Grundler and G. U. Flechsig, *Electrochim. Acta.*, **1998**, *43*, 3451.

[37] P. Grundler, *Fres. J. Anal. Chem.*, **1998**, *362*, 180.
[38] P. Grundler and A. Kirbs, *Electroanalysis*, **1999**, *11*, 223.
[39] P. Grundler, *Fres. J. Anal. Chem.*, **2000**, *367*, 324.
[40] P. Grundler and D. Degenring, *J. Electroanal. Chem.*, **2001**, *512*, 74.
[41] P. Grundler and D. Degenring, *Electroanalysis*, **2001**, *13*, 755.
[42] M. Jasinski, A. Kirbs, M. Schmehl, and P. Grundler, *Electrochem. Commun.*, **1999**, *1*, 26.
[43] M. Jasinski, P. Grundler, G. U. Flechsig, and J. Wang, *Electroanalysis*, **2001**, *13*, 34.
[44] T. Voss, P. Grundler, C. M. A. Brett, and A. M. O. Brett, *J. Pharm. Biomed. Anal.*, **1999**, *19*, 127.
[45] T. Voss, A. Kirbs, and P. Grundler, *Fres.J. Anal. Chem.*, **2000**, *367*, 320.
[46] J. Wang, P. Grundler, G. U. Flechsig, M. Jasinski, J. M. Lu, J. Y. Wang, Z. Q. Zhao, and B. M. Tian, *Anal. Chim. Acta.*, **1999**, *396*, 33.
[47] J. Wang, P. Grundler, G. U. Flechsig, M. Jasinski, G. Rivas, E. Sahlin, and J. L. L. Paz, *Anal. Chem.*, **2000**, *72*, 3752.
[48] T. Zerihun and P. Grundler, *J. Electroanal. Chem.*, **1996**, *404*, 243.
[49] T. Zerihun and P. Grundler, *J. Electroanal. Chem.*, **1998**, *441*, 57.
[50] S. Baranski, *Anal. Chem.*, **2002**, *74*, 1294.
[51] R. G. Compton, B. A. Coles, and F. Marken, *Chem. Commun.*, **1998**, 2595.
[52] F. Marken, Y. C. Tsai, B. A. Coles, S. L. Matthews, and R. G. Compton, *New J. Chem.*, **2000**, *24*, 653.
[53] F. Marken, S. L. Matthews, R. G. Compton, and B. A. Coles, *Electroanalysis*, **2000**, *12*, 267.
[54] F. Marken, Y. C. Tsai, A. J. Saterlay, B. A. Coles, D. Tibbetts, K. Holt, C. H. Goeting, J. S. Foord, and R. G. Compton, *J. Solid State Electrochem.*, **2001**, *5*, 313.
[55] Y. C. Tsai, B. A. Coles, K. Holt, J. S. Foord, F. Marken, and R. G. Compton, *Electroanalysis*, **2001**, *13*, 831.
[56] Y. C. Tsai, B. A. Coles, R. G. Compton, and F. Marken, *Electroanalysis*, **2001**, *13*, 639.
[57] Y. C. Tsai, B. A. Coles, R. G. Compton, and F. Marken, *J. Am. Chem. Soc.*, **2002**, *124*, 9784.
[58] F. L. Qiu, R. G. Compton, B. A. Coles, and F. Marken, *J. Electroanal. Chem.*, **2000**, *492*, 150.
[59] W. C. Waggener, *Rev. Sci. Instruments*, **1959**, *30*, 788.
[60] M. E. Indig, *Corros. Control Low-Cost Reliab, Proc.* – 12th Int. Corros. Congr., **1993**, 4224.
[61] A. Sala and C. Ranninger, *Revista Iberoamericana de Corrosion y Proteccion*, **1985**, *16*, 17.
[62] A. J. Bard, *J. Electrochem. Soc.*, **1988**, *135*, 1939.
[63] R. Cabrera, E. Garcia, and A. J. Bard, *J. Electroanal. Chem.*, **1989**, *260*, 457.
[64] R. Cabrera and A. J. Bard, *J. Electroanal. Chem.*, **1989**, *273*, 147.
[65] R. M. Crooks and A. J. Bard, *J. Phys. Chem.*, **1987**, *91*, 1274.
[66] R. M. Crooks and A. J. Bard, *J. Electroanal. Chem.*, **1988**, *240*, 253.
[67] R. M. Crooks and A. J. Bard, *J. Electroanal. Chem.*, **1988**, *243*, 117.
[68] W. M. Flarsheim, Y.-M. Tsou, I. Trachtenburg, K. P. Johnston, and A. J. Bard, *J. Phys. Chem.*, **1986**, *90*, 3857.
[69] W. M. Flarsheim, A. J. Bard, and K. P. Johnston, *J. Phys. Chem.*, **1989**, *93*, 4234.
[70] C.-Y. Liu, S. R. Snyder, and A. J. Bard, *J. Phys. Chem. B*, **1997**, *101*, 1180.
[71] C. McDonald, F.-R. F. Fan, and A. J. Bard, *J. Phys. Chem.*, **1986**, *90*, 196.
[72] P. Abbot and N. E. Durling, *PCCP*, **2001**, *3*, 579.
[73] P. Abbot, S. Corr, N. E. Durling, and E. G. Hope, *J. Chem. Eng. Data*, **2002**, *47*, 900.
[74] P. Abbot and C. A. Eardley, *J. Phys. Chem. B*, **1999**, *103*.
[75] P. Abbot and C. A. Eardley, *J. Phys. Chem. B*, **2000**, *104*, 9351.
[76] P. Abbot and J. C. Harper, *J. Chem. Soc. Faraday Trans.*, **1996**, *92*, 3895.
[77] P. Abbot, C. A. Eardley, and J. E. Scheirer, *PhysChemChemPhys.*, **2001**, *3*, 3722.
[78] Bandi, M. Specht, T. Weimer, and K. Schaber, *Energy Conversion and Management*, **1995**, *36*, 899.
[79] V. Novoselova, V. A. Khokhlov, and V. Y. Shishkin, *Russian J. Appl. Chem.*, **2001**, *74*, 1672.
[80] V. A. Khokhlov and M. V. Smirnov, *Zh. Prikl. Khim*, **1979**, *1979*, 1528.
[81] S. N. Lvov and D. D. Macdonald, *Electrochem. Soc. Proc.*, **1997**, *39*, 746.
[82] S. R. Jacob, Q. Hong, B. A. Coles, and R. G. Compton, *J. Phys. Chem. B*, **1999**, *103*, 2963.
[83] C. Metaxas, *Foundations of Electroheat*, Wiley, New York, **1996**.
[84] R. L. Cowan and R. W. Staehle, *J. Electrochem. Soc.*, **1971**, *118*, 1969.
[85] T. E. Rummery and D. D. Macdonald, *Whiteshell Nucl. Res. Establ.*, At. Energy Canada Ltd., Pinawa, MB, Can., **1973**.
[86] D. Macdonald, *Whiteshell Nucl. Res. Establ.*, At. Energy Canada Ltd., Pinawa, MB, Can., **1972**.
[87] D. MacDonald and T. E. Rummery, *Whiteshell Nucl. Res. Establ.*,At. Energy Canada Ltd., Pinawa, MB, Can., **1973**.
[88] D. D. Macdonald, G. R. Shierman, and P. Butler, *Whiteshell Nucl Res. Establ.*,At. Energy Canada Ltd., Pinawa, MB, Can., **1972**.

[89] W. Edenborough and R. G. Robins, *Electrochim. Acta*, **1969**, *14*, 1285.
[90] J. DeBethune, T. S. Licht, and N. Swendeman, *J. Electrochem. Soc.*, **1959**, *106*, 616.
[91] R. Salvi and A. J. DeBethune, *J. Electrochem. Soc.*, **1961**, *108*, 672.
[92] R. J. Raridon, *Measurements of temperature coefficients in aqueous systems up to 200 °C using packed-column techniques,* Vanderbilt University, Nashville, TN, **1959,** 107 pp.
[93] A. Noyes, *Carnegie Institute Publication No. 63:1,* **1908**.
[94] G. Faita, P. Longhi, and T. Mussini, *J. Electrochem. Soc.*, **1967**, *114*, 340.
[95] S. Stene, *Rec. Trav. Chim.* **1930**, *49*, 1133.
[96] M. H. Lietzke and R. W. Stoughton, *J. Phys. Chem.*, **1963**, *67*, 2573.
[97] M. B. Towns, R. S. Greeley, and M. H. Lietzke, *J. Phys. Chem.*, **1960**, *64*, 1861.
[98] M. H. Lietzke and R. W. Stoughton, *J. Am. Chem. Soc.*, **1953**, *75*, 5226.
[99] O. V. Ingruber, *Ind Chemist*, **1956**, *32*, 513.
[100] V. P. Kondrat'ev and S. V. Gorbachev, *Zhur. Fiz. Khim*, **1961**, *35*, 671.
[101] W. N. Greer, *Trans. Electrochem. Soc.*, **1937**, *72*, 12.
[102] M. Lepeintre, C. Mahieu, and J. Monjou, *Compt. Rend.*, **1965**, *261*, 3389.
[103] M. H. Lietzke, in *International Conference on High-Temperature High-Pressure Electrochemistry in Aqueous Solutions (NACE)*, University of Surrey, **1973**.
[104] M. H. Lietzke and R. W. Stoughton, *J. Chem. Education*, **1962**, *39*, 230.
[105] K. E. Heusler, in *High-Temperature High-Pressure Electrochemistry Aqueous Solutions Conference*, **1976**.
[106] M Rudolph, D.P. Reddy and S.W. Feldberg, *Anal. Chem.*, **1994**, *66*, 589
[107] AV. Covington, R. G. Bates and R. A. Durst, *Pure and Appl. Chem.,* **1985,** *57*, 531
[108] S. Rondinini, P. R. Mussini and T. Mussini, *Pure and Appl. Chem.*, **1987**, *59*, 1549.
[109] S. Rondinini, *Anal. Bioanal. Chem.*, **2002**, *374*, 813.
[110] F. G. K. Baucke, *Anal. Bioanal. Chem.*, **2002**, *374*, 772
[111] R. P. Buck, S. Rondinini, A. K. Covington, F. G. K. Baucke, C. M. A. Brett, M. F. Camões, M. J. T. Milton, T. Mussini, R. Naumann, K. W. Pratt, P. Spitzer and G. S. Wilson, *Pure Appl. Chem.*, **2002**, *74*, 2169.

Chapter 13: "High-Pressure Electrochemistry: a Review"

The purpose of this chapter is to detail the experimental pressurising apparatus for electroanalytical measurements at high pressures and to review the relevant literature on the effect of pressure on electrode processes and on the properties of aqueous electrolyte solutions. A review paper based on this chapter has been published in Electroanalysis [1].

13.1 Introduction

The impetus behind studying high-pressure electrochemistry has stemmed on the one hand from the particular needs of modern technology and the geological and marine sciences for knowledge of the behaviour of materials under extreme conditions, and on the other hand from realisation that the application of pressure can give new types of fundamental information [2-4]. It can be appreciated that resorting to high pressure techniques is a matter of necessity rather than a choice in situations such as: hydrothermal systems, autoclave procedures and oceanographic analysis/marine science. However, electrochemistry at high pressures can be utilised as a useful tool for insights into the thermodynamic and kinetic aspects of a wide range of redox reactions. The data produced provide information on formal redox potentials, electron transfer rates, ion-solvent interactions and the diffusion properties of the species.

A survey of the literature reveals that electrochemical measurements at high pressures have been performed for over a century. Early studies were concerned mainly with the effect of pressure on the ionic conductance of different electrolyte solutions [5-19] and its effect on the electromotive force (emf) of electrochemical cells [10,20-22]. Detailed accounts of these results have been produced previously and readers are pointed to the following articles for a more thorough overview of these early experiments [4,5,13,23-30]. However, it has since been observed that these early studies often lacked reproducibility and accuracy [24], which can be attributed to the practical difficulties and the complicated experimental apparatus [31] required to record accurate measurements at high pressure.

Problems such as durability and tightness of the apparatus, contamination by hydraulic fluids, fragility of the reference electrode and unreliability of the feed-throughs that take the electrical signals through the pressure vessel wall are often reported [2,3]. Other technical obstacles related to properties of the working electrode

material, preparation of its surface, construction of the cell and availability of suitable reference electrodes have also been observed [31,32]. In addition, it has been found that some electrochemically active couples are not sufficiently stable over the time required to complete a cycle of measurements at various pressures (experiments at high pressure require a full working day, placing stringent demands on the chemical stability of the couple being studied) [3,31]. In view of these difficulties in high pressure work it is not surprising that few early experimentalists took up the challenge of undertaking such measurements!

However, most of these limitations have been overcome over the last 15 years as standard items of high pressure equipment have become readily available and as such removed much of the experimental difficulty [2,3,31,33]. A range of high pressure vessels, pumps, gauges, etc., can be obtained from engineering companies specialising in high pressure equipment and assembled without special tools or facilities. Material with high mechanical strength and chemical inertness are available and pressure can, therefore, reasonably be regarded as a normal practical variable rather than as a formal thermodynamic parameter.

A further problem which today remains and is often exacerbated under these measurements when using a stationary working electrode is keeping the surface of the electrode clean. In the 1960's Hills and co-workers successfully developed an adaptation of the dropping and hanging mercury electrodes for high pressure polarography studies [25]. In their case, the problem of reproducibility was overcome as the electrode surface was continually refreshed. However, this technique is not widely used and as such other methodologies are required. Electrochemical cleaning by cycling the potential such that gas bubbles are formed on the electrode surface and aid in the removal of deposits provides a 'neat' way of overcoming these problems [3].

The introduction of these techniques and the availability of the materials required for these measurements, have stimulated interest in the possibilities of high pressure electrochemistry. This interest has led to a considerable amount of data being produced mainly concerned with the measurements of molar volume changes associated with redox processes involving coordination complexes. Hence, pressure has finally taken its proper place with temperature [34] as an easily accessible thermodynamic variable for electrochemical measurements.

The bulk of this chapter has been split into six sections. The first section deals with the experimental apparatus for high pressure measurements. The second discusses the electrolytic conductance and galvanic for cell emf measurements carried out at high pressures. The third describes the effect of pressure on specific electrode processes. The fourth deals with the pressure effects on kinetics and thermodynamics of reactions of metal complexes at electrodes. The fifth covers the application of pressure to specific systems with practical applications, and, finally, the last section is a brief overview of the relevant recent literature on voltammetry at high temperature and high pressure.

13.2 High Pressure Experimental Setups

13.2.1 Pressurisation Methodologies

Traditionally, high pressure assemblies consisted, essentially, of a high pressure generation unit and a general purpose pressure vessel, (Figure 13.1) whose design depended on the purpose of the experiment and on the fluid to be contained. [24]. Many of the initial high pressure electrochemical experiments were carried out using solutions contained directly in steel pressure vessels [24]. However these vessels were found to corrode and contaminate the sample and therefore to minimise these problems, the inside of each vessel was lined or plated with platinum, gold, silver or

titanium [35],. For the set-up shown in figure 13.1 it was found convenient to use large pressure vessels (i.e, internal diameter of 3-5 cm, 30-50 cm long) so that glass electrochemical cells, which had a typical capacity of 10-50 mL, could be accommodated [4].

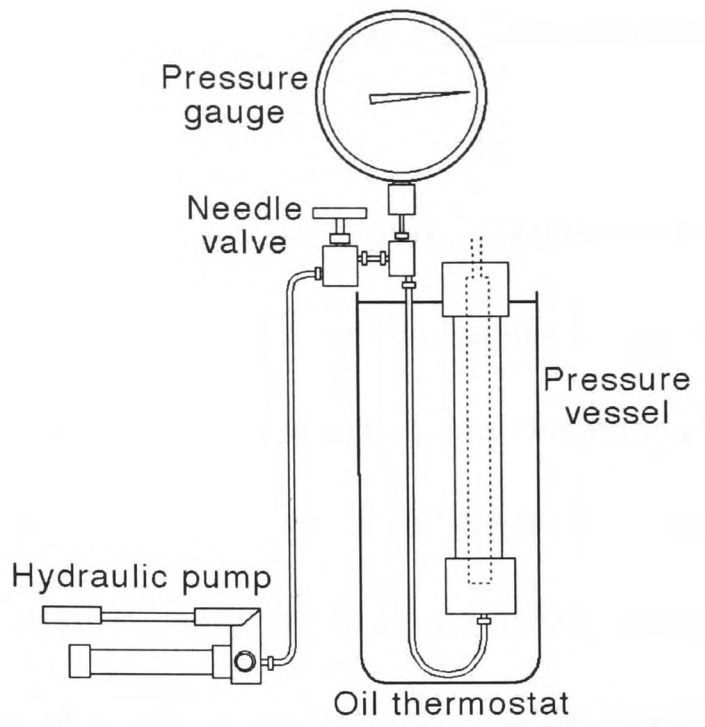


Figure 13.1: An early high pressure assembly for electrochemical measurements in the range 1-5,000 atmospheres (adapted from [24]).

The five main methodologies [13] of generating high pressure in liquids are: (a) the use of a hydrostatic head of liquid, (b) the onset of a phase change in the media being studied, (c) the generation of a chemical reaction or an explosion (d) the thermal expansion of the material and (e) the intrusion of a piston into the cell. The advantages and disadvantages of the first three of these methods have been discussed elsewhere [13] and need not to be considered in detail here. The last two methods are the preferred pressurising methods for electrochemical measurements and are discussed next.

13.2.1.1 Thermal expansion of the material

A common methodology for generating pressure within a vessel is *via* the heating of the solvent in which the experiment is being conducted. These experiments are undertaken in an autoclave as already discussed in the previous chapter (Chapter 12,

Section 12.2.1). Experiments using autoclaves require a design that utilizes materials that can safely withstand both the pressures and temperatures reached during an experiment. A number of vessel liners have been developed for use at high pressures and temperatures and these are described in Chapter 12, Section 12.2.1. By judicious choice of the material, studies of hydrothermal and corrosion reactions have been made at temperatures in excess of 200 °C.

However, this method has the undesirable limitation of the pressure generated being dependent on the temperature and composition of the vessel's contents. When carrying out studies at elevated temperatures in aqueous media it has been shown that the reactivity of water increases causing two problems. First, it is difficult to maintain a glass apparatus or a constant composition of electrolyte; second, the electrochemical oxidation and reduction of water occurs with increasing readiness as the temperature increases and often overshadows the electrode processes of interest.

13.2.1.2 Pressure generation by the intrusion of a piston into a cylinder

A simple approach to generate increased pressure in a cell is to employ an electrically or hand-operated hydraulic displacement pump to drive a piston into the cell. In this case the pressurised fluid is conveyed from the pump to the experimental system by steel capillary tubing of high tensile strength [13]. Given that water freezes at about 900 MPa (~9 kbar) at room temperature, a compressed-air-driven hydraulic pump with a fail-safe electronic controller, or a 200 MPa (~2 kbar) hand pump with a pressure intensifier have been reported for aqueous solution studies where the internal free volume of the pressure vessel is some hundreds of millilitres. A screw press is more convenient to use when the volume of the fluid to be compressed is only of the order of 10 mL [2,3].

Pressure is transmitted to the pressure vessel through a separator with a free piston to keep the hydraulic fluid out of the electrochemical cell. The pressurising fluid entering the electrochemical cell from the separator must be an electrical insulator and free from easily oxidizable or reducible impurities: hexanes [36], octanes, clean hydrocarbon white oil [2,3], heptane [37], or a mixture of isooctane and methylcyclohexane (10:90) [38] have given good performances and working pressures up to 10 kbar [38] are obtainable. These solvents are preferred to water or kerosene which were used in the past [39]. It can be foreseen that the upper limit of the pressures that can be reached by compressing a liquid in a piston-cylinder will be due to the freezing of the fluid or the possible rupture of the cylinders or piston.

It has been shown that contamination between the pressurising fluid and the test solution can occur; however this can be prevented by using inert separators such as mercury, flexible diaphragms or bellows [39] or pistons [40]. Sealing of the pressure vessels is achieved by means of rubber O-rings supported when necessary by a steel-backing ring to prevent extrusion of the rubber between the body of the pressure vessel and the plug or cap. These O-rings are usually tailored to the requirements of the experiment and as such a whole range of materials can be used (eg. PTFE, Teflon or Fluon, or steel lens rings [24]).

Gases have also been employed for pressurising cells [24]. In this case a piston is placed between the liquid and the gas to prevent dissolution of the latter into the pump fluid and the possible formation of fogs and foams in the gas lines due to rapid decompression. An unlimited volume of fluid at high pressure can then be continuously delivered with a diaphragm pump in which a reciprocating piston forces oil into and out of one half of a lenticular chamber divided, in the plane of the lens, by a flexible steel diaphragm. By means of a series of valves, the gas is emitted to the outer half where it is compressed by the flexing of the diaphragm and expelled at high

pressure. However, because the pressure-volume energy of a compressed gas is much greater than for a liquid, the application of pressure with an externally supplied gas is not recommended [3]. Nevertheless, Jovancicevic and Bockris [41] describe a device in which electrode kinetics measurements were recorded up to 2 kbar by the evolution of a large supply of hydrogen gas in a small volume.

As electrochemical measurements are taken within the pressurised cell also the electrical connections into the cell have to be pressure tight. For lower pressures and temperatures below 100 °C, nylon cones and mica-rubber sandwiches are generally employed as seals [24]. However, above this temperature ceramic cones are used or, alternatively, sealing is accomplished by leading the thin wires through a resin plug of Araldite [24,42] which could in turn be forced into conical seating, under liquid pressure, to give a pressure-tight seal.

The measurement of the pressure in the system is usually obtained by using commercially available gauges. Transducer gauges are limited to 2,000 atm, electronic or Bourdon gauges can sense pressure up to 10,000 atm. The pressure coefficient of electrolytic conductance measurements has also been suggested as a pressure gauge [15]. In this case, because of freezing of the solution, the pressure range is restricted to 5,000 atm.

We now turn our attention to the various electrochemical cells utilised in high pressure measurements.

13.2.2 Electrochemical Cells

Outlined below are the details of a range of electrochemical cells used for various electrochemical measurements.

13.2.2.1 Conductivity cells

Conductivity measurements have been recorded since the early 1950's and as such a plethora of designs are described in the literature. Early cell designs (1953) such as those reported by Jamieson were constructed from Teflon (polytetrafluoroethene) with platinised platinum used as electrodes [40]. The pressure was transmitted to the solution inside the cell by a piston. However, the design suffered from the misalignment of the two electrodes at high pressures and the cell constant was found to change [4]. At a similar time Buchanan and Hamann [11] constructed a glass cell in which pressure was transmitted by liquid mercury. The cell was immersed in insulating oil inside a high-tensile steel pressure vessel in a thermostat tank: the oil transmitted pressure from a separate commercial hand pump and was sealed in the vessel. The conductivity cell had conventional square platinised platinum foil electrodes. However, mercury, which was used to separate the electrolyte from the pressure fluid, was found to be not entirely inert and caused contamination. Furthermore, the cell could not be use for pressures greater than 3 kbar because of cracks occurring at the glass/metal seals. A comparison of the glass cell and Teflon cell showed that the cell constant was more dependent on the pressure in the Teflon cell because of the greater compressibility of Teflon and the fact that it undergoes phase transitions involving discontinuous contractions at high pressure [4]. To combat this, Ellis [19] devised a cell in which the electrodes were mounted on a separate glass spacer so that their separation was independent of the shrinkage of the Teflon body and the problem of the cell constant changing was overcome.

Hamann described an arrangement for measuring electrical conductivities of shock-compressed liquids up to 200 kbar [4]. The conductivity cell was a polyethene cylinder containing platinised electrodes mounted in polyethylene plugs that could be pushed into the cell to vary the distance between the electrodes and the explosive

charge and so varying the pressure in different experiments. This set-up was used to measure the conductivity of pure water and aqueous solutions to shock pressures as high as 200 kbar. A large increase in the conductivity was observed indicating that water and a number of other liquids investigated were good conductors under shock wave pressures. This conductivity data was used to estimate the mobilities of the ions under shock conditions and the ionisation product K_w of shock-compressed water [4].

Since these early designs several modifications have been made to produce a leak free cell which is stable over a wide range of pressures (1-2,250 atm) [44]. Saluja [45] has developed a conductance cell which is built directly into a hydraulic piston-cylinder allowing measurements to be taken up to 27 kbar. Finally, Ho and co-workers [46-48] have designed and constructed a flow-through high pressure electrical conductance cell to measure limiting molar conductance and ion association constants of dilute aqueous solutions with high precision at high pressures (up to 300 MPa) and at high temperatures (up to 600°C).

13.2.2.2 EMF cells

Figure 13.2 shows the experimental set-up used by Hamann [4] for emf measurements up to 2 kbar on the cell:

Ag, AgCl | HCl (0.1 N) | glass | KCl (0.1 N) + KOH | AgCl, Ag

This experimental arrangement was similar to the one used by Disteche [49]. The cell was mounted in a steel pressure vessel analogous to that described by Buchanan [11] for conductivity measurements. The HCl solution and the Ag/AgCl electrode, constituting the left-hand side of the cell, were contained in an open-topped commercial electrode made from a rare earth glass which had a negligible alkaline error at pH 13. The right-hand half of the cell, comprising the KCl and KOH solution and another AgCl/AgCl electrode, was held in a surrounding beaker.

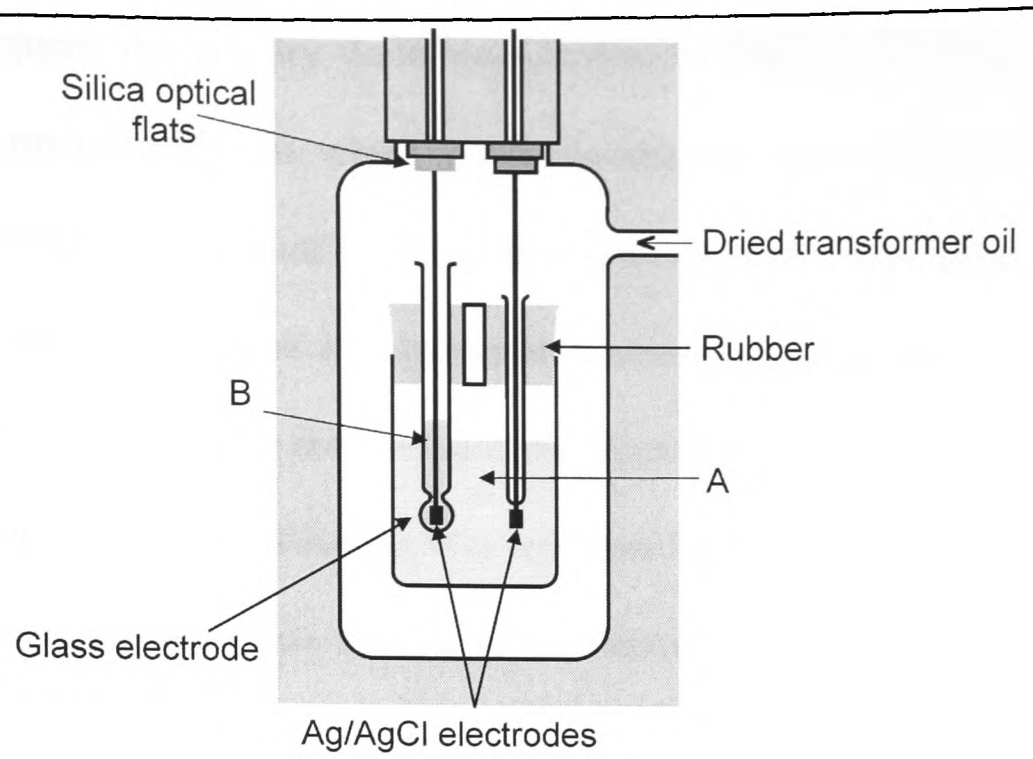


Figure 13.2: Experimental set-up used by Hamann (adapted from [4]) for emf measurements up to 2 kbar on the cell: Ag, AgCl | HCl (0.1 N) | glass | KCl (0.1 N) + KOH | AgCl, Ag. The subscripts A and B refer to solutions outside and inside the glass electrode, respectively.

Pressure was transmitted equally to the two halves by a light hydraulic fluid (dried transformer oil), which surrounded the whole cell. The asymmetry potential of the glass membrane was found to be several millivolts and independent of the pressure to within 0.5 mV between 1 and 2,000 atmospheres. This arrangement was used to measure the K_w of water up to 2 kbar (see Section 13.3.2) [50].

13.2.2.3 Three electrode cells

Several different cell arrangements have been utilised for electrochemical studies at high pressure which incorporate three electrodes. Doine *et al.* [36] first developed a stainless steel pressure vessel which was pressurised with a hand-pump and intensifier and tested up to 300 MPa (~3 kbar). In this case mixing between the pressurising fluid (hexane) and the hydraulic oil was prevented using a large cylindrical separator with a free piston. The sample cell was constructed from Teflon. The working electrode was either a Pt or Au wire, with a Pt wire acting as the counter electrode. Au rod reference electrode completed the cell assembly.

Subsequent designs by Sachinidis and co-workers [51] employed a high pressure electrochemical cell which could be reliably and accurately operated at pressures up to 1.5 kbar (Figure 13.3). This cell was applied to the study of a range of redox reactions and processes in aqueous and non-aqueous solvent systems [51-53] (Section 13.4.2). In this case the electrochemical cell consisted of a Pt or Au working electrode, a Pt counter and a $Ag/AgNO_3$ reference electrode, and was mounted on a 90 mm diameter stainless bomb using a Teflon support. The bomb was pressurised by hydraulic oil from a hand pump and the pressure was measured on a Bourdon type high pressure gauge.

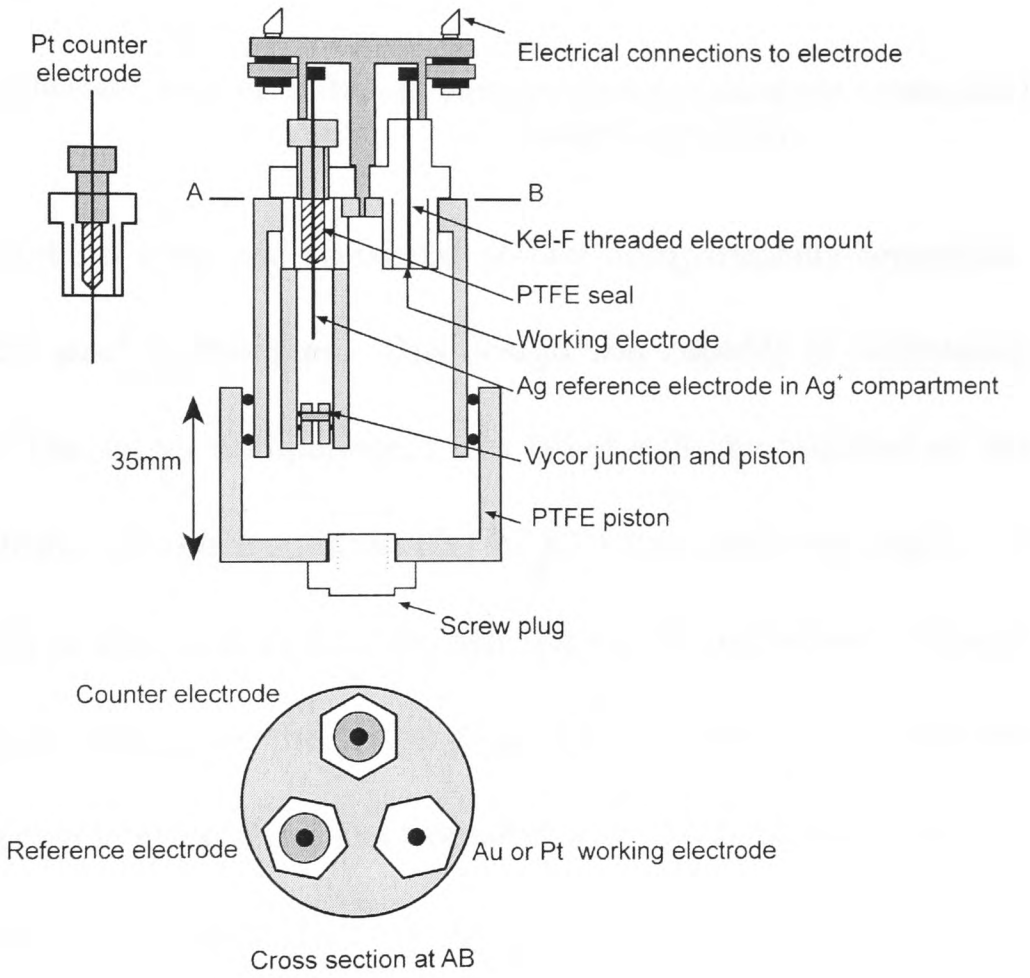


Figure 13.3: A schematic drawing of the high pressure electrochemical cell constructed by Sachinidis *et al.* (adapted from [51]).

Thermostatting of the bomb at 25 ± 0.1 °C was achieved by circulation of water through the thermosetting jacket surrounding the bomb. Because of the low thermal transmission of the polymeric material of the cell and the unstirred oil used to generate pressure in the steel bomb, thermostatting is slow hence a pressure "run" takes a full day [51].

A similar cell has been developed by Faulkner *et al.* [38] (Figure 13.4).

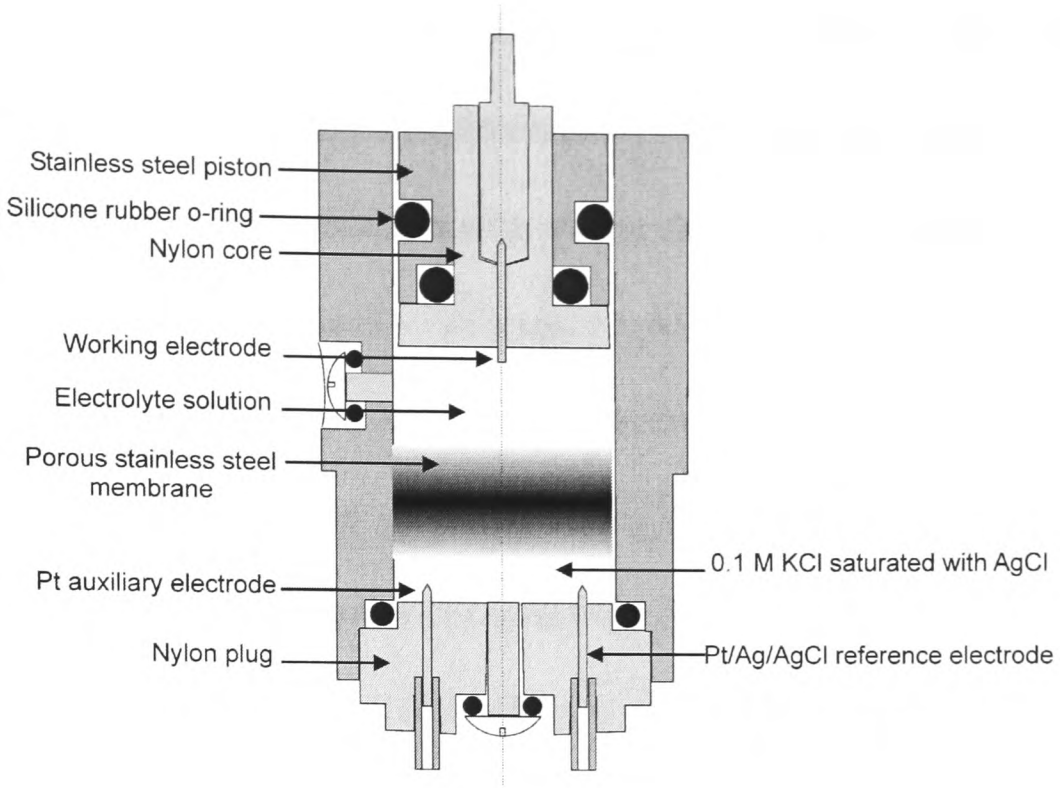


Figure 13.4: A schematic drawing of the high pressure electrochemical cell constructed by Faulkner *et al.* (adapted from [38]).

The cell was 3.4 cm long and consisted of two compartments separated by a pair of porous stainless steel membranes. This design was capable of withstanding pressures up to 10 kbar. The upper compartment was filled with the solution of interest and the lower one with the reference solution (0.1 M KCl saturated with AgCl). A Nylon plug was threaded in at the lower end of the cell (facing the reference compartment). Then Pt pins were press-fitted into the Nylon plug. One served as a counter and the other as a reference electrode after being electroplated with silver and anodised in HCl to form a AgCl film. The suitability of this reference electrode for high pressure measurements was demonstrated [38]. The pressure was transmitted into the cell by a stainless steel piston that slid freely into the working compartment in response to the compression of the fluid surrounding the cell. The piston had a Nylon core in which a Au or Pt rod, working electrode was press fitted. The pressure transmitting fluid was a nonconductive mixture of isooctane and methylcyclohexane (10:90).

The Calgary cell [3] (Figure 13.5 (a)) is an adaptation of Doine's cell [36] in which compression of the reference electrode is allowed by mounting a Vycor frit in a

free piston. Instead of saturated KCl solution, the reference compartment is filled with 4 M aqueous KCl to prevent dissolution or precipitation of KCl as the pressure is changed which may cause drift of the cell potential. In this case the working electrode is Pt, Au wire or a glassy carbon electrode with a Pt or Au counter electrode.

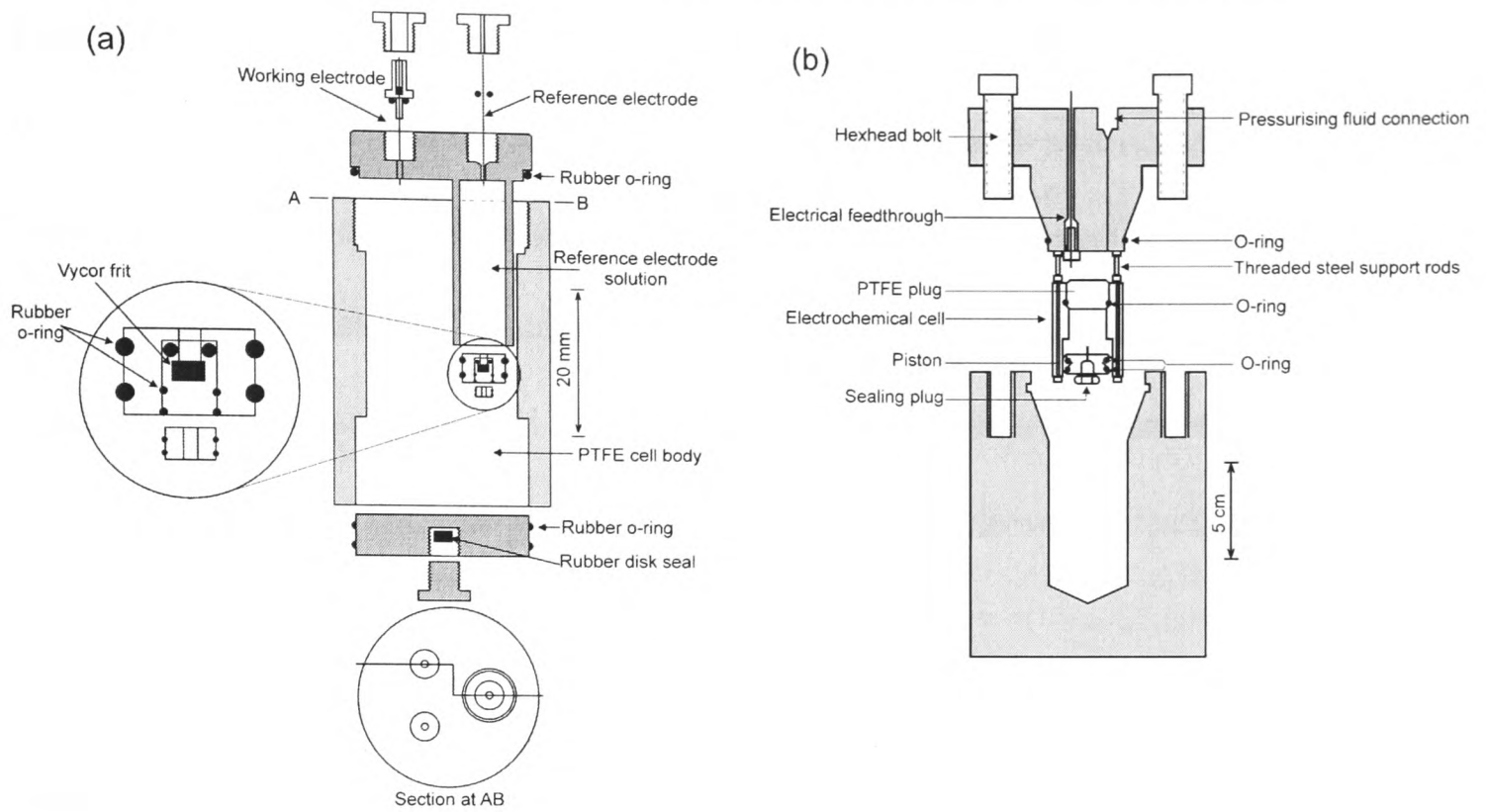


Figure 13.5: A schematic drawing of: (a) the Calgary high pressure electrochemical cell and (b) the pressure vessel for the Calgary high pressure electrochemical cell constructed by Swaddle *et al.* (adapted from [3]).

Thermal equilibration within ±0.05 °C is achieved by circulating water through the aluminium jacket surrounding the stainless steel pressure vessel (Figure 13.5 (b)). As already mentioned this is a slow process requiring 75 minutes initially and 45-50 minutes after each pressure change (since adiabatic compression and decompression respectively rise and lower the temperature of the pressure vessel contents). Before each measurement the working electrode is cleaned electrochemically by cycling the potential at least three times between the most positive potential to be scanned and the hydrogen evolution potential. Consequently, a full cycle of measurements normally requires a full day.

Golas and co-workers [31] have recently described a complete apparatus for voltammetric measurements at high pressure (up to 0.8 GPa, or ~8 kbar) and provided

practical advice on how to prepare and maintain the electrodes used in such experiments [31,32,54]. The apparatus for high pressure (up to 0.8 GPa) electrochemical measurements consisted of four components: a high pressure chamber with pressure control system, a press, an electrochemical analyser and, finally, an electrochemical cell with a set of electrodes. The high pressure chamber was made by the High Pressure Research Center UNIPRESS (Warsaw) and consists of a double steel jacket (an inner steel jacket and an outer safety steel jacket) and a mobile piston. The head of the piston is equipped with a Manganin pressure gauge MPG 10 and, in addition, the piston is provided with nine high pressure electric connections, an electric socket, a holder for the electrochemical cell and a double washer seal made of brass and rubber.

Two versions of the electrochemical cells were used for different experiments: a short one-compartment cell (dimensions: 3 cm long x 1.3 cm wide) and a long two-compartment cell (dimensions: 4.4 cm long x 1.9 cm wide). The short one was an adaptation of the design of Faulkner *et al.* [38] described above and consisted of a steel tube closed at one end by a threaded nylon plug with the Ag/AgCl reference and the auxiliary Pt electrodes embedded in it. The other end was closed by a mobile piston which consisted of an internal threaded steel ring with an external undercutting for a rubber-o-ring and a threaded, sealed epoxy-resin with a disk working electrode. The long one was also constructed on the basis of the design of Faulkner *et al.* [38] but inside the steel tube there was a specially designed movable sealed piston. The time required to prepare the apparatus for high pressure measurements was estimated to be between 45 and 60 minutes with two further hours required to reach the pressure of 0.8 GPa [31].

Stevenson and White [37] have developed a high pressure electrochemical cell (Figure 13.6) capable of using microdisk techniques for quantitative investigations of

organic electrochemical reactions at pressure up to 1 kbar in the absence of an inert solvent. In these systems, the solution comprises a polar organic liquid, e.g. nitrobenzene, and a small quantity of a dissociated supporting electrolyte, e.g. 0.2 M tetra-n-butylammonium hexafluorophosphate.

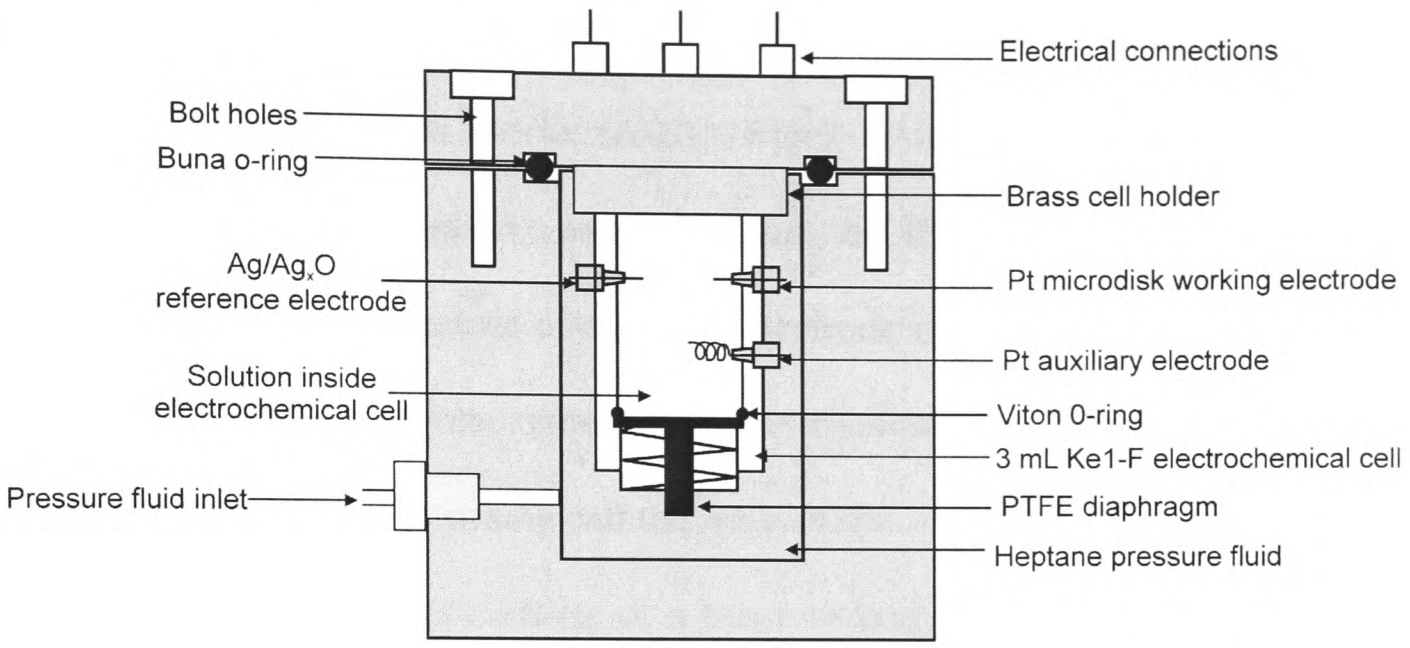


Figure 13.6: A schematic drawing of the electrochemical cell enclosed in the high pressure cell used by Stevenson and White (adapted from [37])

The high pressure cell is cylindrical with a 3 cm thick lid which is sealed to the base using a Buna O-ring. The electrochemical apparatus consists of a single-compartment 3 mL Ke1-F cell equipped with a Ag/Ag_2O reference electrode, a Pt wire counter electrode and a Pt microdisk electrode (nominal radius = 12.5 μm). It is held in place inside the high pressure cell by a brass collar attached to the lid. A thin Teflon diaphragm located on the bottom of the electrochemical cell is used to transfer the pressure between the heptane in the high pressure cell and the electrochemical solution. The pressure exerted by the heptane causes the diaphragm to compress the electrochemical solution until the pressures inside and outside the electrochemical cell are equalised. The cell pressure was measured using a pressure gauge with an estimated uncertainty of ±3 bar.

A novel high pressure sonoelectrochemical cell has been constructed by Compton *et al.* [55], the designs of which are detailed in figure 13.7. This allows the employment of high-intensity ultrasound emitted from an ultrasonic horn probe to be used in a cell pressurised up to 100 bar.

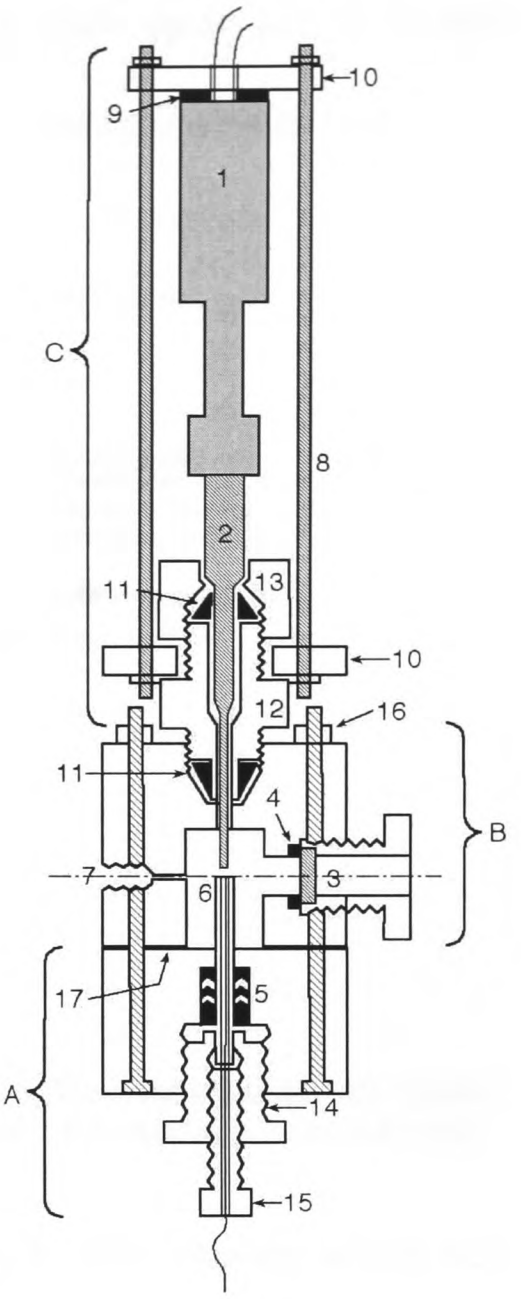


Figure 13.7: A schematic drawing of the high pressure (up to 100 bar) sono-electrochemical cell constructed by Compton *et al.*. [55]. (1) Ultrasound converter; (2) tip horn; (3) sapphire window; (4) PTFE O-ring; (5) PTFE gaskets and Ti washers; (6) 25 μm Pt microelectrode; (7) inlet; (8) brass threaded bars; (9) PTFE washer; (10) aluminium disk; (11) ¼ in. PTFE cone; (12) titanium double nut; (13) titanium counternut; (14) brass nut; (15) brass counternut; (16) tensile bolt; (17) gold O-ring.

It consists of three main blocks (A-C). Block A is constructed from titanium and contains a Pt microelectrode wire. Sealing of the microelectrode is achieved by PTFE gaskets compressed by titanium washers against the glass casing and the walls of the titanium block. Block B consists of a titanium body with two sapphire windows which allow observation of the cell interior under pressure. Three HPLC inlets are used for the Ag quasi-reference electrode, the gas inlet and a temperature sensor. A quasi-reference electrode was coiled around the glass tube of the microdisk working electrode. Blocks A and C are tightly held in place by five tensile bolts with gold O-rings providing the pressure sealing.

Block C contains the ultrasonic horn probe which delivers the ultrasound to the electrochemical cell. The probe is placed directly opposite the working electrode in a 'face-on' geometry. The electrochemical data were recorded using a bipotentiostat configured in such a way that the horn potential was set to +0 V versus the Ag pseudo reference electrode to avoid undetected currents flowing to or from the horn tip.

Compton *et al.* [56] have also constructed a simple and inexpensive high-temperature electrochemical cell capable of withstanding pressures of up to ca. 5 atmospheres and which allows measurements to be made up to 115 °C in both aqueous and non-aqueous solvents. A schematic design is shown in Figure 13.8.

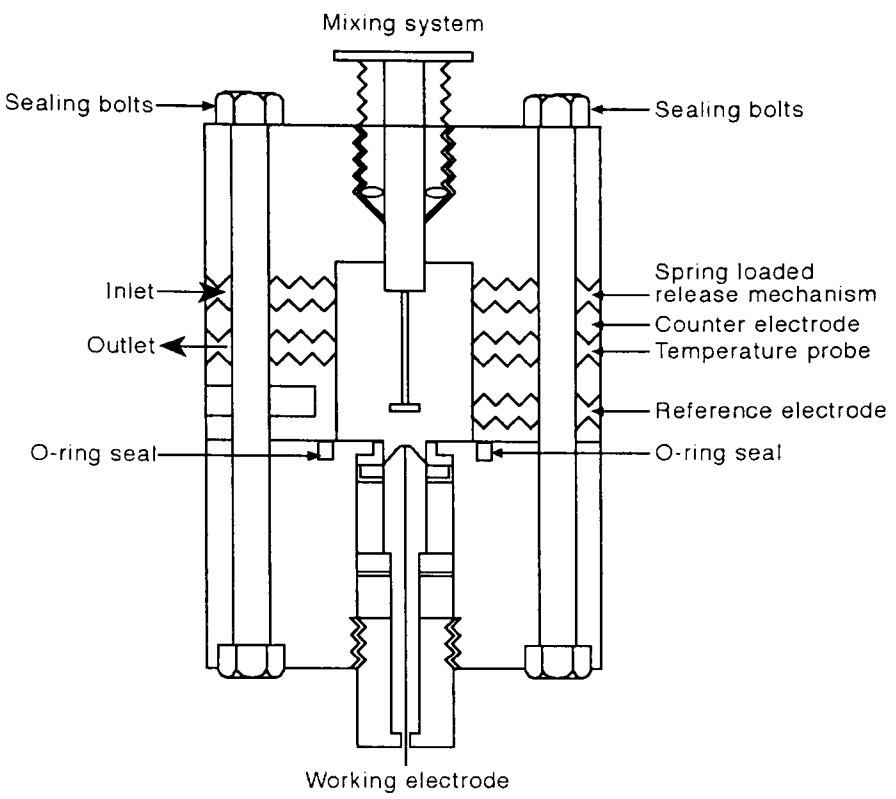


Figure 13.8: A schematic drawing of the high-temperature (up to 115 °C) electrochemical cell capable of withstanding pressures of up to ca. 5 atmospheres. Cell dimensions: 8.5 cm long x 3 cm wide [56].

The cell (dimensions: 8.5 cm long x 3 cm wide) was made from titanium which was then baked at 600 °C for three days to electrically passivate all the surfaces of the titanium with a film of titanium oxide. A 10 μm diameter Pt disc electrode sealed in Pyrex glass acted as the working electrode with a Pt coil counter electrode and a Ag wire reference electrode. The counter and reference electrode leads were taken out of the cell through passivated titanium tubing (3 mm diameter) and were sealed in place with Torr Seal. This tubing was clamped in place using standard HPLC fittings to ensure a seal capable of withstanding the pressure exerted when the solvent exceeded its boiling point. The temperature inside the cell was measured using a Pt/PtRh thermocouple. Uniform heating of the cell was achieved by circulating high pressure

steam from a pressure cooker via insulated stainless steel tubing, through channels within the cell wall.

13.2.2.4 Polarography measurements at high pressure

As discussed above, one of the main obstacles when performing high pressure electrochemical measurements at solid electrodes is fouling of the electrode due to accumulation of material which cannot be removed from the electrode surfaces during a series of measurements.

Initial studies attempting to overcome this limitation, focused on the use of polarographic measurements at high pressure. Unlike the surface of solid electrodes, which may become contaminated over a long period, the surface of a mercury electrode is continually refreshed. Hills and co-workers [24,25,57-61] have described a successful adaptation of dropping mercury electrode polarography at high pressure, however, the technique has not been widely applied. Polarographic measurements have been used to obtain average currents (i.e., averaged over the drop life) as a function of applied voltage over the pressure range 1-3 kbar [25]. It was shown that for fast electrode processes, such measurements allowed the estimation of diffusion coefficients and ionic concentrations, whereas slow reactions could be analysed to give rate constants for the electrode process. These results are reviewed elsewhere [25] and briefly summarised in section 13.3.3.1.

13.3 High Pressure Electrochemical Measurements

Outlined below is a summary of the main electrochemical experiments that have been carried out at high pressures and the results obtained.

13.3.1 Conductance Measurements

Conductance experiments can provide an insight into the properties of bulk solutions, as well as being the preferred methods for determining ionisation constants compared to the electromotive force (emf, see section 13.3.2) method at high pressures [24]. The emf method has been shown to be more difficult to employ under pressure. However, it is more reliable than the conductivity method in the case of very weak electrolytes [24].

Upon application of pressure to an electrolyte solution two main effects are observed; first, the ionic mobilities will be altered and, second, in the case of weak electrolytes and ion pairs, the degree of dissociation will increase. These effects are thermodynamically related to the decrease in the total volume that accompanies ionisation reactions [24]. The experimental evidence for this increase is reported in the literature [4,5,11,13,30]. In particular Hamman [4] reported a critical compilation of the effects of pressure on ionisation equilibria and of volume changes for the ionisation of weak electrolyte. Therefore, only a brief summary is given below.

Hamman and Strauss [62] and Ellis [16,18,19] initially studied conductimetrically aqueous solutions of weak acids at high pressure. More data have been reported by Horne [63] for the dissociation of the HSO_4^- ion up to 1,500 atm, and by Franck *et al.* [28] who expanded the range of pressure investigated to 8,000 atm. Owen and Brinkley [9] investigated the variation with pressure of the dissociation constant of water and of weak acids up to pressure of 1 kbar. Conductance measurements have also been used to measure the dissociation constant of ion pairs at high pressures [6-8,64] and have provided a convenient means of studying the influence of pressure on the association of ions into micelles [4].

Overall, these results reveal that a number of errors in conductance measurements at high pressure are often encountered. These are outlined here and

help to explain some discrepancies observed between different sets of data. First, temperature control is difficult due to the compression of liquid causing adiabatic heating which is typically 10 °C per kbar. Second, solvent conductance is problematic (for example, it has been shown that the conductivity of pure water increases by a factor of about 16 between 1 bar and 10 kbar, having a value of about $9 \times 10^{-7}\ \Omega^{-1}\ cm^{-1}$ at 25 °C) [4]. To overcome this, the solutions are usually made in water with a conductivity of the order of $10^{-6}\ \Omega^{-1}\ cm^{-1}$, a value which is roughly trebled at 3 kbar [4]. Third, the dimensions of the cell may cause error. It can be envisaged that as pressure is applied to the cell, the cell and its electrodes change dimensions and this alters the cell constant. Fourth, contamination and leakage of the sample, and finally the compressibility of the solutions may also result in error. As the solutions contract under pressure (by as much as 19% at 3 kbar) the concentration of electrolyte increases.

Finally, the resistance and capacitance of substituted $M_2O_{11}Al_2O_3$ (where M = Li, Na and K) crystals, were measured on a Wayne Kerr radio frequency bridge at pressure up to 4,000 atmospheres produced by a hydraulic press acting on the piston of the steel pressure cell assembly [65]. The ionic conductivity was found to increase linearly up to 4,000 atm with M = Li, to remain constant for M = Na, and to decrease for M = K. The diffusion of ions was found to be dependent on the activation volume of the crystal lattice in the vicinity of the mobile cation. In the β-Al_2O_3 lattice, Na ions move without serious steric hindrance, whereas K-substituted β-Al_2O_3 requires lattice expansion. Conversely, the net effect of Li ion motion is a local contraction of the lattice.

We now turn our attentions to the study of EMF measurements at high pressures.

13.3.2 EMF Measurements

Early studies of the effect of pressure on cell emfs were carried out by Cohen and Piepenbroek [10]. Since these early studies measurements of the cell emfs have also been used to obtain ionisation constant values at high pressure. At atmospheric pressure, the emf method is the one normally used to measure ionisation constants because of its experimental simplicity and its accuracy. Unfortunately, however, at high pressure hydrogen electrodes have been revealed to be awkward to use as their potential changes enormously with pressure simply because of the very large compressibility of gaseous hydrogen. For example, as early as 1922 MacInnes and co-worker [20-22] found that the emf of the Pt, H_2 (p atm) | HCl (aq) | Hg_2Cl_2 | Hg, cell increased by 100 mV between 1 and 1,000 bars, masking any more subtle changes in the solution. Furthermore, there is the serious theoretical problem of properly allowing for the large change of free energy which occurs when compressing hydrogen over an aqueous solution [4]. Hills and Kinnibrugh [24] addressed this problem by compressing a solution saturated with hydrogen at atmospheric pressure and assuming that the solution contained a constant concentration of dissolved hydrogen. The results obtained with this cell were however not in good agreement with the literature values [4]. Heusler and Gaiser [66] have described a gas-free saturated hydrogen electrode with a Ag/AgCl reference electrode capable of operating up to 2.5 kbar.

The problems associated with the hydrogen electrode were by-passed by Disteche [49,67-70] who showed that it is possible to use a glass electrode to obtain ionisation constants as a function of pressure provided that the pressure is allowed to act equally on both sides of the membrane. Disteche [49,67-70] used the glass electrodes to measure the effect of pressure on the ionisation constants of water and of some weak acids in water and the results showed a good agreement with those obtained by conductivity methods [4]. He also obtained evidence that the ionisation

constant of water, K_w, is considerably greater at 1,000 atmospheres than 1 atmosphere which was confirmed by measurements using the Ag | AgCl | HCl(aq) | glass | KCl+KOH (aq.) | AgCl | Ag cell [50] and other measurements [71,72]. These findings by Distèche helped in the development of a glass electrode to measure the pH of sea water [49,67].

Finally, measurements of the ionisation constant of water as a function of pressure were carried out by Whitfield [71] and Linov and Kryukov [72] and their experimental values of K_w were found to be in agreement with that reported by Hamann. [4]

Next the study of kinetic voltammetry at elevated pressures will be summarised.

13.3.3 Electrode Processes

13.3.3.1 Diffusion-controlled electrode processes

(a) Mercury electrodes

The use of the mercury electrode at high pressure was first reported by Mairanovskii *et al.* [73] who investigated the electroreduction of several metal ions in 0.1 M KCl and found practically no change in the limiting currents up to 3 kbar.

The pressure dependence of the double layer capacity at the mercury-solution interface was studied by taking measurements of capacitance at a dropping mercury electrode [61]. The pressure was transmitted via the head of mercury and an inflatable plastic bag in which the mercury was collected without either creating a back-pressure or an additional head-pressure through distension of the bag. Multiple leads through the top closure enabled impedance measurements to be made on a controlled and timed dropping electrode. The results illustrated significant changes in the volume

accompanying the adsorption or desorption of water in the inner region of the double layer.

The rate of the hydrogen evolution reaction on mercury in aqueous 0.1 M HCl up to 1.5 kbar hydrostatic pressure has also been measured [39] using a hanging drop Hg electrode to avoid the complications associated with the changing geometry of an expanding drop. The current densities at a constant overpotential were found to be pressure dependent. A negative volume of activation (-3.4 cm^3 mol^{-1}) for the hydrogen evolution reaction was found, which is in agreement with subsequent results published by Conway [74].

Ellis and Hill [25] have also reported the use of the dropping mercury electrode at high temperature (up to 250 °C) and relatively high pressure (up to 100 bar). The results revealed that reversible polarograms were obtained for aqueous solution of cadmium, zinc and indium ions.

The electroreduction of $CuSO_4$ in 0.5 M KCl has been studied [75] using DC polarography and no change at all in the limiting current with applied pressure up to 3 kbar was observed. However, this was found to be in contradiction with the results of Lim [12] who investigated the same system at a stationary Pt microelectrode and found a significant decrease in the limiting current when the pressures increased up to 3 kbar. This discrepancy was attributed to the fact that DC polarisation is always liable to give anomalous results when using long polarisation times [25].

(b) Microelectrodes

As discussed in Chapter 1 (Section 1.7) microelectrodes display several advantages over conventional electrodes such as convergent diffusion and enhanced mass transport, very small currents and small iR losses which enable their use in two-electrode system, reduction of the double layer capacitance which allows fast voltammetric measurements to be made and, finally, the possibility of measurements

of microvolumes. It is therefore some what surprising that only a few studies describe the use of microdisk electrodes in high pressure electrochemical experiments [3,12,31,32,37,38,54,76].

The use of microelectrodes at high pressures was first reported in 1958 by Ewald [12] who investigated the reduction of Cu^{2+} to Cu^{+} relative to a saturated calomel electrode in 0.5 M KCl up to 303 MPa. From the half-wave potential (which was found to be independent of concentration but was moved to a more negative value by an increase in pressure of 3,000 atm), the volume of reaction ΔV_{SCE} for the cell was evaluated to be 23 $\pm$0.7 $cm^3\ mol^{-1}$.

However, it was the work by Faulkner *et al.* [31,32,54] which pioneered the use of Pt ultramicroelectrodes in high pressure cyclic voltammetry experiments. They measured the pressure dependence of the diffusion coefficients of $Fe(CN)_6^{3-}$ and O_2 in aqueous KCl [32]. These were chosen because the reaction products do not accumulate on the electrode surface and both system have been well described under ambient pressure. For the ferri/ferrocyanide systems [32] it was found that the cyclic voltammograms shifted toward more positive potentials (with increasing pressure) and their slopes decreased in a manner consistent with a slowing of the electrode kinetics for pressure above 0.4 GPa. The reduction of $Fe(CN)_6^{3-}$ was clearly favoured by pressure and the volume of activation changed from about -5.5 $cm^3\ mol^{-1}$ at 0.05 GPa to approximately -1.5 $cm^3\ mol^{-1}$ at 0.8 GPa suggesting that the volume of the transition state is smaller that of the reactants in the rate determining step. It was also found that the diffusion coefficient , D, was almost halved when the pressure was elevated from 0.1 GPa to 0.8 GPa (D= 0.76 x 10^{-5} $cm^2\ s^{-1}$ at 0 GPa and 0.47 x 10^{-5} $cm^2\ s^{-1}$ at 0.8 GPa). This was attributed mostly to the change of viscosity, η, because the product $D\eta$ did not change greatly with pressure.

The voltammetric and chronoamperometric measurements for the reduction of oxygen [32] showed analogous results whereby the waves shifted towards positive potentials when pressure increased thus the volume of the transition state is smaller than that of the reactants in the rate determining step. Once again the diffusion coefficient decreased with increasing pressure due to the changing of the viscosity of the solution; $D\eta$ varied only slightly with pressure.

Other systems studied for the effects of pressure on the electrode potential include horse heart cytochrome *c* [77], $M(bipy)_3^{3+/2+}$ (M = Co, Fe) and α-(hydroxyethyl)ferrocene$^{+/0}$ [38]. These results will be discussed in Section 13.4.5.

Finally, Stevenson and White [37] investigated the one electron reduction of acetophenone (AP) and nitrobenzene (NB) at a Pt microdisk in a small quantity of a dissociated supporting electrolyte, e.g., 0.2 M tetra-n-butylammonium hexafluorophosphate, and between 1 and 1,000 bar. The cell (Figure 13.7) consisted of an Ag/Ag_xO reference electrode, a Pt wire counter electrode (1 cm in length) and a Pt microdisk working electrode. The steady-state limiting currents obtained for the reduction of each species showed a linear decrease with increasing pressure for both systems. The apparent diffusivities of these liquids were calculated from limiting currents and compared to bulk solution molecular diffusivities measured for a redox-active molecule (decamethylferrocene, DMFc) added to the solutions at low concentration (16 mM). The same dependency on pressure for AP and NB and DMFc was found, thereby suggesting that the dependence of the limiting current on pressure for undiluted organic redox liquids can be predicted *a priori* from the bulk viscosity data over the same pressure range. Therefore, they concluded that the transport-limited currents for the reduction of these organic liquids are determined solely by diffusive processes.

13.3.3.2 Effects of pressure on electrodeposition and stripping analysis

Golas has studied the reduction of Hg^{2+} to Hg^0 at iridium microelectrodes and the reduction of Pb^{2+} to Pb^0 at mercury-coated electrodes [32,54]. A three-electrode system with Pt wire as the counter electrode and Ag/AgCl as the reference electrode was used.

Chronoamperometric transients and cyclic voltammograms of 10 mM Hg (I) in 0.1 M $HClO_4$ were obtained at an iridium microelectrode under pressure from 1 kbar to 6 kbar and compared to those obtained under ambient pressure [32]. The process of nucleation was found to be strongly pressure-dependent completing in less than 0.3 sec at 6 kbar. The thermodynamics of electroplating were improved by pressure as the cathodic peak was shifted by approximately 40 mV/kbar in the pressure range from 0 to 4 kbar.

The decrease of the separation of cathodic and anodic peaks on the cyclic voltammograms with increasing pressure suggested that the process becomes more reversible at elevated pressure. An increase in the cathodic peak current was also observed, and was attributed to the improved nucleation kinetics and possibly also to an increase of the number of active sites where mercury nuclei may start to grow.

Golas [32] also noted that over the range of pressure investigated the decrease of the diffusion coefficient cannot be compensated by the effective increase in Hg (I) concentration because of the compressibility of the aqueous solution. The Hg (I) concentration can be assumed to change from 10 mM at ambient pressure to 11.5 mM at 5 kbar.

The reduction of Pb^{2+} to Pb^0 at mercury coated electrodes was carried out [32] as it is well known that metallic lead forms an amalgam with mercury. Thus the product does not accumulate directly on the surface. Mercury-coated electrodes of different thickness were made and their performance at high pressure tested using this

reaction process. The peak potentials of the lead oxidation from mercury were found to be independent of pressure; however the kinetics of electrodissolution of lead were not favoured by increased pressure. The performance of the electrode was found to be dependent on the thickness and shape of the mercury film.

13.4 Volumes of Activation and Electrode Potentials

13.4.1 Theory

The effect of pressure P on a true thermodynamic equilibrium constant K° can be represented as the volume of reaction, ΔV^o, which is the sum of the partial molal volumes of the products minus that of the reactants as given by: [78]

$$(\partial \ln K^0 / \partial P)_T = -\Delta V^0 / RT \qquad (13.1)$$

where T is the temperature in Kelvin and R is the gas constant.

For electrochemical reactions [2,3,79], this can be expressed in terms of the standard electrode potential change ΔE^0 (the standard potential of the oxidant half-reaction minus that of the reductant half-reaction):

$$\ln K^0 = nF\Delta E^0 / RT \qquad (13.2)$$

$$\Delta V^0 = -nF(\partial \Delta E^0 / \partial P)_T \qquad (13.3)$$

where n is the number of moles of electrons transferred and F is the Faraday constant. From these equations it follows that a change in volume induced by the application of pressure will affect the standard potential of a redox couple.

Determination of ΔV^o from the algebraic sum of the partial molal volumes of all the entities involved in the reaction is, in principle, possible, but inaccurate (in cases such as when stable solid salts of one or more of the reacting solute species cannot be made in purity high enough for densimetric measurements) and valid only at infinite dilution. In contrast, ΔV^o values calculated by means of electrochemical measurements on a solution are *conditional* (i.e., at some practical value of ionic

strength) rather than standard values and can be made even when one of the redox partners is of limited long-term stability.

13.4.2 Pressure Effects on the Redox Potential of Metal Complexes

Table 13.1 contains a compilation of the experimental cell reaction volumes determined from electrochemical measurements at elevated pressure by different authors for the reduction of transition metal complexes in aqueous solution at 25 °C.

Table 13.1: *Experimental cell reaction volumes for the reduction of transition metal complexes in aqueous solutions at 25 °C. The values $\Delta V_{Ag/AgCl}$ are normalised against the Ag/AgCl electrode and assumed to be independent of pressure (0 - 200 MPa), unless otherwise indicated. Ligands abbreviations: bipy = 2,2'-bipyridine; diamsar = 1,8-diamino-3,6,10,16,19-hexaazabicyclo [6.6.6]eicosane (diaminosarcophagine); en = 1,2-diaminoethane(ethylenediamine); phen = 1,10-phenanthroline; sep = 1,3,6,8,10,13,16,19-octaazabicyclo[6.6.6]eicosane (sepulchrate); tacn = 1,4,7-triazacyclononane ([9]aneN$_3$); ttcn = 1,4,7 trithiacyclononane; isn = isonicotinamide; py = pyridine; lut = 3,5-lutidine.*

Couple/electrode	Medium	Ionic Strength (mol L^{-1})	$\Delta V_{Ag/AgCl}$ (cm^3 mol^{-1})	Ref.
$Fe(CN)_6^{3-/4-}$/Au	KNO_3	0.030	-39.9 ± 0.6	[52]
$Fe(CN)_6^{3-/4-}$/Au	KNO_3	0.030	-38.4 ± 0.6	[51]
$Fe(CN)_6^{3-/4-}$/Au	KNO_3	0.010	-39.6 ± 0.6	[52]
$Fe(CN)_6^{3-/4-}$/Au	KNO_3	0.010	-35.0 ± 1.2	[51]
$Fe(CN)_6^{3-/4-}$/Au	$NaNO_3$	0.10	-36.1 ± 1.3	[52]
$Fe(CN)_6^{3-/4-}$/Au	$Ba(NO_3)_2$	0.81	-42.4± 0.7	[52]
$Fe(CN)_6^{3-/4-}$/Au	$Ba(NO_3)_2$	0.30	-42.0 ± 1.4	[52]
$Fe(CN)_6^{3-/4-}$/Au	$Ba(NO_3)_2$	0.03	-38.9 ± 0.6	[52]
$Fe(CN)_6^{3-/4-}$/Au	$Sr(NO_3)_2$	0.30	-41.6 ± 0.8	[52]
$Fe(CN)_6^{3-/4-}$/Au	$La(NO_3)_3$	6.0	-23.6 ± 0.7	[52]
$Fe(CN)_6^{3-/4-}$/Au	$La(NO_3)_3$	0.60	-2.9.5 ± 0.4	[52]
$Fe(CN)_6^{3-/4-}$/Au	$La(NO_3)_3$	0.06	-30.4 ± 0.5	[52]
$Fe(CN)_6^{3-/4-}$/Au	$La(NO_3)_3$	0.01	-32.3 ± 0.5	[52]
$Fe(CN)_6^{3-/4-}$/Au	(Li,Na,K)Cl	1.0	-35	[80]
$Fe(CN)_6^{3-/4-}$/Au	KNO_3	1.00	-34.6 ± 0.4	[51]
$Fe(CN)_6^{3-/4-}$/Au	KNO_3	1.00	-35.8 ± 0.5	[52]
$Fe(CN)_6^{3-/4-}$/Au	KNO_3	0.33	-38.7 ± 0.9	[52]
$Fe(CN)_6^{3-/4-}$/Au	KNO_3	0.30	-37.6 ± 0.6	[51]
$Fe(CN)_6^{3-/4-}$/Au	KNO_3	0.10	-34.4 ± 0.6	[51]
$Fe(CN)_6^{3-/4-}$/Au	KNO_3	0.10	-39.3 ± 0.5	[52]
$Fe(CN)_6^{3-/4-}$/Pt	KCl	0.1	ca. -34	[54]
$Fe(CN)_6^{3-/4-}$/Pt	KCl	1.0	-38.3 ± 1.0	[36]
$Fe(CN)_6^{3-/4-}$/Pt	KCl	0.51	-36.6 ± 0.7	[36]
$Fe(CN)_6^{3-/4-}$/Pt	KCl	0.28	-36.2 ± 0.8	[36]
$Fe(CN)_6^{3-/4-}$/Pt	LiCl	0.28	-37.1 ± 1.3	[36]
$Fe(CN)_6^{3-/4-}$/Pt	K_2SO_4	0.28	-34.4 ± 0.6	[36]
$Fe(C_5H_5)^{2+/0}$/SAM/Au	$NaClO_4$	1.0	-10 to -22	[81]
$(NH_3)_5Ru^{III}Cyt^{II} \leftrightarrow (NH_3)_5Ru^{II}Cyt^{III}$	$NaClO_4$	0.1	31.7 ± 1.2	[82]

Couple/electrode	Medium	Ionic Strength (mol L^{-1})	$\Delta V_{Ag/AgCl}$ (cm^3 mol^{-1})	Ref.
trans-$(NH_3)_4$ (isn)$Ru^{III}Cyt^{II}$ ↔ *trans*-$(NH_3)_4$ (isn)$Ru^{II}Cyt^{III}$	$NaClO_4$	0.1	21.1 ± 1.0	[82]
trans-$(NH_3)_4$ (py)$Ru^{III}Cyt^{II}$ ↔ *trans*-$(NH_3)_4$ (py)$Ru^{II}Cyt^{III}$	$NaClO_4$	0.1	23.3 ± 0.6	[82]
trans-$(NH_3)_4$ (3,5-lut)$Ru^{III}Cyt^{II}$ ↔ *trans*-$(NH_3)_4$ (3,5-lut)$Ru^{II}Cyt^{III}$	$NaClO_4$	0.1	21.1 ± 0.8	[82]
$Fe(H_20)_6^{3+/2+}$/Pt	$HClO_4$/ $NaClO_4$	0.5	5.5 ± 0.8	[83]
$Fe(H_20)_6^{3+/2+}$/Pt	CF_3SO_3H	0.28	5.0 ± 0.3	[36]
$Fe(H_20)_6^{3+/2+}$/Au	$HClO_4$	1.0	4.6 ± 0.3	[53]
$Fe(H_20)_6^{3+/2+}$/Au	$HClO_4$	0.1	2.6 ± 1.4	[53]
$Fe(H_20)_6^{3+/2+}$/Au	$HClO_4$	0.1	7.0 ± 0.4	[84]
$Fe(phen)_3^{3+/2+}$/Pt	Na_2SO_4	0.1	15.3 ± 0.7	[83]
$Fe(phen)_3^{3+/2+}$/Pt	NaCl	0.1	14.2 ± 0.7	[84]
$Fe(phen)_3^{3+/2+}$/Au	KNO_3	1.00	9.6 ± 1.0	[52]
$Fe(phen)_3^{3+/2+}$/Au	KNO_3	0.25	9.0 ± 0.3	[52]
$Fe(bipy)_3^{3+/2+}$/Au	KNO_3	1.00	10.9 ± 0.3	[52]
$Fe(bipy)_3^{3+/2+}$/Au	KNO_3	0.10	11.2± 0.5	[52]
$Fe(bipy)_3^{3+/2+}$/Pt	KNO_3	0.10	18[a,b]	[38]
$Fe(bipy)_2(CN)_2^{+/0}$/Au	KNO_3	1.00	-3.7 ± 0.5	[52]
$Fe(bipy)_2(CN)_2^{+/0}$/Au	KNO_3	0.010	-3.6 ± 0.6	[52]
$Fe(bipy)_2(CN)_4^{-/2-}$/Au	KNO_3	1.00	-22.8 ± 0.6	[52]
$Fe(bipy)_2(CN)_4^{-/2-}$/Au	KNO_3	0.010	-26.7 ± 0.36	[52]
$Fe(phen)(CN)_4^{-/2-}$/Au	KNO_3	1.00	-22.6± 0.8	[52]
$Fe(phen)_2(CN)_2^{-/2-}$/Pt	NaCl	0.1	0	[84]
$Cu(aq.)^{2+/0}$/Cu	$NaNO_3$	0.1	2.8	[51,52]
$Cd^{2+/0}$/Hg	NaCl	4.0	10.7	[85]
$Cr(bipy)_3^{3+/2+}$/Hg(Au)	KNO_3	0.1	11.0 ± 1.0	[53]
$Mo(CN)_8^{3-/4-}$/Au	$NaClO_4$	0.5	-29.8.0 ± 1.0	[86,87]
$W(CN)_8^{3-/4-}$/$C_{(gl)}$	KCl	0.5	-27.5 ± 0.8	[86,87]
$CH_3CHOH(C_5H_4)$	KNO_3	0.1	-0.8[a,c]	[86]
$Os(CN)_6^{3-/4-}$/Pt	KCl	0.6	-33.4 ± 0.9	[86]
$Co(bipy)_3^{3+/2+}$/Au	KNO_3	0.1	23.9 ± 0.9	[53]
$Co(bipy)_3^{3+/2+}$/Pt	KNO_3	0.1	29.2[a,d]	[38]
$Co(bipy)_3^{3+/2+}$/Pt	NaCl	0.1	27.1 ± 1.4	[84]
$Co(terpy)_3^{3+/2+}$/Pt	NaCl	0.1	30.8 ± 1.5	[84]
$Co(en)_3^{3+/2+}$/Pt	KCl	0.5	26.7 ± 0.7	[83]
$Co(en)_3^{3+/2+}$/Hg(Au)	KNO_3	0.1	29.8 ± 0.5	[53]
$Co(diamsar)^{3+/2+}$/Au	$NaClO_4$	0.1	17.4 ± 0.5	[88]
$Co(diamsarH_2)^{5+/4+}$/Au	$HClO_4$/ $NaClO_4$	0.13	19.5 ± 0.8	[88]
$Co(sep)^{3+/2+}$/Pt	KCl	1.0	13.5 ± 0.4	[36]
$Co(sep)^{3+/2+}$/Pt	KCl	0.28	13.9 ± 0.5	[36]
$Co(sep)^{3+/2+}$/Pt	KCl	0.5	15.8 ± 0.5	[83]
$Co(ttcn)^{3+/2+}$/Pt	$NaClO_4$	0.1	24.4 ± 1.0	[83]
$Co(ttcn)^{3+/2+}$/Pt	CF_3SO_3H	0.26	21.1 ± 0.3	[89]
$Co(ttcn)^{3+/2+}$/Pt	KCl	0.26	20.6 ± 0.2	[89]
$Co(ttcn)^{3+/2+}$/Pt	KCl	1.1	21.8 ± 0.5	[89]
$Co(ttcn)^{3+/2+}$/Pt	NaCl	0.3	21.4 ± 1.1	[84]
$Ni(tacn)^{3+/2+}$/Pt	NaCl	0.1	24.7 ± 1.2	[84]
$Ru(H_2O)_6^{3+/2+}$/Au	$NaClO_4$	0.1	2.4 ± 0.7	[53]
$Ru(H_2O)_6^{3+/2+}$/Au	$HClO_4$	0.1	3.0 ± 0.6	[53]
$Ru(NH_3)_6^{3+/2+}$/Au	KNO_3	0.1	20.2 ± 0.4	[53]

Couple/electrode	Medium	Ionic Strength (mol L^{-1})	$\Delta V_{Ag/AgCl}$ (cm^3 mol^{-1})	Ref.
$Ru(NH_3)_6^{3+/2+}$/Hg(Au)	KCl	0.1	19.7 ± 0.6	[53]
$Ru(en)_3^{3+/2+}$/Hg(Au)	KNO_3	0.1	16.9 ± 0.6	[53]
Horse Heart Cytochrome *c* $^{III/II}$	NaCl	0.1	-23[a,e]	[77]
Horse Heart Cytochrome *c* $^{III/II}$	$NaClO_4$	0.1	-14.0 ± 0.5	[82]

[a] Pressure dependent: value at 100 MPa.
[b] Ranges from 39.5 cm^3 mol^{-1} at 0 MPa to 4.0 cm^3 mol^{-1} at 1 GPa.
[c] Ranges from 1.9 cm^3 mol^{-1} at 0 MPa to -3.8 cm^3 mol^{-1} at 500 MPa; nearly constant at -3.7 cm^3 mol^{-1} from 0.5 to 1.0 GPa
[d] Ranges from 55.1 cm^3 mol^{-1} at 0 MPa to 12.5 cm^3 mol^{-1} at 1 GPa.
[e] Ranges from -27 cm^3 mol^{-1} at 0 kbar to -3 cm^3 mol^{-1} at 5 kbar.

A few high–pressure electrochemical experiments were also carried out in acetonitrile with respect to a $Ag/AgClO_4$ (0.01 M in 0.1 M Et_4ClO_4) reference electrode by Sachinidis [53] and have been listed in Table 13.2.

Table 13.2: *Cell reaction molar volume for complex-ion couples in acetonitrile using a 1 mm Au disk working electrode and a $Ag/AgClO_4$ (0.01 M), 0.1 N Et_4NClO_4 reference electrode at 298 K [53]. Ligands abbreviations: phen = 1,10-phenanthroline, bipy = 2,2'-bipyridine.*

Couple	ΔV_{cell} (cm^3 mol^{-1})
$Fe(cp)_2^{+/0}$	-9.9 ± 0.5
$Fe(phen)_3^{3+/2+}$	-1.5 ± 1.1
$Co(phen)_3^{3+/2+}$	+15.0 ± 0.9
$Co(bipy)_3^{3+/2+}$	+14.0 ± 1.4

From these tables it can be seen that, despite the difficulty of obtaining reproducible electrochemical results from pressurised systems (see introduction) a general good agreement between the data reported by different authors is found. Furthermore, several studies for the ferri/ferrocyanide couple have been undertaken [36,51,52] in different electrolytes showing that for this couple the $\Delta V_{complex}$ (complex-ion reduction volume) is almost independent of the nature or concentration of the electrolyte.

The issue of how to evaluate the contributions of the separate half-cells to the experimental volume change (ΔV_{cell}) associated with the reduction of a complex-ion couple was first addressed by Sachinidis. The "Sachinidis-Shalders-Tregolan principle" [51-53] permits the separation of the contribution to ΔV_{cell} of the reference electrode (ΔV_{ref}) and of the redox couple of interest ($\Delta V_{complex}$). Then, $\Delta V_{complex}$ for

the couple can be split into intrinsic (ΔV_{intr}) and electrostrictive (ΔV_{elec}) components. ΔV_{intr} reflects bond length and conformational changes in the structure of the complex, while ΔV_{elec} reflects the contraction or the expansion of the surrounding solvent in response to the change in charge on the complex accompanying the redox reaction thereby providing much otherwise inaccessible information on the solvational and structural changes accompanying redox processes. This applies both in aqueous and non-aqueous solutions.

The estimated intrinsic and electrostrictive contributions for a range of couples were studied in aqueous solutions [36,52,53,83] and are summarised in Table 13.3.

Table 13.3: *Electrostrictive and intrinsic contributions to various M(III)/(II)-complex reduction volumes (cm^3 mol^{-1}) in aqueous solution at 298 K (Italicised data are calculated from the other two sets of data for that system. Ligands abbreviations: bipy = 2,2'-bipyridine; en = 1,2-diaminoethane(ethylenediamine); phen = 1,10-phenanthroline.*

Redox Couple	$\Delta V_{complex}$ (cm^3 mol^{-1})	ΔV_{elec} (cm^3 mol^{-1})	ΔV_{intr} (cm^3 mol^{-1})	Ref.
$Fe(H_2O)_6^{3+/2+}$	+14.0[a]	+4.4	9.6	[36]
$Fe(H_2O)_6^{3+/2+}$	+14.5[b]	+4.9	9.6	[83]
$Fe(H_2O)_6^{3+/2+}$	+12.7[c,d]	+3.1	9.6	[52]
$Fe(H_2O)_6^{3+/2+}$	+13.6[e]	+4.0	9.6	[53]
$Fe(phen)_3^{3+/2+}$	+19.1[f]	*+19.1*	0	[52]
$Fe(bipy)_3^{3+/2+}$	+21.3[g]	*+21.3*	0	[52]
$Ru(en)_3^{3+/2+}$	+27.0[c,h]	+25.9	1.1	[52,53]
$Ru(NH_3)_6^{3+/2+}$	+30.3[c,h,i]	+27.7	2.6	[52,53]
$Ru(NH_3)_6^{3+/2+}$	+29.8[c,d,h]	+27.2	2.6	[52,53]
$Ru(H_2O)_6^{3+/2+}$	+12.5[c]	+6.8	6.7	[52]
$Ru(H_2O)_6^{3+/2+}$	+13.1[c,d]	+6.4	6.7	[52]
$Cr(bipy)_3^{3+/2+}$	+21.1[h]	*+21.1*	0	[53]
$Co(phen)_3^{3+/2+}$	+34.4	+19.1	15.3	[52,53]
$Co(phen)_3^{3+/2+}$	+34.4	+19.1	16.5	[53]
$Co(phen)_3^{3+/2+}$	+34.4	+20.7	13.7	[52,53]
$Co(bipy)_3^{3+/2+}$	+34.0[c,h]	+21.3	12.7	[52,53]
$Co(en)_3^{3+/2+}$	+39.9[c,h]	+28.0	11.9	[52,53]

[a] I=0.28 mol L^{-1} CF_3SO_3H; assumes $\Delta V_{ref}(Ag/AgCl)$ of -9 cm^3 mol^{-1}.
[b] I=0.5 mol L^{-1} $HClO_4/NaClO_4$; assumes $\Delta V_{ref}(Ag/AgCl)$ of -9 cm^3 mol^{-1}.
[c] Assumes $\Delta V_{ref}(Ag/Ag^+)$ of -13 cm^3 mol^{-1}.
[d] I=0.1 mol L^{-1} $HClO_4$.
[e] I=1.0 mol L^{-1} $HClO_4$; assumes $\Delta V_{ref}(Ag/Ag^+)$ of -11.9 cm^3 mol^{-1}
[f] I=0.25 mol L^{-1} KNO_3
[g] I=0.25 mol L^{-1} KNO_3.
[h] I=0.10 mol L^{-1} KNO_3.
[i] Using Au(Hg) working electrode.

It can be seen that the electrostrictive volume change is around 20 cm^3 mol^{-1} for the larger tri-phen and tri-bipy systems, increasing to approximately 26 cm^3 mol^{-1} for the

smaller tris-en and hexamine complexes. Where ΔV_{intr} is anticipated to be zero (i.e., $Fe(bipy)_3^{3+/2+}$ [52], $Fe(phen)_3^{3+/2+}$ [52], and $Cr(bipy)_3^{3+/2+}$ [53]) the volume of activation for the complex ($\Delta V_{complex}$) is very similar and is attributed to ΔV_{elec} alone. Under the assumption that this will be the electrostrictive contribution to $\Delta V_{complex}$ for couples such as $Co(phen)_3^{3+/2+}$ $Co(bpy)_3^{3+/2+}$, Sachinidis [53] concluded that intrinsic changes contribute around half of the +34 $cm^3\ mol^{-1}$ associated with these reductions.

Franklin and Mathew measured apparent volumes of activation for the metal electrodeposition reactions:

$$M(H_20)_6^{z+}(aq) + ze^- \rightarrow M(s) + 6\ H_2O \qquad (13.4)$$

for M = Ni [90-92], Co and Ag [92] from a variety of electrolyte solutions.

The volume of activations for the electron-transfer step were determined from the effect of pressure (0-1,750 atmospheres) on the exchange current density, i_o, at constant overvoltage η according to [57]:

$$\Delta V_{ideal}^* = -RT\,(\partial \ln i_o / \partial P)_{\eta,T} \qquad (13.5)$$

The volume of activation is the sum of an intrinsic part, ΔV^*_{int} related to bond-making and bond-breaking, and a solvational part, $\Delta V^*_{sol,}$ relating to the loss of solvent ligand molecules attached to the reacting substances. In dilute solutions, the volumes of activation were found to be equal to +13 $cm^3\ mol^{-1}$ for Co and Ni and +10 $cm^3\ mol^{-1}$ for Ag. Given that the volumes of activation for water exchange on $Co(H_2O)_6^{2+}$ and $Ni(H_2O)_6^{2+}$ are +6.1 and +7.2 $cm^3\ mol^{-1}$ respectively, Franklin deduced that the rate determining first step en route to the formation of a desolvated atom of elemental metal during the activation process for electrodeposition was the loss of two water molecules (one from the electrode surface, one from the first coordination sphere of the aqueous ion).

Results obtained in the presence of other additives showed that one water molecule was lost in boric acid and more concentrated chloride solutions [91] and of

sulfonate [92] and thiocyanate [90] in the deposition of nickel while none were lost in thiocyanate solutions [90]. Franklin interpreted these findings in terms of an outer-sphere electron-transfer bridge between the electrode and the metal ion in the case of thiocyanate [90] and inner-sphere bridges in the cases of chloride and boric acid [91].

Swaddle [3,93,94] details an empirical equation which relates the molar volume of aqua-ions to their coordination number, according to which the volume change expected for complete removal of one water molecule from the first coordination sphere of a metal aqua-ion to bulk solution is about +13 $cm^3\ mol^{-1}$, with only a slight dependence on ionic charge or size. Hence, Swaddle reinterpreted Franklin's experimental results discussed above and suggested that the rate determining first step in electrodeposition of a metal is the removal of one water ligand from the metal ion, without dehydration of the electrode surface, thereby allowing a sufficiently close approach of the central metal ion to the electrode for electron transfer to occur. When significant concentrations of chloride, thiocyanate, or azide ions are present, these anions become coordinated to the metal ion and provide efficient (inner-sphere) bridges [91]. Conversely, for Ag^+, complexation with ammonia, which cannot act as a bridge for electron transfer, increases the volume of activation to +21 $cm^3\ mol^{-1}$.

13.4.3 Pressure Effects on the Kinetics of Electrode Reactions of Metal Complexes

Table 13.4 summarises the rate constants k_{el} and the corresponding volume of activation $\Delta V_{el}^{\ddagger}$ for electrode reactions determined as a function of pressure up to 200 MPa using alternating current (AC) voltammetry by Swaddle and co-workers in their Calgary laboratories [83,86,88,89,95-99]. The analogous quantities for the corresponding homogeneous self-exchange reactions in bulk solution are also reported for comparison.

Table 13.4: *Rate constants and volumes of activation for self-exchange reactions at electrodes and in homogeneous aqueous solution obtained as a function of pressure up to 200 MPa using alternating current (AC) voltammetry at 25 ℃ by Swaddle and co-workers in their Calgary laboratories [83,86,88,89,95-99] Ligands abbreviations: bipy = 2,2'-bipyridine; diamsar = 1,8-diamino-3,6,10,16,19-hexaazabicyclo[6.6.6]eicosane (diaminosarcophagine); en = 1,2-diaminoethane(ethylenediamine); phen = 1,10-phenanthroline; sep = 1,3,6,8,10,13,16,19-octaazabicyclo[6.6.6]eicosane (sepulchrate); ttcn = 1,4,7 trithiacyclononane.*

Couple/Electrode	**Medium (mol L^{-1})[a]**	**k_{el}^0 (cm s^{-1})**	**$\Delta V_{el}^{\ddagger}$**	**$k_{el}^{0\,b}$ (L mol^{-1} s^{-1})**	**$\Delta V_{el}^{\ddagger c}$ (cm^3 mol^{-1})**	**Ref.**
$Co(phen)_3^{3+/2+}$/Pt	0.1 NaCl	0.108 ± 0.002	-9.1 ± 0.4	6.7 (0.10)	-17.6 ± 0.7	[83,96]
$Co(en)_3^{3+/2+}$/Pt [d]	0.5 KCl	0036 ± 0.001	-8.3 ± 0.5	8×10^{-5} (0.5)	-15.5 ± 0.8	[83,95,100]
$Fe(H_2O)_6^{3+/2+}$/Pt	0.5 $HClO_4$/Na ClO_4	0.0207± 0.0005	-5.5 ± 0.2	4.8 (0.5)	-11.1 ± 0.5	[83,97]
$Co(diamsar)^{3+/2+}$/Pt	0.1 $NaClO_4$ (pH 9)	0.0162 ± 0.0007	-3.5 ± 0.2	0.48 (0.14)	-10.4 ± 0.5	[83,88]
$Co(diamsarH_2)^{5+/4+}$/Au	0.13 $HClO_4$/Na ClO_4	0.010 ± 0.001	-3.8± 0.3	0.05 (0.4)	-9.6 ± 0.8	[83,88]
$Co(sep)^{3+/2+}$/Pt	0.5 KCl	0.091 ± 0.001	-3.0 ± 0.4	5.0 (0.2)	-6.4± 0.2	[83,89,95,98]
$Co(ttcn)_2^{3+/2+}$/Pt	0.1 $NaClO_4$	0.27 ± 0.02	-2.8 ± 0.7	9.5×10^4 (0.1)	-4.8 ± 0.2	[83,89,98]
$Fe(phen)_3^{3+/2+}$/Pt	0.1 Na_2SO_4	0.300 ± 0.003	-1.6 ± 0.1	1.4×10^7 (0.3)	-2.2 ± 0.1	[83,99]
$Fe(CN)_6^{3-/4-}$/Pt	0.5 KCl	0.072 ± 0.005	+11.9 ± 1.4	2.6×10^4 [e]	+22 ± 2	[83,95,101]
$Os(CN)_6^{3-/4-}$/C(glassy)	0.6 KCl	0.040 ± 0.005	+9.7 ± 0.7	3.1×10^4 [f]	+18.5 ± 0.8	[86,87]
$Mo(CN)_6^{3-/4-}$/Au	0.1 $NaClO_4$ (pH 2.7)	0.053 ± 0.001	+7.3 ± 0.7	3.1×10^4 [g]	+14.6 ± 0.5	[86,87]
$Mo(CN)_6^{3-/4-}$/C(glassy)	0.5 $(Et_4N)Cl$	0.18 ± 0.03	-4.4 ± 0.5	6×10^4 [h]	-8.2 ± 0.6	[86,87]
$W(CN)_8^{3-/4-}$/Pt	0.5 KCl	0.161 ± 0.008	+10.8 ± 0.4	1.0×10^4 [i]	+12.5 ± 1.1	[86,87]

[a] Medium for k_{el}^0 and $\Delta V_{el}^{\ddagger}$ measurements.
[b] Ionic Strength I (mol L^{-1}) in parenthesis.
[c] See reference for details of medium and temperature.
[d] A total of 0.2 mol L^{-1} 1,2-diaminoethane (en) is present.
[e] 0.08 mol L^{-1} $K_4Fe(CN)_6$, 0.002 mol L^{-1} $K_3Fe(CN)_6$.
[f] 0.19 mol L^{-1} $K_4Os(CN)_6$, 0.01 mol L^{-1} $K_3Os(CN)_6$.
[g] 0.078 mol L^{-1} $K_4Mo(CN)_6$, 0.01 mol L^{-1} $K_3Mo(CN)_8$.
[h] 0.069 mol L^{-1} $(Et_4N)_4Mo(CN)_8$, 0.007 mol L^{-1} $(Et_4N)_3Mo(CN)_8$.
[i] 0.23 mol L^{-1} $K_4W(CN)_8$, 0.014 mol L^{-1} $K_3W(CN)_8$.

This shows that for typical aqueous electrode reactions the volumes of activation for heterogeneous electron transfer ($\Delta V_{el}^{\ddagger}$) are one-half of those for homogeneous (bimolecular) electron transfer ($\Delta V_{ex}^{\ddagger}$) in the same couple, with the same algebraic

sign, as can generally be accounted by an extension of Marcus theory [102-105] developed for the latter. This is referred to by Swaddle [2,3,95] as the fifty-percent rule and can be written as:

$$\Delta V_{el}^{\ddagger} = 1/2\ \Delta V_{ex}^{\ddagger} \qquad (13.6)$$

13.4.4 Effects of Solvents Dynamics at Elevated Pressures

Given that the viscosity is roughly exponentially dependent on pressure over the first few hundred MPa for common solvents other than water, kinetic studies of electrode reactions at high pressures are potentially capable of providing evidence of the possible involvement of solvent dynamics (solvent friction) in non-aqueous systems without changing the solvent chemically.

In the case of water, pressure breaks up ice-like local structures in the liquid phase. As a consequence, the η vs P plot at low temperatures passes through a shallow minimum around 50 - 100 MPa and at 25 °C is almost flat to 200 MPa. Hence, for a given couple, if any pressure effects (retardations) on k_{el} observed in aqueous solutions are truly due to solvent dynamic effects, they will be absent in H_2O at 25 °C. Normally, volumes of activation for cationic couples undergoing electron transfer at an electrode are expected to be moderately negative [83] thus a markedly positive value for non-aqueous solvent would indicate the incursion of solvent dynamics.

Fu *et al.* [106] have measured volumes of activation for the reduction of $Co(bipy)_3^{3+}$ at a Pt electrode in acetonitrile, acetone, propylene carbonate and water. The results suggest that the fifty-percent rule (Section 4.3) also applies to $\Delta V_{el}^{\ddagger}$ for electrode reactions in non-aqueous media but its effect is swamped by solvent dynamical contributions so that $\Delta V_{el}^{\ddagger}$ is invariably positive [2,3,106].

Yeomans and co-workers [107] investigated the effect of the presence of the anions PF_6^-, BF_4^-, ClO_4^-, and tosylate on the potential of the Ru(III)/(II) redox

processes in a series of mono-, di-, and trinuclear complexes involving polypyridyl ligands. The anions were found to give rise to a cathodic shift in the respective redox potentials in the sequence PF_6^- < BF_4^- ~ ClO_4^- < tosylate, with the magnitude of the shift being largest for the tri-nuclear and smallest for the mononuclear species. The molar volume changes for successive redox couples in di- and tri- nuclear complexes were found to be invariant and consistent for mononucleus species suggesting the occurrence of isolated Ru(III)/(II) processes in all complexes and that the electrostrictive effects on solvents are limited to a very short range.

13.4.5 Effects of Pressure on the Electrochemistry of Proteins

Cruanes *et al.* [77] pioneered the use of high-pressure electrochemistry for protein characterisation and demonstrated that high pressure electrochemical measurements of metalloproteins may provide valuable thermodynamic information as well as insights into the structural (through ΔV) and dynamic (through compressibilities) differences between their oxidised and reduced forms. They measured the formal redox potentials for horse heart cytochrome *c* over the pressure range 0 - 500 MPa using a gold electrode. To avoid adsorption of the metalloprotein on the electrode surface, the gold electrode was coated with L-cysteine, a strongly adsorbed monolayer of a suitable electron transfer promoter.

The pressure effect on the iron(III)(II) centre in horse heart cytochrome *c* relative to Ag/AgCl was also investigated by Sun and co-workers [82] but the results are in disagreement with those reported by Cruanes [77].

Cruanes [77] observed a reaction volume of -24 cm^3 mol^{-1} (Table 13.1) which was ascribed to the volume collapse associated with the reduction of cytochrome *c*. In contrast, Sun [82] reported no major change in volume during the electron transfer. Discrepancies between the two sets of results may have originated in medium effect of

chloride *vs.* perchlorate and in the use of a different electrode modifier agent (L-cysteine) [77] and 4,4'-dipydyldisulfide [82] (Table 13.1). It is also worth mentioning that Sun confined his investigation to a maximum value of pressure of 200 MPa. In contrast, Cruanes' investigation covered a wide range of pressure (0 - 500 MPa) but yielded a curved plot of ΔE versus P, the interpretation of which is further complicated by a possible change in response of the Ag/AgCl reference electrode observed around 300 MPa.

13.4.6 Effect of Pressure on the Electrochemistry of Self-Assembled Monolayers (SAMs) and Quaternised Poly-4-VinylPyridine (QPVP) films

Faulkner and co-workers [81] studied the electrochemical behaviour of ferrocene-terminated self-assembled monolayers (SAMs) on gold electrodes in 1 M $NaClO_4$ at hydrostatic pressures from 0.001 to 6 kbar. The oxidation of surface-bound neutral ferrocene to ferrocenium was found to be disfavoured by compression. This effect was attributed to the steric characteristics of the oxidation step, which involves a volume expansion relative to that of ferrocene in solution, probably related to a structural transformation of the monolayer and a need for counterion complexation.

Faulkner *et al.* [108] have reported electrochemical studies of quaternised poly-4-vinylpyridine (QPVP) films placed on electrode surfaces, loaded with ferricyanide ions and exposed to 0.1 M KNO_3, at pressure from ambient to 8 kbar. At atmospheric pressure the films have a gel-type structure and the electrochemical responses show the expected thin-layer behaviour for the electron-diffusional process. However, with compression, a new process governed by semi-infinite linear diffusion gradually takes place. The results indicate that the propagation of charge is drastically restricted under high pressure. Overall the data provide evidence that compression alters the microstructure of the film. Interestingly, the decrease in volume that accompanies the

reduction of ferrocyanide incorporated into the film was found to be about -30 cm^3 mol^{-1} which is the same value obtained for ferricyanide in solution (Table 13.1).

13.5 Application of Pressure to Specific Electrochemical Systems

13.5.1 Electrochemistry of Superoxide at Elevated Pressures (up to 10 atmospheres)

Alnashef *et al.* [109] have recently investigated the electrochemical behaviour of the superoxide ion ($O_2^{\bullet -}$) in acetonitrile as a function of pressure up to 10 atmospheres with tetraethylammonium perchlorate (TEAP) as the supporting electrolyte. The pressurised cell was constructed from a 1-in diameter Swagelock cross tubing. A Pt wire (0.13 mm diameter) acted as a quasi-reference electrode and Pt mesh having surface areas of 0.5 and 1 cm^2 acted as working and counter electrode, respectively. The electrodes were sealed in the cross cell with the aid of Conax Teflon fittings.

Cyclic voltammograms obtained in the pressure cell at several values of oxygen overpressure (from 1 to 10.88 atmospheres) showed that the rate of the superoxide generation increased as expected because of the increased solubility of oxygen according to Henry's law. Cyclic voltammograms were also obtained keeping the oxygen pressure constant at 160 psi (10.88 atmospheres) and varying the CO_2 overpressure (1, 2.36 and 3.72 atmospheres) and these revealed that the addition of gaseous CO_2 enhanced the oxygen reduction but inhibited the reverse (oxidation) reaction of superoxide to oxygen in a manner consistent with the irreversible formation of a peroxydicarbonate ion.

13.5.2 High Pressure Electrochemical Promotion of Ammonia Synthesis over an Industrial Iron Catalyst

Yiokari *et al.* [110] reported the first investigation of the effect of electrochemical promotion or nonfaradaic electrochemical modification of catalytic activity (NEMCA effect) in a high pressure (50 atmospheres) reactor.

The system studied was ammonia synthesis over an industrial iron catalyst. The experimental set up consisted of a 300 cm^3 high pressure reactor vessel, an analysis unit and a gas feed unit. A 24-pellet cell unit was constructed and suspended inside the vessel which was operated at 50 atmospheres.

The catalyst was loaded on high-proton conductive disks. Silver reference and counter electrodes were deposited on the other side of the disks by applying GC electronics silver followed by drying in air at 120 °C. Specially built machinable ceramic (Macor) holders were used to support the catalyst pellets.

The reactor head was equipped with a transducer gland that fitted three gold wires used to keep all 24 of the working, counter and reference electrodes, respectively, connected in parallel. By means of these three wires, constant external potentials or constant current was applied via a galvanostat-potentiostat.

It was found that the catalytical activity of the industrial iron catalyst for ammonia synthesis could be enhanced by up to 1,300% by interfacing the catalyst with the proton conductor $CaIn_{10}Zr_{0.9}O_{3-\alpha}$ and by supplying protons to the catalyst via application of a potential (typically -1.0 V) between the catalyst and the counter electrode. The results could in principle lead to a substantial decrease in the operating temperature and pressure of ammonia synthesis reactors.

13.5.3 High Pressure Sono-Electrochemistry

The combination of high pressure and ultrasound assisted electrochemistry was pioneered by Compton *et al.* [55]. A novel high pressure sonoelectrochemical cell (Figure 13.8) was developed employing high-intensity ultrasound emitted from an ultrasonic horn probe and tested up to a static pressure up to 100 bar without any noticeable leak over a period of several hours. The effect of pressurising the sonoelectrochemical cell with Ar and CO_2 was studied by recording cyclic voltammograms for the reversible $Ru(NH_3)_6^{3+/2+}$ couple at a 25 μm diameter Pt electrode under silent conditions and in the presence of ultrasound. Under silent conditions, a change in pressure up to 60 bar did not alter the diffusion limited current for the reduction process. However, two different types of behaviour were observed. First, at a given pressure and at a low ultrasonic power, no cavitation occurred. Second, after a pressure dependent threshold in ultrasound power, the onset of cavitation at the electrode/solution interface was observed and this resulted in a remarkable increase in the mean transport limited current.

Furthermore, the threshold for the cavitation process was found to be strongly dependent on the type of pressurising gas. In the presence of argon a nearly linear increase in the threshold for cavitation was observed and at a relatively mild 30 bar level cavitation could no longer be induced with the available power. However, in the presence of carbon dioxide the threshold for cavitation appeared at lower ultrasound power and even decreased at higher pressures (> 40bar). The observed phenomena were explained in terms of the mechanical pressure, the surface tension and the formation of a CO_2 phase.

Given the detected current enhancement even in the presence of "soft" cavitation, liquids near the critical point can be considered very suitable solvents for

efficient sonoelectrochemical processes even at high pressure, which may have interesting applications in Super Critical Electrochemistry (Section 13.6).

13.6 Voltammetry at High Temperatures and High Pressures

The study of hydrothermal solutions at elevated pressures poses a number of problems such as the risk of thermoelectric effects, the corrosive nature of the electrolyte solution toward many metals, the dissolution or leaching of silica or silicate-based vessels, the softening or decomposition of many plastic structural materials such as Teflon and the increased solubility of reference electrode components such as AgCl [111]. As a result, there still a great scarcity of thermodynamic data in the supercritical environment.

By far the most comprehensive study is that carried out by Bard *et al.* have been engaged in extracting quantitative and qualitative electrochemical data from a number of inorganic and organic species in near-critical or supercritical media such as water, ammonia, SO_2 and acetonitrile [76,112-121]. Research in this area is of technological interest because of the unique solvent properties of materials in the critical region, including improved transport conditions, which has led to their extensive use in extraction and separation science. They also hold clear advantages for electrosynthesis.

A lot of effort was made in the design of cells and electrodes that allow precise measurements under extreme conditions of high temperature and pressure. Aqueous solutions under these conditions are very corrosive and can attack most metal and dissolve quartz and Pyrex glass, leading to equipment failure and solution contamination. An alumina tube was used as the electrochemical cell in their earlier experiments [76,113,115] because alumina had the desired properties of chemical inertness to hot water and a high volume resistivity (reducing stay electric fields within

the cell during measurements) but it was revealed to be brittle and often cracked during a heating cycle. A stainless steel pressure vessel with silica liner was also used [114] but this exhibited problems with dissolution by water at high temperature.

An improved electrochemical cell [121] based on an oxidised titanium tube that showed excellent mechanical and chemical stability was therefore constructed. The central section of the cell consisted of a 6.35 mm o.d. Ti tube with a 0.89 mm diameter wall thickness and a length of 10 cm. The tube contained the solution under high pressure and was the only section of the cell that was heated by wrapping the tube in a flexible electric heating tape. All the 316 stainless and Hastelloy parts in the original design were also changed to titanium, eliminating the contamination from metal corrosion.

Macroscopic electrodes used in the earlier experiments [114,115] showed significant iR drops that limited the accuracy of the measurements. Ultramicroelectrodes of Pt sealed in Pyrex were then used in one instance [76] but the Pyrex electrode appeared to suffer from corrosion and current leakage. Finally, the electrode design was improved [121] and Pt UMEs mounted in a special glass (Corning 8870, 50-60% PbO, 25-35% SiO_2, 5-10% K_2CO_3, 0.1-0.5% SbO_3) were the sensors of choice as they were showed to be resistant toward leaching by supercritical water at temperature up to 385 °C and pressure up to 270 bar.

The measurement of pH in high temperature aqueous systems is a major challenge [122,123]. Problems such as irreversibility, drift and errors (in some cases up to ±0.5 pH units) are so often encountered that it is still not easy to routinely carry out highly accurate experiments at temperature above 100 °C [123]. However, in recent years Macdonald's group has made important advances in the measurement of pH in high temperature and supercritical water [124-134]. They carried out high quality potentiometric measurements (accuracy from 3 to 10 mV) using a flow-through

technique along with a flow-through external pressure-balanced Ag/AgCl reference electrode (EPBRE) in which the electroactive element is maintained at room temperature via a non-isothermal electrolyte bridge [124] thereby overcoming the problem with the value of the thermal liquid junction potentials varying ± 150 mV depending on the nature of the electrolyte bridge and the thermal gradient across it. Other pH sensing electrodes that they have successfully developed include a tungsten oxide [128], glass electrodes for moderately high temperature (200-250 °C) [125], and a YZS (yttrium-stabilised zirconia) pH sensitive membrane electrode [126,127] containing a Hg/HgO internal element fitted into an autoclave contained in a once through/recirculating flow loop that operates in a single-phase mode at both sub and supercritical temperatures (temperatures from 200 and 390 °C and pressure of 255 bar). They also developed Pd-Pt electrodes for measuring dissolved H_2 in supercritical media [129].

Developments have also been made in electrochemical investigations for corrosion testing in high temperature water. Jayasekera and co-workers [135,136] investigated the anodic dissolution of iron and cathodic reduction of oxygen in ammonium chloride solutions over the temperature range 30-150 °C and at a total pressure up to 780 kPa using the rotating disk electrode technique. The industrial importance of this reaction is in the production of synthetic rutile via the Becher Process which involves the high temperature reduction of ilmenite followed by the forced corrosion of metallic iron from the reduced ilmenite matrix. Results from a series of pressure leaching trials showed that, by carrying out this reaction at above ambient oxygen partial pressures and at elevated temperatures, the corrosion rate can be significantly increased above that achieved in the conventional aeration process. Electrochemical corrosion rate measurements for corrosion of stainless steel in high temperature water have also been reported [137-139].

Some high temperature and high pressure studies have also been carried out in non-polar solvents such chlorodifluoromethane [140], trifluoromethane [141,142], in difluoromethane [143-146] and CO_2 [147,148]. The limited publications on non-polar Super Critical Fluids (SCFs) as compared to the polar SCFs discussed above is primarily due to the low solubility of electrolytes and the associated high solution resistance [143].

13.7 Conclusion

High pressure electrochemical studies are potentially dangerous and less immediately implemented than conventional investigations. Technical obstacles related to properties of the working electrode material, preparation of its surface, availability of suitable reference electrodes, and the need for specially designed high pressure equipment and cells may account for the relative lack of experimental data on electrochemistry at high pressures. However, this chapter has shown that the limitations and experimental difficulties associated with high pressure electrochemical experiments encountered in earlier studies have finally been overcome in the last 10-15 years and, consequently, the interest in high pressure electrochemistry has since grown and will grow further.

Initial electrochemical experiments carried out at high pressure were almost completely restricted to electrolytic conductance and galvanic cell emf measurements, the former receiving more attention. However, in the last two decades there has been an increasing interest in the study of electrode kinetics at high pressure and of the effect of pressure on redox equilibria. As a consequence, a considerable amount of data, mainly concerned with the measurements of molar volume changes associated with redox processes has now become available, in both aqueous and non-aqueous solvents. This has allowed the accurate determination of activation and reaction

volumes for a large number of redox couples which has led to a better understanding of solute-solvent interactions in electron-transfer phenomena, reaction kinetics, and mass and charge transport mechanisms. Such information is finding application describing chemical processes in areas from classical coordination chemistry to reactions of proteins.

The number of electrochemical studies in the area of SCFs has also expanded in recent years because of the awareness of the unique solvent properties of materials in the critical region which, combined with the improved mass transport conditions, holds clear advantages in practical applications such as electrosynthesis and separation science.

Finally, high pressure electrochemistry has provided an improved understanding of a variety of different processes under non-classical conditions with potential application to technological problems involving elevated pressure such as the measurement of pH at the bottom of the ocean.

13.8 Chapter 13 References

[1] D. Giovanelli, N. L. Lawrence, R. G. Compton, *Electroanalysis* **2004**, *16*, 789.
[2] T. W. Swaddle, in *High Pressure Chemistry: Synthetic, Mechanistic, and Supercritical Applications* (Eds: R. van Eldik, F. G. Klarner), Wiley-VCH, Weinheim **2002**, pp. 161-183.
[3] T. W. Swaddle, P. A. Tregolan, *Coord. Chem. Rev.* **1999**, *187*, 225.
[4] S. D. Hamann, in *Modern Aspects of Electrochemistry* (Eds: B. E. Conway, J. O. M. Bockris), Plenum Press, New York-London **1974**, pp. 47-158.
[5] P. W. Bridgam, *The Physics of High Pressure*, Bells and Sons, London, **1931**.
[6] L. H. Adams, *J. Am. Chem. Soc.* **1931**, *53*, 3769.
[7] L. H. Adams, R. E. Hall, *J. Wash. Acad. Sci.* **1931**, *21*, 183.
[8] L. H. Adams, R. E. Hall, *J. Phys. Chem.* **1931**, *35*, 2145.
[9] B. B. Owen, S. R. Brinkley, *Chem. Revs.* **1941**, *29*, 461.
[10] E. Cohen, P. K., *Z. Phys. Chem. A* **1934**, *A167*, 365.
[11] J. Buchanan, S. D. Hamann, *Trans. Farad. Soc.* **1953**, *49*, 1425.
[12] A. H. Ewald, S. C. Lim, *J. Phys. Chem.* **1957**, *61*, 1443.
[13] S. D. Hamann, *Physico-Chemical Effects of Pressure*, Butterworths Scientific Publications, London, **1957**.
[14] A. J. Ellis, W. S. Fyfe, R. I. Rutherford, A. Fischer, J. Vaughan, *J. Chem. Phys.* **1959**, *31*, 176.
[15] A. J. Ellis, *J. Sci. Instr.* **1962**, *39*, 464.
[16] A. J. Ellis, *J. Chem. Soc.* **1963**, 2299.
[17] A. J. Ellis, D. W. Anderson, *J. Chem. Soc.* **1961**, 4678.
[18] A. J. Ellis, D. W. Anderson, *J. Chem. Soc.* **1961**, 1765.
[19] A. J. Ellis, *J. Chem. Soc.* **1959**, 3689.
[20] W. R. Hainsworth, *Science* **1921**, *53*, 578.
[21] W. R. Hainsworth, D. A. MacInnes, *J. Am. Chem. Soc.* **1922**, *44*, 1021.

[22] W. R. Hainsworth, H. J. Rowley, D. A. MacInnes, *J. Am. Chem. Soc.* **1924**, *46*, 1437.
[23] R. S. Bradley, D. C. Munro, *High Pressure Chemistry*, Pergamon, New York, **1965**.
[24] G. J. Hills, P. J. Ovenden, in *Advances in Electrochemistry and Electrochemical Engineering*, John Wiley and Sons, **1966**, pp. 185-247.
[25] G. J. Hills, *Talanta* **1965**, *12*, 1317.
[26] E. U. Franck, *Journal de Chimie Physique et de Physico-Chimie Biologique* **1969**, 9.
[27] E. U. Franck, *Pure Appl. Chem.* **1970**, *24*, 13.
[28] E. U. Franck, J. E. Savolainen, W. L. Marshall, *Rev. Sci. Instr.* **1962**, *33*, 115.
[29] W. L. Marshall, *Rev. Pure Appl. Chem.* **1968**, *18*, 167.
[30] R. A. Horne, in *Advances in High Pressure Research* (Ed. R. S. Bradley), Academic press, London and New York **1969**, pp. 169-223.
[31] J. Gorecki, J. Golas, *Electroanalysis* **1996**, *8*, 630.
[32] J. Golas, H. G. Drickamer, L. R. Faulkner, *Acta Chim. Hung.* **1992**, *129*, 497.
[33] T. W. Swaddle, in *High Pressure Techniques in Chemistry and Physics: A Practical Approach* (Eds: W. Holzapfel, N. Isaacs), Oxford University Press, **1997**, pp. 343 pp.
[34] G. G. Wildgoose, D. Giovanelli, N. S. Lawrence, R. G. Compton, *Electroanalysis* **2004**, *16*, 421.
[35] W. C. Waggener, *Rev. Sci. Instr.* **1959**, *30*, 788.
[36] H. Doine, T. W. Whitcombe, T. W. Swaddle, *Can. J. Chem.* **1992**, *70*, 81.
[37] K. J. Stevenson, H. S. White, *J. Phys. Chem.* **1996**, *100*, 18818.
[38] M. T. Cruanes, H. G. Drickamer, L. R. Faulkner, *J. Phys. Chem.* **1992**, *96*, 9888.
[39] G. J. Hills, D. R. Kinnibrugh, *J. Electrochem. Soc.* **1966**, *113*, 1111.
[40] J. C. Jamieson, *J. Chem. Phys.* **1953**, *21*, 1385.
[41] V. Jovancicevic, J. O. M. Bockris, *Rev. Sci. Instr.* **1987**, *58*, 1251.
[42] K. S. Balain, C. J. Bergeron, *Rev. Sci. Instr.* **1959**, *30*, 1058.
[43] R. J. Withey, E. Whalley, *Trans. Faraday Soc.* **1963**, *59*, 895.
[44] A. B. Gancy, S. B. Brummer, *J. Electrochem. Soc.* **1968**, *115*, 804.
[45] P. P. S. Saluja, C. Cameron, M. A. Floriano, A. Lavergne, G. E. McLaurin, E. Whalley, *Rev. Sci. Instr.* **1986**, *57*, 2791.
[46] P. C. Ho, H. Bianchi, D. A. Palmer, R. H. Wood, *J. Sol. Chem.* **2000**, *29*, 217.
[47] P. C. Ho, D. A. Palmer, R. H. Wood, *J. Phys. Chem. B* **2000**, *104*, 12084.
[48] P. C. Ho, D. A. Palmer, M. S. Gruszkiewicz, *J. Phys. Chem. B* **2001**, *105*, 1260.
[49] A. Disteche, *J. Electrochem. Soc.* **1962**, *109*, 1084.
[50] S. D. Hamann, *J. Phys. Chem.* **1963**, *67*, 2233.
[51] J. Sachinidis, R. D. Shalders, P. A. Tregloan, *J. Electroanal. Chem.* **1992**, *327*, 219.
[52] J. I. Sachinidis, R. D. Shalders, P. A. Tregloan, *Inorg. Chem.* **1994**, *33*, 6180.
[53] J. I. Sachinidis, R. D. Shalders, P. A. Tregloan, *Inorg. Chem.* **1996**, *35*, 2497.
[54] J. Golas, H. G. Drickamer, L. R. Faulkner, *J. Phys. Chem.* **1991**, *95*, 10191.
[55] D. F. Goldfarb, H. R. Corti, F. Marken, R. G. Compton, *J. Phys. Chem. A* **1998**, *102*, 8888.
[56] G. G. Wildgoose, N. S. Lawrence, B. A. Coles, L. Jiang, T. G. J. Jones, R. G. Compton, *Phys. Chem. Chem. Phys.* **2003**, *5*, 4219.
[57] G. J. Hills, in *Advances in High Pressure Research* (Ed. R. S. Bradley), Academic Press, London and New York **1969**, pp. 225-255.
[58] G. Hills, *Symposia of the Society for Experimental Biology* **1972**, *26*, 1.
[59] G. J. Hills, R. Payne, *Trans. Faraday Soc.* **1965**, *61*, 316.
[60] G. J. Hills, H. Hoiland, *J. Coll. Interf. Science* **1984**, *99*, 463.
[61] G. J. Hills, R. Payne, *Trans. Faraday Soc.* **1965**, *61*, 326.
[62] S. D. Hamann, W. Strauss, *Trans. Faraday Soc.* **1955**, *51*, 1684.
[63] R. A. Horne, R. A. Courant, G. R. Frysinger, *J. Chem. Soc.* **1964**, 1515.
[64] F. H. Fisher, *J. Phys. Chem.* **1962**, *66*, 1607.
[65] R. H. Radzilowski, J. T. Kummer, *J. Electrochem. Soc.* **1971**, *118*, 714.
[66] K. E. Heusler, L. Gaiser, *Ber. Bunsenges.* **1969**, *73*, 1059.
[67] A. Disteche, *Rev. Sci. Instr.* **1959**, *30*, 474.
[68] A. Disteche, S. Disteche, *J. Electrochem. Soc.* **1967**, *114*, 330.
[69] A. Disteche, S. Disteche, *J. Electrochem. Soc.* **1965**, *112*, 350.
[70] A. Disteche, *Symposia of Society for Experimental Biology* **1972**, *26*, 27.
[71] M. Whitfield, *J. Chem. Eng. Data* **1972**, *17*, 124.
[72] E. D. Linov, P. A. Kryukov, *Seriya Khimicheskikh Nauk* **1972**, *4*, 10.
[73] S. G. Mairanovskii, M. G. Gonikberg, A. A. Opekunov, *Dokl. Akad. Nauk SSSR* **1958**, *123*, 312.
[74] B. E. Conway, J. C. Currie, *J. Electrochem. Soc.* **1978**, *125*, 252.
[75] K. Hayashi, I. Kono, *Jpn. J. Physiol.* **1958**, *8*, 246.
[76] W. M. Flarsheim, A. J. Bard, K. P. Johnston, *J. Phys. Chem.* **1989**, *93*, 4234.

[77] M. T. Cruanes, K. K. Rodgers, S. G. Sligar, *J. Am. Chem. Soc.* **1992**, *114*, 9660.
[78] P. W. Atkins, J. De Paulo, *Atkins' Physical Chemistry*, 7th Ed., Oxford University Press, Oxford, **2002**.
[79] A. M. Bond, in *Broadening Electrochemical Horizons*, Oxford University Press, Oxford **2002**, pp. 123-128.
[80] M. Sato, T. Yamada, in *High Pressure Science and Technology* (Eds: B. Vodar, P. Marteau), Pergamon, Oxford **1980**, pp. 812.
[81] M. T. Cruanes, H. G. Drickamer, L. R. Faulkner, *Langmuir* **1995**, *11*, 4089.
[82] J. Sun, J. F. Wishart, R. van Eldik, R. D. Shalders, T. W. Swaddle, *J. Am. Chem. Soc.* **1995**, *117*, 2600.
[83] Y. Fu, T. W. Swaddle, *J. Am. Chem. Soc.* **1997**, *119*, 7137.
[84] M. Matsumoto, I. Tarumi, S. Funahashi, T. Noda, H. D. Tagaki, *Z. Naturforschung* **1997**, *52B*, 1087.
[85] P. Krasinski, M. Tkacz, B. Baranowski, Z. Galus, *J. Electroanal. Chem.* **1991**, *308*, 189.
[86] Y. Fu, T. W. Swaddle, *Inorg. Chem.* **1999**, *38*, 876.
[87] P. Metelski, T. W. Swaddle, *Inorg. Chem.* **1999**, *38*, 301.
[88] R. D. Shalders, T. W. Swaddle, *Inorg. Chem.* **1995**, *34*, 4815.
[89] M. R. Grace, H. Takagi, T. W. Swaddle, *Inorg. Chem.* **1994**, *33*, 1915.
[90] T. C. Franklin, S. A. Mathew, *J. Electrochem. Soc.* **1987**, *134*, 760.
[91] T. C. Franklin, S. A. Mathew, *J. Electrochem. Soc.* **1988**, *135*, 2725.
[92] T. C. Franklin, S. A. Mathew, *J. Electrochem. Soc.* **1989**, *136*, 3627.
[93] T. W. Swaddle, M. K. S. Mak, *Can. J. Chem.* **1983**, *64*, 473.
[94] T. W. Swaddle, *Inorg. Chem.* **1983**, *22*, 2663.
[95] Y. Fu, T. W. Swaddle, *Chem. Commun.* **1996**, 1171.
[96] M. R. Grace, T. W. Swaddle, *Inorg. Chem.* **1993**, *32*, 5597.
[97] W. H. Jolley, D. R. Stranks, T. W. Swaddle, *Inorg. Chem.* **1990**, *29*, 1948.
[98] H. Doine, T. W. Swaddle, *Inorg. Chem.* **1991**, *30*, 1858.
[99] H. Doine, T. W. Swaddle, *Can. J. Chem.* **1988**, *66*, 2763.
[100] W. H. Jolley, D. R. Stranks, T. W. Swaddle, *Inorg. Chem.* **1990**, *29*, 385.
[101] H. D. Tagaki, T. W. Swaddle, *Inorg. Chem.* **1992**, *31*, 4669.
[102] R. A. Marcus, *Can. J. Chem.* **1959**, *37*, 155.
[103] R. A. Marcus, *J. Phys. Chem.* **1963**, *67*, 853.
[104] R. A. Marcus, *J. Chem. Phys.* **1965**, *43*, 679.
[105] R. A. Marcus, *Electrochim. Acta* **1968**, *13*, 995.
[106] Y. Fu, A. S. Cole, T. W. Swaddle, *J. Am. Chem. Soc.* **1999**, *121*, 10410.
[107] B. D. Yeomans, L. S. Kelso, P. A. Tregolan, F. R. Keene, *Eur. J. Inorg. Chem.* **2001**, 239.
[108] M. T. Cruanes, H. G. Drickamer, L. R. Faulkner, *J. Phys. Chem.* **1996**, *100*, 16613.
[109] I. M. AlNashef, M. L. Leonard, M. A. Matthews, J. W. Weidner, *Ind. Eng. Chem. Res.* **2002**, *41*, 4475.
[110] C. G. Yiokari, G. E. Pitselis, D. G. Polydoros, A. D. Katsaounis, C. G. Vayenas, *J. Phys. Chem. A* **2000**, *104*, 10600.
[111] D. d. G. Jones, H. G. Masterson, in *Advances in corrosion science and technology* (Eds: M. G. Fontana, R. W. Staehle), Plenum Press, New York-London **1970**, pp. 1-49.
[112] F. A. Uribe, P. R. Sharp, A. J. Bard, *J. Electroanal. Chem.* **1983**, *152*, 173.
[113] A. J. Bard, W. M. Flarsheim, K. P. Johnston, *J. Electrochem. Soc.* **1988**, *135*, 1939.
[114] A. C. McDonald, F. R. F. Fan, A. J. Bard, *J. Phys. Chem.* **1986**, *90*, 196.
[115] W. M. Flarsheim, Y. M. Tsou, I. Trachtenberg, K. P. Johnston, A. J. Bard, *J. Phys. Chem.* **1986**, *90*, 3857.
[116] R. M. Crooks, A. J. Bard, *J. Phys. Chem.* **1987**, *91*, 1274.
[117] R. M. Crooks, A. J. Bard, *J. Electroanal. Chem.* **1988**, *240*, 253.
[118] R. M. Crooks, A. J. Bard, *J. Electroanal. Chem.* **1988**, *243*, 117.
[119] C. R. Cabrera, E. Garcia, A. J. Bard, *J. Electroanal. Chem.* **1989**, *260*, 457.
[120] C. R. Cabrera, A. J. Bard, *J. Electroanal. Chem.* **1989**, *273*, 147.
[121] C.-y. Liu, S. R. Snyder, A. J. Bard, *J. Phys. Chem. B* **1997**, *101*, 1180.
[122] D. D. Macdonald, in *Modern Aspects of Electrochemistry* (Eds: B. E. Conway, J. O. M. Bockris), Plenum Press, New York **1975**, pp. 141-195.
[123] S. N. Lvov, D. D. Macdonald, *Proceedings - Electrochemical Society* **1997**, *97-39*, 746.
[124] S. N. Lvov, D. D. Macdonald, *J. Electroanal. Chem.* **1996**, *403*, 25.
[125] L. B. Kriksunov, D. D. Macdonald, *Sens. Actuators, B* **1994**, *22*, 201.
[126] D. D. Macdonald, S. Hettiarachchi, H. Song, K. Makela, E. Emerson, M. Ben-Haim, *J. Solut. Chem.* **1992**, *21*, 849.
[127] S. Hettiarachchi, K. Makela, H. Song, D. D. Macdonald, *J. Electrochem. Soc.* **1992**, *139*, L3.
[128] L. B. Kriksunov, P. J. Millet, D. D. Macdonald, *J. Electrochem. Soc.* **1994**, *141*, 3002.

[129] C.-y. Liu, D. D. Macdonald, *J. Supercrit. Fluids* **1995**, *8*, 263.
[130] R. Biswas, S. N. Lvov, Z. Ahmad, D. D. Macdonald, *Proc. - Electrochem. Soc.* **1997**, *97-13*, 340.
[131] S. N. Lvov, H. Gao, D. Kouznetsov, I. Balachov, D. D. Macdonald, *Fluid Phase Equilib.* **1998**, *150*, 515.
[132] S. N. Lvov, X. Y. Zhou, D. D. Macdonald, *J. Electroanal. Chem.* **1999**, *463*, 146.
[133] S. N. Lvov, X. Y. Zhou, S. M. Ulyanov, A. V. Bandura, *Chem. Geol.* **2000**, *167*, 105.
[134] S. N. Lvov, X. Y. Zhou, S. M. Ulyanov, D. D. Macdonald Potentiometric measurements of association constants and pH in high temperature HCl(aq) solutions. *Steam, Water, and Hydrothermal Systems: Physics and Chemistry Meeting the Needs of Industry, Proceedings of the International Conference on the Properties of Water and Steam, 13th, Toronto, ON, Canada, Sept. 12-16, 1999*, 2000; pp 653-660.
[135] S. Jayasekera, J. Avraamides, S. I. Bailey, L. Shaw, *Publications of the Australasian Institute of Mining and Metallurgy* **1994**, *4/94*, 123.
[136] S. Jayasekera, Y. Marinovich, J. Avraamides, S. I. Bailey, *Hydrometallurgy* **1995**, *39*, 183.
[137] T. Fujii, in *Predictive methods for assessing corrosion damage to BWR piping and PWR steam generators* (Eds: H. Okada, R. W. Staehle), National Association of Corrosion Engineers, Houston, Texas **1978**, pp. 107-111.
[138] J. C. Danko, M. E. Indig, in *Predictive methods for assessing corrosion damage to BWR piping and PWR steam generators* (Eds: H. Okada, R. W. Staehle), National Association of Corrosion Engineers, Houston, Texas **1978**, pp. 112-116.
[139] J. Takabayashi, M. Hishida, in *Predictive methods for assessing corrosion damage to BWR piping and PWR steam generators* (Eds: H. Okada, R. W. Staehle), National Association of Corrosion Engineers, Houston, Texas **1978**, pp. 116-127.
[140] S. A. Olsen, D. E. Tallman, *Anal. Chem.* **1994**, *66*, 503.
[141] S. A. Olsen, D. E. Tallman, *Anal. Chem.* **1996**, *68*, 2054.
[142] D. F. Goldfarb, H. R. Corti, *Electrochem. Comm.* **2000**, *2*, 663.
[143] A. P. Abbott, N. E. Durling, *Phys. Chem. Chem. Phys.* **2001**, *3*, 579.
[144] A. P. Abbott, S. Corr, N. E. Durling, E. G. Hope, *J. Chem. Eng. Data* **2002**, *47*, 900.
[145] A. P. Abbott, C. A. Eardley, *J. Phys. Chem. B* **1999**, *103*, 6157.
[146] A. P. Abbott, C. A. Eardley, *J. Phys. Chem. B* **2000**, *104*, 9351.
[147] A. P. Abbott, J. C. Harper, *J. Chem. Soc. Farad. Trans.* **1996**, *92*, 3895.
[148] D. Niehaus, M. Philips, A. Michael, R. M. Wightman, *J. Phys. Chem.* **1989**, *93*, 6232.

Chapter 14: "Electrochemical Determination of Sulfide at High Temperatures *via* Its Electrochemically Initiated Reaction with diethyl-p-phenylenediamine (DEPD) in N,N,'-dimethylformamide (DMF)"

In Part 1 the electrochemical oxidation of DEPD both in the absence (Chapter 5) and in the presence of sulfide (Chapter 6) was investigated in DMF. It was shown that, at room temperature, sulfide can react with the doubly oxidised $DEPD^+$ species in a 1,4-Michael addition to produce an enhancement in the second limiting current (Chapter 6, Scheme 6.2). The results detailed previously produced a linear detection range for sulfide dependent on the concentration of DEPD present with a linear range of 37 – 3000 μM and a limit of detection of 6 μM sulfide obtainable at a 66 μm Pt electrode when 0.5 mM DEPD was present in solution. However, in order to determine sulfide at these room temperatures, specific reaction conditions were needed in order to ensure that sufficient amounts of the $DEPD^{\bullet}$ were present at the electrode surface such that further oxidation could occur to form the $DEPD^+$ species (Chapter 6, Scheme 6.1). In this chapter we will shown how these restrictions can be lifted by increasing the temperature of the solution as the equilibrium for the proton transfer is pushed further to the products. This would therefore aid in the determination of sulfide at elevated temperatures (up to 70 °C) and might hold important implications for sulfide detection in the oilfield industry. The bulk of the experiments were conducted by Gregory G. Wildgoose, then a part II student in the group jointly supervised by myself, Dr. N. Lawrence and Prof. R. Compton. The results detailed below have been published in Electroanalysis [1].

14.1 Introduction

As discussed in Chapter 3, determination of hydrogen sulfide has gained significant importance within the analytical community due to its toxicity. The ubiquity of the gas within oil and gas reserves can pose problems to workers on the rig as H_2S can enter drilling muds from subsurface formations and/or be generated by sulphate-reducing bacteria present in stored muds. It is therefore desirable to develop fast and sensitive H_2S sensors capable of measuring up to the demands of oilfield applications (namely high temperatures and pressures [2-5]). As discussed in Chapter 5, the electrochemical oxidation of DEPD in the absence of sulfide follows an $EC_{rev}ECE$ pathway (Chapter 5, scheme 5.1, [6]). The nature of the electrode process is such that, at room temperature, for small electrode radii of less than 100 μm and low DEPD concentrations the second oxidation wave is immeasurably small and therefore sulfide sensing under these conditions becomes impossible. It was found that the determination of sulfide could only occur under the conditions of large electrode size or high concentrations of the indicator solution (for example a 0.5 mM DEPD solution required an electrode with at least a 31 μm radius, Chapter 6, Figure 6.3, [7]). In order to relieve the constraints on the sensing system (electrode radii, concentration of DEPD), the effects of temperature on the system were studied. It was anticipated that both the equilibrium constant for the proton transfer step and the rate of dimerisation would be affected by increasing the temperature, thereby enhancing the second limiting current. Analysis of the voltammetric response at microdisc electrodes measured as a function of temperature yielded a value of +83 kJ mol^{-1} for the enthalpy of reaction for the proton transfer step and a value of +43 kJ mol^{-1} for the activation energy of the dimerisation reaction. Furthermore it was shown that sulfide sensing was possible using this system up to temperatures of 70 °C.

14.2 Experimental

14.2.1 Electrochemical Equipment

Electrochemical measurements were recorded using a PalmSens potentiostat (Houten, Netherlands) controlled by an iPAQ H3760 pocket computer (Compaq, U.S) with a standard three-electrode configuration. A glassy carbon macro electrode (GC, 0.0707 cm^2) or platinum electrode (diameter = 40 μm) acted as the working electrodes (see below). A platinum electrode acted as the counter electrode and Pt or Ag wire pseudo reference electrodes completed the cell assembly. Sulfide additions were prepared by utilising the cell arrangement detailed in Chapter 6 (Figure 6.1).

14.2.2 Uniformly Heated Cell

High-temperature (up to 70 °C) cyclic voltammetry recorded at macroelectrodes was undertaken using a double wall glass cell thermostatted at the appropriate temperature through the circulation of water from a heated bath.

14.2.3 Heated Microdisc Setup

The microelectrode high-temperature experiments were carried out using a cell approximately 10 cm^3 in volume heated by hot air circulation within a small box of insulating material with a front glass wall. A Pt resistance thermometer was used to control the air temperature and a thermocouple in contact with the solution was used to read the temperature during the voltammetric scans. A 40 μm diameter platinum disc (99.99 %, Goodfellow Cambridge, UK) sealed in Pyrex glass was used as the working electrode, with a platinum coil counter electrode and a Ag wire was used as the reference electrode.

The diffusion coefficients were calculated from the steady-state limiting currents by using the following equation for a microdisc electrode of radius r_o [8] after correction for changes in the solution density [9].

$$I_{lim} = 4\ n\ F\ D\ C\ r_o \qquad (14.1)$$

The use of microelectrodes under isothermal conditions, however, was limited to temperatures below 120 – 125 °C in DMF. The formation of bubbles at the electrode surface, observed at higher temperatures, gave unsuitable voltammograms with poorly defined limiting plateaux.

14.3 Results and Discussion

14.3.1 Electrochemical Oxidation of DEPD in DMF at Elevated Temperatures

In Chapter 5 the electrochemical oxidation of DEPD in DMF was studied at room temperature primarily by examining the linear sweep voltammetry obtained at a range of different sizes of microelectrodes and different concentrations of DEPD. The voltammetric response obtained was correspondingly modelled and shown to follow $EC_{rev}ECE$ reaction (Chapter 6, Scheme 6.1). In this reaction scheme the parent DEPD is first oxidised at the electrode surface to a radical cation species $DEPD^{+\bullet}$. This loses a proton to another parent DEPD molecule to form the corresponding radical species $DEPD^{\bullet}$, which can then be oxidised further to the di-imine species $DEPD^{+}$. The latter can then undergo dimerisation and further oxidation. The rate constant for the reversible proton transfer step was found to be in the order of 10^{12}-10^{13} cm^3 mol^{-1} s^{-1} and the corresponding equilibrium constant was found to be equal 1. The rate constant for the dimerisation process was estimated to be *ca.* 1.2 x 10^7 cm^3 mol^{-1} s^{-1}.

The results obtained at room temperature revealed that the nature of this electrode process is such that for small electrode radii of less than 100 μm and low DEPD concentrations the second oxidation wave is immeasurably small. Under these conditions very specific concentration ranges and electrode sizes have to be utlilised. Therefore, in order to improve the electrode response of the second oxidation wave at low concentrations and small electrode radii, the effect of increasing the temperature of the solution on the electrode response was investigated. This was predicted to have the

effect of changing the equilibrium constant for the proton transfer step such that more of the DEPD$^{\bullet}$ species might be formed, and therefore more would be available to detect sulfide. In addition, an increase of the rate constant of the dimerisation process was anticipated, again aided the sought detection.

Initial voltammetric characterisation for the oxidation of DEPD in DMF at elevated temperatures was carried out at a glassy carbon electrode using cyclic voltammetry in a thermally jacketed cell heated by a thermostated water bath, thereby allowing temperatures up to 70 °C to be obtained. The corresponding voltammetric responses (scan rate = 100 mV s^{-1}) for a 0.25 mM solution of DEPD in DMF (0.2 M TBAP) to increasing temperature (from 20 to 70 °C) are detailed in figure 14.1.

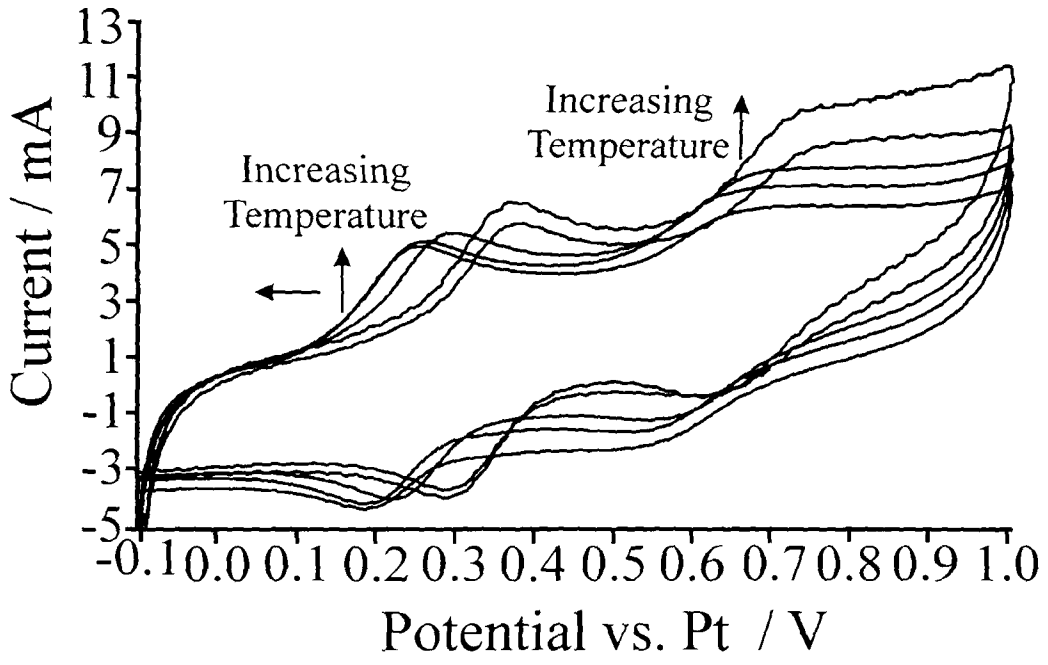


Figure 14.1: The cyclic voltammetric responses (scan rate = 100 mV s-1) for a solution containing 0.25 mM DEPD in DMF (0.2 M TBAP) to increasing temperature (from 20 to 70 °C).

These reveal two oxidative waves at +0.25 V and +0.66 V which can be attributed to the oxidation of DEPD and of DEPD$^{\bullet}$, respectively (Chapter 6, Scheme 6.1). Upon reversal of the scan, a broad reductive wave is observed at +0.62 V corresponding to the reduction of the di-imine species back to DEPD$^{\bullet}$ followed by a second sharper wave at +0.18 V corresponding to the reduction of DEPD$^{\bullet+}$ back to the parent DEPD species. This type of electrochemical behaviour is in agreement with that recorded at room temperatures (Chapter 6). An enhancement in the magnitude of the peak

currents for all the redox processes is observed as the temperature is raised consistent with the increased mass transport of the species to the electrode surface at the elevated temperatures. A shift in the oxidation potential towards more positive potentials occurs when the temperature is raised which might be due in part to changes in the pseudo-reference electrode couple. A quantitative examination of the ratio of the second oxidation peak current to the first oxidation peak current shows an increase from ca. 0.75 at 20 °C to ca 1.16 at 70 °C suggesting that the proton transfer is an endothermic process and so, as the temperature is increased, more $DEPD^{\bullet}$ is formed and therefore oxidised.

Analysis of the first oxidation peak current as a function of square root of scan rate at each temperature studied (from 20 to 70 °C) is detailed in figure 14.2 (a). An increase in the gradient of each plot is observed as the temperature is increased.

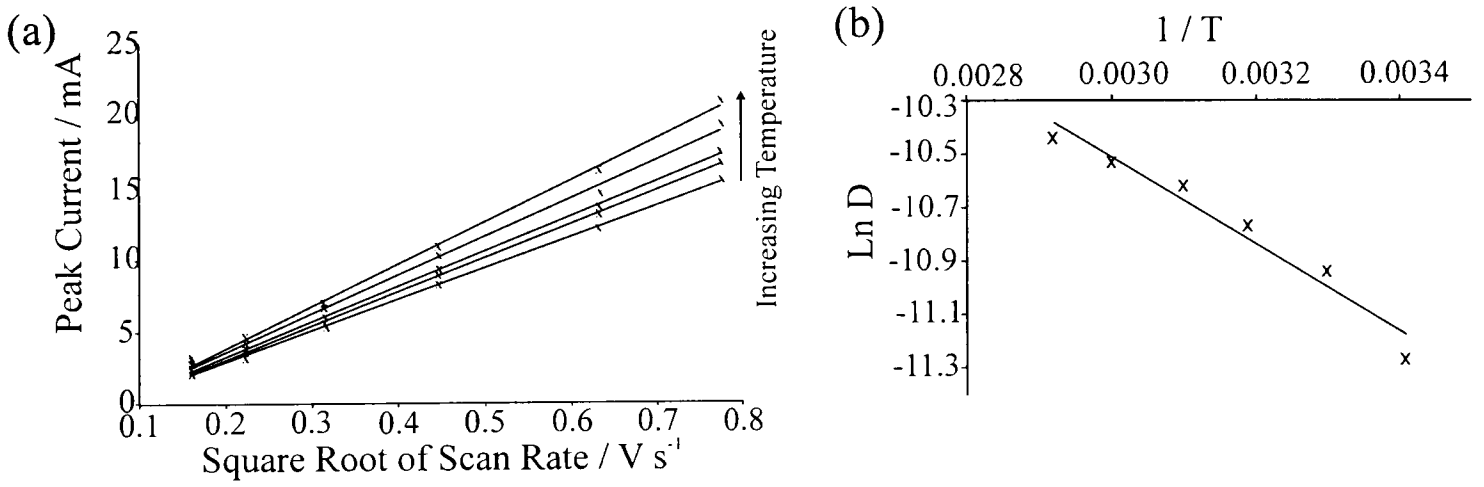


Figure 14.2: (a) Plots of the first oxidation peak current against square root of scan rate for each temperature studied (from 20 to 70 °C) and (b) An Arrhenius plot of ln D against 1/T.

These Randles-Ševčik plots allow the determination of the experimental diffusion coefficient of the DEPD species at each temperature from the equation [8]. In determining these values it was assumed that the electrode process relative o the first oxidation wave is fully reversible and n is close to one at 25 °C. Next, the dependence of the diffusion coefficient with temperature is analysed in terms of the Arrhenius equation:

$$D = D_o \exp(-E_A / RT) \qquad (14.2)$$

where D is the diffusion coefficient, D_o is a constant, E_A is the activation energy for the diffusion process, R is the molar gas constant (= 8.314 J K^{-1} mol^{-1}) and T is the temperature. Therefore a plot of ln D vs. $1/T$ yields a straight line (figure 14.2 (b)), the slope of which leads to the determination of the activation energy and the intercept produces a value for D_o. The corresponding values for D_o and E_a for the diffusion of DEPD in DMF were found to be 3.5 x 10^{-3} cm^2 s^{-1} and 13.5 kJ mol^{-1} respectively, which is in good agreement with the temperature dependence of the diffusion of other phenylenediamine species in acetonitrile [10].

In order to corroborate these results for both D_o and E_A and the fact that it was qualitatively observed that the ratio of the first peak current to the second peak current increases at higher temperatures, a second set of experiments were carried out using the heated microdisc experiment detailed in section 14.2.3. In these experiments the steady state linear sweep voltammetry obtained from a 20 μm radius platinum microdisc working electrode was examined over a temperature from 20 to 130 °C, which is a significantly larger temperature range than that obtainable from the thermally jacketed cell used above. The corresponding steady state linear sweep voltammograms obtained from a solution containing 0.5 mM DEPD (0.2 M TBAP) at various temperatures from 20 to 90 °C are shown in figure 14.3. These show two oxidative processes occurring at +0.23 V (*vs.* Pt) and +0.62 V (*vs.* Pt) and can be attributed to the oxidation of the parent DEPD and $DEPD^{\bullet}$ species respectively, in accordance with the reaction process detailed in scheme 6.1 (Chapter 6). Once again, as the temperature is raised, an increase in both the first and second limiting currents is observed, consistent with an increase in the mass transport of the species in solution.

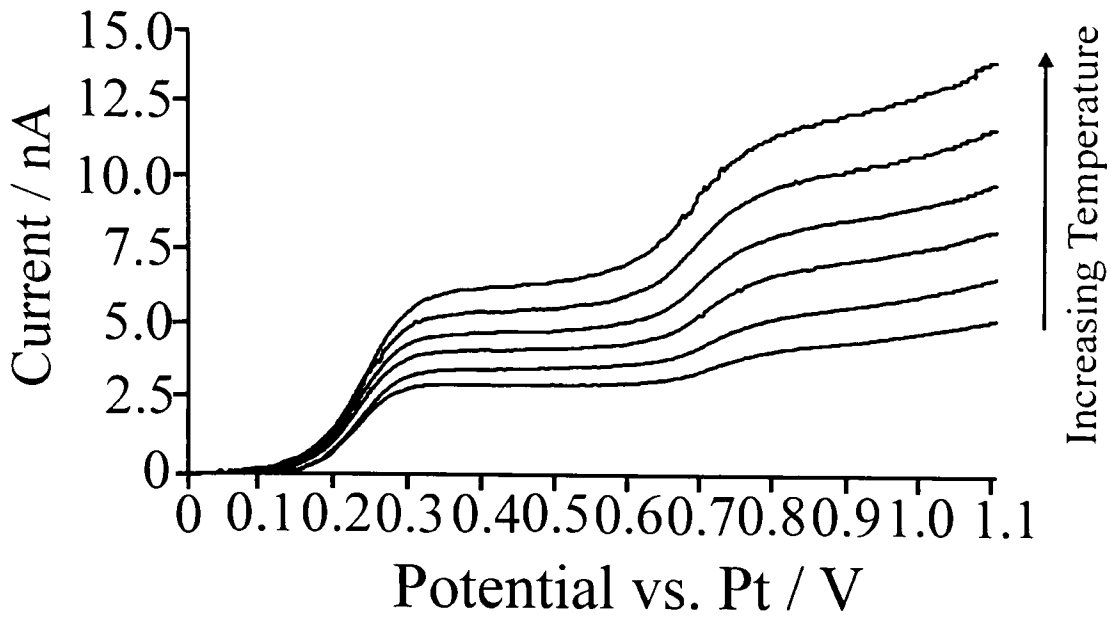


Figure 14.3: Steady state linear sweep voltammograms (scan rate = 5 mV s^{-1}) obtained at a 20 μm platinum microdisc in a 0.5 mM solution of DEPD (0.2 M TBAP) at various temperatures (from 20 to 90 °C).

However, at higher temperatures (*ca.* 130 °C), although an increase in both the first and second limiting currents is still observed, the enhancement in the second oxidation peak current is lower than expected (*vide infra*). This can be tentatively attributed to the increased rate of formation of polymeric species on the electrode surface at the higher temperatures.

Further examination of the voltammetric responses by analysis of both the first and second limiting currents over a concentration range from 0.25 to 1.0 mM DEPD reveals three factors. First, a plot of the first limiting current, I_l, against concentration of DEPD at each temperature studied as depicted in figure 14.4 (a) allows the determination of the diffusion coefficient at each temperature by use of equation 14.1 detailed above. A plot of ln *D vs* 1/T for the heated microdisc data yielded values for D_o and E_a of 3.4 x 10^{-3} cm^2 s^{-1} and 14.5 kJ mol^{-1} respectively which is in good agreement with that detailed above for the independent cyclic voltammetry data.

Secondly, a plot of the ratio of the second to the first limiting current as a function of temperature obtained from the responses depicted in figure 14.3 is detailed in figure 14.4 (b). This shows that, as the temperature of the solution is increased, the ratio of

the peak currents tends towards one, which is quantitatively consistent with that found using the cyclic voltammetry data detailed previously.

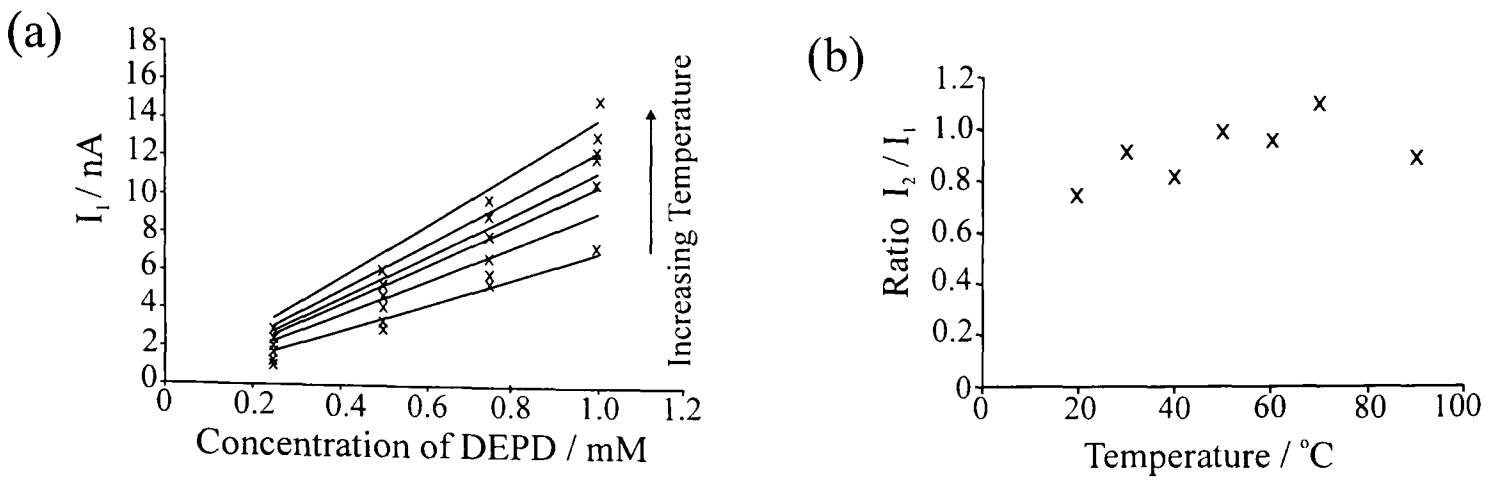


Figure 14.4: (a) Plots of the first limiting current as a function of DEPD concentration present in the solution at each temperature studied (from 20 to 90 °C) and (b) Plot of the ratio of the first limiting current to the second limiting current (I_2/I_1)for a 0.5 mM solution of DEPD as a function of temperature (see text)

This behaviour was observed at each concentration of DEPD studied (0.25 to 1 mM) and suggests the formation of more of the DEPD$^{\bullet}$ radical species at the electrode surface and an increase in the rate constant for the dimerisation process (*vide infra*). It can also be seen that at the higher temperatures (> 70 °C) the ratio of the first limiting current to the second drops below one and this might be attributed to enhanced 'fouling' of the electrode surface by polymeric species; more of the latter may likely be formed at elevated temperatures.

In order to produce quantitative data for both changes in the equilibrium constant k_1 for the proton transfer step and the rate of dimerisation k_2 at these elevated temperatures the modelling of the $EC_{rev}ECE$ reaction process discussed previously (Chapter 5) was utilised. For this purpose O. V. Klymenko used the working surface for the EC_{rev} reaction presented in Chapter 5 (Figure 5.5) to obtain the values of the rate constant k_1 and the equilibrium constant K_{eq} (where $K_{eq} = k_1/k_{-1}$) (see Scheme 5.1) for every temperature investigated. The application of the fitting procedure for the first wave current revealed that the value of the rate constant k_1 remains high at all

temperatures considered (it is of the order of 10^{12} - 10^{13} cm^3 mol^{-1} s^{-1}) while the value of K_{eq} increases with increasing temperature (Table 14.1).

Table 14.1: *The variation of both the equilibrium constant ($K_{eq} = k_1/k_{-1}$) for the proton transfer step and the rate constant (k_2) for the dimerisation process at elevated temperatures (see Chapter 5, Scheme 5.1).*

Temperature / Kelvin	$K_{eq} = k_1/k_{-1}$	k_2 / cm^3 mol^{-1} s^{-1}
293	0.2	1.00×10^8
303	1	8.00×10^7
313	6.2	1.00×10^9
323	5.9	1.00×10^9
333	33	3.50×10^8
343	34	5.01×10^8

A Van't Hoff plot of ln K_{eq} against $1/T$ is detailed in figure 14.5 and is linear as expected and yielded a value of +82.7 kJ mol^{-1} for the enthalpy of reaction. The fact that the equilibrium constant increases with temperature and the enthalpy of reaction is positive shows that the proton transfer is an endothermic process.

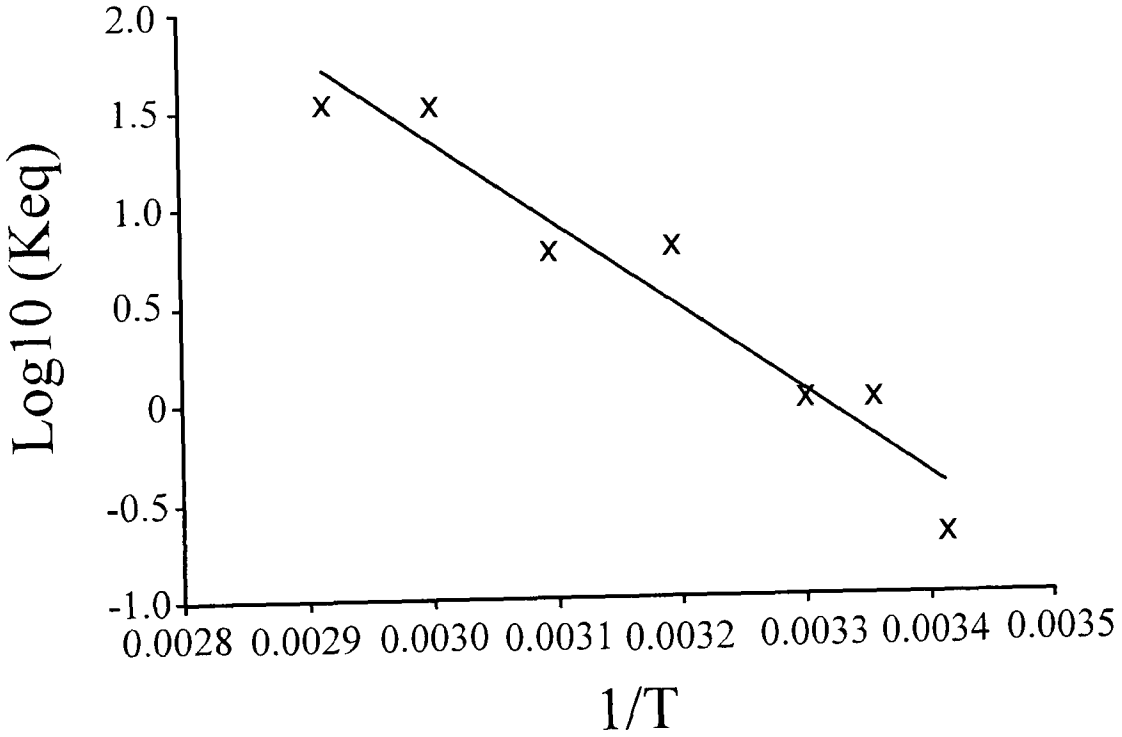


Figure 14.5: A Van't Hoff plot for the data detailed in table 14.1 for the equilibrium constant of the proton transfer step.

The values of k_1 and K_{eq} for every temperature were then used for the second wave current fitting procedure. To this end the working surfaces were generated by O. V. Klymenko for different values of the equilibrium constant K corresponding to different temperatures. Subsequently, the values of k_2 were found by solving the minimisation

problem. The obtained reaction rates for k_2 are detailed in Table 14.1 (only temperatures where electrode fouling was not observed were modelled). An Arrhenius plot of ln k_2 against 1/T (not shown) gave a value for the activation energy of the dimerisation reaction of +43 kJ mol^{-1}.

14.3.2 Electrochemically Initiated Determination of Sulfide in DMF at Elevated Temperatures

The effect of temperature on the electrochemically initiated reaction of sulfide with DEPD was next examined using the heated microdisc set-up decribed in Section 14.2.3. The corresponding voltammetric responses obtained at 70 °C and 90 °C for a solution containing 0.5 mM DEPD (0.2 M TBAP) at a 20 μm Pt microdisc to increasing additions of sulfide (0 – 900 μM) are detailed in figure 14.6 (a) and (b), respectively.

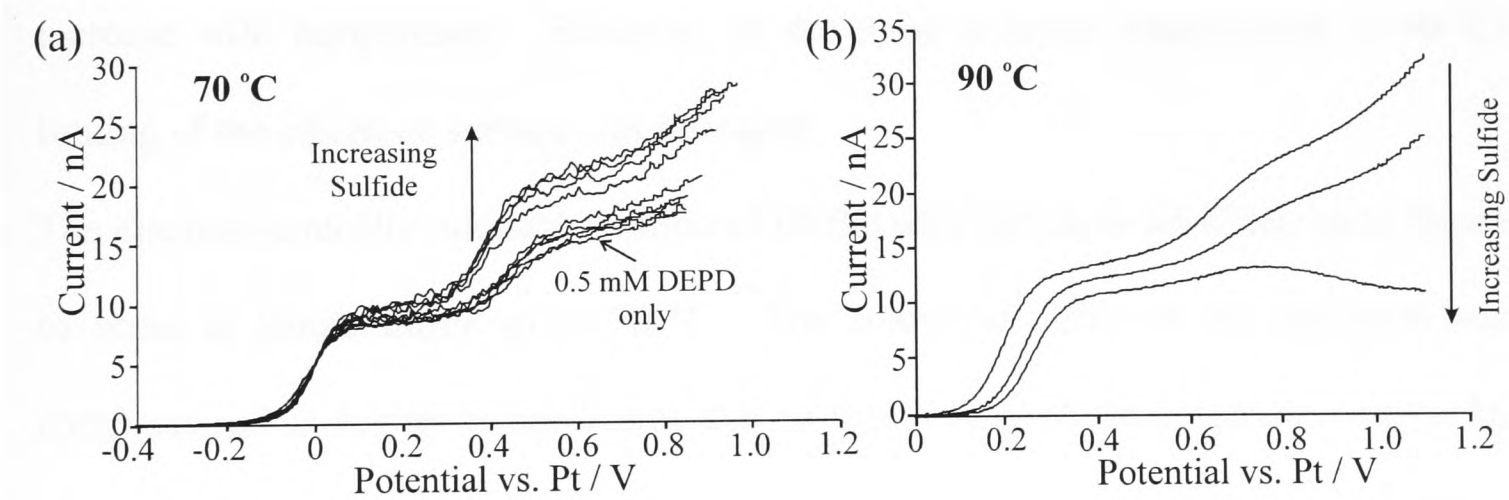


Figure 14.6: Steady state linear sweep voltammograms responses obtained at an 20 μm microdisc for a solution containing 0.5 mM DEPD (0.2 M TBAP) to increasing additions of sulfide (0 to 900 μM) at (a) 70 °C and (b) 90 °C.

As it can be seen from figure 14.6 (a), upon addition of sulfide to the solution at 70 °C an increase in the second limiting current is observed, analogous to that observed previously at room temperatures (Chapter 6). This suggests that the sulfide is attacking the doubly oxidised $DEPD^+$ species, with the resulting adduct being oxidised directly at the electrode surface as detailed in scheme 6.2, Chapter 6. However, as

shown in figure 14.6 (b) at the higher temperatures (90 °C), a 'fall off' in the both limiting currents occurs and this can be attributed to the formation of polymeric or oligomeric species on the electrode surface.

14.4 Conclusion

The electrochemical oxidation of DEPD in DMF has been studied over a wide temperature range from 20 to 130 °C. The resulting steady state linear sweep voltammetric response produces an enhancement in the second limiting current as the temperature is increased and can be attributed to the effects of temperature on the rates of reaction for the previously determined $EC_{rev}ECE$ process (Chapter 5). Computational modelling of the reaction process was carried out by O. V. Klymenko and revealed that the equilibrium process for the proton transfer reaction is an endothermic process. The rate constant for the dimerisation process was also found to increase with temperature. However, at the more extreme temperatures (> 90 °C) fouling of the electrode surface was observed.

The electrochemically initiated reaction of DEPD with sulfide in DMF has been shown to occur at temperatures up to 70 °C. The analytical utility of the approach was compromised at higher temperatures due to the fouling of the electrode surface by adsorbing species. It can be foreseen that these problems of electrode fouling maybe overcome by the use of single shot individually addressable arrays of microelectrodes or by the use of pulse techniques whereby the electrode would be held at oxidising potential for a short period of time thereby minimising the time in which accumulation of the species to the electrode surface can occur.

14.5 Chapter 14 References

[1] G. G. Wildgoose, D. Giovanelli, O. V. Klymenko, N. S. Lawrence, L. Jiang, T. G. J. Jones, R. G. Compton, *Electroanalysis* **2004**, *16*, 337.

[2] W. L. Orr, J. S. Sinninghe Damste, in *Geochemistry of Sulphur in Fossil Fuels, ACS Symposium Serie 429* (Eds: W. L. Orr, C. M. White), American Chemical Society, Washington D.C. **1990**.

[3] A. C. Aplin, M. L. Coleman, in *The Geochemistry of Reservoirs* (Eds: J. M. Cubitt, W. A. England) London **1995**, pp. 303.

[4] R. D. Kane, R. J. Horvath, M. S. Cayard, *Wet H2S cracking of carbon steels and weldments*, NACE International, Houston, **1996**.

[5] M. R. Carlson, W. B. Cawston Obatining PVT data for very sour retrograde condensate gas and volatile oil reservoirs: a multi-disciplinary approach. *SPE Gas Tech. Conf.,*: Calgary, April-May 1996.

[6] O. V. Klymenko, D. Giovanelli, N. S. Lawrence, N. V. Rees, L. Jiang, T. G. J. Jones, R. G. Compton, *Electroanalysis* **2003**, *15*, 949.

[7] D. Giovanelli, N. S. Lawrence, O. V. Klymenko, L. Jiang, T. G. J. Jones, R. G. Compton, *Electroanalysis* **2003**, *15*, 961.

[8] C. M. A. Brett, A. M. O. Brett, *Electrochemistry Principles, Methods and Applications*, Oxord University Press, Oxford, **1993**.

[9] V. M. M. Lobo, *Handbook of Electrolyte Solutions*, Elsevier, Amsterdam, **1989**.

[10] B. A. Coles, M. J. Moorcroft, R. G. Compton, *J. Electroanal. Chem.* **2001**, *513*, 8.

Chapter 15: "Elevated Temperature Electrochemical Studies of Nickel Oxide Modified Nickel (NOMN) Electrodes in Acidic Media in the Presence of Sulfide"

In Chapter 8 we have shown that quantitative measurements of sulfide can be obtained at a nickel oxide modified nickel (NOMN) electrode immersed in acidic solution. In this chapter the effect of temperature (from 25 to 70 °C) on the response of the NOMN electrode to increasing additions of sulfide is examined. The results detailed show that as the temperature is increased the sensitivity towards the determination of sulfide increases. The bulk of experimental work was conducted by Ian Streeter, a summer vacation student in the group jointly supervised by myself, Dr. N. Lawrence and Prof. R. Compton. The findings of this chapter have been published in Electroanalysis [1].

15.1 Introduction

In Chapter 7 and Chapter 8 we have discussed the use of modified nickel electrodes in alkaline and acidic media respectively, as a means of determining hydrogen sulfide. It was shown that sensing of sulfide at a nickel oxide modified nickel (NOMN) electrode in acidic media (Chapter 8, Section 8.1, [2]) provided improved limits of detection and sensitivities than that observed under alkaline media (Chapter 7, [3]). The approach was further developed into the use of nickel modified screen printed carbon (Ni-SPC) electrodes as economical and disposable sensors for sulfide (Chapter 8, Section 8.2, [4]).

This chapter examines the effect of temperature on the response of sulfide at a NOMN electrode in acidic solution. The results detailed herein show how the application of temperature to the system provides improved sensitivity for the determination of sulfide.

15.2 Experimental

Rotating disk analysis was conducted using an Oxford Electrodes motor controller with the three electrode arrangement.

Heating of the cell was carried out using a double wall glass cell thermostatted at the appropriate temperature through the circulation of water from a heated bath.

15.3 Results and Discussion

Initial characterisation was carried out using cyclic voltammetry as means of assessing the effect of temperature on the stability of the nickel oxide layer. Figure 15.1 depicts the initial voltammetric scan of the nickel electrode (= 0.5 cm diameter) when it was first placed in a pH 4 acetate buffer solution at (a) 24 °C, (b) 40 °C, and (c) 70 °C. Also overlaid are the fifth consecutive scan and a voltammogram recorded after the

electrode has been left in solution for one minute.

Analysis of the initial voltammetric response obtained at 24 °C reveals an oxidative wave at +0.30 V, which is followed by a current plateau from +0.30 V to +1.0 V. This is consistent with our previous observations (Chapter 8, section 8.1.3.1) and can be rationalised as follows: the oxidative peak corresponds to the active dissolution of nickel and the oxidative current is probably due to the presence of a protective film formed by oxide species which is known as an active-passive transition state [5-11]. Upon reversal of the first scan no reduction wave is observed indicating that this passive state is retained. Analysis of the fifth voltammetric scan reveals that the passive NiO remains as no electrochemical signal is observed in the potential range studied. Finally it is shown that the NiO layer is stable over time as the voltammetric scan recorded after the electrode was allowed to stand in solution for a period of one minute revealed no appreciable oxidative or reductive waves.

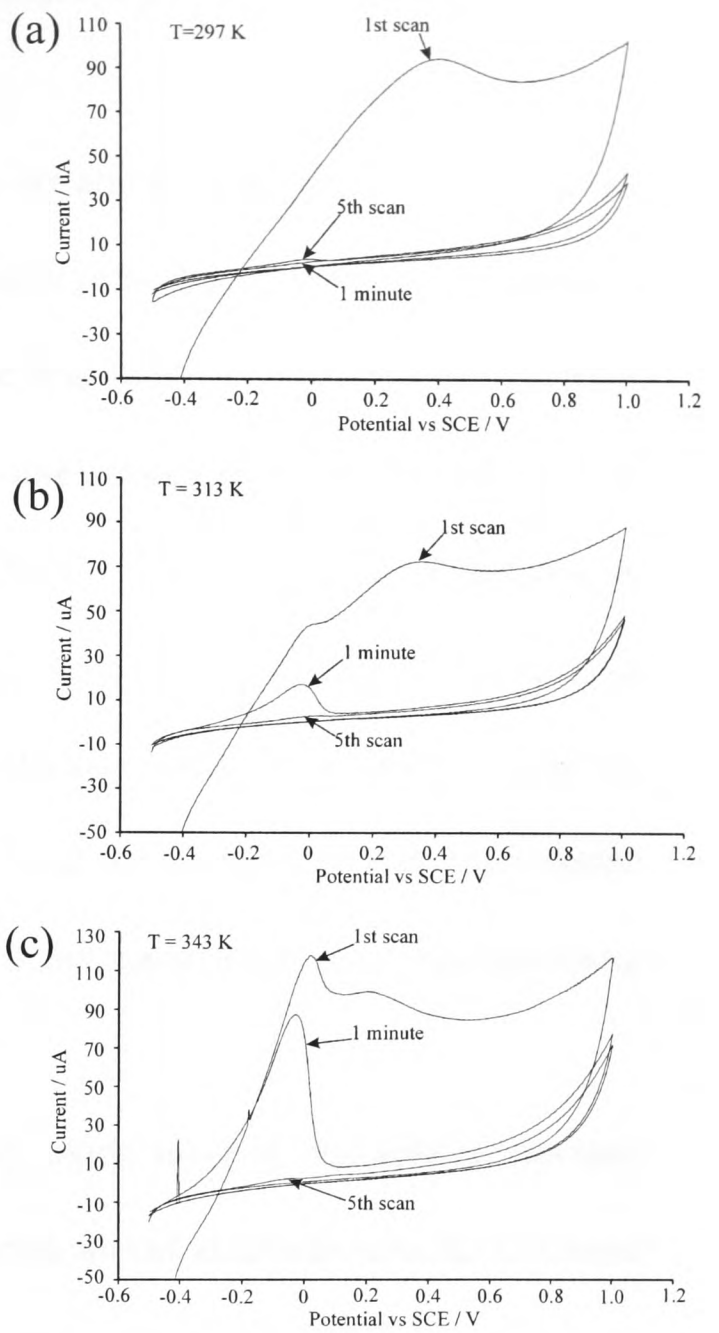


Figure 15.1: Cyclic voltammetric response (100 mV s^{-1}) obtained at a nickel electrode placed in 0.1 M acetate buffer solution (pH 4) at: (a) 24 °C, (b) 40 °C and (c) 70 °C. Detailed are the first and fifth consecutive scan along with a response recorded one minute after the fifth scan in which the electrode stood in the solution during this time.

Figures 15.1 (b) and (c) detail the analogous set of voltammetric scans recorded at 40 and 70 °C respectively. These responses reveal that the initial voltammetric scan produces a broad oxidative wave consistent with that observed at 24 °C. The amount of charge passed during the oxidative scan increases with temperature suggesting that

the rate of Ni dissolution from the electrode surface increases as the temperature is raised.

Once again the fifth consecutive cycle reveals no appreciable voltammetric feature indicating that the NiO layer is stable upon repetitive scanning over the temperature range from 24 to 70 °C. However, analysis of the response obtained after the electrode was allowed to stand in solution for a period of one minute reveals the occurrence of an oxidative process at -0.05 V at both 40 and 70 °C. The occurrence of this feature might be due either to a breakdown in the passivating film or a sharp increase in its rate of dissolution as the temperature rises. An obvious additional explanation for the emergence of the peak at high temperature is that the dissolution and passivation reactions are competitive as would be the case if the passivating film was becoming porous at temperature above 40 °C.

These findings suggest that the protective nickel oxide layer is unstable at elevated temperature. In order to combat this, a rotating disk nickel electrode was next utilised to replenish the nickel oxide layer by continuous potential cycling. First we examined the voltammetric response of 10 repetitive cycles of the nickel rotating disk electrode from 25 to 50 °C while it was being rotated at 20 Hz in order to ensure that no change was observed for the formation of the NiO layer. The corresponding current-potential profiles showed that the first scan produced a broad oxidative wave at +0.30 V consistent with that observed under stationary conditions. The subsequent scans reveal no appreciable voltammetric features occurring in the potential range studied, thereby showing that the nickel oxide layer was stable under these conditions. Similar responses were observed over the entire temperature range studied (25 – 50 °C).

Next the response of the NiO layer to increasing sulfide concentrations was examined. Figure 15.2 (a) details the initial ten voltammetric cycles recorded after the introduction of 10 μM sulfide to the pH 4 acetate buffer solution at 30 °C.

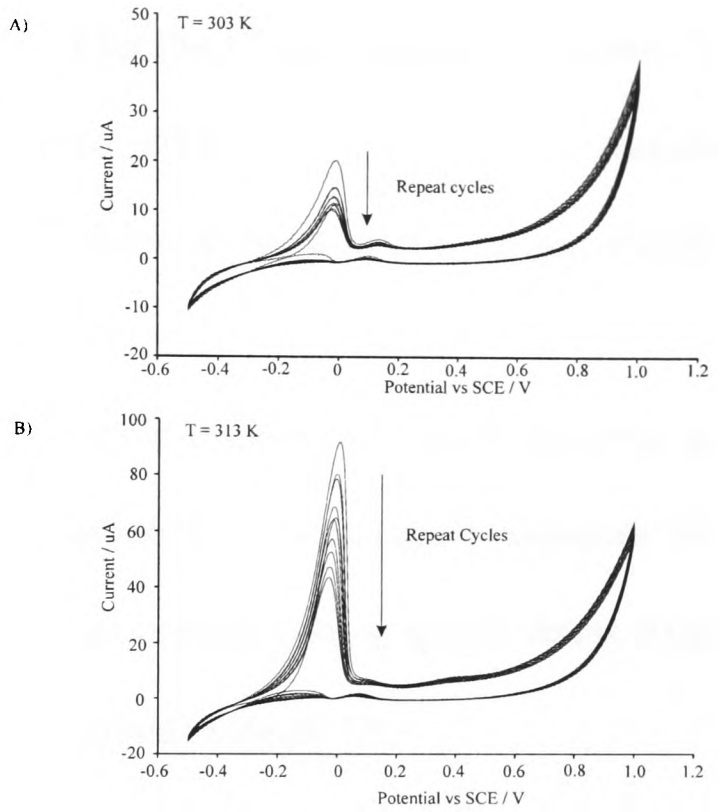


Figure 15.2: Ten consecutive cyclic voltammograms (100 mV s^{-1}) obtained at a nickel electrode placed in 0.1 M acetate buffer solution (pH 4) in the presence of 10 μM sulfide at (a) 30 °C, (b) 40 °C and (c) 70 °C.

This illustrates that upon the addition of sulfide to the solution a large stripping like oxidation wave is observed at -0.01 V along with a smaller oxidation process at +0.1 V. This type of electrochemical behaviour is consistent with our previous observations (Chapter 8) and can be attributed to initial formation of a NiS layer and its subsequent stripping from the electrode surface as discussed in Chapter 8 (scheme 8.1). Upon repetitive cycling the two waves begin to diminish as the NiS layer is stripped from the electrode surface. The corresponding responses obtained at 40 and 70 °C are illustrated in figures 15.2 (b) and 15.2 (c), respectively. Once again the initial response reveals a large oxidation wave at –0.02 V consistent with stripping of the newly formed NiS layer. Upon repetitive scanning the peak current decreases analogous to that observed at 30 °C (figure 15.2 (a)). This 'fall off' was found to be enhanced at these temperatures compared to that observed at 30 °C due to the increased fouling of the electrode surface. Analysis of the oxidative wave shows that both the charge passed and peak currents obtained increase as the temperature rose, which can be attributed to the increased rate of NiS formation at the elevated

temperatures. To avoid problems associated with the fouling of the electrode observed at elevated temperature (i.e., 70 °C) all subsequent studies were carried out at a maximum temperature of 50 °C.

Plots of ln I (where I is the peak oxidative current for the 1st scan) against 1/T (where T is the temperature of the solution) were found to yield a straight line and a pseudo activation energy of 73 kJ mol^{-1} for the surface chemical reaction of hydrogen sulfide with the nickel oxide layer (Scheme 8.1, Chapter 8).

Next the effect of the rotation speed on voltammetric response of the Ni electrode in the presence of sulfide was examined. The corresponding voltammetric responses for a pH 4 acetate solution containing 10 μM sulfide at various rotation speeds (from 10 to 30 Hz) obtained at a scan rate of 80 mV s^{-1} are detailed in figure 15.3.

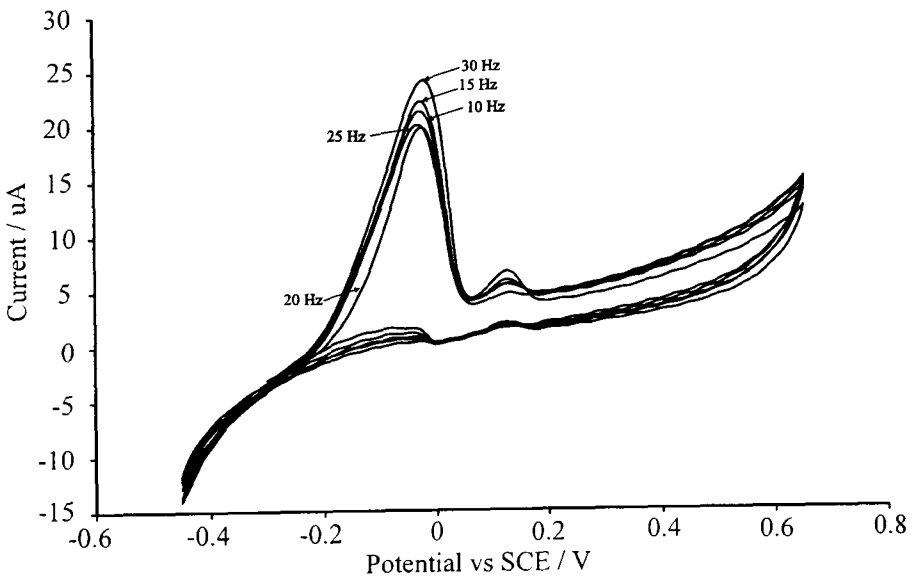


Figure 15.3: The effect of rotation speed (10 to 30 Hz) on the voltammetric response obtained at a passivated NiO layer in the presence of 10 μM sulfide

These reveal the occurrence of oxidative process at –0.01 V consistent with stripping of the NiS layer. However, both the peak current and charge associated with this oxidative wave were found to independent of the rotation speed. This is a significant finding as it suggests that the rotation speed of the electrode does not have to be monitored during the experiment.

In order to assess the viability of the proposed protocol for sensing sulfide at elevated temperatures two strategies were employed. The first examined the response obtained

at a rotating NOMN electrode at 50 °C when sulfide was added consecutively into the solution with no cleaning of the electrode surface between each response. The corresponding voltammetric waves obtained when 1 to 9 μM sulfide was introduced into the cell (pH 4 acetate, 50 °C) are detailed in figure 15.4 (a).

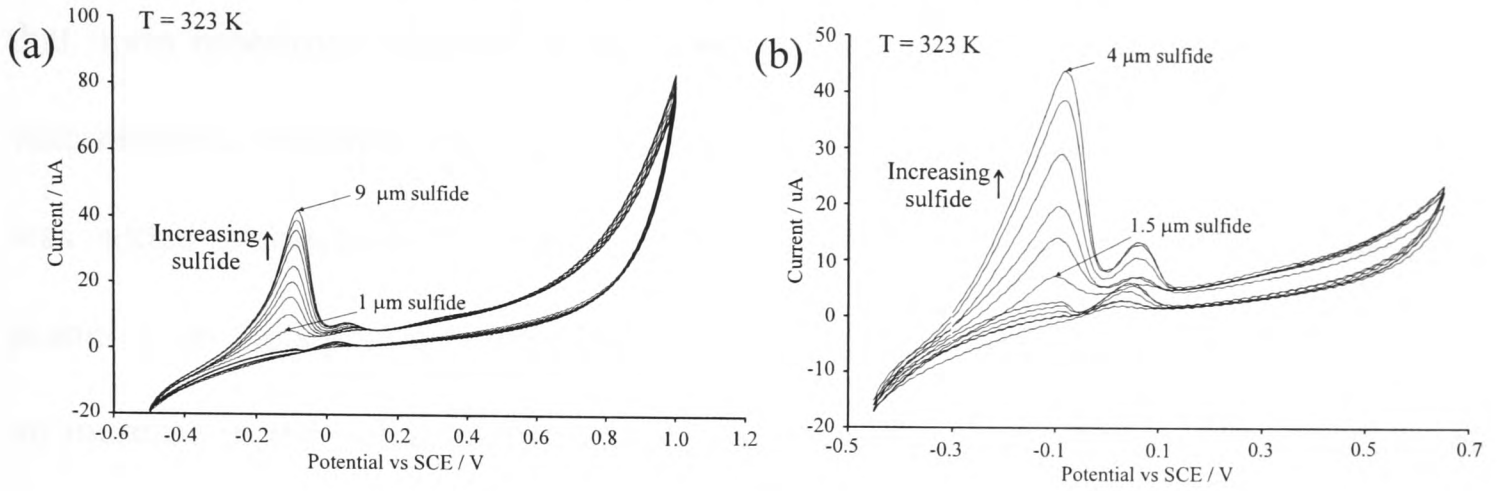


Figure 15.4: Cyclic voltammograms detailing the response of the NiO layer to consecutively increasing additions of sulfide in pH 4 acetate buffer (a) with no cleaning of the electrode surface between each addition of (from 1 to 9 μM sulfide) and (b) with cleaning of the electrode surface and subsequent formation of the NiO layer between each addition of sulfide (from 1.5 to 4μM sulfide)

It can be seen that, as the concentration of sulfide is increased, an enhancement is observed in the oxidative peak current, consistent with that observed previously at room temperature. Analysis of the corresponding standard addition plot produced a linear range from 1 to 9 μM (sensitivity = 4.94 A M^{-1}, r^2 = 0.99) and a limit of detection of 0.47 μM. These results offer an improvement in terms of sensitivity for the determination of sulfide compared to that observed at room temperature (Chapter 8).

The second approach examined the response obtained at a rotating NOMN electrode at 50 °C when sulfide was introduced consecutively into the solution with cleaning of the electrode surface and subsequent formation of the NiO layer between each addition. The corresponding current-potential profiles are detailed in figure 15.4 (b). It can be seen that as the concentration of sulfide is increased an enhancement is observed in the oxidation peak current consistent with further accumulation and stripping of sulfide from the electrode surface. Analysis of the corresponding standard addition plot

produced a linear range from 1.5 to 4 μM (sensitivity = 13.5 A M^{-1}, r^2 = 0.99) and a limit of detection of 1.25 μM. A comparison of the approaches reveals that the second methodology provides a greater sensitivity for the determination of sulfide. This can be rationalised by analysis of the results detailed in figure 15.2. These figures showed that upon repetitive scanning in the presence of a fixed concentration of sulfide the voltammetric response was found to decrease. In the experiments where the sulfide was added consecutively, there will be a coupling between the effect of repetitive scanning on the signal causing a decrease and the introduction of fresh sulfide causing an increase in the voltammetric signal. This coupling compromises the sensitivity of the voltammetric signal compared to the response obtained when a fresh NiO layer was formed prior to the addition.

Finally, this second approach in which a new NiO layer was formed prior to the addition of sulfide was examined over the temperature range from 25 to 50 ^{O}C. This was carried out in order to examine how the analytical parameters were affected by the application of temperature to the system. The corresponding parameters obtained are detailed in table 15.1 and reveal that as the temperature is increased the sensitivity towards the detection of sulfide increases.

Table 15.1: *The effect of temperature on the response of sulfide obtained at a nickel rotating disk electrode (20 Hz) in 0.1 M acetate buffer solution (pH 4).*

Temperature / °C	Linear Range / μM	Sensitivity / A M^{-1}	LoD/ μM
25	4 - 12	3.4	4.0
40	2 - 8	9.1	1.5
50	1.5 - 10	13.5	1.25

15.4 Conclusion

The above results detail the effect of temperature on the analytical determination of sulfide at a NOMN electrode in acidic media (pH 4 acetate buffer). It was found initially that the NiO layer became increasingly unstable as the temperature was

increased. This instability was overcome by repetitive potential scanning of the NiO layer to produce a stable electrochemical signal. It was further shown that upon the introduction of sulfide to the solution a stripping like response was observed over the entire temperature range (25 – 70 °C). The analytical parameters of the methodology were examined and these revealed that raising the temperature of the solution increases the sensitivity for the determination of sulfide. This protocol could foreseeable be used for the determination of low concentrations of sulfide under high temperature conditions, such those to be encountered in the oilfield environment.

15.5 Chapter 14 References

[1] I. Streeter, D. Giovanelli, G. G. Wildgoose, N. S. Lawrence, L. Jiang, T. G. J. Jones, R. G. Compton, *Electroanalysis* **2004**,*16*, 1205.
[2] D. Giovanelli, N. S. Lawrence, L. Jiang, T. G. J. Jones, R. G. Compton, *Analyst* **2003**, *128*, 173.
[3] D. Giovanelli, N. S. Lawrence, L. Jiang, T. G. J. Jones, R. G. Compton, *Sens. and Actuators, B* **2003**, *B88*, 320.
[4] D. Giovanelli, N. S. Lawrence, S. J. Wilkins, L. Jiang, T. G. J. Jones, R. G. Compton, *Talanta* **2003**, *61*, 211.
[5] A. Jouanneau, M. Keddam, M. C. Petit, *Electrochim. Acta* **1976**, *21*, 287.
[6] J. R. Vilche, A. J. Arvia, *Lat. Am. J. Chem. Appl. Chem.* **1979**, *9*, 35.
[7] J. R. Vilche, A. J. Arvia, *Corros. Sci.* **1978**, *18*, 441.
[8] S. G. Real, M. R. Barbosa, J. R. Vilche, A. J. Arvia, *J. Electrochem. Soc.* **1990**, *137*, 1696.
[9] S. G. Real, J. R. Vilche, A. J. Arvia, *Corros. Sci.* **1980**, *20*, 563.
[10] M. R. Barbosa, J. A. Bastos, J. J. Gracia-Jareno, F. Vicente, *Electrochim. Acta* **1998**, *44*, 957.
[11] M. R. Barbosa, S. G. Real, J. R. Vilche, A. J. Arvia, *J. Electrochem. Soc.* **1988**, *135*, 1077.

Appendix 1: Fick's Laws of Diffusion

Outlined below are the derivations of Fick's two laws of diffusion.

A1.1 Fick's First Law of Diffusion

This derivation requires a simple model. Consider a volume of electrolyte solution where the concentration of the diffusing ionic species is constant in the yz-plane but varies in the xy-plane. The cuboid of solution considered is evenly divided into two by a plane (T) of area A (figure A1.1). The diffusion occurs normal to this plane with the outer planes L and R situated at a distance of $\langle x^2 \rangle^{1/2}$ (the mean distance travelled by an ion in a time interval t) from the plane T ensuring that, provided the ions are moving in the specified direction, all the ions in each compartment cross the plane.

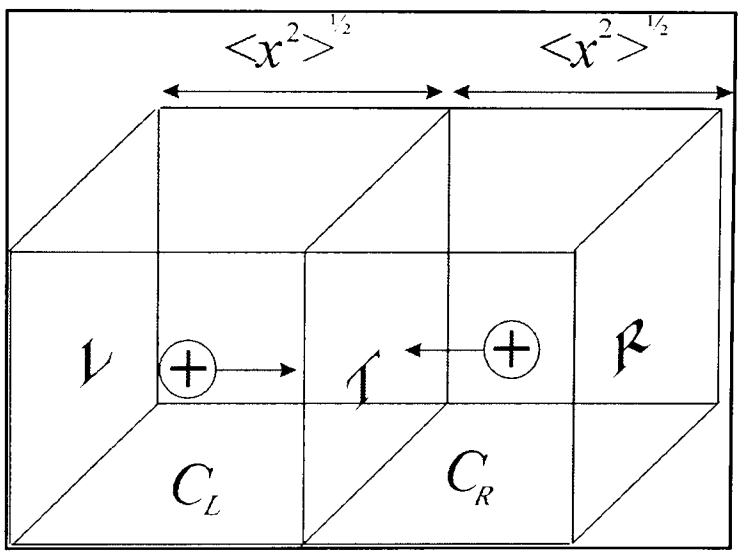


Figure A1.1 Cuboid of solution used to model random walk processes

As the ions are 'random walking', statistically only half the ions will be moving towards the plane T at any given time. Thus in a time interval t,

Number of ions making the L → T crossing is $\frac{1}{2}\left(\sqrt{\langle x^2 \rangle} A C_L\right)$ (A1.1)

Number of ions making the R → T crossing is $\frac{1}{2}\left(\sqrt{\langle x^2 \rangle} A C_R\right)$ (A1.2)

where C_L and C_R are the concentrations of ions in the respective compartments. The total diffusive flux J (mol m^{-2} s^{-1}) of ions across the plane T in the L → R direction is

$$J = \frac{1}{2}\frac{\sqrt{\langle x^2 \rangle}}{t}[C_L - C_R] \quad \text{(A1.3)}$$

The concentration gradient (dc/dx) in the L → R direction can then be written

$$\frac{dc}{dx} = \frac{[C_R - C_L]}{\sqrt{\langle x^2 \rangle}} \equiv -\frac{[C_L - C_R]}{\sqrt{\langle x^2 \rangle}} \tag{A1.4}$$

If the two expressions are then combined the following expression results

$$J = -\frac{1}{2}\frac{\langle x^2 \rangle}{t}\frac{dc}{dx} \tag{A1.5}$$

This is analogous to Fick's first law where

$$D = \frac{\langle x^2 \rangle}{2t} \tag{A1.6}$$

thus

$$\langle x^2 \rangle = 2Dt \tag{A1.7}$$

hence the parameters x and D are related.

A1.2 Fick's Second Law of Diffusion

As for the first law only planar diffusion is considered. Considering a small region of volume Adx and the concentration changes which occur within this region of volume in the time interval t and t + dt,

No. of moles in the region at time t+dt	-	No.moles in the region at time t	=	No. of moles entering across plane at x	- No. of moles leaving across plane at x+dx

or

$$c(x, t + dt)\, A dx - c(x, t)\, A dx = J(x,t)\, A dt - J(x + dx,t)\, A dt \tag{A1.8}$$

where $J(x, t)$ is the flux in the x-direction (mol cm^{-2} s^{-1}) such that

$$[c(x, t + dt) - c(x, t)]\, dx = [J(x,t) - J(x + dx,t)]\, dt \tag{A1.9}$$

when rearranged gives

$$\frac{\partial}{\partial t} c(x,t) + \frac{\partial}{\partial x} J(x,t) = 0 \tag{A1.10}$$

If J(x,t) is substituted for Fick's first law then Fick's second law is obtained

$$\frac{\partial}{\partial t}c(x,t) = D\frac{\partial^2}{\partial x^2}c(x,t) \qquad (A1.11)$$

This shows that from using a simple statistical model the diffusion of molecules can be mathematically expressed in the form of Fick's laws.

Appendix 2: "Chemicals and Suppliers"

Compound	Formula	Supplier
Acetic Acid	CH_3CO_2H	Fisons
Acetonitrile	CH_3CN	Fisher
Acetone	CH_3COCH_3	Fischer
Alumina		Buehler, IL
Ammonia	NH_3	BOC
Ammonium hexafluorophospate	NH_4PF_6	Aldrich
Benzonitrile	C_6H_5CN	Aldrich
Boric Acid	H_3BO_3	Aldrich
Diamond paste		Kemet
Dimethylglyoxime	$C_4H_8N_2O_2$	Aldrich
4, 4-Diethyl-p-phenylenediamine	$NH_2C_6H_4N(C_2H_5)_2$	Aldrich
4, 4-Dimethyl-p-phenylenediamine	$NH_2C_6H_4N(CH_3)_2$	Aldrich
Dimethylsulfoxide	C_2H_6OS	BDH
2,3-Dimethoxy-5-methyl-1,4-benzoquinone	$(H_3CO)_2(H_3C)C_6HO_2$	Lancaster
2,3-Dimethoxy-p-benzoquinone	$HOC_6H_2(CH_3)_2OH$	Lancaster
N,N'-Diphenyl-p-phenylenediamine	$(C_6H_6)NHC_6H_4NH(C_6H_6)$	Aldrich
3,5-Di-tert-butyl-o-benzoquinone	$C_6H_2O_2(C_4H_9)_2$	Lancaster
1-Ethyl-3-methylimidazoliumbis (trifluoromethylsulfonyl)imide	[EMIM]N$(Tf)_2$ (See Chapter 9)	See Chapter 9
Ferrocene	$Fe(C_5H_5)_2$	Aldrich
Hydrogen Chloride	HCl	Aldrich
Hydroquinone	$C_6H_4(OH)_2$	Aldrich
ICN Alumina N-supergrade		(ICN Biomedicals, Germany)
Litium Chloride	LiCl	Aldrich
Hypophosphorous Acid	H_3PO_2	Aldrich
N,N'-Dimethyformamide	C_3H_7NO	Aldrich
Nitrogen	N_2	BOC
p-Benzoquinone	OC_6H_4O	Aldrich
p-Phenylenediamine	$H_2NC_6H_4NH_2$	BDH
Phosphoric Acid	H_3PO_4	Aldrich
Potassium Chloride	KCl	Fluka
Potassium dihydrogen Phosphate	KH_2PO_4	Acros
Potassium ferricyanide (III)	$K_3Fe(CN)_6$	Aldrich
Potassium ferrocyanide (II) trihydrate	$K_2Fe(CN)_6{\cdot}3H_2O$	Aldrich
Potassium monohydrogen Phosphate	K_2HPO_4	Aldrich
Propylcyanide	$CH_3CH_2CH_2CN$	Fisher
Rubidium Chloride	RbCl	Aldrich
Sodium Hydroxide	NaOH	BDH
Sodium Sulfide	$Na_2S{\cdot}9H_2O$	Fisons
Sulfuric Acid	H_2SO_4	Aldrich
Tetrabutylammonium bromide	$(CH_3CH_2CH_2CH_2)_4NBr$	Fluka
Tetrabutylammonium nitrate	$(CH_3CH_2CH_2CH_2)_4NNO_3$	Fluka
Tetrabutylammonium perchlorate	$(CH_3CH_2CH_2CH_2)_4NClO_4$	Fluka
2,3,5,6-tetrachloro-1,4-benzoquinone	$C_6Cl_4O_2$	Aldrich
Tetramethylammonium chloride	$(CH_3)_4NCl$	Fluka

Appendix 3: "The Wilke Chang Relationship"

Diffusion coefficients can be predicted for several organic species in dilute aqueous or organic media using the Wilke-Chang semi-empirical expression [1]:

$$D = 7.4\text{x}10^{-8} \frac{(\chi M)^{1/2} T}{\nu \, V^{0.6}} \qquad \text{(A3.1)}$$

where T is the temperature of the solution in Kelvin, M is the molecular weight of the solvent in g mol^{-1}, χ is the association parameter introduced to define the effective molecular weight of the solvent with respect to the diffusion process (see Table A3.1), ν is the viscosity in cP (= 0.89 cP in the case of water at 25 °C) and V is the molar volume of the solute at the normal boiling point estimated for complex molecules from atomic contributions as defined by La Bas [2] (see Table A3.2 and A3.3). For the systems studied by Wilke and Chang, the average error contained within equation (A3.1) was about 10 %.

Table A3.1: *Association parameter, χ, for different solvents*

Solvent	Association parameter, χ
Water	2.6
Methyl Alcohol	1.9
Ethyl Alcohol	1.5
Benzene	1
Ether	1
Heptane	1

Table A3.2: *Atomic contributions for the calculation of molar volumes as defined by La Bas*

Atom	Atomic Volume / cm^3 mol^{-1}
Carbon	14.8
Hydrogen	3.7
Nitrogen	15.6
Nitrogen in primary amines	10.5
Nitrogen in secondary amines	12.0

Table A3.3: *Volume deductions necessary for cyclic and aromatic structures during calculations of molar volumes as defined by La Bas*

Cyclic / Aromatic Structure	Volume Deduction / $cm^3\ mol^{-1}$
3-membered ring	6.0
4-membered ring	8.5
5-membered ring	11.5
6-membered ring	15.0

A3.1 References

[1] C. R. Wilke, P. Chang, *A.I Ch. E. Journal*, **1955**, *1*, 264.
[2] J. H. Perry, *Chemical Engineers Handbook*, McGraw-Hill Book Company, Inc., **1950**